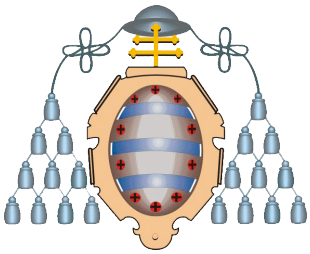

UNIVERSIDAD DE OVIEDO

Departamento de Química Física y Analítica

Programa de Doctorado: Análisis químico, bioquímico y estructural avanzado

(Mención de Calidad)

NEW ANALYTICAL STRATEGIES FOR QUANTITATIVE AND SPATIALLY RESOLVED DIRECT SOLID ANALYSIS BY LA-ICP-MS

DISSERTATION

Ioana Konz

Oviedo, 2014

RESUMEN DEL CONTENIDO DE TESIS DOCTORAL

1.- Título de la Tesis	
Español/Otro Idioma: **Nuevas estrategias analíticas para el análisis cuantitativo y con resolución espacial de sólidos empleando LA-ICP-MS**	Inglés: **New analytical strategies for quantitative and spatially resolved direct solid analysis by LA-ICP-MS**

2.- Autor	
Nombre: **Ioana Konz**	
Programa de Doctorado: **Análisis químico, bioquímico y estructural avanzado. Mención de calidad**	
Órgano responsable: **Universidad de Oviedo**	

RESUMEN (en español)

La ablación láser acoplada a un plasma de acoplamiento inductivo con espectrometría de masas (LA-ICP-MS) se está convirtiendo en una tecnología dominante para el muestreo directo de sólidos en química analítica. La ablación láser se refiere al proceso en el cual una intensa energía suministrada por un pulso láser se utiliza para arrancar una pequeña cantidad de material. Los beneficios del empleo de la ablación láser para la introducción de la muestra en el ICP-MS son múltiples e incluyen la simplificación de la preparación de muestras así como la reducción del riesgo de contaminación e interferencias espectrales debido a la ausencia de disolventes y ácidos utilizados para la digestión de la muestra. Además, el acoplamiento del sistema de ablación láser a un ICP-MS es una herramienta muy prometedora para el análisis directo de cualquier tipo de sólidos con una detección altamente sensible y selectiva proporcionando información elemental e isotópica con resolución espacial en el rango de las micras. Por lo tanto, la técnica LA-ICP-MS puede proporcionar importante información cualitativa y cuantitativa con alta resolución lateral y profundidad en una amplia variedad de aplicaciones.

En este contexto, el objetivo principal de la presente Tesis Doctoral es el **desarrollo de nuevas estrategias analíticas para el análisis cuantitativo y con resolución espacial de sólidos empleando LA-ICP-MS**. Este objectivo general se abordó a través de cuatro objectivos parciales cuyas investigaciones se resumen a continuación:

1. Varios tipos de defectos pueden ocurrir en la producción de vidrios homogéneos y con recubrimientos, poniendo en peligro su función y uso y, por lo tanto, la calidad del producto final. En este capítulo, se llevó a cabo la **caracterización de defectos locales en vidrios recubiertos**, así como la determinación de su posición en el vidrio (es decir, en el substrato de vidrio homogéneo, en la interfase o en las capas del recubrimiento). El objetivo final era poder identificar las posibles fuentes de contaminación en el proceso de producción; aspecto de importancia crucial en el proceso de fabricación de los vidrios, así como en su control de calidad.
2. En el segundo capítulo, se desarrolló un nuevo método de **análisis directo para la cuantificación absoluta de la transferrina del suero humano separada por electroforesis en gel**. La estrategia propuesta combina la GE-LA-ICP-MS con el análisis por dilución isotópica especifica utilizando transferrina saturada isotópicamente enriquecida con ^{57}Fe. Dicha metodología proporciona resultados exactos y precisos con tiempos de análisis significativamente menores a los recogidos en la

bibliografía para otras metodologías. En comparación con los métodos alternativos de cuantificación, no se requieren materiales de referencia ni curvas de calibración. Además, la selección adecuada de la estrategia de ablación láser y la preparación de la muestra resultó ser crucial para asegurar la exactitud y buena precisión de los análisis.

3. Debido a la urgente necesidad en los análisis "*imaging*" empleando LA-ICP-MS por estándares internos fiables y capaces de corregir los efectos de matriz, las variaciones de la masa arrancada y transportada así como las desviaciones instrumentales, en el tercer capítulo se presenta el **desarrollo de una estrategia novedosa de corrección interna** en estudios de "*imaging*". El método se basa en la deposición de una capa fina de oro en la superficie de la muestra a analizar y el uso de la señal de $^{197}Au^{+}$ para la normalización interna. El método propuesto se aplicó al "*imaging*" cualitativo de Mg, Fe y Cu en tejidos oculares embebidos en parafina. El potencial analítico se demostró por la realización de estudios de reproducibilidad usando secciones de ojo humano del mismo donante y con diez ojos diferentes de donantes adultos.

4. Con el fin de realizar análisis por LA-ICP-MS en secciones de tejido congelado, una celda de ablación láser que permita trabajar a bajas temperaturas es esencial para mantener la integridad de las muestras durante todo el tiempo de análisis y, por lo tanto, para obtener una buena resolución lateral y garantizar análisis fiable. En la primera parte de este capítulo, se llevó a cabo **el diseño y la fabricación de una celda de ablación láser refrigerada por un sistema Peltier**. Las características más notables de la celda de ablación son el sistema de refrigeración interno y el termopar sensible que permite la medición de la temperatura directamente en la superficie de la muestra. Además, el evacuado rápido de la celda fue alcanzado por restringir el volumen efectivo de expansión del aerosol generado por el láser y una geometría de entrada y salida de gas cuidadosamente diseñada favoreciendo los flujos laminares del gas de arrastre.

   La segunda parte de este capítulo fue dedicada a la aplicación del método de estandarización interna propuesto en el capítulo 3 y la celda de ablación láser criogénica para la **generación de imagenes elementales cuantitativas en secciones de lente humana**. La cuantificación se realizó por calibración externa utilizando estandares sintéticos de tejido homogenizado ("*matrix-matched tissue standards*"). Los resultados obtenidos por "*imaging*" LA-ICP-MS han sido corroborados mediante el análisis por dilución isotópica-ICP-MS después de la digestión ácida de las muestras (lente humana y cápsulas) como método de referencia.

RESUMEN (en Inglés)

Laser ablation is becoming an important technology for direct solid sampling in analytical chemistry. Laser ablation refers to the process in which an intense burst of energy delivered by a short laser pulse is used to ablate a small amount of material. The most essential and noticeable benefits of laser ablation for sample introduction are the simplification of sample preparation and the reduction of the risk of contamination and spectral interferences due to the absence of solvents and acids used for digestion. Furthermore, the coupling of laser ablation to a mass spectrometer with inductively coupled plasma as ion source is a very promising tool for the direct analysis of solids with a highly sensitive and selective detection enabling the analysis of elemental and isotopic information with spatial resolution in the µm range. Thus, laser ablation inductively coupled plasma mass spectrometry (LA-ICP-MS) can provide important qualitative and quantitative information with high lateral and depth resolution in a wide variety of applications.

In this context, the main objective of the present dissertation is the development of **new analytical strategies for quantitative and spatially resolved direct solid analysis by LA-ICP-MS**. In this general line, different partial objectives have been addressed:

1. Various types of glass defects may occur in the production of homogeneous and coated glasses, endangering their function and usage and, thereby, the quality of the product. In the first chapter, LA-ICP-MS was applied to the **characterization of local defects in coated glasses** as well as their position in the glass sample (i.e., in the homogeneous glass substrate, in the interface or in the layers of the coating), in order to identify potential sources of contamination in the production process; aspect of crucial importance in the manufacturing process as well as in quality control.
2. In the second chapter, a new **direct sampling method for the absolute quantification of human serum transferrin separated by gel electrophoresis** was developed. The proposed species-specific GE-LA-ICP-IDMS strategy using a saturated transferrin isotopically enriched with ^{57}Fe provides accurate and precise results with significantly reduced analysis times compared to those already published. Compared with alternative quantification methods, no calibration curves or standard reference materials are necessary. The appropriate selection of the laser ablation strategy and the sample preparation was found to be crucial to ensure good precision and accuracy.
3. LA-ICP-MS imaging analyses require reliable internal standards able to correct for matrix effects, variations in ablated and transported mass and instrumental drifts. In the third chapter, a **novel internal standard correction strategy** based on the deposition of a thin gold film on the sample surface and the use of the $^{197}Au^{+}$ signal for internal normalization is developed. The proposed approach was applied to elemental bioimaging of Mg, Fe and Cu in eye tissue sections. The analytical performance was demonstrated by reproducibility studies using human eye sections from the same donor and with ten different eyes from adult donors.
4. In order to perform LA-ICP-MS analyses in frozen tissue section, a laser ablation cell that allows working at low temperatures is essential to maintain the integrity of the samples throughout the entire analysis time and thus, to obtain a good lateral resolution and ensure reliable analysis. In the first part of this chapter the **design and assembling of a Peltier-cooled laser ablation cell** was carried out. The most remarkable features of the developed ablation cell are the internal refrigeration system and the sensitive thermocouple which allows the temperature measurement directly on sample surface. Furthermore, reasonable washout times of the chamber was achieved by restricting the effective volume of expansion of the laser-generated aerosol and a carefully designed gas inflow and outflow geometry favoring laminar gas flows.

   The second part of this chapter was devoted to the application of the internal standardization method proposed in chapter 3 and the developed cryogenic laser ablation cell for the **quantitative bioimaging of human lens sections**. Quantification was carried out by external calibration using synthetic matrix-matched tissue standards. The obtained results by imaging LA-ICP-MS have been corroborated by isotope dilution analysis ICP-MS after acid digestion of the human lens and lens capsules as the reference method.

Contents

List of figures **II**

List of tables **XIII**

Glossary **XV**

1 Generic Introduction **1**

2 Objectives/Objectivos **5**

3 Fundamentals **11**

3.1 Inductively coupled plasma mass spectrometry (ICP-MS) 11

3.1.1 Sample introduction system 11

3.1.2 Inductively coupled plasma source 12

3.1.3 The interface region 13

3.1.4 The ion focusing system 14

3.1.5 Mass analyzer 15

3.1.6 The ion detector 18

3.1.7 Interferences in ICP-MS 19

3.2 Laser ablation (LA) 20

3.2.1 Discovery and developments 20

3.2.2 Basic concepts of solid sampling by laser ablation 22

3.2.3 The ablation process and particle generation 23

3.2.4 Aerosol transport 32

3.2.5 Quantification strategies in LA-ICP-MS 37

3.3 Applications of LA-ICP-MS 44

3.3.1 Detection of proteins after gel electrophoretic separation . . . 45

3.3.2 Elemental imaging of biological tissues 57

4 Experimental **68**

4.1 Instrumentation 68

4.2 Procedures 73

5 Results and discussion **79**
5.1 Analysis of local defects in coated glasses 79
5.1.1 Introduction 79
5.1.2 Samples 82
5.1.3 LA-ICP-MS parameters 83
5.1.4 Depth profile analysis by LA-ICP-MS 84
5.2 Analysis of metalloproteins separated by gel electrophoresis: Absolute quantification of human serum transferrin 91
5.2.1 Introduction 91
5.2.2 Samples 99
5.2.3 Optimization of GE-LA-ICP-MS parameters for the analysis of gels 99
5.2.4 External calibration for the quantification of transferrin in human serum samples 110
5.2.5 Isotope dilution analysis for the absolute quantification of transferrin in human serum samples 122
5.3 Qualitative elemental bioimaging in soft tissues: Development of a novel internal standard correction strategy 137
5.3.1 Introduction 137
5.3.2 Samples and selection of region of interest 140
5.3.3 Optimization of LA-ICP-MS parameters for bioimaging of ocular tissue 141
5.3.4 Evaluation of a thin gold film for internal standard correction 150
5.3.5 Application of the gold normalization approach to reproducibility studies 156
5.4 Development of a cryogenic laser ablation cell for quantitative elemental bioimaging in frozen tissues 161
5.4.1 Introduction 161
5.4.2 Development of a Peltier-cooled laser ablation cell 166
5.4.3 Quantitative elemental bioimaging in human eye lens sections 184

6 Conclusions/Conclusiones **195**

7 Suggestions for future research **201**

Bibliography **203**

Appendix **241**

List of Figures

1.1 Selection of common synonyms for "laser ablation" found in earlier literature. 3

3.1 Schematic view of a plasma torch. Adapted from [47] 13
3.2 Schematic illustration of the space charge effect and its impact on the ion beam. 15
3.3 The path of an ion through an electron multiplier tube. 18
3.4 Idealized model for LA-ICP-MS analyses [101]. 22
3.5 Ablated mass *versus* laser fluence: The effect of plasma shielding. . . 25
3.6 Laser-matter interaction during nanosecond pulses (left) and femtosecond pulses (right) [125]. 27
3.7 Particle size distributions (left) and chemical composition (right) determined for nanosecond LA of brass. The last fraction indicated by asterisk acts as a separator for particles >3.5 μm [104]. 28
3.8 Two classes of particles (fibrous and spherical particles) of aerosol particles of the standard reference material NIST 610 collected on a filter membrane [129]. 28
3.9 Particle size distribution in dependence of the carrier gas. Adapted from [90] 29
3.10 Particle formation by hydrodynamic sputtering due to Kelvin-Helmholtz-instabilities [103]. 31
3.11 Theoretical transport loss of particles in a horizontal tube (length 1 m, inner diameter 4 mm) with argon and helium as transport gases (flow rate 1 L min^{-1}) in dependence on particle diameter [101]. 33
3.12 Simulation of the velocity field built up inside a cylindrical ablation cell (radius 22.5 mm, height 20 mm) equipped with inlet nozzles of 2.0 mm diameter assuming a helium flow rate of 1.0 L min^{-1} [142]. . . . 35
3.13 Schematic view of an ablation cell with sampling tube for fast aerosol transport. Adapted from [137] 36
3.14 Classification of calibration methods used in LA-ICP-MS 38

3.15 ^{195}Pt profiles obtained by LA-ICP-MS from the analysis of a Pt-enriched blood serum sample using native and denaturing PAGE [235]. 50
3.16 Schematic diagram with mass spectrometric techniques used for protein analysis in 2D gels of Alzheimer's disease brain proteins, including transient signals obtained by LA-ICP-MS for $^{56}Fe^{+}$ in selected proteins spots and blank [223]. 53
3.17 Scheme of a laser ablation sampling from a microarray with multiple analytes on each spot, and transient signals of mixing element-tagged antibodies obtained by LA-ICP-MS from spots of dried droplets on a glass slide: Eu^{3+}-labeled anti-AFP, Sm^{3+}-labeled anti-PSA (prostate-specific antigen) and colloidal Au-labeled GAH (goat-anti-human IgG) [241]. 56
3.18 Light micrographs and LA-ICP-MS images obtained for $^{232}Th^{+}$, $^{238}U^{+}$ and $^{239}Pu^{+}$ in paratracheal lymph node (A) and lung tissue (B) from an occupationally exposed person [246]. 59
3.19 Quantitative metal images of Cu, Zn, Fe and Mn representative for each group (control, 2 h, 7 days and 28 days after the last of five daily MPTP injections) [254]. 60
3.20 Intensity ratio of $^{195}Pt^{+}/^{34}S^{+}$ along a hair strand obtained by LA-ICP-MS from a patient treated with four 100 mg doses of cisplatin [283]. . 64

4.1 Scheme of the laser ablation system used in this study. 68
4.2 Dependence of the laser fluence from the spot size. 70
4.3 Scheme of the Thermo Element 2 ICP-MS instrument used in this study. 71
4.4 Workflow of the preparation of matrix-matched laboratory standards used for quantification of images obtained by LA-ICP-MS. 77

5.1 Schematic two-dimensional illustration of the atomic arrangement in (A) crystal and (B) glass. 79
5.2 Step-by-step manufacturing of float glass [297, 298]. 81
5.3 Schematic composition of the nanoscale layers of the analyzed glasses. 82
5.4 Selected glass samples for LA-ICP-MS analyses. Local defects are marked with a circle. 82
5.5 LA-ICP-MS signals of $^{24}Mg^{+}$, $^{31}P^{+}$, $^{32}S^{+}$, $^{35}Cl^{+}$ and $^{44}Ca^{+}$ for a coated glass without defects (blank analysis). 84
5.6 Crater shape obtained by profilometer for the coated glass without defect after LA-ICP-MS analysis. 85

5.7 LA-ICP-MS signals of $^{24}Mg^+$, $^{31}P^+$, $^{32}S^+$, $^{35}Cl^+$ and $^{44}Ca^+$ for the analysis of the coated glass 1 with local defect. 86

5.8 Optical microscope images of a local defect in the coated glass 1 before (A) and after (B) LA-ICP-MS analysis, SEM image inside the crater after ablation of the defect (C) and resulting crater profile by profilometry (D). 87

5.9 LA-ICP-MS signals of $^{24}Mg^+$, $^{31}P^+$, $^{32}S^+$, $^{35}Cl^+$ and $^{44}Ca^+$ for the analysis of the coated glass 2 with local defect. 88

5.10 Optical microscope images of a local defect in the coated glass 2 before (A) and after (B) LA-ICP-MS analysis, SEM image inside the crater after ablation of the defect (C) and resulting crater profile by profilometry (D). 89

5.11 Optical microscope images of two local defects (A and B) in the coated glass 3 before LA-ICP-MS analysis. 89

5.12 LA-ICP-MS signals of $^{24}Mg^+$, $^{31}P^+$, $^{32}S^+$, $^{35}Cl^+$ and $^{44}Ca^+$ for the analysis of the coated glass 3 with local defect. 90

5.13 Periodic table of elements. Chemical elements important for the human are highlighted in color [311]. 91

5.14 Hyphenated techniques for speciation analysis 94

5.15 Structure of the N-terminal part of human transferrin. The iron-binding site is highlighted in red. 98

5.16 Workflow for the optimization of experimental parameters for the analysis of gels. 99

5.17 Analysis of free ^{56}Fe after treatment of Tf with SDS, SDS and DTT and without any treatment. 101

5.18 Optimization of sample dilution and %T of the resolving gel under denaturing conditions (SDS-PAGE) using human serum samples. . . . 103

5.19 Optimization of %T of the resolving gel under native conditions using human serum samples. 104

5.20 Influence of the gel drying method on the LA-ICP-MS signal. 105

5.21 Experimental set-up for (A) dry plasma conditions: direct introduction of the laser generated aerosol and (B) wet plasma conditions: mixing of the laser-generated aerosol with a nebulized solution using a glass Y-piece. 106

5.22 Dependence of the net signal intensity from the laser energy using a pulse repetition rate of 20 Hz, a scan speed of 45 μm s^{-1} and a spot size of 200 μm (all signals are gas blank corrected). 107

5.23 Dependence of the signal intensity from the pulse repetition rate using a laser energy of 100%, a scan speed of 45 μm s^{-1} and a spot size of 200 μm (all signals are gas blank corrected). 108

5.24 Dependence of the signal intensity from the spot size using a laser energy of 100%, a pulse repetition rate of 20 Hz and a scan speed of 45 μm s^{-1} (all signals are gas blank corrected). 109

5.25 Dependence of the signal intensity from the scan speed using a laser energy of 100%, a pulse repetition rate of 20 Hz and a spot size of 200 μm (all signals are gas blank corrected). 109

5.26 Example of a gel used for calibration (left) and obtained ^{32}S and ^{56}Fe profiles by LA-ICP-MS (right). 110

5.27 (A) ^{1}H- and (B) ^{13}C-NMR spectra of the reaction product (*E*)-3-iodoacrylamide. 113

5.28 Calibration curves for $^{56}Fe^{+}$ (left) and $^{32}S^{+}$ (right) obtained for gels dried with glycerol in dry plasma conditions for different transferrin concentrations (all values are gas blank corrected). 114

5.29 Calibration curves for $^{56}Fe^{+}$ (left) and $^{32}S^{+}$ (right) obtained for gels dried without glycerol in dry plasma conditions for different transferrin concentrations (all values are gas blank corrected). 114

5.30 Calibration curves for $^{56}Fe^{+}$ (left) and $^{32}S^{+}$ (right) obtained for gels dried with glycerol in wet plasma conditions for different transferrin concentrations (all values are gas blank corrected). 115

5.31 Calibration curves for $^{56}Fe^{+}$ (left) and $^{32}S^{+}$ (right) obtained for gels dried without glycerol in wet plasma conditions for different transferrin concentrations (all values are gas blank corrected). 116

5.32 Overview of the different ablation strategies. 116

5.33 Calibration curves for $^{56}Fe^{+}$ applying single line (left) and multiple line ablation strategy (right). All values are gas blank and IS (^{13}C) corrected. 117

5.34 Native 1D-PAGE of natural saturated Tf and detection of ^{56}Fe by LA-ICP-MS. (A) Ablation of the protein spot horizontally to migration direction and (B) ablation of the protein spot perpendicular to migration direction. 118

5.35 Calibration curve for $^{56}Fe^{+}$ and $^{32}S^{+}$ applying the single line ablation strategy perpendicular to the migration direction using unstained gels. All values are gas blank and IS (^{13}C) corrected. 119

5.36 Electropherogram of ^{56}Fe obtained after native 1D-PAGE of a certified human serum sample. 120

5.37 Saturation of apo-transferrin with $^{56}FeCl_3$ at different concentrations and incubation times. 123

5.38 Recovery of Fe (in the form of Fe-citrate) after ultrafiltration of Fe-citrate solutions with different Fe-to-citrate ratios through membrane filters with a molecular cut-off of 10 kDa. 127

5.39 Saturation of apo-transferrin with ^{56}Fe-citrate at different concentrations and incubation times. 128

5.40 Stability of saturated and filtrated apo-transferrin standard over a period of four weeks (stored at 4°C). 130

5.41 Stability of saturated apo-transferrin standard at two different incubation temperatures after four weeks under different storage conditions. 130

5.42 Native gel after staining with Coomassie Blue (2 μg Tf). Left lane - isotopically enriched ^{57}Fe-Tf; Right lane - natural abundance Tf. . . . 132

5.43 Profiles obtained by LA-ICP-MS for ^{56}Fe, ^{57}Fe and their isotopic ratio using a mixture of the CRM and the isotopically enriched ^{57}Fe-Tf (13 μg ^{nat}Fe-Tf:14 μg ^{57}Fe-Tf). 133

5.44 Uncertainty budgets obtained for representative analysis of CRM by A) species-specific isotope dilution analysis using the linear regression slope data treatment and B) external calibration. 136

5.45 Schematic diagram of the human eye [347]. 139

5.46 A) Graphical representation of the structures of the anterior chamber of the eye [359]. B) Histology of the anterior chamber of the eye [360] 140

5.47 Workflow for the optimization of experimental parameters for bioimaging in ocular tissues. 141

5.48 LA-ICP-MS analysis of 10 μm thick section. A) Histological image obtained after laser ablation analysis, B) 3D-image of the analyzed area by CLSM, crater profiles obtained C) across and D) along ablated line. 144

5.49 LA-ICP-MS analysis of 25 μm thick section. A) Histological image obtained after laser ablation analysis, B) 3D-image of the analyzed area by CLSM, crater profiles obtained C) across and D) along ablated line. 145
5.50 LA-ICP-MS analysis of 160 μm thick section. A) Histological image obtained after laser ablation analysis, B) 3D-image of the analyzed area by CLSM, crater profiles obtained C) across and D) along ablated line. 146
5.51 Graphical representation of the penetration depth *versus* tissue section thickness. Standard deviation values were calculated from the mean of three independent measurements. 146
5.52 Dependence of the $^{56}Fe^{+}$ signal response (integrated profile area) from the laser energy using a pulse repetition rate of 20 Hz, a scan speed of 5 μm s^{-1} and a spot size of 10 μm (all signals are gas blank corrected). 148
5.53 Dependence of the $^{56}Fe^{+}$ signal response (integrated profile area) from the pulse repetition rate using a laser energy of 100%, a scan speed of 5 μm s^{-1} and a spot size of 10 μm (all signals are gas blank corrected). 148
5.54 Graphical representation of the dependence of the lateral resolution from the scan speed, maintaining laser energy, pulse repetition rate, spot size and ICP-MS acquisition times constant. 149
5.55 The effect of varying the laser scan speed on image dimensions [293]. 150
5.56 A) Histological image of the anterior segment in a paraffin-embedded human eye tissue section, analyzed by LA-ICP-MS, showing the different structures of ophthalmological interest. B) Elemental distribution of $^{24}Mg^{+}$, $^{56}Fe^{+}$ and $^{63}Cu^{+}$ in the tissue section measured by LA-ICP-MS without internal standard correction (left), with $^{13}C^{+}$ (middle) and $^{197}Au^{+}$ (right) as IS. 152
5.57 Histological images of the analyzed zones in the ocular tissue sections (left) and corresponding elemental distribution of $^{13}C^{+}$ and $^{197}Au^{+}$ obtained by LA-ICP-MS. A) Sample with the thin Au layer deposited on the top of the tissue section. B) Sample with the thin Au layer deposited directly on the glass substrate (below the tissue section). . 153
5.58 3D pictures of the imaging area in ocular tissue sections (thickness 15 μm) after laser ablation analysis obtained by CLSM. A) without Au coating and B) with thin Au film deposited on sample surface. The histological images (left upper corner, respectively) show the analyzed area before laser ablation analysis. 154

5.59 SEM images of the collected aerosol particles produced in different ocular structures. These images show the different kinds of transported particles observed but are not representative of the total transported mass. A) iris, B) ciliary body, C) cornea and D) paraffin. 155
5.60 Elemental distribution of $^{24}Mg^+$, $^{56}Fe^+$ and $^{63}Cu^+$ in three adjacent ocular tissue sections of the same donor measured by LA-ICP-MS without internal standard correction (blank corrected signals) and using $^{197}Au^+$ as IS (upper and lower row, respectively). 157
5.61 Elemental distribution of $^{24}Mg^+$, $^{56}Fe^+$ and $^{63}Cu^+$ in human eye sections of three normal donors measured by LA-ICP-MS with corrected signal intensities using $^{197}Au^+$ as IS. 158
5.62 Schematics of the cryogenically cooled ablation cells proposed by the working groups of Feldmann (A), Becker (B) and Müller (C) [152, 365, 366]. 162
5.63 Schemes of the sample preparation and quantification processes used in two novel calibration strategies for the quantitative elemental imaging of biological tissues by LA-ICP-MS. (A) Internal standard scheme for elemental imaging and workflow of the quantification process with film standards. (B) Preparation of frozen matrix-matched standards [150, 370]. 164
5.64 Gas flow models showing gas velocities (m s^{-1}) at the ablation area using Ansys CFX 11.0. A) single, circular gas in- and outflow, B) single, circular gas inflow and funnel-shaped gas outflow and C) four side-by-side, circular gas inflows and funnel-shaped gas outflow. . . . 168
5.65 Internal refrigeration system of the developed ablation cell. 169
5.66 Hardware set-up of the refrigeration system (internal and external). . 170
5.67 Temperature diagram of a cooling cycle to a pre-determined sample temperature of -20°C in a long-time test (17h). The first 40 minutes are zoomed-in in the inset. 171
5.68 Zoom of signal rise and decay at -20°C of $^{59}Co^+$, $^{107}Ag^+$, $^{137}Ba^+$, $^{232}Th^+$ and $^{238}U^+$ for the calculation of the washout times (signal decay to background level). 172
5.69 Comparison of the aerosol washout of $^{59}Co^+$, $^{107}Ag^+$, $^{137}Ba^+$, $^{232}Th^+$ and $^{238}U^+$ after 90 s of laser ablation at room temperature (20°C) (black columns) and -20°C (gray columns). RSD of 10 different analyses is represented by error bars. 174

5.70 LA-ICP-MS profile obtained for $^{59}Co^{+}$, $^{139}La^{+}$, $^{232}Th^{+}$ and $^{238}U^{+}$ in a long-term stability test using the ablation cell at room temperature. Selected area (dashed line) was used for calculation of TRSD. 175

5.71 Raw intensities of $^{59}Co^{+}$ (lower signal intensity) and $^{238}U^{+}$ (higher signal intensity) in dependence of the analysis temperature (20°C black line and -20°C gray line) obtained for LA-ICP-MS analysis of glass SRM NIST 612. 175

5.72 Detailed schematic view of the developed Peltier-cooled laser ablation cell showing the main components, such as (1) removable lid with single, circular gas inflow and funnel-shaped gas outflow, (2) specially coated quartz crystal transparent for the employed laser wavelength, (3) cell base containing the internal refrigeration system, (4) sample, (5) temperature sensor, (6) sample substrate, (7) cooling plate, (8) insulating plate, (9) Peltier elements, (10) cooling coil and (11) connections for the circulating refrigerant fluid. 177

5.73 Instrumental set-up of the LA-ICP-MS system including the developed Peltier-cooled laser ablation cell. 178

5.74 Restriction of the visibility of the sample due to condensation of water vapor on the window incorporated in the cell base during a period of 10 min. 179

5.75 A) Modification of the ablation cell by installation of a series of consecutive closed air chambers in the cell base. B) Images taken of the sample by the CCD camera of the laser system showing a constant translucence of the window incorporated in the cell base. 179

5.76 A) Condensation of water vapor on the coated quartz crystal in the removable lid after 50 min. B) Constant air flow above the ablation cell led to the elimination and prevention of the condensation process for at least 24 h. 180

5.77 Histological images of frozen tissue sections of an anterior segment of the porcine eye and elemental images obtained by LA-ICP-MS for $^{56}Fe^{+}$, $^{63}Cu^{+}$ and $^{64}Zn^{+}$ at A) 20°C and B) -20°C. 182

5.78 Microscope images of fresh leaves from *Solanum lycopersicum* and elemental images obtained by LA-ICP-MS for $^{63}Cu^{+}$ and $^{127}I^{+}$ at A) 20°C and B) -5°C. 183

5.79 Schematic diagram of a cross-section of the mammalian lens. 185

5.80 Depth profiles obtained for $^{56}Fe^{+}$, $^{63}Cu^{+}$ and $^{64}Zn^{+}$ in freshly dissected bovine lens by LA-ICP-MS: lens analyzed in the anterior pole with the capsule (red line/arrow), in the anterior pole without the capsule and the epithelial cell layer (black line/arrow) and on the posterior pole of the lens (blue line/arrow). 187
5.81 Elemental distribution obtained for $^{56}Fe^{+}$, $^{63}Cu^{+}$ and $^{64}Zn^{+}$ in a thin section of a matrix-matched tissue standard by LA-ICP-MS. 189
5.82 Calibration curves obtained for $^{56}Fe^{+}$, $^{63}Cu^{+}$ and $^{64}Zn^{+}$ ($^{197}Au^{+}$ as internal standard) by LA-ICP-MS using three matrix-matched laboratory standards of human eye lens homogenates. Standard deviation values are calculated from the mean of ten independent analyses. . . . 190
5.83 Microscope image of the analyzed human lens section (up left) and reconstructed elemental images for $^{56}Fe^{+}$, $^{63}Cu^{+}$ and $^{64}Zn^{+}$ after internal standard correction with $^{197}Au^{+}$. 191

List of Tables

1.1 The basic laser analytical processes in atomic spectroscopy 2

3.1 Figures of merit of ICP-MS and LA-ICP-MS in material science [82]. 21
3.2 Summary of relevant parameters and their effect in LA-ICP-MS [16]. 23
3.3 Selected applications of GE-LA-ICP-MS. 47
3.4 Selected applications of 2D mapping of hard biological samples by LA-ICP-MS. 62

4.1 Protocols for gel preparation. 74

5.1 Optimized parameters used for the analysis of glasses by LA-ICP-MS. 83
5.2 Phosphorus, sulfur and chlorine isotopes, corresponding interferences and required resolution. 84
5.3 Optimized parameters used for the analysis of gels by LA-ICP-MS. . 100
5.4 Electrophoretically separable protein fractions in human serum. . . . 102
5.5 Comparison of different ablation strategies and sample preparation procedures for Tf quantification. 121
5.6 Summary of the quantitative results of the different transferrin saturation methods using $FeCl_3$. 125
5.7 Summary of the quantitative results of the different transferrin saturation methods using Fe-citrate. 128
5.8 Determination of Tf concentrations in a serum reference material and human serum samples by species-specific GE-LA-ICP-IDMS using three different data treatment approaches[a]. 135
5.9 Optimized parameters used for the analysis of paraffin-embedded ocular tissue samples by LA-ICP-MS. 142
5.10 Optimized parameters used for optimization and evaluation of the developed Peltier-cooled laser ablation cell by LA-ICP-MS. 173
5.11 Precision and accuracy obtained for silver, barium and lead isotope ratio measurements at two analysis temperatures using the glass SRM NIST 612. 176

5.12 Instrumental procedure of the developed Peltier-cooled laser ablation cell 181
5.13 Optimized parameters used for the analysis of frozen ocular tissue samples by LA-ICP-MS. 186
5.14 Approximate and determined concentrations of $^{56}Fe^{+}$, $^{63}Cu^{+}$ and $^{64}Zn^{+}$ in the homogenized tissue standards. 189
5.15 Comparison of Fe, Cu and Zn concentrations in human lens without capsule (nuclear and cortical) and lens capsule obtained by LA-ICP-MS and IDA-ICP-MS. LA-ICP-MS concentrations correspond to the estimated average value from *figure 5.81*. IDA-ICP-MS uncertainties show result from standard deviations of the mean of five independent analyses of five individuals. 193

7.1 List of reagents used throughout this work. 241

Glossary

AC	Affinity Chromatography
ACN	Acetonitrile
AcOH	Acetic Acid
AFP	α-Fetoprotein Protein
APS	Ammonium Persulfate
BN	Blue Native
BSA	Bovine Serum Albumin
CEA	Carcinoembryonic Antigen
CEC	Capillary Electrochromatography
CLSM	Confocal Laser Scanning Microscopy
CZE	Capillary Zone Electrophoresis
DOTA	1,4,7,10-Tetraazacyclododecane-1,4,7,10-Tetraacetic Acid
DTT	Dithiothreitol
EMC	Extracellular Matrix
EMT	Electron Multiplier Tube
EPMA	Electron Probe Microanalysis
ESI	Electrospray Ionization
FFPE	Formalin-Fixed Paraffin-Embedded
FT-ICR	Fourier Transform Ion Cyclotron Resonance
GAH	Goat-Anti-Human IgG
GE	Gel Electrophoresis
HCL	Hollow Cathode Lamp

HDL	High Density Lipoprotein
HPLC	High Performance Liquid Chromatography
HR	High Resolution
HSA	Human Serum Albumin
ICP-AES	Inductively Coupled Plasma Atomic Emission Spectrometry
ICP-MS	Inductively Coupled Plasma Mass Spectrometry
IDA	Isotope Dilution Analysis
IDMS	Isotope Dilution Mass Spectrometry
IEF	Isoelectric Focusing
IEX	Ion Exchange Chromatography
IgG	Immunoglobuline G
IR	Isotope Ratio
IS	Internal Standard
LA	Laser Ablation
LA-ICP-MS	Laser Ablation Inductively Plasma Mass Spectrometry
LA-ICP-OES	Laser Ablation Inductively Plasma Optical Emission Spectroscopy
LAPIS	Laser Photoionization Spectroscopy
LAPIS	Thermal Lens Spectroscopy
LAS	Laser Absorption Spectroscopy
LASER	Light Amplification by Stimulated Emission of Radiation
LDL	Low Density Lipoprotein
LIBS	Laser Induced Breakdown Spectroscopy
LIF	Laser Induced Fluorescence
LIMS	Laser Ionization Mass Spectrometry
MALDI	Matrix Assisted Laser Desorption Ionization
MC	Multicollector
MEKC	Micellar Electrokinetic Chromatography
NMR	Nuclear Magnetic Resonance Spectroscopy

PAGE	Polyacrylamide Gel Electrophoresis
pHMB	p-Hydroxymercuribenzoic Acid
PSA	Prostate-Specific Antigen
PTS	Photothermal Lens Spectroscopy
PVDF	Polyvinyl Difluoride
Py	Pyridine
R	Resolution
ROI	Region Of Interest
RP	Reversed Phase Chromatography
RSD	Relative Standard Deviation
RT	Room Temperature
SD	Standard Deviation
SDS	Sodium Dodecyl Sulfate
SEC	Size Exclusion Chromatography
SEM	Scanning Electron Microscopy
SF	Sector Field
SOD	Superoxide Dismutase
TEMED	Tetramethylethylenediamine
TOF	Time-of-Flight
TRSD	Temporal Relative Standard Deviation
XRF	X-Ray Fluorescence

1 Generic Introduction

> *"It is still a matter of wonder how the Martians are able to slay men so swiftly and so silently. Many think that in some way they are able to generate an intense heat in a chamber of practically absolute non-conductivity. This intense heat they project in a parallel beam against any object they choose, by means of a polished parabolic mirror of unknown composition, much as the parabolic mirror of a lighthouse projects a beam of light. But no one has absolutely proved these details. However it is done, it is certain that a beam of heat is the essence of the matter. Heat, and invisible, instead of visible, light. Whatever is combustible flashes into flame at its touch, lead runs like water, it softens iron, cracks and melts glass, and when it falls upon water, incontinently that explodes into steam."*
>
> H. G. Wells, *The War of the Worlds* (1898) [1]

This quote is taken from the famous science-fiction classic "The war of the worlds" published over 100 years ago by the British author Herbert George Wells and is probably the first description of what nowadays is employed, fortunately with peaceable intentions, in most areas of science: the laser, which is an acronym for Light Amplification by Stimulated Emission of Radiation. At that times Wells - a graduated natural scientist with honors - already formulated some of the characteristic properties of laser light, as well as their influence on matter, but only in the year 1960 Maiman developed the ruby laser as the first working laser system [2].

In the following years, the theoretical fundamentals of laser-matter interaction have been examined [3] and first analytical applications have been described. These were documented under the name "laser microprobe analysis" and based on the measurement of emission spectra [4, 5]. The first mass spectrometric hyphenation was realized in 1963 by Honig and Woolston for the analysis of a variety of solid inorganic compounds [6]. The great amount of books and publications about developments of either new laser sources or new analytical techniques, based upon some of the peculiar properties of laser light, as well as their applications published to date are an impressive evidence of the scientific importance of this field.

In the area of analytical chemistry, the developments made in laser technology opened up new possibilities, both by improvements of traditional analytical processes (absorption and fluorescence) and by introduction of new analytical techniques, such as laser photoionization spectroscopy (LAPIS) and photothermal lens spectroscopy (PTS or TLS). The laser analytical techniques can be classified on the basis of the physical process caused by interaction of laser radiation with matter. An overview of these processes is collected in *table 1.1*.

Table 1.1: The basic laser analytical processes in atomic spectroscopy

Process	**Description**	**Technique**
Absorption	Use of lasers as primary sources for atomic absorption measurements, e.g., as hollow cathode lamps (HCLs).	LAS
Emission	Use of lasers tightly focused on a solid, liquid or gaseous sample (target) to create a plasma from which atomic and ionic emission of the target constituents is measured.	LIBS
Fluorescence	Use of lasers as excitation sources to pump atoms into selected excited states from which radiative de-excitation is measured.	LIF
Ionization	Use of lasers to pump atoms in highly excited levels from which collisional ionization occurs or to photoionize selectively the atoms. The charges formed are measured (e.g., in flames) or the ions formed are introduced into a time-of-flight mass spectrometry.	LIMS
Ablation	Use of lasers as a sampling device to generate atoms, molecules and particles from a target sample, which are transported into an excitation source, e.g., a plasma.	LA-ICP-MS/OES

Among the techniques reported in *table 1.1*, in the past years a trend can be recognized towards ablation techniques, in particular with mass spectrometric detection. However, the term "laser ablation" was not always consistently used, particularly in older publications, as the same process was described by a wide variety of synonyms (see *figure 1.1*). Only from the mid-80's, the removal of material from a solid or liquid surface by radiation with a high-energy laser was consistently referred to as laser ablation.

In 1985 Gray [7] presented, as the first, laser ablation hyphenated to inductively

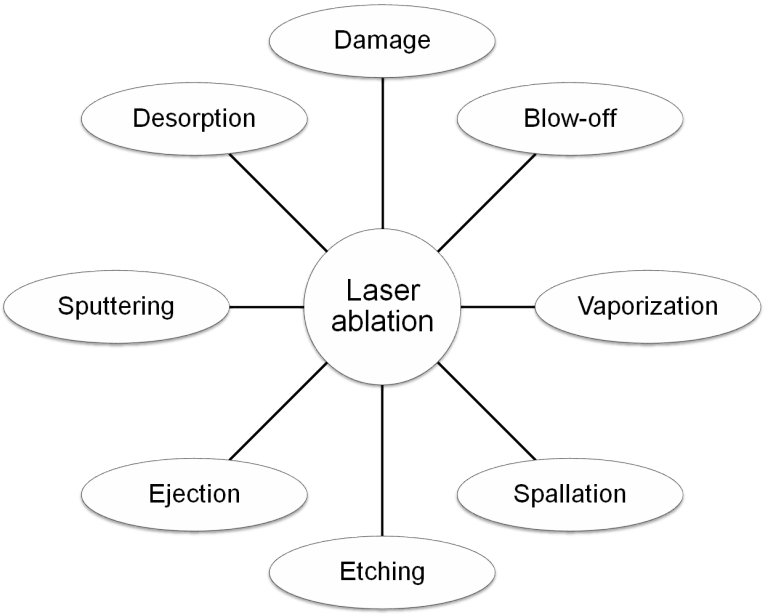

Figure 1.1: Selection of common synonyms for "laser ablation" found in earlier literature.

coupled plasma mass spectrometry (ICP-MS). The studies were in general driven by the idea to have a method at hand that would allow the sensitive determination of elements in all solid samples without laborsome, potentially erroneous and time-consuming sample preparation. The potential advantages of laser ablation for sample introduction are manifold:

1. Sample preparation is drastically reduced.
2. The analysis of conducting and non-conducting samples is possible.
3. The absence of solvents and acids used for digestion reduces the risk of contamination and possible interferences.
4. Elemental and isotopic information can be obtained with spatial resolution in the micrometer range, with limits of detection and at a speed, which no other technique available could provide [8, 9].

While in Gray's work laser spot diameters of 0.5 - 0.7 mm were employed, LA-ICP-MS evolved and established itself since then as a real microanalytic technique. LA-ICP-MS initially was regarded as little suitable for quantitative determinations. This was mainly attributed to insufficient precision and reproducibility of the ablation process [10, 11]. In the meantime, thanks to reference materials and internal

standardization procedures, quantitative results are achievable comparable to those from solution analysis. Several review articles summarize the state-of-the-art of the laser ablation technique [11–19]. In the beginning, mainly metallic and inorganic samples were analyzed [8, 12] representing the class of material analyzed in the first chapter of this doctoral thesis. Over the past years, the laser ablation technique was increasingly applied to environmental, organic and biological samples [20, 21]. The sample characteristics of this new class differ enormously compared to the metallic and inorganic materials, being generally much softer. Thereby, laser-tissue interactions change drastically and pose new challenges to the analytical chemist, bringing us to the background of the second chapter of the present dissertation. Nowadays, one of the most prominent application is the generation of elemental distribution maps in all kind of samples, especially in biological tissues [22, 23]. Here again, new questions, such as the reliability of the elemental distribution in biological tissue sections obtained by LA-ICP-MS, bring up new challenges for investigators and represents the topic of the third and forth chapter of this doctoral thesis.

2 Objectives/Objectivos

The field of laser ablation inductively coupled plasma mass spectrometry for the direct analysis of major, minor and trace elements in a wide variety of solid samples is continuously growing, because of its inherent advantage compared to alternative elemental approaches, which usually require dissolution steps prior to the final analysis. Due to its unique features, LA-ICP-MS allows trace element and isotopic analyses of solids, including microanalysis and depth profiling, with excellent lateral and depth resolution at trace concentration levels. Moreover, the coupling of the laser system to a magnetic sector field mass analyzer provides low limits of detection and high mass resolution, which overcomes many problems related to isobaric and polyatomic interferences.

In this context, the main objective of this work is the **development and application of new analytical strategies for quantitative and spatially resolved direct solid analysis by LA-ICP-MS**. This general aim has been pursued through the specific following objectives:

1. **Analysis of local defects in coated glasses:** Various types of glass defects may occur in the production of homogeneous and coated glasses, endangering their function and usage and, thereby, the quality of the product. Furthermore, glass defects are undesirable because they cause significant costs to manufacturing industries. In general, characterization of such defects presents a real challenge due to their size, position inside the glass and complex chemical and mineralogical properties. In addition, not only the identification of the impurities is necessary but also their position in the glass sample (i.e., in the homogeneous glass substrate, in the interface or in the layers of the coating), in order to identify potential sources of contamination in the production process; aspect of crucial importance in the manufacturing process as well as in quality control. Due to the small size of the local defects (diameter of the defect were between 200 and 800 μm) and the low concentration of the impurities the use of a highly sensitive microanalytic technique is indispensable.

   In this vein, the main objective of this study will be the identification of P, S and Cl trace impurities in relevant local defects of coated glasses. For the study,

several glass samples coated with layers of metals and oxides in the nanometer range were selected.

2. **Analysis of metalloproteins separated by gel electrophoresis: Absolute quantification of human serum transferrin:** Polyacrylamide gel electrophoresis (PAGE), employed in either the monodimensional or two-dimensional mode is the well accepted state-of-the-art technique for the separation of proteins. However, their accurate quantitative analysis is still one major task for analytical chemists. There is an urgent need for reliable absolute quantification methods for proteins in various concentration levels, particularly in the lowest concentration level found in important biological samples as for example blood derived samples or urine.

   The aim in this chapter will be the development and validation of a species-specific LA-ICP-IDMS method to achieve a sensitive, fast and accurate absolute quantification of transferrin. The proposed approach is based on the use of an isotopically enriched ^{57}Fe-Tf complex to quantify natural Tf in human serum samples after non-denaturing monodimensional gel electrophoretic separation (1D-PAGE). A critical evaluation of novel external calibration strategies and the species-specific IDMS quantification method, in terms of precision, accuracy and analysis time will be presented.

3. **Qualitative trace elemental imaging in paraffin-embedded ocular tissue sections:** Elemental bioimaging analytical techniques with adequate spatial resolution are today of crucial interest in life science studies to achieve a deeper understanding of the role of metal ions in biological systems. However, both in qualitative and quantitative elemental imaging correction of the LA-ICP-MS signal for matrix effects, variations in ablated and transported mass and instrumental drifts still presents a great challenge.

   Thus, the aim of this chapter will be the development of a novel internal standard correction strategy for qualitative elemental imaging by LA-ICP-MS. The proposed strategy is based on the deposition of a homogeneous thin gold film on the tissue surface and the use of the $^{197}Au^+$ signal as internal standard for normalization. A structurally complex biological sample (thin section from paraffin-embedded human eyes) will be used as model tissue and the bio-metal distribution ($^{24}Mg^+$, $^{56}Fe^+$ and $^{63}Cu^+$) will be investigated in the structures of the anterior segment of the eye. Reproducibility studies with samples both from the same donor and different individuals will be performed to evaluate

the potential of the novel IS correction approach with $^{197}Au^{+}$ as the internal standard.

4. **Quantitative bioimaging of trace elements in native frozen tissue sections using a custom-built cryogenic laser ablation cell:** Beside the correction of the analytical signal for effects distorting the result, there is another important factor influencing the outcome of the direct analysis of biological tissues. In this vein, it has been demonstrated, that cryogenic conditions, both for the sample preparation step and the LA-ICP-MS analysis, are preferable for metal determination in biological samples.

   In this chapter, the design, assembly and testing of the analytical performance of a new custom-built Peltier-cooled laser ablation cell will be performed using both inorganic glass and biological samples. Furthermore, the proposed cryogenic ablation cell will be employed for the quantitative determination of elemental distribution in human eye lens sections.

Objectivos

El campo de la ablación láser acoplado a un espectrómetro de masas con fuente de plasma de acoplamiento inductivo para el análisis directo de elementos mayoritarios, minoritarios y elementos traza en una amplia variedad de muestras sólidas está creciendo continuamente, debido a su inherente ventaja en comparación con técnicas elementales alternativas, que generalmente requieren pasos de disolución antes del análisis. Debido a sus características únicas, LA-ICP-MS permite el análisis de elementos traza e isotópico directamente desde el sólido, incluyendo microanálisis y perfiles de profundidad, con excelente resolución lateral y profundidad a niveles de concentración muy bajos. Por otra parte, el acoplamiento del sistema láser a un analizador de masas de doble enfoque proporciona bajos límites de detección y un alto poder de resolución, que supera muchos problemas relacionados con interferencias isobáricas y poliatómicas.

En este contexto, el objetivo principal de la presente Tesis Doctoral es el **desarrollo y aplicación de nuevas estrategias analíticas para el análisis cuantitativo y con resolución espacial de sólidos empleando LA-ICP-MS**. Este objetivo general se abordará a través de los siguientes objetivos parciales especificos:

1. **Análisis de defectos locales en vidrios recubiertos:** Varios tipos de defectos pueden ocurrir en la producción de vidrios homogéneos y con recubrim-

iento, poniendo en peligro su función y uso y, por tanto, la calidad del producto. Además, los defectos en los vidrios son indeseables porque ocasionan costos significativos para las industrias manufactureras. En general, la caracterización de tales defectos presenta un verdadero desafío debido a su tamaño, posición dentro del vidrio y las características químicas y mineralógicas complejas. Además, no solo es necesario identificar las impurezas sino también su posición en la muestra, con el fin de identificar las posibles fuentes de contaminación en el proceso de producción de los vidrios; aspecto de crucial importancia en el proceso de fabricación así como en el control de calidad. Debido al tamaño reducido de los defectos locales (en el rango de 200 a 800 μm de diámetro) y la baja concentración de las impurezas el uso de una técnica microanalítica altamente sensible es indispensable .

En este sentido, el principal objetivo de este estudio será identificar la naturaleza de las impurezas presentes en defectos locales en vidrios recubiertos mediante el uso de la técnica LA-ICP-MS. Para el estudio se han seleccionado varios vidrios recubiertos con capas de metales y óxidos en el rango de los nanómetros.

2. **Análisis de metaloproteinas separadas por electroforesis en gel: cuantificación absoluta de la transferrina del suero humano:** La electroforesis de proteínas en gel con una matriz de poliacrilamida es sin duda una de las técnicas más ampliamente usadas para caracterizar mezclas complejas de proteínas debido a sus numerosas ventajas, entre las que destaca su gran poder de separación. Sin embargo, en la actualidad su precisión en análisis cuantitativos sigue siendo un reto importante para los químicos analíticos. Existe una necesidad urgente de desarrollo de métodos de cuantificación absoluta fiables para proteínas a varios niveles de concentración, pero con un interés especial para proteínas a niveles muy bajos de concentración que se pueden encontrar en muestras como sangre u orina.

   El objetivo de este capítulo será el desarrollo y la validación de un método de dilución isotópica especifica empleando LA-ICP-MS para lograr una sensible, rápida y precisa cuantificación absoluta de la metaloproteína transferrina. La estrategia propuesta se basa en el uso de un complejo ^{57}Fe-Tf isotópicamente enriquecido para cuantificar Tf natural en muestras de suero humano después de la separación electroforética nativa en una dimension (1D-PAGE). Se presentará una evaluación crítica de nuevas estrategias de calibración externa y el método de cuantificación por dilución isotópica especifica, en cuanto a la precisión, la

exactitud y el tiempo de análisis.

3. **Generación de imágenes cualitativas en secciones de tejido ocular embebido en parafina:** Las técnicas analíticas basadas en la generación de imágenes elementales con suficiente resolución espacial son hoy en día de crucial interés en los estudios de las ciencias de la vida para lograr una comprensión más profunda del papel de los metales en los sistemas biológicos. Sin embargo, la corrección de la señal de LA-ICP-MS por efectos de matriz, variaciones de la masa arrancada y transportada así como las desviaciones instrumentales tanto para imágenes elementales cualitativas y cuantitativas aún presenta un gran desafío.

   Así, el objetivo de este capítulo será el desarrollo de una nueva estrategia de corrección interna para le generación de imágenes elementales cualitativas empleando LA-ICP-MS. La estrategia propuesta se basa en la deposición de una capa fina y homogénea de oro sobre la superficie de la muestra y el uso de la señal de $^{197}Au^{+}$ como patrón interno para la normalización. Una muestra biológica estructuralmente compleja (sección de ojo humano embebido en parafina) será utilizada como tejido modelo investigándose la distribución de metales ($^{24}Mg^{+}$, $^{56}Fe^{+}$ y $^{63}Cu^{+}$) en las estructuras del segmento anterior del ojo. Se llevarán a cabo estudios de reproducibilidad con muestras tanto del mismo donante como de diferentes individuos para evaluar el potencial del método de corrección con $^{197}Au^{+}$ como patrón interno.

4. **Generación de imágenes cuantitativas en secciones de tejido ocular congelado utilizando una celda de ablación criogénica de diseño propio:** Además de la corrección de la señal analítica por efectos que podrían distorsionar el resultado final, hay otro factor que influye en el resultado del análisis directo de tejidos biológicos. En este sentido, se ha demostrado, que condiciones criogénicas, tanto para la etapa de preparación de muestras como para el análisis por LA-ICP-MS, son preferibles para la determinación de metales en muestras biológicas.

   Por lo tanto, en este capítulo se llevará a cabo el diseño, la fabricación y la evaluació analítica de una nueva celda de ablación con un sistema de enfriamiento basado en elementos Peltier utilizando muestras inorgánicas y biológicas. Además, la celda de ablación criogénica se usará para la generación de imágenes cuantitativas que representarán la distribución de elementos traza en secciones de lente humana.

3 Fundamentals

3.1 Inductively coupled plasma mass spectrometry (ICP-MS)

In the early 80s inductively coupled plasma mass spectrometry (ICP-MS) was introduced as an analytical technique by Houk and coworkers [24]. Even though the basic layout has remained unchanged, important improvements in terms of detection limits, linear dynamic range of the detection and robustness established ICP-MS to one of the key techniques for the analysis of trace and ultra-trace elements in inorganic, organic and biological samples [25–27]. Today, detection limits for high-resolution sector-field instruments are in the pg g^{-1} range or below for a multitude of the elements. In total, more than 70 elements can be measured by this technique. Furthermore, the mass spectrum provides not only elemental concentrations but also isotopic information.

In ICP-MS instruments there are six main steps to be considered. The first one is the sample introduction. Measurements in solution are performed using any kind of solution nebulization. Solid samples can be introduced using a broad variety of sample introduction systems. In a second step, the analytes are guided into the ICP source for vaporization, atomization and ionization. Subsequently, the generated ions are extracted through an interface into a high vacuum enclosure, where they are focused by a series of lenses, separated according to their mass to charge ratio in the mass analyzer and finally counted by a detector. In the following, each of these steps will be described briefly.

3.1.1 Sample introduction system

The majority of applications of mass spectrometry with inductively coupled plasma deal with the analysis of liquid samples. However, the stoichiometric transfer of the sample into an aerosol and subsequently into the plasma source still continues to be the weak link in this system as a shift in the elemental composition would bias the analytical results. For analytes in solution, there exists a variety of different sample introduction systems. The conventional technique is solution nebulization by a pneumatic nebulizer with concurrent separation of large droplets from the aerosol

in a spray chamber. The low efficiency (1-2% reaches the ICP) and the high sample consumption of 1-2 ml min^{-1} are the main drawbacks of this technique [28, 29]. Therefore, high-efficiency nebulizers were developed consuming less than 200 μl min^{-1} of solution [30–32]. The low sample consumption is an advantage when the sample volume is limited or expensive and also for chromatographic coupling techniques. It further reduces plasma effects if, for example, analytes in organic matrices have to be measured.

An approach to improve the nebulization efficiency was the development of direct injection nebulizers, where the sample is nebulized directly into the ICP [33, 34]. However, the larger amount of solution introduced (compared to conventional nebulization) causes enhanced matrix effects. The combination of direct injection with high efficiency nebulizers reduces matrix effects [35] but is more expensive than conventional sample introduction systems. Other techniques for liquid sample introduction are ultrasonic nebulizers with high [36] and low [37] sample consumption, monodisperse dried microparticulate injectors [38, 39] and also electrothermal vaporization [40–42].

For solid samples, spark ablation (restricted to conducting samples) [12, 43] or laser ablation (*section 3.2*) [12, 19, 44] are the commonly used sample introduction techniques.

3.1.2 Inductively coupled plasma source

In the mid-sixties, Greenfield [45] and Fassel [46] reported about the possibility of using inductively coupled plasma as an excitation source for element analysis. Since then, the basic apparatus has changed little (see *figure 3.1*).

An atmospheric ICP is formed in a quartz torch that consists of three tubes of varying diameter. The aerosol carrier gas ($\leq$ 1 L min^{-1}) flows through the inner tube and is enclosed by the auxiliary gas with a similar flow rate. The main function of the auxiliary gas flow is the positioning of the formed plasma relative to the front end of the torch. Since the plasma can reach temperatures of up to 10,000 K, an excess cooling gas flow of argon (15-17 L min^{-1}) through the outermost tube shields the glass torch and prevents it from melting. By a high-frequency generator (27.1 MHz or 40.6 MHz) power is directed via a load coil to the plasma gas. By igniting an initial spark several electrons are introduced into the resulting strong alternating electromagnetic field. The accelerated electrons collide with argon atoms forming positively charged argon ions and further electrons. The resulting chain reaction leads to the formation of

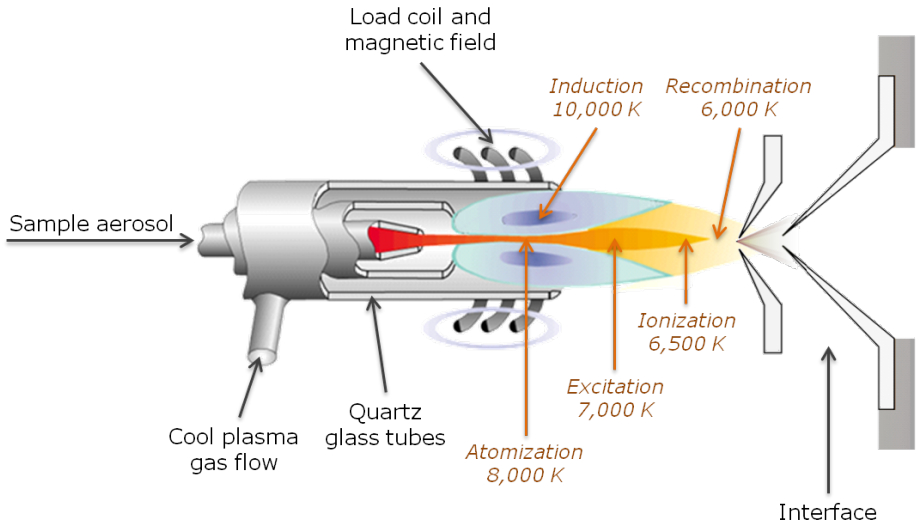

Figure 3.1: Schematic view of a plasma torch. Adapted from [47]

a plasma which can be maintained as long as power above a threshold value (typically 600 to 1,500 W) is supplied. The effective energy transfer by the numerous collision processes and the dwell time of the sample in the plasma of a few milliseconds leads to its drying, ashing, atomization, excitation and ionization. Subsequently, the charged atoms are transmitted into the interface region.

Argon as a plasma gas is a suitable selection due to its relatively high first ionization potential of 15.8 eV. This allows the ionization of most elements, more than 50 of them by more than 90% [25]. Only He, F and Ne have higher first ionization potentials and are therefore not ionizable in an argon plasma. Elements with high ionization potentials (but lower than Ar) are difficult to be ionized (e.g. N, O, Cl, Br). Most elements have their second ionization potential close to or higher than the 15.8 eV of Ar so doubly charged ions are therefore rare. The ions generated in the ICP at ambient pressure pass via an interface to the mass analyzer.

3.1.3 The interface region

The interface is used to bridge the huge pressure difference between the atmospheric pressure at which the plasma is generated and the high vacuum of the mass spectrometer. The separation of the ions takes place in a high vacuum, since here their mean free path is sufficiently large to prevent most of the collisions between the analyte ions and other molecules. Otherwise, the transmission of the ions could be reduced by the collisions taking place, which would lead to a deterioration of the detection capability. The transition from atmospheric pressure to high vacuum, however, was

for a long time a significant challenge, which led to the delayed commercialization of ICP-MS equipments.

The interface consists of two consecutive metallic cones with diameters of less than 1 mm. They are usually made of nickel, but for particularly corrosive samples they are made of platinum [29]. In the gap between the first cone (sampler cone) and the second (skimmer cone) the vacuum is maintained at about 10^{-3} bar whereas in the region behind the skimmer a pressure of up to 10^{-6} bar prevails.

Mainly because the sampler cone is exposed to very high temperatures, both cones are mounted in a holder made of a highly thermally conductive material such as copper or aluminum which is water-cooled.

Another problem in the development of the interface was an impinging phenomenon that is referred to as secondary discharge. This is an electrical discharge between the plasma source and the sampler cone which may shorten the life of the interface and impair the measurement. Due to the secondary discharge the ions can develop very different kinetic energies, making the focusing in the ion optics significantly difficult. This effect can be minimized by using a guard or shield electrode.

The ions that successfully pass through the skimmer cone orifice are accelerated by a high voltage potential gradient and passed through a series of focusing lenses.

3.1.4 The ion focusing system

Due to the fact that there is both between the cones and behind the skimmer cone a negative pressure compared to the pressure in the region of the plasma, the generated ions are drawn automatically from the plasma through the interface in the section of the ion optics. The concept of ion optics is somewhat misleading, since it is not a classical form of optics. This area is made up of many different metal plates and cylinders which are under voltage and thus can influence the trajectory of the ions.

Not only the analyte ions are generated in the plasma, but also other particles, molecule ions from the matrix, neutral atoms and photons. These can lower the efficiency of the system in different ways. Photons as well as cations can trigger a cascade of electrons and thus the detection of a signal (EMT, see *section 3.1.6*). Due to the large number of photons formed in the plasma, this could lead to an overloading of the detector, for which reason these are usually stopped by a photon blocker (e.g. a plate perpendicular to the flight path).

A phenomenon that is called mass bias occurs during the transport of the ions previously generated in the plasma. The main reason for this is assumed to be in so-called space charge effect and is described briefly below.

The inductively coupled plasma has to be electrically neutral, because for each generated positively charged particle, it always creates also an electron or an anion. However, on closer inspection of the plasma, a spatial separation of charge can be observed (see *figure 3.2*).

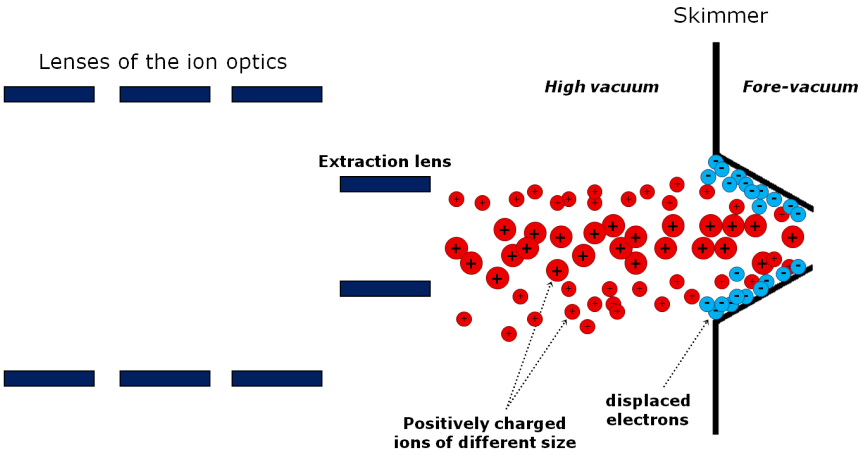

Figure 3.2: Schematic illustration of the space charge effect and its impact on the ion beam.

If there is a high charge density at the skimmer, an overlapping of the Debye spheres of the charge carriers and thus repulsion effects occur. Due to the lower mass and therefore kinetic energy of the electrons they diffuse, more than the heavier, positively charged ions, to the edge of the ion beam. In the center remains a positive charge. But not only the light electrons are affected, smaller and lighter cations are more defocused than heavy elements. Since the ion optics preferably focuses the middle part of the ion beam, this represents the main cause of the discrimination of the lighter isotopes in isotope ratio measurements. The frequently observed signal depression of lighter elements in the presence of many heavy elements in the matrix can also be explained by the space charge effects.

Finally, the focused ion beam carrying the positively charged analyte ions is finally guided into the mass analyzer.

3.1.5 Mass analyzer

Various mass spectrometers use an ICP as ion source. Quadrupole [24, 25, 48], sector field (SF) instruments [49] and time of flight (TOF) [50–53] are commercially

available. Additionally, ICP coupling has also been reported with ion trap MS [54] and Fourier transform ion cyclotron resonance (FT-ICR) MS [55]. These instruments differ in some important characteristics that play a significant role in the analysis of miscellaneous samples.

- The smallest and largest detectable mass characterizes the analyzable range. This varies depending on the physical separation principle on the spectrometer.
- The sensitivity of an analyzer is described in terms of permeability (transmission) and indicates the number of ions reaching the detector, compared to the number of formed ions.
- Another important aspect is the scan rate which considers the time needed for a scan, or more precisely, the time needed to record a mass spectrum. This represents the pure measurement time including the time required by the analyzer to reach again the initial state. This factor is especially important for time-dependent measurements.
- An important criterion of mass analyzers is the resolution R and reflects the separation properties between two adjacent peaks (*equation 3.1*), where m is the nominal mass of target analyte and Δm the mass difference between target and interference mass.

$$R = \frac{m}{\Delta m} \tag{3.1}$$

One of the earliest and nowadays with about 90% mostly applied technique is the quadrupole mass filter. The possibility to use an electromagnetic quadrupole for mass separation was first published by Wolfgang Paul in 1953 [56]. Compared to other analyzers the quadrupole became accepted as a cheap and robust routine technique adequate for high throughput and trace analyses. It consists of four cylindrical or hyperbolic, parallel arranged electrodes of the same length and same diameter. By placing a direct current (DC) field on one pair of rods and a radio frequency (RF) field on the opposite pair, only ions of a certain mass to charge ratio are kept in stable trajectories and are thus analyzed in the subsequent detector. The other ions are ejected from the quadrupole. The typically achieved mass resolution of about R<300 is adequate for most of the applications but insufficient for many elements that are prone to suffer spectral interferences from argon, solvent or sample matrix. In order

to overcome this problem, a new approach called "collision/reaction cell" technology, positioned in front of a conventional quadrupole mass filter, has been developed to eliminate or reduce certain interferences from the ion beam [57–59].

Generally, quadrupole mass analyzers allow fast scanning of about 40 different elements within 0.5 s, however, the measurements are still sequential. For rapidly changing transient signals, this leads to spectral skewing effects. This can be the case when a laser ablation is used as sample introduction system, especially for single pulse analysis [60] or if the mass scan time is close to the laser ablation frequency for fast flushing cells [44].

The limitations in the quadrupole resolving power has led to the development of high resolution (HR) spectrometers based on the double-focusing magnetic-sector design. Here, the ions are separated in a magnetic field (B-field) according to their mass to charge ratio followed by the discrimination by kinetic energy in an electric field (E-field) (inverse Nier-Johnson geometry). In this way, higher mass resolutions up to R=10,000 are achievable which is adequate to resolve molecular interferences from the mass spectrum [49, 61]. However, isobaric interferences require even higher mass resolutions and can therefore not be separated by commercially available ICP-MS instruments. Two main types of instruments can be distinguished. By scanning of the B- and E-fields, sequential measurement of the mass spectrum is possible with slower scan speeds than quadrupole instruments. However, using special arrangements, very fast scan speeds comparable to those of quadrupole mass analyzers can be achieved [62]. Besides high resolving power, other attractive features of HR-ICP-MS are their high sensitivity combined with low background levels and an excellent precision.

The demand for ultrahigh-precision data was the driving force for the development of an instrument based on the previously described design but with multiple detectors. This technique is commonly referred to as multicollector (MC) ICP-MS and is mainly used for precise isotopic studies of various samples [63–67].

The time-of-flight mass spectrometer was also adapted for use in an ICP-MS system. All TOF-MS instruments are based on the same fundamental principle that the kinetic energy of an ion is directly proportional to its mass and velocity. Thus, charged molecule ions generated in the ion source are accelerated by a short high-voltage pulse. This gives all ions the same kinetic energy so they can subsequently be separated in a field-free high-vacuum chamber due to different migration velocities depending on the mass to charge ratio [68]. The main advantage of TOF-ICP-MS

is the simultaneous ion extraction and the fast sequential measurement of the entire mass range within a few microseconds. This is especially important when the sample volume is limited or for high precision measurements necessary in isotope ratio analyses.

3.1.6 The ion detector

On exiting from the mass analyzer the ions will sequentially strike the detector. Several types of detectors are available, whereby the electron multiplier tube (EMT) is the most common. Two different types of electron multiplier can be used, continuous or discrete dynode, while both are based on the same working principle: a curved glass tube or a row of consecutive electrodes are coated with an easily ionizable metal (e.g. Cs). Once an ion strikes the active surface of the dynode, one or more electrons are released. These electrons are accelerated in a potential difference down the tube (or to the next dynode) where in turn they expulse new electrons. Hence, an exponential cascade of electrons rapidly builds up and this amplification leads to a measurable pulse (see *figure 3.3*).

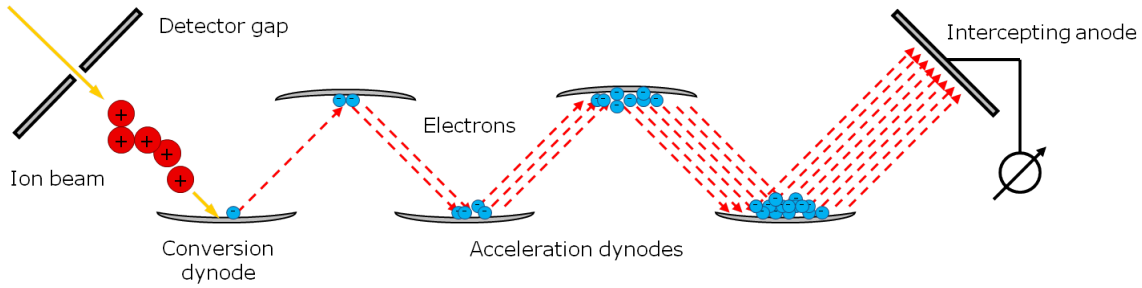

Figure 3.3: The path of an ion through an electron multiplier tube.

For preserving and extending the lifetime of the detector, a so-called dual system can be applied. In this case, the resulting signal is collected in two different sites, talking about an analog and a digital pulse signal. The pulse-counting (digital) mode shuts off automatically when an ion current of about 10^6 ions per second is registered in order to avoid congestion and thus premature aging. The further signal acquisition is then only done in the analog mode at the midpoint dynode, which has a lower sensitivity by about a factor of 100. This will turn off only at an ion current of about 10^9 ions per second.

3.1.7 Interferences in ICP-MS

The analysis by ICP-MS is limited by the existence of interferences, ranked according to their origin. It can be distinguished between non-spectral and spectral interferences.

To **non-spectral interferences** is usually referred as effects that are caused by the matrix. They can be divided into two categories:

- Reversible matrix effects can have many causes and usually lead to signal suppression, less commonly to signal amplification. The reversibility implies that this effect lasts only as long as a matrix is brought into the plasma.

- Irreversible matrix effects are due to deposition of particles (e.g. salts) on the interface and lead to a gradual decrease of the signal intensity. Even after the end of the matrix supply, the impact of this effect is observed.

Spectral interferences are caused by elemental or molecular ions of the same nominal mass as the analyte ion and lead to the superposition of the sought signal. Here, isobaric and molecular interferences are distinguished.

- Isobaric interferences are referred to isotopes of different elements with the same nominal mass (e.g. ^{40}Ar and ^{40}Ca) that cannot be distinguished depending on the resolution of the mass spectrometer. The emergence of this interference can be corrected, by analyzing other isotopes of the involved elements (if existent) and recalculate the actual value by using the natural isotopic abundances. Nevertheless, this principle is flawed. The same principle can also be applied when elements have a low second ionization potential and therefore reach the detector as doubly positively charged ions. One example is the interference of $^{138}Ba^{2+}$, which is detected at a mass of 69 and thus interferes with the analysis of the ^{69}Ga isotope.

- Molecular or polyatomic interferences (argides, oxides, carbides) are usually formed in the plasma by the actual plasma gas, the solvent and the sample matrix, and even by the presence of oxygen or nitrogen from the surrounding air. If they have the same m/z ratio as the analyte ions (e.g. $^{40}Ar^{16}O^{+}$ and $^{56}Fe^{+}$) they can be distinguished only with difficulty. The elimination or minimization of the interferences is usually performed by instrumental methods and were briefly described in *section 3.1.5*.

3.2 Laser ablation (LA)

3.2.1 Discovery and developments

In 1981 Thompson presented the coupling of a laser ablation (LA) equipment with an inductively coupled plasma atomic emission spectrometer (ICP-AES) [69]. Four years later, this new form of sample uptake was hyphenated by Alan Gray with an ICP mass spectrometer [7] benefiting in this way from the better analytical performances of the ICP-MS compared to the ICP-AES. Since then, this method has evolved into a widely employed technique in qualitative and quantitative analyses of major, minor, trace and ultratrace elements, as well as for the determination of isotope ratios of solids samples [11, 20, 70, 71].

Despite the nature of the focused laser beam, in the earlier works LA-ICP-MS was mainly employed for bulk analyses of homogeneous solid materials. However, as essential properties of the samples are frequently related to the distribution of the elements, techniques providing this information are highly advantageous. In this vein, the relatively small diameter of the laser beam permits the spatial characterization of structures in solid samples with lateral and in-depth resolution in the μm and nm range, respectively, allowing, for example, the analysis of geological samples, such as for example, rocks, meteorites, and in particular their small inclusions [72, 73]. As the damages of the solid samples after the laser impact are minimal, further applications can be found in forensics [74, 75] as well as the examination of archaeological specimens [76, 77]. Lately, LA-ICP-MS is also increasingly applied to address biological and medical questions [78–80]. The use of this technique on electrophoretic gels allows the study of metal proteins in the blood serum [81] or the determination of elemental distributions in biological tissue sections [22].

The advantages of direct solid analysis by LA-ICP-MS over conventional nebulization ICP-MS are presented in *table 3.1*.

Firstly, the direct laser vaporization of solid samples requires only minimal sample preparation, minimizing the risk of contamination by the used solvents [82]. In this way almost all solids can be introduced directly into the mass analyzer by laser ablation without prior treatment. Another benefit consists in a much lower required sample volume. The general sample up-take rate for laser ablation ranges between 0.0001 and 0.1 μg s^{-1} [19], so that theoretically for homogeneous samples a total sample volume of a sand grain is required. Thus, despite ablated sample quantities

Table 3.1: Figures of merit of ICP-MS and LA-ICP-MS in material science [82].

	ICP-MS	**LA-ICP-MS**
Sample preparation	Often simple	Small or no
Quantification possibility	Excellent	Difficult, SRM required
Detection limits	0.001-0.1 pg mL^{-1}	0.0001-0.1 $\mu g\ g^{-1}$
Amount of sample	From ng to fg range	From mg to μg range
Precision	$\pm$1-5%	$\pm$2-10%
Spatially resolved analysis	No	Lateral resolution >10 μm
Depth profiling analysis	No	Depth resolution >1 μm
Time consuming step	Sample preparation	Quantification
Contamination risk	High	Low
Limitations	Interferences	Interferences, inhomogeneity

in the low μg range, detection limits in the lower ng g^{-1} range can be achieved due to the extremely high sensitivity of the ICP-MS. Additionally, using laser ablation for sample introduction, analyses with high lateral resolution can be performed, so that the spatial distribution of elements in inhomogeneous samples can be detected. This information is lost during the chemical digestion of the solid sample so that in this case only bulk data are available. Finally, the specific feature of a dry plasma, i.e. the absence of solvents and thus the drastically diminished presence of oxygen directly in contact with the analyte (apart from ambient air), reduces significantly the formation of polyatomic interferences based on oxides.

Although the theoretical fundamentals of this relatively new analysis technique have been increasingly investigated since its introduction the process of laser ablation is not yet understood in its entirety.

Initially, mainly basic factors such as the influence of the transport tube length on the signal shape [83] or the dependency of the ablated mass on the laser wavelength [84] were investigated. Several works also focused on the fractionation effects during the ablation process [85] and their resulting consequences [86, 87] as well as on important variables such as the particle size distribution [88–90], pulse duration [91–93] or ablation chamber layout [94, 95]. In recent years, there is also an increasing number of publications dealing with model simulations [95–100], answering questions regarding the laser ablation process. However, this learning process is not yet complete and will probably still demand more years of intensive investigation.

3.2.2 Basic concepts of solid sampling by laser ablation

In the analysis of a solid sample by LA-ICP-MS three stages can be considered which are undergoing a continuous process of optimization:

- Ablation process and aerosol generation
- Aerosol transport
- Atomization and ionization of the particles in the ICP

An idealized model for solid sampling by LA-ICP-MS is represented in *figure 3.4*:

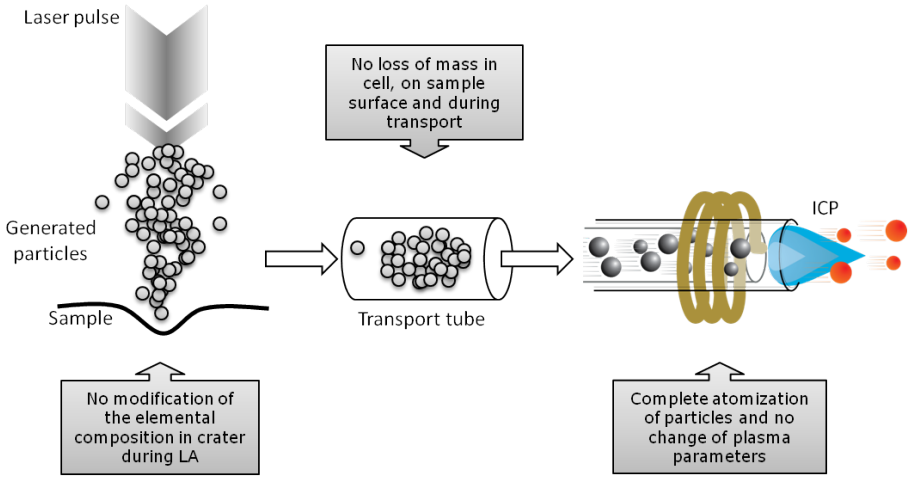

Figure 3.4: Idealized model for LA-ICP-MS analyses [101].

In the first stage, a pulsed laser beam focused on the target surface ablates a certain amount of sample mass forming a well-defined crater with sharp borders. The ablated mass forms with the gas phase, the so-called carrier gas, a fine aerosol, whose particles have exactly the same stoichiometric composition as the original sample. The sample matrix adjacent to the crater remains chemically and physically unchanged and the ablated material is not re-deposited onto the surface of the sample.

In the second stage, the formed particles are transported, without any loss from the place of ablation, out of the ablation cell through the transport tubing and the injector of the ICP-torch into the plasma. There is a very small effective total volume with no dead zones, thus, very sharp signals are obtained without memory effects (due to long washout times of the ablation cell).

In the last stage, the particles are atomized and ionized completely in the ICP without affecting the plasma parameters.

Unfortunately, the real conditions differ from the ideal requirements. In order to approximate as much as possible, a profound understanding of the entire system and the laser-matter-interaction is indispensable. The degree of deviation depends on the sample characteristics and the choice of experimental conditions. A summary of the relevant parameters and their influence in LA-ICP-MS analysis is given in *table 3.2*.

Table 3.2: Summary of relevant parameters and their effect in LA-ICP-MS [16].

	Sample material	**Laser**	**Transport system**	**ICP-MS**
Parameters	Absorbance	Wavelength	Cell volume	Rf-Power
	Reflectivity	Pulse length	Tubing diameter	Plasma potential
	Heat capacity	Spot size	Tubing length	Gas Flows
	Heat conductivity	Fluency	Gas composition	Gas composition
		Irradiance		Torch position
		Repetition rate		Torch config.
		Ablation mode		Interface pressure
		Gas environment		Ion lens settings
				Data Acquisition
	⇓	⇓	⇓	⇓
Influence	Ablation rate	Penetration depth	Gas velocity	Plasma temp.
	Surface* composition	Surface temp.	Signal dispersion	Vaporization
	Surface* morphology	Ablation rate	Transport efficiency	Atomization
		Vapor composition		Ionization
		Particle-size distribution		Ion extraction
		Aerosol composition		Ion transmission
		Transported material		Sensitivity
				Mass bias
				Duty cycle

* Volume, which is affected by the laser radiation and vaporized or melted material

In the following the fundamental stages of the LA-ICP-MS process and their influence on the analytical results will be revised.

3.2.3 The ablation process and particle generation

The term "ablation" derives from the Latin "ablare" and means "carry off/away". It describes the actual sampling by laser radiation without giving any indication of the present mechanism. Two distinctive particle formation mechanisms occur during the ablation of solid material:

In the first place, there is the pure interaction of laser radiation with the solid

surface. In addition, secondary processes take place that lead to the mobilization of the solid phase and thus affect the composition of the formed aerosol. Comparable to a tiny explosion, both solid and melted particles are expulsed from the surface (hydrodynamic sputtering), which subsequently are transported by the carrier gas to the ICP-MS and thereby contribute to the analytic result [102, 103].

3.2.3.1 Laser-matter-interaction

The interaction between the laser pulse and the solid sample can be explained fundamentally by the occurrence of absorption phenomena and the resultant effects. It is strongly dependent on the laser wavelength, the laser energy density (fluence) and the pulse duration [87, 104]. For lasers with pulse durations longer than one nanosecond - as used in this work - the most suitable model to describe the ablation process is based on the rapid absorption of energy by the target causing a fast heating, melting and evaporation of the sample surface [105, 106].

Vaporization of matter is typically achieved, depending on the sample characteristics, applying laser irradiances between 10^4 and 10^{10} W cm^{-2}. At low laser irradiances, the generated vapor above the sample surface is of low density and mainly transparent for the laser beam. The transmissivity of the vapor is reduced with increasing laser fluence, as saturation of vapor results in the condensation of particles in the submicrometer range due to the expansion of the vapor and its consequential cooling [107]. For high laser frequencies the generated aerosol particles may cause scattering effects, and, depending on the particle size and the employed laser wavelength, absorption effects, so that the laser energy reaching the solid surface could be reduced [108]. In addition, the generated vapor shows a different refraction index compared to the pure carrier gas, which may cause defocusing of the laser beam.

Plasma shielding

For fluences above a threshold value (10^7 to 10^{10} W cm^{-2}) - depending on the sample matrix and the laser wavelength - the vapor is partly ionized. It comes to the formation of a plasma in front of the target whose optical density will increase with higher power densities. The laser beam will be partially absorbed before it reaches the sample surface, which is also referred to as plasma shielding [105, 109–112]. As a result, the amount of ablated material per pulse in dependence of the laser fluence exhibits at first a linear behavior, but flattens out at higher fluence values due to energy losses of the laser beam by vapor and particle absorption (see *figure 3.5*).

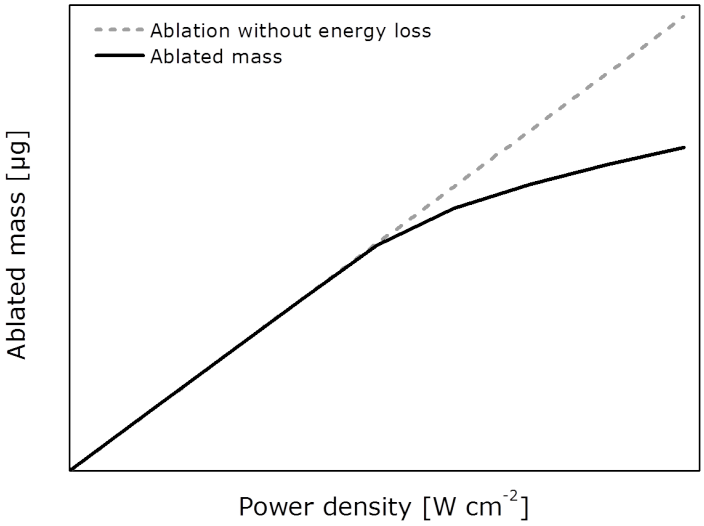

Figure 3.5: Ablated mass *versus* laser fluence: The effect of plasma shielding.

The effect of plasma shielding is, besides the fluence, strongly dependent on the wavelength of the laser used. From the ultraviolet (UV) to the visible range the effect gets more pronounced, while for IR lasers the effect is so strong that, depending on the matrix, it does not leave sufficient energy available for target evaporation [84, 96, 113–115]. Consequently, the use of UV lasers has prevailed in modern LA-ICP-MS analysis (266 nm, 213 nm, 193 nm, 157 nm) [87, 116].

As the clouds of ionized matter formed by strong plasma shielding are very irregularly shaped, this can lead to irreproducible ablation rate which in turn is reflected in the analysis by low precision and accuracy [117].

Strong plasma shielding can also cause that the solid surface adjacent to the actual ablation spot is physically and chemically subject to change, reducing in this way the lateral resolution of the LA-ICP-MS [84].

Furthermore, it was observed that the type of carrier gas has an influence on the formation of a plasma during the ablation process. Comparison of the noble gases helium and argon has shown that a significantly smaller plasma is formed in helium atmosphere. This can be explained by a faster removal of thermal energy away from the laser induced plasma due to the almost one order of magnitude higher thermal conductivity of helium compared to argon. As a consequence, a much lower plasma shielding effect can be observed in helium compared with argon [90].

Matrix dependence

Besides the reduction of plasma shielding effects, another advantage of using shorter wavelengths is the decrease of the matrix dependency of the ablation [84, 116]. This can be explained by the lower target surface reflectivity [114] leading to a higher energy yield of the laser pulse for the ablation process [96].

On the other hand the absorption in the UV range increases in general with shorter wavelengths [118]. As a consequence the penetration depth of the laser beam into the sample matrix decreases [116], so that a higher energy per volume is transferred to the sample. Thus, a decrease of the minimum fluence threshold value necessary to induce the ablation process is observed for shorter wavelengths [87].

Fractionation effects during the ablation process

As already described at the beginning of this section the most suitable model to describe the ablation process is based on fast heating, melting and evaporation of the sample surface. On this background, differences in the stoichiometric composition of the aerosol particles in comparison to the solid sample can be explained. There is considerable evidence that volatile elements and compounds are particularly prone to be enriched in the aerosol. As this phenomenon can be traced back to a fractional evaporation process, this effect is referred to as fractionation effect [85].

Additionally, there are another two effects that are embraced by the term "fractionation effect" in the literature. They are linked to the transport of the formed aerosol and the decomposition of the particles in the ICP and will be further discussed in the respective sections (*section 3.2.4.1* and *section 3.2.3.2*).

The fractionation effect of the ablation process is, just as the matrix dependency, strongly influenced by the laser wavelength as well as pulse duration [87, 119]. As already described before, the shorter the wavelength the lower is the penetration of the laser beam into the sample surface. Thus, for the ablation with a constant energy density (J cm^{-2}) the irradiated volume is less resulting in a higher volume energy density (J cm^{-3}) and ultimately in a higher temperature. In addition, the energy is transferred to the matrix in less time when shorter pulse durations (and constant energy density) are employed. Both of these factors lead to an increase of the power density in the irradiated volume (J s^{-1} cm^{-3}). This causes very high temperatures in a strongly limited area so that the evaporation process is faster than the time needed to form an evaporation equilibrium in the vapor/melt interface, resulting in less fractionation effects [99, 103].

A physical property of the sample, which can result in a higher fractionation effect, is a high heat conduction coefficient. Especially with longer pulses (ns range), this leads to a higher loss of the laser energy due to heating of adjacent, not ablated, material (see *figure 3.6*). In that case, an evaporation equilibrium can be established and fractional evaporation occurs [99]. Metals in general have a high heat conduction coefficient. Therefore, the fractionation effect is particularly pronounced in metals and alloys compared to other solid materials (such as glass) [120].

This model is also supported by comparing ablation with laser pulse durations in the fs-range. Here, the laser pulse duration (10^{-15} s) is shorter than the electron cooling time (10^{-13} to 10^{-12} s) and the lattice heating time ($>10^{-12}$ s) [121–124], so neither thermal conduction nor the establishment of an evaporation equilibrium prior to the actual ablation can take place (see *figure 3.6*). Thus, under optimized conditions, the fractionation effect caused by the laser pulse duration is nearly negligible [91].

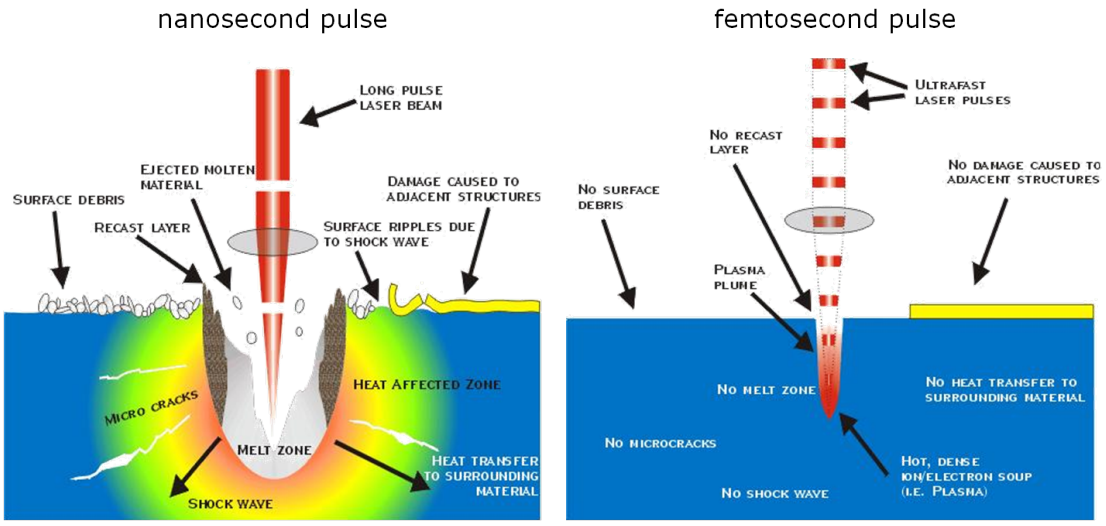

Figure 3.6: Laser-matter interaction during nanosecond pulses (left) and femtosecond pulses (right) [125].

3.2.3.2 Particle generation through secondary processes

The particle size distribution of a laser ablation aerosol generally ranges from a few hundred picometers to a few micrometers [104, 126]. Typically, two maxima can be observed suggesting the presence of at least two particle formation mechanisms. Both fractions can show big variations in their chemical composition, as it was demonstrated for the analysis of brass (Cu/Zn 1.53:1) using laser ablation (laser wavelength 775 nm,

5 ns pulse duration). *Figure 3.7* shows the obtained particle distribution (left) and their chemical composition depending on the size (right). It could be observed that in the fraction with particle sizes smaller than 100 nm the more volatile zinc (boiling point 1180 K) was significantly enriched compared to copper (boiling point 2835 K), while in the size fraction over 100 nm the opposite case was detected.

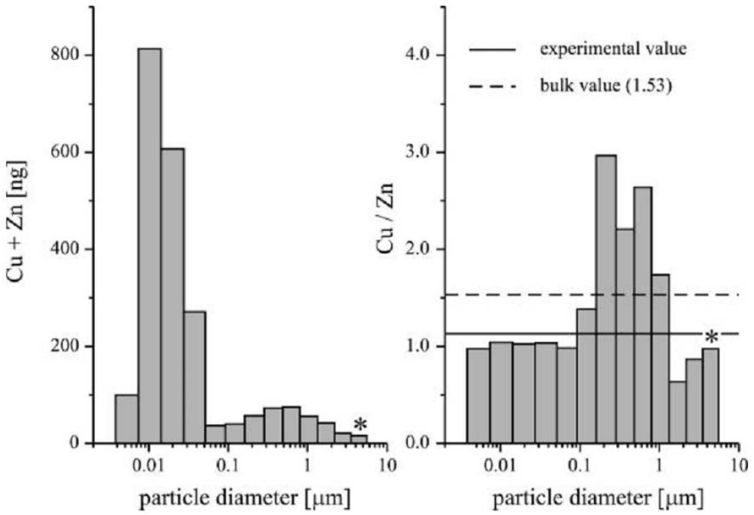

Figure 3.7: Particle size distributions (left) and chemical composition (right) determined for nanosecond LA of brass. The last fraction indicated by asterisk acts as a separator for particles >3.5 μm [104].

Microscopic images of filtered particles also confirm the hypothesis that at least two independent particle formation mechanisms exist, as two classes of particles where observed: fibrous agglomerates and large spherical particles [127–129] (see *figure 3.8*).

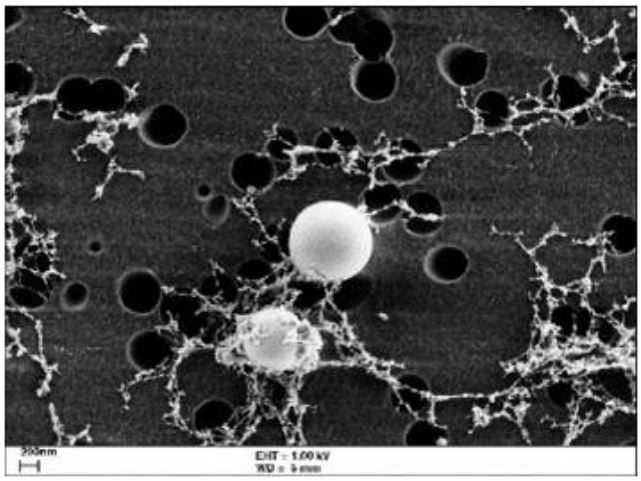

Figure 3.8: Two classes of particles (fibrous and spherical particles) of aerosol particles of the standard reference material NIST 610 collected on a filter membrane [129].

Primary particles and influence of the carrier gas

During the ablation process a microplasma of up to 6000°C [130] (containing the ablated material) is generated on the sample surface which expands into the ambient gas. The expansion itself as well as the interaction with the carrier gas has strong cooling effects provoking the saturation of the vapor. As a consequence desublimation occurs forcing the evaporated material to precipitate as fine particles forming the actual solid aerosol. The particle size distribution, their shape as well as the elemental composition resulting from this mechanism are heavily dependent on the ambient pressure, the type of ambient gas and the sample matrix itself. Ablation in a LA-ICP-MS analysis is performed at atmospheric pressure, thus, the expansion of the vaporized sample material takes place in the so-called ablation gas.

Argon and helium are generally used for this purpose. However, the use of helium as ablation gas instead of argon has shown to increase the sensitivity by a factor of two to four [86] and reduce the amount of deposited material around the ablation zone. It has been suggested that the rapid removal of thermal energy from the laser induced plasma in a helium environment inhibits the condensation of smaller particles into larger ones. These larger particles are prone to deposition near the ablation crater [131] and suffer incomplete decomposition in the ICP [90] (see *figure 3.9*).

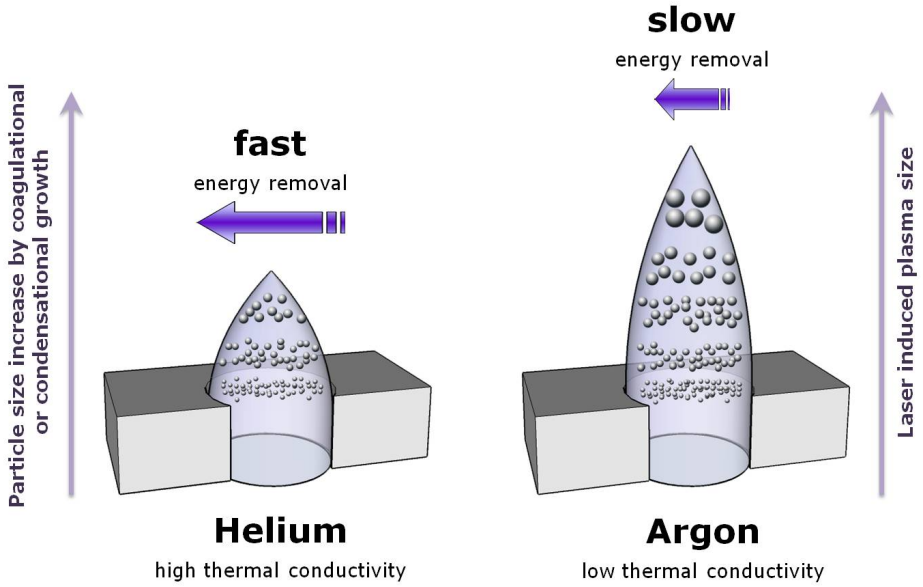

Figure 3.9: Particle size distribution in dependence of the carrier gas. Adapted from [90]

On this primary nanoscale condensation nuclei further material is accumulated until the particles solidify due to cooling effects. In this vein, in ablation gases with high thermal conductivity, such as helium, this process is much faster than in gases

with lower thermal conductivity. Thus, the time span for the particle growth due to condensation processes is much shorter for helium than for argon.

This particle formation mechanism is able to explain particle sizes up to approximately 100 nm [105] and is largely independent from the laser wavelength. In order to explain the formation of particles with sizes up to 10 μm there are several mechanisms: on the one hand, the primary nanoparticles generated by vapor condensation collide with each other forming filamentary agglomerates [128], maintaining the initial particle size distribution [132]. On the other hand, the formation of large spherical particles can be observed, which are based on a different formation mechanism, as the hydrodynamic sputtering.

Particles through hydrodynamic sputtering

Horn and Günther investigated the influence of different laser wavelengths (193 nm *versus* 266 nm) on the ablation and the subsequent analysis using LA-ICP-MS [133]. In this comparative work, all other parameters such as sample matrix, ablation apparatus, carrier gas, spot diameter and energy per pulse were kept constant. Experiments showed that the total amount of ablated mass was independent from the wavelength used. However, the sensitivity was found to be lower at longer wavelengths. This was mainly attributed to a shift in the particle size distribution to larger particles for longer wavelengths, which in turn cannot be completely atomized and ionized in the ICP. At first glance these findings seem to be contrary to the above mentioned mechanism for primary particles, which was demonstrated to be independent of the laser wavelength.

Thus, the cause for the difference must lie in large particles that are subject to a different formation mechanism which is dependent on the laser wavelength. This points to the already mentioned large, spherical particles, whose formation can be explained by a mechanism known as hydrodynamic sputtering [103].

In simplified terms, this process can be described by means of the effect of a laser pulse on matter. During the irradiation of a surface with a laser, a thin layer of molten material is formed, which is heated up very fast resulting in evaporation of the liquid matter. This sudden evaporation process causes a pressure gradient above the surface and the cloud of gaseous matter begins to expand.

The expansion of the plasma parallel to the melt surface excites microscopic waves. The effort to maintain a small surface and to reduce the amplitude of the waves

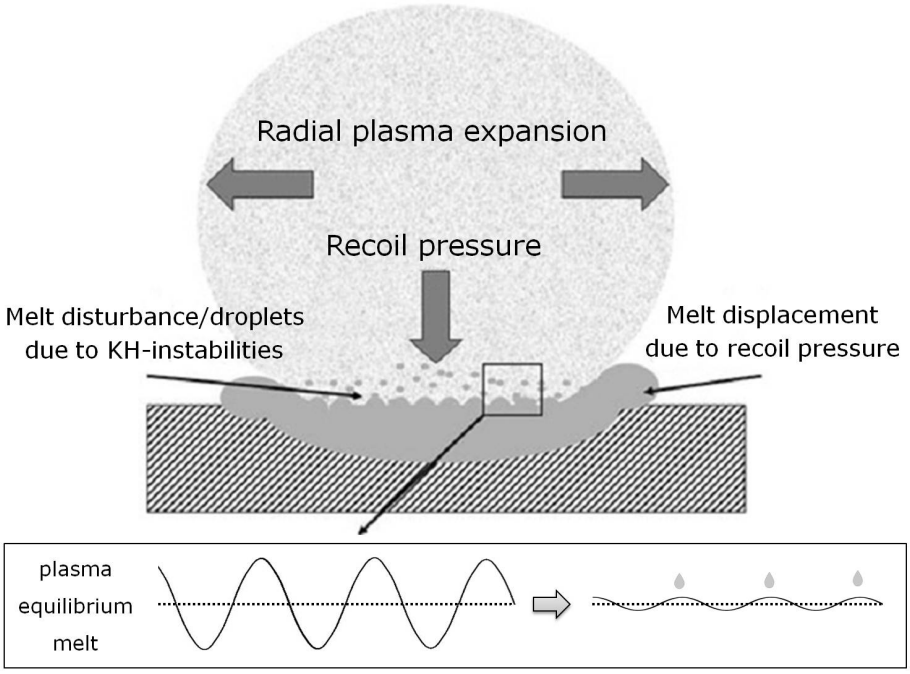

Figure 3.10: Particle formation by hydrodynamic sputtering due to Kelvin-Helmholtz-instabilities [103].

yields in so-called Kelvin-Helmholtz instabilities [134], which, under certain conditions, result in the ejection of a droplet from the wave crest. These are swept away by the expanding plasma gas and finally form part of the particle size spectrum (see *figure 3.10*). Particles formed in this way therefore arise from the melt and have a spherical shape. Their diameters range between 100 nm and approximately 1 μm and are limited by the thickness of the melt layer, as well as its viscosity. The formation is therefore dependent on the wavelength, as the thickness of the melt layer is determined by the laser wavelength [116].

The formation of the melt layer also depends on the pulse duration of the laser. For laser pulse durations in the range of the oscillation period of the atoms (femtoseconds) in the solid matter, the energy transfer is so quickly that almost no melt layer is formed and thus hardly any spherical particles are formed by hydrodynamic sputtering (see figure 3.6) [104].

Fractionation effects due to hydrodynamic sputtering

As already described in the anterior section, the fractional evaporation process of solids during the ablation leads to an enrichment of the more volatile elements in the gas phase, whereas the less volatile elements are concentrated in the melt layer. Since the mechanism of hydrodynamic sputtering yields large aerosol particles (0.1 to 1 μm)

originating from this melt layer, it can be explained, why in the particle size spectrum the large spherical particles are enriched with the less volatile elements [104]. This effect reduces the actual elemental fractionation, but cannot fully obliterate it. As a result of its dependency on wavelength and pulse duration, the particle formation by hydrodynamic sputtering cannot take place to the same extent as the formation of the primary particles. Additionally, the complete decomposition and ionization of the large spherical particles (>0.15 μm diameter) in the plasma of the ICP-MS is no longer guaranteed resulting in the so-called fractionation effect in the ICP. [135].

3.2.4 Aerosol transport

Two factors describe the transport of laser-generated aerosol into the plasma: the efficiency of the transfer and its velocity. Essentially, the transfer velocity depends on the gas flow rate, the volume of the ablation cell and the transport tubing length to the ICP-MS. The transfer efficiency of the aerosol is dependent on the particle size distribution, the carrier gas, the ablation cell design and the total transport distance. Early studies on the transport efficiency of laser-generated aerosols yielded somewhat inconsistent values ranging from 10% up to 60% for nanosecond laser systems. [83, 136]. For femtosecond lasers transport efficiencies in the range of 80% are reported [137, 138]. The causes of these large differences are treated in the following.

3.2.4.1 Particle size restriction and fractionation effects during transport

After the expansion of the laser-generated aerosol into the carrier gas the aerosol particles are accelerated in flow direction by friction with the gas molecules, until they all have the same velocity. Subsequently, the aerosol is transported out of the ablation cell through the transport tubing to the plasma. However, several factors prevent that particles of all sizes reach the plasma. These include diffusion, gravity and inertia of the particles.

The diffusion limits the transport of particles that are smaller than the mean free path of the gas particles of the carrier gas. Such small particles do not collide often enough with gas particles from the gas stream in order to be transported with the flow. For helium the mean free path at room temperature and ambient pressure is 200 nm and for argon approximately 72 nm [139]. The smaller the particle, the stronger the impact of this effect.

For particles in the μm range, gravity affects the efficiency of the transport. This phenomenon can be explained as follows: in horizontally positioned tubings, as they are common in the LA-ICP-MS, the maximum drop height from which a particle can

fall to the ground is determined by the inner diameter of the tubes. The particle settling velocity is constant and principally determined by its radius (besides constants, such as gravitational acceleration, viscosity and density of the carrier gas, as well as the density of the particles). The larger the radius, the faster the fall of the particle. In case that the vertical path covered by a particle along the entire horizontal length, is greater than the maximum drop height, the particle will be deposited of the inner surface of the transport tube and will not reach the ICP [140].

Assuming a 1 m long horizontal tube with an inner diameter of 4 mm and a gas flow rate (He or Ar) of 1 L min^{-1}, the calculated transport losses in dependence of the particle size and taking into account diffusion and gravitational losses can be represented as shown in *figure 3.11*.

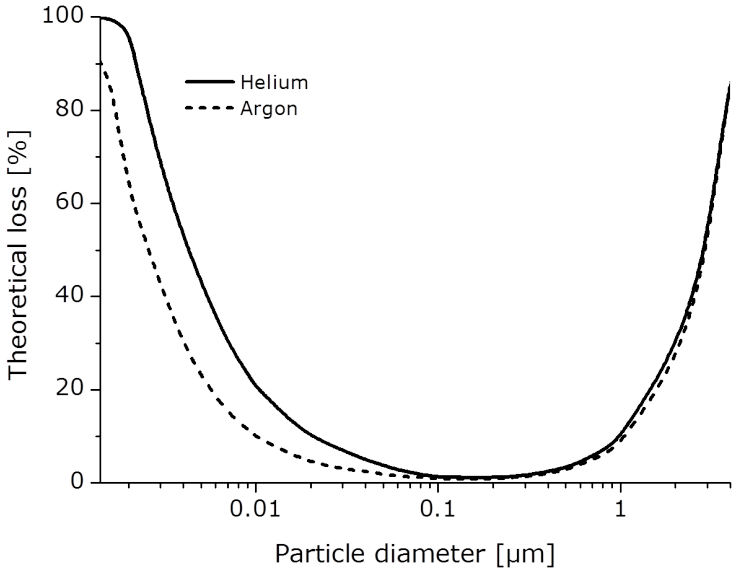

Figure 3.11: Theoretical transport loss of particles in a horizontal tube (length 1 m, inner diameter 4 mm) with argon and helium as transport gases (flow rate 1 L min^{-1}) in dependence on particle diameter [101].

Another reason for transport losses is the inertia of the particles. If the aerosol is directed through tight curves, large particles settle on the inner walls of the transport tube directed by the centrifugal force. This follows a similar mechanism as the gravity-related losses, but instead of gravitational acceleration, the centrifugal force due to the inertia of the particle accelerates the particles in the direction of the wall. Bigger particles have a larger moment of inertia and therefore are rather deposited on the walls than smaller particles.

As the chemical composition of the aerosol particles is dependent on the particle

size and differs from the original composition of the solid sample, a size-dependent transport ultimately affects the result of the analysis. This effect is called fractionation effect during the transport process. By the use of femtosecond lasers, the particle size distribution of the aerosol can be reduced so that only small size-dependent transport losses occur.

3.2.4.2 Carrier gas flow

The flow rate of the carrier gas is an essential parameter in the transport velocity and efficiency of the aerosol into the plasma of the ICP-MS, the temporal resolution of the aerosol composition, as well as the degree of decomposition of the particles in the plasma and hereby the signal stability. At low gas flow rates, the transport of the aerosol particles to the plasma takes longer, and thus, more particles can settle from the vapor phase onto the walls of the transport tube and are no longer detected by the mass analyzer. On the other hand, higher flow rates are favorable for high resolution time-resolved analyses, since the time for backmixing of the aerosol particles by diffusion is shorter. However, there is a threshold value, from which large particles can no longer be completely vaporized in the inductively coupled plasma. Too high gas flow rates reduce the residence time of the particles in the plasma so that they emerge from the plasma undecomposed and are deposited on the vacuum interface. This leads to poor signal stability [141].

Furthermore it is generally recommended to mix the helium aerosol with argon right before entering the plasma torch in order to abet the vaporization of the particles and the ionization of the atoms [131]. The sample aerosol-containing helium stream is introduced centrally into the torch so that the thermal energy of the ICP is transferred more efficiently to the outer borders of the sample aerosol. Due to the presence of argon in the center of the sample aerosol a more homogeneous energy distribution can be achieved resulting in a higher temperature in the analytical zone and thus, in higher decomposition efficiencies.

The flow pattern of helium for flow rates typically used in LA-ICP-MS (0.5 to 2 L min^{-1}) shows in general laminar behavior, which means, that there is no complete mixing of the aerosol throughout the entire ablation cell volume. In the case of short distances between ablation cell and the ICP (<20 cm) this can reduce the degree of aerosol homogenization resulting in higher standard deviations compared to the ones obtained under turbulent conditions [142].

When using argon instead of helium, a gas flow rate of >0.75 L min^{-1} and an inlet opening diameter of 0.5 mm, it is possible to create turbulent flow conditions in the ablation cell. Although this leads to an improvement in the precision of the results the washout times of the aerosol from the ablation cell are longer than under laminar flow conditions, resulting in a poorer temporal resolution of the element signal.

3.2.4.3 Ablation cell design

The design of the ablation cell is, apart the carrier gas flow rate, of great importance for a fast and efficient transport of the sample aerosol into the plasma of the ICP-MS. Crucial factors are here the shape and volume of the ablation cell itself, as well as the nature of the gas inlet (with or without nozzle). Together with the type of carrier gas and the gas flow rate, they determine whether there is a laminar or turbulent flow inside the ablation cell. In laminar flows obtained by using helium (see *figure 3.12*) a large part of the laser-generated aerosol is captured by the gas stream and directly transferred to the ICP-MS without any turbulences [142].

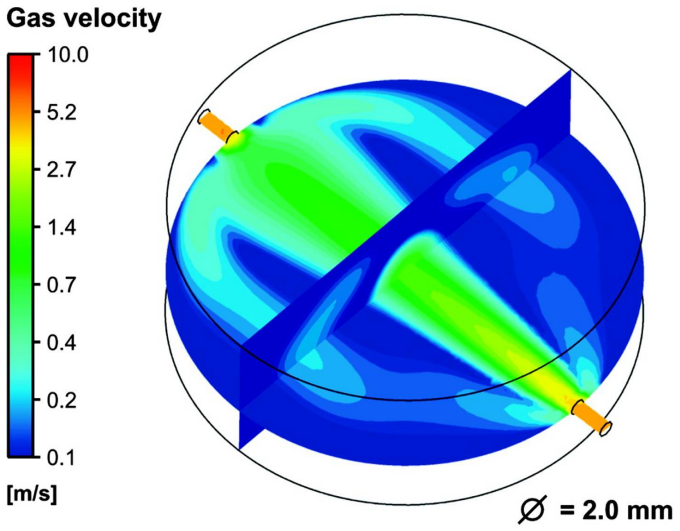

Figure 3.12: Simulation of the velocity field built up inside a cylindrical ablation cell (radius 22.5 mm, height 20 mm) equipped with inlet nozzles of 2.0 mm diameter assuming a helium flow rate of 1.0 L min^{-1} [142].

As a result, shorter washout times are achievable compared to turbulent flow conditions. However, under laminar conditions dead zones can occur, so that part of the sample aerosol settles out and is no longer transported and detected in the ICP-MS. Moreover, for laminar flow conditions and large ablation cells the transport efficiency of the aerosol is strongly dependent on the sampling position inside the cell [143].

The use of argon as ablation gas and by choosing the appropriate parameters (small inlet nozzles <1 mm, high flow rates >1 L min^{-1}) enables the generation of turbulent flow conditions in the ablation cell. Here, the laser-generated aerosol from one pulse is distributed all over the entire volume of the ablation cell and constantly transported out of the cell. The larger the cell volume, the longer it takes for the aerosol to be transported out of the cell.

In order to achieve turbulent flow conditions, the diameter of the inlet nozzle must be very small. This leads to higher gas velocities at the cell inlet and to faster homogenization of the aerosol in the entire cell volume. In this case, no dead zones are formed, so that the geometry of the cell has no influence on the washout times and aerosol recoveries.

Turbulent flow conditions are desirable, with regard the homogeneity of the aerosol, but not achievable with helium under normal conditions due to its low viscosity. Therefore, a trend towards new ablation cell designs can be noted where the formed aerosol is collected inside a small sampling tube which is placed directly above the sample surface [83, 95, 100, 137]. In that way, the effective volume into which the expansion of the aerosol takes place is kept as small as possible (see *figure 3.13*).

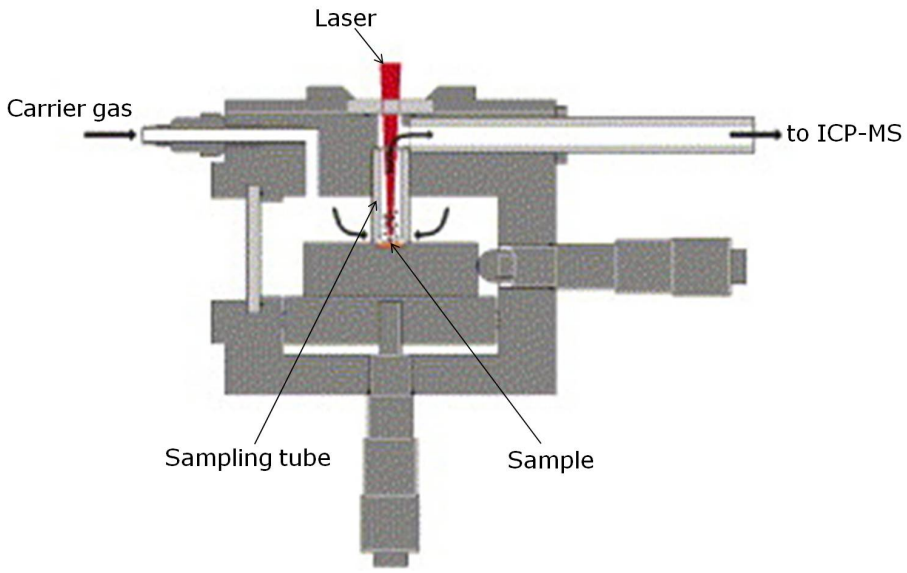

Figure 3.13: Schematic view of an ablation cell with sampling tube for fast aerosol transport. Adapted from [137]

This new design entails high transport efficiencies and avoids the formation of dead zones. In this way, extremely short washing times and high temporal resolution of the ICP-MS signal are achieved, enabling analyses with high spatial resolution and depth profiling analyses. The inner dimensions of the sampling tube must not fall below a

threshold value in order to avoid collisions of the expanding, liquid aerosol particles with the walls provoking their deposition.

Lindner et al. recently performed a theoretical simulation of the effect of an additional argon flow right above the ablation spot [100]. The ablation itself can take place in pure helium, but the subsequent transport is carried out with the help of argon, resulting in a better homogenization of the aerosol due to a more turbulent flow.

3.2.4.4 Transport tubing

The tubing length that connects the sample chamber with the ICP determines both the transfer time for the aerosol to reach the atomization source and the longitudinal diffusion (peak width). The longer the line, the later will the signal appear in the mass spectrometer and the broadened it will be.

Furthermore, the tubing length affects the transport efficiency, as there is an increased possibility that larger particles settle out due to gravity or inertia. As both effects have a greater impact on larger particles and the chemical composition of the particles is size dependent, greater tubing lengths also come along with higher fractionation effects. In general, it could be observed that up to a certain degree the deposited particles inside the transport tubings do not lead to any memory effects or contamination in subsequent analyses, as, once stuck to the tubing walls, they are not resuspended into the gas stream [143].

3.2.5 Quantification strategies in LA-ICP-MS

A major difficulty in laser ablation ICP-MS still is the correct and reliable absolute quantification of element concentrations due to the high matrix dependence of this form of sample uptake. In this vein, the use of internal standards (IS) is indispensable to improve the precision of the analysis. An internal standard is a known concentration of an element that is present in the sample that is analyzed. An effective IS should behave in a similar manner to the analyte during the ablation process, transport and in the ICP source. Additionally, it should be homogeneously distributed within the sample, which is one of the crucial requirements to obtain accurate measurements. For non-homogenized, solid samples, as they are often used in laser ablation analyses, the introduction of the aforementioned IS is normally not possible. Both in qualitative and quantitative elemental analyses by LA-ICP-MS, different IS have been investigated to account for matrix effects as well as for variations in ablated mass,

transported mass and instrumental drift normally present in laser-based analysis techniques.

Internal standardization can be performed for inorganic as well as organic or biological samples by monitoring an element already present in the sample, such as $^{43}Ca^{+}$ [144] or $^{13}C^{+}$ [145–147], respectively. If no homogeneously distributed element is available, the production of pressed pellets [148] or homogenized tissue standards [149] can be performed. In both cases, the internal standard is added to the homogenized sample in an adequate concentration. The complete homogenization of the sample is a crucial factor and can be laborious increasing the risk of contamination. Finally, another approach for the analysis of thin samples using LA-ICP-MS is the introduction of a standard directly under the sample and their simultaneous ablation [150]. Here, the ablation parameters must be chosen so that both layers are completely ablated.

Apart from the selection of an appropriate internal standard, the choice of an adequate quantification strategy is also crucial. Here several methods have already been described in the literature which can be mainly classified into calibration with solid or liquid standards (*figure 3.14*) and will be discussed briefly in the following.

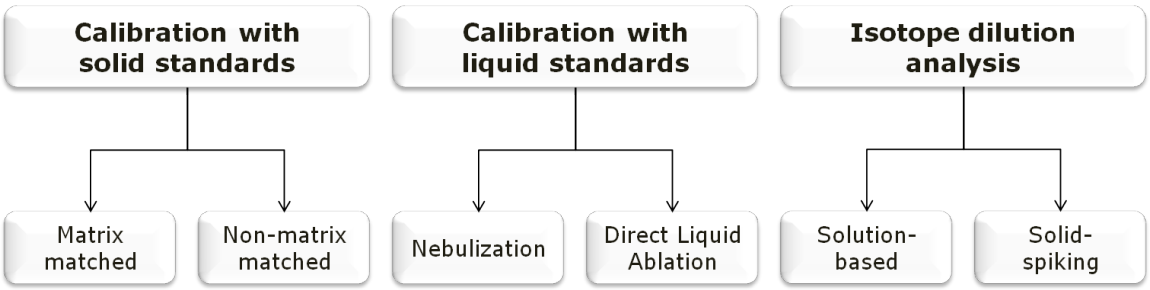

Figure 3.14: Classification of calibration methods used in LA-ICP-MS

3.2.5.1 Calibration with solid standards

Matrix-matched calibration

Most reliable quantitative studies are based on the use of matrix-matched standards using certified reference materials. As an example, the quantitative elemental determination in glass samples is performed using the widely-employed standard reference materials NIST 610 and NIST 612 [151]. Also the use of a CRM for single-point cali-

bration in the quantification of trace elements in sheep liver [152] or the preparation of pressed pellets of lyophilized CRMs for the quantification of Cu, Zn and Fe in rat brain [153] have been reported. Unfortunately, for the majority of solid matrices no certified reference materials are available.

When no adequate reference material is commercially available, matrix-matched standards can also be synthetically prepared. Here, two different strategies can be distinguished. Firstly, the standard addition quantification approach, which is a method often used in analytical chemistry where sample matrix also contributes to the analytical signal. It involves adding known amounts of the standards to aliquots of the processed sample. The sample matrix must not be changed, i.e. may not be significantly diluted by the addition of the standard. The measured intensities are then plotted *versus* the increasing concentrations of the standards, the Y-intercept being defined by the blank sample (aliquot of the processed sample without addition of standard). When the resulting regression line is extrapolated to zero intensity, the point of interception of the abscissa is the endogenous concentration of the analyte in the sample. This method provides excellent results if the increases of the standard concentrations are in the range of the real analyte concentration in the sample. The practical implementation of this calibration strategy for LA-ICP-MS analyses is hampered by a major difficulty: the introduction of the standards into the solid sample is usually difficult and sometimes even impossible. Thus, this strategy could only be applied in exceptional cases.

Similarly to the previously mentioned strategy, the preparation of synthetic matrix-matched standards is also used for the quantification by external calibration. Here, the production of pressed pellets [154], homogenized tissue standards [149] or fused glass beads [155] have been proposed. However, apart from a potentially time-consuming sample preparation step, these standards are prone to contamination and inhomogeneities of the added elements.

Non-matrix-matched calibration

The use of non-matrix-matched, solid standards has also been proposed [156, 157], although the expansion of the quantification approach to other matrices than the calibration standard is not advisable due to variations in the size classification of the aerosol particles and the high matrix dependence in general [158]. Here, the determination of conversion factors specific for each matrix and element are necessary in order to correlate the calibration signal to the sample signal. The determination

of such factors, however, is associated with a significant additional effort and must be repeated prior each new adjustment of the analytical parameters.

A promising, generally applicable method in order to overcome the calibration problems of LA-ICP-MS is the use of UV-fs-lasers [92, 93, 137]. The combination of short wavelengths with the short pulse duration results in a reduced matrix dependency to such extent, that a nearly matrix-independent calibration becomes possible [159, 160]. Additionally, the current development of this approach shows a trend towards shorter wavelengths, such as 266 nm [92, 161] and 196 nm [162]. An end of this development still does not seem in sight as the obtained results still present greater errors, than they occur in the analysis of liquid samples by ICP-MS.

A further, substantial drawback to this approach is the cost and the handling of UV-fs-lasers, as femtosecond lasers are usually extremely expensive ($>10^6$ Euro) and shorter UV wavelengths are not trivial to handle. In particular, the extreme absorption of wavelengths shorter than 200 nm extends to most substances, including commonly used optical materials, such as synthetic fused silica and air, so that the optical path of the laser beam needs to be flooded with a non-absorbing gas [118].

3.2.5.2 Calibration with liquids

Nebulization of aqueous standards

On-line solution-based calibration procedures have also been investigated for quantitative analysis [163–166]. The dual sample/standard approach was proposed to produce quantitative information in the absence of solid calibration standards: the laser-generated aerosol is mixed with the aerosol generated by nebulization of an aqueous calibration standard. Three different solution-based calibrations have been proposed:

- The nebulizer gas flow coming from an ultrasonic nebulizer is used as the carrier gas flow for laser ablation. During solution calibration the sample target is simultaneously ablated with a focused laser beam [163, 164].

- A micronebulizer is inserted into the laser ablation cell and standard solutions with increasing concentration are nebulized during the ablation of the sample [165].

- The dry aerosol produced by laser ablation of the sample and the wet aerosol generated by pneumatic nebulization of standard solutions are carried by two

separated flows of Ar and directly introduced in the injector tube of the ICP through two different apertures [166].

Several problems arise from the proposed solution-based calibrations and hamper their implementation in routine quantification analyses. The main drawback is that the ablation process itself is strongly matrix dependent and this is not taken into account by any of the proposed methods, since the calibration is carried out independently from the ablation. Those methods also do not consider the transport efficiency of the ablated material into the ICP and their subsequent decomposition and ionization, which have a direct impact on the signal intensity. Under constant ablation conditions, those methods could only allow a relative, secondary calibration. A further disadvantage is that those approaches change the plasma conditions to a wet plasma. As a consequence, oxide-based polyatomic interferences are produced, which in turn raise the need for high-resolution or collision cell-based ICP mass spectrometers.

A slightly improved quantification using liquid standards is achieved if a desolvation unit is connected to the nebulizer, transforming the wet aerosol into a dry one [167–169]. The quantification is carried out by the simultaneous measurement of the two mass flows (ablation aerosol and dried nebulizer aerosol). For an accurate quantification both mass flows must be known, which is particularly complicated for the ablation aerosol so that short-term fluctuations in the ablation cannot be corrected. In this vein, an in-line mass transport measurement cell can be introduced, which enabled the determination of the amount of debris transported to the plasma as the result of the laser ablation of a wide variety of samples [170].

Direct liquid ablation

In order to overcome the problems of interferences due to oxide formation reported for dual sample introduction systems and the heterogeneous trace element distribution in in-house manufactured solid standards, a new calibration approach has been proposed [171]. In this case, microliter quantities of aqueous solutions are introduced into a Teflon vessel covered with a plastic film and placed in the ablation chamber. The film is shot through with a number of laser pulses and the solution then directly ablated.

Summarizing, it can be said that, all mentioned calibration strategies are external calibrations, which are neither able to correct for inhomogeneities in the sample nor take into account the sampling rates or aerosol transport efficiencies.

3.2.5.3 Isotope dilution analysis

In the search for more accurate quantification strategies an alternative approach has been proposed for reliable quantitative analyses by LA-ICP-MS. Isotope dilution analysis (IDA) or isotope dilution mass spectrometry (IDMS) is a well-known analytical technique based on the measurement of isotope ratios in samples, where the isotopic composition has been altered by addition of a known amount of an isotopically enriched element. Since only isotope ratios (IR) are necessary for quantification, no external calibration or internal standardization is needed. Here, an isotope of the target element itself is used to correct for various types of disturbances before and during analysis, because the different isotopes of an element are expected to behave similarly (at least at the level of precision required for isotope dilution) and can be considered as almost perfect internal standards. Isotope dilution analysis is also known to be a very versatile technique as there are many examples for its use with various analytes and as well different instrumental techniques [172, 174].

All elements that have at least two stable isotopes (on the time scale of the measurement) and whose isotope ratio is determined exactly by mass spectrometry can be analyzed. To a sample of unknown concentration and generally natural isotopic composition a spike is given, which contains the sought element in a non-natural isotope ratio. After complete mixing of sample and spike the resulting altered isotope ratio can be determined exactly by mass spectrometry. The relationship between the amount of both components in the mixture and the isotope ratio can be expressed in the isotope dilution equation (see *equation 3.2*).

$$c_S = c_{Sp} \cdot \frac{m_{Sp}}{m_S} \cdot \frac{M_S}{M_{Sp}} \cdot \frac{A^b_{Sp}}{A^a_S} \cdot \frac{R_m - R_{Sp}}{1 - R_m R_S} \tag{3.2}$$

with: c_S: concentration of the sample
c_{Sp}: concentration of the spike
m_S, m_{Sp}: mass taken of the sample and the spike, respectively
M_S, M_{Sp}: atomic weight of the element in the sample and the spike, respectively
$A^b{}_{Sp}$: abundance of the enriched isotope b in the spike
$A^a{}_S$: abundance of the most abundant isotope a in the sample
R_m: isotope ratio (a/b) in the mixture
R_{Sp}: isotope ratio (a/b) of the spike
R_S: isotope ratio (b/a) in the sample

Thus, the concentration of the sample can be calculated with the known isotopic abundances of the sample and the spike, the concentration of the spike, and the measured isotope ratio of the mixed sample.

So far, the combination of LA-ICP-MS and IDA has been investigated for the direct determination of trace elements in a wide variety of solid samples (e.g., soils, coals, sediments, mosses, road dusts, hair samples, petroleum products, etc.) using two different strategies.

Solution-based isotope dilution analysis

Online isotope dilution analysis was performed by introducing a dry aerosol of a nebulized isotopically enriched spike solution into the ablation chamber during the laser ablation of the sample [175, 176]. However, as already discussed previously, such liquid-based methodology is only able to correct for errors derived from the detection step and not for those derived from the ablation processes.

Solid-spiking isotope dilution analysis

A different quantification methodology based on the addition of the corresponding isotope-enriched spike solutions to the powdered sample, and the subsequent drying and pressing of the isotopically enriched sample, has been widely investigated by the group of Heumann [148, 177–179]. This methodology allows the matrix-matched quantification of elemental concentrations without any external standard correction for all signal variations during the analysis, either derived from the instrumental drift or varying mass ablation rates. Nevertheless, the required addition, homogenization, and drying of the liquid spike solutions to each sample of interest increase considerably the total analysis time, particularly when a large number of samples have to be analyzed. To overcome the tedious synthesis process with the isotope-enriched spike solutions, an alternative sample preparation strategy has been proposed [180]. The direct and simultaneous determination of trace elements in soil and sediment samples was accomplished by fs-LA-ICP-IDMS with the development of a solid-spiking sample preparation procedure based on the synthesis of a unique isotopically enriched solid spike and the preparation of isotope-diluted blend pellets for each sample of interest.

Several drawbacks limit the application of this quantification strategy. On the one hand, the spiking of a solid with a solution can sometimes be troublesome since the analyte in liquid state can gradually concentrate due to solvent evaporation during the drying process. Even a thorough blending may subsequently turn out to be

insufficient, resulting in an inhomogeneous distribution of the analyte. Additionally, pelletization can prove difficult with certain matrices without the use of binders, which may represent a source of metallic contamination.

This quantification strategy by IDA is only valid for determinations of the total amount of the element of interest in a given sample. Nevertheless, it can also be used for the quantification of a specific species of interest, if the spike is added in the same chemical form, and only the isotope ratio for this species is determined experimentally. This so-called species-specific isotope dilution analysis requires the synthesis of the compound using enriched stable isotopes and its handling without possible contaminations with the element with natural composition. The main advantage of this quantification method is, that from the moment of complete mixture of the sample and the spike and therefore complete isotopic mixing, errors occurring during sample preparation (e.g. losses) or analysis (e.g. matrix effects, elemental fractionation during ablation) do not affect the accuracy of the analytical result, as all errors affect all isotopes in the same way and therefore do not change the finally measured isotope ratio [181].

3.3 Applications of LA-ICP-MS

Laser ablation ICP-MS is nowadays the most frequently used inorganic mass spectrometric technique for a fast and sensitive multielement determination at the trace and ultratrace levels, for speciation analysis, and for the precise and accurate isotopic analysis of a wide variety of solid samples [20–22, 78, 118, 160, 182–187]. This is demonstrated by a significant increase of LA-ICP-MS installations worldwide and, along with that, a rapid increase in the number of analytical publications on LA-ICP-MS for trace and isotope analysis in environmental materials, geological, biological and medical samples, in chemical and technical products, in nuclear and radioactive waste materials. Furthermore, LA-ICP-MS is being increasingly used for the characterization of high-purity materials (e.g. metals, alloys, semiconductors, insulators such as ceramic oxides, nitrides or carbides), which are very important for materials science [23, 71, 188–191].

As the main focus of the present doctoral thesis will be placed on biological samples, applications of LA-ICP-MS to this area will be described more in detail in the following.

Many efforts and advances have been made in the last years for a comprehensive study of metalloproteins as well as metal- or heteroatom-containing proteins, basically dealing with the structures and functions of the metal sites as well as the biological implications of those metal/heteroatom-biomolecules interactions. The great challenge in this research area is the combination of specificity of analytical response with the different element species and sensitivity. The latter can cause difficulties because of the complex composition of biological samples, the low concentration level of the species of interest and, additionally, the very small volumes to analyze. Therefore, the use of analytical techniques with high spatial resolution as well as high sensitivity for metal determination is indispensable.

Biological metal-relevant information can be addressed at different levels. Most often trace elements are determined in the bulk of biological material after homogenization of the sample of interest, and often, after acid digestion. This approach is as frequent as useless in most of the cases because it ignores not only the speciation of an element but also its spatial distribution. It could be stated that the meaning and value of trace element relevant information in biological environment increase with the sampling resolution and, therefore, strong requirements on both the sensitivity and the spatial resolution of the detection technique have to be settled [192, 193]. In this sense, LA-ICP-MS has been established during the last decade as a powerful tool for the elemental analysis within biological and medical samples because of its excellent analytical performance. Here, two types of approaches can be distinguished: the analysis of proteins after their separation by gel electrophoresis and the qualitative and quantitative imaging of elements in biological tissues. In the following sections both strategies will be revised.

3.3.1 Detection of proteins after gel electrophoretic separation

The main analytical tools for the analysis of proteins include chromatographic or electrophoretic separation of the target biomolecules and their subsequent identification by molecular MS techniques, using both an electrospray (ESI) or a matrix-assisted laser desorption ionization (MALDI) source [194, 195]. Several alternative strategies have been developed to investigate the chemical speciation of the metal bound to the protein, including LA-ICP-MS in combination with a high resolution separation technique. Gel electrophoresis (GE) , with its unique ability to resolve thousands of proteins in a single run, is a powerful tool routinely used in biochemical, medical and molecular biology laboratories today. Traditionally, detection of the metals of interest relied on autoradiography, so radioactively labeled metals have to be used.

Alternative techniques have been investigated for the detection of metals in the gels [196] and, in this sense, the potential of LA-ICP-MS was successfully demonstrated for the detection of phosphorylated proteins, selenoproteins and other metalloproteins [197–199]. Error sources in GE-LA-ICP-MS analysis can be related, both to the behavior of the species of interest during sample preparation and electrophoretic separation processes, as well as to the laser-matter interaction. A significant number of studies were dedicated to the optimization of the effective separation of metal-binding proteins (e.g. their stability during GE and post-separation gel treatment); however, accurate quantitative analysis still remains an important challenge and, as yet, there is no consensus regarding a preferred calibration approach.

Table 3.3 gives an overview of some selected LA-ICP-MS applications for the detection of heteroatom- or metal-containing proteins after gel electrophoretic separation. Additionally, if no detectable element is present in the sought biomolecule, labeling strategies can be employed.

3.3.1.1 Analysis of heteroatom-containing proteins

The first work dealing with basic studies on the detection of trace elements in gels after an electrophoretic separation using LA-ICP-MS was published in 1998 by Neilsen et al. for the analysis of Co binding serum proteins [81]. Since its introduction, GE-LA-ICP-MS has been applied for qualitative and quantitative analysis of different types of proteins. A substantial part of the applications deals with heteroatom-containing proteins, such as selenoproteins [198, 200–208] and phosphoproteins [209–213]. Some of these works will be revised in the following.

Chéry et al. [200] studied the capabilities of LA-ICP-MS for the detection of selenoproteins in red blood cells extracts and in yeast after one- and two-dimensional (1D and 2D) separations using polyacrylamide gels (PAGE). Limits of detection, linearity and repeatability were evaluated for a whole range of elements by using hydrated gels with standard solutions, showing that detection can be at least semi-quantitative (a linear dependence of the signal with concentration was observed).

An alternative approach for the detection of heteroatom-containing proteins by LA-ICP-MS is the use of GE in combination with electroblotting onto nitrocellulose or polyvinyl difluoride (PVDF) membranes. In such a way, proteins can be detected not only directly in agarose or polyacrylamide gels but also after blotting onto membranes.

Table 3.3: Selected applications of GE-LA-ICP-MS.

1D-GE	*2D-GE*	*Blotting*	*Mol. MS*	**Element**	**Material/Matrix**	**Reference**
				Heteroatom-containing proteins		
✓				Se	Protein standard	[198]
✓	✓			Se	Red blood cells, yeast	[200]
✓				Se	Protein extracts (fish, bird)	[201]
✓	✓			Se	Yeast	[206]
✓		✓		Se	Protein standard, cell lines	[205]
✓		✓		P	Protein standard	[209]
✓		✓		P	Bacterial & eukaryotic cytoplasma	[211]
✓		✓		P	Protein standard	[212, 213]
✓		✓	✓	Se	Human plasma	[208]
✓			✓	Se	Protein extracts (fish)	[207]
	✓		✓	Se	Yeast	[202, 203]
✓			✓	Se	Protein standard	[204]
	✓		✓	P	Protein standard, human serum	[210]
				Metal-containing proteins		
✓				Zn, Cd	Plant	[214]
✓				S, Fe	Protein standard	[215]
✓				Cu, Zn	Protein standard	[216]
	✓			Al, Si, P, S, Cu, Zn	Protein extracts (human brain)	[197]
✓			✓	Cr, Fe, Ni, Cu, Zn, Cd, Pb	Protein extracts (rat kidney, liver)	[217]
✓			✓	Cu, Zn	Protein standard	[218]
✓			✓	Pt	Cell lines	[219]
	✓		✓	P, Fe, Cu, Zn	Yeast	[220]
	✓		✓	Na, Mg, Ca, Ti, Fe, Zn, Sr, Ag	Human serum	[221]
	✓		✓	P, Cu, Zn, U	Protein extracts (human brain)	[222–224]
	✓		✓	Mg, Cu, Zn, Ag	Plant	[225]
				Labeled proteins		
✓		✓		Au	Cells	[79]
✓				Hg	Protein standard	[226]
✓		✓		I, Lanthanides	Protein standard	[227]
✓		✓		I, Eu	Microsomes	[228]
✓		✓		Lanthanides	Microsomes	[229]
✓		✓		I	Protein standard	[230]
✓		✓		I	Protein standard, microsomes	[231]
✓		✓		Eu, Tb, Ho	Protein standard	[232]

This strategy looks promising, particularly for the analysis of phosphoproteins: a trace matrix separation can be achieved to reduce blanks from buffers used for sample preparation (e.g. in SDS-PAGE) and the proteins are enriched in a thin surface layer which is auspicious for laser ablation analysis. Nevertheless, losses during blotting are often mentioned as a limiting factor [233]. Krüger et al. [211] investigated the analysis of protein phosphorylation stoichiometry comparing two analytical strategies: the combination of 1D-GE, protein blotting onto PVDF membranes followed by the analysis by LA-ICP-MS, and the combination of 1D-GE, in-gel digestion of the protein spots with subsequent analysis by capillary liquid chromatography ICP-MS. Both strategies were evaluated with standard phosphoproteins and applied to the analysis of cytoplasmatic proteome of bacterial and eukaryotic cells, showing consistent quantitative results. For LA-ICP-MS analysis, the surface of the blot membrane was scanned line by line with the laser beam in order to simultaneous monitoring ^{31}P and ^{34}S; 2D images were obtained from the analysis of the PVDF-blot, which were equal to results obtained by conventional staining techniques. One intense and one faint band were visible in the ^{31}P image, indicating that the corresponding proteins were phosphorylated. The phosphorylation stoichiometry was then calculated from the integral of their ^{31}P and ^{34}S signals and, in contrast to ICP-MS analysis, the sensitivity for ^{31}P and ^{34}S detection was constant over the whole blot. Recently, the analysis of protein blots by LA-ICP-MS has been employed for the detection of phosphoprotein standards [212, 213] and selenium-containing proteins in African catfish [207]. In all cases the authors indicated a favorable ablation of the blotting membranes due to lower volumes introduced into the ICP-MS and the higher surface density of the analytes. Nevertheless, significant differences in signal intensities between membranes were found and, therefore, sample preparation procedures need to be carefully optimized.

Most of the developments in the area of protein research would not have been possible without the combination of both inorganic and organic MS techniques. These latter are characterized by the soft ionization of the analyte, allowing the transfer of ionized large biomolecules into the gas phase and their posterior analysis by MS. Nowadays, it is possible to find a large number of applications related to a multidimensional approach, which can be briefly described throughout the following steps:

- Separation of proteins by 1D or 2D-GE
- Specific detection of heteroatoms or metals in the gels spots by LA-ICP-MS
- In-gel trypsin digestion of the spots of interest
- Identification of peptides by ESI-MS or MALDI-MS.

Thus, it is possible to carry out not only the detection of heteroatom or metal-containing proteins in the samples of interest but also the identification of the proteins.

Concerning selenoproteins, Ballihaut et al. [194] discussed in a review article the recent advances in MS techniques for the detection and identification of this type of proteins after separation by GE. In this case, the use of an ICP-MS equipped with a collision cell was essential to allow interference-free detection of the most-abundant ^{80}Se isotope, which, in turn, is the prerequisite of attaining detection limits for selenium in the low ng g^{-1} range. The authors demonstrated that the ablation of the protein spots was a linear function of the concentration and that quantification could be carried out using external calibration without the need for more sophisticated strategies. On the other hand, the efficient extraction of selenium-proteins from the gel and their identification by organic MS techniques is difficult due to the poor ionization of selenomethionine-containing peptides and the rich isotopic pattern of Se. In any case, it should be stressed that GE-LA-ICP-MS has been efficiently applied for the qualitative and quantitative detection of selenium-containing proteins in several applications [203–205, 208, 234].

Besides MALDI-MS, the use of electrospray MS for protein identification after electrophoretic separation has been rapidly growing. In this vein, a novel integrated approach for the analysis of intact yeast selenium-containing proteins purified by GE was proposed [202] consisting of three stages: high-resolution 2D-GE for establishing high-reproducible reference proteins map, LA-ICP-MS for Se detection and, finally, ESI-MS for proteins identification. In such a way, up to ten selenium-containing proteins were successfully characterized in the mass range 9-20 kDa. However, several limitations were found for the proposed methodology related to the low concentration of selenoproteins and to the fact that intact proteins with masses greater than 20 kDa were difficult to extract from the gels (and also to analyze by ESI-MS due to decreasing signal intensity and mass accuracy for large masses). Therefore, although LA-ICP-MS allows the rapid detection of selenium-containing proteins in the gel spots, the proteins identification by molecular MS techniques still requires the use of multistep sample preparation or pre-concentration procedures.

3.3.1.2 Analysis of metal-containing proteins

In all previously mentioned applications, the sought elements are incorporated in the protein structure and, therefore, the heteroatom-protein binding is not broken during

electrophoretic separation. However, metal-binding proteins in which the metal is not covalently bound can undergo loss of the metal during electrophoretic separation (especially using denaturing PAGE) being this a serious pitfall that researchers have to face. Therefore, the development of new strategies for the separation of proteins without breaking the metal-protein bond or, at least, the use of accurate and precise quantification strategies able to correct the possible losses are necessary.

Several authors reported studies on metal losses in proteins during GE [206, 214, 215, 217, 235]. In most cases, the use of native PAGE instead of denaturing PAGE was proposed as the best option to minimize the possible losses. McLeod's group [235] investigated the behavior of Pt-serum binding proteins by LA-ICP-MS after both native and denaturing PAGE. As can be seen in *figure 3.15*, representative Pt signals were obtained for the proteins of interest using native PAGE, whereas no signals were found after denaturing separation conditions.

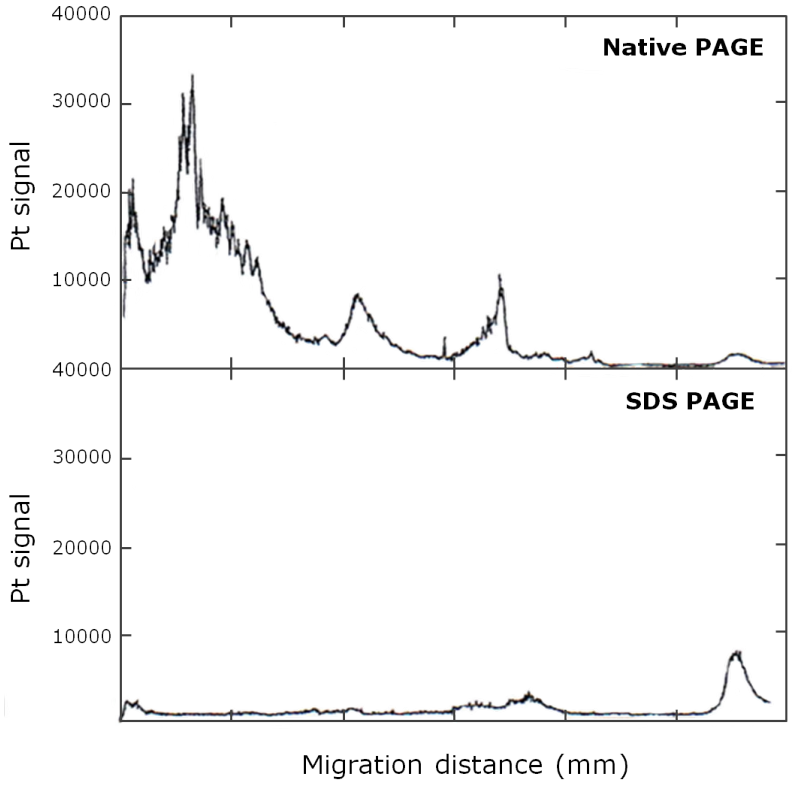

Figure 3.15: ^{195}Pt profiles obtained by LA-ICP-MS from the analysis of a Pt-enriched blood serum sample using native and denaturing PAGE [235].

These results showed that metalloprotein complexes may have limited thermodynamic stability and, therefore, they should be studied under native rather than denaturing conditions. This finding was confirmed by a different study, where the use

of native PAGE, such as Blue Native (BN) PAGE, where all denaturing agents are left out of the GE, was found to avoid possible vanadium losses of serum proteins [206]. In this vein, the use of BN PAGE separation conditions allowed also a fast detection of several essential and toxic metals in small amounts of rat kidney and liver samples by LA-ICP-MS [217]. The dried gels were analyzed in single line scan modus by LA-ICP-MS and Cu, Zn, Cd, Cr, Fe and Pb were easily detected in the separated protein bands of BN gels. For rat kidney proteins, together with the occurrence of Zn and Cu traces of Cd and Pb were observed at 65 kDa, whereas in the BN-PAGE from the rat liver sample Zn, Cu, Fe and Cr were detected in different proteins. Moreover, Jakubowski et al. [214, 215] investigated the ability of LA-ICP-MS for the analysis of Cd- and Zn-binding proteins in plant samples and Fe-containing proteins (cytochrome C, hemoglobin, transferrin and ferritin) after both anodal native and denaturing PAGE. Results showed that denaturing PAGE was unsuitable for the absolute quantification of proteins via the metal due to its partial loss during separation. Although anodal native PAGE, which preserves the native protein structure, is a powerful alternative it has to pay the cost of molecular weight calibration.

Not only 1D electrophoretic separation can be employed for the analysis of metalloproteins by LA-ICP-MS; Human brain proteins [220, 222, 224] and yeast mitochondrial proteins [80] were analyzed by LA-ICP-MS after 2D isoelectric focusing/sodiumdodecyl sulfate (SDS) PAGE and 2D BN/SDS-PAGE. The authors demonstrated that stable metal-protein complexes can survive denaturing and reducing conditions during the separation of proteins in the second dimension, but also that these conditions partly release the naturally bound metal ions of non-stable metal-complexes.

On the other hand, tracer experiments were also performed by GE-LA-ICP-MS to study the formation ability of bovine serum proteins to exchange Zn and Cu as a function of time by using an isotopic enriched ^{65}Cu spike [218]. 1D-BN-PAGE gels with separated bovine serum proteins were doped with an enriched isotope copper tracer. Results showed that the exchange of Zn bonded to bovine serum albumin by Cu takes place in a short time of about 1 min. Therefore, it could be concluded that the binding of Cu with BSA seems to be more stable than the binding with Zn and that the exchange of Zn with Cu is a very fast reaction. Such metal exchange was also observed for tau protein isoforms as a target protein in Alzheimer's disease [216]. Enriched isotope tracers (^{65}Cu and ^{67}Zn) were doped to 1D gels of separated tau protein isoforms after GE and ^{65}Cu/^{63}Cu and ^{67}Zn/^{64}Zn isotope ratios were measured by LA-ICP-MS in several protein bands. The isotope analysis by LA-ICP-MS

indicated certain proteins with a natural isotope composition of Cu or Zn. Furthermore, Cu-containing tau protein isoforms with a changed $^{65}Cu/^{63}Cu$ isotope ratio in comparison to the isotope composition in nature were also determined, indicating an isotope exchange of Cu containing tau protein isoforms during the tracer experiments. Therefore, it can be concluded that the formation of new metal-containing tau protein complexes during the tracer experiments in the 1D gel had occurred. The identification of the tau protein isoforms was carried out by MALDI-MS after tryptic digestion of the protein gel bands. In this case, no metal containing proteins were identified in the mass spectra, being this attributed to the fragmentary sequence coverage of the tryptic peptides of tau proteins isoforms eluted from the gel band.

As already described for the heteroatom-containing protein, the subsequent identification of the proteins after in-gel tryptic digestion by molecular MS is also performed for metal-containing proteins. The separation of yeast mitochondrial proteins was investigated by 2D-GE and, subsequently, LA-ICP-MS was successfully used to rapidly screen for the presence of P, Fe, Cu and Zn in the different spots of the gel [80, 220]. Next, the phosphorus containing proteins were identified by MALDI-MS. The complementary data obtained from both techniques showed to be particularly valuable for the identification of complex protein mixtures. In this particular case, the identification of subunits Atp1p and Atp2p of the ATPase was performed, being the results confirmed by Western blot analysis using antibodies directed against phosphorylated amino acids. The same authors have utilized the combination of atomic and molecular MS techniques for the identification and characterization of several human proteins from Alzheimer's disease brain [222, 223]. After separation of a brain protein mixture by 2D-GE, the protein spots were screened by LA-ICP-MS in respect to P, S, Cu, Zn and Fe content. Then, several selected protein spots were excised and analyzed by MALDI-MS after tryptic digestion. In such a way, the characterization of human brain proteins in respect to their structure, sequence, phosphorylation state and metal content could be carried out. *Figure 3.16* collects a schematic diagram with the techniques employed for the analysis of the proteins as well as the information obtained with each of them.

Recently, such multidimensional strategy was applied to a study where serum samples from untreated bipolar disorder patients were compared to those from patients treated with Li and also to control individuals [221]. The serum samples from these three groups were pooled according to their category, separated by 2D-GE and, then,

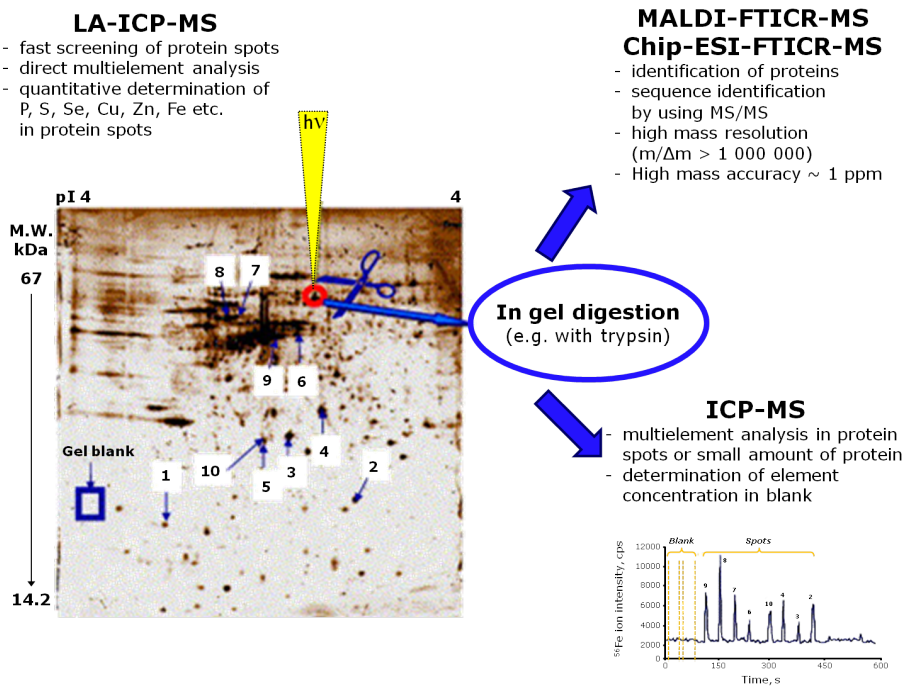

Figure 3.16: Schematic diagram with mass spectrometric techniques used for protein analysis in 2D gels of Alzheimer's disease brain proteins, including transient signals obtained by LA-ICP-MS for $^{56}Fe^{+}$ in selected proteins spots and blank [223].

scanned by LA-ICP-MS to determine the metals bound to the protein spots. Three ablation strategies for metal detection in proteins were tested, including imaging, line scan through the spots and micro-local analysis of the spots. The imaging mode was found to be advantageous for allowing the visualization of Ag, Mg, Zn, Fe, Ca, Na, Sr, and Ti distributions along the proteins contained in a gel region. Moreover, 32 serum proteins associated with the metals previously detected by LA-ICP-MS were identified by MALDI-MS. Results showed that, comparing control and bipolar disorder patients, a differentiation was observed in terms of metals bound to proteins (e.g. Mn was only detected in the control group, whereas K and Ti were only found in the bipolar disorder patient groups) by using LA-ICP-MS and MALDI-MS as complementary techniques.

Following a similar procedure, the potential of LA-ICP-MS together with ESI-MS for the detection and identification of protein drug targets from whole cell systems was investigated [219]. Proteins from Escherichia coli cells, which had been incubated with cisplatin, were partially separated by GE and the gel lanes were then scanned by LA-ICP-MS. Platinum distribution through the gel was found to be not proportional to the distribution of protein, suggesting that this element has, to some extent, specific protein targets within the cell. Next, the band with the highest Pt content relative

to the amount of protein was selected for peptide fingerprinting by ESI-MS (after the band was excised from the gel, digested with trypsin and the resultant peptides extracted). The masses and sequences of these peptides were combined to produce a peptide fingerprint indicating that a single protein was present in the gel fragment, which was unambiguously identified as Outer Membrane Protein A.

3.3.1.3 Elemental tagging for proteins

As has been previously described, LA-ICP-MS technique has been successfully used for the measurement of heteroatoms which are directly associated with proteins in tissues in a wide variety of applications. In order to apply this technique for the analysis of biomolecules which do not have detectable elements naturally present in their structure, labeling strategies with metal or heteroatom tags can be employed as a promising tool [199, 236, 237]. Different approaches have been investigated for specific detection of proteins, such as labeling with antibodies or metal chelates and by using covalent-bound labels. Although there are many examples of elemental labeling for quantitative peptides and protein analysis by ICP-MS so far, investigations to assess the analytical performance of LA-ICP-MS in combination with those approaches still are scarce.

Bettmer et al. [236] have recently revised the ability to specifically mark antibodies with an element for the use of ICP-MS as detector in immunoassays. This strategy was firstly described by Zhang et al. [238] for the determination of thyroid-stimulating hormone in human serum. Lanthanides are the most widely used elements for this type of studies because of their absence in biological systems and the high stability of their complexes. Waeting et al. [227] investigated the labeling of three different polyclonal antibodies with iodine and lanthanides for detection of the elements by LA-ICP-MS on Western blot membranes. Results showed that only the labeling of antibodies using p-SCN-Bn-DOTA lanthanide chelates could be applied successfully in the Western blot approach, whereas for iodine an unspecific binding and a too low sensitivity was observed. An alternative to this method is the use of metal cluster as the antibody tag, which can increase the detection limits in LA-ICP-MS measurements increasing the number of metal atoms used in the cluster. Müller et al. [79] employed gold cluster labeled antibodies for the determination of Mre11, a protein involved in DNA-repair mechanisms. In this study, the separation of proteins of cell lysates by 1D-GE was followed by a transfer to a blotting membrane and protein marking with antibodies, which were covalently attached to gold nanoparticles, be-

fore LA-ICP-MS analysis.

The feasibility of selecting elemental tags which do not produce interfering signals during analysis allows also the possibility to perform two or more analytical determinations simultaneously in one sample [239, 240]. The potential of immunoassays with element-tagged antibody (or antigen) in combination with LA-ICP-MS detection for multiplexing assay has been demonstrated in several applications [227–229]. Waeting et al. [229] presented a method for the multi-parametric and simultaneous quantitative determination of several cytochromes P450 in liver microsomes of both untreated and induced treated rats (with different chemicals, including carcinogens and drugs) by LA-ICP-MS. Liver microsomal proteins were separated by SDS-PAGE and subsequently blotted onto nitrocellulose membranes. Resultant blots were simultaneously incubated with 5 different lanthanide labeled antibodies, using an additional one as IS. Subsequently the lanes were ablated by the laser beam and analyzed by ICP-MS for ^{165}Ho, ^{169}Tm, ^{175}Lu, ^{153}Eu, ^{159}Tb and ^{141}Pr. In such a way, multiple isoforms of cytochromes P450 enzymes were quantitatively and simultaneously determined by LA-ICP-MS.

In some specific applications the use of a high-resolution separation technique can be circumvented. Here, protein microarrays provide a powerful multiplexing approach to detect proteins, monitor their expression levels as well as to investigate protein interactions and functions. The potential of LA-ICP-MS in combination with protein microarray technology and multielemental tag of immunoassay was recently explored for the detection of three model proteins [241]. In this study, α-Fetoprotein IgG (AFP), carcinoembryonic antigen (CEA) and human IgG were identified on the basis of sandwich-type immunoreactions on a microarray with Sm^{3+}-labeled AFP, Eu^{3+}-labeled CEA and Au nanoparticles-labeled IgG as labeled antibodies, respectively. *Figure 3.17* shows a scheme of laser ablation sampling for multiple analytes on each spot of a microarray and the transient signals of mixing element-tagged antibodies obtained by LA-ICP-MS from spots of dried droplets on a glass slide. Experimental results proved that LA-ICP-MS can determine multiple proteins from each spot of the microarray with a spatial resolution at micrometer range. Additionally, it was observed that the sensitivity of the proposed method (detection limits in the range of 0.012-0.2 ng mL^{-1} at the concentration of 1.0 ng mL^{-1} of proteins) could be further increased if all of the tags were nanoparticles instead of rare-earth ions.

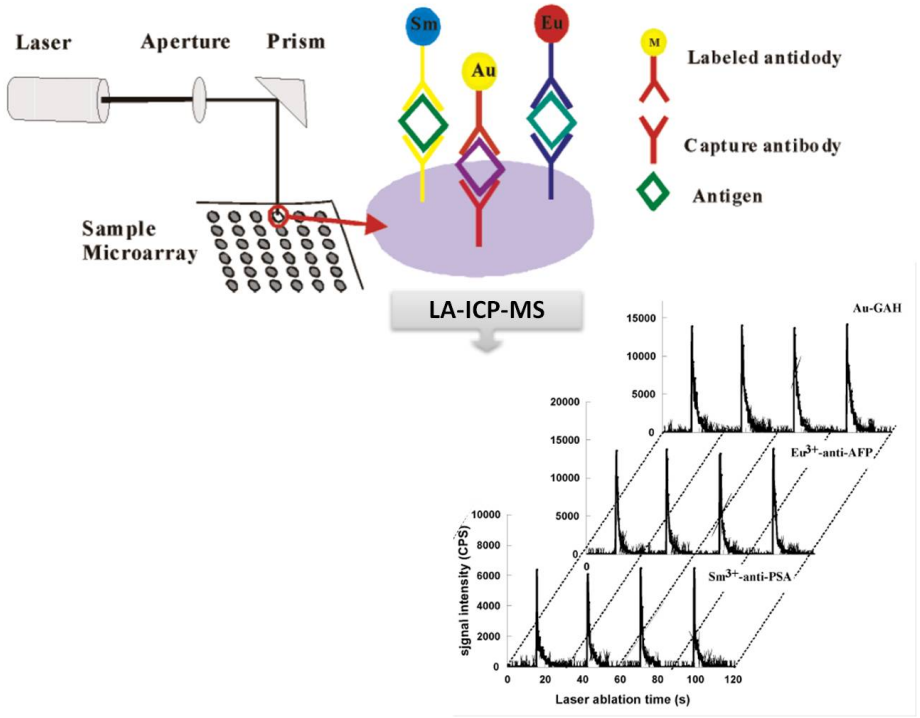

Figure 3.17: Scheme of a laser ablation sampling from a microarray with multiple analytes on each spot, and transient signals of mixing element-tagged antibodies obtained by LA-ICP-MS from spots of dried droplets on a glass slide: Eu^{3+}-labeled anti-AFP, Sm^{3+}-labeled anti-PSA (prostate-specific antigen) and colloidal Au-labeled GAH (goat-anti-human IgG) [241].

Beside the use of element-tagged antibodies, protein labeling can also be performed by using small molecules that form covalent bonds. Protein iodination has proved to be a simple, cheap and efficient method for labeling by covalent binding of heteroatom to a protein. Different protocols for protein iodination have been applied for the detection using LA-ICP-MS of intact proteins separated by SDS-PAGE and electroblotted onto nitrocellulose membrane [230, 231]. The efficiency iodination of single proteins (lysozyme, BSA, cytochrome C450 and β-casein), whole proteome (microsomal proteome of rats) and antibodies (anti-bovine casein, anti-BSA) with potassium triiodide has been demonstrated with minimal losses of antigen properties and antibody binding to iodinated proteins [231]. Moreover, compared with previous experiences applying lanthanide labeled antibodies for detection of antigens, the labeling of a whole proteome or of molecular weight markers looks very promising just to have all relevant information measured simultaneously by LA-ICP-MS.

On the other hand, mercury tag can be also employed for protein derivatization since mercury can form highly-stable covalent bonds with free sulfhydryl groups in proteins. Recently, Kutscher et al. [226] studied the potential of mercury tag for

the sensitive detection of ovalbumin protein from PAGE gels after reaction with p-hydroxymercuribenzoic acid (pHMB) using LA-ICP-MS. For quantification purposes, the use of label-specific IDMS (using ^{199}Hg enriched pHMB) was found to improve precision and accuracy of the results.

An alternative approach for specific detection of proteins is the labeling with metal chelates. A metal ion can be attached to a biological molecule via bi-functional chelating agents, which contain a metal chelating group and a second functional group capable of forming a covalent union to the desired molecule. Among several metal chelates described in the literature, lanthanide DOTA chelate (1,4,7,10-tetraazacyclododecane-1,4,7,10-tetraacetic acid) seems to be the most versatile [199]. The use of such chelate has been successfully applied for multi-element labeling of proteins separated by SDS-PAGE [232]. Detection was performed by LA-ICP-MS after electroblotting of the target proteins onto nitrocellulose membranes. Two different proteins (BSA and hen egg white lysozyme) were labeled with the commercially available chelating compound DOTA containing stable isotopes of Eu, Tb and Ho. Compared to previous strategies reported using iodine [230], the one described in this work was found to be more laborious and time-consuming, but it was convincing because it can be applied for development of multi-element labeling procedures of proteins (and antibodies).

Summarizing, it can be said, that the high sensitivity and spatial resolution, absolute quantification capability, robustness and ability to carry out isotope ratio measurements with great accuracy open new avenues to LA-ICP-MS applications in protein analysis. In fact, information provided by LA-ICP-MS has demonstrated to be complementary to that achieved by present molecular MS instruments. Finally, it should be highlighted that the combination of LA-ICP-MS and protein fingerprinting methods contributes to overcome some of the current limitations of common proteomics approaches.

3.3.2 Elemental imaging of biological tissues

Bioimaging analytical techniques are today of key interest in life science studies and have been rapidly growing in biological and medical applications. In recent years, LA-ICP-MS has demonstrated its huge ability as an alternative tool, capable of delivering both qualitative and quantitative imaging of elements (especially metals) in biological tissues [22, 242, 243].

3.3.2.1 Elemental bioimaging of soft tissues

The first work dealing with the analysis of fresh soft tissue samples by LA-ICP-MS was published in 2002 for the analysis of thin sections of lamb's liver and kidney [152]. The proof-of-concept of 2D mapping of biological tissues by LA-ICP-MS was next reported for the analysis of Cu and Zn in thin sections of sheep liver [147]. Two different ablation modes were investigated; raster scans of single shots or linear scans, in which the laser moves with a certain speed while ablating. In general, the line scan takes more time and more material is ablated and transported into the ICP plasma. The maximum resolution for the raster scan is $\sim$10 μm, whereas for the line scan the resolution depends on the scan speed and data acquisition. The use of carbon as an IS was tested because its content in dry mass of tissues is reasonably constant; this allows correction for differences in the laser fluctuation, surface roughness and changes in the absorption coefficient of the tissue. Results showed that the use of carbon improved the precision of Cu and Zn measurements around a 1.5-fold factor. Moreover, the ability of LA-ICP-MS for elemental bioimaging in biological tissues was proved, showing the potential of this technique for the determination of small changes in the elemental concentration as well as the non-uniform spatial distribution of the elements.

Since its introduction, the application of LA-ICP-MS for the study of elements distributions in soft matrices (e.g. mouse kidney and hearth tissues [244, 245], human lymph nodes and respiratory tissues [145, 246], liver biopsy, breast cancer and prostate tissues [247, 248]) is continuously growing. It is well-known that platinum complexes are currently used for the treatment of several types of cancer and, therefore, micro-local analysis of platinum distribution in tissue sections may contribute to the optimization of platinum therapies. In this vein, 2D imaging of Cu, Zn and Pt distribution in kidney tissues from a mouse 60 min after injection of cisplatin by using LA-ICP-MS was reported [244]. The results showed that Cu was enriched in the capsule and outer cortex, Zn in the inner part of the cortex composed of tubules and the Pt concentration followed a centripetal gradient with clear medullar enrichment. Thus, it was demonstrated that scanning LA-ICP-MS may be helpful in the development of new platinum complexes for the treatment of various cancers.

Concerning the analysis of cancerogenous tissues, the potential of elemental bioimaging by LA-ICP-MS was demonstrated for the identification of metastatic melanoma within single lymph nodes of human tissues according to relative trace element con-

centrations [145]. Construction of 2D maps presented as single elements or ratios of elements ($^{31}P^+/^{34}S^+$ and $^{31}P^+/^{66}Zn^+$) showed clear images of the melanoma and adjacent non-tumorous tissues. An excellent correlation was found between decreased relative P concentration and the presence of the tumor, which was confirmed by comparison with standard histopathology. In general, no significant variations in concentrations of S, Fe, Cu and Zn were observed when imaged as separate isotopes. However, a clear increased $^{31}P^+/^{34}S^+$ ratio in the peritumoural lymphoid tissue was found compared with the metastatic tumor as well as a slightly different perspective on the tumor boundary for the $^{31}P^+/^{66}Zn^+$ ratio. In addition, an interesting application of LA-ICP-MS for visualization and quantitative determination of the localized mass concentrations of Th, U and Pu in human respiratory tissues (lymph node and lung samples), for both chronic natural background and occupationally exposed people was described [246]. *Figure 3.18* shows light micrographs and LA-ICP-MS images obtained for $^{232}Th^+$, $^{238}U^+$ and $^{239}Pu^+$ in paratracheal lymph node (see *figure 3.18A*) and lung tissue (see *figure 3.18B*) samples from an occupationally exposed person.

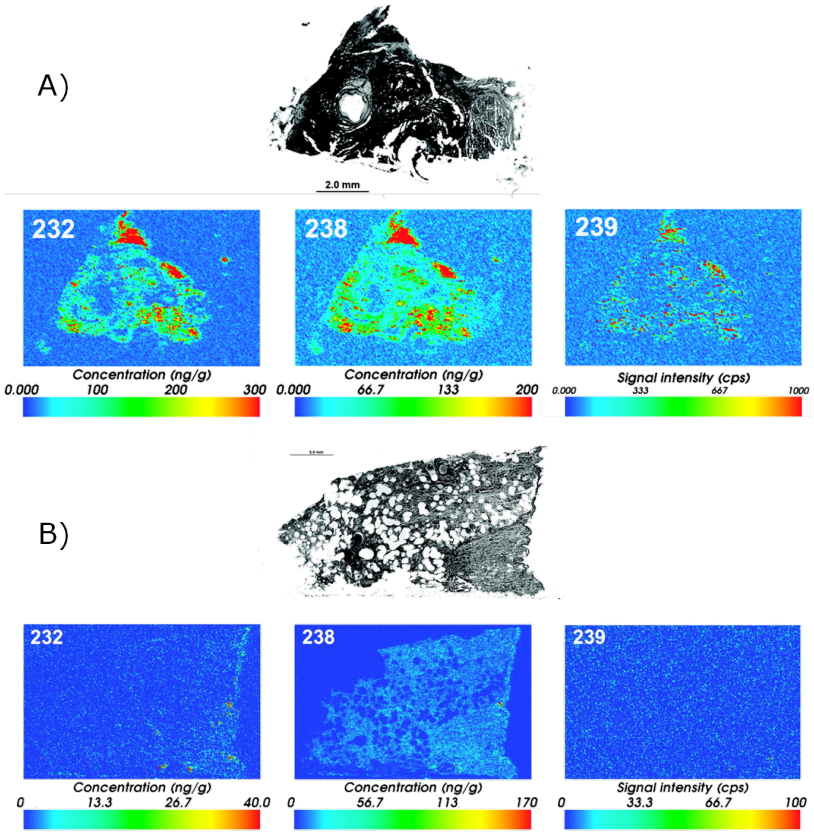

Figure 3.18: Light micrographs and LA-ICP-MS images obtained for $^{232}Th^+$, $^{238}U^+$ and $^{239}Pu^+$ in paratracheal lymph node (A) and lung tissue (B) from an occupationally exposed person [246].

Experimental results revealed a highly inhomogeneous distributions of Th, U and Pu isotopes in lymph nodes and lung tissues, indicating localized aggregation of the inhaled particles for both chronic natural background and acute occupational actinide exposures.

In the last years, LA-ICP-MS has been increasingly employed for metal and non-metal imaging in brain tissue sections [146, 249–258]. It is known that metal accumulations in the brain appear to be directly linked to neurodegenerative processes (e.g. Alzheimer's, Parkinson's or Wilson's diseases, ageing and ischemia). Thus, bioimaging of metals in thin tissue sections of brain is a challenging topic in analytical chemistry and can be established as a new emerging field in brain research, providing information on the pathophysiology, pharmacology and toxicology of elements of interest.

The potential of LA-ICP-MS was demonstrated to produce large series of quantitative maps of Cu, Zn, Fe and Mn in native brain sections of mice subchronically intoxicated with neurotoxin MPTP (1-methyl-4-phenyl-1,2,3,6-tetrahydropyridin) as a model of Parkinson's disease [254]. A defined sample area of a brain tissue was ablated line by line with a focused laser beam. The distribution profiles of the metals were quantified using matrix-matched synthetic laboratory standards prepared from brain homogenates of analogous control mice doped with trace elements of defined concentrations. *Figure 3.19* illustrates the quantitative LA-ICP-MS images obtained for Cu, Zn and Fe in brain sections from mice treated with the neurotoxin MPTP (2 h, 7 days and 28 days after the last injection) compared to controls.

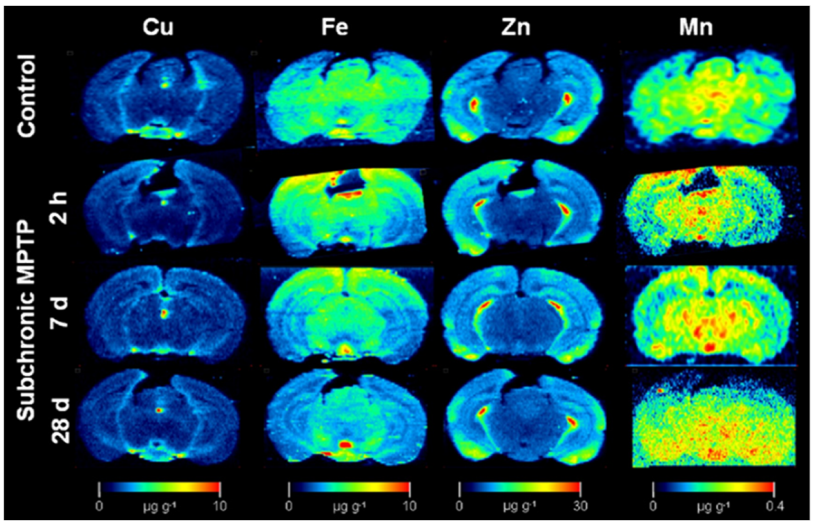

Figure 3.19: Quantitative metal images of Cu, Zn, Fe and Mn representative for each group (control, 2 h, 7 days and 28 days after the last of five daily MPTP injections) [254].

Clear effects of enrichment of Cu in the ventricle, Fe in the interpeduncular nucleus and Zn in the hippocampus area of Parkinson's were observed in diseased mouse brain compared to the control brain. These findings underline the value of routine micro-local analytical techniques in the life sciences and confirm a role of Cu availability in Parkinson's disease.

In other application, Zoriy et al. [252] reported the quantitative imaging of element distribution in histological sections of glioblastoma multiforme, the most common primary human brain tumor, by LA-ICP-MS. Frozen sections from three different human glioblastoma specimens as well as matrix-matched laboratory standards with defined concentrations of the elements of interest were prepared for the calibration of analytical data. Cu and Zn distributions showed a similar localization, with maximum ion intensities in the same region, which histologically corresponded to areas of intratumoral haemorrhage, being both elements completely lacking within the tumor. Moreover, it was found that the concentrations of all measured elements were lower in glioblastoma multiforme compared to the control brain.

3.3.2.2 Elemental bioimaging of hard tissues

LA-ICP-MS offers also the possibility to obtain spatially resolved information of hard biological matrices, such as tree barks [259], lichens [260], corals [261, 262], shells [263, 264], fish otoliths and scales [265–268], bird feathers [269] and horns [270]. Some details of the selected applications are collected in *table 3.4*, showing the diversity of samples that can be analyzed by LA-ICP-MS. Although this selection is fairly arbitrary, it gives some ideas about the growth of areas in LA-ICP-MS applications to hard tissues. Marine samples, particularly corals and fish otoliths, constitute a great part of the studies while the analysis of mosses, barks and plants have received relatively little attention so far. On the other hand, the analysis of human teeth, nails and hair samples have been rapidly growing in the last years, focusing on problems related to human nutrition and health as well as on the assessment of migration patterns of prehistoric species [78, 183, 271–274]. It should be stated that, while the analysis of blood samples for trace metals determination provides information concerning recent exposure, the analysis of hard tissues (e.g. teeth, nails and hair) offers insight into a period of several months, or even years, and is preferable since the samples are non-invasively collected and easily stored.

Table 3.4: Selected applications of 2D mapping of hard biological samples by LA-ICP-MS.

Matrix	**Application**	**Reference**
Barks	Characterization of tree bark samples from different regions with high and low pollution burden; identification of areas with different degrees of environmental impact.	[259]
Lichens	Quantitative elemental bioimaging of Pb in lichens from a heavily anthropogenic impacted area of maritime Antarctica.	[260]
Corals	Study of several metals and rare earth elements in coral samples to create environmental records of pulse events (e.g. contamination spills) and seasonal cycles.	[261, 262]
Shells	Determination of natural and anthropogenic changes in coastal upwelling regions and study of patterns of trace elemental distribution throughout the shells from which the chronology of elemental uptake as a diagnostic tool for investigating toxic element uptake.	[263, 264]
Otoliths	Evaluation of migration patterns and fingerprint of the local environmental or geochemical conditions.	[265–267]
Scales	Spatial elemental analysis of carp fishes (lateral resolved and depth-profiling analysis) to study the elemental distribution of matrix elements and substituents.	[268]
Feathers	Comparative study of elemental distribution of external versus internal metal contamination of feathers in wild peregrine and urban birds.	[269]
Horns	Assessment of migration patterns by accumulation of trace elements in keratin-rich tissues.	[270]
Teeth	Chronological record of individuals' nutritional status and anthropogenic trace metal exposure during development.	[78, 274]
Nails	Study of long-term chronological variations of metals as well as depth distribution patterns.	[183, 271]
Hair	Investigation of element distributions along hair strands; study of metals intoxication in human bodies.	[183, 272, 273]

Several authors have recently proved the potential of LA-ICP-MS for spatially resolved analyses through bio-monitoring of longitudinal distributions of heavy-metals (e.g. Pb, Hg, As and U) in single hair strands [275–278]. The quantitative analysis was carried out in all cases by external calibration, using digested hair samples [275, 277], pressed pellets of powdered hair [276, 278] or hair strands immersed into solutions of defined element concentrations [278] as matrix-matched laboratory standards. Different heavy-metal concentrations were found across the hair samples depending on exposure times or ingestion periods. Moreover, the use of a single strand of hair as a bio-indicator tissue for the determination of toxic elements contamination (As and U, respectively) coming from drinking waters was also reported [279, 280]. Results showed that LA-ICP-MS can be successfully used for the rapid identification and screening of toxic and nutritionally important elements in hair; there is need for only one hair strand for the analysis and it is possible to conveniently track changes in concentration that occur over time. Thus, intake effects of toxic elements on the human body can be monitored using hair samples as a bioassay medium, even several weeks or months after the exposure. In addition, chronic exposure due to changes in dietary habits or environmental factors could be distinguished from acute, or accidental, exposure incidents.

Taking into account the relationship between diet and recent migration through the measurement of hair carbon, nitrogen, and sulfur isotope ratios in modern humans living [281], the ability of LA coupled to a multicollector ICP-MS for the measurement of sulfur isotope ratios in human hair was investigated [282]. Three individual subjects were employed in the study (two residents in the UK and one traveler that had been in the UK for a just over a month before the analysis and had visited four different countries within the 6 months prior to sample collection); preliminary results showed the ability of the proposed method to measure variations in human hair strands and the potential correlation between geographical movements and variations in sulfur isotopic composition. $^{34}S/^{32}S$ isotope amount ratio measurements were performed along 4.3 cm of hair strand (it should contain information related to the past 3-9 months from the day of sample collection) using a well-characterized horse hair sample as an external standard to correct for instrumental mass bias effects. Furthermore, LA-ICP-MS has been effectively applied to analysis in medical research through the monitoring of Pt in hair strands from a patient who had been treated with cisplatin in cancer therapy [283]. Matrix-matched laboratory standards were used for quantification purposes by using tufts of hair, from a volunteer without any history of Pt exposure, incubated in different Pt solutions. These Pt-enriched strands

were used for external calibration using ^{34}S as IS. The patient was treated with four cycles of cisplatin at 3-week intervals and, as can be seen in *figure 3.20*, LA-ICP-MS profile showed four peaks that can be attributed to the different treatment cycles (i.e. to each dose of cisplatin). Additionally, a smaller peak preceded the major peak in all replicates, indicating absorption of Pt by hair in two steps.

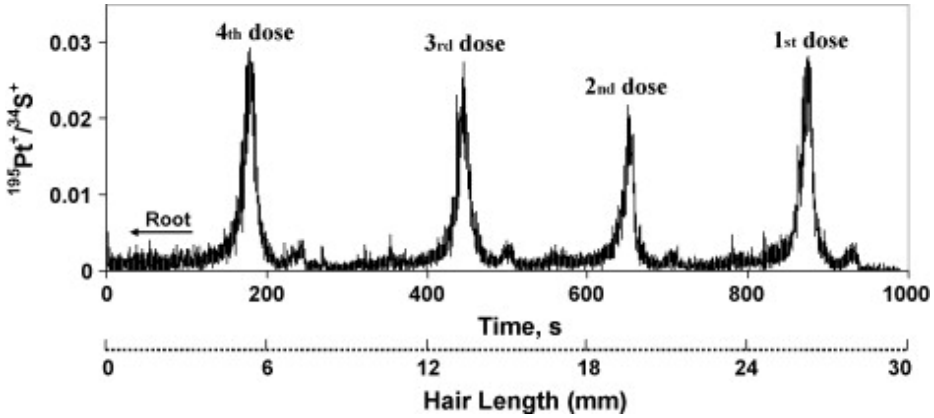

Figure 3.20: Intensity ratio of $^{195}Pt^+/^{34}S^+$ along a hair strand obtained by LA-ICP-MS from a patient treated with four 100 mg doses of cisplatin [283].

In addition to these results, the potential of LA-ICP-MS for elemental bioimaging of trace elements in teeth and bone samples has been recently demonstrated by several authors [284–287]. Recently, micro-spatial analyses of a prehistoric bear tooth were reported, being the choice of investigated chemical elements further motivated by their importance in paleozoology [288]. For example, the Sr/Ca and Ba/Ca ratios generally contain information about the nutrition, especially the proportion of foodstuff of animal and vegetable origin in the diet and, therefore, these ratios can differ in geographic regions with different Sr, Ba, and Ca content in the environment. Results demonstrated that the seasonal fluctuations of Sr/Ca and Sr/Ba ratios can be detected by LA-ICP-MS, indicating the migration of the selected bear between his hibernaculum and the place where the fossils were found. On the other hand, Sr isotope ratios in teeth can be also investigated to assess geographic origins or migration behavior of the investigated species [289, 290]. Copeland et al. [289] employed LA-ICP-MC-MS for measuring Sr isotope ratios in fossil teeth. The proposed methodology includes the determination of background cave $^{87}Sr/^{86}Sr$ values and comparison of Sr concentrations and isotope ratios in fossil enamel versus dentine of individual rodent teeth. In general, enamel is more resistant to diagenetic contamination than dentine because of its essentially non-porous structure with relatively large crystals and low organic component; enamel Sr retains a more biogenic value than dentine Sr

in the same teeth. Experimental results showed that the total concentration of Sr in modern and fossil enamel from the selected area was statistically indistinguishable. Moreover, little evidence of diagenetic Sr was found in the fossil enamel, whereas the fossil dentine may contain up to 50% diagenetic Sr.

3.3.2.3 Bioimaging of element-tagged proteins

A further application of LA-ICP-MS is related to the measurement of element-tagged immunoassay for imaging purposes, providing a new strategy for direct quantification measurement and mapping of peptides and proteins in different types of tissues [248, 249, 291]. Hutchinson et al. [249] reported the potential of LA-ICP-MS for the detection and imaging of β-amyloid (Aβ) protein in immunohistochemical sections from brains of a transgenic mouse model of Alzheimer's disease. Localization of amyloid precursor protein and Aβ peptide in histological sections of brain tissue was obtained using Eu and Ni-coupled antibodies. LA-ICP-MS analysis proved to be a valuable tool for imaging of Aβ deposits. One striking difference was found between the ^{60}Ni and the ^{153}Eu maps; the ^{60}Ni map provided a full recovery of the anatomy of the tissue, whereas the ^{153}Eu map visualized only the Aβ deposits with no anatomical recovery. Moreover, distribution maps of endogenous metal trace elements in the brain sections could be also obtained simultaneously with the Eu and Ni data. The potential of immunohistochemistry and LA-ICP-MS have been also demonstrated for imaging of cancer biomarkers [291]. The distribution of two breast cancer-associated proteins (MUC-1 and HER2) was studied based on multiple line scanning of tissue sections by the laser beam and the subsequent measurement of relevant Au/Ag tagged antibodies bound to the tissue. Results showed a good correlation of feature information between optical microscopy and LA-ICP-MS measurements, allowing analysis with high sensitivity and sufficiently good resolution to permit fine scale feature mapping at the cellular level.

The same strategy was also applied in post-mortem imaging of Gd spatial distribution in a mouse tumor model, post-administration of PEGylated Gd liposomal nanoparticles [292]. Experimental results showed the Gd distribution maps within the tissue by the analysis of a single 7 μm thick section of the tumor (2 h post-administration of PEGylated Gd liposomal nanoparticles). It was found that the major accumulations of Gd and, therefore, of Gd liposomal nanoparticles were within the peripheral viable tumor areas.

Despite the potential of LA-ICP-MS and the use of advanced focusing techniques, spatial resolution, sensitivity and data acquisition speed remain limitations of LA-ICP-MS to achieve high resolution images. Concerning the spatial resolution, although LA-ICP-MS analyses can be carried out using, for example, a 10 μm spot size, the spatial resolution also depends on the integration time of the MS instrument and the washout time of the laser-generated aerosol through the transport system, including the ablation cell and transport tubing. Moreover, typical data acquisition times for a 5 mm^2 specimen can vary from over 2 h for a low resolution image to more than 30 h for a more detailed image. For some applications, high resolution images are desirable to distinguish fine details, such as the substantia nigra in brains of Parkinsonism mouse models [251] and, therefore, LA-ICP-MS require significant reductions in analysis time to remain at the forefront of accessible μm-scale element imaging technology. Thus, a carefully selection of both laser and ICP-MS parameters has to be performed for each sample of interest to achieve the optimal analysis conditions in terms of sensitivity, spatial resolution and analysis time.

Other important parameters, such as the relationship between laser scan speed, MS dwell time, and image resolution for the purposes of speeding up typical total acquisition times for image construction by LA-ICP-MS have been investigated [293]. Quantitative experiments were run using 30 μm thick sections of brain from adult wild-type mice. It was observed that the original relative dimensions of the samples are maintained in LA-ICP-MS images if the laser scan speed is equal to the laser spot diameter divided by the scan cycles time in the MS. Thus, the maximum laser scan speed may be calculated from dwell times, the number of m/z measured, and the detection limits required. A comparison between the elemental imaging capabilities of LA-ICP-MS and micro-X ray fluorescence (XRF) spectrometry was carried out for the model organism Daphnia magna in terms of detection power and spatial resolution [294]. Experimental results showed that spatial resolution of LA-ICP-MS seems to be higher than that provided by micro-XRF. However, wash-out effects and spikes disturb the image quality to some extent. In the same way, a complementary method was reported for quantitative high spatially resolved imaging of trace elements in heterogeneous media using LA-ICP-MS and synchrotron micro-XRF [295]. Results showed that combining the outputs achievable by the two independent techniques enhances the imaging capabilities significantly; the qualitative high resolution image of synchrotron micro-XRF was in good agreement with the quantitative image recorded by LA-ICP-MS. Nevertheless, the efficiency of LA-ICP-MS measurements was low due to the slow washout of the ablation cell; a faster aerosol transportation

system is required to improve the spatial resolution and avoid the signal deconvolution of experimental data (necessary to obtain higher quality imaging by decreasing the contribution of shot to shot overlap).

4 Experimental

4.1 Instrumentation

Laser system

For the direct introduction of solid samples a nanosecond laser ablation system LSX 213 (CETAC LSX 213, Cetac Technologies, Omaha, NE, USA) was used. The LSX-213 employs a Nd:YAG laser, frequency quintupled to the ultraviolet wavelength of 213 nm. A scheme of the instrument is presented in *figure 4.1*.

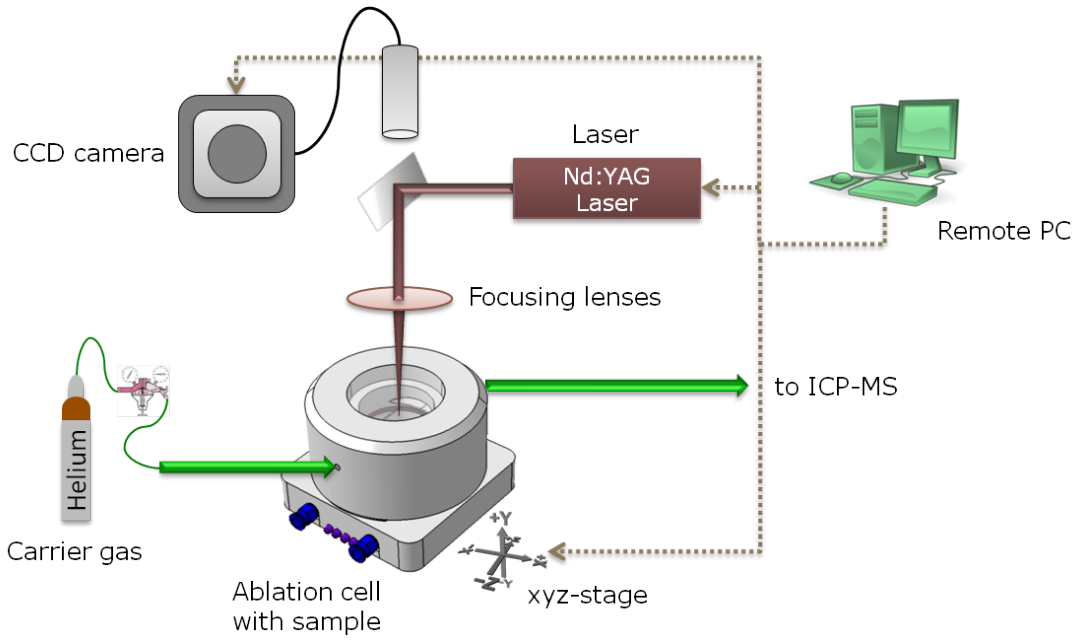

Figure 4.1: Scheme of the laser ablation system used in this study.

The laser output energy is adjustable from 0-100% with a maximum value of 5.6 mJ. These features provide a nearly uniform energy profile ("flat-top profile") across all spot sizes ranging 10 μm to 200 μm and, consequently, a flat-bottomed (>90%) crater on the sample. Due to the non-ideal flat-top profile the laser energy does not fully scale across the whole spot size, thus, a compensation factor for each spot size needs to be accounted for. An approximation curve is given by the following equation (provided by CETAC):

$$\text{Energy factor} = -7.445 \cdot 10^{-10} \cdot (\text{spot area})^2 + 5.397 \cdot 10^{-5} \cdot (\text{spot area}) \qquad (4.1)$$

Note, that the spot area is given in microns. Applying this equation, a multiplication factor is obtained, which can be used to calculate the energy delivered to the sample surface from the attenuated raw beam. So, for example, for 80% energy an attenuated raw beam of $(5.6 \cdot 0.8)$ 4.48 mJ is obtained. Using a 100 μm spot size, the correction factor would use a spot area of 7854 μm^2, and an energy factor of 0.38 would result in this example. This correction factor is then multiplied by the attenuated raw beam energy $(4.48 \cdot 0.38)$ to give delivered energy of 1.69 mJ.

With the corrected energy values, the energy density per surface area (fluence J cm^{-}2) can be calculated using the following equation:

$$\text{Energy density} = \frac{\text{corrected laser energy}}{\text{spot area}} \qquad (4.2)$$

Taking into account the previously mentioned example, the calculated fluence for 80% energy and a 100 μm spot size would be 21.56 J cm^{-2}. Due to the instrumental characteristics, both energy and energy density reaching the sample surface are dependent on the spot size. The graphical representation of the relation fluence to spot size for a specific energy value of 80% based on the approximation curve (see *equation 4.1)* is shown in *figure 4.2*.

The LSX-213 sampling cell is mounted on an X-Y-Z translation stage, with a step size of 0.25 μm. It provides X-Y positioning control for laser targeting on the sample and is under computer control. The Z-axis is used to focus the laser via the CCD camera viewing system. The sample image is viewed directly in the DigiLaz 213™ Software. For LA-ICP-MS measurements a laser ablation chamber providing an effective volume of 60 cm^3 was employed, which ensured fast washout times. Additionally, for the analysis of frozen samples, the commercial ablation cell from CETAC was replaced by a novel cryogenically cooled ablation cell. The ablation cell was built in-house and specially designed for the analysis of cryogenic tissue sections. The ablated material was transported through high-purity tubes (Teflon-lined Tygon® tubing, $\frac{1}{4}$" OD, $\frac{1}{8}$" ID) into the inductively coupled plasma using helium as the carrier gas. The coupling of the laser ablation system to the ICP-MS was carried out either in dry or wet plasma conditions. In the former case, the transport tubing carrying the laser

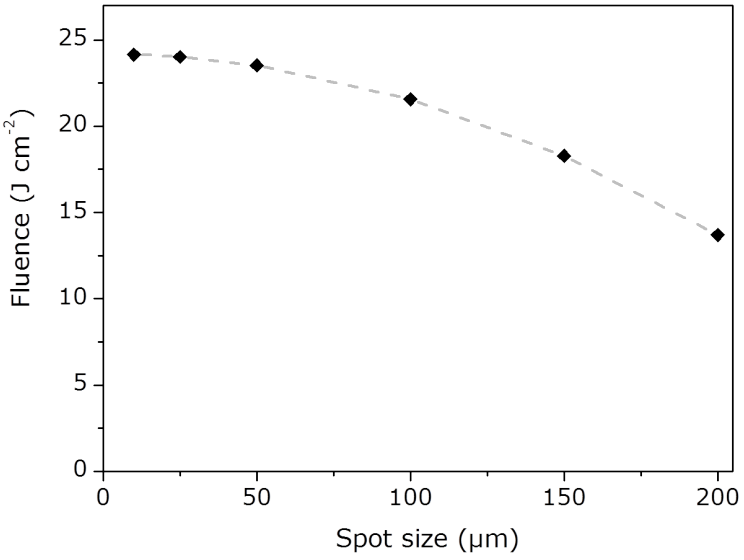

Figure 4.2: Dependence of the laser fluence from the spot size.

generated aerosol was directly connected to the ICP torch. In the latter case, the laser aerosol was mixed with a liquid aerosol generated by means of a concentric nebulizer, using a home-made Y-piece of glass before introduction into the plasma. The laser ablation was daily tuned by continuous ablation of a reference glass sample (SRM NIST 612) for maximum intensity of $^{59}Co^{+}$, $^{139}La^{+}$, $^{232}Th^{+}$ and $^{238}U^{+}$ and low elemental fractionation (by optimizing the $^{238}U^{+}/^{232}Th^{+}$ ratio to 1). The laser parameters were 150 μm spot size, 70% laser energy, 10 Hz repetition rate and 20 μm s^{-1} scan speed, 1000 and 500 mL min^{-1} for He and Ar flow rate, respectively.

Inductively coupled plasma mass spectrometer

Element-specific detection was carried out using a double-focusing sector field ICP-MS (Element 2, Thermo Fisher Scientific, Bremen, Germany) at medium mass resolution (R=4000) in order to avoid spectral interferences on the determination of the sought elements. A scheme of the instrument can be found in *figure 4.3*.

The spectrometer is equipped with three fixed resolutions and is able to switch the positions of the entrance and exit slits which offers maximum stability and reproducibility of resolutions. The instrument was tuned daily with a multi-element tuning solution containing 1 ng g^{-1} of lithium, indium and uranium for maximum intensity and low oxide formation. The most important parameters proved to be the torch position and the lens voltages (focus, X- and Y-deflection and shape). Apart from

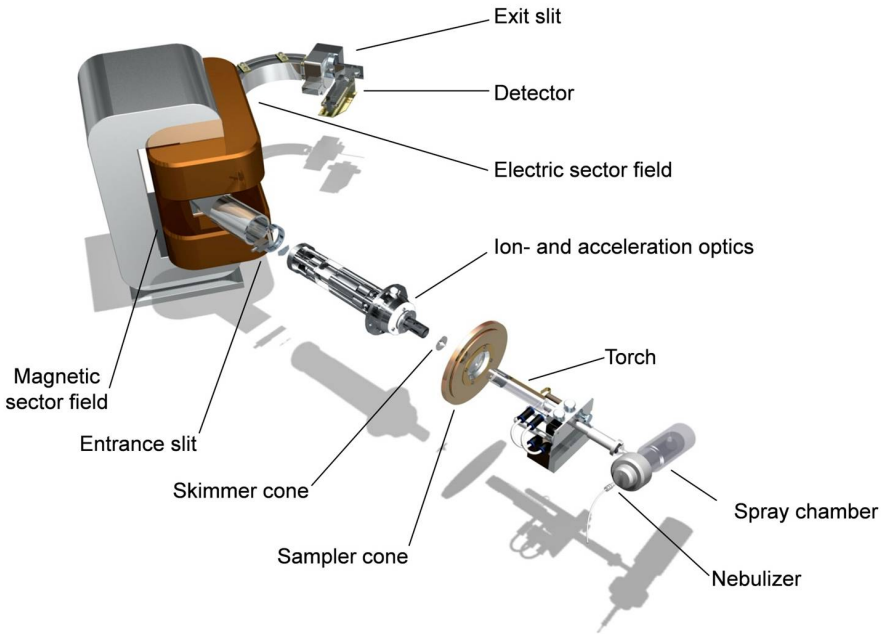

Figure 4.3: Scheme of the Thermo Element 2 ICP-MS instrument used in this study.

that, measuring in medium resolution necessitates an exact determination of mass offset of the investigated elements. This was done daily with a solution containing the sought elements at appropriate concentrations. For measurements with conventional nebulization, a concentric nebulizer (Meinhard) with a flow rate of about 1 mL min^{-1} and a double-pass Scott type spray chamber were used. Typical instrumental parameters are displayed in the corresponding sections.

Gel electrophoresis

The separation of proteins was performed using a 1-D vertical mini-gel electrophoresis system (Mini-PROTEAN® Tetra Cell, Bio-Rad Laboratories, Hercules, CA, USA). Gels were handcast using a spacer plate with 0.75 mm thickness and a 10-well comb.

Sputter coating unit

Metal coating for SEM analyses was performed with a Balzers SCD 004 Sputter Coating Unit at intensity levels of 20 mA under argon atmosphere ($7 \cdot 10^{-2}$ atm) during 3 minutes.

Metal coating of tissue sections was performed during 40 s using the same sputter coating unit as above.

Microtome tissue cutting

Tissues samples embedded in paraffin were cut in sections of varying thicknesses using a Microm HM 360 (Thermo Fisher Scientific, Bremen, Germany), mounted on microscope glass slides and dried for 24 h at 37°C.

Thin sample sections of frozen samples were obtained using a Microm HM 550 cryostat (Thermo Fisher Scientific, Bremen, Germany), mounted on microscope glass slides and stored over dry ice until analysis.

Tissue homogenizer

Homogenization of tissue samples was performed using an Art-Miccra D-8 homogenizer (ART Prozess- & Labortechnik GmbH & Co. KG, Müllheim, Germany)

Spectrophotometer UV/Vis

For the studies of the saturation grade of Tf with Fe and its stability in time depending on the storage an UV/Vis spectrophotometer (Thermo Spectronic™ GENESYS™ 20, Thermo Scientific, Bremen Germany) was used. It covers the wavelength range from 325 to 1100 nm with an accuracy of ± 2 nm.

Confocal laser scanning microscopy (CLSM)

High-resolution 3D images of tissue samples were generated by sequential acquisition using a Leica TCS SP2 AOBS spectral confocal microscope equipped with a Ar/Kr laser, at 488 nm in reflection mode, a Plan Apochromat 10X/0.40 CS objective lens operated in dry conditions, without band-pass filter. Stacks of images were collected every 1 μm along the z-axis. 3D images and crater profiles were generated and visualized with Leica Confocal Software.

Profilometer

Laser generated crater depths were measured with a profilometer (KLA-Tencor/P-15, USA) by measuring two profile traces in different directions across the center of each crater.

The Au layer thickness used as internal standard in imaging studies was determined on cross-sectioned witness samples by using a mechanical step profilometer (XP1 - Ambios technology, USA).

Scanning electron microscopy (SEM)

The morphology of the laser generated craters was investigated using a JEOL JSM

6360 instrument (JEOL Ltd, Japan). The electron beam voltages used were 10 kV and 15 kV.

Laser generated aerosol particles collected on polycarbonate membrane filters were investigated using a JEOL 6610LV instrument (JEOL Ltd, Japan) operated at 5 kV.

Imaging software

Two dimensional images of elemental distributions in tissue sections were created using Origin® software.

Computational fluid dynamic modeling

To validate the assumptions about the gas flow patterns within the designed ablation cell, the gas flow dynamics were modeled with Ansys CFX 11.0 using an optimized fine numerical grid of about 0.8 million elements. The fluid was set to helium at standard temperature and pressure (STP). The boundary conditions, i.e., inflow and outflow were based on experimental data and set to a mass flow of $2.9767 \cdot 10^{-3}$ g s^{-1} at 25°C ($\widehat{=}$ 1 L min^{-1}).

4.2 Procedures

Gel preparation

The characteristics of the stacking and resolving gel are usually described by the total monomer concentration (%T) and the weight percentage of the crosslinker (%C). Their definitions are given in *equation 4.3* and *4.4*.

$$\%T = \frac{\text{weight (acrylamide + bisacrylamide)}}{\text{total weight of solution}} \cdot 100 \tag{4.3}$$

$$\%C = \frac{\text{weight (bisacrylamide)}}{\text{weight (acrylamide + bisacrylamide)}} \cdot 100 \tag{4.4}$$

All separations were carried out following an optimized standard procedure with handcast gels in denaturing and native conditions. The preparation protocols for the native and denaturing stacking and resolving gels are given in *table 4.1*.

The total volume of 10 mL was sufficient for two mini-gels. It is worth mentioning, that both the radical initiator (APS) and the catalyst (TEMED) are added immediately before the gel solution is filled between the glass plates. Before the elec-

Table 4.1: Protocols for gel preparation.

Chemical	**Native gel** %T=8, %C=0.7	**Denaturing gel** %T=10, %C=0.9	**Stacking gel**[a] %T=4, %C=0.3
Milli-Q water	4.8 mL	4 mL	6.1 mL
Tris-HCl 1.5 M, pH=8.8	2.5 ml	2.5 mL	
Tris-HCl 0.5 M, pH=6.8			2.5 mL
SDS 10%		0.1 mL	0.1 mL[b]
Acrylamide (%T=30) / Bisacrylamide (%C=2.6)	2.6 mL	3.4 mL	1.3 mL
APS 10%	0.1 mL	0.1 mL	0.1 mL
TEMED	0.01 mL	0.01 mL	0.01 mL

a) For both native and denaturing PAGE

b) Only for denaturing PAGE

trophoretic separation all samples were mixed with the loading buffer (ratio 4:1 sample to buffer) which consisted of 150 mM Tris-HCl (pH=8.8), 50% glycerol, bromophenol blue and 0.4% SDS (only for denaturing PAGE). In the case of the denaturing conditions, the mixture was heated to 90°C for 5 min. for a better reaction of the detergent (SDS) with the proteins. The samples were run immediately to avoid any undesirable additional reactions or denaturation. For the electrophoresis buffer 3 g Tris, 14.4 g glycine and 1 g SDS (only for denaturing PAGE) were diluted in 1000 mL Milli-Q water. The final pH of the buffer was 8.3.

The electrophoresis was generally run at constant 300 V for 20 min. Following electrophoresis the gel cassettes were dismantled and the mini-gels were stained in freshly prepared and filtered Coomassie Blue staining solution (10% acetic acid, 20% methanol) for 30 min and destained in 10% acetic acid with 50% methanol until the gel background was clear. The gels were then placed in glycerol for 2 min and dried for a few hours at room temperature or in an oven at 70°C on filter paper (Whatman® paper). Subsequently, they were covered with a transparent plastic film (Saran™ Film) to protect them against contamination until analysis. Finally, the gels were cut and attached to a glass slide using double-sided tape before mounting into the ablation cell. The attempt was made to carry out the analysis by LA-ICP-MS on the same day (not later than two days after preparation in order) to avoid diffusion of the proteins within the gel or into the substrate.

Saturation of apo-transferrin standard with ^{nat}Fe-citrate

For the saturation of the transferrin standard, 3 mg of the protein were dissolved in 250 μL of a physiological medium, which consisted of 50 mM Tris and 150 mM NaCl (pH 7.4). This solution was diluted 1:1 with a model solution containing 20 mM ammonium bicarbonate, 150 mM NaCl and 300 μM sodium citrate (pH 7.4). Next, 250 μL of the previously synthesized 1:1000 Fe-citrate ($\sim$ 7-fold iron excess) were added. The appropriate amount of Milli-Q water was added to obtain a final volume of 1 mL. The mixture was finally thoroughly stirred and incubated for one hour at room temperature.

Saturation of apo-transferrin standard with ^{57}Fe-citrate

Concerning the synthesis of ^{57}Fe-Tf, 250 μL of an Apo-Tf standard solution in a physiological medium was diluted 1:1 with the model solution used for incubations. The Apo-Tf was then saturated with the ^{57}Fe-citrate solution previously synthesized following the same incubation procedure used for the natural abundance Fe-citrate.

Saturation of serum transferrin with ^{nat}Fe-citrate

For the saturation of serum transferrin, 150 μL of serum (clinical or serum certified for Tf concentration CRM ERM-DA740k) were diluted with 250 μL of the physiological medium and 250 μL of the model solution. To the mixture 50 μL of the freshly synthesized 1:1000 Fe-citrate solution ($\sim$ 7-fold iron excess with respect to the expected Fe-Tf concentration) and 300 μL Milli-Q water were added to obtain a final volume of 1 mL. The mixture was finally thoroughly stirred and incubated for one hour at room temperature.

Conventional protocol for paraffin-embedding of eyes

Paraffin-embedded eye sections were kindly provided by the Fundación de Investigación Oftalmológica - Instituto Oftalmológico Fernández-Vega (Oviedo, Spain). For the preparation of the thin sections, first, the eyes were fixed in a solution containing 4% formaldehyde/4% formaldehyde + picric acid for about 2 h. After washing of the samples with phosphate buffer for 10 min (3x) paraffin-embedding was performed (FFPE) following a conventional protocol. For that, the fixed and washed samples were placed in histology molds and submitted to several washing steps with different solvents in order to replace the water of the samples with paraffin. The protocol consisted of the following steps:

- Immersion in ethanol 70% for 1 h.
- Immersion in ethanol 80% for 1 h.
- Immersion in ethanol 80% for 1 h.
- Immersion in ethanol 96% for 1 h.
- Immersion in ethanol 96% for 1 h.
- Immersion in ethanol 100% for 1 h.
- Immersion in ethanol 100% for 1 h.
- Immersion in ethanol 100% for 1 h.
- Immersion in xylene for 1 $\frac{1}{2}$ h.
- Immersion in xylene for 1 $\frac{1}{2}$ h.
- Immersion in paraffin for 2 h.
- Immersion in paraffin for 2 h.

Subsequently, the paraffin block containing the sample was formed and sections through the eye bulbs were prepared using a microtome. The thin slices were mounted on glass microscope slides and dried for 24 h at 37°C.

Conventional protocol for native frozen eyes

The native frozen tissue sections from bovine, porcine or human eyes were also provided by the Fundación de Investigación Oftalmológica - Instituto Oftalmológico Fernández-Vega. In this case, porcine and bovine eyes were collected from a local slaughterhouse (Matadero Central de Asturias, Oviedo, Spain) while human eyes from adult normal donors (cadavers) ranging in age from 45 to 65 years were obtained 24 h post-mortem through the Hospital Universitario Central de Asturias (HUCA, Oviedo, Spain). Whole eyes or dissected eye lenses were directly frozen at -80°C without any further treatment. For LA-ICP-MS, eyes or lenses were embedded in Optimal Cutting Temperature Compound, cut in a cryostat at -20°C and mounted on microscope glass slides.

Preparation of homogenized matrix-matched tissue standards

The preparation procedure of the synthetic matrix-matched tissue standards is summarized in *figure 4.4*.

Briefly, eye lenses from human donors (10 lenses) were thoroughly homogenized. The homogenate (total weight 1.8 g) was divided into four aliquots (200 mg each). Three of them were spiked (total volume 150 μL) with increasing concentrations of the desired standard metal solutions ($\sim$300 μg g^{-1}); to the forth sample the same volume of 0.1% HNO_3 was added and was used as blank. The total weight of the

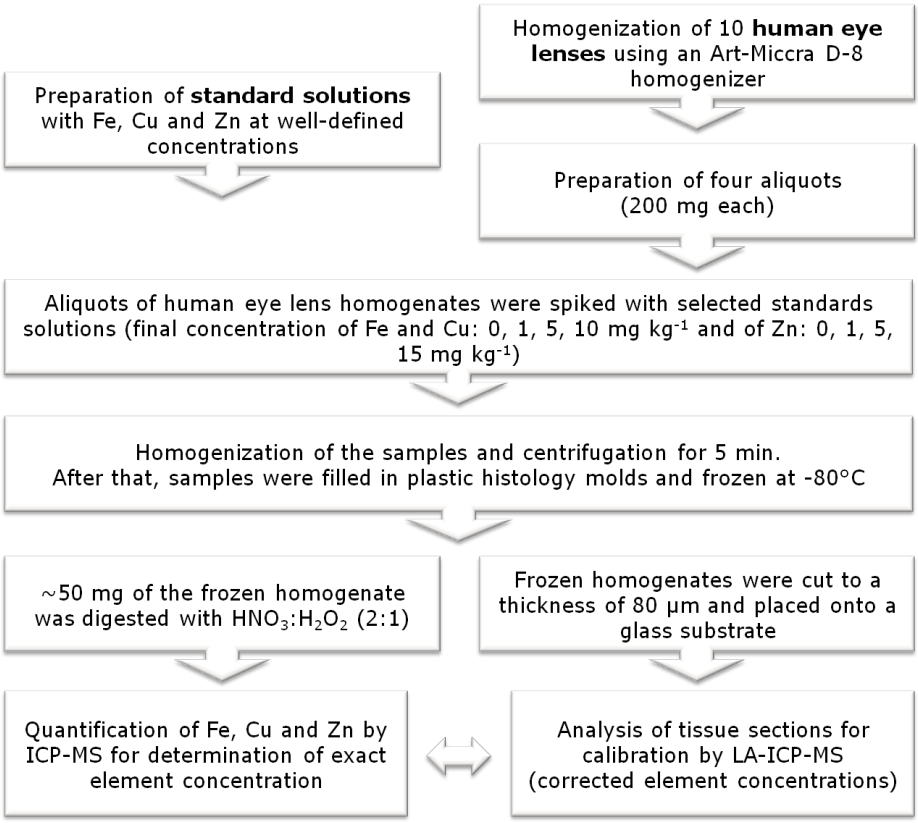

Figure 4.4: Workflow of the preparation of matrix-matched laboratory standards used for quantification of images obtained by LA-ICP-MS.

final samples was about 350 mg. All samples were carefully homogenized and centrifuged for 5 min and then filled into 0.5 cm^3 plastic histology molds and frozen at -80°C. To evaluate the Fe, Cu and Zn concentration in the prepared matrix-matched standards an aliquot of 50 mg of each standard was digested in 3 mL HNO_3 and 1.5 mL H_2O_2 in an ultrasonic bath for one hour (or until the resulting solution turned colorless). The digested solutions were analyzed by ICP-MS (external calibration) for determination of the multi-element concentrations. The frozen matrix-matched tissue standards were cut in a cryostat at -20°C to 80 μm tissue thickness and metalized with Au.

Metallization of thin tissue section with gold

In order to apply the internal standard correction approach using a thin gold film on the sample surface, the corresponding tissue sections were metalized during 40 s with Au. In the case of the frozen sections, special attention was paid in order to maintain the integrity of the sample during the time of the experiment. In this vein, lens sections were mounted on glass microscope slides and placed on copper plates

previously frozen in liquid nitrogen for the deposition of thin Au film. The total duration of the deposition process was below 5 min and no thawing or decomposition effect of the samples was observed.

Sample mineralization

The quantitative measurement of Fe, Cu and Zn levels in bovine eye lens and lens capsules and from human donors were assessed by conventional nebulization ICP-MS. For that, five bovine and human eye lenses were digested in 3 mL of concentrated HNO_3 and 1.5 mL H_2O_2 separately. The corresponding lens capsules were digested using 300 μL HNO_3 and 150 μL H_2O_2. Digested samples were diluted in 1% (v/v) HNO_3 prior to ICP-MS analysis and finally the metal concentrations were determined by IDMS. As controls, preparatory blank tubes (no tissue added) were treated in the same manner as the samples. The proposed mineralization procedure for the bovine and human eye lenses and lens capsules produced homogeneous solutions and no insoluble residues were observed.

5 Results and discussion

5.1 Analysis of local defects in coated glasses

5.1.1 Introduction

Glass (from Germanic "glasa" = the shining, shimmering) is an amorphous non-crystalline solid, typically brittle and optically transparent. Materials, known in everyday life as glass (like drinking glass, window glass or light bulbs) are only part of the diversity of glasses.

Although glass is one of the oldest man made materials, there is still confusion in many aspects of its atomic structure. The now generally accepted interpretation of the structure is the network hypothesis, which was established by Zachariasen in 1932, and says that in glass there are basically the same bound states as in a crystal. For example, most of the glasses contain silica as main component and exist in the form of SiO_4 tetrahedra (see *figure 5.1)* [296].

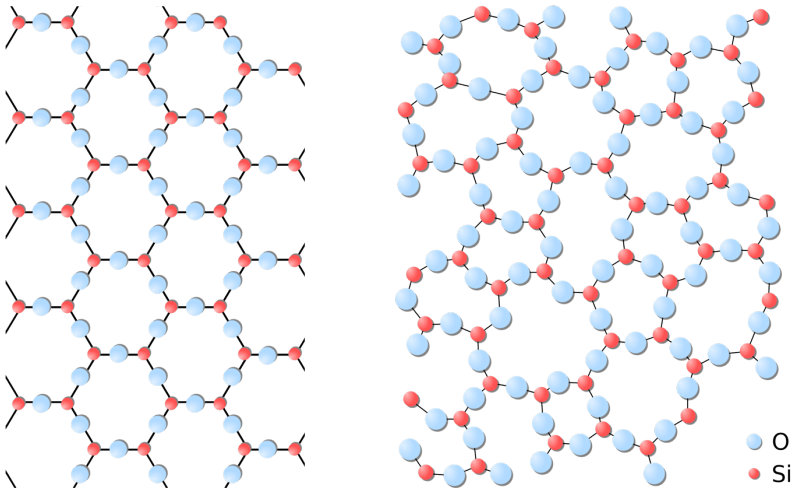

Figure 5.1: Schematic two-dimensional illustration of the atomic arrangement in (A) crystal and (B) glass.

Strictly speaking, glass is an inorganic product of fusion which solidifies substantially without crystallization, more precisely, a material which has been cooled down

too quickly through its glass transition to the solid state without allowing the formation of crystals as they exist for example in quartz.

Glasses play an essential role in science and industry because of its optical (transparency), physical (electrical resistance, low thermal conductivity) and chemical (resistant to corrosion) properties that made them suitable for many different applications. The glass industry is generally divided into container glass, flat glass and special glass manufacture. Container glass is a type of glass used, for example, for the production of bottles, jars and bowls and is usually machine-blown, whereas products of higher quality like glass blocks and drinking glasses are pressed. Flat glass is a type of glass initially formed in planes and is commonly used for window glasses, as a precursor for automotive glasses and many more applications. The flat glass is industrially manufactured by the float process since the 1960s and currently supplies about 95% of the total flat glass industry.

Float glass uses common glass making raw materials like sand, soda ash, dolomite, limestone and salt cake which are mixed and fed together into a furnace where they are molten at 1100°C. The purified pasty-liquid glass melt runs continuously from one side into an oblong bath of molten tin in which the about $\frac{2}{3}$ lighter glass floats and spreads out evenly like an oil film. Because of the surface tensions of tin and the molten glass very smooth surfaces are generated. At the cooler end of the bath the frozen, about 600°C hot glass is drawn out continuously and passed through an annealing lehr, where it is cooled down free from distortion. After an optical quality control the glass is cut into the required pieces (see *figure 5.2*).

Various types of glass defects (e.g. knots, striate, crystals, metallic inclusions, bubbles, etc.) may occur in the production of homogeneous and coated glasses, endangering their function and usage by reducing the mechanical strength, inducing stress or producing optical inhomogeneities which may lower its functional properties, and, thereby, the quality of the product. In general, characterization of such defects presents a real challenge due to their complex chemical and mineralogical properties and, therefore, a multimethod approach is required [299, 300].

The fast and reliable depth profiling analysis of local defects in coated glasses is of critical importance to assist the optimization of the synthesis procedures as well as to evaluate their manufacturing quality. Most of the earlier work on glass analysis using

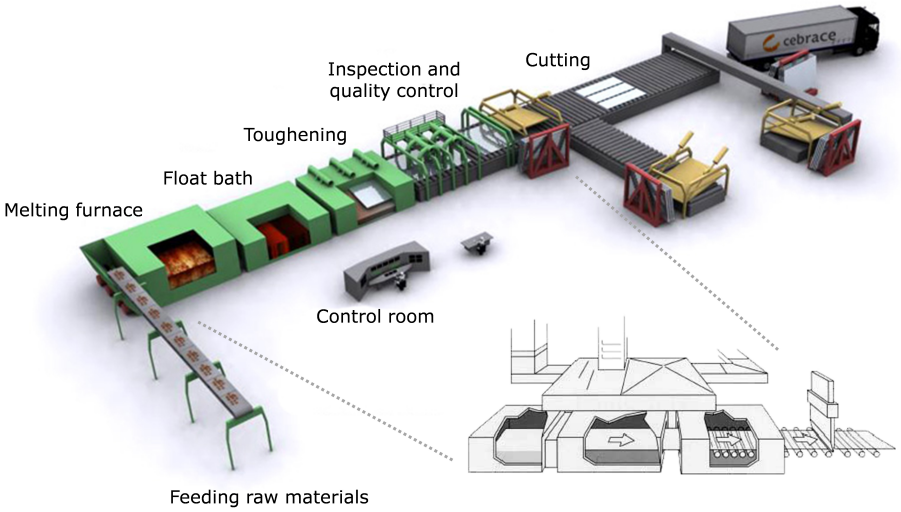

Figure 5.2: Step-by-step manufacturing of float glass [297, 298].

LA-ICP-MS has been focused on sampling strategies, evaluation of laser parameters and development on quantification methodologies for the analysis of homogeneous glasses [133, 301–305]. However, studies on depth profiling analysis of coated glasses by LA-ICP-MS are still scarce [306, 307] and few attempts have been done for the characterization of local defects in thin films [308, 309]. In such cases, only major components of glass specimens (Na_2O, Al_2O_3, SiO_2, K_2O, ZrO_2 and BaO) were investigated and the sources of defects were attributed to high intrinsic compressive stress in the thin films.

Preliminary analysis of the coated glasses selected in this work were performed by the manufacturing company using electron probe microanalysis (EPMA) and P, S, and Cl were found to be possible impurities in the local defects. Due to the low concentration of such elements and the limited depth resolution of EPMA for the analysis of thin films in the nanometer range, it was not possible to distinguish the position of the impurities in the samples and only averaged information on composition was obtained, which was not enough to define the possible contamination sources.

Objective

In this section, the presence of P, S and Cl trace impurities in relevant local defects of coated glasses is investigated by using LA-ICP-MS. Several coated glasses with metallic and oxide layers in the nanometer range were selected for the study. As the local defects appear during the temperate treatments, used to increase the strength

of the glasses, the main goal of this work is the identification and localization (i.e. at the glass substrate, the interface or the coating) of the impurities that promote the local defects in order to identify possible contamination sources, an aspect of critical importance in the glass manufacturing process. With knowledge of the elemental composition of the impurities, the origin of the contamination source could be found and, thus, appropriate actions could be taken for their prevention in the synthesis of glasses.

5.1.2 Samples

A set of coated glasses with antireflective and thermal properties was provided by the glass manufacturing company Saint Gobain Glass (Avilés, Spain). The glass samples, which were taken during the production, consisted of a homogeneous glass substrate (6 mm thick) coated with various metallic and oxide layers (Ag, ZnO and Al_2O_3) in the nanometer range (below 200 nm overall thickness) (see *figure 5.3*). All selected glasses had local defects, not easily detected by the human eye because of their reduced size (200-800 μm in diameter).

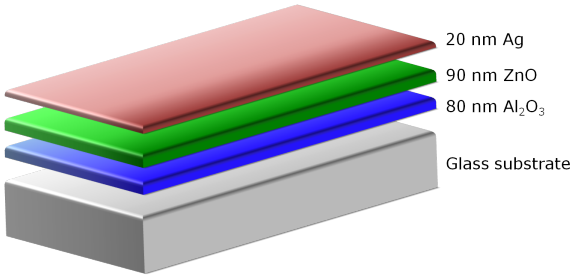

Figure 5.3: Schematic composition of the nanoscale layers of the analyzed glasses.

Figure 5.4 shows an image on the three analyzed glass samples. The areas with the local defects are highlighted in different colors.

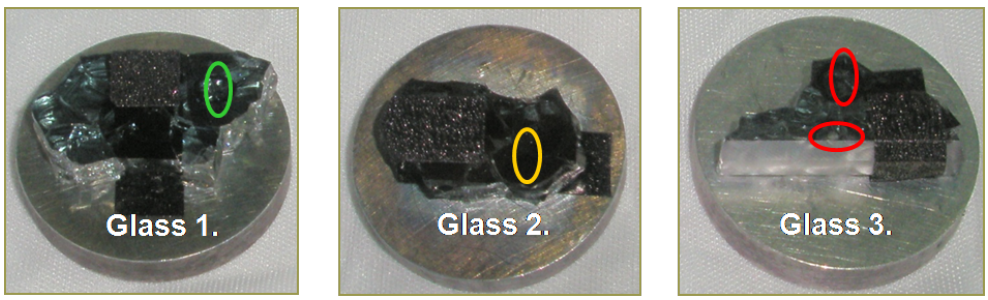

Figure 5.4: Selected glass samples for LA-ICP-MS analyses. Local defects are marked with a circle.

5.1.3 LA-ICP-MS parameters

The general tuning of the LA-ICP-MS system was performed daily as described in the Experimental chapter (*section 4.1*). For the characterization of the local defects, first, the selection of the ablation strategy and the LA-ICP-MS conditions was carried out. In order to perform depth profiling analysis, the single point ablation mode was employed throughout the experiments. Moreover, a low laser repetition rate was used to avoid mixing of information coming from different laser pulses and, thus, 30 s of delay time was chosen between two laser pulses. Spot sizes of 200 μm were selected for the analysis as a compromise between high sensitivity, necessary to detect trace impurities, and good depth/diameter ratio. The optimized operating conditions are summarized in *table 5.1*.

Table 5.1: Optimized parameters used for the analysis of glasses by LA-ICP-MS.

System	Parameter	Value
ICP-MS	RF power	1325 W
	Cooling gas	15 L min^{-1}
	Auxiliary gas	0.8 L min^{-1}
	Carrier gas (Ar)	0.4 L min^{-1}
	Cones	Ni (Skimmer and Sampler)
	Mass resolution	4000
	Isotopes monitored	^{24}Mg, ^{43}Ca, ^{44}Ca (glass substrate) ^{31}P, ^{32}S, ^{34}S, ^{35}Cl (local defects)
	Acquisition time	2.8 s
	Mass window	50%
LA system	Laser energy	100% (5.6 mJ)
	Repetition rate	0.033 Hz (1 shot and 30 s delay time)
	Spot size	200 μm
	Ablation mode	Single point
	Carrier gas (He)	1 L min^{-1}

Due to important and well-known polyatomic interferences on phosphorus, sulfur and chlorine detection [310] (see *table 5.2*), the analyses were performed working in medium resolution of the ICP-MS (R=4000).

Table 5.2: Phosphorus, sulfur and chlorine isotopes, corresponding interferences and required resolution.

Isotope	Interference	Resolution
^{31}P	$^{14}N^{16}O^{1}H^{+}$	966
^{32}S	$^{16}O_2{}^{+}$	1801
	$^{18}O^{14}N^{+}$	1060
^{34}S	$^{16}O^{18}O^{+}$	1296
	$^{68}Zn^{2+}$	6236
^{35}Cl	$^{16}O^{18}O^{1}H^{+}$	1058
	$^{34}S^{1}H^{+}$	5113

5.1.4 Depth profile analysis by LA-ICP-MS

Blank analyses of the glasses in a location without defects were always performed to check the background levels of the impurity elements. Additionally, these analyses allowed us to get preliminary information about the thickness of the coating. *Figure 5.5* shows a typical profile obtained by LA-ICP-MS for the analysis of a coated glass without defects.

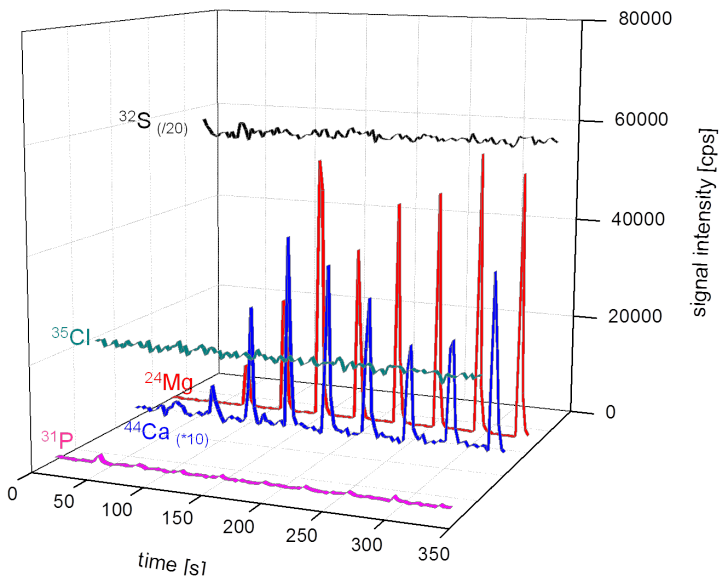

Figure 5.5: LA-ICP-MS signals of $^{24}Mg^{+}$, $^{31}P^{+}$, $^{32}S^{+}$, $^{35}Cl^{+}$ and $^{44}Ca^{+}$ for a coated glass without defects (blank analysis).

This profile gives an early indication of the compositions of the glass. Each peak

represents one laser shot, increasingly penetrating the sample. As can be seen, a stable background signal was found for $^{32}S^{+}$ and $^{35}Cl^{+}$, and only a slight increase of $^{31}P^{+}$ ion signal was observed in the first laser pulse. $^{24}Mg^{+}$ and $^{44}Ca^{+}$ ion signals, coming from the glass substrate, progressively increased from the second to the fourth laser pulses, indicating that the homogeneous glass substrate was reached at the fourth laser pulse and, therefore, that the first, second and third pulses correspond to the analysis of the thin films and the coating/glass interface.

On the other hand, in order to evaluate if the ablation rate (nanometers per laser pulse) and, thus if the depth of the craters changed when analyzing the local defects or the blank surfaces, the crater shapes were studied by profilometry. *Figure 5.6* shows the crater shape obtained after LA-ICP-MS analysis for a glass without defects. As can be seen, a rather Gaussian profile was obtained. Moreover, the depth of the crater was determined to ∼400 nm. Taking into account the number of single shots (9), a sputtering rate around 45 nm per pulse can be calculated.

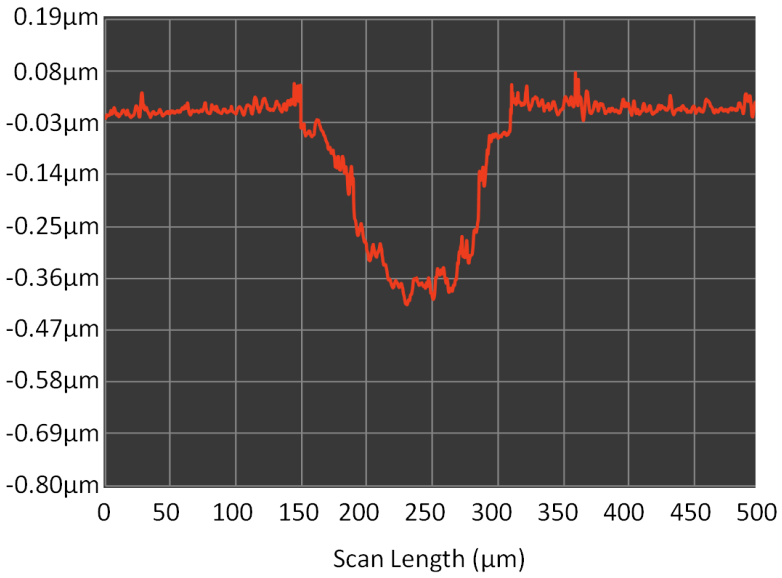

Figure 5.6: Crater shape obtained by profilometer for the coated glass without defect after LA-ICP-MS analysis.

Next, the analysis of the local defects in the coated glasses was carried out for all the selected specimens. Three types of defects, depending on the element identified in the impurity by LA-ICP-MS, were found in the samples. Increased intensity of P, S and Cl were determined in the local defects, whereas just background levels of those elements were always found in the glass location without defects.

Glass 1

In comparison to the blank analysis (see *figure 5.5*), *figure 5.7* shows the obtained depth profile of the ablation inside the impurity. Due to the size of the impurity, two analyses next to each other could be performed, both showing similar results.

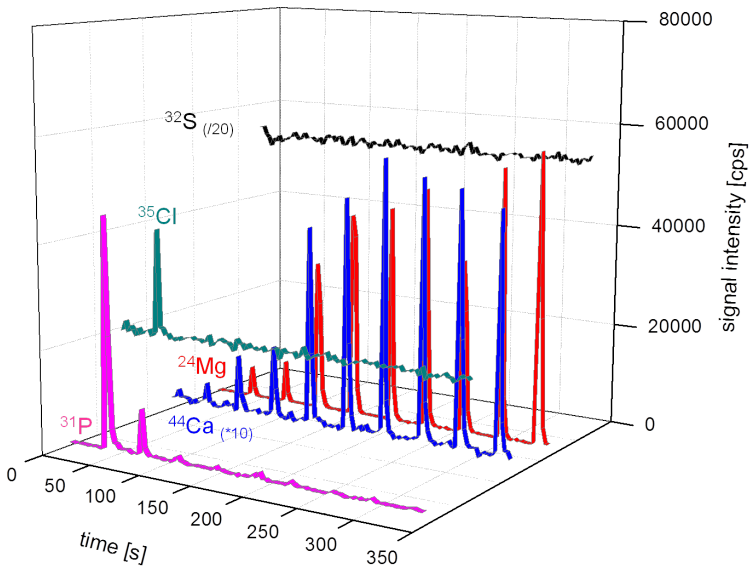

Figure 5.7: LA-ICP-MS signals of $^{24}Mg^+$, $^{31}P^+$, $^{32}S^+$, $^{35}Cl^+$ and $^{44}Ca^+$ for the analysis of the coated glass 1 with local defect.

The obtained results demonstrate clearly the identification of phosphorus and chlorine in the local defect. However, the main goal of this work is not only the identification of impurities present at the local defects but also the recognition of their depth position to detect the possible contamination sources. As can be observed in *figure 5.7*, $^{31}P^+$ and $^{35}Cl^+$ ion signals were found in the two first laser pulses, where the signals coming from the glass substrate were negligible or rather low. Therefore, it could be stated that the impurities are located in the coating of the samples and not in the homogeneous glass substrate. Additionally, $^{31}P^+$ and $^{35}Cl^+$ exhibited always the highest signals at the first laser pulse, which could also indicate that the impurities are in the thin metallic and oxide films and not in the coating/substrate interface.

In order to evaluate the sputtering rate inside the local defect, the crater depth was determined by profilometry. *Figure 5.8* collects some pictures of the impurity of the glass sample, where (A) and (B) were taken with the optical microscope of the laser system and (C) with a scanning electron microscope. Additionally, the resulting

crater was measured using a profilometer (D).

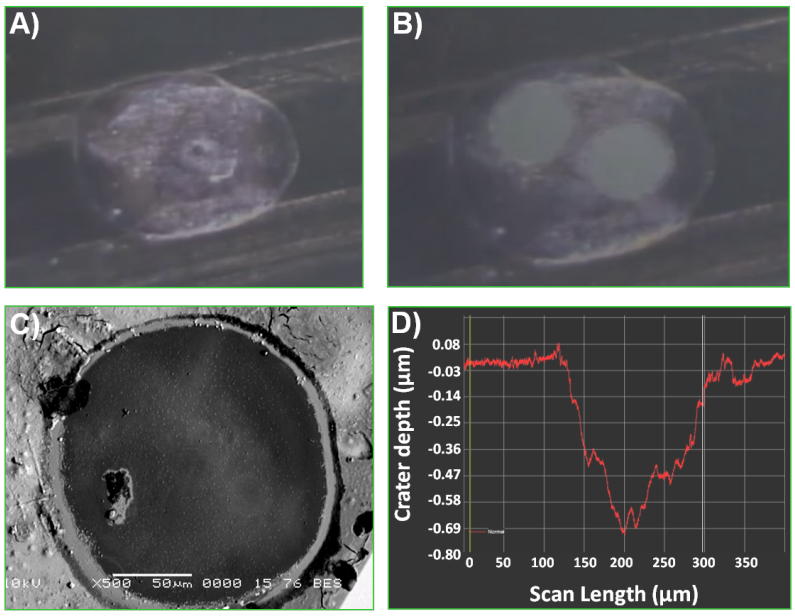

Figure 5.8: Optical microscope images of a local defect in the coated glass 1 before (A) and after (B) LA-ICP-MS analysis, SEM image inside the crater after ablation of the defect (C) and resulting crater profile by profilometry (D).

The crater profile inside the local defect exhibits, similar to the crater profile of the blank analysis (see *figure 5.6*), a Gaussian profile with some irregularities, which could be attributed, at least partly, to the structure of the defect itself. The depth of the crater was different to the one obtained in the blank analysis, showing a penetration depth of around 700 nm. With the known number of laser shots and the depth of the crater the sputtering rate could be calculated to ∼80 nm per pulse, which indicates a thickness of the coating of this glass sample of a few hundred nanometers and the presence of the impurity in the first 100-200 nm.

Such differences observed on the ablation rates for the analysis of spots with and without defects can be mainly attributed to changes in the sample morphology and, therefore, to an altered action of the laser beam during the analysis. Additionally, the possible mixing of the different metallic and oxides layers inside the local defect could change the laser absorption characteristics of the glasses. In any case, as can be seen in *Figure 5.8C*, SEM images obtained inside the local defects showed a crater with a well-defined structure and without big redeposited particles; only small particles can be observed in the SEM image and a negligible redeposition at the crater edges.

Glass 2

Following the procedure from the previous experiment, first a blank analysis was performed in the sample by choosing an analysis location without defect. The obtained profiles were very similar to the ones shown in *figure 5.5*, confirming that the base elements of the glass are detected from the third laser shot. This indicates that before only the layers on the top of the sample are ablated. The obtained results for the analysis of the local defect are represented in *figure 5.9*. In this impurity only chlorine could be found, and again, like in the previous analysis only in the first pulse, which suggest its presence in the upper layers of the sample.

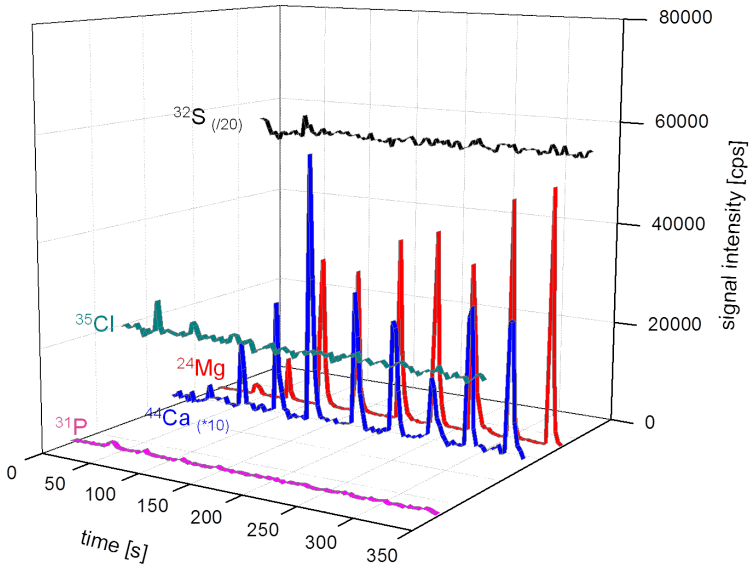

Figure 5.9: LA-ICP-MS signals of $^{24}Mg^+$, $^{31}P^+$, $^{32}S^+$, $^{35}Cl^+$ and $^{44}Ca^+$ for the analysis of the coated glass 2 with local defect.

Figure 5.10 shows some pictures of the impurity of the glass sample. With the known number of laser shots and the depth of the crater the sputtering rate could be calculated and gave a value similar to the previous one (glass 2) of about 100 nm per pulse. As chlorine was detected only in the first pulse, it suggest its presence in the upper layers of the sample.

Glass 3

The third and last glass sample showed two different local defects which are shown in *figure 5.11*.

The two investigated impurities seem to be physically slightly different from each other, as the defect A presents a cracked surface. An analysis in the center of the local

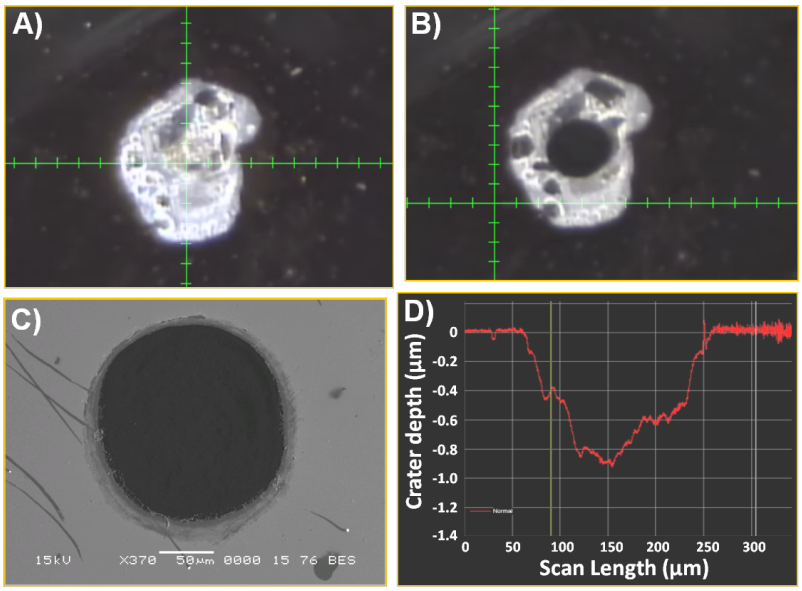

Figure 5.10: Optical microscope images of a local defect in the coated glass 2 before (A) and after (B) LA-ICP-MS analysis, SEM image inside the crater after ablation of the defect (C) and resulting crater profile by profilometry (D).

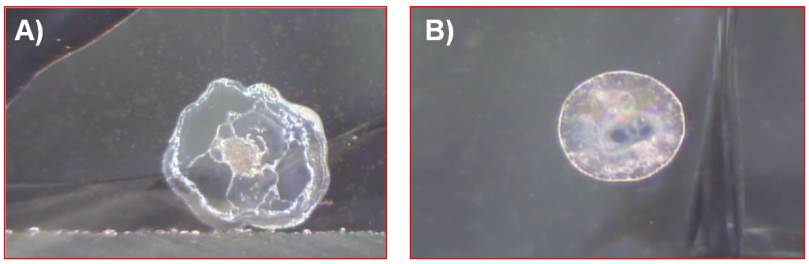

Figure 5.11: Optical microscope images of two local defects (A and B) in the coated glass 3 before LA-ICP-MS analysis.

defect A revealed a profile corresponding perfectly to a blank analysis, containing the base elements (Mg and Ca) from the first shot without any presence of phosphorus, sulfur or chlorine. This could indicate the rupture of the layers down to the substrate and thus its direct ablation. On the other hand, the analysis of the local defect A at the edge and of the defect B resulted in very similar profiles, which is exemplarily shown in *figure 5.12*.

In both impurities, the presence of the three suspected elements was clearly observed, presenting significantly higher signal intensities than those previously obtained for glasses 1 and 2. In this case the resulting crater depth was not measured and, therefore, no information of the sputtering rate is available (i.e. the higher signal intensity cannot be automatically related to higher concentrations of the elements). Nevertheless, it can be assumed that higher contamination was in the defect since the

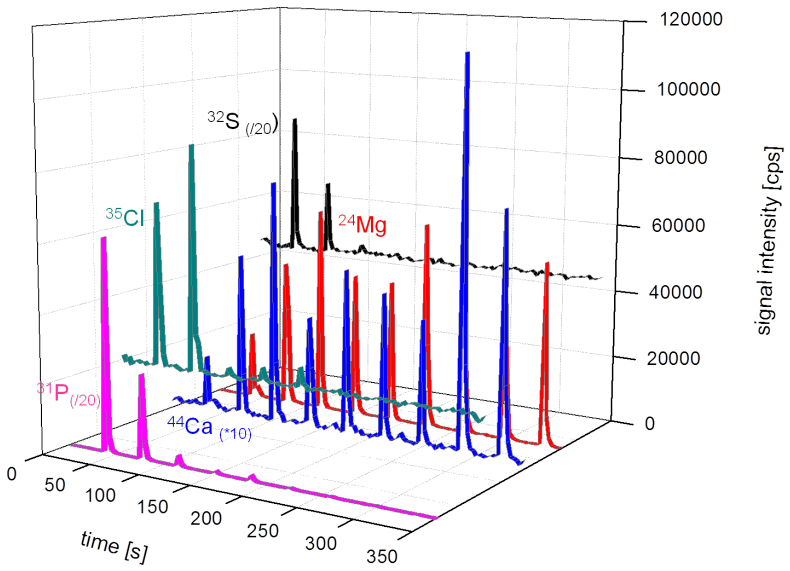

Figure 5.12: LA-ICP-MS signals of $^{24}Mg^+$, $^{31}P^+$, $^{32}S^+$, $^{35}Cl^+$ and $^{44}Ca^+$ for the analysis of the coated glass 3 with local defect.

signal intensities of the base elements (such as magnesium) are comparable to both obtained in the blank analysis as well as in former analyses of the other glass samples. As already observed in the LA-ICP-MS profiles of the local defect in glasses 1 and 2, the elements characteristic for the impurity were found up to the third laser pulse indicating their presence in the coating of the glass. However, as no information is available about the crater depths, no conclusions can be made about the localization in depth of the defect.

In this work, the ability of LA-ICP-MS for the direct and simultaneous analysis of P, S, and Cl in local defects of coated glasses was successfully demonstrated. Analysis by LA-ICP-MS was performed after the optimization of experimental conditions (e.g. laser energy, repetition rate, spot diameter, and He flow rate) and, in order to determine if the impurity is present in the layers of the sample or in the glass substrate, a low repetition rate (1 Hz) with a delay of 30 s between laser shots was selected. In all cases, a "blank" analysis on the glass surface without defect was performed for comparison. Depending on the defect, one, two or three of the elements were perfectly identified and, in all cases, impurities were found in the first laser pulses indicating their presence in the coating of the glass.

5.2 Analysis of metalloproteins separated by gel electrophoresis: Absolute quantification of human serum transferrin

5.2.1 Introduction

Water, proteins, carbohydrates, lipids, and nucleic acids are important biomolecules in human body. In fact, these five types of substances make up 96% of the body's mass. These compounds are made up largely of four different chemical elements: oxygen, carbon, hydrogen, and nitrogen. Although these four elements are very important, the body also requires a number of other elements to stay healthy (*figure 5.13*). The quantity elements represent a proportion of about 3% of body weight and perform diverse important functions, such as maintenance of the bone and cellular structure (Ca), the storage of chemical energy (P), muscle and nerve functioning or protein biosynthesis (Mg). In addition, in the human body there can be found small amounts of certain elements, called trace elements, which are characterized as those, whose daily supply does not exceed 25 mg [311]. Here, it has to be distinguished between essential trace elements, those whose essential character is undetermined and those without essential properties. Essential elements are all those, whose absence in the human organism lead to heavy and/or irreversible damage, such as Fe, Cu, I, Se, Zn. Other trace elements can also be found in the human body, although they do not have any known essential function or they are known to be toxic like arsenic, lead or cadmium. Their presence is mainly attributed to similarities to essential elements.

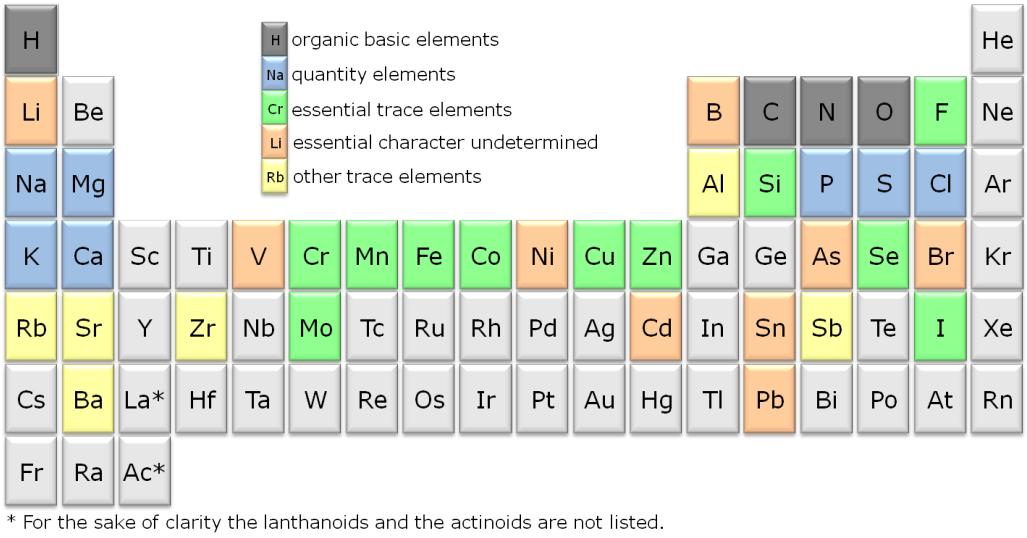

Figure 5.13: Periodic table of elements. Chemical elements important for the human are highlighted in color [311].

More than one third of all proteins require an essential metal as cofactor, usually a transition metal, e.g. Cu, Fe, Zn or Mo. A relatively new field of research has gained great importance in modern bioanalytical chemistry because of the emerging interest of the mechanisms by which metals are sensed, stored or incorporated as a cofactor and their interactions, transformations and functions in biological systems. Important terms that are used in the bibliography are summarized below: [312–314].

Metallomics: Qualitative and/or quantitative study of a metallome, interactions and functional connections of metal ions and their species with genes, metabolites and other biomolecules within organisms and ecosystems. It implies:

- A focus on metals or metalloids (e.g. Fe, Se) in a biological context, without the extension to biologically important non-metals such as sulfur or phosphorus.
- A correlation (statistical, structural or functional) of the element concentration blueprint or element speciation with the genome.
- A systematic, comprehensive or global approach.

Metallome: The term metallome refers to the entirety of metal and metalloid species within a cell or tissue type, their identity, quantity and localization. It encompasses, among others, the inorganic species (ionome) and protein complexes (metalloproteome). Deciphering a metallome will thus give following information:

- How an element (metal or metalloid) is distributed among the cellular compartments of a given cell type.
- Its coordination environment; in which biomolecule it is incorporated or by which bioligand it is complexed.
- The concentrations of the individual metal species present.

Metalloprotein: In contrast to the above mentioned the function of this protein is conferred by a metal, which means, that the protein must have a (coordinate) covalent bond to a metal. It can be distinguished between different functions, e.g. catalytic activity, implication in electron-transfer reactions of redox-active metal ions or stabilization of the protein tertiary or quaternary structure. Thereby the metal is usually bound as a hydrated ion or a metal-containing cofactor.

Metal-binding protein: Class of proteins which complex a metal due to the existence of a thermodynamic equilibrium in the system. In this case the metal has no particular influence on the function of the molecule.

Metallometabolite: Metal complex with an endogenous bioligand produced by a biochemical reaction or biosynthesized by an organism exposed to metal stress, or a biologically altered metallobiomolecule that had been deliberately introduced into an organism (e.g. as metallodrug).

In the last years many efforts and advances have been made for a comprehensive study of metalloproteins, basically dealing with the structures and functions of the metal sites as well as the biological implications of these interactions. In addition, the bioavailability and toxicity of the elements also depend on their chemical forms. Speciation analysis is aiming to define and quantify the distribution of a target element between the different species in which it occurs [315]. Today it is well accepted that such information is mandatory for a complete understanding of the processes occurring in biological systems. However, speciation analyses are often difficult because of the lability of most of the biological species, the complex composition of the samples, the low concentration of some species and additionally the very small volumes (up to nanoliters) to analyze. Therefore the use of techniques with high resolution for separation as well as high sensitivity is mandatory.

A benchmark in speciation analysis was the hyphenation of a powerful separation technique (chromatographic or electrophoretic) with a sensitive element-specific detector (e.g. ICP-MS). The current state-of-the-art of hyphenated techniques for the bioinorganic speciation analysis is schematically shown in *figure 5.14*. Different separation techniques can be combined (on-line or off-line) to either ICP-MS for sensitive element-specific detection or to mass spectrometry with soft ionization for structural identification. ICP-MS and ESI/MALDI-MS provide complementary data for the sensitive detection, quantification and identification of metallo-biomolecules.

The coupling of HPLC, employing different separation mechanisms with ICP-MS, has been the most widely used and reviewed [313, 316, 317]. Furthermore, taking advantage of the low sample-volume requirements, high plate number (peak efficiency), the ability to separate positive, neutral and negatively charged species in a single run, and, generally, short run times, the hyphenation of capillary electrophoresis to ICP-MS is widely employed [318, 319]. Sensitivity is, however, becoming a key issue

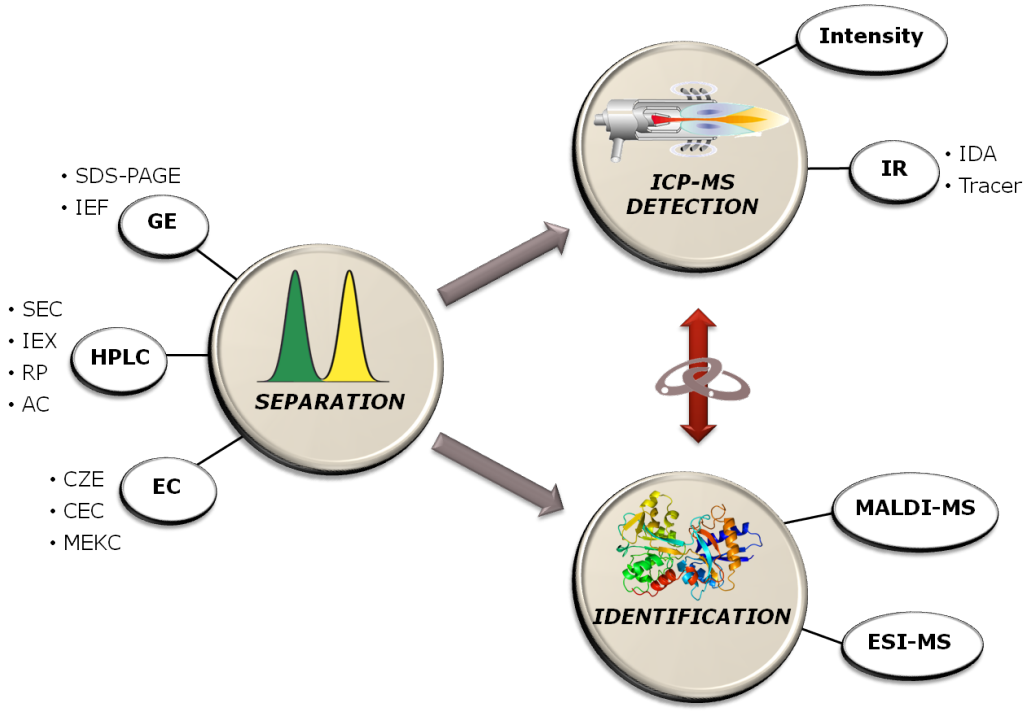

Figure 5.14: Hyphenated techniques for speciation analysis

when capillary separation techniques are used or when the target sample amount is very small.

Gel electrophoresis, employed in either the monodimensional (1D) or two-dimensional (2D) and with its unique ability to resolve thousands of proteins in a single run, is a powerful tool used routinely in biochemical, medical and molecular biology laboratories. In fact, such routine tool has contributed significantly to clarify key bioscience issues, opening many new biological and clinical avenues. Classical detection methods in GE employ specific chemical reactions, resulting in visible spots in the gel. The analyte biomolecule can be extracted from the spot in the gel and characterized by molecular MS. One of the main limitations of GE techniques is to achieve the absolute quantification of the corresponding protein. An alternative approach consisting of the direct analysis of gels using laser ablation ICP-MS was first reported by Neilsen et al. in 1998 [81]. The manifold applications arising during the following years have already been described in the Fundamentals chapter, *section 3.3* on page 48ff.

The principal difficulty in the use of PAGE-LA-ICP-MS in metallomics is the need for preservation of the metal ion bound to the protein of interest. Proteins containing

covalently incorporated metals (e.g. selenoproteins) can be analyzed easily with very low detection limits, as shown by Chéry et al. [200] and Ballihaut et al. [320]. But many metal-complexes with proteins (e.g. transferrin) are labile and can be destroyed by denaturation of the protein (e.g. during SDS-PAGE). Additionally, not only the nature of the electrophoretic separation can alter the metal-protein binding. There are several studies devoted to investigate the stability of metalloproteins during GE and post-separation gel treatments [321–323]. Raab et al. [321] have recently reported a study on the conditions necessary for an effective and accurate application of GE-LA-ICP-MS for the analysis of metal-binding proteins. Experimental results showed some important remarks:

- It is necessary to use native separation conditions for most metalloproteins, since SDS and other denaturing agents destabilize most metal-protein complexes.
- The use of unstained gels is recommended, as elemental loss during staining procedures with silver or Coomassie Blue was observed to be generally very high.
- Although several gels drying processes can be employed, the use of glycerol followed by heating proved to be a suitable method of drying without extensive element loss.
- Elemental contamination of gels surface should be avoided by using clean-room facilities when available.

Therefore, it can be concluded that a separation protocol for proteins alone cannot be directly extrapolated to metal-protein complexes and a careful assessment of the separation parameters and post-separation gel treatments has to take place for each specific application.

However, most of the efforts devoted to metallomics using GE-LA-ICP-MS have focused on developing methods that enable efficient identification of proteins in complex samples whereas protein quantification studies are comparatively scarce. Quantitative protein analysis is nowadays one of the main challenges in analytical and bioanalytical sciences since it can provide additional information for understanding pathological and biochemical pathways within biological systems [324]. It has been demonstrated that the natural presence of a heteroelement in a given protein enables the application of elemental MS in the field of metalloproteomics, making possible a robust and sensitive approach for protein quantification [199, 325]. Different calibration strategies

have been investigated for the quantitative analysis of proteins separated by GE using LA-ICP-MS, being the proposed strategies mainly focused on external calibration and the use of isotope dilution mass spectrometry (IDMS).

External calibration methods have been traditionally used for quantitative protein analysis by GE-LA-ICP-MS using protein standards. Several examples can be found in the literature for the analysis of selenoproteins, phosphoproteins and metalloproteins [194, 201, 209, 220, 320, 326]. External calibration was carried out by the separation in the gels of a model protein standard at different concentration levels. Protein bands were then scanned by the laser beam in the direction of electrophoresis migration and the calibration curve was obtained by the integration of LA-ICP-MS profiles. In such a way, it is possible to perform the quantification of a protein not only of the same species than that used in the standard but also for other species [201, 209, 220]. As an alternative procedure, the hydration of the gels with standard solutions of increasing concentrations for the sought elements has been also investigated [200, 327]. The main drawback of this approach is the difficulty to ensure the homogeneous distribution of the elements in the gel and, also, that the gel contains the analyte at the desired concentration after hydration. In addition, this strategy is not applicable for proteins electroblotted onto nitrocellulose or PVDF membranes. Becker et al. [210] proposed a new quantification procedure using a solution-based calibration, where an ultrasonic nebulizer for the nebulization of calibration standard solutions was coupled to the laser ablation chamber. Co was added as an internal standard element to the gel after separation of the protein mixture for correction of possible variations of gel ablation rate from point to point. The proposed method was used for the direct quantification of protein-phosphorus contents in human tau proteins. Nevertheless, it should be stated that an important prerequisite is needed for its correct application; the particles size distribution of the laser-generated aerosol has to be well represented by the ultrasonically generated aerosol and it has to be constant during ablation. Moreover, transport, vaporization and ionization must be identical for both types of aerosol, which is hard to achieve.

Those approaches are external calibration methods and neither consider the behavior of proteins under the conditions used for electrophoresis nor compensate for possible non homogeneities in a protein spot. Thus, alternative quantification strategies, such as the use of IDMS have been recently proposed for quantitative protein analysis by GE-LA-ICP-MS. Isotope dilution mass spectrometry (IDMS) is internationally

regarded as an absolute measurement method directly traceable to the International System of Units [172, 173]. In contrast to other calibration approaches, the analytical result is not affected by signal drifts, matrix effects or analyte losses. Therefore, quantification of metalloproteins by GE-LA-ICP-MS can be improved by the addition of an isotopically enriched protein at the beginning of the sample preparation procedure (species-specific spiking); the electrophoretic separation, analyte losses or transformations of the species will not affect the final results. Additionally, LA-ICP-IDMS can also correct for some common fractionation and matrix effects that cannot be controlled using other calibration procedures.

So far, investigations to assess the analytical performance of IDMS in combination with GE-LA-ICP-MS are scarce [181, 226]. Deitrich et al. [181] reported the use of an isotopically enriched ^{65}Cu, ^{68}Zn-superoxide dismutase (SOD) complex in an attempt to quantify natural SOD in a spiked liver extract subjected to native 1D-PAGE. The stability of the isotopically enriched metal-protein complex was carefully investigated. However, the absolute quantification capabilities of IDMS were not demonstrated, since the analysis of reference materials to validate the quantification approach was lacking.

Objective

The aim of this chapter is the development and validation of a species-specific LA-ICP-IDMS methodology to achieve a sensitive, fast and accurate absolute quantification of transferrin (Tf) metalloprotein in serum samples. Transferrin has been selected as model metalloprotein due to its important role in the iron metabolism of the human body. The most common analytical approaches for absolute quantification of Tf in serum samples are based on separations by chromatography [328] or electrophoresis [329] techniques followed by an iron-specific detector such as an ICP-MS. The proposed method is based on the use of an isotopically enriched ^{57}Fe-Tf complex to quantify natural Tf in human serum samples, after native one-dimensional GE separation (1D-PAGE). A critical evaluation of novel external calibration strategies and the species-specific IDMS quantification method, in terms of precision, accuracy and analysis time was performed. The proposed species-specific GE-LA-ICP-IDMS method was validated analyzing a certified reference serum material.

5.2.1.1 Biological relevance of transferrin

Iron represents a paradox for living systems by being essential for a wide variety of metabolic processes (oxygen transport, electron transport, DNA synthesis, etc.) but

also having the potential to cause deleterious effects. Because of iron's virtual insolubility and potential toxicity under physiological conditions, specialized molecules for the acquisition, transport, and storage of iron in a soluble, nontoxic form have evolved to meet cellular and organism iron requirements. Physiologically, the majority of cells in the organism acquire iron from a well-characterized plasma protein; transferrin.

Transferrin is a glycoprotein which is produced by the liver and mainly responsible for iron ion delivery in vertebrates. It has two binding sites for Fe^{3+} ions, with which it binds free iron in serum tightly but reversibly (*figure 5.15*) and transports it into cells, where it is transferred to transferrin receptors.

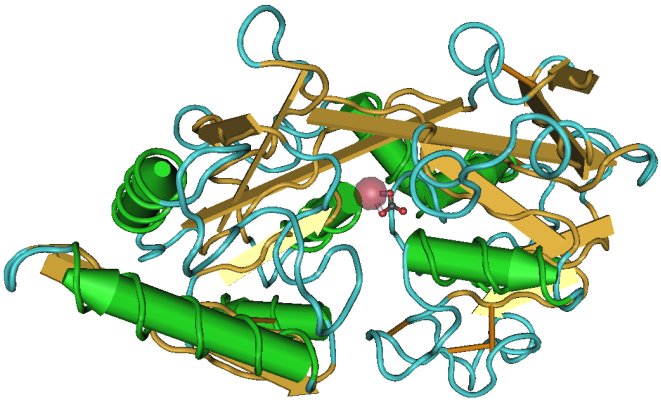

Figure 5.15: Structure of the N-terminal part of human transferrin. The iron-binding site is highlighted in red.

There are four main isoforms of transferrin: pentasialo, tetrasialo, trisialo and disialo isoform. With a share of 4% of plasma proteins transferrin is the fourth most common protein in blood plasma. The standard concentration in human serum is about 2.5 mg mL^{-1} [330]. An increase of the transferrin level is observed in iron deficiency and pregnancy. A decrease of this level occurs in chronic inflammations, cancer, iron overload or hemolysis. Generally, the transferrin saturation is about 30%. In cases of excess of iron the saturation may increase and therefore the binding capacity of transferrin may be quickly exhausted, so that there remains free iron in the blood plasma, which is toxic. At full saturation of transferrin, the plasma can absorb about 12 mg of iron, a comparatively small amount. The bound iron in transferrin is approximately 0.1% of total iron in the human organism.

5.2.2 Samples

Human serum holo-transferrin (protein standard) was used for all optimization experiments as well as for the quantification by external calibration. For the saturation of protein with isotopically enriched ^{57}Fe human serum apo-transferrin (protein standard) was employed. The certified reference material (CRM) ERM-DA470k/IFCC (serum protein reference material) was selected for the validation of the proposed quantification methodology. Moreover, a pool of human serum samples from healthy volunteers was kindly provided by the Laboratory for Clinical Analysis (Central University Hospital of Asturias, Spain).

5.2.3 Optimization of GE-LA-ICP-MS parameters for the analysis of gels

The general tuning of the LA-ICP-MS system was performed daily as described in the Experimental chapter (*section 4.1*). For the analysis of gels by LA-ICP-MS the additional optimization of several parameters illustrated in *figure 5.16* is required.

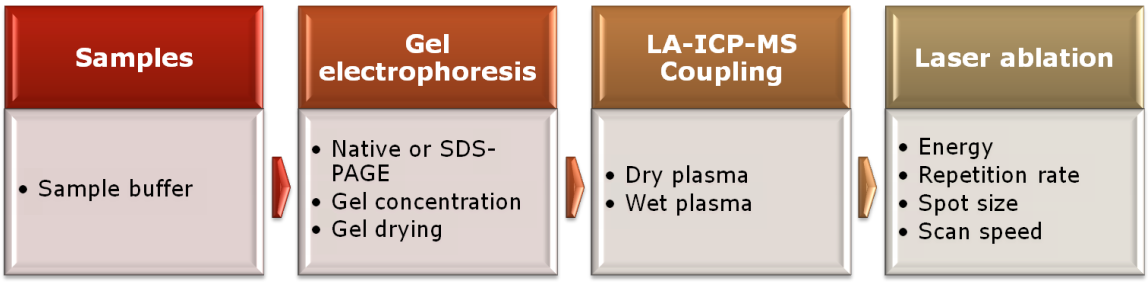

Figure 5.16: Workflow for the optimization of experimental parameters for the analysis of gels.

Each of them will be discussed in detail in the following. The optimized conditions are summarized in *table 5.3*.

5.2.3.1 Sample buffer preparation

Prior to the electrophoretic separation, both protein standards and serum samples were mixed with the sample buffer. Typically employed sample buffers in gel electrophoresis (Bio-Rad Laemmli sample buffer) contain, additionally to the reagents mentioned in *table 5.3*, β-mercaptoethanol, which is used to reduce disulfide bonds.

Table 5.3: Optimized parameters used for the analysis of gels by LA-ICP-MS.

System	Parameter	Value
ICP-MS	RF power	1325 W
	Cooling gas	15 L min^{-1}
	Auxiliary gas	0.8 L min^{-1}
	Carrier gas (Ar)	0.4 L min^{-1} (dry plasma) 0.6 L min^{-1} (wet plasma)
	Cones	Ni (Skimmer and Sampler)
	Mass resolution	4000
	Isotopes monitored	^{13}C, ^{32}S, ^{34}S, ^{54}Fe, ^{56}Fe, ^{57}Fe, ^{58}Fe, ^{69}Ga, ^{71}Ga
	Acquisition time	1.7 s
	Mass window	100%
LA system	Laser energy	100% (5.6 mJ)
	Repetition rate	20 Hz
	Spot size	200 μm
	Scan speed	40 μm s^{-1}
	Ablation mode	Single line scan
	Carrier gas (He)	1.0 L min^{-1} (dry plasma) 0.8 L min^{-1} (wet plasma)
GE system	%T Resolving gel	10 (SDS-PAGE) 8 (Native PAGE)
	%C Resolving gel	0.9 (SDS-PAGE) 0.7 (Native PAGE)
	%T Stacking gel	4
	%C Stacking gel	0.3
	Electrophoresis buffer	25 mM Tris, 200 mM Glycine, (3.5 mM SDS*)
	Sample buffer	150 mM Tris-HCl, pH=8.8, 50% Glycerol, bromophenol blue, (0.4% SDS*)
	Voltage	const. 300 V
	Electrophoresis duration	$\sim$ 20 min

* only in denaturing gels

In an initial study, stock solutions of 15 nM Tf at different pH values (6.5, 6.8, 7.4, 8.0 and 8.8) were divided into three aliquots. The first aliquot was mixed with the sample buffer containing SDS and dithiothreitol (DTT) which can be used instead of β-mercaptoethanol. The second aliquot was treated only with SDS and the last aliquot was diluted with the corresponding amount of buffer without reducing agents. After incubation, the samples were centrifuged in order to separate possible free iron and the protein solution as well as the filtrate were quantified by external calibration. The obtained results are shown in *figure 5.17*.

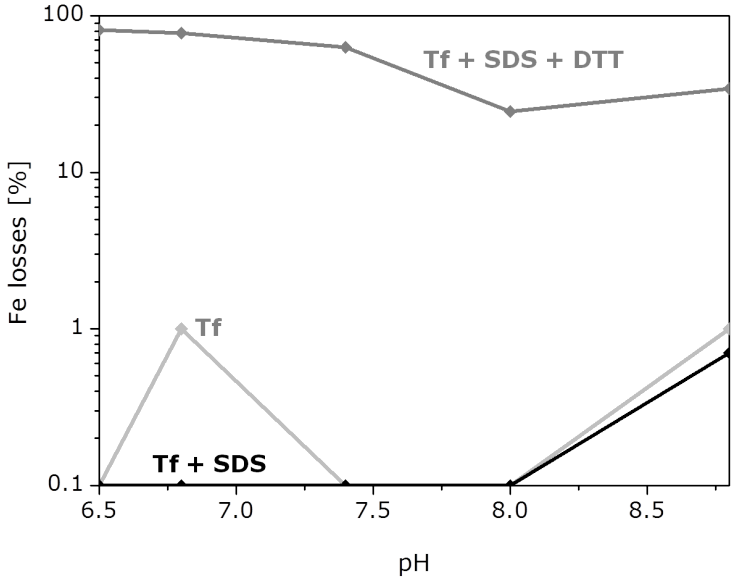

Figure 5.17: Analysis of free ^{56}Fe after treatment of Tf with SDS, SDS and DTT and without any treatment.

As it can be seen, the addition of SDS, although disrupting non-covalent bonds, does not lead to a loss of the bound metal as observed for the untreated Tf sample (free iron <1%). On the other hand, the reducing agent DTT leads to a nearly complete loss of the coordinated metal. Therefore, all further SDS-PAGE experiments were performed without the addition of reducing agents.

5.2.3.2 Optimization of gel electrophoretic conditions

Native and SDS-PAGE separation and gel concentration

As the main objective of this work is the quantification of transferrin in clinical samples, first of all the optimization of the electrophoretic separation of the proteins

in human serum was carried out. Typically, the serum proteins are divided into five groups, which can be separated from each other by electrophoretic methods (*table 5.4*).

Table 5.4: Electrophoretically separable protein fractions in human serum.

Fraction	**Important proteins**	**Concentration [mg mL^{-1}]**
Albumin	Albumin	43
α_1-Globulin	α_1-Lipoprotein (HDL) α_1-Antitrypsin Transcortin	3
α_2-Globulin	α_2-Macroglobulin α_2-Haptoglobin α_2-Glycoprotein	7
β-Globulin	β-Lipoprotein (LDL) Transferrin Hemopexin	9
γ-Globulin	Immunoglobulin G Immunoglobulin A Immunoglobulin M Immunoglobulin D Immunoglobulin E	11

Due to the enormous range of concentration between about 43 mg mL^{-1} of albumin and 2.5 mg mL^{-1} of transferrin, the dilution of the sample is important not to overload the gel, but still see the less abundant transferrin. On the other hand, also the concentration (%T) of the resolving gel is important to ensure the separation of transferrin from other serum proteins. Additionally, as SDS-PAGE provokes a denaturation of the proteins, this could lead to a loss of the transferrin associated iron and therefore distort the quantification of the protein. For this reason, separations under denaturing and native conditions have been investigated.

A summary of the optimization of the concentration (%T) of the resolving gel and the dilution of the human serum under denaturing conditions is shown in *figure 5.18*. As can be seen in the first gel in the upper line (A), working with either undiluted human serum or diluted 1:1 leads to an overload of the gel and therefore the proteins cannot be separated. A dilution of 1:10 offers quite good results, while the final dilution of 1:100 leads to a loss of the transferrin spot because of its low

concentration. Thus, all further studies with human serum samples were performed using a 1:10 dilution.

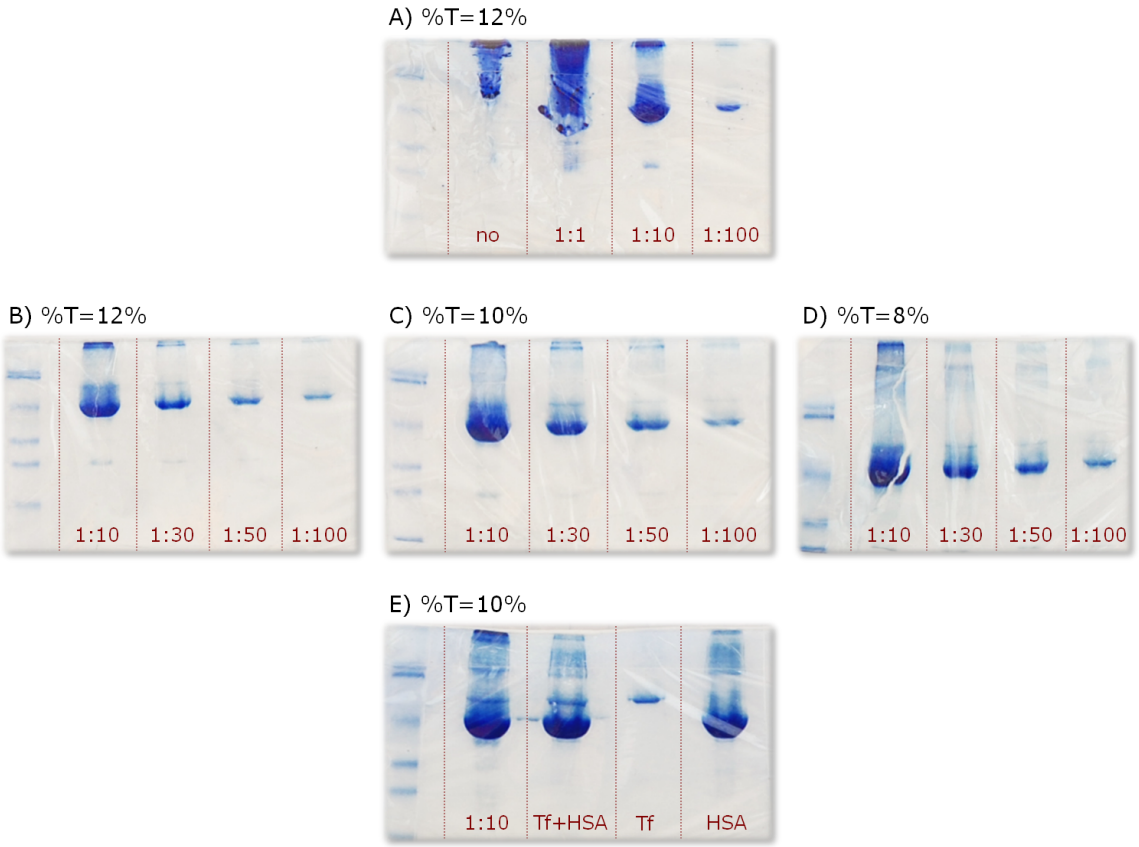

Figure 5.18: Optimization of sample dilution and %T of the resolving gel under denaturing conditions (SDS-PAGE) using human serum samples.

Several concentrations (%T) were investigated, ranging from 6% to 14%. The results obtained for three representative %T-concentrations are shown in the middle row of *figure 5.18* (gels B, C and D). As it can be seen, all concentrations are suitable for the proper separation of human serum proteins. However, further studies under denaturing conditions were performed using a resolving gel of 10%. For the identification of the proteins of interest, gel (E) also shows, additionally to a 1:10 diluted serum sample, the protein standards of transferrin (Tf) and human serum albumin (HSA) separated under the previously optimized conditions.

As the dilution of the sample had already been optimized under denaturing conditions, for the separation under native conditions only the dilution 1:10 was used (see *figure 5.19*). The finally selected concentrations of the gels were %T=10 for SDS-PAGE and %T=8 for native PAGE and are summarized in *table 5.3* (page 102).

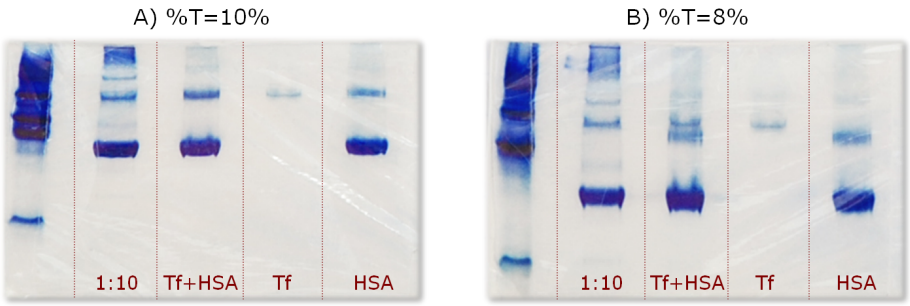

Figure 5.19: Optimization of %T of the resolving gel under native conditions using human serum samples.

Comparing the resulting gels of SDS-PAGE and native PAGE several observations can be made. On the one hand, the proteins spots in the native gels are better defined. On the other hand, in contrast to SDS-PAGE, here, the transferrin spot is separated completely from all other proteins, which facilitates its quantification. This is due to a slightly different separation mechanism between SDS-PAGE and the native PAGE. In the latter there is no addition of any denaturing agent, such as sodium dodecyl sulfate, to the sample, which results in a separation of the proteins depending on their size and additionally, with even more influence, due to their own charge. This leads to the clear separation of two proteins of similar molecular weight (Tf and HSA).

Drying of the gels for LA-ICP-MS analysis

The absorption of the laser energy is heavily dependent on the sample matrix. Therefore, three different drying processes for gels have been investigated.

1. The gel was placed in glycerol for 2 min, mounted on filter paper and then air-dried until no further change in the texture of the sample was observed (up to one day).

2. The gel was placed in glycerol for 2 min, mounted on filter paper and dried in an oven at 70°C, which resulted not only in a faster drying process (a few hours) but also in a slightly more rigid texture of the gel.

3. The gel was air-dried directly on the filter paper after the electrophoresis. This resulted in a very thin, plastic-like texture of the sample.

The gels were analyzed by LA-ICP-MS in dry plasma conditions (for experimental parameters, see *table 5.3*, page 102) monitoring sulfur. In *figure 5.20* the LA-ICP-MS profiles obtained can be seen.

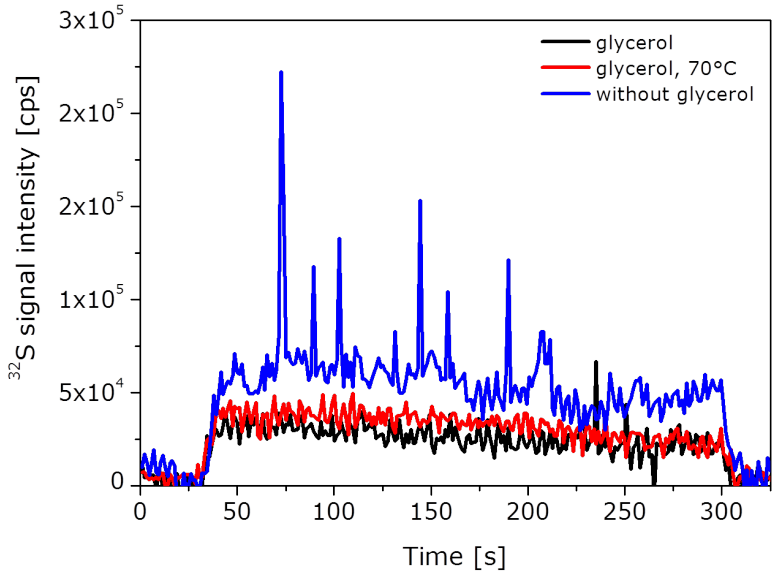

Figure 5.20: Influence of the gel drying method on the LA-ICP-MS signal.

As can be seen, the profile obtained for the gel dried with glycerol (black line) is quite stable. In comparison, the profile of the gel dried with glycerol at 70°C gives a slightly higher signal (red line). The highest signal intensities are obtained with the plastic-like gels, corresponding to the gel dried without glycerol (blue line), nevertheless, it shows more instabilities with a lot of spikes along the profile which are due to cracks in the gel that occur during the drying process. Therefore, for further analyses, only two drying methods were taken into account, trying to compare the benefits of a stable signal (drying with glycerol at 70°C) to higher intensities (drying without glycerol).

5.2.3.3 Dry and wet plasma conditions

Laser ablation analysis can be performed in two different modes: dry and wet plasma conditions, which consist of the analysis of the dry aerosol formed in the ablation cell or the addition of a solution to the dry aerosol before entering the plasma torch, respectively. Both operation modes require different experimental set-ups, which are shown in *figure 5.21*.

The dry plasma conditions are obtained by connecting the sample out tubing of the laser ablation system directly to the torch of the ICP, trying to keep the length as short as possible to avoid excessive laser-generated particles losses.

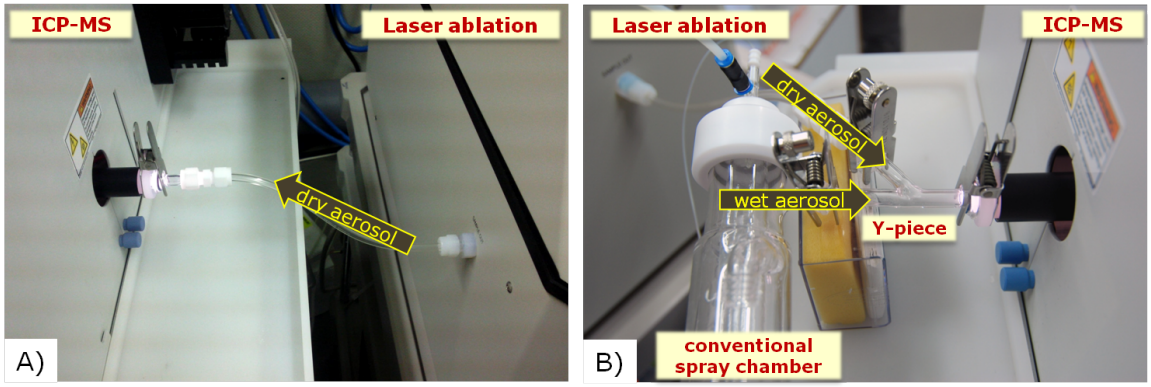

Figure 5.21: Experimental set-up for (A) dry plasma conditions: direct introduction of the laser generated aerosol and (B) wet plasma conditions: mixing of the laser-generated aerosol with a nebulized solution using a glass Y-piece.

For the wet plasma conditions a glass Y-piece serves to mix the laser generated aerosol with the wet aerosol formed in the spray chamber just before entering the torch of the ICP. By introducing an additional wet aerosol the sensitivity can be increased due to a reduction of the ICP-MS load effects [331] and possible carbon depositions on the cones are also reduced. Another major difference in the experimental set-up of dry and wet plasma is the introduction of the nebulization gas (argon) into the ICP-MS. In the case of the dry plasma conditions, the argon flow is introduced into the tubing system of the LA and mixed with the helium flow before entering the torch of the ICP. In contrast to this, in wet plasma conditions the argon is only used for the conventional nebulization of the solution and does not enter the laser ablation system. In both cases helium was used as carrier gas for the transport of the laser-generated aerosol through the ablation cell.

Both gas flows (carrier gas - helium, nebulization gas - argon) have an enormous influence on the sensitivity and the elemental fractionation effects. Therefore, a careful optimization was performed, taking into account, that each gas flows depends on the other one and cannot be considered separately. For this reason, both gas flows were varied dependent on each other until maximum intensities and optimal U/Th ratio were achieved. The optimized parameters for both operating modes can be seen in *table 5.3* (page 102). Due to the significant increase in sensitivity (see *section 5.2.4.2*), for all further GE-LA-ICP-MS analyses wet plasma conditions were used.

5.2.3.4 Optimization of laser parameters for the analysis of gels

In order to obtain elemental information of the proteins after electrophoretic separation, a single line across the stained proteins spot was ablated. To maintain the

same ablation conditions for the tuning of the laser parameters and the subsequent analyses the same ablation strategy was chosen.

The four important parameters of the laser system (laser energy, pulse repetition rate, laser spot size and scan speed) were optimized by monitoring ^{13}C. Optimization was carried out for maximum signal intensity taking into account the gas blank.

The **laser output energy** is adjustable from 0-100% (0-5.6 mJ). Depending on the applied laser energy the laser beam penetrates more or less into the sample and, therefore, ablates different amounts of material. As the gels are dried on filter paper the laser energy was adjusted in such a way, that only the gel was ablated without reaching the support. First, a scan speed of 45 μm s^{-1}, a laser spot size of 200 μm and a pulse repetition rate of 20 Hz were applied for the analysis. As can be seen in *figure 5.22*, as it was expected, the net signal intensities of ^{13}C increased with higher laser energies.

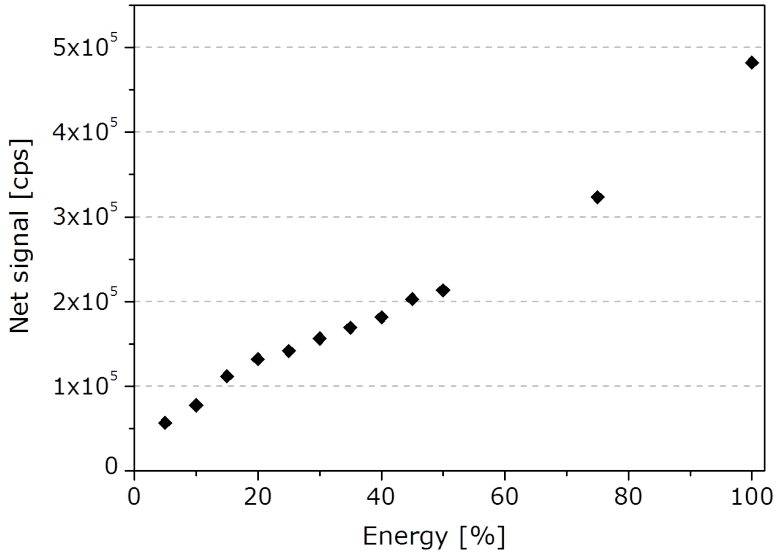

Figure 5.22: Dependence of the net signal intensity from the laser energy using a pulse repetition rate of 20 Hz, a scan speed of 45 μm s^{-1} and a spot size of 200 μm (all signals are gas blank corrected).

The pulse **repetition rate** is controlled via the laser Q-switch and can be varied from 1-20 Hz. *Figure 5.23* shows the dependence of the signal intensity from the repetition rate using a laser energy of 100%. The energy value was selected to obtain a considerable signal in spite of the expectable decreasing intensity at lower frequencies. From the results obtained it can be concluded, that increasing the pulse repetition

rate leads to higher signal intensities. Thus, for all further analyses a repetition rate of 20 Hz was chosen.

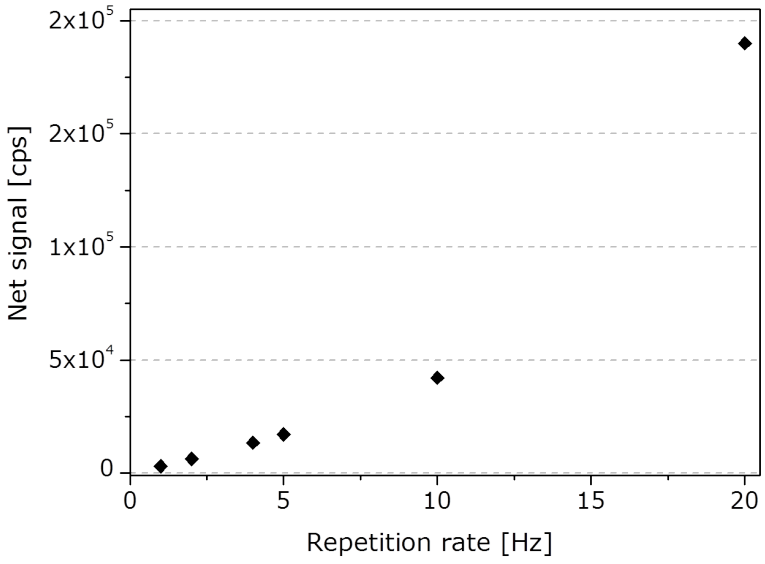

Figure 5.23: Dependence of the signal intensity from the pulse repetition rate using a laser energy of 100%, a scan speed of 45 μm s^{-1} and a spot size of 200 μm (all signals are gas blank corrected).

The **spot size** correlates directly with the quantity of the ablated material, and therefore its influence on the signal intensity needs to be investigated. The adjustable spot sizes vary between 10-200 μm. Ablating more material leads to an increase of the signal intensity, which is clearly shown in *figure 5.24*. As in the present study the lateral resolution was not very critical, the maximum spot size of 200 μm was chosen in order to ensure maximum sensitivity.

The ablation cell is mounted on an X-Y-Z translation stage. The translation stage provides X-Y positioning control for laser targeting on the sample and also for movement of the sample during line scans while the Z-axis is used to focus the laser on the sample surface. The velocity of the X-Y translation needs to be optimized, as this is also correlated with the quantity of ablated material and therefore with the signal intensity. *Figure 5.25* shows the dependence of the signal intensity from the **scan speed**. At slow velocities of the X-Y translation (10-30 μm s^{-1}), the penetration of the laser beam into the sample is high and thus the paper substrate is also ablated. This is related to the multiple ablation of the same area due to the overlapping of the laser spot diameters. At higher scan speeds (>50 μm s^{-1}) this overlapping does not occur to this extent and, therefore, the penetration and the quantity of ablated

material is less. This results in a signal decrease. The selected scan speed for further analyses was 40 μm s^{-1}.

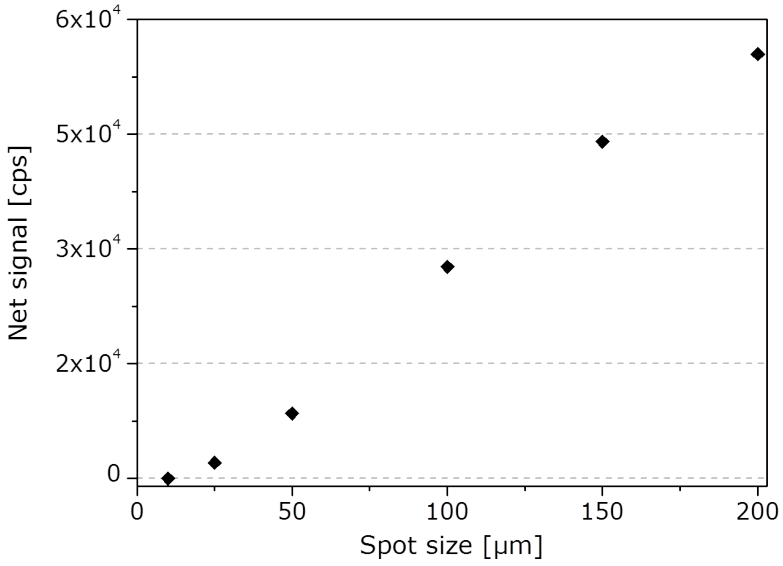

Figure 5.24: Dependence of the signal intensity from the spot size using a laser energy of 100%, a pulse repetition rate of 20 Hz and a scan speed of 45 μm s^{-1} (all signals are gas blank corrected).

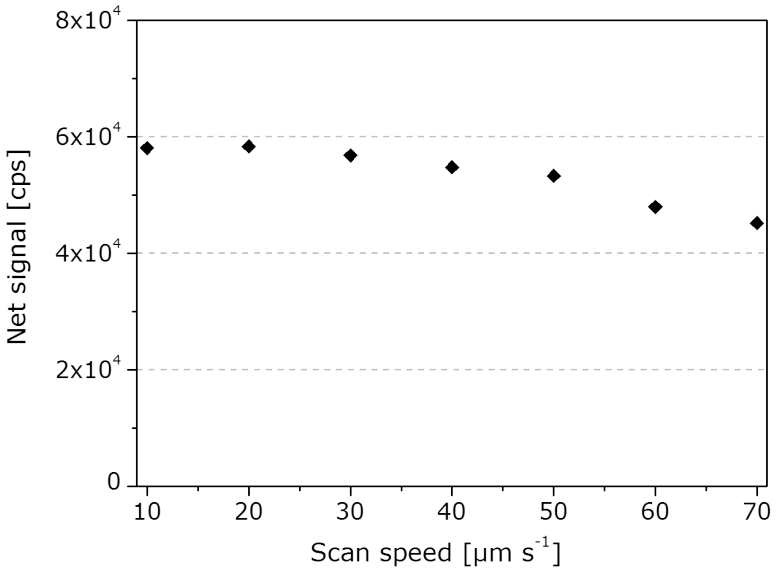

Figure 5.25: Dependence of the signal intensity from the scan speed using a laser energy of 100%, a pulse repetition rate of 20 Hz and a spot size of 200 μm (all signals are gas blank corrected).

A summary of the optimized parameters used for all further analyses is shown in *table 5.3* on page 102.

5.2.4 External calibration for the quantification of transferrin in human serum samples

After the optimization of the experimental parameters (see corresponding sections) LA-ICP-MS was applied for the quantification of transferrin in gels by external calibration. For this purpose, native gels (%T=8) were prepared and 10 μL with increasing protein amount (from 1.5 to 14.5 μg holo-transferrin) were loaded into every second lane. The empty lanes in between the samples were filled with sample buffer to guarantee a homogeneous running pattern. After separation of proteins and Coomassie staining the gel lanes were scanned in migration direction using the optimized parameters for ICP-MS, laser ablation and gel electrophoresis given in *table 5.3* on page 102. The lanes are translated under the laser beam, while the sought elements, Fe and S, are monitored and the corresponding signal intensities plotted as a function of the migration distance. In this way, an electropherogram is obtained. *Figure 5.26* shows an example of a gel used for calibration (left). In the right part of the image, the resulting profiles of the laser ablation, monitoring sulfur and iron, are shown. The highlighted area on the left, which frames the protein spot with a concentration of 14.5 μg transferrin, was zoomed in and corresponds to the profiles in the right part of the picture.

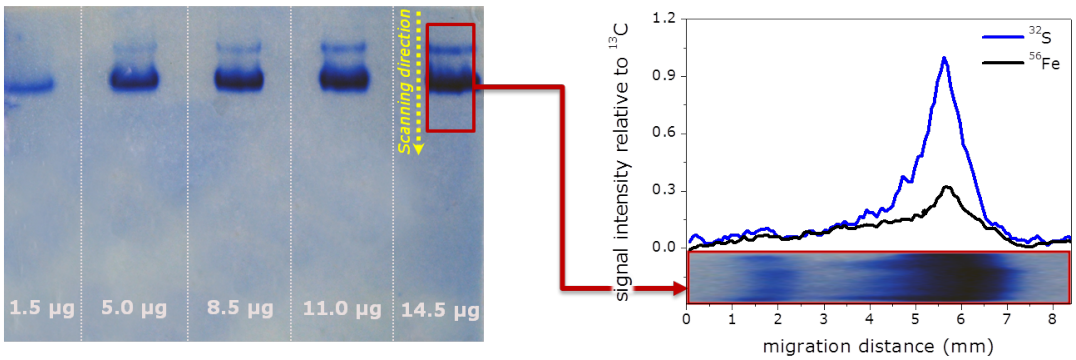

Figure 5.26: Example of a gel used for calibration (left) and obtained ^{32}S and ^{56}Fe profiles by LA-ICP-MS (right).

With the purpose of quantification, the obtained Fe and S peaks in the profiles were integrated with Origin® software and the resulting areas were plotted against the Fe or S concentration, respectively (calibration curves).

5.2.4.1 Internal standardization

In general, quantification in GE-LA-ICP-MS still remains a great challenge as there is no proof for reproducible ablation processes, especially in a sensitive matter such as a gel, which is absolutely necessary for accurate quantification. One way to overcome this problem is the use of an internal standard. As already mentioned in *section 3.2.5*, although highly controversial, the ^{13}C signal is generally employed in GE-LA-ICP-MS applications due to its homogeneous distribution in the gel. Thus, as an alternative, iodine was investigated as a possible internal standard. In order to ensure the homogeneity of the iodine throughout the gel, iodinated acrylamide (2- or 3-iodoacrylamide) was synthesized.

Synthetic route 1

The first attempt to synthesize the iodinated monomer was carried out following the synthetic route proposed by Ruel et al. in 1998 [332]. For that, acrylamide was mixed with iodine in the presence of diethyl ether, acetonitrile (ACN) and pyridine (Py) for 48 h at room temperature.

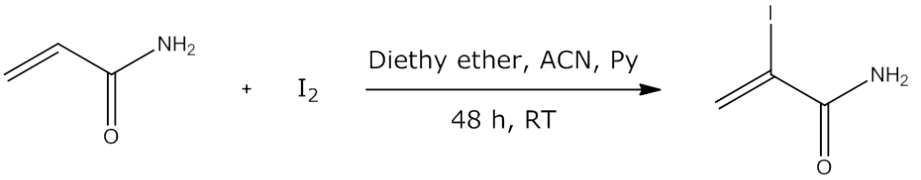

acrylamide 2-iodoacrylamide

After completion of the reaction time, the product molecule structure was determined by ^{1}H-NMR-spectroscopy. However, no satisfactory results were obtained, as the spectrum indicated polymerization of the monomer (either of the reactant acrylamide or the product).

Synthetic route 2

The second attempt was divided into two steps. First the synthesis of the intermediate 2,3-diiodopropannamide was carried out by the reaction of acrylamide with iodine in the presence of dichloromethane during 11 days at room temperature. Subsequently, the elimination of iodide was achieved by the addition of pyridine to the reaction mixture and stirring for 2 days at room temperature.

After a reaction time of three hours of the second step the product molecule structure was determined by ^{1}H-NMR. The obtained spectrum showed the clear presence of the reactant with traces of the desired product. However, after completion of the

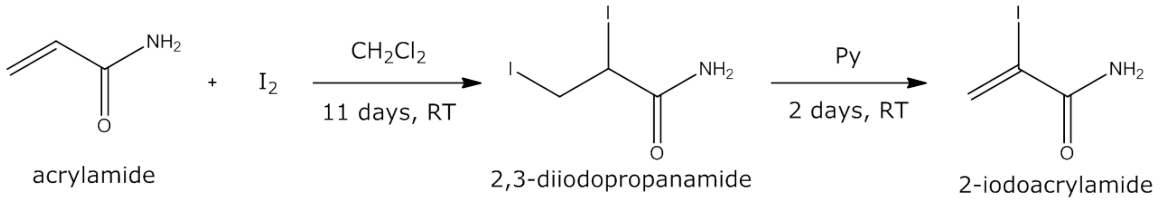

entire reaction time, ^{1}H-NMR-spectroscopy revealed the absence of both reactant and product, probably due to polymerization.

Synthetic route 3

The third synthesis route was based on the work of Ma et al. [333]. The reaction is based on the mixing of propiolamide with lithium iodide in the presence of acetic acid (AcOH) and stirring of the mixture for 22 hours at 90°C.

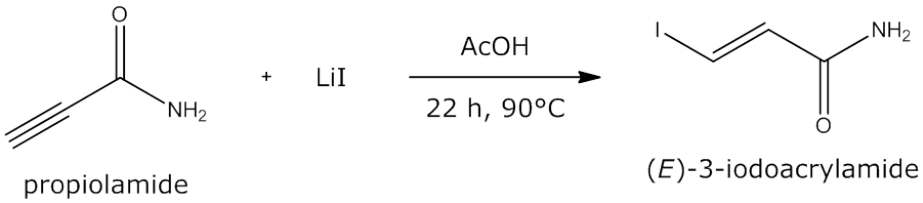

After completion of the reaction time, the product molecule structure was determined by ^{1}H- and ^{13}C-NMR. The obtained spectra are shown in *figure 5.27*, where the left spectrum (A) shows the application to hydrogen and the spectrum on the right (B) shows the application to carbon.

As it can be seen, the synthesis of the monomer (*E*)-3-iodoacrylamide was successful, as all peaks present in both spectra can be attributed to the hydrogens (in the ^{1}H-spectrum) and carbons (in the ^{13}C-spectrum) of the product. Thus, (*E*)-3-iodoacrylamide was used for the copolymerization experiments.

After the successful synthesis of the iodinated monomer, this was mixed in an appropriate amount with the conventional monomer solution (30% acrylamide/0.8% bisacrylamide). After complete mixing of the components the copolymerization was initiated. Due to the covalent bond of iodine to carbon, which should ensure its presence in the gel and the good sensitivity of an ICP-MS for this element, investigations were carried out to review the capability of this internal standardization. Subsequent studies showed, however, that the iodine is unexpectedly lost during polymerization, and therefore cannot serve for the internal correction. Thus, as the following experiments were performed in order to optimize the analysis conditions (wet or dry plasma,

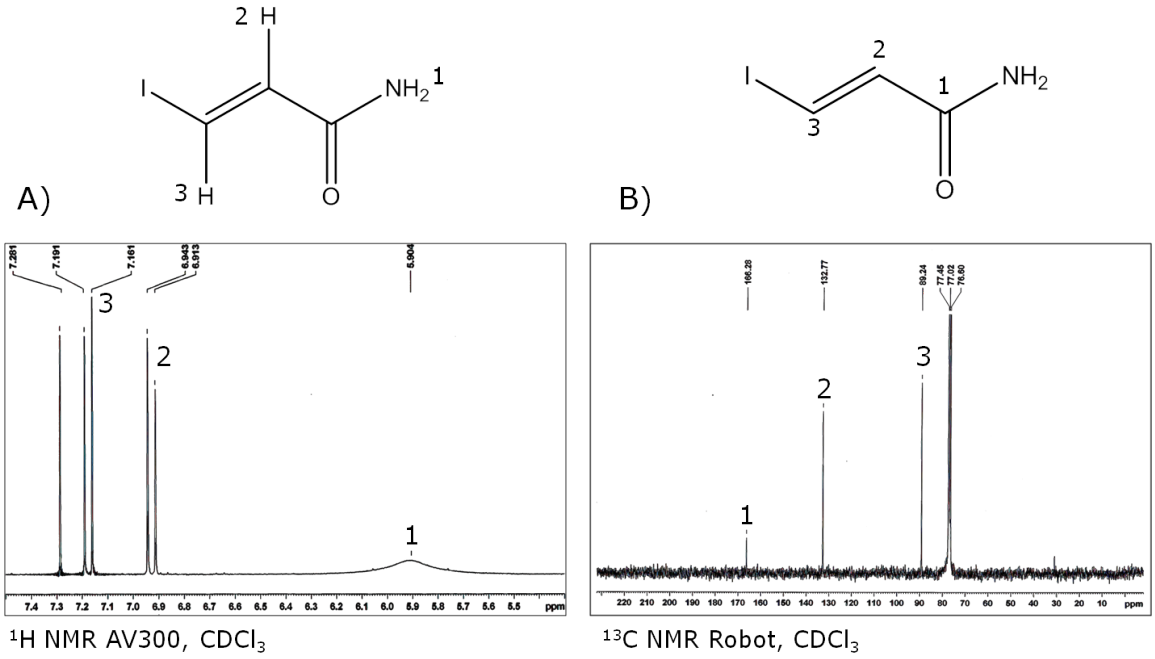

Figure 5.27: (A) ^{1}H- and (B) ^{13}C-NMR spectra of the reaction product (*E*)-3-iodoacrylamide.

gels dried with or without glycerol), no internal standardization of the net signals of $^{56}Fe^+$ and $^{32}S^+$ were was conducted.

5.2.4.2 Comparison of different analysis conditions

As already mentioned before, there are two different operating modes in laser ablation, which are distinguished by the additional introduction of a nebulized solution in wet plasma conditions, compared to dry plasma conditions. As the supply of a wet aerosol into the plasma changes its properties, the following analyses were performed comparing both conditions. Additionally, as the texture of the matrix has great influence on the ablation process, both drying methods, with and without glycerol, were also investigated for the calibration. In all cases, gels containing increasing amounts of holo-transferrin standard were prepared and treated accordingly.

Calibration in dry plasma conditions using gels dried with glycerol at 70°C

The analysis of gels dried with glycerol by LA-ICP-MS under dry plasma conditions resulted in small and broad peaks, especially in the case of the iron profiles, so that their integration was hindered. Particularly in the case of the lower concentrations the distinction of the signal peak from the base line was difficult and for the smallest protein amount (1.5 μg transferrin) integration not possible. *Figure 5.28* shows the resulting calibration curves for $^{56}Fe^+$ (left) and $^{32}S^+$ (right).

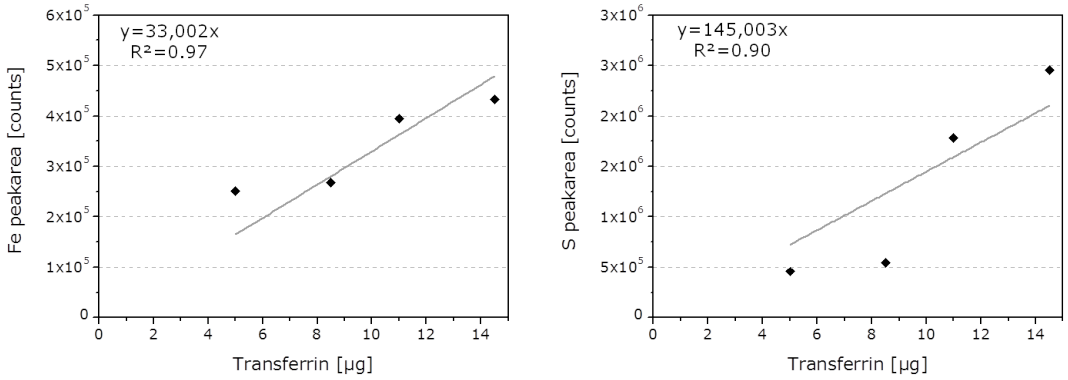

Figure 5.28: Calibration curves for $^{56}Fe^{+}$ (left) and $^{32}S^{+}$ (right) obtained for gels dried with glycerol in dry plasma conditions for different transferrin concentrations (all values are gas blank corrected).

Calibration in dry plasma conditions using gels dried without glycerol

In general, it could be observed, that the ablation of gels dried without glycerol led to slightly higher signals. All peaks could clearly be distinguished from the base line, even for the lowest concentration, resulting in calibration lines with a higher slope and better correlation coefficients, as it is shown in *figure 5.29*.

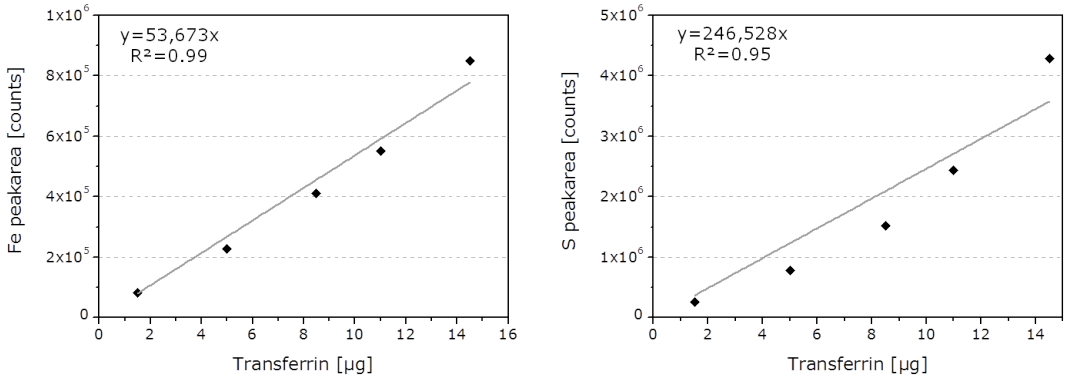

Figure 5.29: Calibration curves for $^{56}Fe^{+}$ (left) and $^{32}S^{+}$ (right) obtained for gels dried without glycerol in dry plasma conditions for different transferrin concentrations (all values are gas blank corrected).

These results could indicate that, on one hand, the absorption efficiency of the laser is increased for a more solid-like sample matrix causing a more efficient ablation of the material (less heat dissipation and melting processes) and, on the other hand, that the formed aerosol particles have a higher transport and ionization efficiency.

Calibration in wet plasma conditions using gels dried with glycerol at 70°C

In the case of the wet plasma conditions, the continuous nebulization of a 10 ng g^{-1} gallium solution was performed. In this way, fluctuations of the ICP-MS signal in the course of the day could be determined. However, no significant signal drifts could be observed, neither during one analysis nor between the first and last analysis of the day (up to 18 hours).

Figure 5.30 shows the calibration curves for $^{56}Fe^{+}$ and $^{32}S^{+}$ obtained working in wet plasma conditions and with gels dried with glycerol in an oven at 70°C.

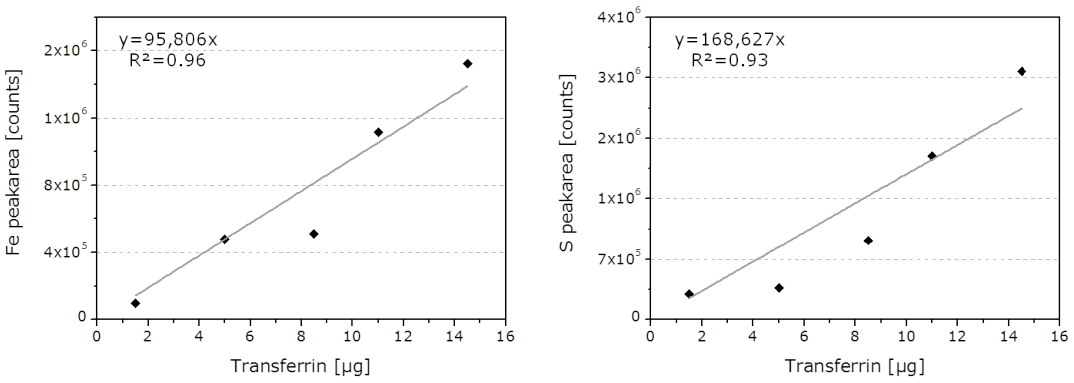

Figure 5.30: Calibration curves for $^{56}Fe^{+}$ (left) and $^{32}S^{+}$ (right) obtained for gels dried with glycerol in wet plasma conditions for different transferrin concentrations (all values are gas blank corrected).

The additional introduction of a wet aerosol resulted in a considerable increase of the signal intensities, especially in the case of iron. The enhanced sensitivity is very clear when the slopes of the individual calibration lines of iron are compared: "dry plasma, with glycerol" (m=33,002) < "dry plasma, without glycerol" (m=53,673) < "wet plasma, with glycerol"' (m=95,806), giving a general increase by about a factor of 3. Additionally, the resulting coefficients of determination in this analysis are very satisfactory.

Calibration in wet plasma conditions using gels dried without glycerol

Figure 5.31 shows the results obtained working in wet plasma conditions and with gels dried without glycerol.

In this analysis the combination of the more plastic-like gels dried without glycerol and the introduction of an additional wet aerosol into the plasma did not lead to a significant increase in sensitivity. As the gels dried without glycerol were much more fragile compared to those soaked in glycerol, the finally chosen analysis conditions implied gels dried with glycerol and wet plasma conditions.

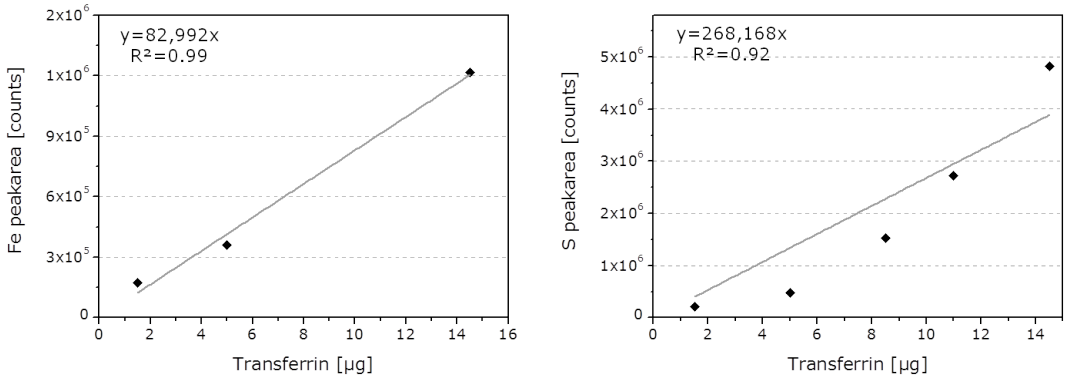

Figure 5.31: Calibration curves for $^{56}Fe^{+}$ (left) and $^{32}S^{+}$ (right) obtained for gels dried without glycerol in wet plasma conditions for different transferrin concentrations (all values are gas blank corrected).

5.2.4.3 Comparison of different ablation strategies

For the analysis of electrophoretic gels by LA-ICP-MS different ablation strategies can be employed (see *figure 5.32*). Advantages and drawbacks of each approach will be discussed in the following.

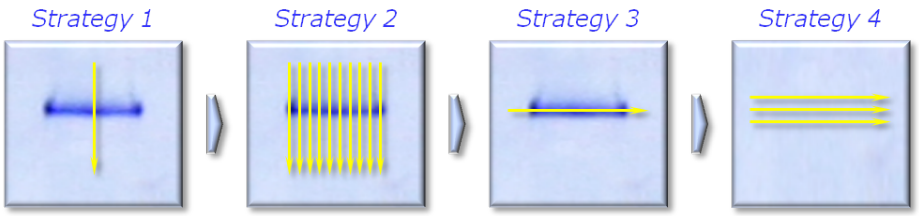

Figure 5.32: Overview of the different ablation strategies.

Up to date, conventional external calibration after gel electrophoresis by LA-ICP-MS was carried out by line scan ablation of the Coomassie stained protein spot in direction of the electrophoretic migration. In this vein, a triplicate of each holo-transferrin amount (2, 4 and 6 μg) was prepared and each protein spot was ablated once (single line ablation) corresponding to **Strategy 1** in *figure 5.32*. In order to improve counting statistics, the ablation of the same protein spot ten times was also investigated (multiple line ablation) denominated as **Strategy 2**. *Figure 5.33* demonstrates that ablation at the optimized conditions is a linear function of the concentration, where the left graph shows the calibration curve obtained for the single line ablation (n=3, 1 line per spot) and the graph on the right represents the results obtained for the multiple line ablation (n=30, 10 lines per spot). With the purpose

of quantification, the obtained peaks in the profiles were corrected with the internal standard, integrated with Origin® software and plotted against the applied amount of protein.

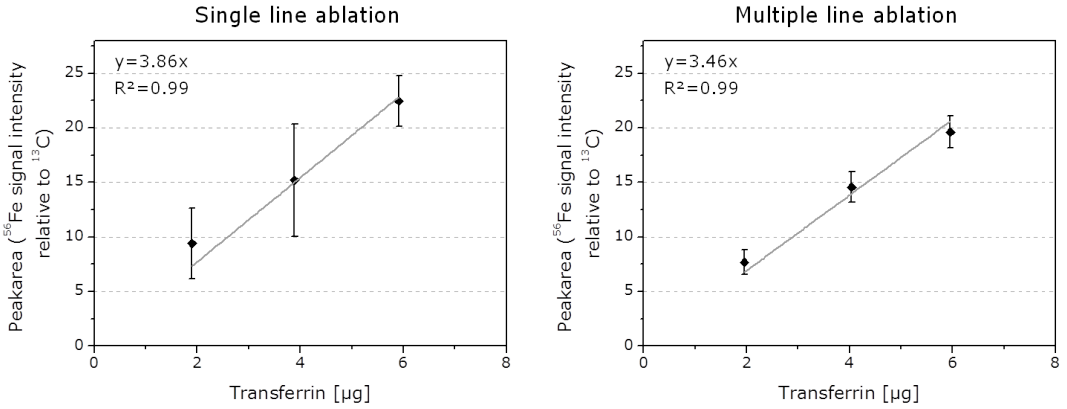

Figure 5.33: Calibration curves for $^{56}Fe^{+}$ applying single line (left) and multiple line ablation strategy (right). All values are gas blank and IS (^{13}C) corrected.

Taking a look to both graphs it is evident, that, although working under the same conditions as in *figure 5.30* (wet plasma conditions and gels dried with glycerol at 70°C), a clear improvement for the calibration curves was obtained due to the internal standard correction. Furthermore, as expected, the multiple line ablation resulted in significantly lower RSD values (error bars) and, thus, improved accuracy. Nevertheless, it needs to be taken into account that the multiple line ablation also involves a tenfold longer analysis time.

In order to overcome the difficulties of the relatively inhomogeneous distribution of the protein inside the spot and the diffusion due to the electrophoretic separation, a different ablation strategy has been investigated. *Figure 5.34* shows an example of a gel used for calibration (left). In the right part of the image, the resulting ^{56}Fe profiles of laser ablation corresponding to the two different ablation strategies applied are shown. The upper profile (A) shows the electropherogram obtained applying the conventional horizontal ablation strategy, which means in direction of the electrophoretic migration. It is clear that due to diffusion caused by the electrophoretic migration, no clear borders of the protein bands are visible. However, the intensity maximum of the ^{56}Fe signal is clearly located in the center of the protein spot. Thus, a single line ablation in the direction perpendicular of electrophoretic migration (one line in the middle of each protein spot) was performed (**Strategy 3**). *Figure 5.34B* shows the electropherogram obtained by changing the ablation strategy to perpendicular to the

direction of the electrophoretic migration. In contrast to the upper profile here is the ^{56}Fe signal is clearly defined and there is no diffusion. Therefore, the ablation of the protein was performed perpendicular to the electrophoretic migration direction in the center of the spot.

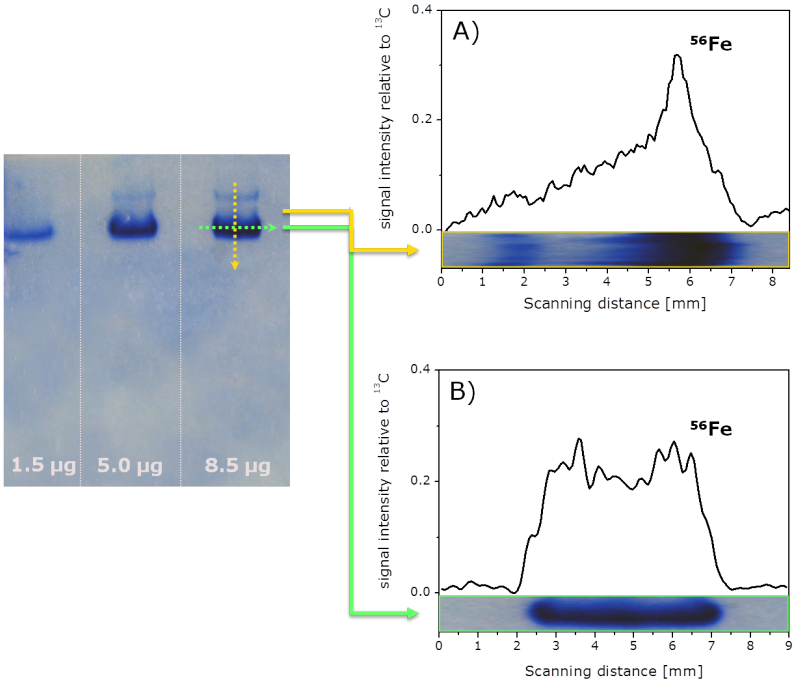

Figure 5.34: Native 1D-PAGE of natural saturated Tf and detection of ^{56}Fe by LA-ICP-MS. (A) Ablation of the protein spot horizontally to migration direction and (B) ablation of the protein spot perpendicular to migration direction.

A triplicate of each holo-Tf concentration was prepared and each spot was ablated once. The obtained profiles were corrected with the internal standard and the area corresponding to the protein spot was plotted against the amount of protein obtaining a correlation coefficient of R^2=0.99.

It has been recently reported by several authors [181, 323] that Coomassie Blue staining of the gels prior to LA-ICP-MS analysis can be a metals contamination source, increasing e.g. the Fe background in the gel and masks the real Fe content of the protein. Moreover, the reproducibility of the staining and destaining stages is quite low due to the amount of the dye in the protein spot and, therefore, the concentration of the exogenous Fe, strongly depends on the duration and homogeneity of each stage. Aiming at avoiding such contamination in the following non-stained gels were analyzed using the optimized ablation strategy perpendicular to the migration direction. Since

the proteins in the gel tend to diffuse after the electrophoretic separation, action must be taken in order to fix them in the gel. This is achieved by denaturation of the protein, which in turn can be performed either chemically (by lowering the pH to 3) or thermally (by heating to 70°C). Comparative studies, in which Tf was quantified in a certified reference material, have shown that the thermal method led to more precise and exact results.

Following the optimized procedure, a triplicate of each concentration (absolute amount of protein between 2 and 10 μg) was prepared and each spot was ablated. As the spot in the unstained gel is not visible, a larger area needed to be analyzed to ensure the ablation of the protein spot in its maximum. Therefore, the ablation of three lines per spot was carried out (**Strategy 4**). After integration of the obtained signals in the spot center, the following calibration lines were obtained (see *figure 5.35*).

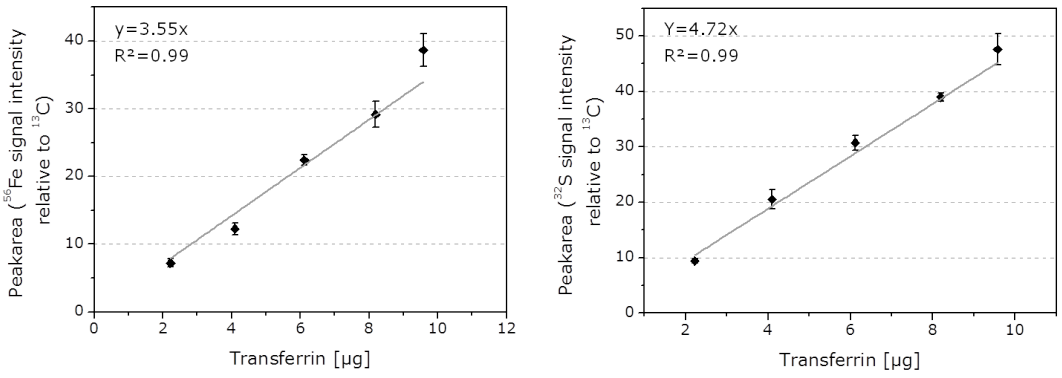

Figure 5.35: Calibration curve for $^{56}Fe^{+}$ and $^{32}S^{+}$ applying the single line ablation strategy perpendicular to the migration direction using unstained gels. All values are gas blank and IS (^{13}C) corrected.

The obtained results for both calibration curves (^{56}Fe and ^{32}S) shown very good linearity and reproducibility, confirming, that the most adequate strategy for the analysis of protein bands in gels implies the ablation of the non-stained spot perpendicular to the migration direction.

5.2.4.4 Determination of Tf concentrations in a serum reference material by external calibration GE-LA-ICP-MS

For evaluation of the methods accuracies, a reference serum sample certified for total Tf was analyzed using the proposed strategies. *Figure 5.36* shows the obtained

electropherogram and the resulting signal intensities for ^{56}Fe. As can be seen, Fe is present to a low extent coordinated to the immunoglobulins in the first 5 mm and to a higher extent to Tf (at 9 mm) and albumin (at 18 mm).

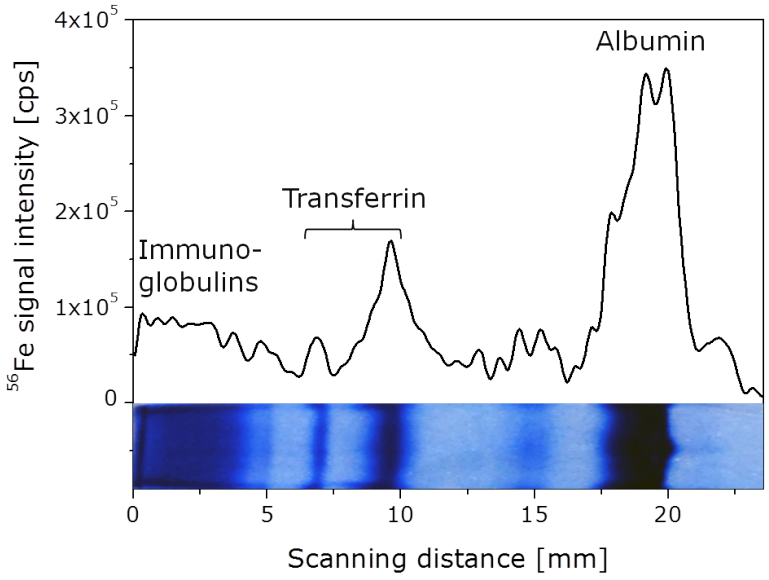

Figure 5.36: Electropherogram of ^{56}Fe obtained after native 1D-PAGE of a certified human serum sample.

The spot corresponding to the Tf was ablated in total either 3 or 30 times in three different replicates of the same sample. The obtained results for the determination of total Tf using single line calibration (**Strategy 1**) were 2.45 ± 0.76 g L^{-1} and showed an acceptable agreement with the certified value (2.36 ± 0.08 g L^{-1}), but with very high RSDs (∼ 31%). By quantification of total Tf using multiple line calibration (**Strategy 2**) an amount of 2.21 ± 0.10 g L^{-1} was found. The precision for the analysis of Tf in the certified serum sample (calculated as the RSD of 30 line scans) was of about 5%.

By changing the strategy to ablation of the protein spot perpendicular to the migration direction (**Strategy 3**) the obtained results for the quantification of total Tf (2.07 ± 0.30 g L^{-1}) showed an acceptable agreement with the certified value (2.36 ± 0.08 g L^{-1}) with lower RSDs than the single line ablation previously described (∼ 14%). Although it shows higher RSDs than the ones obtained by multiple line ablation strategy, the time factor needs to be taken into account, as the analysis by multiple line ablation takes about 18 hours (including 5-point calibration and one

sample) and the analysis with the changed ablation strategy (perpendicular to migration direction) less than two hours (including 5-point calibration and one sample).

Finally, the concentration of total Tf using the ablation strategy perpendicular to the migration direction in unstained gels (**Strategy 4**) was determined to 2.25 ± 0.18 g L^{-1}, which is in good agreement with the certified value (2.36 ± 0.08 g L^{-1}) with low RSDs (8%). In addition to Fe, S can also be used for quantification as it is present in the protein in form of the amino acids methionine and cysteine. The corresponding calibration curve is shown in *figure 5.40* (right). The quantification of Tf in a certified reference material gave a value of 2.52 ± 0.24 g L^{-1}, which coincides quite well with the certified value.

A summary of the results for the quantification of Tf in a certified human serum by external calibration is listed in *table 5.5*. The precision of the measurements was calculated based on 1s-standard deviation from three independent replicates. In addition, the table shows for comparison the required analysis time for each calibration and the obtained limits of detection for Tf. To calculate the limits of detection the 3s criterion ($3s_b/S$) was employed, where s_b is the standard deviation of five independent measurements of the blank value (ablation of a pure polyacrylamide gel without protein spot) in cps and S is the sensitivity for the corresponding analyte isotope obtained by measuring the reference material ERM-DA470k.

Table 5.5: Comparison of different ablation strategies and sample preparation procedures for Tf quantification.

Sample preparation	**LA strategy**	**Tf in CRM**[a] g L^{-1}	**LOD Tf** g L^{-1}	**Time**[b]
Stained gel (n=3)	horizontally	2.45 ± 0.76	0.7	1.5 h
Stained gel (n=30)	horizontally	2.21 ± 0.10	0.7	18 h
Stained gel (n=3)	perpendicularly	2.07 ± 0.30	0.7	1.5 h
Non-stained gel (n=3)	perpendicularly	2.25 ± 0.18	0.2	4.5 h

a) CRM ERM-DA740k: certified value 2.36 ± 0.08 g L^{-1}

b) Analysis time required for a 5-point calibration and one sample (triplicate measurements)

As can be seen in *table 5.5*, the Tf concentrations determined by external calibration in stained and non-stained gels were in well agreement with the certified values (within the given uncertainties). However, the required analysis time as well as the

accuracy and precision were strongly dependent upon the conditions selected for the sample preparation and ablation strategy.

The Tf concentration determined by external calibration in stained gels using a single line ablation strategy (one line per protein spot) in the same direction of migration (denoted as horizontally) showed results in agreement with the certified value, but a high standard deviation is apparent (RSD 30%). As expected, increasing the number of analysis (10 single line ablations per protein spot) the precision obtained was significantly better (5% RSD). However, the sample analysis time (including a 5-point calibration and triplicate measurements of standards and sample) increases from 1.5 h to 18 h for the multiple line ablation strategy. By changing the sampling strategy from horizontally to perpendicularly (to migration direction) both RSD (31% and 14%, respectively) and analysis time could be lowered at a time. Such improvement in the precision could be attributed to a better counting statistics (the laser beam stays longer on the protein spot) and to a more homogeneous Fe distribution throughout the spot in this direction. It should be noted that the precision obtained for Tf quantification in this case was significantly worse than that for multiple ablation (14% *versus* 5%), but the analysis time was drastically reduced. Finally, using the optimized strategy and analyzing unstained gels the possibility for Fe contamination could be repealed, which resulted in improved limits of detection for Tf compared to the previous calibration strategies and also low RSDs and analysis time. In this way, as little as 2 g L^{-1} Tf could easily be detected resulting in limits of detection for the protein of 0.2 g L^{-1}, which is below the ones reported by other authors [181].

5.2.5 Isotope dilution analysis for the absolute quantification of transferrin in human serum samples

As already described in the introduction of this chapter, species-specific isotope dilution analysis is a good alternative to the usually applied quantification methods, correcting for any analyte losses, matrix effects or elemental fractionation during sample preparation or the ablation process. The main requisite of this strategy is the availability of the species of interest (here, transferrin) isotopically enriched in ^{57}Fe. Therefore, different procedures have been investigated for their suitability to protein saturation with natural iron in order to transfer the optimal strategy to the synthesis of ^{57}Fe-transferrin. In the following section they will be explained in detail.

5.2.5.1 Synthesis and purification of ^{nat}Fe-transferrin using iron(III) chloride

Incubation of apo-transferrin standard with $FeCl_3$

The preparation of the saturated transferrin standard, also known as holo-transferrin, was carried out following the procedure detailed in *section 4.2*. Briefly, 3 mg of the apo-transferrin standard (transferrin free of iron) were dissolved in 1 mL Milli-Q water. The solution was stirred by Vortex until complete dissolution. Then, 25 μL of a solution of 500 mM sodium bicarbonate, as synergistic anion, and 25 μL of a 10 mM $FeCl_3$ solution was added and incubated at room temperature [334].

The saturation grade of transferrin can be followed spectrophotometrically. In the case of the binding of two irons to the active sites of the transferrin, the domains close to surround the metal with the ligands. A phenolate-to-iron charge transfer transition at 465 nm arising from the binding of iron to two tyrosine ligands is characteristic for the color of the Fe-transferrin complex. Therefore, in the case of total saturation of transferrin (molar ratio two iron : one transferrin) a maximum in the absorbance at the wavelength 465 nm is observed. In this way, the effects of the iron concentration and the incubation time for the transferrin saturation have been investigated. In *figure 5.37* the absorbance at 465 nm is plotted against the concentration of iron used for saturation. The various lines represent different times of incubation.

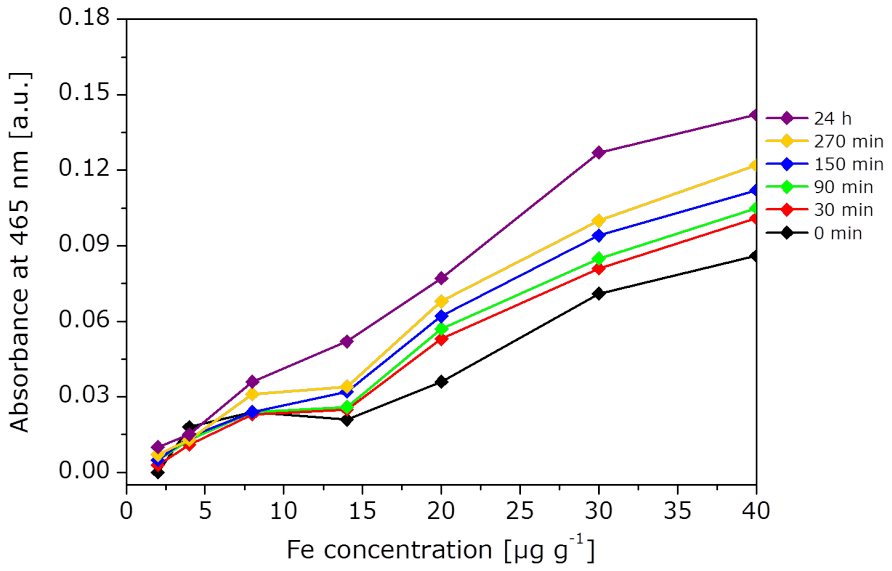

Figure 5.37: Saturation of apo-transferrin with $^{56}FeCl_3$ at different concentrations and incubation times.

As it is evident from the graph, the absorbance does not reach a plateau at any time and for any concentration representing the total saturation of the protein with iron. In theory, due to the quantity of protein used for this experiment, a concentration of 4 μg g^{-1} of iron is sufficient for the occupation of all binding sites of transferrin. In order to elucidate, why up to a 20-fold excess of iron is not sufficient for Tf saturation, a closer look was taken to the ferric chemistry after protein purification.

Purification of saturated protein

The solution chemistry of ferric ions (Fe^{3+}) is complicated by their high affinity for oxo ligands and ability to form high molecular weight polymers as well as low molecular weight oligomeric and monomeric species. As a result of the high charge density, these cations interact with both water and hydroxide anions in aqueous solutions. Oxygen is able to cross-link the hydrated cations to form dimers and oligomeric species, finally generating insoluble ferrihydrate species with a maximal molecular mass of around 150 kDa. This condensation reaction occurs rapidly at neutral pH. To avoid the precipitation of iron, three different attempts were made:

1. Saturation of Tf in Milli-Q water.
2. Saturation of Tf in Milli-Q water with adjustment of the pH value of the final mixture to pH 5.
3. Saturation of Tf in 250 mM ammonium acetate.

For protein purification ultracentrifugation (Amicon® Ultracentrifugal filter, molecular cut-off 10 kDa) was employed. This step is necessary as a great excess of iron to the protein solution is added, which in the subsequent electrophoretic separation could lead to a contamination of the gel and therefore to higher backgrounds in the LA-ICP-MS analysis. Additionally, in the quantification by isotope dilution analysis the elevated amount of isotopically enriched iron not bound to the protein could distort the analytical results. Thus, after saturation of transferrin using the above mentioned methods, 100 μL of the final solution was added to the Amicon Ultra Filter device and centrifuged at 14,000 g for 15 min. The protein fraction (retained in the upper part of the filter) was washed with 100 μL of Milli-Q water and centrifuged again at 14,000 g for 10 min. This step was repeated twice more. Finally, the Fe-transferrin complex was reconstituted in 100 μL of Milli-Q water by inversion of the Amicon filter and a brief (2 min) centrifugation at 1,000 g. This washing step was repeated twice more. The following solutions were quantified using isotope dilution for their content of iron (with ^{57}Fe spike) and sulfur (with ^{34}S spike) by ICP-MS:

1. *The unfiltrated solution of the saturated transferrin*, to obtain the total concentration of iron and sulfur in the sample. The sulfur concentration represents the amount of protein, as in theory all the sulfur is bound to the protein. The iron concentration reflects the amount of iron used for saturation, including the iron bound to the protein.

2. *The filtrate*, theoretically only containing the excess of iron used for incubation.

3. *The recovered filter residue*, containing the purified saturated transferrin.

After quantification, recoveries were determined for both, iron and sulfur and the molar ratio iron to transferrin was calculated. In the ideal case of the total saturation of the protein and complete removal of any unbound iron this ratio is 2, as two equivalents of iron are needed to saturate one mole of transferrin.

All investigated saturation methods were verified for their suitability not only by spectrophotometric measurement, but also by quantification of their content of iron and sulfur after the purification by ultracentrifugation. The following table (*table 5.6*) provides a summary of all results obtained, showing the applied saturation method and its corresponding molar ratio of iron to transferrin. In all quantification analyses the obtained recoveries for iron (according to the employed amount of iron for incubation) and sulfur (corresponding to the weighed amount of protein) were above 95%.

Table 5.6: Summary of the quantitative results of the different transferrin saturation methods using $FeCl_3$.

Saturation method	**Molar ratio Fe:Tf***
$FeCl_3$ in Milli-Q water	7.82 ± 0.07
$FeCl_3$ in Milli-Q water, pH=5	7.65 ± 0.05
$FeCl_3$ in ammonium acetate	8.17 ± 0.09

* Expected ratio: 2

As shown in *table 5.6*, applying all methods resulted in a purified fraction of the saturated transferrin with too much iron. As the protein can bind only a certain amount of iron, it is presumed that the formation of insoluble iron species of high molecular weight takes place, which cannot be separated by ultracentrifugation from

the protein. Additionally, taking into account the previous spectrophotometric results, it can be assumed, that the formed iron species may not be available anymore for Tf saturation. For this reason an alternative saturation method was evaluated.

5.2.5.2 Synthesis and purification of ^{nat}Fe-transferrin using Fe-citrate

In the presence of suitable ligands the above mentioned precipitation of ferryhydrate species in aqueous solution can be minimized. Therefore, the suitability of Fe-Citrate for saturation was investigated. Evans et al. [335] described that the formation of high molecular weight species depends on the iron-to-citrate ratio used for the synthesis. Therefore, the tendency of polymerization and saturation capability of Fe-citrate, synthesized in different ratios, ranging from 1:1 to 1:1000, was investigated.

Synthesis of natural abundance Fe-citrate

Iron citrate solutions were prepared at pH 7.4 to final concentrations of 100 μM iron and various iron-to-citrate molar ratios. Two similar methods (method A and B) were used to prepare iron citrate complexes. In method A, 0.03 g of an ICP-standard solution of natural iron (17.9 mM iron in aqueous 10% HNO_3) was mixed with a calculated volume of citric acid solution (1 M) to give the required iron-to-citrate molar ratio. The pH was adjusted to 7.4 by careful addition of sodium hydroxide solution (either 10 M or 1 M depending on the amount of citrate present). Since the pH adjustment step was very difficult, a second method (method B) was developed. Here, 0.03 g of an ICP-standard solution of iron was mixed with a calculated volume of trisodium citrate (1 M) to give the required iron-to-citrate ratios. The subsequent pH adjustment with sodium hydroxide (1 M) proved to be less problematic in this method.

Permeation of Fe(III)-citrate through membrane filters

To investigate the formation of species with high molecular weight a range of solutions containing different molar ratios of iron-to-citrate were prepared, as described earlier. The solutions were filtrated through ultrafiltration devices with a molecular mass cut-off of 10 kDa. After recovery of the filter residue all three solutions (filtrate, filter residue and unfiltrated sample) were quantified by isotope dilution analysis. The results showed, that only using iron-to-citrate ratios of 1:1000 the formed species had molar masses smaller than 10 kDa (see *figure 5.38*).

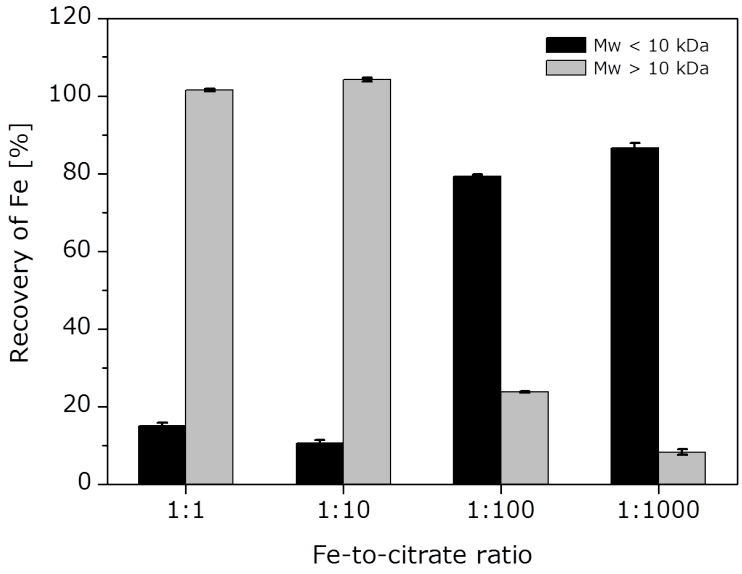

Figure 5.38: Recovery of Fe (in the form of Fe-citrate) after ultrafiltration of Fe-citrate solutions with different Fe-to-citrate ratios through membrane filters with a molecular cut-off of 10 kDa.

Incubation of apo-transferrin standard with Fe-citrate

The saturation of apo-transferrin standard with freshly synthesized Fe-citrate was carried out following the protocol described in *section 4.2*. Briefly, the protein was dissolved in a physiological medium and diluted 1:1 with a model solution containing. Subsequently, the apo-transferrin was saturated with an appropriate amount of the previously synthesized Fe-citrate (1:1000). The mixture was finally thoroughly stirred and incubated at room temperature [336].

The saturation grade of transferrin with iron was verified by measuring the absorbance at 465 nm with a spectrophotometer where different amounts of iron were used with incubation times between 30 minutes and 24 hours. The absorbance at 465 nm was plotted against the concentration of iron used for saturation (see *figure 5.39*). The various lines represent different times of incubation. As it is evident from the graph, using 8 μg g^{-1} or more iron and 60 min of incubation at room temperature (light green line) the absorbance reaches a maximum value that remains nearly constant, independent of iron concentration and incubation time.

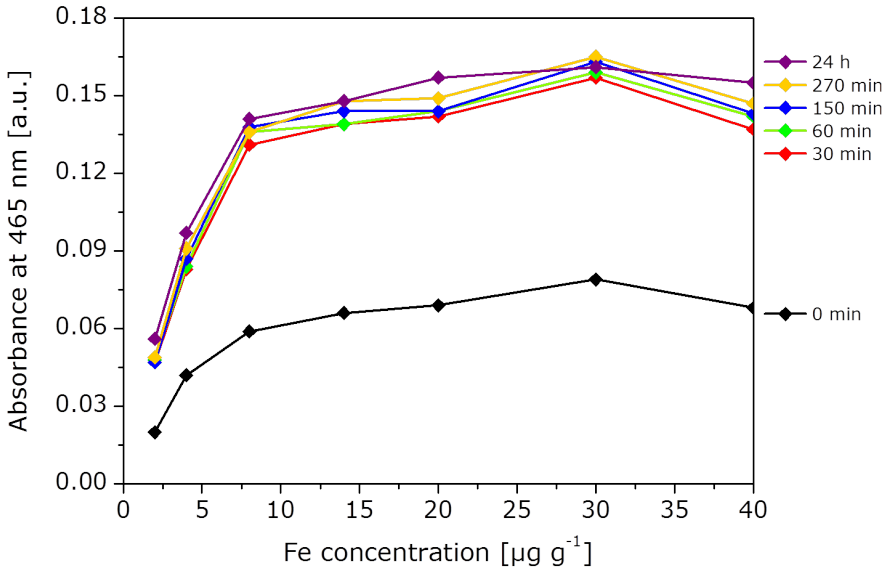

Figure 5.39: Saturation of apo-transferrin with ^{56}Fe-citrate at different concentrations and incubation times.

Purification of saturated protein

Following the procedure described previously, the saturated transferrin was subsequently purified from the excess of iron by ultracentrifugation. The resulting solutions were quantified by isotope dilution analysis for their iron and sulfur content. Recoveries were calculated to be above 96% for both elements. For comparative purposes, the saturation and purification procedure was also performed using a 1:10 Fe-citrate solution. The obtained results are shown in *table 5.7*.

Table 5.7: Summary of the quantitative results of the different transferrin saturation methods using Fe-citrate.

Saturation method	**Molar ratio Fe:Tf***
Fe-citrate (molar ratio 1:10)	5.77 ± 0.44
Fe-citrate (molar ratio 1:1000)	**1.94 ± 0.09**

* Expected ratio: 2

As it was already observed for the saturation of transferrin with $FeCl_3$, the formation of high-molecular species is predominant for low Fe-to-citrate ratios. In this vein, an excess of iron is found in the purified protein fraction. In contrast to this, purification of the transferrin saturated by the second method presented in *table 5.7*

gives both, the degree of saturation and quantitative information. The obtained molar ratio of iron to transferrin was found to be 1.94 ± 0.09, a value in agreement with the expected ratio and with the molar ratio calculated from *figure 5.39* (1.83 ± 0.04). This demonstrates that the synthesis of the Fe-citrate complex was successful and due to the formation of structures of low molecular weight the iron remains available for the saturation of the protein. An iron concentration of 14 μg g^{-1} and an incubation time of one hour were chosen to ensure complete saturation of the protein with the metal.

Stability of the saturated transferrin

Beside the information related to the saturation grade, the absorbance at 280 nm (amino acids with aromatic rings) and 465 nm (iron-to-phenolate complex) were investigated to obtain information on the stability of the formed Fe-transferrin complex. An apo-transferrin solution was divided into four aliquots and saturated under the previously optimized conditions, whereby two different incubation temperature were investigated (room temperature, being the one used up to the present study, and additionally 37°C). Two of the aliquots (one incubated at room temperature and the other one at 37°C) were stored up to four weeks at 4°C, while the other two aliquots were stored at -20°C. The absorbance at 280 nm and 465 nm was determined after 1 h, 2 h, 3 h, 1 d, 1 week, 2 weeks and 4 weeks. The ratio of 280/465 nm gives the amount of protein in relation to the intact Fe-complex present in each solution and thus, provides information about the Fe-transferrin stability. *Figure 5.40* shows the stability of the saturated apo-transferrin incubated at the two investigated temperatures over a period of four weeks.

As can be seen, the mean value for the 280/465 nm ratio of the protein saturated at room temperature (23.8 ± 0.4) was closer to the ratio obtained for the fully saturated holo-transferrin standard (19.6 ± 0.5) than the apo-transferrin incubated at 37°C (27.1 ± 1.6). This indicates, that the saturation of transferrin at room temperature was more efficient than at 37°C. Furthermore, it was observed, that the stability of the Fe-transferrin complex could be ensured during at least four weeks.

The storage conditions have been evaluated, comparing the storage of the saturated protein before and after ultrafiltration (in order to eliminate the excess of iron). Additionally, one aliquot of the unfiltrated protein was filtrated prior to the spectrophotometric analyses. The obtained results are shown in *figure 5.41*.

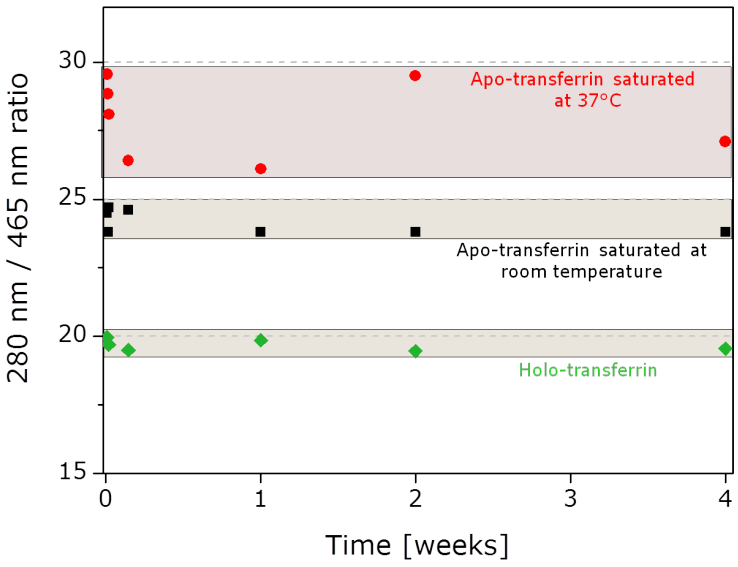

Figure 5.40: Stability of saturated and filtrated apo-transferrin standard over a period of four weeks (stored at 4°C).

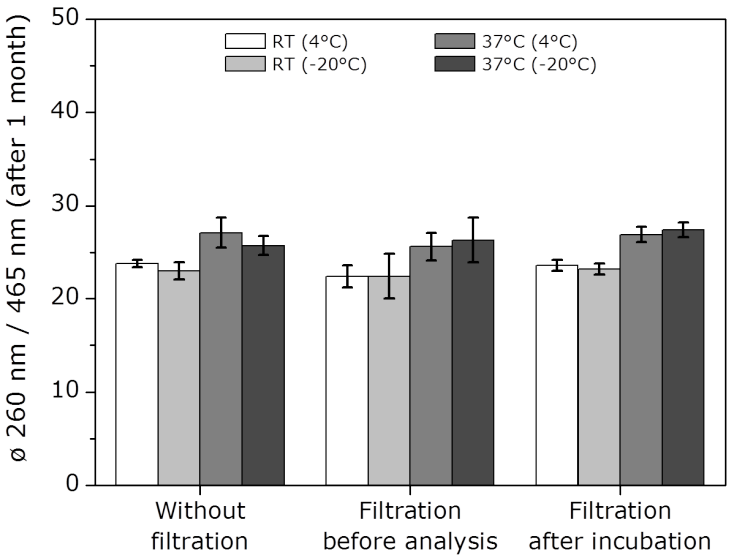

Figure 5.41: Stability of saturated apo-transferrin standard at two different incubation temperatures after four weeks under different storage conditions.

The white and the light gray bars represent the apo-transferrin saturated at room temperature (RT) stored at 4°C and -20°C, respectively, while the mid-gray and dark gray bars show the results for the apo-transferrin incubated at 37°C and stored at the

two investigated temperatures. The ordinate gives the mean values of the 280/465 nm ratios of the entire analysis time (four weeks) and the error bars represent the resulting standard deviation. The saturation of the apo-transferrin at room temperature seems to be more efficient than the incubation at 37°C, confirming the results presented in *figure 5.40*. Furthermore, taking a closer look to the error bars, it can be concluded, that the most favorable storage conditions were found for the filtrated protein right after incubation at 4°C.

5.2.5.3 Preparation and characterization of isotopically enriched ^{57}Fe-transferrin

For the synthesis of the species-specific spike, in this case ^{57}Fe-transferrin, the previously developed procedure was applied (see also *section 4.2*). Briefly, an apo-Tf standard solution in a physiological medium was diluted 1:1 with the model solution used for incubations. The apo-Tf was then saturated with the ^{57}Fe-citrate solution previously synthesized (following the same incubation procedure used for the natural abundance Fe-citrate). After the elimination of the iron excess the molar ratio of ^{57}Fe-Tf was determined to 1.88 ± 0.10%. To demonstrate that the synthesized ^{57}Fe-Tf complex can be used over a large time scale for the analysis of different samples, its stability was studied over a period of one month. No significant changes on the isotopic composition were observed. Additionally, as previously investigated by del Castillo Busto et al. [337], the stability of the ^{57}Fe-Tf complex in solutions containing Fe with natural isotopic composition is very important and, therefore, a study to evaluate whether any free and bioavailable natural Fe is potentially exchangeable was carried out. However, no replacement of ^{57}Fe by natural abundance Fe in the ^{57}Fe-Tf complex was found.

Furthermore, the isotopic composition of the ^{57}Fe-Tf spike was calculated by Fe isotope ratio measurements at medium resolution of the ICP-MS, while the elemental concentration was determined by reverse ICP-IDMS using the corresponding standards of natural isotopic composition. The ^{57}Fe abundance was found to be 94.77 ± 0.12% and the obtained total concentration of Fe was 3.51 ± 0.05 μg g^{-1}.

To perform a successful isotope dilution analysis, it is absolutely necessary to make sure that the isotopically enriched Tf behaves in all steps exactly like natural Tf. Therefore, apo-Tf saturated with natural Fe and isotopically enriched Tf were submitted to gel electrophoretic separation using native 1D-PAGE to compare their migration patterns. *Figure 5.42* shows natural and isotopically enriched Tf standards

of similar concentration after Coomassie Blue staining.

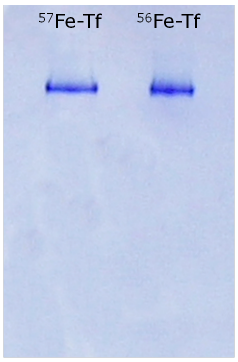

Figure 5.42: Native gel after staining with Coomassie Blue (2 μg Tf). Left lane - isotopically enriched ^{57}Fe-Tf; Right lane - natural abundance Tf.

The migration behavior for natural and isotopically enriched Tf was the same, expressed by a retention factor of R_f=0.25 (migration distance/migration to front), demonstrating that neither the charge nor the structure of the isotopically enriched protein was affected by the labeling procedure. In addition, it has to be stressed that no diffusion of the protein after fixing or protein cross contamination were observed in any analysis.

5.2.5.4 Species-specific isotope dilution GE-LA-ICP-MS analysis

For the quantification of endogenous serum transferrin, a known amount of the ^{57}Fe-Tf spike was added to the certified human serum previously incubated with natural Fe-citrate for saturation (for saturation protocol see *section 4.2*). Samples were vortexed and left at room temperature during 5 min to guarantee the complete mixing and equilibration of Fe-Tf from the sample and the added isotopically enriched ^{57}Fe-Tf. Next, the CRM proteins were separated using native 1D-PAGE and the unstained gels were analyzed by LA-ICP-MS using the optimized ablation strategy perpendicular to the migration direction. As an example, *figure 5.43* shows the ^{56}Fe and ^{57}Fe profiles obtained for the analysis of the CRM and additionally, the resulting isotope ratio ^{56}Fe / ^{57}Fe along the electropherogram (analyte/^{57}Fe-Tf spike ratio corresponding to a 1:1 proportion).

Three different data treatment approaches to calculate the Fe isotope ratios were employed for comparison. First, ^{56}Fe and ^{57}Fe integrated areas within the protein

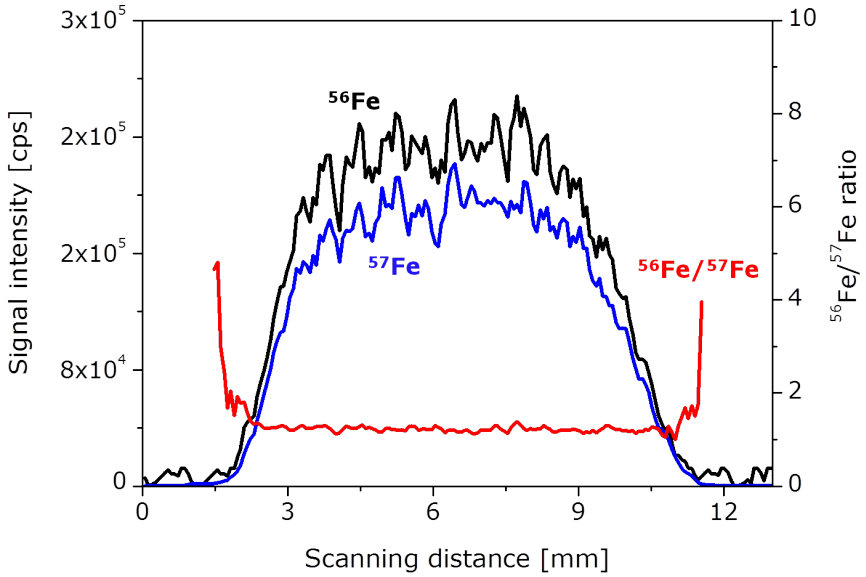

Figure 5.43: Profiles obtained by LA-ICP-MS for ^{56}Fe, ^{57}Fe and their isotopic ratio using a mixture of the CRM and the isotopically enriched ^{57}Fe-Tf (13 μg ^{nat}Fe-Tf:14 μg ^{57}Fe-Tf).

spot along the LA-ICP-MS profiles (denoted as Integration in *table 5.8*) was tested. Secondly, the ^{56}Fe/^{57}Fe point-by-point calculation of average isotope ratios (point-by-point data in *table 5.8*) was used to calculate the quantity of the natural Tf in the sample. Finally, a new strategy of isotopic ratios calculation recently described by Fietzke et al. [338] was also evaluated (corresponding to linear regression slope in *table 5.8*). Here, the described method for calculation of Fe isotope ratios using the INDEX LINEST function of MS EXCEL with the ^{56}Fe and ^{57}Fe signal intensities was applied. This function calculates the statistics for a line by using the "least squares" method to determine a straight line that best fits the obtained data, and then returns an array that describes the line. In such a way, background correction and the subjective influence which may occur by setting the integration limits were avoided, simplifying enormously the evaluation of data. Although the linear regression slope treatment approach has been previously investigated for isotopic ratios measurements with a simultaneous detection by multicollector ICP-MS [338, 339], the successful application of such signal processing using a slow signal acquisition detection could be demonstrated.

Two mass bias correction approaches were investigated in this work by the measurement of natural abundance Fe isotope ratios in polyacrylamide gels of a human serum Tf standard (external correction) and by the continuous nebulization of a 10

ng g^{-1} natural abundance Ga standard solution (internal correction). In both cases, the mass bias factor, K, was calculated using the linear model based on the following equation.

$$K = \frac{(R_{exp} - R_{theo})}{R_{theo} \cdot \Delta M} \tag{5.1}$$

with: K: mass bias factor
R_{exp}: exp. natural IR ($^{56}Fe/^{57}Fe$ for the ext. and $^{69}Ga/^{71}Ga$ for the int. correction
R_{theo}: IUPAC tabulated $^{56}/_{57}$ and $^{69}/_{71}$ isotope ratios
ΔM: mass difference between the isotopes

Comparative studies showed similar results for external and internal correction strategies and the calculated mass bias factor was found to be around -0.07 for the external correction and -0.06 for the internal correction. Thus, differences observed in the calculated Fe concentration by using the proposed species-specific LA-ICP-IDMS methodology were always below 1%. Since similar results were observed using the two strategies, the Ga standard solution was used for all the measurements. This means that the mass bias factor was determined for each sample in the same LA-ICP-MS profile by using a natural Ga standard solution with well-known isotopic composition. The final calculation of the GE-LA-ICP-IDMS results was carried out by using the conventional isotope dilution equation (see *equation 3.2*).

The results obtained for the determination of Fe in the certified reference serum sample by species-specific GE-LA-ICP-IDMS are summarized in *table 5.8*. As can be seen, Tf concentration determined by the proposed species-specific IDMS method was in very good agreement with the certified value, being the precision obtained significantly better than that obtained by external calibration with RSDs in the range of 0.9-2.7% depending on the data treatment procedure. Additionally, the analysis time (LA-ICP-MS measurement time, excluding sample preparation time) was drastically reduced to less than 15 min. Moreover, the quantification by species-specific GE-LA-ICP-IDMS provided accurate and precise results not only by analyzing the protein spot in the center position but also in adjacent ablation lines to the center with deviations from the certified value below 5%. It should be stressed here that by using the linear regression slope data treatment a significant improvement in the precision (0.9% RSD) and in the accuracy of the Tf concentration values were obtained (as compared to the results obtained by the other tested integration and point-by-point approaches). In addition, although a different instrumentation as well as ablation

strategies were employed in previous IDMS approaches for the analysis of soils, sediments and crude and fuel oil samples, the precision obtained for the direct analysis of gels by species-specific LA-ICP-IDMS was significantly better that precisions reported in previous work using IDMS and LA-ICP-MS, where RSD values in the order of 15% were found [340, 341].

Table 5.8: Determination of Tf concentrations in a serum reference material and human serum samples by species-specific GE-LA-ICP-IDMS using three different data treatment approaches[a].

Data treatment	**Tf in CRM**[b] g L^{-1}	**Tf in human serum** g L^{-1}	**Time**[c]
Integration	2.40 ± 0.08	2.48 ± 0.04	15 min
Point-by-point	2.24 ± 0.03	2.24 ± 0.03	15 min
Linear regression slope	2.34 ± 0.02	2.34 ± 0.04	15 min

a) SD values are calculated from the mean of three measurements in three independent gels

b) CRM ERM-DA740k: certified value 2.36 ± 0.08 g L^{-1}

c) Analysis time required for triplicate measurements

Finally, once the validation of the optimal quantification method was guaranteed, by the analysis of the reference serum sample, the analysis of clinical human serum samples from healthy volunteers was performed. A triplicate of a pool of serum samples was separated in native 1D-PAGE and the non-stained gels were analyzed LA-ICP-MS. Quantification was carried out by species-specific isotope dilution analysis. *Table 5.8* collects the results obtained using the three data treatment approaches. As can be observed the Tf concentration obtained showed typical values reported for healthy human serum samples (similar to those obtained for the CRM).

Measurement uncertainty budgets

The uncertainty for each individual measurement of Fe concentration was calculated according to the method proposed by Kragten [342]. When external calibration was applied a relative uncertainty (%) of 13.4% was obtained, whereas for the proposed species-specific IDMS methodology a relative uncertainty of 1.7% was found. Moreover, in order to study the influence of the different factors in the final uncertainty of the concentration values, the full uncertainty budgets for Fe in a representative analysis of the serum CRM using the method proposed by Kragten were calculated.

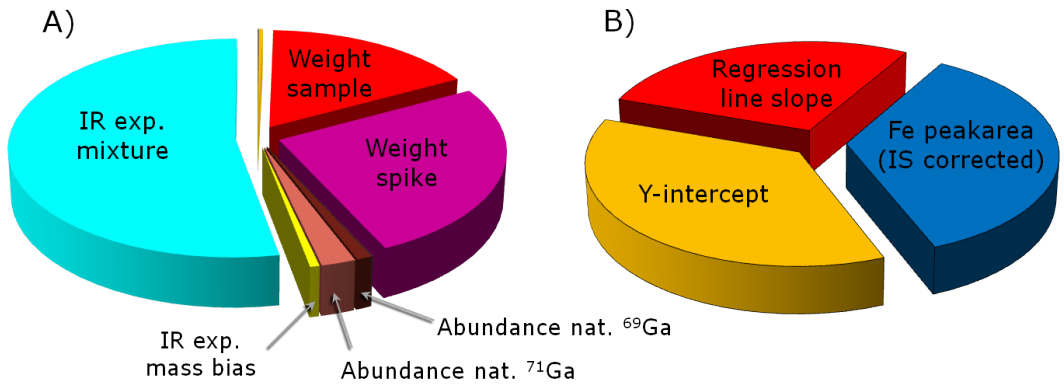

Figure 5.44: Uncertainty budgets obtained for representative analysis of CRM by A) species-specific isotope dilution analysis using the linear regression slope data treatment and B) external calibration.

The corresponding uncertainty budgets demonstrated that the most important contributor to the uncertainty was the measurement of the $^{56}Fe/^{57}Fe$ isotope ratio for the isotope dilution procedure and the measurement of ^{56}Fe and ^{13}C signals and the y-intercept of the calibration curve for the external calibration (see *figure 5.44*). For the sake of clarity, other factors contributing only to a negligible part to the uncertainty budget for the isotope dilution analysis (such as the abundance of the natural ^{56}Fe and ^{56}Fe, the abundance of ^{54}Fe, ^{56}Fe, ^{57}Fe and ^{58}Fe in the enriched spike, the spike concentration and the atomic weight of natural iron) are not shown in the graphical representation (although taken into account in the calculations).

Summarizing, it can be said that, although accurate quantification is still considered as one of the limitations of the routine applicability of laser ablation technique, the potential of GE-LA-ICP-IDMS, using a species-specific tracer for the accurate, precise and time-effective quantification of Tf in clinical samples could be demonstrated. This tool could pave the way to develop new analytical procedures to achieve reliable metal-protein quantifications after gel electrophoretic separation without the need of further laborious sample treatment steps. Such validated approaches could become essential to meet the quality assurance requirements urgently demanded in quantitative heteroatom-tagged protein analyses, overcoming some of the present problems of transparency of the results reported in literature.

5.3 Qualitative elemental bioimaging in soft tissues: Development of a novel internal standard correction strategy

5.3.1 Introduction

Trace elements play a number of important roles throughout nature. In biological systems a wide range of essential trace elements are involved in innumerable physiological processes, from providing structural support as part of an inorganic matrix to acting as cofactors in a variety of enzymatic reactions. Homeostatic imbalance of some essential trace elements have also been implicated in a number of diseases, many arising from the redox-active properties of first-row transition metals [343]. Essential trace elements, for example, such as Fe, Cu, Zn, Se and I are elements that, although present in very small amounts in tissues and bodily fluids, perform a variety of functions essential to sustain life. Their optimal levels are maintained by homeostasis and the surplus or deficit of these elements can lead to various diseases. However, it is worth mentioning, that essential metals are not homogeneously distributed in cells and biological tissues, thus elemental bioimaging studies providing information of the spatial distribution of elements in a given sample are today of crucial interest. The evidence of the scientific importance is mainly demonstrated by the great amount of books, reviews and publications about either new developments of qualitative and quantitative bioimaging techniques as well as their applications to an increasing variety of samples published to date (see *section 3.3.2*).

One of the remaining challenges in qualitative and quantitative bioimaging studies by LA-ICP-MS is the reliability of the obtained elemental data in terms of relative or absolute amounts, mainly due to the severe matrix effects in laser based analyses. In order to account for matrix effects as well as variations in ablated and transported mass and instrumental drifts, different internal standard correction strategies have been proposed so far. The most conventional approach in elemental bioimaging applications employs the $^{13}C^{+}$ signal for internal normalization [145–147]. However, carbon is not always homogeneously distributed within the different structures of soft tissues, so it does not entirely satisfy the requirements of an IS. Moreover, ^{13}C is less sensitive to instrumental fluctuations than the analytes under investigation [153, 344]. Additionally, Frick et al. have recently performed a detailed study of the ablation of carbon-containing matrices demonstrating the formation of two individual phases, a gaseous carbon-containing species and a carbon-containing particle phase [345]. Such fundamental findings line up with the hypothesis that carbon might not be a suitable

IS even if a close matrix matching is performed. Another approach for the analysis of thin samples using LA-ICP-MS is the introduction of a standard directly under the sample and their simultaneous ablation [150]. Here, the ablation parameters must be chosen so that both layers are completely ablated. In addition, the thickness of the sample and the internal standard layer must be known, as well as the concentration of element in the standard layer. The total thickness of both layers must be small compared to the diameter of the laser beam as otherwise the ablation of similar amounts of sample and standard is no longer guaranteed (due to the non-pure flat top energy profile of the laser beam).

Although a few more internal standard correction strategies have been presented in the literature, (see *section 3.2.5*) none of the described methods is generally applicable.

Objective

Based on an intensive study of the existing internal standardization methods, the aim of this chapter was the development of an improved internal standard correction strategy circumventing the drawbacks which put limits to the published approaches. The proposed strategy is based on the deposition of a homogeneous thin gold film on the sample surface and the use of the $^{197}Au^{+}$ signal as IS for normalization. This new approach was compared to the common correction with $^{13}C^{+}$. Analytical performance of the proposed IS regarding changes in the ablation process and/or particle generation and transport to the ICP-MS was studied by using confocal laser scanning microscopy (3D images of the sample surface) and scanning electron microscopy (characterization of the laser-generated aerosol particles). Reproducibility studies were performed to assess the potential of $^{197}Au^{+}$ to correct for inhomogeneous sample compositions, different ablation rates and particle transport; aspects not always taken into account using $^{13}C^{+}$ as IS.

5.3.1.1 The human eye

The eyes are our window to the outside world. We look to orient us, to detect good or dangerous, to make us a picture of the world. Over 90% of all sensory impressions are absorbed through the eyes. Whether it is the colors of a colorful summer meadow, the quick screen graphics in a computer game, or the warning light of an emergency flasher system - all these impressions are redirected over the eyes to the brain for further processing. In other words: who does not see properly, misses something.

In everyday life, the eye is constantly subjected to oxidative stress [346]. This stress has multiple sources, such as daily exposure to sunlight, environmental factors, tobacco smoke, elevated metabolic activity, etc. Generally, the eye can be seen as a system of defense, or wall, facing all this load of environmental stress. The first physical and biochemical barriers are the cornea and aqueous humor inside the anterior chamber, followed by the lens and finally, traversing the vitreous humor, the retina (see *figure 5.45*).

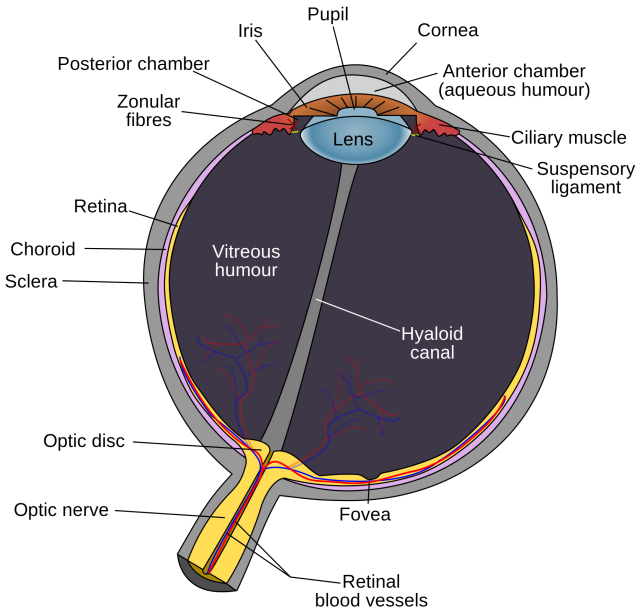

Figure 5.45: Schematic diagram of the human eye [347].

Oxidative damage has also been reported to play a role in several ocular diseases including cataract [348], glaucoma [349] and age-related macular degeneration [350]. In addition, aging has a dramatic role on different eye diseases [351]. Antioxidant enzymes, such as superoxide dismutase (SOD), catalase and glutathione peroxidase (GPx) are known to be effective scavengers of free radicals in lens and retina. Each of these enzymes requires (semi)metals for their function, i.e. SOD requires Zn and Cu (or Mn), catalase requires Fe and GPx requires Se. The study of the species and their functions involved in the defense mechanism against oxidative stress in the eye is of high interest in ocular biology and biochemistry [352]. To date, the most used approaches originated from the genetic [353] and proteomic [354] fields, whereas information related to the metallomics of this tissue is still scarce [355]. In this regard, the number of publications indicating a possible role of Fe and Zn in diseases such as

cataracts, glaucoma and the age-related macular degeneration is increasing [356]. In addition, the relevance of these trace elements in the physiology and pathophysiology of the eye depends not only on their levels, but also on their cellular distribution along the distinct ocular tissues, which to date remain to be studied [357, 358].

5.3.2 Samples and selection of region of interest

Human eye samples from normal donors (cadavers) were obtained post-mortem through the National Disease Research Interchange (Philadelphia, PA, USA). The procedures conformed to the tenets of the Declaration of Helsinki. Eyes were paraffin-embedded following a conventional protocol (for details see *section 4.2*), carefully sliced to about 10-200 μm thickness and deposited on a flat surface (e.g. glass slides).

The **region of interest** (ROI) was selected in collaboration with the Fundación de Investigación Oftalmológica of the Instituto Oftalmológico Fernández Vega (Oviedo, Spain) and is shown in *figure 5.46*.

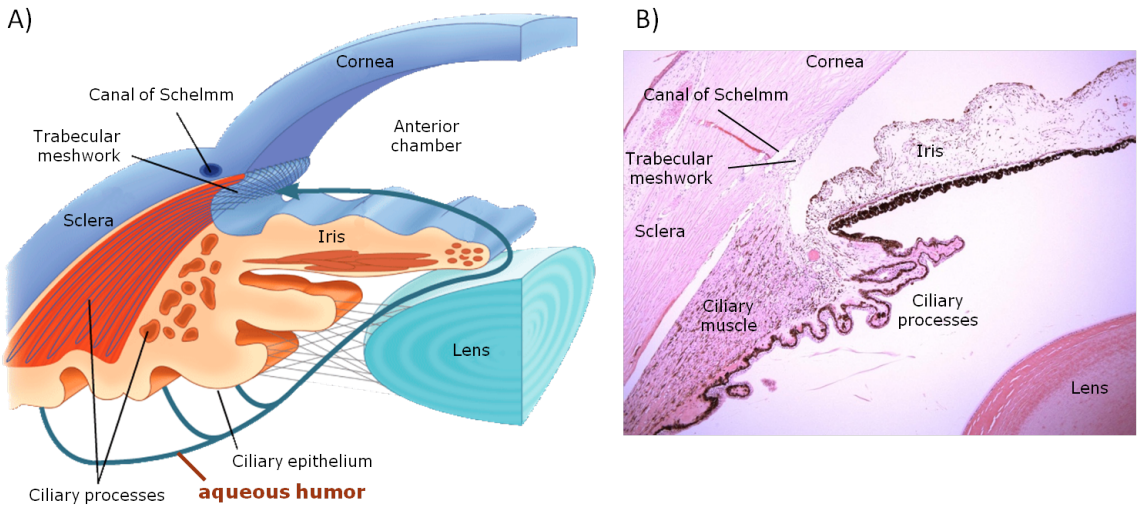

Figure 5.46: A) Graphical representation of the structures of the anterior chamber of the eye [359]. B) Histology of the anterior chamber of the eye [360]

Figure 5.46 shows the structures with significant autonomic functions of the anterior chamber of the eye. The blue arrow in *figure 5.46A* represents the pathway of the aqueous humor. The aqueous humor is produced by the ciliary processes and contains important nutrients for lens and corneal endothelium. Furthermore it serves, with its content of immune factors and its circulation, the removal of potentially harmful agents from the interior of the eye. In the center of the images (A and B) the canal of Schlemm is shown. It is a ring-shaped canal in the eye located in the scleral part

of the iridial angle and forms the central drainage route for the aqueous humor into the blood stream. The canal of Schlemm is covered with a close-meshed network, the trabecular meshwork, mainly responsible to drain the aqueous humor from the anterior chamber into the canal of Schlemm.

Regulation of the intraocular pressure arises from the relationship between production of the aqueous humor and its outflow. If this is not guaranteed or disturbed, an increase in the intraocular pressure can occur, which can lead to glaucoma. Furthermore, an increased pressure inside the eye can damage the optic nerve and lead to blindness. Glaucoma can be roughly divided into two main categories, "open-angle" and "closed-angle" glaucoma. The angle refers to the area between the iris and cornea, through which fluid must flow to escape via the trabecular meshwork. In the case of the "closed-angle" glaucoma draining of the aqueous humor is disturbed due to the constriction between iris and cornea impeding the aqueous humor to reach the trabecular meshwork. On the other side, in the "open-angle" glaucoma, the outflow of the aqueous humor through the trabecular meshwork is reduced due to its degeneration and obstruction and thus less absorption of the aqueous humor. Loss of aqueous humor absorption leads to increased resistance and thus a slow buildup of intraocular pressure. In this context, the selection of the above mentioned ROI for imaging studies by LA-ICP-MS aimed the investigation of the potential influence of metals, metalloproteins, metal-binding proteins or their accumulation in the area of the canal of Schlemm leading to obstruction of the outflow.

5.3.3 Optimization of LA-ICP-MS parameters for bioimaging of ocular tissue

The general tuning of the LA-ICP-MS system was performed daily as described in the Experimental chapter (*section 4.1*). For bioimaging analyses of ocular tissues by LA-ICP-MS the additional optimization of several parameters illustrated in *figure 5.47* is required. The optimized conditions are summarized in *table 5.9*.

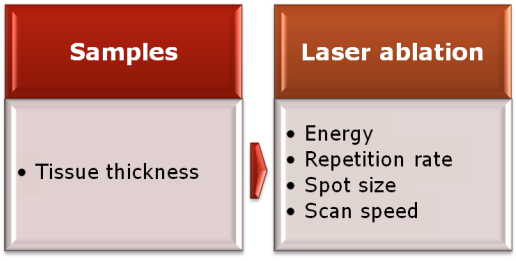

Figure 5.47: Workflow for the optimization of experimental parameters for bioimaging in ocular tissues.

Table 5.9: Optimized parameters used for the analysis of paraffin-embedded ocular tissue samples by LA-ICP-MS.

System	Parameter	Value
ICP-MS	RF power	1330 W
	Cooling gas	15.5 L min^{-1}
	Auxiliary gas	0.8 L min^{-1}
	Carrier gas (Ar)	0.9 L min^{-1}
	Cones	Ni (Skimmer and Sampler)
	Mass resolution	4000
	Isotopes monitored	^{13}C, ^{24}Mg, ^{56}Fe, ^{63}Cu, ^{197}Au
	Acquisition time	1.3 s
	Mass window	100%
LA system	Laser energy	100% (5.6 mJ)
	Repetition rate	20 Hz
	Spot size	10 μm
	Scan speed	6.5 μm s^{-1}
	Ablation mode	Multiple line scan
	Carrier gas (He)	1 L min^{-1}

5.3.3.1 Optimization of the sample tissue thickness

A basic requirement for reliable qualitative and quantitative bioimaging analysis is the complete ablation of the matrix. This task is even more challenging when inhomogeneous tissues with varying local distributions in the low μm range are investigated, an attribute characteristic for nearly all kinds of biological tissues. Therefore, it is very important to study the laser-matter interaction for each kind of sample matrix separately, as it is highly dependent on different factors regarding both the laser properties and the sample characteristics. On the one hand, the optical absorption properties of tissue are governed by the absorption of the constituent biomolecules, such as proteins, DNA, melanin, hemoglobin, and water. However, the variation of their optical activities with wavelength is quite different, leading to different internal energy distributions depending on the employed laser system (ultraviolet, visible or infrared radiation) which drives the ablation process [361]. On the other hand, tissue composition, morphology and mechanical properties also affect the energy transport among tissue constituents and mediate the response to the impacting laser pulse.

Soft biological tissues can be viewed as a material consisting of cells that reside in and attach to an extracellular matrix (ECM), a complex composite material, whose principal components are water, collagen and proteins. The ratio of ECM components to the total tissue mass varies significantly among tissue types. In "cell-continuous" tissues such as liver, the ECM fraction is quite small and consists mostly of proteins. In contrast, "matrix-continuous" tissues such as corneal stroma have very small cellular fraction and consist almost entirely of ECM, with collagen contents up to 35%. The primary function of the ECM is to maintain the structural integrity of the tissue. This can lead to an inhibition of tissue vaporization and material removal during the ablation process. Another aspect of bioimaging analysis of tissues which has great influence on the laser-matter interaction is related to the sample preparation step, as generally there are two different ways to obtain thin tissue sections. In the one case, the fresh tissue is formalin-fixed, frozen and cryogenically cut. In the second case, the tissue is paraffin-embedded and cut to the desired thickness at room temperature. Due to the change in the mechanical properties of the tissue, as a result of the presence or absence of paraffin, the laser-matter interaction may vary and needs to be taken into account when quantitative analysis are intended.

In order to overcome inhomogeneous and irreproducible ablation processes due to the above mentioned aspects, the tissue thickness needs to be optimized to ensure the complete ablation of the sample. In this vein, different tissue thicknesses between 10 and 160 μm of paraffin-embedded eye samples have been investigated. Furthermore, the ablation was performed comparing compartments with different compositions and morphology in order to study different ablation efficiencies. With the purpose to investigate the penetration depth in different zones of ocular tissue, three adjacent lines were ablated using the experimental parameters summarized in *table 5.9*. The formed craters in the analyzed samples were subsequently visualized by confocal laser scanning microscopy generating 3D-images of the samples using Leica Confocal Software. Crater depth and shape were also determined in order to evaluate ablation efficiencies depending on the matrix composition and to assess the optimal tissue thickness. By way of example, in the following the results obtained for three of the investigated tissue thicknesses, 10 μm, 25 μm and 160 μm, will be presented in detail.

The results obtained for a tissue thickness of 10 μm are shown in *figure 5.48*. In particular, image (A) shows the histology of the analyzed sample visualized by the CCD camera of the laser system, (B) shows the 3D-image of the respective area obtained by

confocal laser scanning microscopy (CLSM) and (C) and (D) give information about the obtained crater profiles. As it can be clearly seen, complete ablation of the sample along the entire line could be achieved. The obtained craters across the ablated line were very well defined and in all three adjacent lines reproducible. A crater profile performed along the ablation line shows a flat bottom without unablated residues.

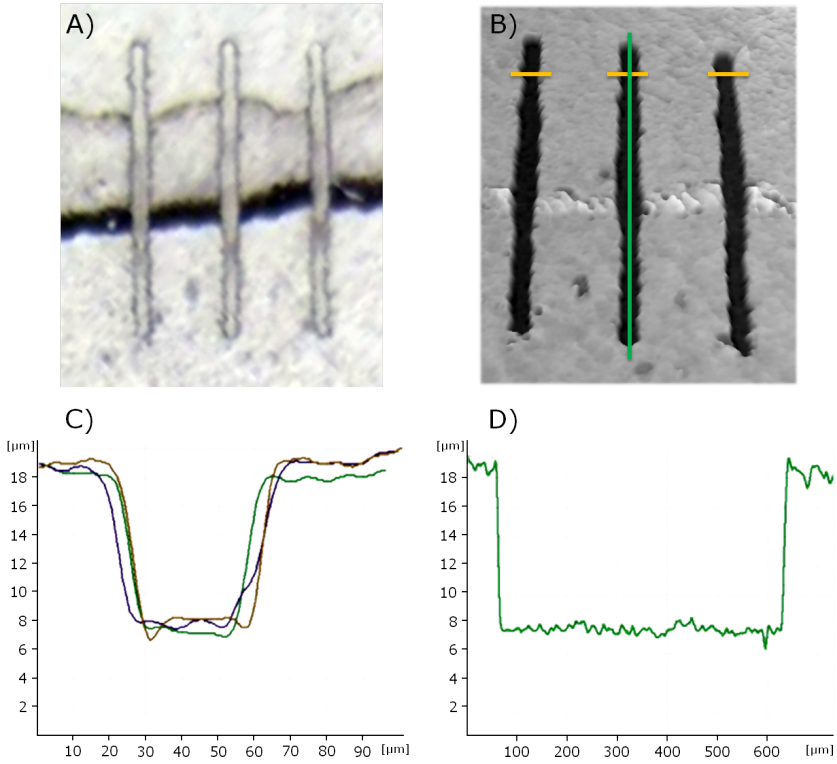

Figure 5.48: LA-ICP-MS analysis of 10 μm thick section. A) Histological image obtained after laser ablation analysis, B) 3D-image of the analyzed area by CLSM, crater profiles obtained C) across and D) along ablated line.

Increasing the tissue thickness to 25 μm led to a slightly different result, as it is summarized in *figure 5.49*. Although the differences in ablation efficiency between the sample thicknesses 10 and 25 μm are already visually distinguishable by comparing the images obtained by the CCD camera of the laser system (*figure 5.48A* and *figure 5.49A*), the demonstration gets even clearer taking a look to the 3D-images obtained by confocal laser scanning microscopy (*figure 5.48B* and *figure 5.49B*). In the case of the thicker sample (25 μm) the ablation line shows irregularities without defined crater borders. By extraction of the crater profiles from the 3D-image across and along the ablation line it can be seen, that no complete ablation of the sample was achieved. When performing qualitative or quantitative bioimaging analyses, this could lead to

irreproducible and unreliable imaging data.

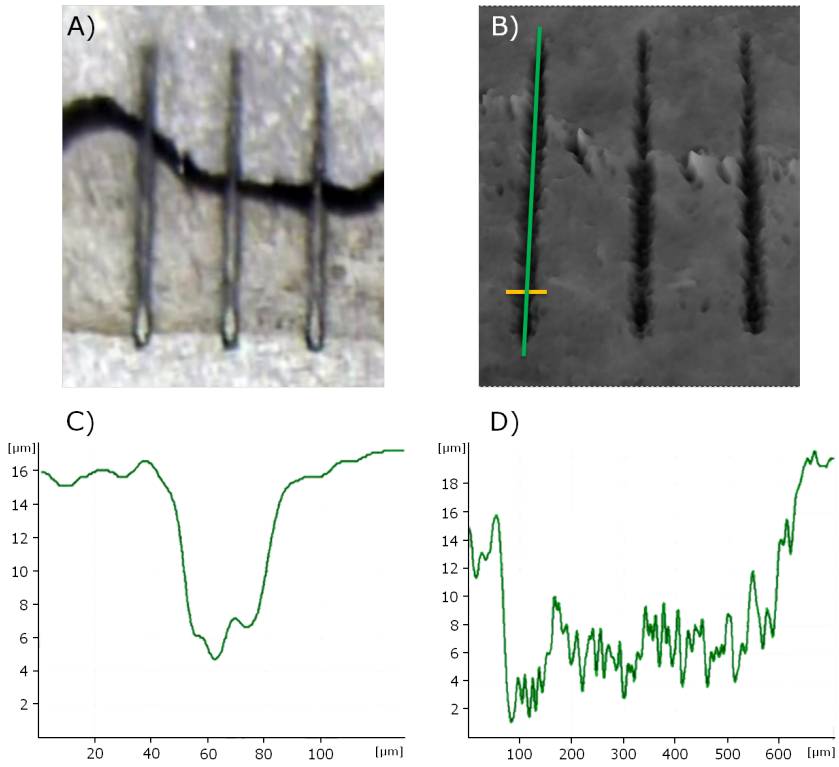

Figure 5.49: LA-ICP-MS analysis of 25 μm thick section. A) Histological image obtained after laser ablation analysis, B) 3D-image of the analyzed area by CLSM, crater profiles obtained C) across and D) along ablated line.

Generally, greater tissue thickness could improve the signal intensity, as more material can be ablated and thus transported to the ICP-MS. However, the penetration capabilities of the laser beam are limited due to the available energy output, as *figure 5.50* shows. The 160 μm tissue section shows clearly incomplete and irreproducible ablation along the three adjacent lines, so the ablation was mainly dominated by the different laser-matter interaction due to the composition of the constituent biomolecules. Furthermore, as can be observed in *figure 5.50D*, the crater profile along the entire line (green line) shows preferential ablation in the compartments containing melanin resulting in higher penetration of the tissue in this region.

A summary of the results obtained for all the investigated tissue thicknesses is shown in *figure 5.51*, where the penetration depth achieved by laser ablation is plotted against the section thickness.

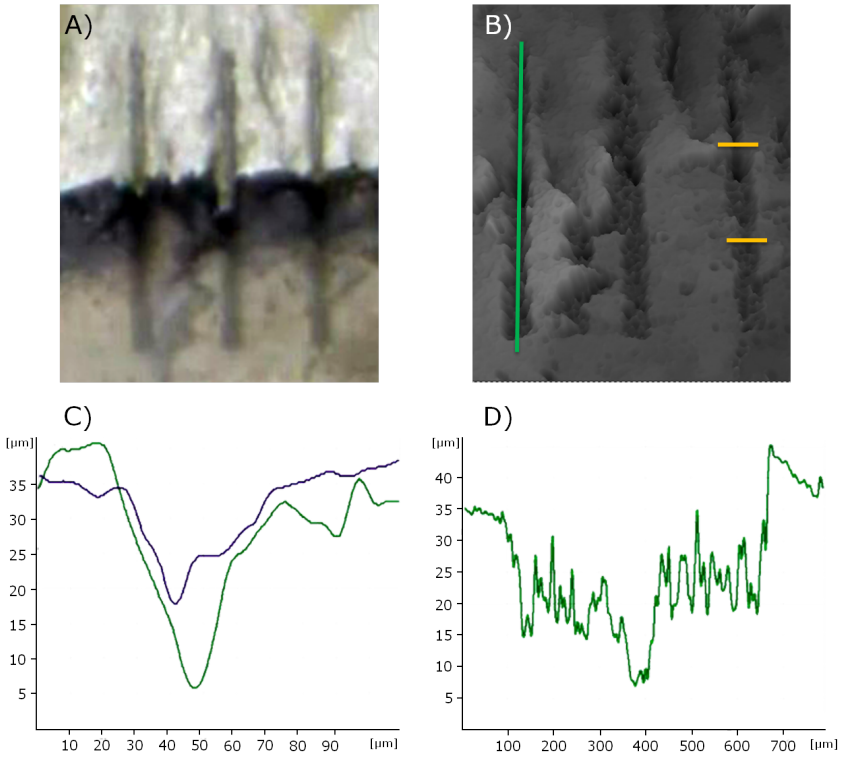

Figure 5.50: LA-ICP-MS analysis of 160 μm thick section. A) Histological image obtained after laser ablation analysis, B) 3D-image of the analyzed area by CLSM, crater profiles obtained C) across and D) along ablated line.

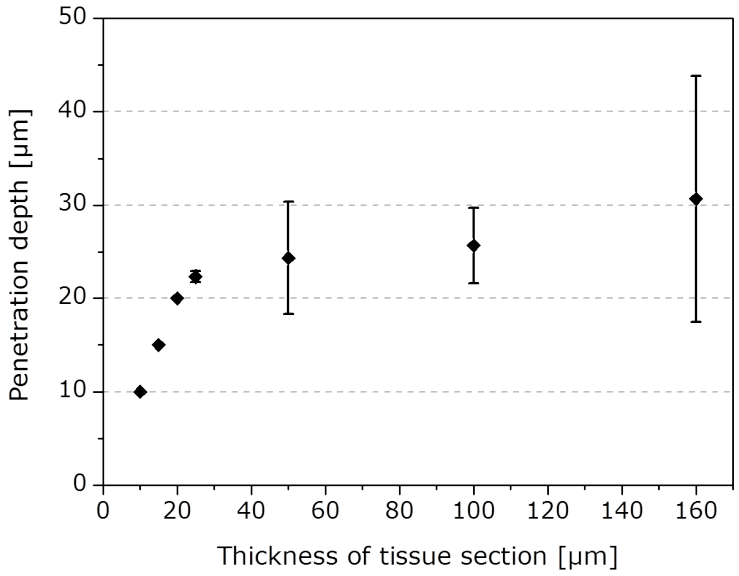

Figure 5.51: Graphical representation of the penetration depth *versus* tissue section thickness. Standard deviation values were calculated from the mean of three independent measurements.

The graphical representation shows a linear correlation between penetration depth and tissue thickness for the first three points, which means, that up to 20 μm section thickness complete ablation of the sample matrix can be ensured. For samples with greater thicknesses than 20 μm the ablation efficiency decreases, reaching a maximum average penetration depth of about 30 μm, independently of the tissue thickness. Furthermore it can be clearly seen, that the interline and intraline homogeneity in the ablation efficiency decreases drastically (represented by the error bars), as at greater section thicknesses the ablation process is influenced mainly by the inhomogeneous sample composition and morphology. Based on these results, all further imaging studies were performed with tissue thicknesses of 15 μm.

5.3.3.2 Optimization of laser parameters for bioimaging of ocular tissues

The important parameters of the laser system (laser energy, pulse repetition rate and scan speed) were optimized by monitoring ^{56}Fe and using a spot size of 10 μm in order to guarantee high lateral resolution. Optimization was carried out for maximum signal intensity by triplicate single line scans through the iris. The recorded LA-ICP-MS signals were integrated over the entire profile to give the dependence of the signal intensity from the corresponding laser parameter. The obtained results (profile area *versus* different values of the optimized parameter) are only indicative, as no homogeneous biological sample was used for the analyses. Thus, differences in integrated areas are dependent on both the optimized parameter as well as the sample characteristic itself.

The **laser energy** was optimized in the range from 0-100%. Due to the small spot size and taking into account the calculations presented in *section 4.1* on page 72ff, the maximum energy value available is ~24 μJ. Thus, applying an energy value of 100% maximum signal intensities without ablation of the subjacent sample substrate was achieved (see *figure 5.52*).

Next, the influence of the **repetition rate** was studied. *Figure 5.53* shows the dependence of the signal intensity from the repetition rate using a laser energy of 100%. As expected, increasing the pulse repetition rate leads to higher signal intensities. Thus, for all further analyses a repetition rate of 20 Hz was chosen.

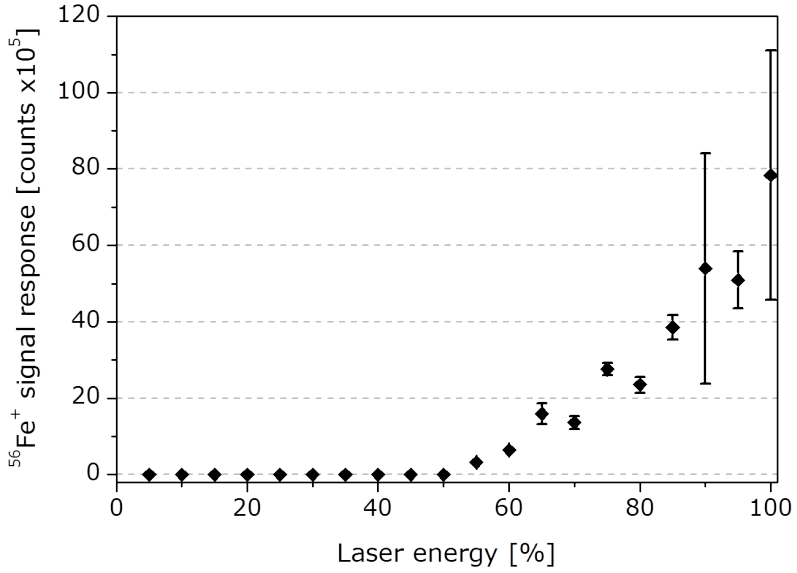

Figure 5.52: Dependence of the $^{56}Fe^{+}$ signal response (integrated profile area) from the laser energy using a pulse repetition rate of 20 Hz, a scan speed of 5 μm s^{-1} and a spot size of 10 μm (all signals are gas blank corrected).

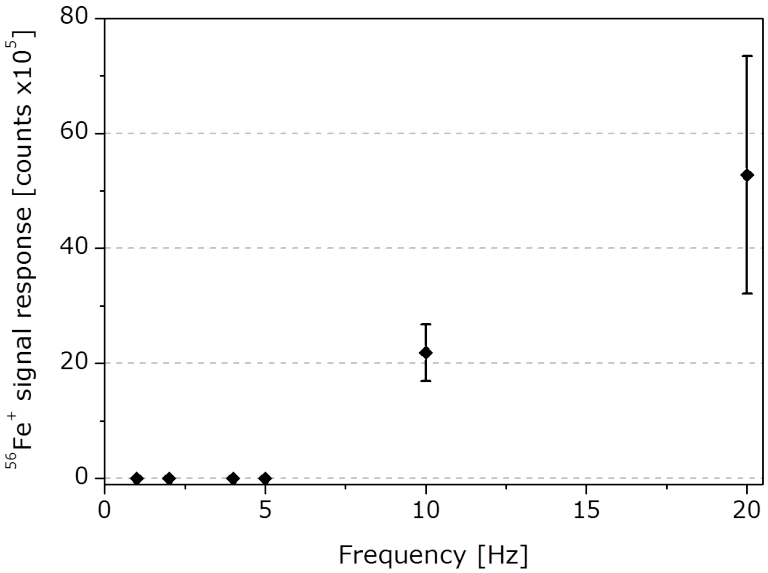

Figure 5.53: Dependence of the $^{56}Fe^{+}$ signal response (integrated profile area) from the pulse repetition rate using a laser energy of 100%, a scan speed of 5 μm s^{-1} and a spot size of 10 μm (all signals are gas blank corrected).

Optimization of the **scan speed** was performed in order to ensure the shortest possible analysis time without losing lateral resolution. *Figure 5.54* shows graphically the dependence of the lateral resolution from the scan speed.

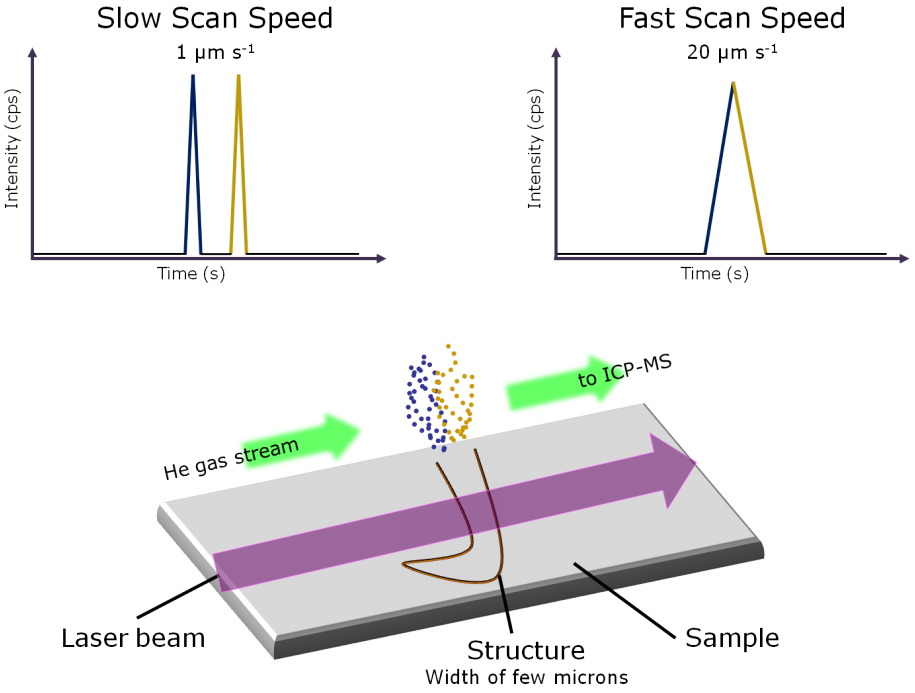

Figure 5.54: Graphical representation of the dependence of the lateral resolution from the scan speed, maintaining laser energy, pulse repetition rate, spot size and ICP-MS acquisition times constant.

As it can be clearly seen, slow scan speeds increase the lateral resolution, as the formed aerosol of one structure is able to evacuate from the ablation cell before the ablation of an adjacent structure takes place. On the contrary, fast scan speeds can lead to a mixture of aerosols from different microstructures and thus, decrease lateral resolution.

Typical bioimaging experiments normally employ scan speeds where the distance traversed in one second is equal to or less than the diameter of the laser beam. For example, a X μm laser spot diameter moving at a scan speed of X μms^{-1} would move X μm in one second. If the acquisition time of the ICP-MS (t_a) is equal to one second, a square pixel representative of X μm is recorded every scan cycle. If t_a is the only variable altered and is either greater or less than one second, a true representation of the relative dimensions is lost and the resulting image is either compressed or expanded (see *figure 5.55*).

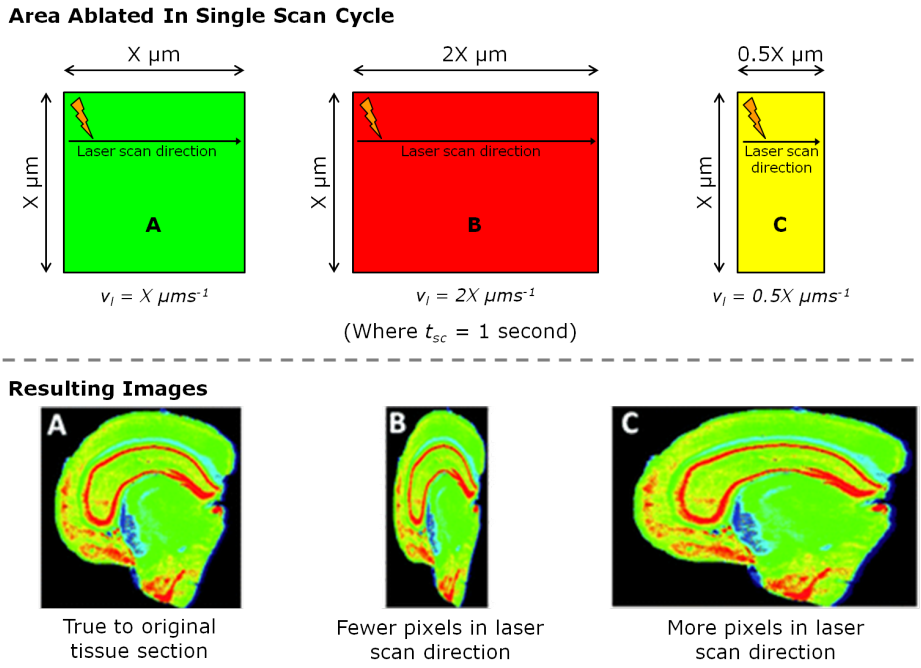

Figure 5.55: The effect of varying the laser scan speed on image dimensions [293].

In order to overcome this problem, the optimal scan speed for a given spot size (in this case 10 μm) was calculated according to the acquisition time defined in each analysis by the mass spectrometer using *equation 5.2*, resulting in a scan speed of 6.5 μms^{-1}:

$$v_l = \frac{X_l}{t_a} \tag{5.2}$$

with: v_l: scan speed
X_l: spot size
t_a: acquisition time of the ICP-MS

A summary of the optimized parameters used for all further analyses is shown in *table 5.9* on page 144.

5.3.4 Evaluation of a thin gold film for internal standard correction

The major source of error in imaging studies by LA-ICP-MS is usually related to inhomogeneities between different tissue structures. Therefore, the use of an effective IS correcting for matrix effects as well as variations in mass ablated, mass transported and instrumental drift is a must for reliable results. In order to experimentally demonstrate that at the optimized experimental parameters the signal intensity measured

for $^{197}Au^+$ is stable, a glass reference material (NIST 612) covered with a thin gold film was analyzed. The signal intensities for the target elements and the internal standard were plotted as a function of time as well as the ratio of the target elements *versus* $^{197}Au^+$ showing in all cases stable signals. The temporal relative standard deviation (TRSD) was calculated to be below 20%, presenting slight differences depending on the analyzed element and/or measuring in low or medium resolution of the mass spectrometer.

In order to evaluate the suitability of gold as an IS for imaging studies in biological tissues, the samples first have to be covered with a thin Au film. Due to the physical process of thin-film deposition by sputtering (see *section 4.1*), homogeneous coatings can be achieved throughout the sample area to be analyzed, which is one of the prerequisites of an adequate IS for imaging studies.

5.3.4.1 Comparison of results for elemental distributions in ocular tissue without normalization and with $^{13}C^+$ or $^{197}Au^+$ as internal standard

For imaging studies a sample area of about 10 mm^2 was selected, containing different tissue compartments of ophthalmological interest, such as ciliary body, ciliary muscle, iris, cornea and the outflow system, including trabecular meshwork and canal of Schlemm (see *figure 5.46*). Tissue structures differ very much in morphology and molecular composition and, as a consequence, also in water and solid matter content.

Figure 5.56 shows the analyzed area (A) and the qualitative elemental distributions of $^{24}Mg^+$, $^{56}Fe^+$ and $^{63}Cu^+$ with gas blank corrected signal intensities (left) and signals corrected with $^{13}C^+$ (middle) or $^{197}Au^+$ (right) as IS (B). As it can be seen in the left (gas blank corrected) images, the three elements seem to be present to different extents in the ocular tissue, while being totally absent in the paraffin matrix. The use of internal standardization at this point is indispensable in order to ensure that the observed signal intensities are not artifacts. Thus, the obtained signal intensities of the sought elements were normalized with the corresponding $^{13}C^+$ signal intensity (middle column), which led to a drastic loss in structure definition compared to the gas blank corrected images (left column). Comparing the elemental distributions resulting after normalization with the $^{13}C^+$ signal with the ones obtained after normalization with the $^{197}Au^+$ signal (right column), apparent conclusions from the images are different: with $^{197}Au^+$ signal as IS, $^{24}Mg^+$ and $^{63}Cu^+$ seemed to be present in the cornea and ciliary muscle, while $^{56}Fe^+$ was clearly identified in the ciliary region.

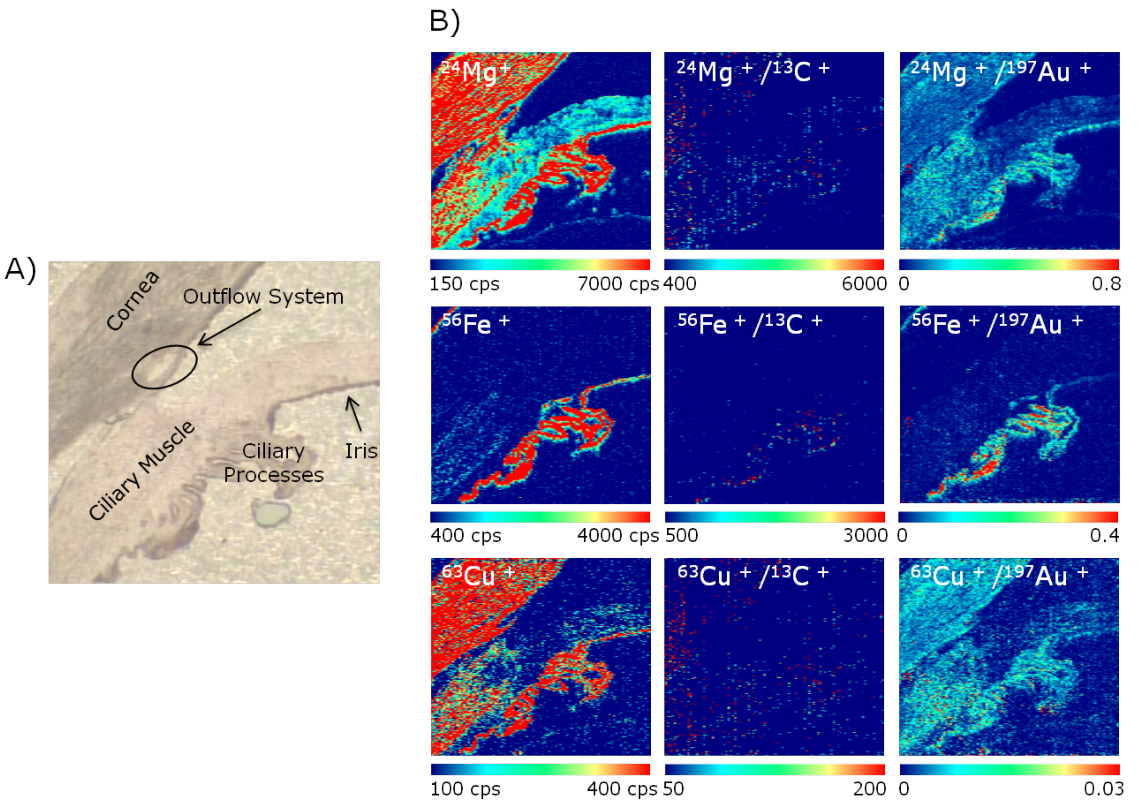

Figure 5.56: A) Histological image of the anterior segment in a paraffin-embedded human eye tissue section, analyzed by LA-ICP-MS, showing the different structures of ophthalmological interest. B) Elemental distribution of $^{24}Mg^+$, $^{56}Fe^+$ and $^{63}Cu^+$ in the tissue section measured by LA-ICP-MS without internal standard correction (left), with $^{13}C^+$ (middle) and $^{197}Au^+$ (right) as IS.

Such different conclusions for the elemental distributions of $^{24}Mg^+$, $^{56}Fe^+$ and $^{63}Cu^+$ in the tissue depending on the IS selected ($^{13}C^+$ or $^{197}Au^+$) raised the question of which of the obtained results reflect the real presence of the sought elements in the analyzed zone of the ocular tissue section. To answer that key question a closer look was taken to the elemental distributions obtained by LA-ICP-MS for $^{13}C^+$ and $^{197}Au^+$. *Figure 5.57A* shows the results obtained for a tissue section with the thin gold layer deposited on the top of the tissue sample. As can be seen, both $^{13}C^+$ and $^{197}Au^+$ show an elemental distribution which fits to the corresponding histological image (left). In the case of $^{13}C^+$ this seems logical, as the distinct tissue compartments are characterized by different cell densities and water content, and therefore, differing carbon content. On the other hand, the finding of elemental distribution of $^{197}Au^+$ which overlaps very well with the histological image of the analyzed zone was a surprising result, as the thin-film deposition by sputtering theoretically ensures a homogeneous distribution of Au within the tissue surface. Perhaps the observed distribution in the elemental

image is caused by accumulation of Au in the different tissue structures during or after the deposition process.

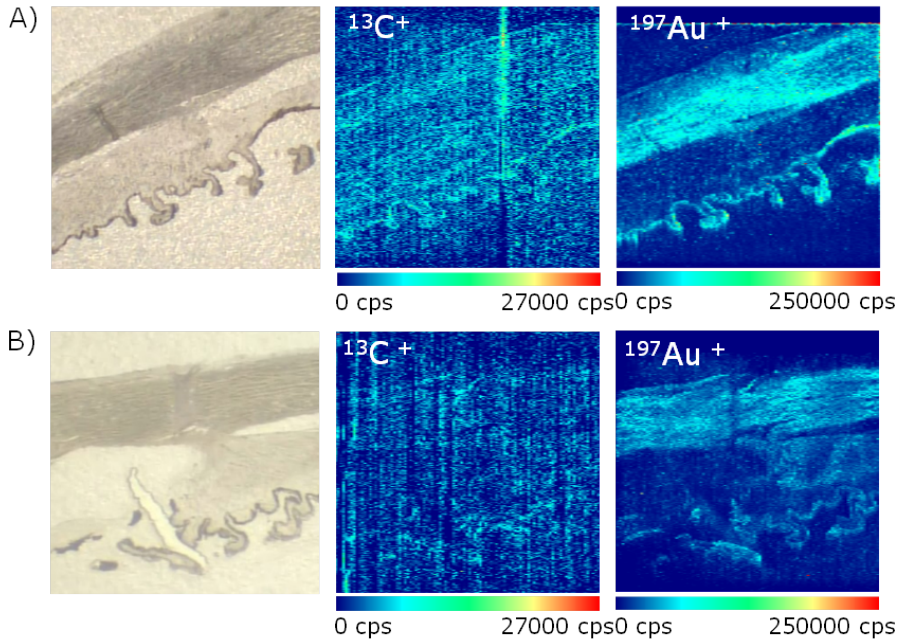

Figure 5.57: Histological images of the analyzed zones in the ocular tissue sections (left) and corresponding elemental distribution of $^{13}C^+$ and $^{197}Au^+$ obtained by LA-ICP-MS. A) Sample with the thin Au layer deposited on the top of the tissue section. B) Sample with the thin Au layer deposited directly on the glass substrate (below the tissue section).

Thus, an alternative sample preparation procedure has been investigated. Here, the thin Au film was deposited directly on the glass substrate and subsequently covered with the tissue section. After laser ablation analysis of the sample, elemental maps for $^{13}C^+$ and $^{197}Au^+$ similar to those shown in *figure 5.57B* were obtained. Remarkably, as in the former sample, the obtained elemental map of $^{197}Au^+$ clearly defines the morphology of the ocular tissue. This indicates, that the change in signal intensities of the IS is not driven by accumulation of the element in different tissue compartments but by changes in the ablation process itself, which depends on the sample composition at every structure. In order to assess this hypothesis a careful characterization of the ablation process was performed.

5.3.4.2 Characterization of the ablation process

Ablation efficiency

As already mentioned before, complete sample ablation is a prerequisite for reproducible and reliable results. In order to reassess if the complete matrix ablation of

the optimized tissue section thickness of 15 μm could also be guaranteed throughout the entire analysis time required for imaging studies (up to 15 h) independently of the tissue composition, the formed imaging craters were visualized by confocal laser scanning microscopy. *Figure 5.58* shows the obtained 3D-images of a sample without Au coating (A) and one with thin Au film deposited on the surface (B). Due to the objective used with a visual window of maximum 1.5 x 1.5 mm, several 3D pictures had to be automatically assembled to the final image.

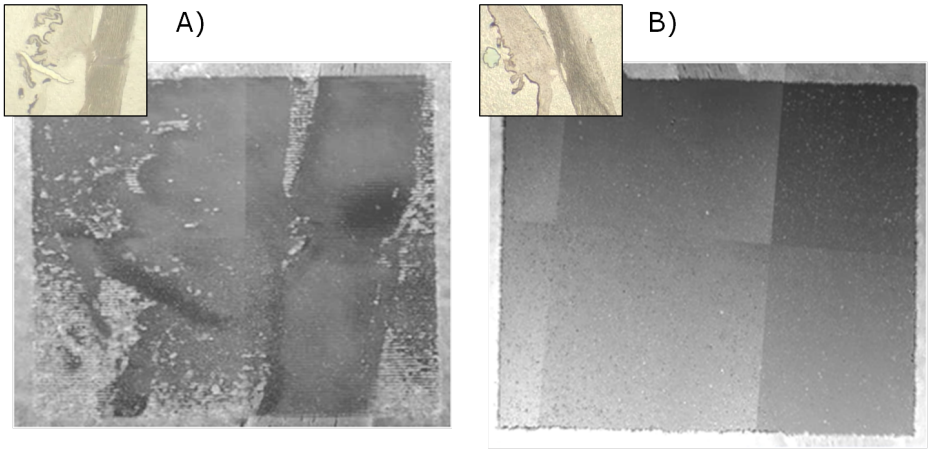

Figure 5.58: 3D pictures of the imaging area in ocular tissue sections (thickness 15 μm) after laser ablation analysis obtained by CLSM. A) without Au coating and B) with thin Au film deposited on sample surface. The histological images (left upper corner, respectively) show the analyzed area before laser ablation analysis.

As it can be seen, although a 15 μm tissue slice was analyzed, the complete ablation of the sample without Au coating (*figure 5.58A*)could not be assured throughout the entire area, as relatively great zones remain unablated. Interestingly, these unablated zones principally coincide with regions of embedding matrix which suggest a high dependence of the ablation efficiency on the sample morphology. In contrast, the analysis of a tissue section covered with a thin Au film (*figure 5.58B*) results in a residue-free ablation of the sample which indicates an increase in ablation efficiency with reduced sample composition dependence. Since the elemental distribution of Au can apparently not be attributed to differences in ablation efficiencies, the morphology of the transported aerosol was examined closer.

Physical characteristics of the transported aerosol

Knowledge about aerosol particle sizes in laser-generated aerosols and fundamental understanding of aerosol formation and particle transport are important aspects to

better understand and improve LA-ICP-MS analysis. In this vein, the laser-generated aerosol obtained from the analysis of different structures of ocular tissues was collected on filters and analyzed by scanning electron microscopy (SEM). It is worth noticing that in order to keep the particle morphology unchanged and to avoid swelling with ambient humidity, the filters were immediately stored after sampling in the presence of silica gel and introduced into the SEM coating unit the same day. Single line analysis, at the optimized laser ablation conditions selected for bioimaging studies was performed at iris, ciliary body and cornea regions as well as at paraffin matrix. The particle collection time was the same for each ablation to better compare the amount of ablated material. *Figure 5.59* shows typical SEM images of the collected aerosol particles obtained in the different ocular structures.

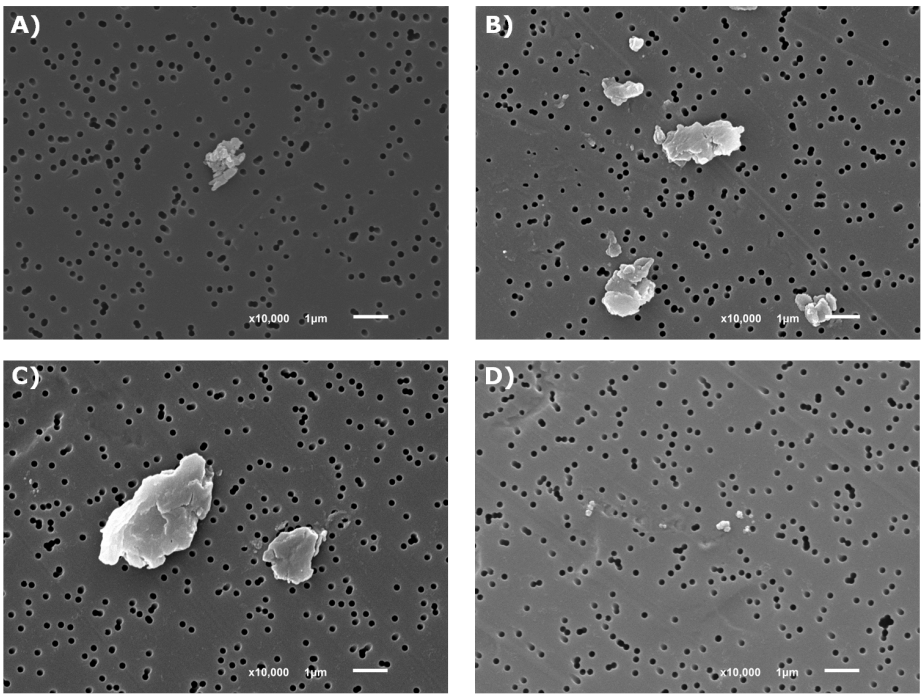

Figure 5.59: SEM images of the collected aerosol particles produced in different ocular structures. These images show the different kinds of transported particles observed but are not representative of the total transported mass. A) iris, B) ciliary body, C) cornea and D) paraffin.

SEM images cannot be used to provide quantitative information about particle size distribution due to the non-uniform distribution of particles on the filter surface. However, they reveal the shape and texture of the particles, which provide crucial information about particle formation processes. For the ablation of ocular structures, such as iris, ciliary body and cornea, a similar amount of particles of comparable size

and morphology was found on the filters (see *Figure 5.59A, B* and *C*, respectively). On the other hand, the ablation of the paraffin matrix provided less particles of generally smaller size (see *Figure 5.59D*). The images obtained corroborate the hypothesis that aerosol formation, particle transport and aerosol atomization are highly dependent on the tissue morphology. This of course leads to variations in element signal response of ICP-MS even when complete sample ablation is assured. Additionally, from an analytical point of view, these results emphasize once more the urgent need for an adequate IS (capable of correcting element-independent response variations) when reproducible and accurate analyses are intended.

5.3.4.3 Influence of the plasma conditions on IS correction with $^{197}Au^{+}$

It has been demonstrated in several works that wet plasma conditions (continuous nebulization of liquid during ablation events) are advantageous for LA-ICP-MS analysis owing to the increased tolerance with respect to different plasma loads. Furthermore, it has been reported that water addition to laser-generated aerosols provides plasma conditions in favor of reduced matrix effects [169, 331]. In order to evaluate if the mentioned benefits of improved sensitivity with reduced matrix effects can also be applied to the imaging studies in ocular tissues performed in the present dissertation, the LA-ICP-MS coupling was carried out in wet plasma conditions using a homemade Y-piece of glass and mixing the laser-generated aerosol with a liquid aerosol (nebulized by means of a concentric nebulizer) before introduction into the plasma. Elemental distributions in the ocular tissue showed that, although an increase of the net signals (background corrected) for all sought elements could be obtained, internal standard correction with $^{197}Au^{+}$ led to comparable results to those obtained in dry plasma conditions. Thus, as no increase in sensitivity and reduced matrix effects could be observed, all further studies were performed in dry plasma conditions.

5.3.5 Application of the gold normalization approach to reproducibility studies

5.3.5.1 Intraindividual study

After careful evaluation of the optimal laser ablation parameters and plasma conditions for imaging studies, the next step was a closer evaluation of the proposed Au-based normalization strategy. Due to the lack of certified reference materials of biological tissues for elemental imaging purposes and the lack of information on distribution of metals in histological tissue sections, reproducibility studies through intra- and interindividual comparisons were performed in order to assess the analytical po-

tential of the approach using $^{197}Au^+$ as IS. It should be stressed that due to the long analysis time needed for obtaining high resolution images (∼15 h), the IS has to correct not only for matrix effects or tissue inhomogeneities within one analysis but also for instrumental drifts. Thus, elemental distribution maps of three adjacent ocular tissue sections of the same donor were performed firstly. *Figure 5.60* shows the images obtained for $^{24}Mg^+$, $^{56}Fe^+$ and $^{63}Cu^+$ of three adjacent tissue sections after LA-ICP-MS analysis.

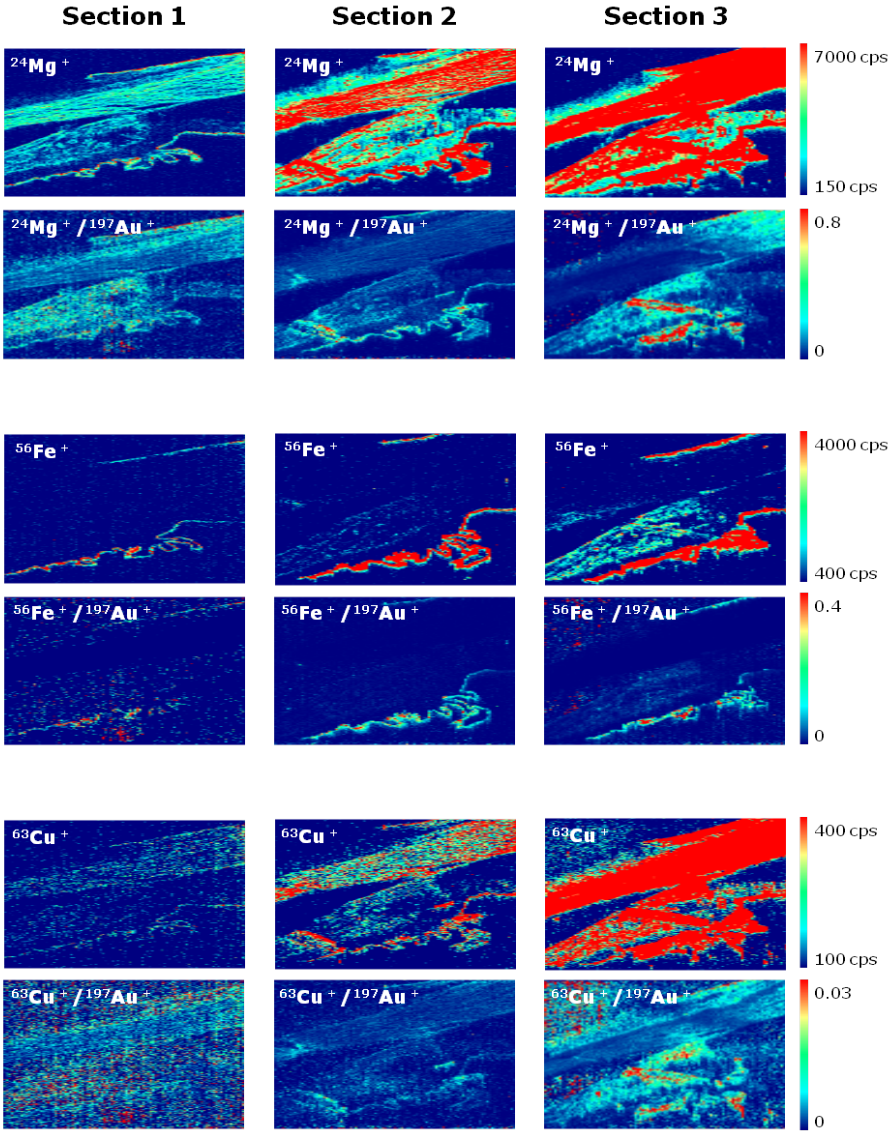

Figure 5.60: Elemental distribution of $^{24}Mg^+$, $^{56}Fe^+$ and $^{63}Cu^+$ in three adjacent ocular tissue sections of the same donor measured by LA-ICP-MS without internal standard correction (blank corrected signals) and using $^{197}Au^+$ as IS (upper and lower row, respectively).

The upper row represents the gas blank corrected signals of the sought elements and the lower row the same images after IS correction with $^{197}Au^+$. As can be seen for the

upper row (uncorrected images), differences in absolute signal intensities between the adjacent sections of one order of magnitude in the case of $^{24}Mg^{+}$, one and a half for $^{56}Fe^{+}$ and up to two orders of magnitude for $^{63}Cu^{+}$ could be observed for the three tissue sections scrutinized, which could lead to a distorted interpretation of the results. The great differences observed in intensities can be explained, at least partially, by daily variations in the laser ablation and ICP-MS systems, apart from real elemental differences in the three individual tissue sections. Such element-independent response variations could be compensated by applying the proposed approach of IS correction with $^{197}Au^{+}$ and differences in relative signal intensities were reduced drastically.

5.3.5.2 Interindividual study

Next, the study was extended to the comparison of $^{24}Mg^{+}$, $^{56}Fe^{+}$ and $^{63}Cu^{+}$ elemental distribution in sections of eleven different eyes from donors. As an example, *Figure 5.61* collects images obtained by LA-ICP-MS for eye-sections from three distinct donors.

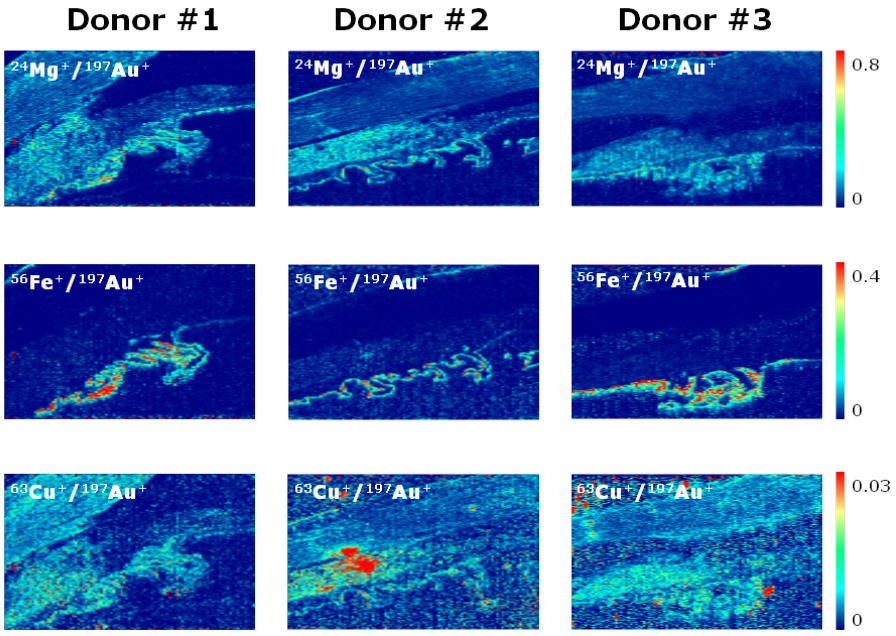

Figure 5.61: Elemental distribution of $^{24}Mg^{+}$, $^{56}Fe^{+}$ and $^{63}Cu^{+}$ in human eye sections of three normal donors measured by LA-ICP-MS with corrected signal intensities using $^{197}Au^{+}$ as IS.

Although slight differences between the elemental images can be observed, they could be attributed mainly to biological differences in elemental concentrations, characteristic for each individual. In any case, it should be stressed that the observed

reproducibility in terms of relative signal intensities is still maintained. As can be seen, $^{24}Mg^+$, $^{56}Fe^+$ and $^{63}Cu^+$ were not equally distributed along ocular structures: $^{56}Fe^+$ was found to be concentrated in ciliary body, while $^{24}Mg^+$ and $^{63}Cu^+$ was mainly present in ciliary body and muscle. In other words, using the developed Au IS methodology the reproducibility of LA-ICP-MS analysis can be significantly improved allowing more reliable comparative studies.

As a conclusion, the principle advantages of the application of a thin $^{197}Au^+$ layer on the top of the sample for internal standardization are summarized in the following:

1. Fast and ease in sample treatment. No additional sample preparation is required, as for example for the preparation of matrix-matched standards of polymeric films.

2. Homogeneous distribution of the internal standard is ensured due the characteristics of sample preparation (metal deposition by sputtering). This aspect is not provided in inhomogeneous tissues by any other element already present in the sample.

3. Significant enhancement of ablation efficiency, ensuring the complete sample ablation, even when long analysis times are required.

4. Correction with $^{197}Au^+$ accounts for different aerosol formation, transport and ionization, while $^{13}C^+$ cannot ensure the correction of these element-independent response variations.

5. Capability to distinguish between artifacts and real elemental signals, an aspect not taken into account by $^{13}C^+$.

6. Significant improvement of the reproducibility, offering the possibility for reliable long-term intra- and inter-patient studies.

5.4 Development of a cryogenic laser ablation cell for quantitative elemental bioimaging in frozen tissues

5.4.1 Introduction

The analysis of soft tissue samples by LA-ICP-MS is generally carried out using, either formalin-fixed and paraffin-embedded (FFPE), or native frozen (stored at temperatures around -70°C) sections. FFPE has been in use for over a century for histologic preparation of clinical tissue samples. Formalin fixation results in crosslinking of proteins, but when paired with impregnation with paraffin and the exclusion of water, results in a remarkably stable biospecimen [362]. Furthermore, FFPE processing provides an ideal architectural preservation and stabilization of cellular details. These morphological features are affected when the tissue is preserved by freezing [363]. Nevertheless, due to the numerous washing and embedding steps in a conventional FFPE protocol, distortion of the initial metal concentration might occur due to metal leaching, especially of diffusible metal ions. In this vein, it was recently shown that the concentration of some metals (e.g. Fe) in samples embedded in paraffin is lower than the concentrations detected in cryogenic samples. This fact could be due to leaching of metals from tissues in formalin solution or during the process of inclusion in paraffin [364]. As LA-ICP-MS analysis is based on the determination of these metals, native freezing is the preferable sample preparation procedure. Additionally, analysis of frozen tissue sections reduces errors occurring during LA-ICP-MS analysis due to fractionation effects, molecular ion formation, as well as evaporation of the water from the vicinity of the laser shot [365].

In order to perform LA-ICP-MS analyses in frozen tissue section, the application of cooled laser ablation cells (commercially available from selected laser ablation companies or developed in research laboratories) has proved to be advantageous, not only for the analysis of cryo-preserved materials but also for dried biological samples [165, 365]. Currently there are three commercially available cryogenic laser ablation cells:

1. Cryocell System 10 - GeoMed Analytical, LLC (Boston, USA)
2. CryoLAC - W. Ludolph GmbH (Germany)
3. Cryocell - New Wave Research, Electro Scientific Industries Europe Ltd.

Additionally, three types of cooled ablation cells developed in the groups of Feldmann, Becker and Müller [152, 365, 366] have been successfully employed for elemental

analysis of frozen samples by LA-ICP-MS. *Figure 5.62* shows the schematic diagrams of these ablation cells.

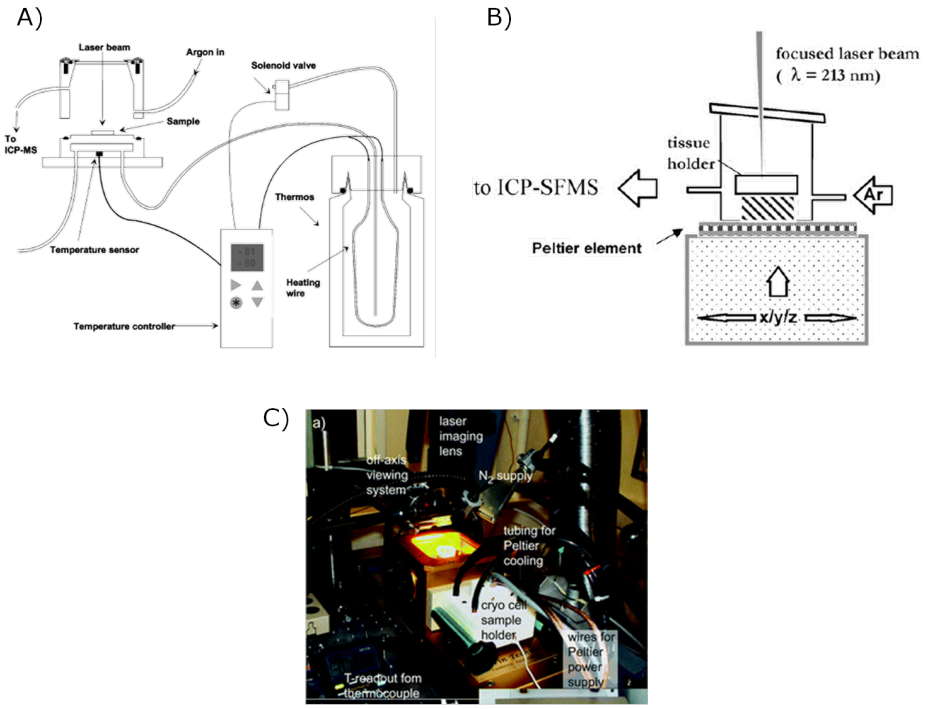

Figure 5.62: Schematics of the cryogenically cooled ablation cells proposed by the working groups of Feldmann (A), Becker (B) and Müller (C) [152, 365, 366].

Feldmann et al. [152] proposed a cryogenically cooled ablation cell with a temperature sensor and a copper cooling coil in the bottom of the cell. The sensor was connected to a temperature controller, which regulates the liquid nitrogen supply stored in a Dewar to the ablation cell by a solenoid valve. In this case, the temperature can be controlled from -20°C to -100°C. Becker et al. [365] developed a cooled PFA laser ablation cell. The cooling system is arranged using two Peltier elements in serial connection under the target holder made of Al. Using this setup a temperature of the target holder of about -15°C was observed. This experimental arrangement showed high signals stability, leading to good precision and accuracy of analytical data as demonstrated for uranium isotope ratio measurements on thin sections of brain samples. Müller et al. [366] designed specifically an ablation cell for the analysis of ice cores and uses also Peltier elements as the cooling device.

Despite the different designs and cooling mechanism of the mentioned cryogenic cells all have in common, that the temperature control is carried out in the structural

components of the cell such as the target holder and not in the sample itself. During a laser ablation process significant thermals effects occur, which may affect the sample, both directly in the irradiated surface and in adjacent areas. Therefore, a direct and precise control and an adjustment of the sample temperature throughout LA-ICP-MS analysis is mandatory, particularly when working with biological samples which have to be preserved in cryogenic conditions during the long analysis time generally needed for obtaining high-resolution images.

An additional aspect when it comes to imaging studies of samples with structures in the micrometer range (e.g. inclusions in geological samples or distribution of metals in human tissue sections) is the precise and clear visualization of the sample. All of the proposed ablation cells which comprise a sample cooling system present an opaque cell base, normally a copper or aluminum block, for which the illumination of the sample can only be performed from above. In some cases, this could turn out to be insufficient to distinguish microstructures and thus, impede high lateral resolution analyses.

On the other hand, irrespective of the sample preparation procedures, probably the most serious limitation of LA-ICP-MS for elemental bioimaging is the lack of reliable validated quantification strategies. A summary of the commonly applied approaches is given in *section 3.2.5* on page 41.

Most quantitative studies have relied upon certified reference materials or, specially, the preparation of matrix-matched laboratory standards. Examples of the former include the use of a CRM (LGC 7112) for single-point calibration in the quantification of trace elements in sheep liver [152] or the use of pressed pellets of CRMs (TORT-2, DOLT-2 and DORM-2) for quantification of Cu, Zn and Fe in rat brain sections [153]. However, the most commonly employed calibration strategy is based on the use of matrix-matched standards prepared by spiking the tissues of interest with known amounts of aqueous standards [146, 244, 252, 253, 255, 367–369]. Briefly, a set of matrix-matched homogenized laboratory standards are prepared with defined elemental concentrations. Homogenized tissue standards are frozen and cut into 20-100 μm sections and mounted on glass slides. The set of laboratory standards and the tissue are then analyzed under the same experimental conditions. The final elemental concentrations in the prepared standards are verified (e.g. by ICP-MS) and their homogeneity can be investigated using LA-ICP-MS. Becker et al. [165] reported regression coefficients of the calibration curves of >0.9 using this methodology for the analysis of P, S, Fe, Cu, Zn, Th and U in human brain samples. Nevertheless, it should be noted that this strategy does not take into account the inhomogeneity of

the biomedical tissues such as differences in water content and density. Therefore, it is not possible to guarantee a similar behavior of samples and standards during the ablation process, the transport of the laser-generated aerosol and once in the ICP.

Two novel calibration approaches have been recently proposed for quantitative elemental imaging of biomedical tissues by LA-ICP-MS. Austin et al. [150] investigated the use of thin film coated calibration standards prepared by spin coating. Quantification of Cu and Zn in chicken breast tissue was performed by correlating the obtained signal intensity with the calibration curves from the spin coated standards (metal spiked polymethylmethacrylate films) using Y and Ru as IS. *Figure 5.63A* illustrates the concept of ablation of the sample together with a film containing IS and the workflow of the quantification process.

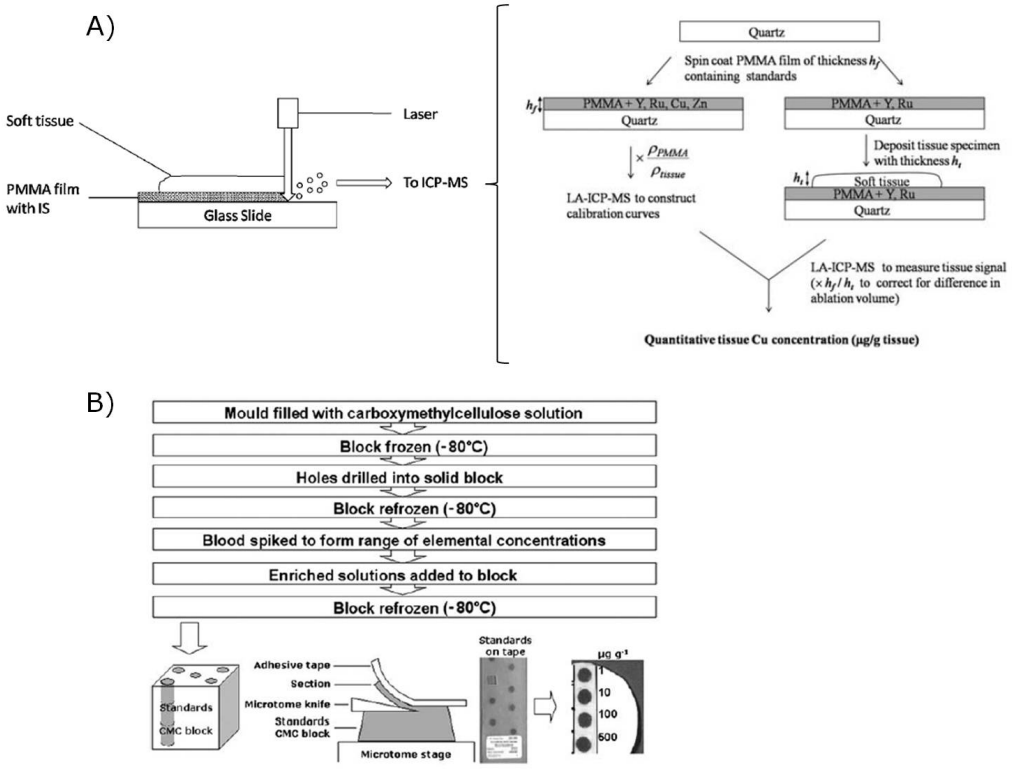

Figure 5.63: Schemes of the sample preparation and quantification processes used in two novel calibration strategies for the quantitative elemental imaging of biological tissues by LA-ICP-MS. (A) Internal standard scheme for elemental imaging and workflow of the quantification process with film standards. (B) Preparation of frozen matrix-matched standards [150, 370].

The tissue samples were frozen and slices precisely cut at 20 μm thickness and placed on top of spin coated quartz. It was observed that the polymer matrix ablated in a similar way to soft tissue samples, provided a much simpler, faster and more reliable

quantification methodology in comparison to homogenized tissue standards. On the other hand, Pugh et al. [370] proposed an alternative strategy for the quantitative imaging of Sr, Gd and Pt. The procedure is relatively simple and is based on spiking whole blood or blood serum with known amounts of elemental standards. Enriched aliquots are next frozen in a customized block and then subjected to cryomicrotom cutting, thus realizing sections of comparable thickness to real samples (in the range of 20-60 μm). Preparation of thin section standards is represented in *figure 5.63B*. The proposed approach ensures samples and standards are matched not only in terms of chemical matrix, but also physical dimensions (i.e. section thickness). Moreover, freeze-drying, which is the norm in biological CRM production, is used in sample preparation and this should permit long-term storage and stability of prepared thin sections.

As an alternative strategy, on-line solution-based calibration has been developed and applied for quantitative analysis of biological tissues using LA-ICP-MS [165, 166]. The dual sample/standard method can provide quantitative data in the absence of solid calibration standard and has already been discussed in *section 3.2.5.2*.

Objective

Taking into account the previously mentioned, the aim of this chapter was the design, assembling and evaluation of a novel Peltier-cooled laser ablation cell. It is worth mentioning that the engineering of the ablation cell was performed by the technology center Fundación Prodintec (Avilés, Spain). Special attention was devoted to the cell design and temperature measurement in order to develop a cryogenic ablation cell totally suitable for high resolution elemental bioimaging studies. The analytical figures of merit were determined using a glass reference material (NIST 612) and biological tissue sections (eye section from a native frozen porcine eye and freshly harvested flower leaves).

Finally, combining the features of the internal standardization approach presented in the anterior section for qualitative imaging analyses (*section 5.3*) and the development of a cooled laser ablation cell, the quantitative elemental bioimaging of frozen human eye lens sections by LA-ICP-MS was carried out. Due to the lack of appropriate certified reference materials able to validate the quantitative results obtained by LA-ICP-MS, the elemental concentrations determined in the biological sections remain countervailable. Thus, the quantitative imaging results were assessed and compared with an alternative more conventional quantitative approach: isotope dilution mass spectrometry combined to conventional nebulization ICP-MS.

5.4.2 Development of a Peltier-cooled laser ablation cell

5.4.2.1 Prerequisites

As described previously, there are several commercially available cryogenically cooled laser ablation cells. Thus, the decision to design and assemble a new cooled laser ablation cell was mainly driven by the idea to overcome existing limitations presented by the other cells and, therefore, improve performance capabilities. In order to do so, first a careful and thorough evaluation of the crucial prerequisites was performed which are summarized in the following:

- The **materials** employed for the construction of the ablation cell should be adapted to the specific needs, i.e. thermally and electrically insulating materials for the corpus and other components with insulating properties and, on the contrary, materials with high thermal conductivity for the cooling system.

- The ablation cell should provide a small **internal volume** into which the expansion of the laser generated aerosol takes place. In such way, short washout times should be ensured, a factor especially important for high resolution bioimaging analyses. Furthermore, the ablation cell should provide a pre-determined outer volume in order to be mounted onto the X-Y-Z translation stage of the laser system (CETAC LSX-213).

- The design of the **in- and outflow system** of the carrier gas should provide a laminar gas flow pattern in order to facilitate the fast and efficient transport of the aerosol out of the ablation cell.

- The **cooling system** of the ablation cell should ensure efficient and stable cooling of the sample to the desired temperature. Furthermore, the cooling system should be able to control the temperature of the sample itself dynamically and correct for possible fluctuations throughout the analysis time.

- The **illumination** of the sample should be optimized in such way, that macro- and microstructures of the analyzed sample are optimally visible.

- The ablation cell should be completely **airtight** in order to enable laser ablation analysis.

- The design, assembling and reproduction of the ablation cell should be **competitive** with the commercial models.

5.4.2.2 Design and assembling

Construction material

For the ablation cell casing (cell base and removable lid) an insulating material with an appropriate thermal transmission coefficient such as synthetic polyamide was chosen, due to its extreme durability and strength. This is an important factor for the efficient cooling of the sample due to the prevalent strong temperature gradient between the inside and the outside of the cell. The dimensioning of the ablation cell casing also pre-determines the space available for the subcomponents, such as internal cooling system, temperature sensor, sample holder and internal volume for the ablation aerosol expansion. The cooling of the ablation cell is realized by thermoelectric cooling using Peltier elements. In this vein, an insulating plate also made of polyamide is employed to thermally separate the hot and cold side of the devices.

As with the criteria for the insulating material, other components of the ablation cell also need a selection of materials according to their function. The cooling plate which also serves as sample holder and the cooling coil as internal heat exchanger require materials with high thermal conductivity in order to ensure rapid thermal kinetics. This is directly correlated with the rapidity of reaction of the system to temperature fluctuations and with the limitation of temperature variations of the sample with a precision of $\pm$ 0.1°C For the manufacturing of the cooling plate ultimately high purity copper was chosen, whereas the cooling coil was made of aluminum.

Ablation cell volume

The external volume of the ablation cell was pre-defined by the translation stage of the laser system in order to replace the commercial CETAC ablation cell without the need for sophisticated tools or adapters.

On the other hand, one main application area of the cooled ablation cell is the analysis of frozen tissue sections. In general, these are mounted on microscopic glass slides with a standard size of 26 x 76 mm. In order to minimize the number of analysis preparation steps (e.g. cutting of the sample substrate) which increase the risk of sample thawing or contamination, the internal dimensions were calculated to incorporate a untreated standard microscope slide. This was realized by an indentation in the cooling plate.

For elemental imaging analyses with high lateral resolution the evacuation of the ablation cell should be as fast as possible to avoid mixing of the aerosols from different spots and therefore ensure discrimination of information from the adjacent sampling positions. One crucial point here is the internal volume of the ablation into which the

expansion of the laser generated aerosol takes place. In the proposed ablation cell the internal free volume is defined by the design of the removable lid. In a first attempt, a cell volume of 20 cm^3 was chosen and used for all studies performed in the present chapter.

In- and outflow system

Numerous investigations have shown that the geometry and volume of a laser ablation cell could affect the size and distribution of laser-generated particles, dispersion and transport efficiency of the aerosol, gas flow pattern and velocity, and ICP-MS signal response [94, 137, 142, 143, 371]. Furthermore it was shown, that ablation under turbulent gas-flow conditions is not advantageous since the ablated particles follow the flow lines of the gas and are redistributed over the whole volume, resulting in longer wash-out times. In contrast, if the ablation takes place under laminar flow conditions much shorter wash-out times can be achieved [94]. In this vein, different ablation cell designs have been investigated with regard to the gas inflow and outflow: (A) single, circular gas in- and outflow, (B) single, circular gas inflow and funnel-shaped gas outflow and (C) four side-by-side, circular gas inflows and funnel-shaped gas outflow (see *figure 5.64*)

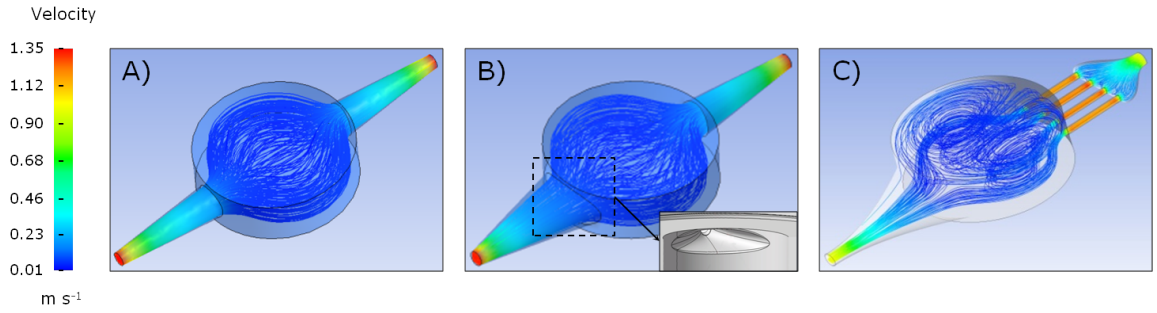

Figure 5.64: Gas flow models showing gas velocities (m s^{-1}) at the ablation area using Ansys CFX 11.0. A) single, circular gas in- and outflow, B) single, circular gas inflow and funnel-shaped gas outflow and C) four side-by-side, circular gas inflows and funnel-shaped gas outflow.

As can be seen in *figure 5.64A* and *5.64B*, laminar gas flows could be obtained with the investigated cell designs (single, circular gas in- and outflow and single, circular gas inflow and funnel-shaped gas outflow, respectively). On the other hand, the latter gas inflow design using four side-by-side, circular gas inflows resulted in turbulent gas flow patterns (see *figure 5.64C*). In order to evaluate if the different gas in- and outflow designs have an influences on the analytical result, single line ablations in a certified glass sample (NIST 612) were performed at room temperature (20°C).

LA-ICP-MS experiments showed, that higher signal intensities with smaller RSDs, less elemental fractionation and higher accuracy and precision in isotope ratio analysis were obtained using cell design (B) compared to the other two configurations (A and C). Therefore, all further characterization experiments were performed with the laser ablation cell design B (single, circular gas inflow and funnel-shaped gas outflow).

Cooling system

The heart of the developed ablation cell is the internal refrigeration system, which is entirely located in the cell base (see *figure 5.65*).

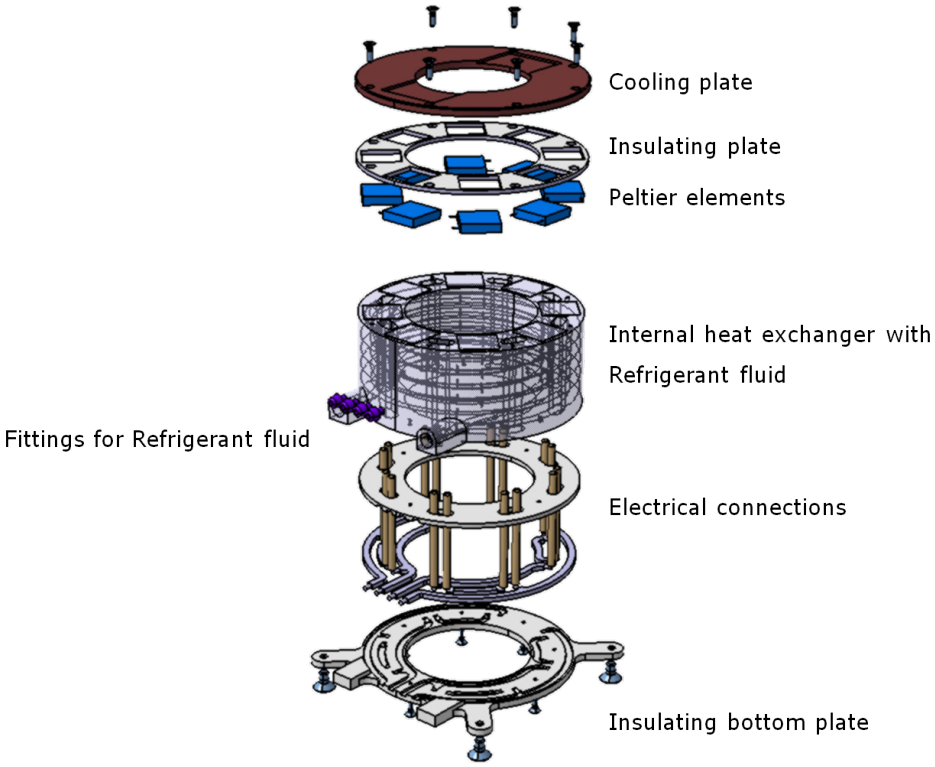

Figure 5.65: Internal refrigeration system of the developed ablation cell.

It consists of a cooling plate which is made of high purity copper and contains the indentation for the sample substrate. Cooling of the sample is carried out by a system of eight small (1 x 1 cm) Peltier elements placed in a circular arrangement below and in direct contact with the cooling plate. Due to the operation mode of a Peltier an insulating plate is necessary in order to thermally separate the cold side of the Peltier (in contact with the cooling plate) from the hot one. For the extraction of the heat generated on the hot side of the Peltier elements a refrigerant fluid such as

polypropylene glycol is guided through a cooling coil below the Peltier elements. The selection of the coil-shaped heat exchanger was based on its high efficiency of heat extraction in a reduced space. Additionally, it offers the possibility to be placed close to the inner walls of the cell base, producing a peephole in the center of the cell. This peephole is of pivotal importance for the adequate illumination of the sample, as it enables the passage of light originating from a set of LEDs placed below the ablation cell. In this way, the visibility of the sample can be significantly enhanced due to a better light-dark contrast, a feature which is not provided by the existing cryogenic laser ablation cells.

The internal refrigeration system is controlled by a sensitive thermocouple. Such temperature sensor is a thin and flexible wire offering the possibility to be placed anywhere inside the ablation cell (e.g. directly on the sample surface). In this vein, a rigorous temperature control of the sample surface can be assured down to -25°C. For the continuous temperature control a custom-built software has been developed, offering additionally the possibility to extract the data from the cooling cycle.

Due to the continuous necessity of heat extraction from the Peltier elements inside the ablation cell, an additional external cooling system is employed. The heated refrigerant fluid originating from the internal cooling system is thermoelectrically cooled in the external heat exchanger. By means of an electrical pump the chilled refrigerant fluid is redirected to the internal cooling system building in such way a closed circuit (see *figure 5.66*).

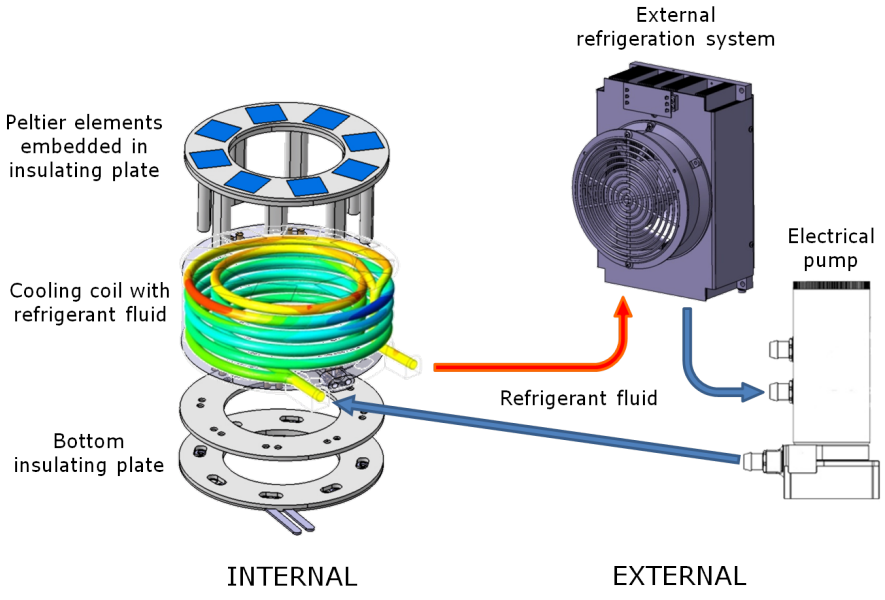

Figure 5.66: Hardware set-up of the refrigeration system (internal and external).

Some elemental imaging analyses can last up to several hours depending on the sample size and required lateral sample resolution. During this time a reliable control of the sample temperature has to be ensured. For this reason, the stability of the temperature measurement was first evaluated in a long-time test using the glass sample (SRM NIST 612). *Figure 5.67* shows the temperature diagram obtained during a cooling cycle of the cryogenic cell for an analysis of 17 hours. The inset shows a zoom of the first 40 min of the cooling cycle.

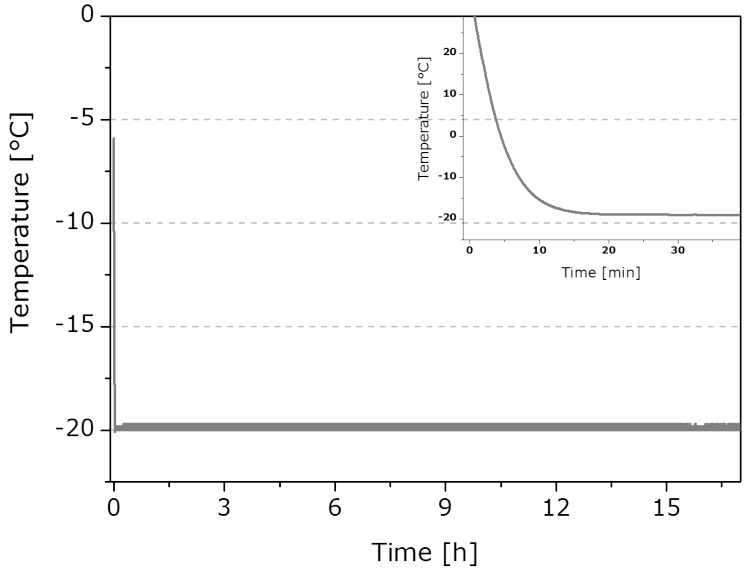

Figure 5.67: Temperature diagram of a cooling cycle to a pre-determined sample temperature of -20°C in a long-time test (17h). The first 40 minutes are zoomed-in in the inset.

As can be seen, the sample surface reaches a temperature of -20°C in less than 20 min. In addition, it is noteworthy that the working temperature is stable, with a deviation of ±0.2°C over the 17 hours period. Thus, the sample integrity and also constant working conditions can be ensured throughout the entire analysis time. Furthermore, temperature fluctuations can be corrected by placing the temperature sensor directly on the sample surface. This possibility was neglected in the previously reported cell designs where the temperature sensor is localized below the target holder. Temperature fluctuations, e.g. caused by the helium carrier gas flow [366], would result in a warming of the sample surface and even in a temperature gradient within the sample. A similar problem arises when thick samples with low thermal diffusivity (e.g. bones, teeth, etc.) are analyzed: the temperature of the sample surface (where the ablation process takes place) does not necessarily correlate with the temperature

in the target holder and, thus, reliability and reproducibility of analysis conditions cannot be ensured. Both aspects are taken into account and those parameters can be instantly corrected by using the developed cryogenic cell with on-sample temperature control.

5.4.2.3 Optimization and evaluation of the Peltier-cooled laser ablation cell

For testing the performance of the proposed laser ablation cell, the reference glass sample SRM NIST 612 was placed on a microscope slide in the center of the cell. Single line ablations were performed under the optimized conditions summarized in *table 5.10* and aimed to evaluate washout times, signal intensity and stability, reproducibility as well as accuracy and precision for isotope ratio measurements.

Short **washout times** of the laser ablation cell and efficient transport of the laser ablated material to the ICP are crucial parameters for LA-ICP-MS imaging with high lateral resolution. In order to determine the washout times (the time required for signals to drop to background level after the last laser pulse) of the cell design B (single, circular gas inflow and funnel-shaped gas outflow) line scans were performed at room temperature (20°C) and at -20°C. *Figure 5.68* shows exemplary the LA-ICP-MS profiles for $^{59}Co^{+}$, $^{107}Ag^{+}$, $^{137}Ba^{+}$, $^{232}Th^{+}$ and $^{238}U^{+}$ obtained at -20°C.

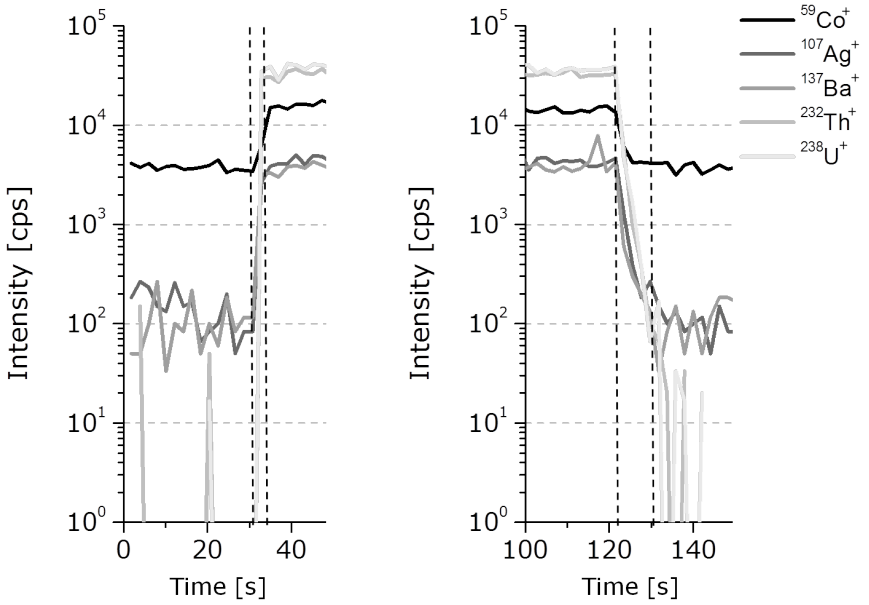

Figure 5.68: Zoom of signal rise and decay at -20°C of $^{59}Co^{+}$, $^{107}Ag^{+}$, $^{137}Ba^{+}$, $^{232}Th^{+}$ and $^{238}U^{+}$ for the calculation of the washout times (signal decay to background level).

Table 5.10: Optimized parameters used for optimization and evaluation of the developed Peltier-cooled laser ablation cell by LA-ICP-MS.

System	Parameter	Value
ICP-MS	RF power	1330 W
	Cooling gas	15.5 L min^{-1}
	Auxiliary gas	0.8 L min^{-1}
	Carrier gas (Ar)	0.5 L min^{-1} (NIST 612) 0.9 L min^{-1} (Biological tissue)
	Cones	Ni (Skimmer and Sampler)
	Mass resolution	4000
	Isotopes monitored	^{56}Fe, ^{59}Co, ^{63}Cu, ^{64}Zn, ^{107}Ag, ^{109}Ag, ^{135}Ba, ^{137}Ba, ^{206}Pb, ^{208}Pb, ^{232}Th, ^{238}U
	Acquisition time	2.1 s (NIST 612) 1.4 s (Biological tissue)
	Mass window	100%
LA system	Laser energy	70% (∼3.5 mJ) (NIST 612) 100% (5.6 mJ) (Eye section) 30% (∼1.7 mJ) (Flower leaf)
	Repetition rate	10 Hz (NIST 612) 20 Hz (Eye section) 10 Hz (Flower leaf)
	Spot size	50 μm (NIST 612) 10 μm (Eye section) 200 μm (Flower leaf)
	Scan speed	50 μm s^{-1} (NIST 612) 10 μm s^{-1} (Eye section) 200 μm s^{-1} (Flower leaf)
	Ablation mode	Single line scan (NIST 612) Multiple line scan (Biological tissue)
	Distance between lines	10 μm (Eye section) 60 μm (Flower leaf)
	Cryogenic cell temperature	-20°C (Eye section) -5°C (Flower leaf)
	Carrier gas (He)	1 L min^{-1} (NIST 612) 0.9 L min^{-1} (Biological tissue)

As can be seen, signal rise after switching the laser on is ∼2 s. Furthermore, a reasonably fast decay of the signal to background level within less than 10 s for all elements both of higher and lower signal intensities can be observed. *Figure 5.69* summarizes the obtained washout times for the investigated isotopes at room temperature (black columns) and -20°C (gray columns). As can be seen, in all cases faster washout times were obtained when working in cryogenic conditions with better reproducibility (represented by error bars from 10 consecutive analyses).

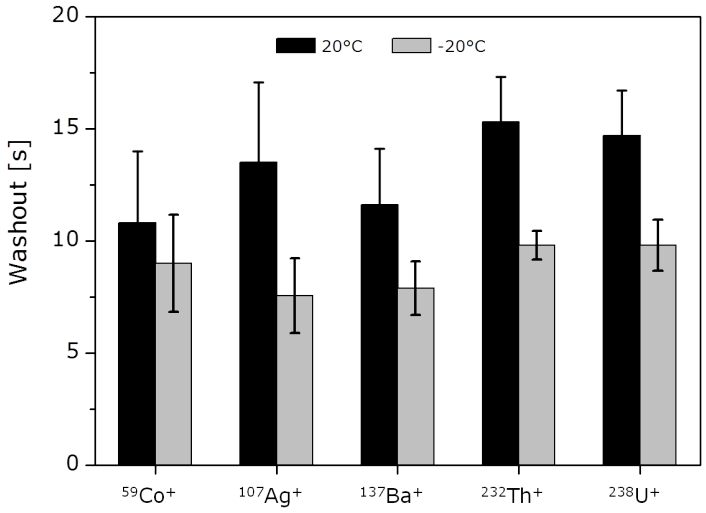

Figure 5.69: Comparison of the aerosol washout of $^{59}Co^+$, $^{107}Ag^+$, $^{137}Ba^+$, $^{232}Th^+$ and $^{238}U^+$ after 90 s of laser ablation at room temperature (20°C) (black columns) and -20°C (gray columns). RSD of 10 different analyses is represented by error bars.

Further experiments performed on the glass reference material were focused on features such as absolute **signal intensity**, **stability** along the analysis time as well as on **reproducibility**, **accuracy and precision** of isotope ratio measurements at different temperatures. Different ablation strategies were employed: (i) long-term (6 min) single line ablation to evaluate signal stability (temporal relative standard deviation), and (ii) consecutive single line ablations (n=10) to evaluate reproducibility. *Figure 5.70* shows the time resolved signal intensities obtained for $^{59}Co^+$, $^{139}La^+$, $^{232}Th^+$ and $^{238}U^+$ from a single line ablation over a period of 6 min at room temperature. As can be seen, stable signals were obtained for the investigated elements with TRSDs below 7%. Furthermore, the LA-ICP-MS profile obtained for $^{59}Co^+$ and $^{238}U^+$ in 10 consecutive single lines (in this case the individual analysis time was 90 s) at two different temperatures is represented in *figure 5.71*.

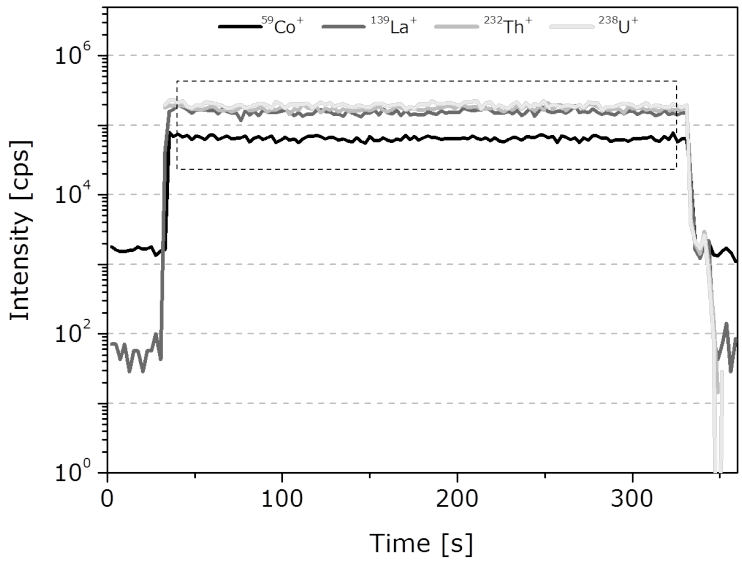

Figure 5.70: LA-ICP-MS profile obtained for $^{59}Co^{+}$, $^{139}La^{+}$, $^{232}Th^{+}$ and $^{238}U^{+}$ in a long-term stability test using the ablation cell at room temperature. Selected area (dashed line) was used for calculation of TRSD.

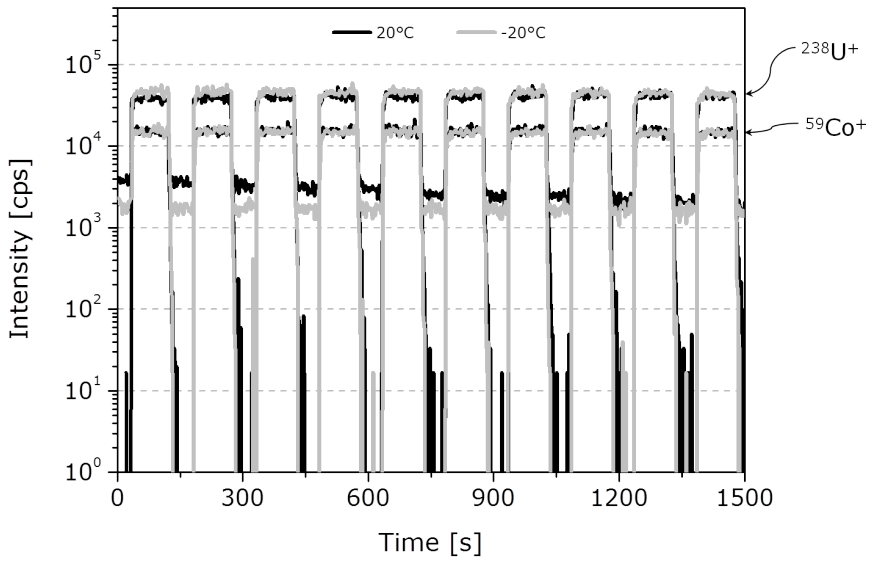

Figure 5.71: Raw intensities of $^{59}Co^{+}$ (lower signal intensity) and $^{238}U^{+}$ (higher signal intensity) in dependence of the analysis temperature (20°C black line and -20°C gray line) obtained for LA-ICP-MS analysis of glass SRM NIST 612.

Relative standard deviations of signal intensities over the entire analysis time for all investigated masses ($^{59}Co^{+}$, $^{107}Ag^{+}$, $^{109}Ag^{+}$, $^{135}Ba^{+}$, $^{137}Ba^{+}$, $^{232}Th^{+}$ and $^{238}U^{+}$)

were found to be below 3.7% at room temperature and below 3.1% when the sample is maintained at -20°C. Furthermore, individual signal stability of the elements under study ranged between 7.3-12.4% working at room temperature and between 6.6-11.7% at cryogenic conditions. Taking into account the ICP-MS drift (about 4% for liquid nebulization during 5 min analysis) the TRSD obtained for LA-ICP-MS analysis with the proposed cryogenic cell can be considered quite good.

The accuracy and precision of natural isotope ratios measurement were also measured at different temperatures for silver, barium and lead using SRM NIST 612. The obtained results are presented in *table 5.11*.

Table 5.11: Precision and accuracy obtained for silver, barium and lead isotope ratio measurements at two analysis temperatures using the glass SRM NIST 612.

Temperature	**IR**	**Measured IR**	**SD** (n=10)	**Accuracy** (%)	**Natural IR**
20°C	$^{107}Ag^+/^{109}Ag^+$	1.028	0.024	4.5	1.076
	$^{135}Ba^+/^{137}Ba^+$	0.611	0.013	4.1	0.587
	$^{206}Pb^+/^{208}Pb^+$	0.466	0.001	1.3	0.460
-20°C	$^{107}Ag^+/^{109}Ag^+$	1.034	0.018	3.9	1.076
	$^{135}Ba^+/^{137}Ba^+$	0.602	0.015	2.6	0.587
	$^{206}Pb^+/^{208}Pb^+$	0.461	0.002	0.3	0.460

Experimental results showed that with the ablation cell at room temperature, the accuracy (deviation from the natural isotope ratio) was in the range of 1.3-4.5%. Comparable results were obtained when the ablation cell was operated under cryogenic conditions (-20°C). Here, the determined accuracy turned out to be 0.3-3.9%. The precision (RSD, n=10) of the analyses at both investigated temperatures was also comparable. Since a glass reference material was used in this experiment no significant temperature influence on the analytical performance was expected. However, these results confirm that the proposed ablation cell does not contribute to loss of isotope signals by working at cryogenic conditions and that changes in analytical signals are purely sample dependent. Hence, the obtained results demonstrate that the proposed ablation cell is able to provide good elemental sensitivity and reproducibility, as well as high accuracy and precision for isotope ratio measurements, both at room temperature and using cryogenic conditions (-20°C).

5.4.2.4 Final Peltier-cooled laser ablation cell design

The final design of the developed cryogenic laser ablation cell is shown in *figure 5.72* pinpointing some of the key components, such as the removable lid with the single, circular gas inflow and funnel-shaped gas outflow, the specially coated quartz crystal transparent for the employed laser wavelength, the cell base containing the internal refrigeration system, the temperature sensor in form of a thin and flexible wire, the glass microscope slide which is generally used as sample substrate, the cooling plate made of high purity copper, the insulating plate responsible for the separation of the hot and cold side of the Peltier elements, the cooling coil for extraction of the heat from the Peltier elements and the connections for the circulating refrigerant fluid.

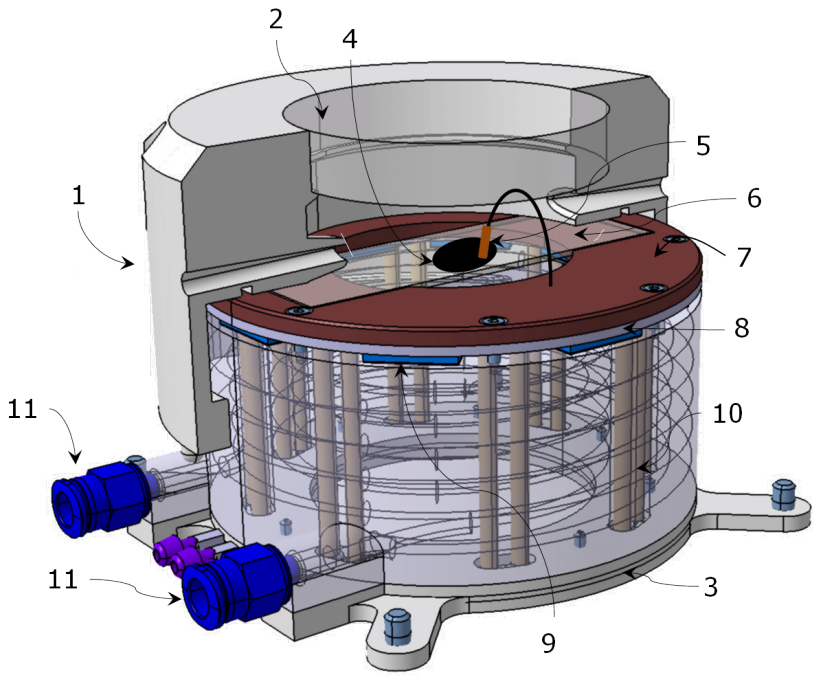

Figure 5.72: Detailed schematic view of the developed Peltier-cooled laser ablation cell showing the main components, such as (1) removable lid with single, circular gas inflow and funnel-shaped gas outflow, (2) specially coated quartz crystal transparent for the employed laser wavelength, (3) cell base containing the internal refrigeration system, (4) sample, (5) temperature sensor, (6) sample substrate, (7) cooling plate, (8) insulating plate, (9) Peltier elements, (10) cooling coil and (11) connections for the circulating refrigerant fluid.

Moreover, *figure 5.73* shows a schematic view of the instrumental set-up of the LA-ICP-MS system with the developed ablation cell.

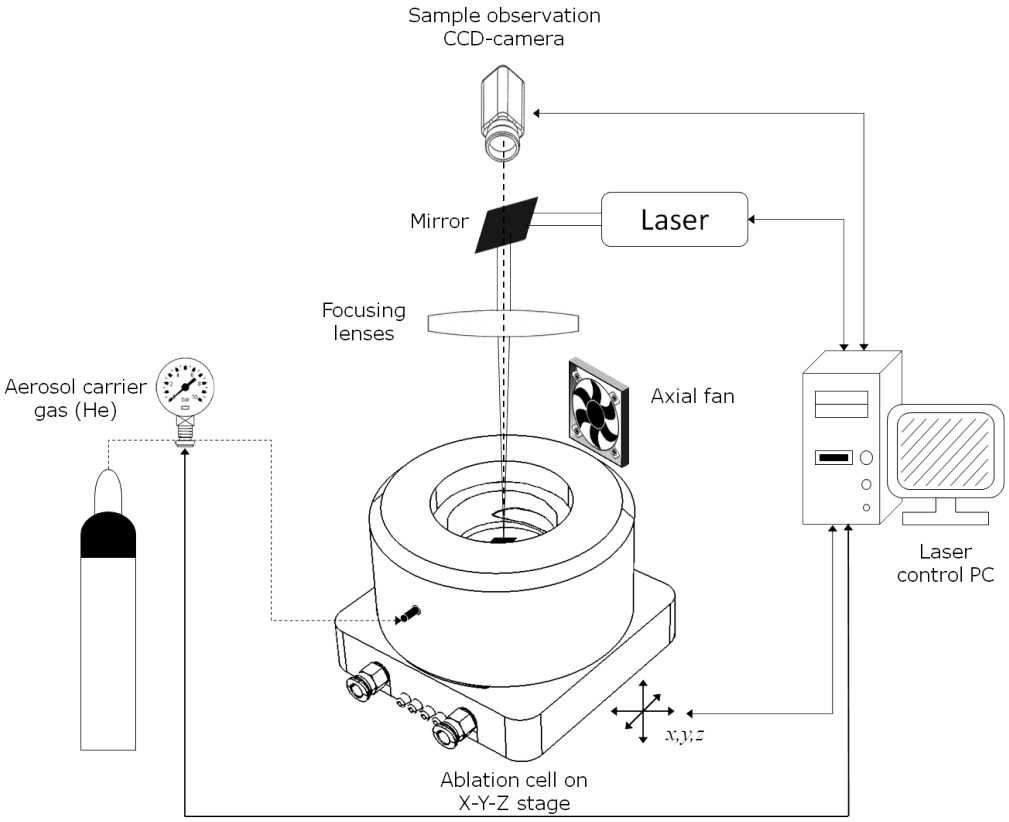

Figure 5.73: Instrumental set-up of the LA-ICP-MS system including the developed Peltier-cooled laser ablation cell.

As it can be seen, the general set-up remained unchanged compared to the set-up employed for the analyses using the commercial CETAC laser ablation cell (see *figure 4.1* on page 72). However, preliminary experiments working in cryogenic conditions revealed condensation problems on both ablation cell windows (in the removable lid and the cell base). Due to the great temperature difference between the inside of the ablation cell and the ambient atmosphere (up to 50°C) the water vapor in the air condenses into a liquid after making contact with the surface of the ablation cell. Here, two cases need to be distinguished:

1. Due to the proximity of the window incorporated in the cell base to the internal refrigeration system its surface temperature is also significantly lowered to below 0°C. Thus, the water vapor condensing on the window instantly freezes forming a layer of ice of about 0.5 cm thickness. The effect of such layer of ice on the laser ablation analysis is shown in *figure 5.74*.

   The condensation process is very fast limiting the translucence within a very short time. Although the actual LA-ICP-MS analysis might not be influenced by

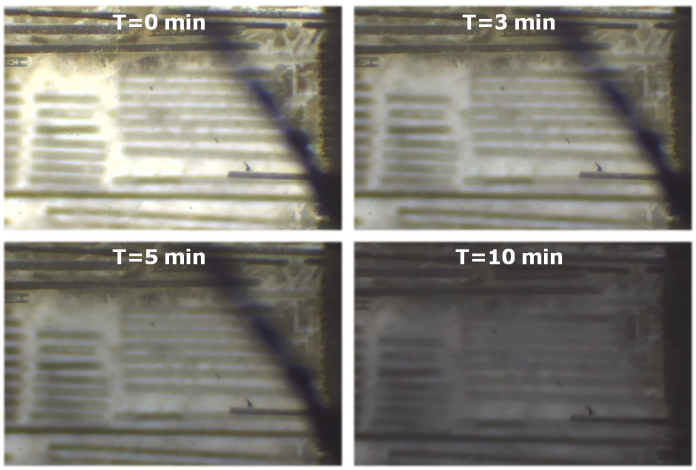

Figure 5.74: Restriction of the visibility of the sample due to condensation of water vapor on the window incorporated in the cell base during a period of 10 min.

the loss of light, the effect severely hampers the visibility of the sample especially when morphologically complex tissues with microstructures are analyzed. In order to overcome this problem, a series of consecutive, closed air chambers was installed in the cell base. In such way, the temperature gradient between the window and the ambiance is gradually reduced inhibiting the condensation process. *Figure 5.75A* shows a schematic view of the retrofitting of the cell while *figure 5.75B* shows that with the modification the intensity of the translucent light remains constant without restriction (images collected up to 50 min).

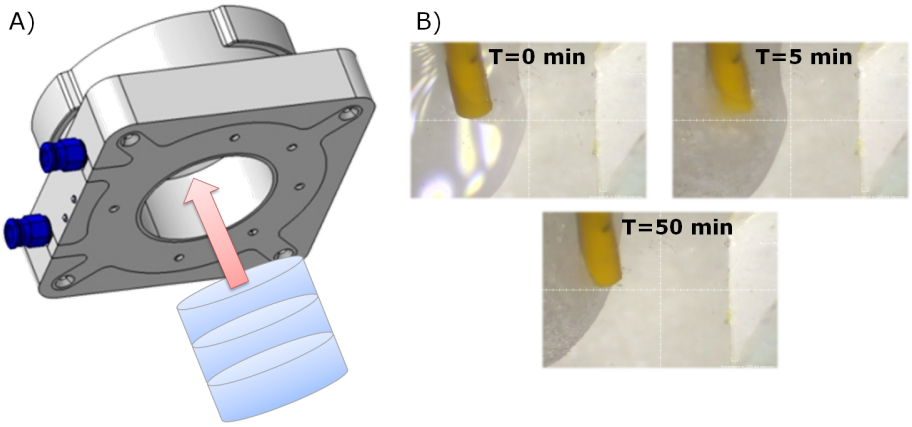

Figure 5.75: A) Modification of the ablation cell by installation of a series of consecutive closed air chambers in the cell base. B) Images taken of the sample by the CCD camera of the laser system showing a constant translucence of the window incorporated in the cell base.

2. Although the temperature gradient between the quartz crystal in the removable lid and the ambiance is not as pronounced as for the window located in the cell base, condensation process occur also here. In contrast to the former case, this effect influences not only the visibility of the sample (see *figure 5.76A*) but also the analysis by LA-ICP-MS, as the laser beam is absorbed by the layer of condensed humidity and thus, the ablation efficiency is drastically reduced. Several solutions have been evaluated and the installation of a constant air flow above the ablation cell by means of an axial fan emerged as the most promising one (see *figure 5.73*). In such way, any condensation process could be immediately reversed and subsequently prevented for a period of at least 24 h (see *figure 5.76B*).

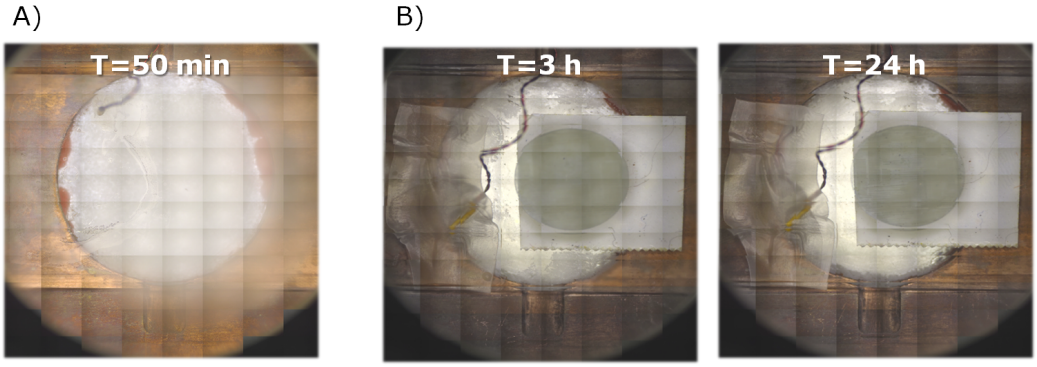

Figure 5.76: A) Condensation of water vapor on the coated quartz crystal in the removable lid after 50 min. B) Constant air flow above the ablation cell led to the elimination and prevention of the condensation process for at least 24 h.

It is worth mentioning, that in spite of the successful engineering of the cryogenic laser ablation cell, its application for LA-ICP-MS analyses would not have been accomplished without the previously mentioned slight modifications.

The last step before the implementation of the developed and evaluated Peltier-cooled laser ablation cell in LA-ICP-MS analyses was the characterization of the instrumental procedure, which is summarized in *table 5.12*.

For the correct commissioning of the cooled ablation cell first the external refrigeration system is turned on. When it reaches a operating temperature between 1 and -1°C the internal refrigeration system can be switched on. The pre-cooling process is necessary to facilitate the rapid cooling of the internal cooling system and thus of the sample. In order to maintain the sample integrity and its frozen state, the sample is placed inside the ablation cell when the internal temperature sensor registers a

Table 5.12: Instrumental procedure of the developed Peltier-cooled laser ablation cell

	Step	Description	Time
1.	Switch on external cooling	Cooling of external Peltier system to at least 1°C (better -1°C).	∼ 15 min
2.	Switch on internal cooling	Cooling of cell interior to below 0°C.	∼ 5 min
3.	Place sample	Place frozen sample on substrate inside the cell.	∼ 2 min
4.	Sample cooling to determined temperature	Wait until desired analysis temperature is reached.	∼ 10 min
5.	Turn on carrier gas flow	When the sample reached the desired temperature, turn on the carrier gas flow rate.	

temperature slightly below the freezing point. The sensory tip of the thermocouple is placed on the sample surface and the sample is cooled down to the pre-determined temperature. Finally, although this is not necessarily the last step, the carrier gas flow rate can be turned on.

5.4.2.5 Elemental bioimaging of frozen eye tissue sections

After the thorough characterization of the proposed laser ablation cell for a model inorganic sample, the influence of the sample temperature was studied for biological tissues analysis. For that, the bio-metal distribution of $^{56}Fe^{+}$, $^{63}Cu^{+}$ and $^{64}Zn^{+}$ in the structures of the anterior segment of the eye, including the iris, ciliary body, cornea and trabecular meshwork was investigated by LA-ICP-MS at room temperature and at -20°C. Porcine eyes, provided by the Fundación de Investigación Oftalmológica - Instituto Oftalmológico Fernández-Vega (Oviedo, Spain), were collected from a local slaughterhouse (Matadero Central de Asturias, Oviedo, Spain) and directly frozen at -80°C. For LA-ICP-MS, the eyes were embedded in Optimal Cutting Temperature compound and cut in a cryostat at -20°C (tissue thickness 20 μm). The experimental operating parameters for the analysis of the histological sections of the eye are summarized in *table 5.10*. In *figure 5.77* the histological images of the analyzed samples and the qualitative elemental images obtained by LA-ICP-MS for $^{56}Fe^{+}$, $^{63}Cu^{+}$ and $^{64}Zn^{+}$ at 20°C and at -20°C (*figures 5.77A* and *5.77B*, respectively) are presented.

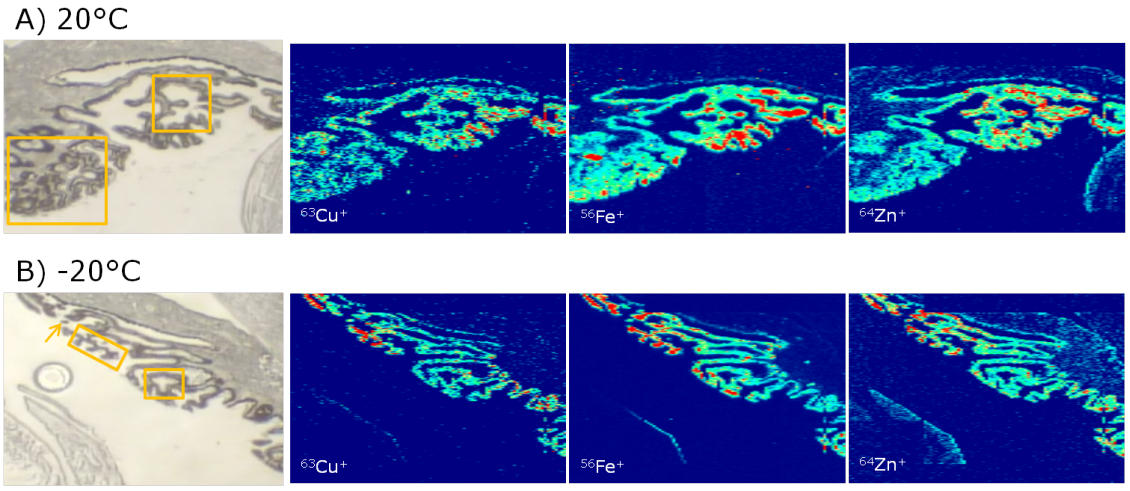

Figure 5.77: Histological images of frozen tissue sections of an anterior segment of the porcine eye and elemental images obtained by LA-ICP-MS for $^{56}Fe^{+}$, $^{63}Cu^{+}$ and $^{64}Zn^{+}$ at A) 20°C and B) -20°C.

As can be seen, a noticeable enhancement of the lateral resolution was obtained when working in cryogenic conditions. The elemental images obtained for $^{56}Fe^{+}$, $^{63}Cu^{+}$ and $^{64}Zn^{+}$ are less blurred when the sample temperature was fixed at -20°C. This cryogenic effect is especially clear in the highlighted zones of the histological images (orange squares and arrow of *figure 5.77*). For the analysis at 20°C (see *figure 5.77A*), the areas in the highlighted zones showed a poorer lateral resolution in the elemental images with broadened microstructures. Conversely, when similar areas were analyzed at -20°C the microstructures obtained by LA-ICP-MS images are better defined in terms of morphology and size. The spot indicated by the arrow clearly shows how small (low μm range) and close microstructures (single spot between two ciliary processes) were resolved in the elemental images just by maintaining the sample in cryogenic conditions.

To summarize, the microstructures formed by the ciliary processes were much better resolved at -20°C than using the elemental images obtained at 20°C. This could be explained by less heat dissipation into adjacent structures during the laser impact and, therefore, less tissue damage. Furthermore, favorable ablation efficiency might result in less re-deposition of the ablated aerosol particles (leading to less contamination of neighboring ablation lines).

5.4.2.6 Elemental imaging of fresh flower leaves

In the light of the described results for LA-ICP-MS imaging of soft ocular tissue sections, the developed cryogenic cell was extended to flower leaves (other type of harder biological samples, widely investigated by LA-ICP-MS). For this purpose, freshly harvested tomato leaves (*Solanum lycopersicum L.* cv. "Tres Cantos") were provided by the Department of Plant Nutrition, Experimental Station of Aula Dei, Spanish National Council for Scientific Research (CSIC) (Zaragoza, Spain). Plants were grown in a controlled environment chamber with a photosynthetic photon flux density at leaf height of 350 mmol m^2 s^{-1} photosynthetic active radiation and a 16 h-22°C/8 h-19°C, day/night regime. Leaves were harvested immediately before the laser ablation analysis to avoid drying and shrinking of the sample and fixed on glass microscope slides using double-sided tape. For LA-ICP-MS imaging studies the center part of the leaf was chosen, covering zones of leaf blade, midvein and veins. The experimental conditions employed for LA-ICP-MS analysis are also summarized in *table 5.10*. The results for the elemental distribution obtained for $^{63}Cu^+$ and $^{127}I^+$ in the flower leaves at 20°C and at -5°C are presented in *figures 5.78A* and *5.78B*, respectively. The same laser ablation conditions were employed at both temperatures, namely a laser beam diameter of 200 μm and a distance between adjacent lines of 60 μm.

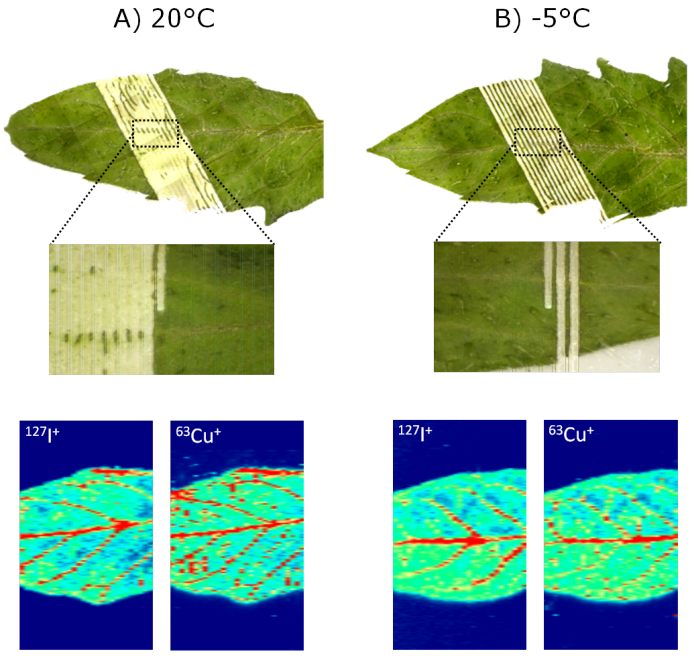

Figure 5.78: Microscope images of fresh leaves from *Solanum lycopersicum* and elemental images obtained by LA-ICP-MS for $^{63}Cu^+$ and $^{127}I^+$ at A) 20°C and B) -5°C.

A comparison of the microscope images of the leaves analyzed at 20°C and -5°C shows, at first sight, a clear improvement in the preservation of the sample integrity when maintaining the sample temperature slightly below the freezing point. Due to strong thermal effects provoked by the laser impact, an expansion of the formed crater after laser ablation is observed when the sample is analyzed at 20°C, enlarging the original crater from 200 μm to approximately 300 μm (zoom of microscope image in *figure 5.78A*). Furthermore, the generation of small and volatile leaf artifacts was observed during the ablation process. As can be seen in the corresponding elemental images obtained by LA-ICP-MS, both effects have a direct influence in the ablation of adjacent lines leading to cross-contamination and reducing the lateral resolution. On the other hand, maintaining the sample temperature slightly below the freezing point results in an excellent preservation of the formed laser crater without any thermal expansion, ensuring the integrity of the sample (zoom of microscope image in *figure 5.78B*). Additionally, working at low temperatures showed to prevent cross-contamination due to leaf artifacts and, therefore, no mixing of elemental information from adjacent lines was obtained (resulting in elemental images with less noise and higher lateral resolution).

In the light of the above, it can be concluded, that the application of the cryogenic laser ablation cell to elemental bioimaging studies of biological tissues (although also extendable to any kind of solid sample) provides enhanced lateral resolution and an optimal preservation of the integrity of the sample. Thus subsequently the features of the previously described internal standardization approach and of the cooled laser ablation cell were combined for the generation of quantitative elemental distribution maps of frozen human eye lens sections by LA-ICP-MS.

5.4.3 Quantitative elemental bioimaging in human eye lens sections

The crystalline lens is a transparent, biconvex structure in the eye that, along with the cornea, helps to refract light to be focused on the retina. It is primarily composed of highly elongated fiber cells that are regularly packed to form a spheroidal mass. Anteriorly, the fiber cells are covered by a monolayer of cuboidal epithelial cells, and the complete structure is covered by a thick membrane, the lens capsule. The anterior and posterior poles of the lens face distinct environments, the anterior pole faces the front of the eye whereas the posterior pole the vitreous and back of the eye. The lens itself lacks nerves, blood vessels, or connective tissue. *Figure 5.79* shows a representative cross-section scheme of the mammalian lens.

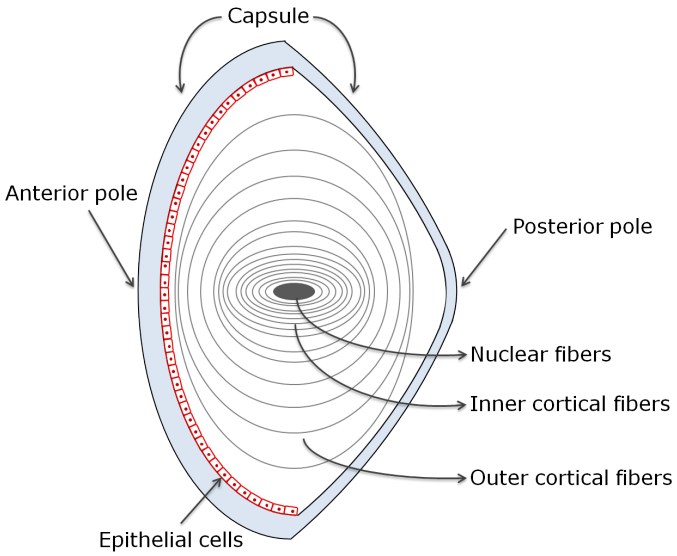

Figure 5.79: Schematic diagram of a cross-section of the mammalian lens.

Amongst other tissues in the mammalian eye, the lens creates a first physical and biochemical barrier to the load of environmental stress acting on the eye. In fact, it is well known that with age the amount of oxidative species increases considerably in the crystalline lens, generating degradation products that can lead to decreased vision or even blindness [372]. Thus, studying the distribution of essential trace elements in the lens, along all its layers, could reveal the importance of this tissue as a defense against oxidative stress.

5.4.3.1 Samples

For depth profiling analysis, bovine eyes were collected from a local slaughterhouse (Matadero Central de Asturias, Oviedo, Spain) and lenses were dissected prior LA-ICP-MS analysis without any further treatment. Additionally, a total of 20 human eyes from adult normal donors (cadavers) ranging in age from 45 to 65 years were also used. Human eyes were obtained 24 h post-mortem through the Hospital Universitario Central de Asturias (HUCA, Oviedo, Spain). The procedures adhere to the tenets of the Declaration of Helsinki, and full ethical approval was obtained from the Clinical Research Ethics Committee at the HUCA. Dissected human lenses were directly frozen at -80°C without any further treatment. For LA-ICP-MS, lenses were embedded in Optimal Cutting Temperature Compound, cut in a cryostat at -20°C (tissue thickness 80 μm) and mounted on microscope glass slides.

5.4.3.2 Optimization of LA-ICP-MS parameters for bioimgaing of frozen tissues

Analyses by LA-ICP-MS were performed after the optimization of the laser parameters (laser energy, repetition rate, spot diameter, scan speed and helium flow rate). The spot diameter was predefined to 50 μm as a compromise between sensitivity and lateral resolution. In such way, the optimal scan speed was calculated, according to *equation 5.2* on page 152, to 32.5 μm s^{-1}. Laser energy and repetition rate were optimized in order to guarantee the complete sample ablation without the subjacent substrate. For the analysis of frozen lens sections, the tissue thickness was optimized to 80 μm, thus increasing the amount of ablated material and consequently the sensitivity. Unless otherwise stated in the text, the optimized operating conditions are summarized in *table 5.13*.

Table 5.13: Optimized parameters used for the analysis of frozen ocular tissue samples by LA-ICP-MS.

System	Parameter	Value
ICP-MS	RF power	1330 W
	Cooling gas	15.5 L min^{-1}
	Auxiliary gas	0.8 L min^{-1}
	Carrier gas (Ar)	0.9 L min^{-1}
	Cones	Ni (Skimmer and Sampler)
	Mass resolution	4000
	Isotopes monitored	^{54}Fe, ^{56}Fe, ^{63}Cu, ^{65}Cu, ^{64}Zn, ^{68}Zn, ^{197}Au
	Acquisition time	1.5 s
	Mass window	100%
LA system	Laser energy	5% (0.3 mJ)
	Repetition rate	10 Hz
	Spot size	50 μm
	Scan speed	32.5 μm s^{-1}
	Ablation mode	Multiple line scan
	Carrier gas (He)	0.9 L min^{-1}
	Cryogenic cell temperature	-20°C

5.4.3.3 Qualitative depth profiling analysis of freshly dissected bovine eye lenses

So far, investigations related to metal content distribution of mammalian lens throughout its different structures have not been performed. To reveal possible trace element distribution in the lens, depth profiling analysis of freshly dissected bovine lenses was conducted. Depth profiling analysis of the trace elements (i.e., Fe, Cu and Zn) through the central anterior-to-posterior pole axis of the lens was attempted using the single point ablation mode (200 μm, 5.6 mJ, 20 Hz, 2000 burst counts).

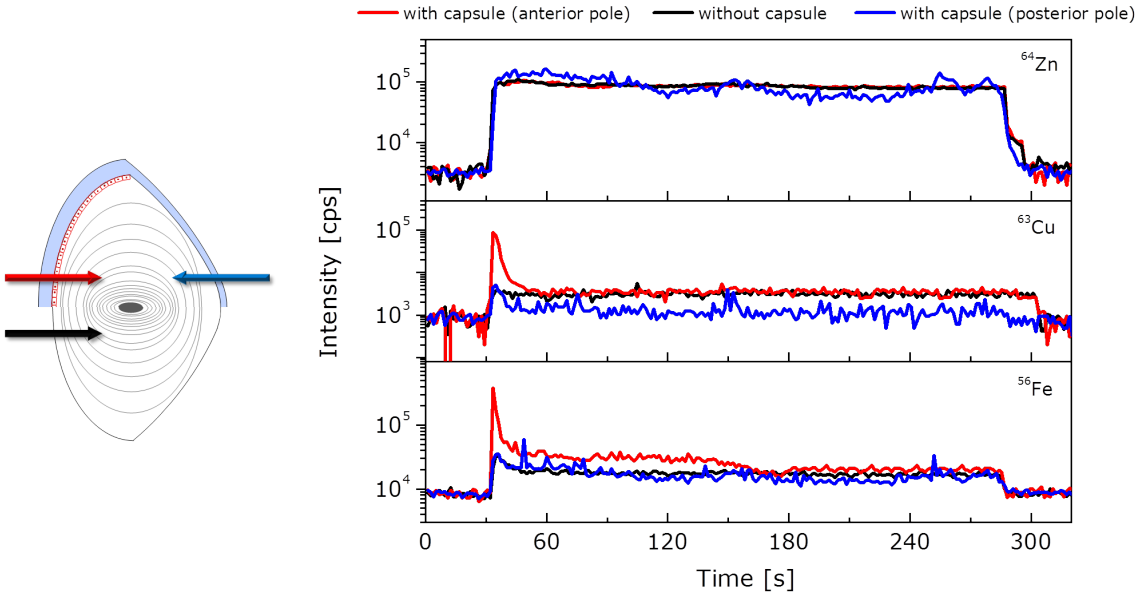

Figure 5.80: Depth profiles obtained for $^{56}Fe^{+}$, $^{63}Cu^{+}$ and $^{64}Zn^{+}$ in freshly dissected bovine lens by LA-ICP-MS: lens analyzed in the anterior pole with the capsule (red line/arrow), in the anterior pole without the capsule and the epithelial cell layer (black line/arrow) and on the posterior pole of the lens (blue line/arrow).

As shown in *figure 5.80*, and following the red arrow in the scheme of the lens and the red line in the obtained LA-ICP-MS profile, $^{56}Fe^{+}$ and $^{63}Cu^{+}$ were detected mainly in the outer layers of the lens (i.e. capsule and/or epithelial cells). To verify whether the detected signals in the lens were restricted to the capsule and/or the epithelial cells two different strategies were employed: analysis of the lens in the posterior pole, where the epithelial cell layer is absent but the capsule is present, and secondly, in the anterior pole of the lens after dissection of the capsule (blue and black lines/arrows, respectively). As it is evident, no $^{56}Fe^{+}$ and $^{63}Cu^{+}$ signal was detected in the first pulses in the posterior pole of the lens in the presence of the capsule neither in the anterior pole when the capsule (and associated cell layer) was absent. The principal

difference between both poles of the lens with respect to the capsule is the associated single cell layer in the anterior pole, suggesting that $^{56}Fe^{+}$ and $^{63}Cu^{+}$ were associated preferentially to the such cell layer of the lens and not to the capsule. Furthermore, LA-ICP-MS profiles also showed no differences in the distribution of $^{64}Zn^{+}$ throughout the lens as the profile of along the anterior-to-posterior poles of the lens appears to be homogenous.

Based on these preliminary qualitative results on the spatial distribution of Fe, Cu and Zn in bovine lenses, the next step was the generation of quantitative bioimages in vertical human eye lens sections.

5.4.3.4 External calibration using matrix-matched tissue standards

The proposed quantification approach consisted of external calibration using matrix-matched tissue standards and ensured that samples and standards were similar not only in terms of chemical matrix, but also in physical dimensions (i.e. section thickness). The preparation of such standards is described in detail in *section 4.2*.

It is judged that one of the main sources of imprecision in data when quantification of biological tissue sections is carried out using matrix-matched tissue standards relates to discontinuities in section structure rather than being linked to instrumental performance. On this account, the homogeneous distribution of the spiked elements for the synthesis of the matrix-matched tissue standards needs to be ensured and confirmed. Therefore, LA-ICP-MS elemental images were produced under the conditions summarized in *table 5.13* using a thin section of matrix-matched tissue standard containing $\sim$0.6 μg g^{-1} Fe, Cu and Zn (see *figure 5.81*). A homogenous distribution was observed in the prepared tissue standards for the three spiked elements. In this way, the obtained ICP-MS signal from the ablation of the tissue standard independently of the ablation position is representative for the corresponding concentration and ensures reproducibility of the external calibration data.

The matrix-matched laboratory standards were carefully characterized and their concentrations were calculated by conventional nebulization ICP-MS after acidic digestion of each corresponding aliquot (details of sample mineralization are given in *section 4.2*). Both the spiked concentration and the determined concentration are summarized in *table 5.14*. The amount spiked prior to homogenization did not necessary fully correlate with the determined concentration, especially in the case of

Zn. These data demonstrate the requirement for characterization of the calibration standards prior to quantification of the tissue section by LA-ICP-MS.

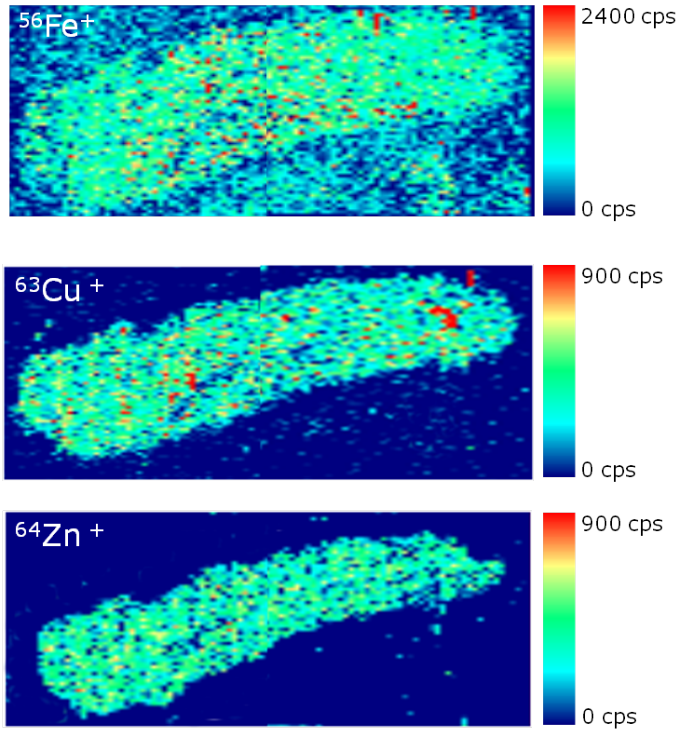

Figure 5.81: Elemental distribution obtained for $^{56}Fe^+$, $^{63}Cu^+$ and $^{64}Zn^+$ in a thin section of a matrix-matched tissue standard by LA-ICP-MS.

Table 5.14: Approximate and determined concentrations of $^{56}Fe^+$, $^{63}Cu^+$ and $^{64}Zn^+$ in the homogenized tissue standards.

Element	**Spiked concentration** ($\mu g\ g^{-1}$)	**Determined concentration** ($\mu g\ g^{-1}$) ± SD (n=3)
Fe	0.70	0.77 ± 0.03
	3.98	4.72 ± 0.15
	9.01	9.19 ± 0.01
Cu	0.81	0.642 ± 0.004
	4.27	3.85 ± 0.02
	9.29	8.35 ± 0.02
Zn	9.29	5.285 ± 0.007
	19.28	14.07 ± 0.05

For the quantification of human eye lens sections the homogenized standard tissue sections were ablated (n=10) immediately before each sample. Calibration curves were constructed by plotting the signal intensity of $^{56}Fe^{+}$, $^{63}Cu^{+}$ and $^{64}Zn^{+}$ (after normalization with the $^{197}Au^{+}$ signal) obtained by LA-ICP-MS *versus* the determined concentrations of the sought elements (see *figure 5.82*).

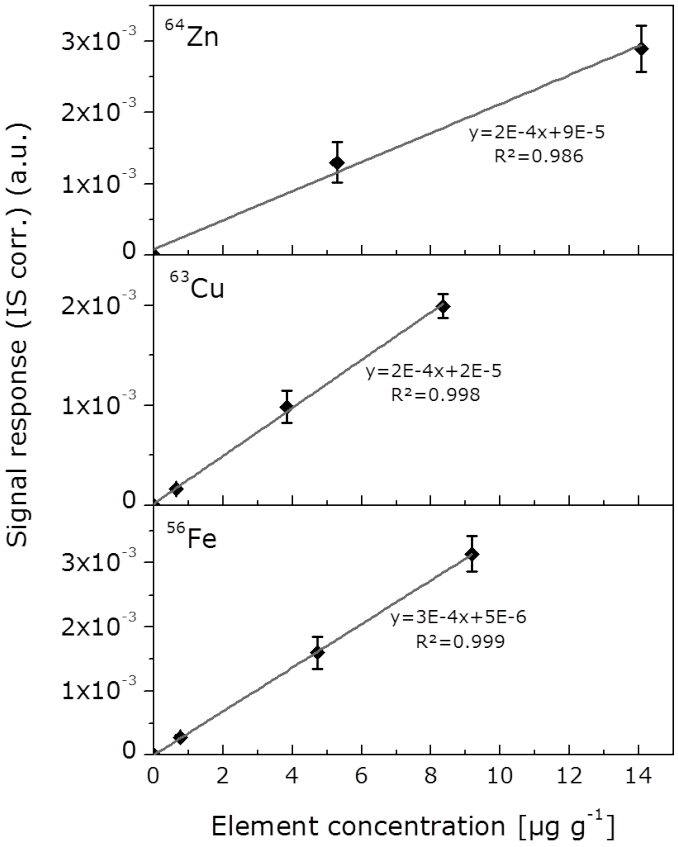

Figure 5.82: Calibration curves obtained for $^{56}Fe^{+}$, $^{63}Cu^{+}$ and $^{64}Zn^{+}$ ($^{197}Au^{+}$ as internal standard) by LA-ICP-MS using three matrix-matched laboratory standards of human eye lens homogenates. Standard deviation values are calculated from the mean of ten independent analyses.

The correlation coefficients of calibration curves obtained from the matrix-matched standards were 0.9999, 0.9980 and 0.9855 for $^{56}Fe^{+}$, $^{63}Cu^{+}$ and $^{64}Zn^{+}$, respectively. Using the obtained linear regressions, each data point (or pixel) resulting from the LA-ICP-MS analysis of human eye lens sections was converted from an intensity / $^{197}Au^{+}$ ratio to $\mu g\ g^{-1}$ concentration, allowing the production of high resolution quantitative images.

5.4.3.5 Quantitative bioimaging of Fe, Cu and Zn in frozen human eye lens sections

Based on the qualitative results obtained by the analysis of freshly dissected bovine lens (*figure 5.80*), next the quantitative determination of the trace elements (i.e. $^{56}Fe^{+}$, $^{63}Cu^{+}$ and $^{64}Zn^{+}$) distribution in transversal frozen sections of human lenses was performed. Lens sections were ablated line by line using a focused laser beam with a spot diameter of 50 μm and two-dimensional images of elemental distribution (analyzed area ~40 mm^2) were obtained. *Figure 5.83* shows a microscope image of the analyzed lens section and the quantitative images obtained by LA-ICP-MS for $^{56}Fe^{+}$, $^{63}Cu^{+}$ and $^{64}Zn^{+}$.

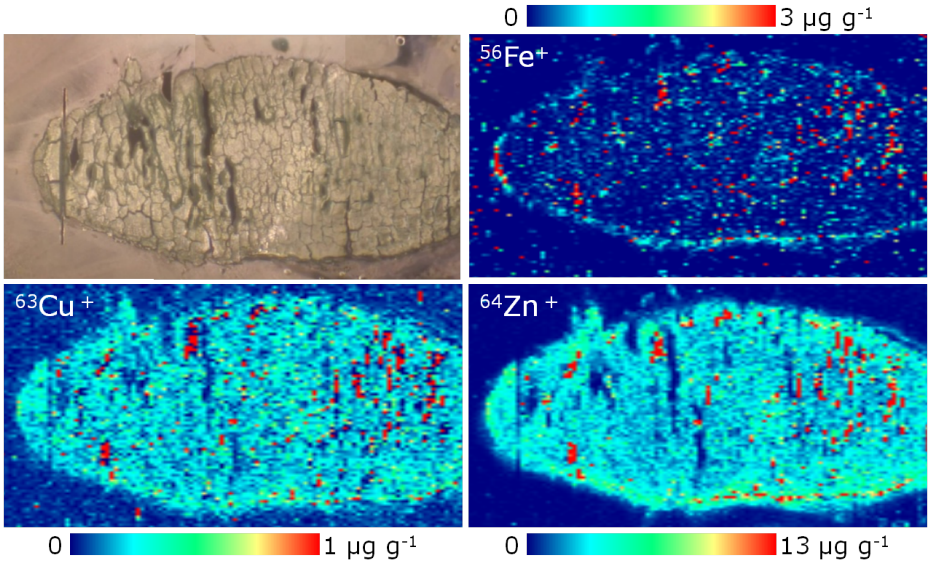

Figure 5.83: Microscope image of the analyzed human lens section (up left) and reconstructed elemental images for $^{56}Fe^{+}$, $^{63}Cu^{+}$ and $^{64}Zn^{+}$ after internal standard correction with $^{197}Au^{+}$.

A relatively homogeneous distribution of the sought elements throughout the human lens was observed. The element concentrations for Fe, Cu and Zn in the lens fibers (i.e. nuclear and cortical) were ~0.3, 0.4 and 8.0 μg g^{-1} of wet tissue, respectively. The average concentration for Fe, Cu and Zn in the capsule at the anterior pole of the lenses were ~1.3, 0.5 and 9.0 μg g^{-1} of wet tissue, respectively (see *table 5.15*). Thus, a homogeneous distribution of $^{63}Cu^{+}$ and $^{64}Zn^{+}$ throughout the entire lens could be found, whereas $^{56}Fe^{+}$ was homogeneously distributed only in the nuclear and cortical fibers and its concentration was higher in the anterior pole of the lens. Due to the employed laser beam diameter of 50 μm the resulting image resolution was not sufficient to determine the increased element concentration more in detail.

By reducing the laser beam diameter to 10 μm the localization in the lens capsule or the associated single cell layer might be possible. Overall it could be observed that Zn was present in the entire lens to a higher extent than Fe and Cu. This observation is in general agreement with reported previous findings [355].

Although bovine and human lenses correspond to different species, LA-ICP-MS images obtained for human lenses were partly in agreement with the results obtained for depth profiling analyses performed in freshly dissected bovine lenses. No significant difference in the distribution of $^{64}Zn^{+}$ between the inner and the outer cortical fibers was found, whereas $^{56}Fe^{+}$ was clearly identified in the anterior pole of the lens. Conversely, the detection of $^{63}Cu^{+}$ observed in the anterior pole of the bovine lens could not be confirmed by similar analysis in the human lens. This could suggest a significant species difference in the distribution of $^{63}Cu^{+}$ in the lens.

5.4.3.6 Determination of Fe, Cu and Zn in human eye lenses by IDA-ICP-MS

Due to the lack of an appropriate certified reference material for the validation of the quantitative bioimaging results an alternative quantification approach was employed. Corroboration was carried out by the use of IDMS in combination with conventional nebulization ICP-MS. For that, a total of five human lenses from adult human eye donors (cadavers) were used for total elemental determinations, after acidic mineralization of the entire lens without capsule and lens capsule, separately. Further details of the sample preparation are given in *section 4.2*. The digested samples were quantified by IDA-ICP-MS using the corresponding enriched isotopes at appropriate concentrations.

Table 5.15 summarizes the Fe, Cu and Zn concentrations obtained by IDA-ICP-MS and LA-ICP-MS in lens fibers and lens capsule. As shown, the estimated concentrations of Fe, Cu and Zn from the LA-ICP-MS image of the human lens were in very good agreement with those determined by the reference technique of IDA-ICP-MS. In addition, no significant differences in Cu and Zn concentrations between lens without capsule and lens capsule were found by the two employed quantification methodologies. It should be stressed here that the increase of Fe concentration localized by LA-ICP-MS in the lens capsule was also confirmed by IDA-ICP-MS measurements, as well as the higher amount of Zn present in the human lens compared to Cu and Fe levels. Slight differences observed between LA-ICP-MS and IDA-ICP-MS results could be mainly attributed to biological differences characterizing each individual.

This demonstrates the reliability of the quantitative results obtained by imaging LA-ICP-MS using the proposed quantification strategy with matrix-matched standards and the adequate internal standard correction strategy.

Table 5.15: Comparison of Fe, Cu and Zn concentrations in human lens without capsule (nuclear and cortical) and lens capsule obtained by LA-ICP-MS and IDA-ICP-MS. LA-ICP-MS concentrations correspond to the estimated average value from *figure 5.81*. IDA-ICP-MS uncertainties show result from standard deviations of the mean of five independent analyses of five individuals.

	Lens without capsule (μg g^{-1} wet tissue)		**Lens capsule** (μg g^{-1} wet tissue)	
	LA-ICP-MS	IDA-ICP-MS	LA-ICP-MS	IDA-ICP-MS
Fe	0.35 - 0.37	0.27 ± 0.10	1.29 - 1.45	1.65 ± 0.41
Cu	0.29 - 0.32	0.23 ± 0.03	0.40 - 0.44	0.39 ± 0.12
Zn	8.7 - 9.5	9.4 ± 1.1	8.7 - 9.3	9.8 ± 2.5

Finally, the difference observed for Cu between bovine and human lenses (Cu was present in the bovine outer layer of the lens whereas it was absent in the human lens) was also verified by applying the same quantification approach. A total of five bovine lenses and the corresponding lens capsules were quantified by ID-ICP-MS after acidic mineralization of the samples. Fe, Cu and Zn concentrations were respectively found to be 0.11 ± 0.02, 0.015 ± 0.007 and 10.74 ± 0.86 μg g^{-1} wet tissue in lens without capsule and 0.98 ± 0.26, 1.32 ± 0.25 and 3.95 ± 1.22 μg g^{-1} wet tissue in lens capsule. According with the data obtained in human lenses, in bovine animals a significantly higher Zn concentration was found compared to Fe and Cu. Additionally, a higher Fe concentration was observed in the lens capsule, compared to the content in lens fibers. In contrast to the results obtained from the human samples, Cu was found to be present in the lens capsule with a 100-fold higher concentration than in the lens itself. These results confirm the previous qualitative depth profiling analysis results observed in freshly dissected bovine lens.

The developed quantification approach using synthetic matrix-matched tissue standards, gold as internal standard and cryogenic temperatures during LA-ICP-MS analysis was successfully applied for the determination of quantitative distributions of trace elements in frozen human eye lens sections. Despite the homogeneous distribution observed for Fe, Cu and Zn in the lens without capsule, the applied methodology was sensitive enough to differentiate between lens fibers and lens capsule, showing an

increase in Fe concentration in the anterior part of the lens. However, investigations with higher spatial resolution need to be performed in order to localize the increased metal concentration in the lens capsule or in the associated single cell layer. The obtained quantitative LA-ICP-MS results for Fe, Cu and Zn in human lens and lens capsule have been confirmed by isotope dilution analysis ICP-MS after acid digestion of the samples as the reference method.

6 Conclusions/Conclusiones

The main conclusions from the **analysis of local defects in coated glasses** are the following:

1. This work demonstrated that LA-ICP-MS can be a highly valuable analytical tool for the fast and sensitive qualitative depth profile characterization of local defect in coated glasses. Moreover, the inherent capability of double-focusing sector field ICP-MS instruments to separate most polyatomic interferences from the analyte ions in the low mass range, working at mass resolving power of 4000 allowed the detection of $^{31}P^{+}$, $^{32}S^{+}$ and $^{35}Cl^{+}$ located preferentially in the local defects. Thus, three different types of defects were successfully identified on the basis of the impurities analyzed in the LA-ICP-MS profiles by comparison with background signals of glasses without defects; with P and Cl (glass 1), Cl (glass 2) and P, S and Cl (glass 3). Furthermore, the craters produced after LA-ICP-MS analysis of the coated glasses (with and without local defects) showed several irregularities along the crater profiles as well as higher ablation rates inside the local defects compared to craters measured for the glasses without defects.

2. Finally, it should be stressed, that the impurities locations could be identified in the thin metallic and oxide films and not in the substrate or in the sample interface. This information was of critical importance for the glass manufacturing company, indicating that contamination sources are mainly related to the thin films deposition process (e.g. pollutants derived from the oils used for the mechanical components of the sputtering lines; rollers, valves, rotating cathodes, etc.).

From **the LA-ICP-MS analysis of metalloproteins separated by gel electrophoresis for the absolute quantification of serum transferrin** the following conclusions can be drawn:

3. The resolution of serum proteins spots in native conditions is better than under denaturing conditions. Apart from that, working under native conditions leads

to the preservation of the native protein structure by which the loss of iron is prevented or at least reduced.

4. Furthermore, the most appropriate method for transferrin saturation with natural and isotopically enriched iron was found to be the incubation with an excess of 1:1000 iron(III) citrate, which was verified spectrophotometrically. By the subsequent purification step, employing centrifugal filter devices, the saturated transferrin could be successfully separated from the excess of iron used for incubation and quantified.

5. Finally, species-specific GE-LA-ICP-IDMS has been demonstrated to provide an accurate, precise, and time-effective strategy for the absolute direct determination of transferrin in serum samples. Compared with alternative quantification methodologies, no calibration curves or standard reference materials are necessary using the ID proposed method. Moreover, the sample analysis time was reduced to less than 15 min and precision and accuracy obtained for the analysis of a CRM were significantly better than those obtained by external calibration. The appropriate selection of the laser ablation strategy (single line ablation in the direction perpendicular to the electrophoretic migration) and of sample preparation (non-denaturing 1D-PAGE and non-stained gels) was found to be crucial to ensure a good precision and accuracy.

From the study of **internal standard correction strategies for reliable qualitative bioimaging analyses** the following can be concluded:

6. A new internal standard correction strategy has been developed for precise and accurate imaging studies in biological tissue sections by LA-ICP-MS. The proposed normalization approach is based on the deposition of a thin gold film on the tissue surface and the use of $^{197}Au^{+}$ signal as internal standard. This time-effective strategy offers the possibility for direct and simultaneous determination of elements distribution in tissue compartments (having different compositions and morphology). Such strategy has been successfully checked to improve the imaging of Mg, Fe and Cu in ocular tissue sections of normal eye donors obtaining high resolution images of the eye outflow system, iris, ciliary body and cornea regions.

The main conclusions from the **development of a cryogenic laser ablation cell for quantitative elemental bioimaging in frozen tissues** are summarized in the following:

7. A cryogenic laser ablation cell with a small internal volume was designed, providing a reasonably washout of the chamber by restricting the effective volume of expansion of the laser-generated aerosol and a carefully designed gas inflow and outflow geometry favoring laminar gas flows. A most remarkable feature of the developed cryogenic cell includes its on-sample temperature control, achieved by using a flexible thermocouple for continuous, robust and reliable control of the temperature on the sample surface throughout the entire analysis time (up to several hours in imaging analysis). Fluctuations of the sample temperature could be so corrected instantly while ablation conditions and sample thermal stability are ensured.

8. The proposed ablation cell provides good elemental sensitivity and reproducibility, as well as high accuracy and precision for isotope ratio measurements, both at 20°C and using cryogenic conditions (-20°C). The image analysis of a morphologically complex soft tissue section in its native frozen state showed a clear enhancement in lateral resolution when maintaining the sample temperature at -20°C compared to the elemental distribution obtained at 20°C. Furthermore, the analysis of harder tissues (freshly harvested flower leaves) showed a better preservation of the sample integrity all along LA imaging analysis if the sample temperature was maintained below the freezing point.

9. The depth profiling analyses in freshly dissected bovine lens revealed the presence of Fe, Cu and Zn. Based on these findings, quantitative elemental images of frozen human lens sections were produced. Despite the homogeneous distribution observed for Fe, Cu and Zn in the lens without capsule, the applied methodology was sensitive enough to differentiate between lens fibers and lens capsule, showing an increase in Fe concentration in the anterior part of the lens. However, investigations with higher spatial resolution need to be performed in order to localize the increased metal concentration in the lens capsule or in the associated single cell layer in the anterior part of the lens.

10. Quantitative LA-ICP-MS results for Fe, Cu and Zn have been assessed in human lens and lens capsule by isotope dilution analysis ICP-MS after acid digestion of the samples as the reference method. Fe increase in the lens capsule was confirmed by IDA-ICP-MS measurements demonstrating the potential of the proposed methodology for quantitative imaging by LA-ICP-MS.

Conclusiones

Las principales conclusiones del **análisis de defectos locales en vidrios recubiertos** son las siguientes:

1. Se ha demonstrado que la técnica de LA-ICP-MS puede ser una herramienta analítica de gran valor para la rápida y sensible caracterización cualitativa de defectos locales en vidrios recubiertos. Por otra parte, la capacidad inherente del ICP-MS de doble enfoque para separar las interferencias poliatómicas de los analitos, ha permitido la detección de $^{31}P^{+}$, $^{32}S^{+}$ y $^{35}Cl^{+}$ localizados preferentemente en los defectos locales. Por lo tanto, tres tipos diferentes de defectos se han identificado con éxito comparando los perfiles en profundidad obtenidos por LA-ICP-MS en las impurezas y en zonas de los vidrios sin defectos; P y Cl (vidrio 1) ,Cl (vidrio 2) y P, S y Cl (vidrio 3). Además, los cráteres producidos después del análisis por LA-ICP-MS (en zonas con y sin defectos locales) mostraron varias irregularidades a lo largo de los perfiles, así como mayores tasas de ablación dentro de los defectos locales en comparación con cráteres en zonas sin defectos .

2. Por último, hay que destacar, que las impurezas se han identificado en las capas metálicas y de óxidos y no en el sustrato o en la interfaz de muestra. Esta información es de importancia crítica para la empresa de fabricación, lo que indica que las fuentes de contaminación están relacionadas principalmente con el proceso de deposición de las capas finas (por ejemplo, los contaminantes derivados de los aceites utilizados para los componentes mecánicos de las líneas de pulverización; rodillos, válvulas, cátodos de rotación, etc .).

Del **análisis por LA-ICP-MS de metaloproteínas separadas por electroforesis en gel para la cuantificación absoluta de la transferrina sérica** se pueden extraer las siguientes conclusiones:

3. La separación de las proteínas séricas en condiciones nativas es mejor que en condiciones desnaturalizantes. Aparte de eso, trabajando bajo condiciones nativas conduce a la preservación de la estructura de la proteína nativa por la que se impide la pérdida del hierro o al menos se reduce.

4. Además, el método más apropiado para la saturación de transferrina con hierro natural y enriquecido isotópicamente es la incubación con un exceso de 1:1000 citrato de hierro, que fue verificado por espectrofotometría. Para la purificación

posterior y cuantificación de la transferrina saturada, se han empleado de filtros de membrana para separar el exceso de hierro utilizado para la incubación.

5. La estrategia propuesta combina la GE-LA-ICP-MS con el análisis por dilución isotópica específica utilizando transferrina saturada isotópicamente enriquecida con ^{57}Fe. Dicha metodología proporciona resultados exactos y precisos con tiempos de análisis significativamente menores a los recogidos en la bibliografía para otras metodologías. En comparación con los métodos alternativos de cuantificación, no se requieren materiales de referencia ni curvas de calibración. Además, la selección adecuada de la estrategia de ablación láser y la preparación de la muestra resultó ser crucial para asegurar la exactitud y buena precisión de los análisis.

Del estudio de una **estrategia novedosa de corrección interna para la generación de imágenes cualitativas fiables en secciones de tejidos biológicos** se puede concluir lo siguiente:

6. Se ha desarrollado una novedosa estrategia de corrección interna para la generación de imágenes cualitativas en secciones de tejidos biológicos por LA-ICP-MS. La normalización se basa en la deposición de una capa fina de oro sobre la superficie del tejido y el uso de la señal de $^{197}Au^{+}$ como patrón interno. El método propuesto se aplicó al "imaging" cualitativo de Mg, Fe y Cu en tejidos oculares embebidos en parafina. El potencial analítico se demostró por la realización de estudios de reproducibilidad usando secciones de ojo humano del mismo donante y con diez ojos diferentes de donantes adultos.

Las principales conclusiones del **desarrollo de una celda de ablación láser refrigerada para la generación de imágenes cuantitativas en secciones congeladas de lente humana** se resumen en los siguientes puntos:

7. Se ha diseñado una celda de ablación láser refrigerada con un pequeño volumen interno, proporcionando una evacuación de la cámara rapida mediante la restricción del volumen efectivo de la expansión del aerosol generado por el láser y una geometría de entrada y salida de gas cuidadosamente diseñada favoreciendo los flujos de gas laminares. Una de las características más notable de la celda criogénica es el uso de un termopar flexible para el control continuo, robusto y fiable de la temperatura de la muestra durante todo el tiempo de análisis (hasta varias horas en el análisis de generación de imágenes). Las fluctuaciones

de la temperatura de la muestra podrían ser corregidas de manera instantánea mientras que las condiciones de ablación y la estabilidad térmica de la muestra están garantizadas.

8. La celda de ablación propuesto proporciona una buena sensibilidad y reproducibilidad elemental, así como una alta exactitud y precisión para el análisis de relaciones isotópicas, tanto a 20°C como usando condiciones criogénicas (-20°C). La imagen elemental de una sección de tejido blando morfológicamente complejo en su estado congelado ha monstrado una clara mejora en la resolución lateral manteniendo la temperatura de la muestra a -20°C en comparación con la distribución elemental obtenida a 20°C. Por otra parte, el análisis de los tejidos más duros (hojas de planta recién cosechadas) han monstrado una mejor preservación de la integridad de la muestra a lo largo del análisis por ablación láser manteniendo la temperatura de la muestra por debajo del punto de congelación.

9. Los análisis en profundidad en lentes bovinos recién diseccionadas han revelado la presencia de Fe, Cu y Zn. A base de estos resultados cualitativos, se han generado imágenes cuantitativas en secciones congeladas de lente humana. A pesar de la distribución homogénea de Fe, Cu y Zn en la lente sin cápsula, la metodología aplicada ha sido lo suficientemente sensible para diferenciar entre las fibras de la lente y la cápsula, que muestra un aumento de la concentración de Fe en la parte anterior de la lente. Sin embargo, investigaciones con mayor resolución lateral será necesarios con el fin de localizar el aumento de la concentración del metal en la cápsula o en la capa de células asociada en la parte anterior de la lente.

10. Resultados cuantitativos obtenidos por LA-ICP-MS en la lente humana se han corroborado por dilución isotópica ICP-MS después de una digestión ácida de las muestras como método de referencia. El aumento de Fe en la cápsula de la lente ha sido confirmado por ID-ICP-MS que demuestra el potencial de la metodología propuesta para la generació de imágenes cuantitativa por LA-ICP-MS.

7 Suggestions for future research

"When one door closes, another door opens [...]."
"Don't keep forever on the public road, going only where others have gone [...]."
Alexander Graham Bell

The investigations presented in this doctoral thesis were focused on some of the main drawbacks of LA-ICP-MS, mainly dealing with internal standardization and quantification strategies. During the present work some practical solutions were demonstrated in order to overcome some specific limitations. However, for the future of LA-ICP-MS, especially in the biomedical research field, several improvements of the described approaches are desirable. These are for example:

- One partial objective of this dissertation was the absolute quantification of serum transferrin by isotope dilution analysis ICP-MS after monodimensional gel electrophoretic separation. However, the state-of-the-art in protein separation is the two-dimensional gel electrophoresis with its exceptional resolving ability. In this vein, further studies could be carried out in order to apply the developed species-specific IDA to the quantification of serum transferrin after 2D-GE. As a result of the separation properties, only small protein spots are obtained, thus special attention should be devoted to the ablation strategy in order to achieve maximum signal intensity. As one might surmise, the proposed quantification strategy with either 1D- or 2D-GE separation is applicable to any protein (after the synthesis of the corresponding species-specific spike, which in some cases might be the weakest link).

- The search for a proper and universally applicable internal standardization approach for both qualitative and quantitative LA-ICP-MS analysis is still in full process. This task is even more challenging if the diversity of the sample matrixes is considered, either within the inorganic as well as organic specimen. From the current point of view, none of the presented strategies in the literature is able to fulfill completely the most important requirements for an ideal internal standard, such as homogeneous distribution of an element not present

in the sample or the similar behavior to the analyte. In this vein, the proposed internal correction approach using a thin gold film deposited on the sample surface seems highly promising. However, further studies could be carried out, extending the application of such approach to a wide variety of matrixes and target elements in order to evaluate if it is universally deployable.

- One of the recent investigation lines in LA-ICP-MS analysis deals with the development of new laser ablation cell, demonstrated by an increasing number of publications. The described designs are generally adapted to the intended application, i.e. ultrafast washout times for analyses with high spatial resolution or sophisticated cooling mechanism for the analysis of frozen samples. As described in this doctoral thesis, the developed Peltier-cooled ablation cell offers several advantages offer existing cryogenic cell models. Nonetheless, this prototype requires various improvements in order to stand out from the crowd. Special attention should be taken to the reduction of the washout times by reconfiguration of the in- and outflow design of the carrier gas or by further restricting of the volume into which the aerosol expansion takes place. Also the temperature measurement on the sample surface could be improved by increasing the robustness of the thermocouple or by installing a non-contact device, such as a pyrometer.

- In the present dissertation as well as in a great number of recently published works, the potential of LA-ICP-MS techniques in biomedical application was demonstrated. More specifically, elemental bioimaging analyses are often used to determine metal distributions and accumulations in specific regions of various biological tissues in order to elucidate their pathogenic effect, e.g. in neurodegenerative diseases. In this vein, according to recent findings, glaucoma is classified as a neurodegenerative disease giving rise to the presumption of the accumulation of certain trace elements in ocular tissue structures. Thus, a continuation of the imaging studies in human ocular tissue presented in this work could focus of the comparison of elemental distributions in eyes from healthy donors and from those with diagnosed glaucoma as well as other eye diseases.

Bibliography

[1] H. G. Wells: **The war of the worlds**; *Heinemann Books*, London (1898)

[2] T. H. Maiman: **Stimulated optical radiation in ruby**; *Nature*, 187 (1960), 493-494

[3] J. F. Ready (Ed.): **Effects of High-Power Laser Radiation**, *Academic*, New York (1971)

[4] C. A. Anderson (Ed.): **Microprobe Analysis**, *John Wiley & Sons*, New York (1973)

[5] R. C. Rosan, M. K. Healy, W. F. McNary: **Spectroscopic ultramicroanalysis with a laser**; *Science*, 142 (1963), 236-237

[6] R. E. Honig, J. R. Woolston: **Laser induced emission of electrons, ions and neutral atoms from solid surfaces**; *Applied Physics Letters*, 2 (1963), 138-139

[7] A. L. Gray: **Solid sample introduction by laser ablation for inductively coupled plasma source mass spectrometry**; *Analyst*, 110 (1985), 551-556

[8] P. Arrowsmith: **Laser ablation of solids for elemental analysis by inductively coupled plasma mass spectrometry**; *Analytical Chemistry*, 59 (1987), 1437-1444

[9] L. Moenke-Blankenburg, T. Schumann, D. Günther, H.-M. Kuss, M. Paul: **Quantitative analysis of glass using inductively coupled plasma atomic emission and mass spectrometry, laser micro-analysis inductively coupled plasma atomic emission spectrometry and laser ablation inductively coupled plasma mass spectrometry**; *Journal of Analytical Atomic Spectroscopy*, 7 (1992), 251-254

[10] A. Raith, R. C. Hutton: **Quantitation methods using laser ablation ICP-MS - Part 1: Analysis of powders**; *Fresenius' Journal of Analytical Chemistry*, 350 (1994), 242-246

[11] S. F. Durrant: **Laser ablation inductively coupled plasma mass spectrometry: Achievements, problems, prospects**; *Journal of Analytical Atomic Spectroscopy*, 14 (1999), 1385-1403

[12] D. Günther, S. E. Jackson, H. P. Longerich: **Laser ablation and arc-spark solid sample introduction into inductively coupled plasma mass spectrometers**; *Spectrochimica Acta, Part B: Atomic Spectroscopy*, 54 (1999), 381-409

[13] K. Niemax: **Laser ablation - Reflections on a very complex technique for solid sampling**; *Fresenius' Journal of Analytical Chemistry*, 370 (2001), 332-340

[14] R. E. Russo, X. Mao, H. Liu, J. Gonzalez, S. S. Mao: **Laser ablation in analytical chemistry - a review**; *Talanta*, 57 (2002), 425-451

[15] E. R. Denoyer, K. J. Fredeen, J. W. Hager: **Laser Ablation-ICPMS**; *Analytical Chemistry*, 75 (2003), 341A-347A

[16] D. Günther, B. Hattendorf: **Solid sample analysis using laser ablation inductively coupled plasma mass spectrometry**; *TrAC - Trends in Analytical Chemistry*, 24 (2005), 255-265

[17] J. Pisonero, D. Günther: **Femtosecond laser ablation inductively coupled plasma mass spectrometry: Fundamentals and capabilities for depth profiling analysis**; *Mass Spectrometry Reviews*, 27 (2008), 609-623

[18] J. Pisonero, B. Fernández, D. Günther: **Critical revision of GD-MS, LA-ICP-MS and SIMS as inorganic mass spectrometric techniques for direct solid analysis**; *Journal of Analytical Atomic Spectroscopy*, 24 (2009), 1145-1160

[19] J. Koch, D. Günther: **Review of the State-of-the-Art of Laser Ablation Inductively Coupled Plasma Mass Spectrometry**; *Applied Spectroscopy*, 65 (2011), 155A-162A

[20] S. F. Durrant, N. I. Ward: **Recent biological and environmental applications of laser ablation inductively coupled plasma mass spectrometry (LA-ICP-MS)**; *Journal of Analytical Atomic Spectroscopy*, 20 (2005), 821-829

[21] W. Castro, J. Hoogewerff, C. Latkoczy, J. R. Almirall: **Application of laser ablation (LA-ICP-SF-MS) for the elemental analysis of bone and teeth samples for discrimination purposes**; *Forensic Science International*, 195 (2010), 17-27

[22] Z. Qin, J. A. Caruso, B. Lai, A. Matusch, J. S. Becker: **Trace metal imaging with high spatial resolution: Applications in biomedicine**; *Metallomics*, 3 (2011), 28-37

[23] D. S. Urgast, J. Feldmann: **Isotope ratio measurements in biological tissues using LA-ICP-MS - possibilities, limitations, and perspectives**; *Journal of Analytical Atomic Spectroscopy*, 28 (2013), 1367-1371

[24] R. S. Houk, V. A. Fassel, G. D. Flesch, H. J. Svec, A. L. Gray, C. E. Taylor: **Inductively Coupled Argon Plasma as an Ion Source for Mass Spectrometric Determination of Trace Elements**; *Analytical Chemistry*, 52 (1980), 2283-2289

[25] R. S. Houk: **Mass spectrometry of inductively coupled plasmas**; *Analytical Chemistry*, 58 (1986), 97A-105A

[26] A. Sanz-Medel, M. Montes-Bayón, J. Bettmer, M. L. Fernández-Sanchez, J. Ruiz Encinar: **ICP-MS for absolute quantification of proteins for heteroatom-tagged, targeted proteomics**; *TrAC - Trends in Analytical Chemistry*, 40 (2012), 52-63

[27] D. Pröfrock, A. Prange: **Inductively coupled plasma-mass spectrometry (ICP-MS) for quantitative analysis in environmental and life sciences: A review of challenges, solutions, and trends**; *Applied Spectroscopy*, 66 (2012), 843-868

[28] S. J. Hill (Ed.): **Inductively Coupled Plasma Spectrometry and its Applications**; *Blackwell*, Oxford (2007)

[29] R. Thomas: **A Beginner's Guide to ICP-MS**; *Spectroscopy*, 16 (2001), 56-60

[30] H. Liu, A. Montaser: **Phase-Doppler diagnostic studies of primary and tertiary aerosols produced by a high-efficiency nebulizer**; *Analytical Chemistry*, 66 (1994), 3233-3242

[31] H. Liu, R. H. Clifford, S. P. Dolan, A. Montaser: **Investigation of a high-efficiency nebulizer and a thimble glass frit nebulizer for elemental analysis of biological materials by inductively coupled plasma-atomic emission spectrometry**; *Spectrochimica Acta, Part B: Atomic Spectroscopy*, 51 (1996), 27-40

[32] J. W. Olesik, J. A. Kinzer, B. Harkleroad: **Inductively coupled plasma optical emission spectrometry using nebulizers with widely different sample consumption rates**; *Analytical Chemistry*, 66 (1996), 2022-2030

[33] K. E. Lawrence, G. W. Rice, V. A. Fassel: **Direct liquid sample introduction for flow injection analysis and liquid chromatography with inductively coupled argon plasma spectrometric detection**; *Analytical Chemistry*, 56 (1984), 289-292

[34] D. R. Wiederin, F. G. Smith, R. S. Houk: **Direct injection nebulization for inductively coupled plasma mass spectrometry**; *Analytical Chemistry*, 63 (1991), 219-225

[35] J. A. McLean, H. Zhang, A. Montaser: **A Direct Injection High-Efficiency Nebulizer for Inductively Coupled Plasma Mass Spectrometry**; *Analytical Chemistry*, 70 (1998), 1012-1020

[36] K. W. Olson, W. J. Haas Jr., V. A. Fassel: **Multielement detection limits and sample nebulization efficiencies of an improved ultrasonic nebulizer and a conventional pneumatic nebulizer in inductively coupled plasma-atomic emission spectrometry**; *Analytical Chemistry*, 49 (1977), 632-637

[37] M. A. Tarr, G. Zhu, R. F. Browner: **Microflow ultrasonic nebulizer for inductively coupled plasma atomic emission spectrometry**; *Analytical Chemistry*, 65 (1993), 1689-1695

[38] J. B. French, B. Etkin, R. Jong: **Monodisperse Dried Microparticulate Injector for Analytical Instrumentation**; *Analytical Chemistry*, 66 (1994), 685-691

[39] J. W. Olesik, S. E. Hobbs: **Monodisperse dried microparticulate injector: A new tool for studying fundamental processes in inductively coupled plasmas**; *Analytical Chemistry*, 66 (1994), 3371-3378

[40] F. Vanhaecke, M. Resano, L. Moens: **Electrothermal vaporisation ICP-mass spectrometry (ETV-ICP-MS) for the determination and speciation of trace elements in solid samples - A review of real-life applications from the author's lab**; *Analytical and Bioanalytical Chemistry*, 374 (2002), 188-195

[41] Z. Arslan, A. J. Paulson: **Solid phase extraction for analysis of biogenic carbonates by electrothermal vaporization inductively coupled plasma mass spectrometry (ETV-ICP-MS)**; *Analytica Chimica Acta*, 476 (2003), 1-13

[42] M. C. Wende, J. A. C. Broekaert: **Direct solid sampling electrothermal vaporization of alumina for analysis by inductively coupled plasma optical emission spectrometry**; *Spectrochimica Acta, Part B: Atomic Spectroscopy*, 57 (2002), 1897-1904

[43] S.-J. Jiang, R. S. Houk: **Arc nebulization for elemental analysis of conducting solids by inductively coupled plasma mass spectrometry**; *Analytical Chemistry*, 58 (1986), 1739-1743

[44] D. Günther, I. Horn, B. Hattendorf: **Recent trends and developments in laser ablation-ICP-mass spectrometry**; *Fresenius' Journal of Analytical Chemistry*, 368 (2000), 4-14

[45] S. Greenfield, C. T. Berry, I. L. Jones: **High-pressure plasmas as spectroscopic emission sources**; *Analyst*, 89 (1964), 713-720

[46] R. H. Wendt, V.A. Fassel: **Induction-coupled plasma spectrometric excitation source**; *Analytical Chemistry*, 37 (1965), 920-922

[47] G. Schwedt: **Analytische Chemie: Grundlagen, Methoden und Praxis**, *Georg Thieme Verlag*, Stuttgart (1995)

[48] K. L. Linge, K. E. Jarvis: **Quadrupole ICP-MS: Introduction to instrumentation, measurement techniques and analytical capabilities**; *Geostandards and Geoanalytical Research*, 33 (2009), 445-467

[49] N. Bradshaw, E. F. H. Hall, N. E. Sanderson: **Plasma source-mass spectrometry using an inductively coupled plasma and a high-resolution quadrupole mass filter**; *Journal of Analytical Atomic Spectroscopy*, 4 (1989), 801-803

[50] D. P. Myers, G. Li, P. P. Mahoney, G. M. Hieftje: **An inductively coupled plasma-time-of-flight mass spectrometer for elemental analysis. Part III: Analytical performance**; *Journal of the American Society for Mass Spectrometry*, 6 (1995), 411-427

[51] P. P. Mahoney, S. J. Ray, G. M. Hieftje: **Time-of-flight mass spectrometry for elemental analysis**; *Applied Spectroscopy*, 51 (1997), 16A-28A

[52] M. Guilhaus: **Essential elements of time-of-flight mass spectrometry in combination with the inductively coupled plasma ion source**; *Spectrochimica Acta, Part B: Atomic Spectroscopy*, 55 (2000), 1511-1525

[53] R. E. Sturgeon, J. W. H. Lam, A. Saint: **Analytical characteristics of a commercial ICP orthogonal acceleration time-of-flight mass spectrometer (ICP-TOFMS)**; *Journal of Analytical Atomic Spectroscopy*, 15 (2000), 607-616

[54] D. W. Koppenaal, C. J. Barinaga, M. R. Smith: **Performance of an inductively coupled plasma source ion trap mass spectrometer**; *Journal of Analytical Atomic Spectroscopy*, 9 (1989), 1053-1058

[55] K. E. Milgram, F. M. White, K. L. Goodner, C. H. Watson, D. W. Koppenaal, C. J. Barinaga, B. H. Smith, J. D. Winefordner, A. G. Marshall, R. S. Houk, J. R. Eyler: **High-Resolution Inductively Coupled Plasma Fourier Transform Ion Cyclotron Resonance Mass Spectrometry**; *Analytical Chemistry*, 69 (1997), 3714-3721

[56] W. Paul, H. Steinwedel: **Ein neues Massenspektrometer ohne Magnetfeld**; *Zeitschrift für Naturforschung*, 8a (1953), 448-450

[57] S. D. Tanner, V. I. Baranov: **Theory, design, and operation of a dynamic reaction cell for ICP-MS**; *Atomic Spectroscopy*, 20 (1999), 45-52

[58] S. D. Tanner, V. I. Baranov, D. R. Bandura: **Reaction cells and collision cells for ICP-MS: A tutorial review**; *Spectrochimica Acta, Part B: Atomic Spectroscopy*, 57 (2002), 1361-1452

[59] I. Feldmann, N. Jakubowski, D. Stuewer: **Application of a hexapole collision and reaction cell in ICP-MS - Part I: Instrumental aspects and operational optimization**; *Fresenius' Journal of Analytical Chemistry*, 365 (1999), 415-421

[60] T. Pettke, C. A. Heinrich, A. C. Ciocan, D. Günther: **Quadrupole mass spectrometry and optical emission spectroscopy: Detection capabilities and representative sampling of short transient signals from laser-ablation**; *Journal of Analytical Atomic Spectroscopy*, 15 (2000), 1149-1156

[61] N. Jakubowski, L. Moens, F. Vanhaecke: **Sector field mass spectrometers in ICP-MS**; *Spectrochimica Acta, Part B: Atomic Spectroscopy*, 53 (1998), 1739-1763

[62] C. Latkoczy, D. Günther: **Enhanced sensitivity in inductively coupled plasma sector field mass spectrometry for direct solid analysis using laser ablation (LA-ICP-SFMS)**; *Journal of Analytical Atomic Spectroscopy*, 17 (2002), 1264-1270

[63] T. Walczyk, F. Von Blanckenburg: **Natural iron isotope variations in human blood**; *Science*, 295 (2002), 2065-2066

[64] M. Rehkämper, M. Schönbächler, C. H. Stirling: **Multiple collector ICP-MS: Introduction to instrumentation, measurement techniques and analytical capabilities**; *Geostandards Newsletter*, 25 (2001), 23-40

[65] T. Pettke, F. Oberli, A. Audétat, M. Guillong, A. C. Simon, J. J. Hanley, L. M. Klemm: **Recent developments in element concentration and isotope ratio analysis of individual fluid inclusions by laser ablation single and multiple collector ICP-MS**; *Ore Geology Reviews*, 44 (2012), 10-38

[66] L. Yang: **Accurate and precise determination of isotopic ratios by MC-ICP-MS: A review**; *Mass Spectrometry Reviews*, 28 (2009), 990-1011

[67] P. Rodríguez-González, V. N. Epov, C. Pecheyran, D. Amouroux, O. F. X. Donard: **Species-specific stable isotope analysis by the hyphenation of chromatographic techniques with MC-ICPMS**; *Mass Spectrometry Reviews*, 31 (2012), 504-521

[68] S. A. Goudsmit: **A time-of-flight mass spectrometer**; *Physical Review*, 74 (1948), 622-623

[69] M. Thompson, J. E. Goulter, F. Sieper: **Laser ablation for the introduction of solid samples into an inductively coupled plasma for atomic-emission spectrometry**; *Analyst*, 106 (1981), 32-39

[70] C.-K. Yang, P.-H. Chi, Y.-C. Lin, Y.-C. Sun, M.-H. Yang: **Development of an on-line isotope dilution laser ablation inductively coupled plasma mass spectrometry (LA-ICP-MS) method for determination of boron in silicon wafers**; *Talanta*, 80 (2010), 1222-1227

[71] J. S. Becker, H. J. Dietze: **State-of-the-art in inorganic mass spectrometry for analysis of high-purity materials**; *International Journal of Mass Spectrometry*, 228 (2003), 127-150

[72] A. Cocherie, M. Robert: **Laser ablation coupled with ICP-MS applied to U-Pb zircon geochronology: A review of recent advances**; *Gondwana Research*, 14 (2008), 597-608

[73] D. Günther, A. Audétat, R. Frischknecht, C. A. Heinrich: **Quantitative analysis of major, minor and trace elements in fluid inclusions using laser ablation-inductively coupled plasma mass spectrometry**; *Journal of Analytical Atomic Spectroscopy*, 13 (1998), 263-270

[74] R. J. Watling, B. F. Lynch, D. Herring: **Use of laser ablation inductively coupled plasma mass spectrometry for fingerprinting scene of crime evidence**; *Journal of Analytical Atomic Spectroscopy*, 12 (1997), 195-203

[75] I. Deconinck, C. Latkoczy, D. Günther, F. Govaert, F. Vanhaecke: **Capabilities of laser ablation-inductively coupled plasma mass spectrometry for (trace) element analysis of car paints for forensic purposes**; *Journal of Analytical Atomic Spectroscopy*, 21 (2006), 279-287

[76] B. Giussani, D. Monticelli, L. Rampazzi: **Role of laser ablation-inductively coupled plasma-mass spectrometry in cultural heritage research: A review**; *Analytica Chimica Acta*, 635 (2009), 6-21

[77] M. Resano, E. García-Ruiz, F. Vanhaecke: **Laser ablation-inductively coupled plasma mass spectrometry in archaeometric research**; *Mass Spectrometry Reviews*, 29 (2010), 55-78

[78] D. Kang, D. Amarasiriwardena, A. H. Goodman: **Application of laser ablation-inductively coupled plasma-mass spectrometry (LA-ICP-MS) to investigate trace metal spatial distributions in human tooth enamel and dentine**

growth layers and pulp; *Analytical and Bioanalytical Chemistry*, 378 (2004), 1608-1615

[79] S. D. Müller, R. A. Diaz-Bone, J. Felix, W. Goedecke: **Detection of specific proteins by laser ablation inductively coupled plasma mass spectrometry (LA-ICP-MS) using gold cluster labelled antibodies**; *Journal of Analytical Atomic Spectroscopy*, 20 (2005), 907-911

[80] U. Krause-Buchholz, J. S. Becker, M. Zoriy, C. Pickhardt, M. Przybylski, G. Rödel, J. S. Becker: **Detection of phosphorylated subunits by combined LA-ICP-MS and MALDI-FTICR-MS analysis in yeast mitochondrial membrane complexes separated by blue native-SDS-PAGE**; *International Journal of Mass Spectrometry*, 248 (2006), 56-60

[81] J. L. Neilsen, A. Abildtrup, J. Christensen, P. Watson, A. Cox, C. W. McLeod: **Laser ablation inductively coupled plasma-mass spectrometry in combination with gel electrophoresis: a new strategy for speciation of metal binding serum proteins**; *Spectrochimica Acta, Part B: Atomic Spectroscopy*, 53 (1998), 339-345

[82] J. S. Becker: **Applications of inductively coupled plasma mass spectrometry and laser ablation inductively coupled plasma mass spectrometry in materials science**; *Spectrochimica Acta, Part B: Atomic Spectroscopy*, 57 (2002), 1805-1820

[83] P. Arrowsmith, S. K. Hughes: **Entrainment and transport of laser ablated plumes for subsequent elemental analysis**; *Applied Spectroscopy*, 42 (1988), 1231-1239

[84] C. Geertsen, A. Briand, F. Chartier, J.-L. Lacour, P. Mauchien, S. Sjöström, J.-M. Mermet: **Comparison between infrared and ultraviolet laser ablation at atmospheric pressure-implications for solid sampling inductively coupled plasma spectrometry**; *Journal of Analytical Atomic Spectrometry*, 9 (1994), 17-22

[85] E. F. Cromwell, P. Arrowsmith: **Fractionation Effects in Laser Ablation Inductively Coupled Plasma Mass Spectrometry**; *Applied Spectroscopy*, 49 (1995), 1652-1660

[86] S. M. Eggins, L. P. J. Kinsley, J. M. G. Shelley: **Deposition and element fractionation processes during atmospheric pressure laser sampling for analysis by ICP-MS**; *Applied Surface Science*, 127 (1998), 278-286

[87] R. E. Russo, X. L. Mao, O. V. Borisov, L. Haichen: **Influence of wavelength on fractionation in laser ablation ICP-MS**; *Journal of Analytical Atomic Spectrometry*, 15 (2000), 1115-1120

[88] S. H. Jeong, O. V. Borisov, J. H. Yoo, X. L. Mao, R. E. Russo: **Effects of particle size distribution on inductively coupled plasma mass spectrometry signal intensity during laser ablation of glass samples**; *Analytical Chemistry*, 71 (1999), 5123-5130

[89] M. Guillong, D. Günther: **Effect of particle size distribution on ICP-induced elemental fractionation in laser ablation-inductively coupled plasma-mass spectrometry**; *Journal of Analytical Atomic Spectrometry*, 17 (2002), 831-837

[90] I. Horn, D. Günther: **The influence of ablation carrier gasses Ar, He and Ne on the particle size distribution and transport efficiencies of laser ablation-induced aerosols: implications for LA-ICP-MS**; *Applied Surface Science*, 207 (2003), 144-147

[91] R. E. Russo, X. Mao, J. J. Gonzalez, S. S. Mao: **Femtosecond laser ablation ICP-MS**; *Journal of Analytical Atomic Spectrometry*, 17 (2002), 1072-1075

[92] J. González, C. Liu, X. Mao, R. E. Russo: **UV-femtosecond laser ablation-ICP-MS for analysis of alloy samples**; *Journal of Analytical Atomic Spectrometry*, 19 (2004), 1165-1168

[93] J. González, S. H. Dundas, C. Y. Liu, X. Mao, R. E. Russo: **UV-femtosecond and nanosecond laser ablation-ICP-MS: internal and external repeatability**; *Journal of Analytical Atomic Spectrometry*, 21 (2006), 778-784

[94] E. L. Gurevich, R. Hergenröder: **A simple laser ICP-MS ablation cell with wash-out time less than 100 ms**; *Journal of Analytical Atomic Spectrometry*, 22 (2007), 1043-1050

[95] D. Autrique, A. Bogaerts, H. Lindner, C. C. Garcia, K. Niemax: **Design analysis of a laser ablation cell for inductively coupled plasma mass spectrometry by numerical simulation**; *Spectrochimica Acta, Part B: Atomic Spectroscopy*, 63 (2008), 257-270

[96] A. Bogaerts, Z. Chen: **Effect of laser parameters on laser ablation and laser-induced plasma formation: A numerical modeling investigation**; *Spectrochimica Acta, Part B: Atomic Spectroscopy*, 60 (2005), 1280-1307

[97] A. Bogaerts, Z. Chen, D. Bleiner: **Laser ablation of copper in different background gases: comparative study by numerical modeling and experiments**; *Journal of Analytical Atomic Spectrometry*, 21 (2006), 384-395

[98] R. Hergenröder: **A model for the generation of small particles in laser ablation ICP-MS**; *Journal of Analytical Atomic Spectrometry*, 21 (2006), 1016-1026

[99] R. Hergenröder: **A model of non-congruent laser ablation as a source of fractionation effects in LA-ICP-MS**; *Journal of Analytical Atomic Spectrometry*, 21 (2006), 505-516

[100] H. Lindner, D. Autrique, J. Pisonero, D. Günther, A. Bogaerts: **Numerical simulation analysis of flow patterns and particle transport in the HEAD laser ablation cell with respect to inductively coupled plasma spectrometry**; *Journal of Analytical Atomic Spectrometry*, 25 (2010), 295-304

[101] C. C. Garcia, H. Lindner, K. Niemax: **Laser ablation inductively coupled plasma mass spectrometry - Current shortcomings, practical suggestions for improving performance, and experiments to guide future development**; *Journal of Analytical Atomic Spectrometry*, 24 (2009), 14-26

[102] R. Hergenröder: **Laser-generated aerosols in laser ablation for inductively coupled plasma spectrometry**; *Spectrochimica Acta, Part B: Atomic Spectroscopy*, 61 (2006), 284-300

[103] R. Hergenröder: **Hydrodynamic sputtering as a possible source for fractionation in LA-ICP-MS**; *Journal of Analytical Atomic Spectrometry*, 21 (2006), 517-524

[104] J. Koch, A. von Bohlen, R. Hergenröder: **Particle size distributions and compositions of aerosols produced by near-IR femto- and nanosecond laser ablation of brass**; *Journal of Analytical Atomic Spectrometry*, 19 (2004), 267-272

[105] A. Bogaerts, Z. Chen, R. Gijbels, A. Vertes: **Laser ablation for analytical sampling: what can we learn from modeling?**; *Spectrochimica Acta, Part B: Atomic Spectroscopy*, 58 (2003), 1867-1893

[106] X. Mao, W.-T. Chan, M. Caetano, M. A. Shannon, R. E. Russo: **Preferential vaporization and plasma shielding during nano-second laser ablation**; *Applied Surface Science*, 96-98 (1996), 126-130

[107] X. Xu: **Phase explosion and its time lag in nanosecond laser ablation**; *Applied Surface Science*, 197-198 (2002), 61-66

[108] G. Callies, H. Schittenhelm, P. Berger, H. Hügel: **Modeling of the expansion of laser-evaporated matter in argon, helium and nitrogen and the condensation of clusters**; *Applied Surface Science*, 127-129 (1998), 134-141

[109] X. Mao, R. E. Russo: **Observation of plasma shielding by measuring transmitted and reflected laser pulse temporal profiles**; *Applied Physics A: Materials Science and Processing*, 64 (1997), 1-6

[110] X. Bai, Q. Ma, M. Perrier, V. Motto-Ros, D. Sabourdy, L. Nguyen, A. Jalocha, J. Yu: **Experimental study of laser-induced plasma: Influence of laser fluence and pulse duration**; *Spectrochimica Acta, Part B: Atomic Spectroscopy*, 87 (2013), 27-35

[111] J. M. Vadillo, J. M. Fernández Romero, C. Rodríguez, J. J. Laserna: **Effect of plasma shielding on laser ablation rate of pure metals at reduced pressure**; *Surface and Interface Analysis*, 27 (1999), 1009-1015

[112] R. E. Russo, X. L. Mao, S. S. Mao: **The physics of laser ablation in microchemical analysis**; *Analytical Chemistry*, 74 (2002), 70A-77A

[113] R. Fabbro, E. Fabre, F. Amiranoff, C. Garban-Labaune, J. Virmont, M. Weinfeld, C. E. Max: **Laser-wavelength dependence of mass-ablation rate and heat-flux inhibition in laser-produced plasmas**; *Physical Review A*, 26 (1982), 2289-2292

[114] X. L. Mao, O. V. Borisov, R. E. Russo: **Enhancements in laser ablation inductively coupled plasma-atomic emission spectrometry based on laser properties and ambient environment**; *Spectrochimica Acta, Part B: Atomic Spectroscopy*, 53 (1998), 731-739

[115] X. L. Mao, A. C. Ciocan, O. V. Borisov, R. E. Russo: **Laser ablation processes investigated using inductively coupled plasma-atomic emission spectroscopy (ICP-AES)**; *Applied Surface Science*, 127-129 (1998), 262-268

[116] M. Guillong, I. Horn, D. Günther: **A comparison of 266 nm, 213 nm and 193 nm produced from a single solid state Nd-YAG laser for laser ablation ICP-MS**; *Journal of Analytical Atomic Spectrometry*, 18 (2003), 1224-1230

[117] M. L. Alexander, M. R. Smith, J. S. Hartman, A. Mendoza, D. W. Koppenaal: **Laser ablation inductively coupled plasma mass spectrometry**; *Applied Surface Science*, 127-129 (1998), 255-261

[118] T. E. Jeffries, S. E. Jackson, H. P. Longerich: **Application of a frequency quintupled Nd-YAG source (λ = 213 nm) for laser ablation inductively coupled**

plasma mass spectrometric analysis of minerals; *Journal of Analytical Atomic Spectrometry*, 13 (1998), 935-940

[119] N. J. Saetveit, S. J. Bajic, D. P. Baldwin, R. S. Houk: **Influence of particle size on fractionation with nanosecond and femtosecond laser ablation in brass by online differential mobility analysis and inductively coupled plasma mass spectrometry**; *Journal of Analytical Atomic Spectrometry*, 23 (2008), 54-61

[120] P. M. Outridge, W. Doherty, D. C. Gregoire: **Ablative and transport fractionation of trace elements during laser sampling of glass and copper**; *Spectrochimica Acta, Part B: Atomic Spectroscopy*, 52 (1997), 2093-2102

[121] D. Von Der Linde, K. Sokolowski-Tinten, J. Bialkowski: **Laser-solid interaction in the femtosecond time regime**; *Applied Surface Science*, 109-110, 1-10

[122] M. Ligges, I. Rajkovic, P. Zhou, O. Posth, C. Hassel, G. Dumpich, D. Von Der Linde: **Observation of ultrafast lattice heating using time resolved electron diffraction**; *Applied Physics Letters*, 94 (2009), 101910

[123] B. Rethfeld, K. Sokolowski-Tinten, D. Von Der Linde, S. I. Anisimov: **Timescales in the response of materials to femtosecond laser excitation**; *Applied Physics A: Materials Science & Processing*, 79 (2004), 767-769

[124] B. N. Chichkov, C. Momma, S. Nolte, F. Von Alvensleben, A. Tünnermann: **Femtosecond, picosecond and nanosecond laser ablation of solids**; *Applied Physics A: Materials Science & Processing*, 63 (1996), 109-115

[125] **http://www.cmxr.com/Education/Introduction.html**; 21^{st} October 2013

[126] J. Koch, H. Lindner, A. Von Bohlen, R. Hergenröder, K. Niemax: **Elemental fractionation of dielectric aerosols produced by near-infrared femtosecond laser ablation of silicate glasses**; *Journal of Analytical Atomic Spectrometry*, 20 (2005), 901-906

[127] J. Pisonero, D. Fliegel, D. Günther: **High efficiency aerosol dispersion cell for laser ablation-ICP-MS**; *Journal of Analytical Atomic Spectrometry*, 21 (2006), 922-931

[128] H. R. Kuhn, D. Günther: **The agglomeration state of nanosecond laser-generated aerosol particles entering the ICP**; *Analytical and Bioanalytical Chemistry*, 383 (2005), 434-441

[129] D. Fliegel, D. Günther: **Low pressure laser ablation coupled to inductively coupled plasma mass spectrometry**; *Spectrochimica Acta, Part B: Atomic Spectroscopy*, 61 (2005), 841-849

[130] B. Wu, Y. C. Shin: **Modeling of nanosecond laser ablation with vapor plasma formation**; *Journal of Applied Physics*, 99 (2009), 84310

[131] D. Günther, C. A. Heinrich: **Enhanced sensitivity in laser ablation-ICP mass spectrometry using helium-argon mixtures as aerosol carrier**; *Journal of Analytical Atomic Spectrometry*, 14 (1999), 1363-1368

[132] H.-R. Kuhn, J. Koch, R. Hergenröder, K. Niemax, M. Kalberer, D. Günther: **Evaluation of different techniques for particle size distribution measurements on laser-generated aerosols**; *Journal of Analytical Atomic Spectrometry*, 20 (2005), 894-900

[133] I. Horn, M. Guillong, D. Günther: **Wavelength dependant ablation rates for metals and silicate glasses using homogenized laser beam profiles - implications for LA-ICP-MS**; *Applied Surface Science*, 182 (2001), 91-102

[134] S. Chandrasekhar: **Hydrodynamic and hydromagnetic stability**, *Clarendon Press*, Oxford (1961)

[135] R. S. Houk, R. K. Winge, X. Chen: **High speed photographic study of wet droplets and solid particles in the inductively coupled plasma**; *Journal of Analytical Atomic Spectrometry*, 12 (1997), 1139-1148

[136] Y. Huang, Y. Shibata, M. Monta: **Micro laser ablation-inductively coupled plasma mass spectrometry. 1. Instrumentation and performance of micro laser ablation system**; *Analytical Chemistry*, 65 (1993), 2999-3003

[137] C. C. Garcia, H. Lindner, K. Niemax: **Transport efficiency in femtosecond laser ablation inductively coupled plasma mass spectrometry applying ablation cells with short and long washout times**; *Spectrochimica Acta, Part B: Atomic Spectroscopy*, 62 (2007), 13-19

[138] C. C. Garcia, M. Wälle, H. Lindner, J. Koch, K. Niemax, D. Günther: **Femtosecond laser ablation inductively coupled plasma mass spectrometry: Transport efficiencies of aerosols released under argon atmosphere and the importance of the focus position**; *Spectrochimica Acta, Part B: Atomic Spectroscopy*, 63 (2008), 271-276

[139] D. R. Lide (Ed.): **CRC Handbook of Chemistry and Physics, Internet Version (http://www.hbcpnetbase.com)**, *CRC Press*, Florida (2005)

[140] P. A. Baron, K. Willeke (Eds): **Aerosol measurements: Principles, techniques and applications**, *John Wiley & Sons*, New York (2005)

[141] D. C. Perdian, S. J. Bajic, D. P. Baldwin, R. S. Houk: **Time-resolved studies of particle effects in laser ablation inductively coupled plasma-mass spectrometry. Part 1. Investigation of nanosecond and femtosecond pulse width lasers and devices for particle size selection**; *Journal of Analytical Atomic Spectrometry*, 23 (2008), 325-335

[142] J. Koch, M. Wälle R. Dietiker, D. Günther: **Analysis of laser-produced aerosols by inductively coupled plasma mass spectrometry: Transport phenomena and elemental fractionation**; *Analytical Chemistry*, 80 (2008), 915-921

[143] D. Bleiner, D. Günther: **Theoretical description and experimental observation of aerosol transport processes in laser ablation inductively coupled plasma mass spectrometry**; *Journal of Analytical Atomic Spectrometry*, 16 (2001), 449-456

[144] B. R. Schöne, Z. Zhang, D. Jacob, D. P. Gillikin, T. Tütken, D. Garbe-Schönberg, T. McConnaughey, A. Soldati: **Effect of organic matrices on the determination of the trace element chemistry (Mg, Sr, Mg/Ca, Sr/Ca) of aragonitic bivalve shells (*Arctica islandica*) - Comparison of ICP-OES and LA-ICP-MS data**; *Geochemical Journal*, 44 (2010), 23-37

[145] D. Hare, F. Burger, C. Austin, F. Fryer, R. Grimm, B. Reedy, R. A. Scolyer, J. F. Thompson, P. Doble: **Elemental bio-imaging of melanoma in lymph node biopsies**; *Analyst*, 134 (2009), 450-453

[146] M. V. Zoriy, M. Dehnhardt, A. Matusch, J. S. Becker: **Comparative imaging of P, S, Fe, Cu, Zn and C in thin sections of rat brain tumor as well as control tissues by laser ablation inductively coupled plasma mass spectrometry**; *Spectrochimica Acta, Part B: Atomic Spectroscopy*, 63 (2008), 375-382

[147] A. Kindness, C. N. Sekaran, J. Feldmann: **Two-Dimensional Mapping of Copper and Zinc in Liver Sections by Laser Ablation-Inductively Coupled Plasma Mass Spectrometry**; *Clinical Chemistry*, 49 (2003), 1916-1923

[148] M. Tibi, K. G. Heumann: **Isotope dilution mass spectrometry as a calibration method for the analysis of trace elements in powder samples by LA-ICP-MS**; *Journal of Analytical Atomic Spectrometry*, 18 (2003), 1076-1081

[149] C. Austin, F. Fryer, J. Lear, D. Bishop, D. Hare, T. Rawling, L. Kirkup, A. McDonagh, P. Doble: **Factors affecting internal standard selection for quantitative elemental bio-imaging of soft tissues by LA-ICP-MS**; *Journal of Analytical Atomic Spectrometry*, 26 (2011), 1494-1501

[150] C. Austin, D. Hare, T. Rawling, A. McDonagh, P.Doble: **Quantification method for elemental bio-imaging by LA-ICP-MS using metal spiked PMMA films**; *Journal of Analytical Atomic Spectrometry*, 25 (2010), 722-725

[151] H.-R. Kuhn, D. Günther: **A quantification strategy in laser ablation ICP-MS based on the transported aerosol particle volume determined by optical particle size measurement**; *Journal of Analytical Atomic Spectrometry*, 21 (2006), 1209-1213

[152] J. Feldmann, A. Kindness, P. Ek: **Laser ablation of soft tissue using a cryogenically cooled ablation cell**; *Journal of Analytical Atomic Spectrometry*, 17 (2002), 813-818

[153] B. Jackson, S. Harper, L. Smith, J. Flinn: **Elemental mapping and quantitative analysis of Cu, Zn, and Fe in rat brain sections by laser ablation ICP-MS**; *Analytical and Bioanalytical Chemistry*, 384 (2006), 951-957

[154] K. Ito, N. Hasebe, R. Sumita, S. Arai, M. Yamamoto, K. Kashiwaya, Y. Ganzawa: **LA-ICP-MS analysis of pressed powder pellets to luminescence geochronology**; *Chemical Geology*, 262 (2009), 131-137

[155] S. M. Eggins: **Laser ablation ICP-MS analysis of geological materials prepared as lithium borate glasses**; *Geostandards Newsletter*, 27 (2003), 147-162

[156] I. Rodushkin, M. D. Axelsson, D. Malinovsky, D. C. Baxter: **Analyte- and matrix-dependent elemental response variations in laser ablation inductively coupled plasma mass spectrometry Part 1. The roles of plasma and ion sampling conditions**; *Journal of Analytical Atomic Spectrometry*, 17 (2002), 1223-1230

[157] I. Rodushkin, M. D. Axelsson, D. Malinovsky, D. C. Baxter: **Analyte- and matrix-dependent elemental response variations in laser ablation inductively coupled plasma mass spectrometry Part 2. Implications for multi-element analyses**; *Journal of Analytical Atomic Spectrometry*, 17 (2002), 1231-1239

[158] C.-A. Craig, K. E. Jarvis, L. J. Clarke: **An assessment of calibration strategies for the quantitative and semiquantitative analysis of calcium carbonate matrices by laser ablation inductively coupled plasma-mass spectrometry (LA-ICP-MS)**; *Journal of Analytical Atomic Spectrometry*, 15 (2000), 1001-1008

[159] F. Poitrasson, X. Mao, S. S. Mao, R. Freydier, R. E. Russo: **Comparison of Ultraviolet Femtosecond and Nanosecond Laser Ablation Inductively Coupled Plasma Mass Spectrometry Analysis in Glass, Monazite, and Zircon**; *Analytical Chemistry*, 75 (2003), 6184-6190

[160] Q. Bian, C. C. Garcia, J. Koch, K. Niemax: **Non-matrix matched calibration of major and minor concentrations of Zn and Cu in brass, aluminium and silicate glass using NIR femtosecond laser ablation inductively coupled plasma mass spectrometry**; *Journal of Analytical Atomic Spectrometry*, 21 (2006), 187-191

[161] V. Možná, J. Pisonero, M. Holá, V. Kanický, D. Günther: **Quantitative analysis of Fe-based samples using ultraviolet nanosecond and femtosecond laser ablation-ICP-MS**; *Journal of Analytical Atomic Spectrometry*, 21 (2006), 1194-1201

[162] I. Horn, F. von Blanckenburg: **Investigation on elemental and isotopic fractionation during 196 nm femtosecond laser ablation multiple collector inductively coupled plasma mass spectrometry**; *Spectrochimica Acta, Part B: Atomic Spectroscopy*, 62 (2007), 410-422

[163] C. Pickhardt, J. S. Becker, H.-J. Dietze: **A new strategy of solution calibration in laser ablation inductively coupled plasma mass spectrometry for multi-element trace analysis of geological samples**; *Fresenius' Journal of Analytical Chemistry*, 368 (2000), 173-181

[164] J. S. Becker, C. Pickhardt, H.-J. Dietze: **Determination of trace elements in high-purity platinum by laser ablation inductively coupled plasma mass spectrometry using solution calibration**; *Journal of Analytical Atomic Spectrometry*, 16 (2001), 603-606

[165] J. S. Becker, M. V. Zoriy, C. Pickhardt, N. Palomero-Gallagher, K. Zilles: **Imaging of copper, zinc, and other elements in thin section of human brain samples (hippocampus) by laser ablation inductively coupled plasma mass spectrometry**; *Analytical Chemistry*, 77 (2005), 3208-3216

[166] D. Pozebon, V. L. Dressler, M. F. Mesko, A. Matusch, J. S. Becker: **Bioimaging of metals in thin mouse brain section by laser ablation inductively coupled plasma mass spectrometry: novel online quantification strategy using aqueous standards**; *Journal of Analytical Atomic Spectrometry*, 25 (2010), 1739-1744

[167] D. Günther, H. Cousin, B. Magyar, I. Leopold: **Calibration studies on dried aerosols for laser ablation-inductively coupled plasma mass spectrometry**; *Journal of Analytical Atomic Spectrometry*, 12 (1997), 165-170

[168] J. J. Leach, L. A. Allen, D. B. Aeschliman, R. S. Houk: **Calibration of laser ablation inductively coupled plasma mass spectrometry using standard additions with dried solution aerosols**; *Analytical Chemistry*, 71 (1999), 440-445

[169] C. O'Connor, B. L. Sharp, P. Evans: **On-line additions of aqueous standards for calibration of laser ablation inductively coupled plasma mass spectrometry: theory and comparison of wet and dry plasma conditions**; *Journal of Analytical Atomic Spectrometry*, 21 (2006), 556-565

[170] R. J. Watling: **In-line mass transport measurement cell for improving quantification in sulfide mineral analysis using laser ablation inductively coupled plasma mass spectrometry**; *Journal of Analytical Atomic Spectrometry*, 13 (1998), 927-934

[171] D. Günther, R. Frischknecht, H.-J. Müschenborn, C. A. Heinrich: **Direct liquid ablation: a new calibration strategy for laser ablation-ICP-MS microanalysis of solids and liquids**; *Fresenius' Journal of Analytical Chemistry*, 359 (1997), 390-393

[172] K. G. Heumann: **Isotope-dilution ICP-MS for trace element determination and speciation: from a reference method to a routine method?**; *Analytical and Bioanalytical Chemistry*, 378 (2004), 318-329

[173] J.I. García Alonso, P. Rodríguez-González: **Isotope Dilution Mass Spectrometry**, *The Royal Society of Chemistry*, Cambridge (2013)

[174] P. Rodríguez-González, J. M. Marchante-Gayón, J. I. Garcia Alonso, A. Sanz-Medel: **Isotope dilution analysis for elemental speciation: A tutorial review**; *Spectrochimica Acta, Part B: Atomic Spectroscopy*, 60 (2005), 151-207

[175] C. Pickhardt, A. V. Izmer, M. V. Zoriy, D. Schaumlöffel, J. S. Becker: **On-line isotope dilution in laser ablation inductively coupled plasma mass spectrometry using a microflow nebulizer inserted in the laser ablation chamber**; *International Journal of Mass Spectrometry*, 248 (2006), 136-141

[176] J. S. Becker, C. Pickhardt, W. Pompe: **Determination of Ag, Tl, and Pb in few milligrams of platinum nanoclusters by on-line isotope dilution in laser ablation inductively coupled plasma mass spectrometry**; *International Journal of Mass Spectrometry*, 237 (2004), 13-17

[177] S. F. Boulyga, K. G. Heumann: **Direct determination of platinum group elements and their distributions in geological and environmental samples at the ng g^{-1} level using LA-ICP-IDMS**; *Analytical and Bioanalytical Chemistry*, 383 (2005), 442-447

[178] S. F. Boulyga, K. G. Heumann: **Direct determination of halogens in powdered geological and environmental samples using isotope dilution laser ablation ICP-MS**; *International Journal of Mass Spectrometry*, 242 (2005), 291-296

[179] S. F. Boulyga, J. Heilmann, K. G. Heumann: **Isotope dilution ICP-MS with laser-assisted sample introduction for direct determination of sulfur in petroleum products**; *Analytical and Bioanalytical Chemistry*, 382 (2005), 1808-1814

[180] B. Fernández, F. Claverie, C. Pécheyran, O. F. X. Donard: **Solid-spiking isotope dilution laser ablation ICP-MS for the direct and simultaneous determination of trace elements in soils and sediments**; *Journal of Analytical Atomic Spectrometry*, 23 (2008), 367-377

[181] C. L. Deitrich, S. Braukmann, A. Raab, C. Munro, B. Pioselli, E. M. Krupp, J. E. Thomas-Oates, J. Feldmann: **Absolute quantification of superoxide dismutase (SOD) using species-specific isotope dilution analysis**; *Analytical and Bioanalytical Chemistry*, 397 (2010), 3515-3524

[182] H. Reinhardt, M. Kriews, H. Miller, C. Lüdke, E. Hoffmann, J. Skole: **Application of LA-ICP-MS in polar ice core studies**; *Analytical and Bioanalytical Chemistry*, 375 (2003), 1265-1275

[183] I. Rodushkin, M. D. Axelsson: **Application of double focusing sector field ICP-MS for multielemental characterization of human hair and nails. Part III. Direct analysis by laser ablation**; *Science of the Total Environment*, 305 (2003), 23-39

[184] M. P. Mateo, C. C. Garcia, R. Hergenröder: **Depth analysis of polymer-coated steel samples using near-infrared femtosecond laser ablation inductively coupled plasma mass spectrometry**; *Analytical Chemistry*, 79 (2007), 4908-4914

[185] J. Pisonero, J. Koch, M. Wälle, W. Hartung, N. D. Spencer, D. Günther: **Capabilities of femtosecond laser ablation inductively coupled plasma mass spectrometry for depth profiling of thin metal coatings**; *Analytical Chemistry*, 79 (2007), 2325-2333

[186] M. Siebold, P. Leidich, M. Bertini, G. Deflorio, J. Feldmann, E. M. Krupp, E. Halmschlager, S. Woodward: **Application of elemental bioimaging using laser ablation ICP-MS in forest pathology: distribution of elements in the bark of *Picea sitchensis* following wounding**; *Analytical and Bioanalytical Chemistry*, 402 (2012), 3323-3331

[187] F. A. Orellana, C. G. Gálvez, M. T. Roldán, C. García-Ruiz: **Applications of laser-ablation-inductively-coupled plasma-mass spectrometry in chemical analysis of forensic evidence**; *TrAC - Trends in Analytical Chemistry*, 42 (2013), 1-34

[188] D. Alamelu, A. K. Choudhary, S. K. Aggarwal: **Determination of impurities in thoria (ThO_2) using Laser Ablation Inductively Coupled Plasma Mass Spectrometry (LA-ICP-MS)**; *Journal of Nuclear Materials*, 406 (2010), 356-359

[189] G. Huelga-Suarez, B. Fernández, M. Moldovan, J. I. G. Alonso: **Detection of transgenerational barium dual-isotope marks in salmon otoliths by means of LA-ICP-MS**; *Analytical and Bioanalytical Chemistry*, 405 (2013), 2901-2909

[190] Y. Liu, Z. Hu, M. Li, S. Gao: **Applications of LA-ICP-MS in the elemental analyses of geological samples**; *Chinese Science Bulletin*, XX (2013), XX-XX

[191] D. Walaszek, M. Senn, M. Faller, L. Philippe, B. Wagner, E. Bulska, A. Ulrich: **Metallurgical and chemical characterization of copper alloy reference materials within laser ablation inductively coupled plasma mass spectrometry: Method development for minimally-invasive analysis of ancient bronze objects**; *Spectrochimica Acta, Part B: Atomic Spectroscopy*, 79-80 (2013), 17-30

[192] R. Lobinski, C. Moulin, R. Ortega: **Imaging and speciation of trace elements in biological environment**; *Biochimie*, 88 (2006), 1591-1604

[193] J. S. Becker: **Inorganic mass spectrometry: principles and applications**; *John Wiley & Sons*, Chichester (2007)

[194] G. Ballihaut, C. Pécheyran, S. Mounicou, H. Preud'homme, R. Grimaud, R. Lobinski: **Multimode detection (LA-ICP-MS, MALDI-MS and nanoHPLC-ESI-MS^2) in 1D and 2D gel electrophoresis for selenium-containing proteins**; *TrAC - Trends in Analytical Chemistry*, 26 (2007), 183-190

[195] J. S. Becker, R. Lobinski, J. S. Becker: **Metal imaging in non-denaturating 2D electrophoresis gels by laser ablation inductively coupled plasma mass spectrometry (LA-ICP-MS) for the detection of metalloproteins**; *Metallomics*, 1 (2009), 312-316

[196] R. Cornelis, J. A. Caruso, H. Crews, K. G. Heumann (Eds): **Handbook of elemental speciation**; *John Wiley & Sons*, Chichester (2003)

[197] J. S. Becker, M. Zoriy, J. S. Becker, C. Pickhardt, M. Przybylski: **Determination of phosphorus and metals in human brain proteins after isolation by gel electrophoresis by laser ablation inductively coupled plasma source mass spectrometry**; *Journal of Analytical Atomic Spectrometry*, 19 (2004), 149-152

[198] F. Claverie, C. Pécheyran, S. Mounicou, G. Ballihaut, B. Fernandez, J. Alexis, R. Lobinski, O. F. X. Donard: **Characterization of the aerosol produced by infrared femtosecond laser ablation of polyacrylamide gels for the sensitive ICP-MS detection of selenoproteins**; *Spectrochimica Acta, Part B: Atomic Spectroscopy*, 64 (2009), 649-658

[199] J. Bettmer, M. Montes Bayón, J. Ruiz Encinar, M. L. Fernández Sánchez, M. d. R. Fernández de la Campa, A. Sanz Medel: **The emerging role of ICP-MS in proteomic analysis**; *Journal of Proteomics*, 72 (2009), 989-1005

[200] C. C. Chéry, D. Günther, R. Cornelis, F. Vanhaecke, L. Moens: **Detection of metals in proteins by means of polyacrylamide gel electrophoresis and laser ablation-inductively coupled plasma-mass spectrometry: Application to selenium**; *Electrophoresis*, 24 (2003), 3305-3313

[201] T. W.-M. Fan, E. Pruszkowski, S. Shuttleworth: **Speciation of selenoproteins in Se-contaminated wildlife by gel electrophoresis and laser ablation-ICP-MS**; *Journal of Analytical Atomic Spectrometry*, 17 (2002), 1621-1623

[202] H. Chassaigne, C. C. Chéry, G. Bordin, F. Vanhaecke, A. R. Rodriguez: **2-Dimensional gel electrophoresis technique for yeast selenium-containing proteins - Sample preparation and MS approaches for processing 2-D gel protein spots**; *Journal of Analytical Atomic Spectrometry*, 19 (2004), 85-95

[203] L. Tastet, D. Schaumlöffel, R. Lobinski: **ICP-MS-assisted proteomics approach to the identification of selenium-containing proteins in selenium-rich yeast**; *Journal of Analytical Atomic Spectrometry*, 23 (2008), 309-317

[204] G. Ballihaut, L. Tastet, C. Pécheyran, B. Bouyssiere, O. Donard, R. Grimaud, R. Lobinski: **Biosynthesis, purification and analysis of selenomethionyl calmodulin by gel electrophoresis-laser ablation-ICP-MS and capillary HPLC-ICP-MS peptide mapping following in-gel tryptic digestion**; *Journal of Analytical Atomic Spectrometry*, 20 (2005), 493-499

[205] J. Bianga, G. Ballihaut, C. Pécheyran, Z. Touat, H. Preud'Homme, S. Mounicou, L. Chavatte, R. Lobinski, J. Szpunar: **Detection of selenoproteins in human cell extracts by laser ablation-ICP MS after separation by polyacrylamide gel electrophoresis and blotting**; *Journal of Analytical Atomic Spectrometry*, 27 (2012), 25-32

[206] C. C. Chéry, L. Moens, R. Cornelis, F. Vanhaecke: **Capabilities and limitations of gel electrophoresis for elemental speciation: A laboratory's experience**; *Pure and Applied Chemistry*, 78 (2006), 91-103

[207] Z. Pedrero, Y. Madrid, C. Cámara, E. Schram, J. B. Luten, I. Feldmann, L. Waentig, H. Hayen, N. Jakubowski: **Screening of selenium containing proteins in the Tris-buffer soluble fraction of African catfish (*Clarias gariepinus*) fillets by laser ablation-ICP-MS after SDS-PAGE and electroblotting onto membranes**; *Journal of Analytical Atomic Spectrometry*, 24 (2009), 775-784

[208] G. Ballihaut, L. E. Kilpatrick, E. L. Kilpatrick, W. C. Davis: **Detection and characterization of selenoproteins by tandem mass spectrometry assisted by laser ablation inductively coupled plasma mass spectrometry: application to human plasma selenoproteins**; *Journal of Analytical Atomic Spectrometry*, 26 (2011), 383-394

[209] P. Marshall, O. Heudi, S. Bains, H. N. Freeman, F. Abou-Shakra, K. Reardon: **The determination of protein phosphorylation on electrophoresis gel blots by laser ablation inductively coupled plasma-mass spectrometry**; *Analyst*, 127 (2002), 459-461

[210] J. S. Becker, S. F. Boulyga, J. S. Becker, C. Pickhardt, E. Damoc, M. Przybylski: **Structural identification and quantification of protein phosphorylations after GE separation using Fourier transform ion cyclotron resonance mass spectrometry and LA-ICP-MS**; *International Journal of Mass Spectrometry*, 228 (2003), 985-997

[211] R. Krüger, D. Kübler, R. Pallissé, A. Burkovski, W. D. Lehmann: **Protein and Proteome Phosphorylation Stoichiometry Analysis by Element Mass Spectrometry**; *Analytical Chemistry*, 78 (2006), 1987-1994

[212] M. Wind, I. Feldmann, N. Jakubowski, W. D. Lehmann: **Spotting and quantification of phosphoproteins purified by gel electrophoresis and laser ablation-element mass spectrometry with phosphorus-31 detection**; *Electrophoresis*, 24 (2003), 1276-1280

[213] A. Venkatachalam, C. U. Koehler, I. Feldmann, P. Lampen, A. Manz, P. H. Roos, N. Jakubowski: **Detection of phosphorylated proteins blotted onto membranes using laser ablation inductively coupled plasma mass spectrometry**; *Journal of Analytical Atomic Spectrometry*, 22 (2007), 1023-1032

[214] A. Polatajko, M. Azzolini, I. Feldmann, T. Stuezel, N. Jakubowski: **Laser ablation-ICP-MS assay development for detecting Cd- and Zn-binding proteins in Cd-exposed *Spinacia oleracea* L.**; *Journal of Analytical Atomic Spectrometry*, 22 (2007), 878-887

[215] M. Garijo Añorbe, J. Messerschmidt, I. Feldmann, N. Jakubowski: **On-line coupling of gel electrophoresis (GE) and inductively coupled plasma-mass spectrometry (ICP-MS) for the detection of Fe in metalloproteins**; *Journal of Analytical Atomic Spectrometry*, 22 (2007), 917-924

[216] J. S. Becker, M. Zoriy, M. Przybylski, J. S. Becker: **Study of formation of Cu- and Zn-containing tau protein using isotopically-enriched tracers by LA-ICP-MS and MALDI-FTICR-MS**; *Journal of Analytical Atomic Spectrometry*, 22 (2007), 63-68

[217] J. S. Becker, S. Mounicou, M. V. Zoriy, J. S. Becker, R. Lobinski: **Analysis of metal-binding proteins separated by non-denaturating gel electrophoresis using matrix-assisted laser desorption/ionization mass spectrometry (MALDI-MS) and laser ablation inductively coupled plasma mass spectrometry (LA-ICP-MS)**; *Talanta*, 76 (2008), 1183-1188

[218] J. S. Becker, D. Pozebon, V. L. Dressler, R. Lobinski, J. S. Becker: **LA-ICP-MS studies of zinc exchange by copper in bovine serum albumin using an isotopic enriched copper tracer**; *Journal of Analytical Atomic Spectrometry*, 23 (2008), 1076-1082

[219] C. S. Allardyce, P. J. Dyson, F. R. Abou-Shakra, H. Birtwistle, J. Coffey: **Inductively coupled plasma mass spectrometry to identify protein drug targets from whole cell systems**; *Chemical Communications*, 24 (2001), 2708-2709

[220] J. S. Becker, M. Zoriy, U. Krause-Buchholz, J. S. Becker, C. Pickhardt, M. Przybylski, W. Pompe, G. Rödel: **In-gel screening of phosphorus, copper, zinc and iron in proteins of yeast mitochondria by LA-ICP-MS and identification of phosphorylated protein structures by MALDI-FT-ICR-MS after separation with two-dimensional gel electrophoresis**; *Journal of Analytical Atomic Spectrometry*, 19 (2004), 1236-1243

[221] A. Sussulini, H. Kratzin, O. Jahn, C. E. M. Banzato, M. A. Z. Arruda, J. S. Becker: **Metallomics studies of human blood serum from treated bipolar disorder patients**; *Analytical Chemistry*, 82 (2010), 5859-5864

[222] J. S. Becker, M. Zoriy, J. S. Becker, C. Pickhardt, E. Damoc, G. Juhacz, M. Palkovits, M. Przybylski: **Determination of Phosphorus-, Copper-, and Zinc-Containing Human Brain Proteins by LA-ICPMS and MALDI-FTICR-MS**; *Analytical Chemistry*, 77 (2005), 5851-5860

[223] J. S. Becker, M. Zoriy, M. Przybylski, J. S. Becker: **High resolution mass spectrometric brain proteomics by MALDI-FTICR-MS combined with determination of P, S, Cu, Zn and Fe by LA-ICP-MS**; *International Journal of Mass Spectrometry*, 261 (2007), 68-73

[224] J. S. Becker, M. Zoriy, C. Pickhardt, M. Przybylski, J. S. Becker: **Investigation of Cu-, Zn- and Fe-containing human brain proteins using isotopic-enriched tracers by LA-ICP-MS and MALDI-FT-ICR-MS**; *International Journal of Mass Spectrometry*, 242 (2005), 135-144

[225] B. Wu, I. Susnea, Y. Chen, M. Przybylski, J. S. Becker: **Study of metal-containing proteins in the roots of *Elsholtzia splendens* using LA-ICP-MS and LC-tandem mass spectrometry**; *International Journal of Mass Spectrometry*, 307 (2011), 85-91

[226] D. J. Kutscher, M. B. Fricker, B. Hattendorf, J. Bettmer, D. Günther: **Systematic studies on the determination of Hg-labelled proteins using laser ablation-ICPMS and isotope dilution analysis**; *Analytical and Bioanalytical Chemistry*, 401 (2011), 2691-2698

[227] L. Waentig, P. H. Roos, N. Jakubowski: **Labelling of antibodies and detection by laser ablation inductively coupled plasma mass spectrometry. PART III. Optimization of antibody labelling for application in a Western blot procedure**; *Journal of Analytical Atomic Spectrometry*, 24 (2009), 924-933

[228] P. H. Roos, A. Venkatachalam, A. Manz, L. Waentig, C. U. Koehler, N. Jakubowski: **Detection of electrophoretically separated cytochromes P450 by element-labelled monoclonal antibodies via laser ablation inductively coupled plasma mass spectrometry**; *Analytical and Bioanalytical Chemistry*, 392 (2008), 1135-1147

[229] L. Waentig, N. Jakubowski, P. H. Roos: **Multi-parametric analysis of cytochrome P450 expression in rat liver microsomes by LA-ICP-MS**; *Journal of Analytical Atomic Spectrometry*, 26 (2011), 310-319

[230] N. Jakubowski, J. Messerschmidt, M. G. Añorbe, L. Waentig, H. Hayen, P. H. Roos: **Labelling of proteins by use of iodination and detection by ICP-MS**; *Journal of Analytical Atomic Spectrometry*, 23 (2008), 1487-1496

[231] L. Waentig, N. Jakubowski, H. Hayen, P. H. Roos: **Iodination of proteins, proteomes and antibodies with potassium triodide for LA-ICP-MS based proteomic analyses**; *Journal of Analytical Atomic Spectrometry*, 26 (2011), 1610-1618

[232] N. Jakubowski, L. Waentig, H. Hayen, A. Venkatachalam, A. Von Bohlen, P. H. Roos, A. Manz: **Labelling of proteins with 2-(4-isothiocyanatobenzyl)-1,4,7,10-tetraazacyclododecane-1,4,7,10-tetraacetic acid and lanthanides and detection by ICP-MS**; *Journal of Analytical Atomic Spectrometry*, 23 (2008), 1497-1507

[233] V. J. Nesatyy, N. W. Ross: **Recovery of intact proteins from silver stained gels**; *Analyst*, 127 (2002), 1180-1187

[234] I. Lopez-Heras, M. Palomo, Y. Madrid: **Selenoproteins: the key factor in selenium essentiality. State of the art analytical techniques for selenoprotein studies**; *Analytical and Bioanalytical Chemistry*, 400 (2011), 1717-1727

[235] R. Ma, C. W. McLeod, K. Tomlinson, R. K. Poole: **Speciation of protein-bound trace elements by gel electrophoresis and atomic spectrometry**; *Electrophoresis*, 25 (2004), 2469-2477

[236] J. Bettmer, N. Jakubowski, A. Prange: **Elemental tagging in inorganic mass spectrometric bioanalysis**; *Analytical and Bioanalytical Chemistry*, 386 (2006), 7-11

[237] A. Tholey, D. Schaumlöffel: **Metal labeling for quantitative protein and proteome analysis using inductively-coupled plasma mass spectrometry**; *TrAC - Trends in Analytical Chemistry*, 2 (2006), 399-408

[238] C. Zhang, F. Wu, Y. Zhang, X. Wang, X. Zhang: **A novel combination of immunoreaction and ICP-MS as a hyphenated technique for the determination of thyroid-stimulating hormone (TSH) in human serum**; *Journal of Analytical Atomic Spectrometry*, 16 (2001), 1393-1396

[239] Z. A. Quinn, V. I. Baranov, S. D. Tanner, J. L. Wrana: **Simultaneous determination of proteins using an element-tagged immunoassay coupled with ICP-MS detection**; *Journal of Analytical Atomic Spectrometry*, 17 (2002), 892-896

[240] A. Sanz-Medel: **ICP-MS for multiplex absolute determinations of proteins**; *Analytical and Bioanalytical Chemistry*, 398 (2010), 1853-1859

[241] S. Hu, S. Zhang, Z. Hu, Z. Xing, X. Zhang: **Detection of Multiple Proteins on One Spot by Laser Ablation Inductively Coupled Plasma Mass Spectrometry and Application to Immuno-Microarray with Element-Tagged Antibodies**; *Analytical Chemistry*, 79 (2007), 923-929

[242] J. S. Becker, M. Zoriy, V. L. Dressler, B. Wu, J. S. Becker: **Imaging of metals and metal-containing species in biological tissues and on gels by LA-ICP-MS: A new analytical strategy for applications in life sciences**; *Pure and Applied Chemistry*, 80 (2008), 2643-2655

[243] J. S. Becker, M. Zoriy, A. Matusch, B. Wu, D. Salber, C. Palm, J. S. Becker: **Bioimaging of metals by laser ablation inductively coupled plasma mass spectrometry (LA-ICP-MS)**; *Mass Spectrometry Reviews*, 29 (2010), 156-175

[244] M. Zoriy, A. Matusch, T. Spruss, J. S. Becker: **Laser ablation inductively coupled plasma mass spectrometry for imaging of copper, zinc, and platinum in thin sections of a kidney from a mouse treated with cis-platin**; *International Journal of Mass Spectrometry*, 260 (2007), 102-106

[245] J. S. Becker, U. Breuer, H.-F. Hsieh, I. Osterholt, U. Kumtabtim, B. Wu, A. Matusch, J. A. Caruso, Z. Qin: **Bioimaging of metals and biomolecules in mouse heart by laser ablation inductively coupled plasma mass spectrometry and secondary ion mass spectrometry**; *Analytical Chemistry*, 82 (2010), 9528-9533

[246] D. Hare, S. Tolmachev, A. James, D. Bishop, C. Austin, F. Fryer, P. Doble: **Elemental bio-imaging of thorium, uranium, and plutonium in tissues from occupationally exposed former nuclear workers**; *Analytical Chemistry*, 82 (2010), 3176-3182

[247] A. G. Sarafanov, T. I. Todorov, A. Kajdacsy-Balla, M. A. Gray, V. Macias, J. A. Centeno: **Analysis of iron, zinc, selenium and cadmium in paraffin-embedded prostate tissue specimens using inductively coupled plasma mass-spectrometry**; *Journal of Trace Elements in Medicine and Biology*, 22 (2008), 305-314

[248] C. Giesen, L. Waentig, T. Mairinger, D. Drescher, J. Kneipp, P. H. Roos, U. Panne, N. Jakubowski: **Iodine as an elemental marker for imaging of single cells and tissue sections by laser ablation inductively coupled plasma mass spectrometry**; *Journal of Analytical Atomic Spectrometry*, 26 (2011), 2160-2165

[249] R. W. Hutchinson, A. G. Cox, C. W. McLeod, P. S. Marshall, A. Harper, E. L. Dawson, D. R. Howlett: **Imaging and spatial distribution of β-amyloid peptide and metal ions in Alzheimer's plaques by laser ablation-inductively coupled plasma-mass spectrometry**; *Analytical Biochemistry*, 346 (2005), 225-233

[250] D. Hare, B. Reedy, R. Grimm, S. Wilkins, I. Volitakis, J. L. George, R. A. Cherny, A. I. Bush, D. I. Finkelstein, P. Doble: **Quantitative elemental bio-imaging of Mn, Fe, Cu and Zn in 6-hydroxydopamine induced Parkinsonism mouse models**; *Metallomics*, 1 (2009), 53-58

[251] D. J. Hare, J. L. George, R. Grimm, S. Wilkins, P. A. Adlard, R. A. Cherny, A. I. Bush, D. I. Finkelstein, P. Doble: **Three-dimensional elemental bio-imaging of Fe, Zn, Cu, Mn and P in a 6-hydroxydopamine lesioned mouse brain**; *Metallomics*, 2 (2010), 745-753

[252] M. V. Zoriy, M. Dehnhardt, G. Reifenberger, K. Zilles, J. S. Becker: **Imaging of Cu, Zn, Pb and U in human brain tumor resections by laser ablation inductively coupled plasma mass spectrometry**; *International Journal of Mass Spectrometry*, 257 (2006), 27-33

[253] J. Dobrowolska, M. Dehnhardt, A. Matusch, M. Zoriy, N. Palomero-Gallagher, P. Koscielniak, K. Zilles, J. S. Becker: **Quantitative imaging of zinc, copper and lead in three distinct regions of the human brain by laser ablation inductively coupled plasma mass spectrometry**; *Talanta*, 74 (2008), 717-723

[254] A. Matusch, C. Depboylu, C. Palm, B. Wu, G. U. Höglinger, M. K.-H. Schäfer, J. S. Becker: **Cerebral Bioimaging of Cu, Fe, Zn, and Mn in the MPTP Mouse Model of Parkinson's Disease Using Laser Ablation Inductively Coupled Plasma Mass Spectrometry (LA-ICP-MS)**; *Journal of the American Society for Mass Spectrometry*, 21 (2010), 161-171

[255] A. Matusch, A. Bauer, J. S. Becker: **Element imaging in formalin fixed slices of human mesencephalon**; *International Journal of Mass Spectrometry*, 307 (2011), 240-244

[256] J. S. Becker: **Bioimaging of metals in brain tissue from micrometre to nanometre scale by laser ablation inductively coupled plasma mass spectrometry: State of the art and perspectives**; *International Journal of Mass Spectrometry*, 289 (2010), 65-75

[257] J. S. Becker, D. Salber: **New mass spectrometric tools in brain research**; *TrAC - Trends in Analytical Chemistry*, 29 (2010), 966-979

[258] J. S. Becker, A. Matusch, J. S. Becker, B. Wu, C. Palm, A. J. Becker, D. Salber: **Mass spectrometric imaging (MSI) of metals using advanced BrainMet techniques for biomedical research**; *International Journal of Mass Spectrometry*, 307 (2011), 3-15

[259] U. Narewski, G. Werner, H. Schulz, C. Vogt: **Application of laser ablation inductively coupled mass spectrometry (LA-ICP-MS) for the determination of major, minor, and trace elements in bark samples**; *Fresenius' Journal of Analytical Chemistry*, 366 (2000), 167-170

[260] M. B. B. Guerra, D. Amarasiriwardena, C. E. G. R. Schaefer, C. D. Pereira, A. A. Spielmann, J. A. Nóbrega, E. R. Pereira-Filho: **Biomonitoring of lead in Antarctic lichens using laser ablation inductively coupled plasma mass spectrometry**; *Journal of Analytical Atomic Spectrometry*, 26 (2011), 2238-2246

[261] L. A. Runnalls, M. L. Coleman: **Record of natural and anthropogenic changes in reef environments (Barbados West Indies) using laser ablation ICP-MS and sclerochronology on coral cores**; *Coral Reefs*, 22 (2003), 416-426

[262] T. Wyndham, M. McCulloch, S. Fallon, C. Alibert: **High-resolution coral records of rare earth elements in coastal seawater: Biogeochemical cycling and a new environmental proxy**; *Geochimica et Cosmochimica Acta*, 68 (2004), 2067-2080

[263] R. K. Takesue, A. van Geen: **Mg/Ca, Sr/Ca, and stable isotopes in modern and Holocene *Protothaca staminea* shells from a northern California coastal upwelling region**; *Geochimica et Cosmochimica Acta*, 68 (2004), 3845-3861

[264] M. D. Seltzer, K. H. Berry: **Laser ablation ICP-MS profiling and semiquantitative determination of trace element concentrations in desert tortoise shells: documenting the uptake of elemental toxicants**; *Science of the Total Environment*, 339 (2005), 253-265

[265] P. A. Hamer, G. P. Jenkins, B. M. Gillanders: **Otolith chemistry of juvenile snapper *Pagrus auratus* in Victorian waters: natural chemical tags and their temporal variation**; *Marine Ecology - Progress Series*, 263 (2003), 261-273

[266] D. Brophy, T. E. Jeffries, B. S. Danilowicz: **Elevated manganese concentrations at the cores of clupeid otoliths: possible environmental, physiological, or structural origins**; *Marine Biology*, 144 (2004), 779-786

[267] H. Tabouret, G. Bareille, F. Claverie, C. Pécheyran, P. Prouzet, O. F. X. Donard: **Simultaneous use of strontium:calcium and barium:calcium ratios in otoliths**

as markers of habitat: Application to the European eel (*Anguilla anguilla*) in the Adour basin, South West France; *Marine Envirnmental Research*, 70 (2010), 35-45

[268] M. Holá, J. Kalvoda, H. Nováková, R. Škoda, V. Kanický: **Possibilities of LA-ICP-MS technique for the spatial elemental analysis of the recent fish scales: Line scan *vs.* depth profiling**; *Applied Surface Science*, 257 (2011), 1932-1940

[269] K. H. Ek, G. M. Morrison, P. Lindberg, S. Rauch: **Comparative tissue distribution of metals in birds in Sweden using ICP-MS and laser ablation ICP-MS**; *Archives of Environmental Contamination and Toxicology*, 47 (2004), 259-269

[270] G. Caumette, S. Ouypornkochagorn, C. M. Scrimgeour, A. Raab, J. Feldmann: **Monitoring the arsenic and iodine exposure of seaweed-eating North Ronaldsay sheep from the gestational and suckling periods to adulthood by using horns as a dietary archive**; *Environmental Science and Technology*, 41 (2007), 2673-2679

[271] S. Hann, C. Latkoczy, T. L. Bereuter, T. Prohaska, G. Stingeder, C. Reiter: **Reconstruction of a case of thallium poisoning using LA-ICP-SFMS**; *International Journal of Legal Medicine*, 119 (2005), 35-39

[272] M. Legrand, R. Lam, M. Jensen-Fontaine, E. D. Salin, H. M. Chan: **Direct detection of mercury in single human hair strands by laser ablation inductively coupled plasma mass spectrometry (LA-ICP-MS)**; *Journal of Analytical Atomic Spectrometry*, 19 (2004), 1287-1288

[273] C. Stadlbauer, T. Prohaska, C. Reiter, A. Knaus, G. Stingeder: **Time-resolved monitoring of heavy-metal intoxication in single hair by laser ablation ICP-DRCMS**; *Analytical and Bioanalytical Chemistry*, 383 (2005), 500-508

[274] T. Prohaska, C. Latkoczy, G. Schultheis, M. Teschler-Nicola, G. Stingeder: **Investigation of Sr isotope ratios in prehistoric human bones and teeth using laser ablation ICP-MS and ICP-MS after Rb/Sr separation**; *Journal of Analytical Atomic Spectrometry*, 17 (2002), 887-891

[275] E. Elish, Z. Karpas, A. Lorber: **Determination of uranium concentration in a single hair strand by LAICPMS applying continuous and single pulse ablation**; *Journal of Analytical Atomic Spectrometry*, 22 (2007), 540-546

[276] M. Legrand, R. Lam, C. J. S. Passos, D. Mergler, E. D. Salin, H. M. Chan: **Analysis of mercury in sequential micrometer segments of single hair strands of fish-eaters**; *Environmental Science and Technology*, 41 (2007), 593-598

[277] L. Bartkus, D. Amarasiriwardena, B. Arriaza, D. Bellis, J. Yañez: **Exploring lead exposure in ancient Chilean mummies using a single strand of hair by laser ablation-inductively coupled plasma-mass spectrometry (LA-ICP-MS)**; *Microchemical Journal*, 98 (2011), 267-274

[278] U. Kumtabtim, A. Matusch, S. U. Dani, A. Siripinyanond, J. S. Becker: **Biomonitoring for arsenic, toxic and essential metals in single hair strands by laser ablation inductively coupled plasma mass spectrometry**; *International Journal of Mass Spectrometry*, 307 (2011), 185-191

[279] S. Steely, D. Amarasiriwardena, J. Jones, J. Yañez: **A rapid approach for assessment of arsenic exposure by elemental analysis of single strand of hair using laser ablation-inductively coupled plasma-mass spectrometry**; *Microchemical Journal*, 86 (2007), 235-240

[280] H. Sela, Z. Karpas, M. Zoriy, C. Pickhardt, J. S. Becker: **Biomonitoring of hair samples by laser ablation inductively coupled plasma mass spectrometry (LA-ICP-MS)**; *International Journal of Mass Spectrometry*, 261 (2007), 199-207

[281] R. Bol, J. Marsh, T. H. E. Heaton: **Multiple stable isotope (^{18}O, ^{13}C, ^{15}N and ^{34}S) analysis of human hair to identify the recent migrants in a rural community in SW England**; *Rapid Communications in Mass Spectrometry*, 21 (2007), 2951-2954

[282] R. Santamaria-Fernandez, J. Giner Martínez-Sierra, J. M. Marchante-Gayón, J. I. García-Alonso, R. Hearn: **Measurement of longitudinal sulfur isotopic variations by laser ablation MC-ICP-MS in single human hair strands**; *Analytical and Bioanalytical Chemistry*, 394 (2009), 225-233

[283] D. Pozebon, V. L. Dressler, A. Matusch, J. S. Becker: **Monitoring of platinum in a single hair by laser ablation inductively coupled plasma mass spectrometry (LA-ICP-MS) after cisplatin treatment for cancer**; *International Journal of Mass Spectrometry*, 272 (2008), 57-62

[284] M. Duval, M. Aubert, J. Hellstrom, R. Grün: **High resolution LA-ICP-MS mapping of U and Th isotopes in an early Pleistocene equid tooth from Fuente Nueva-3 (Orce, Andalusia, Spain)**; *Quaternary Geochronology*, 6 (2011), 458-467

[285] M. Arora, D. Hare, C. Austin, D. R. Smith, P. Doble: **Spatial distribution of manganese in enamel and coronal dentine of human primary teeth**; *Science of the Total Environment*, 409 (2011), 1315-1319

[286] E. A. Hinz, M. J. Kohn: **The effect of tissue structure and soil chemistry on trace element uptake in fossils**; *Geochimica et Cosmochimica Acta*, 74 (2010), 3213-3231

[287] D. Hare, C. Austin, P. Doble, M. Arora: **Elemental bio-imaging of trace elements in teeth using laser ablation-inductively coupled plasma-mass spectrometry**; *Journal of Dentistry*, 39 (2011), 397-403

[288] M. Galiová, J. Kaiser, F. J. Fortes, K. Novotný, R. Malina, L. Prokeš, A. Hrdlička, T. Vaculovič, M. N. Fišáková, J. Svoboda, V. Kanický, J. J. Laserna: **Multielemental analysis of prehistoric animal teeth by laser-induced breakdown spectroscopy and laser ablation inductively coupled plasma mass spectrometry**; *Applied Optics*, 49 (2010), C191-C199

[289] S. R. Copeland, M. Sponheimer, J. A. Lee-Thorp, P. J. le Roux, D. J. de Ruiter, M. P. Richards: **Strontium isotope ratios in fossil teeth from South Africa: Assessing laser ablation MC-ICP-MS analysis and the extent of diagenesis**; *Journal of Archaeological Science*, 37 (2010), 1437-1446

[290] F. G. T. Radloff, L. Mucina, W. J. Bond, P. J. le Roux: **Strontium isotope analyses of large herbivore habitat use in the Cape Fynbos region of South Africa**; *Oecologia*, 164 (2010), 567-578

[291] J. Seuma, J. Bunch, A. Cox, C. McLeod, C. Murray: **Combination of immunohistochemistry and laser ablation ICP mass spectrometry for imaging of cancer biomarkers**; *Proteomics*, 8 (2008), 3775-3784

[292] N. Kamaly, J. A. Pugh, T. L. Kalber, J. Bunch, A. D. Miller, C. W. McLeod, J. D. Bell: **Imaging of gadolinium spatial distribution in tumor tissue by laser ablation inductively coupled plasma mass spectrometry**; *Molecular imaging and biology : MIB : the official publication of the Academy of Molecular Imaging*, 12 (2010), 361-366

[293] J. Lear, D. Hare, P. Adlard, D. Finkelstein, P. Doble: **Improving acquisition times of elemental bio-imaging for quadrupole-based LA-ICP-MS**; *Journal of Analytical Atomic Spectrometry*, 27 (2012), 159-164

[294] D. S. Gholap, A. Izmer, B. De Samber, J. T. van Elteren, V. S. Šelih, R. Evens, K. De Schamphelaere, C. Janssen, L. Balcaen, I. Lindemann, L. Vincze, F. Vanhaecke: **Comparison of laser ablation-inductively coupled plasma-mass spectrometry and micro-X-ray fluorescence spectrometry for elemental imaging in Daphnia magna**; *Analytica Chimica Acta*, 664 (2010), 19-26

[295] H. A. O. Wang, D. Grolimund, L. R. Van Loon, K. Barmettler, C. N. Borca, B. Aeschlimann, D. Günther: **Quantitative chemical imaging of element diffusion into heterogeneous media using LA-ICP-MS, synchrotron microXRF and EXAFS spectroscopy**; *Analytical Chemistry*, 83 (2011), 6259-6266

[296] W. H. Zachariasen: **The atomic arrangement in glass**; *Journal of the American Chemical Society*, 54 (1932), 3841-3851

[297] **http://www.cebrace.com.br/v2**; 3^{rd} September 2013

[298] S. L. Blachford (Ed.): **Automobile Windshield. How Products are Made**; *Gale Cengage*, www.enotes.com (2002); 3^{rd} September 2013

[299] J. Li, Z. L. Wang, T. C. Hufnagel: **Characterization of nanometer-scale defects in metallic glasses by quantitative high-resolution transmission electron microscopy**; *Physical Review B - Condensed Matter and Materials Physics*, 65 (2002), 144201

[300] R. Falcone, P. Galinetto, B. Messiga, E. Negri, M. P. Riccardi, G. Sommariva, M. Verità: **Combined SEM-EDX and μ-Raman spectroscopy for the characterisation of glass/Al-rich refractory interfaces**; *Microchimica Acta*, 161 (2008), 381-386

[301] L. M. Neufeld: **Application of Laser Ablation ICP-MS to the Analysis of Forensic Glass Samples**; *Spectroscopy*, 20 (2005), 31-36

[302] T. Trejos, J. R. Almirall: **Sampling strategies for the analysis of glass fragments by LA-ICP-MS: Part I. Micro-homogeneity study of glass and its application to the interpretation of forensic evidence**; *Talanta*, 67 (2005), 388-395

[303] F. Claverie, B. Fernández, C. Pécheyran, J. Alexis, O. F. X. Donard: **Elemental fractionation effects in high repetition rate IR femtosecond laser ablation ICP-MS analysis of glasses**; *Journal of Analytical Atomic Spectrometry*, 24 (2009), 891-902

[304] M. Humayun, F. A. Davis, M. M. Hirschmann: **Major element analysis of natural silicates by laser ablation ICP-MS**; *Journal of Analytical Atomic Spectrometry*, 25 (2010), 998-1005

[305] M. Wälle, J. Koch, D. Tabersky, K. Hametner, N. D. Zhigadlo, S. Katrych, J. Karpinski, D. Günther: **Analyses of lithium-doped and pure magnesium diboride using ultraviolet nano- and femtosecond laser ablation inductively coupled**

plasma mass spectrometry; *Journal of Analytical Atomic Spectrometry*, 25 (2010), 193-195

[306] A. J. G. Mank, P. R. D. Mason: **A critical assessment of laser ablation ICP-MS as an analytical tool for depth analysis in silica-based glass samples**; *Journal of Analytical Atomic Spectrometry*, 14 (1999), 1143-1153

[307] P. R. D. Mason, A. J. G. Mank: **Depth-resolved analysis in multi-layered glass and metal materials using laser ablation inductively coupled plasma mass spectrometry (LA-ICP-MS)**; *Journal of Analytical Atomic Spectrometry*, 16 (2001), 1381-1388

[308] K. Bange, H. Müller, C. Strubel: **Characterization of defects in glasses and coatings on glasses by microanalytical techniques**; *Microchimica Acta*, 132 (2000), 493-503

[309] H. Müller, C. Strubel, K. Bange: **Characterization and identification of local defects in glass**; *Scanning*, 23 (2001), 14-23

[310] T. W. May, R. H. Wiedmeyer: **A table of polyatomic interferences in ICP-MS**; *Atomic Spectroscopy*, 19 (1998), 150-155

[311] W. Kaim, B. Schwederski: **Bioanorganische Chemie**, *Teubner-Verlag*, Stuttgart (1995)

[312] S. Mounicou, J. Szpunar, R. Lobinski: **Metallomics: the concept and methodology**; *Chemical Society Reviews*, 38 (2009), 1119-1138

[313] J. Szpunar: **Advances in analytical methodology for bioinorganic speciation analysis: metallomics, metalloproteomics and heteroatom-tagged proteomics and metabolomics**; *Analyst*, 130 (2005), 442-465

[314] J. Szpunar: **Metallomics: a new frontier in analytical chemistry**; *Analytical and Bioanalytical Chemistry*, 378 (2004), 54-56

[315] D. M. Templeton, F. Ariese, R. Cornelis, L.-G. Danielsson, H. Muntau, H. P. Van Leeuwen, R. Łobiński: **Guidelines for terms related to chemical speciation and fractionation of elements. Definitions, structural aspects, and methodological approaches**; *Pure and Applied Chemistry*, 72 (2000), 1453-1470

[316] J. Szpunar: **Bio-inorganic speciation analysis by hyphenated techniques**; *Analyst*, 125 (2000), 963-988

[317] M. Montes-Bayón, K. DeNicola, J. A. Caruso: **Liquid chromatography-inductively coupled plasma mass spectrometry**; *Journal of Chromatography A*, 1000 (2003), 457-476

[318] S. S. Kannamkumarath, K. Wrobel, K. Wrobel, C. B'Hymer, J. A. Caruso: **Capillary electrophoresis-inductively coupled plasma-mass spectrometry: An attractive complementary technique for elemental speciation analysis**; *Journal of Chromatography A*, 975 (2002), 245-266

[319] R. Haselberg, G. J. de Jong, G. W. Somsen: **Capillary electrophoresis-mass spectrometry for the analysis of intact proteins**; *Journal of Chromatography A*, 1159 (2007), 81-109

[320] G. Ballihaut, F. Claverie, C. Pécheyran, S. Mounicou, R. Grimaud, R. Lobinski: **Sensitive Detection of Selenoproteins in Gel Electrophoresis by High Repetition Rate Femtosecond Laser Ablation-Inductively Coupled Plasma Mass Spectrometry**; *Analytical Chemistry*, 79 (2007), 6874-6880

[321] A. Raab, B. Pioselli, C. Munro, J. Thomas-Oates, J. Feldmann: **Evaluation of gel electrophoresis conditions for the separation of metal-tagged proteins with subsequent laser ablation ICP-MS detection**; *Electrophoresis*, 30 (2009), 303-314

[322] M. S. Jiménez, M. T. Gomez, L. Rodriguez, L. Martinez, J. R. Castillo: **Some pitfalls in PAGE-LA-ICP-MS for quantitative elemental speciation of dissolved organic matter and metalomics**; *Analytical and Bioanalytical Chemistry*, 393 (2009), 699-707

[323] M. S. Jiménez, L. Rodriguez, M. T. Gomez, J. R. Castillo: **Metal-protein binding losses in proteomic studies by PAGE-LA-ICP-MS**; *Talanta*, 81 (2010), 241-247

[324] J. Bettmer: **Application of isotope dilution ICP-MS techniques to quantitative proteomics**; *Analytical and Bioanalytical Chemistry*, 397 (2010), 3495-3502

[325] A. Sanz-Medel, M. Montes-Bayón, M. d. R. Fernández de la Campa, J. R. Encinar, J. Bettmer: **Elemental mass spectrometry for quantitative proteomics**; *Analytical and Bioanalytical Chemistry*, 390 (2008), 3-16

[326] D. R. Bandura, O. I. Ornatsky, L. Liao: **Characterization of phosphorus content of biological samples by ICP-DRC-MS: potential tool for cancer research**; *Journal of Analytical Atomic Spectrometry*, 19 (2004), 96-100

[327] M. R. B. Binet, R. Ma, C. W. McLeod, R. K. Poole: **Detection and characterization of zinc- and cadmium-binding proteins in Escherichia coli by gel electrophoresis and laser ablation-inductively coupled plasma-mass spectrometry**; *Analytical Biochemistry*, 318 (2003), 30-38

[328] M. Grebe, D. Pröfrock, A. Kakuschke, J. A. C. Broekaert, A. Prange: **Absolute quantification of transferrin in blood samples of harbour seals using HPLC-ICP-MS**; *Metallomics*, 3 (2011), 176-185

[329] V. Sanz-Nebot, P. González, I. Toro, A. Ribes, J. Barbosa: **Characterization of human transferrin glycoforms by capillary electrophoresis and electrospray ionization mass spectrometry**; *Journal of Chromatography B: Analytical Technologies in the Biomedical and Life Sciences*, 798 (2003), 1-7

[330] H. Sun, H. Li, P. J. Sadler: **Transferrin as a Metal Ion Mediator**; *Chemical Reviews*, 99 (1999), 2817-2842

[331] I. Kroslakova, D. Günther: **Elemental fractionation in laser ablation-inductively coupled plasma-mass spectrometry: evidence for mass load induced matrix effects in the ICP during ablation of a silicate glass**; *Journal of Analytical Atomic Spectrometry*, 22 (2007), 51-62

[332] F. S. Ruel, M. P. Braun, C. R. Johnson: **2-(4-Methoxyphenyl)-2-cyclohexen-1-one: Preparation of 2-iodo-2-cyclohexen-1-one and Suzuki coupling with 4-methoxyphenylboronic acid**; *Organic Syntheses Collective Volume*, 75 (1998), 69-76

[333] S. Ma, X. Lu, Z. Li: **A Novel Regio- and Stereospecific Hydrohalogenation Reaction of 2-Propynoic Acid and Its Derivatives**; *Journal of Organic Chemistry*, 57 (1992), 709-713

[334] E. Del Castillo Busto: **Nuevas estrategias analíticas para el estudio de ferroproteínas usadas en el diagnóstico clínico mediante espectrometría de masas**; *Dissertation, University of Oviedo*, (2009)

[335] R. W. Evans, R. Rafique, A. Zarea, C. Rapisarda, R. Cammack, P. J. Evans, J. B. Porter, R. C. Hider: **Nature of non-transferrin-bound iron: Studies on iron citrate complexes and thalassemic sera**; *Journal of Biological Inorganic Chemistry*, 13 (2008), 57-74

[336] A. Sarmiento-González, J. R. Encinar, A. M. Cantarero-Roldán, J. M. Marchante-Gayón, A. Sanz-Medel: **HPLC-ICPMS and stable isotope-labeled approaches**

to assess quantitatively Ti(IV) uptake by transferrin in human blood serum; *Analytical Chemistry*, 80 (2008), 8702-8711

[337] M. E. Del Castillo Busto, M. Montes-Bayón, A. Sanz-Medel: **Accurate Determination of Human Serum Transferrin Isoforms: Exploring Metal-Specific Isotope Dilution Analysis as a Quantitative Proteomic Tool**; *Analytical Chemistry*, 78 (2006), 8218-8226

[338] J. Fietzke, V. Liebetrau, D. Günther, K. Gürs, K. Hametner, K. Zumholz, T. H. Hansteen, A. Eisenhauer: **An alternative data acquisition and evaluation strategy for improved isotope ratio precision using LA-MC-ICP-MS applied to stable and radiogenic strontium isotopes in carbonates**; *Journal of Analytical Atomic Spectrometry*, 23 (2008), 955-961

[339] V. N. Epov, S. Berail, M. Jimenez-Moreno, V. Perrot, C. Pecheyran, D. Amouroux, O. F. X. Donard: **Approach to Measure Isotopic Ratios in Species Using Multicollector-ICPMS Coupled with Chromatography**; *Analytical Chemistry*, 82 (2010), 5652-5662

[340] B. Fernández, F. Claverie, C. Pécheyran, J. Alexis, O. F. X. Donard: **Direct Determination of Trace Elements in Powdered Samples by In-Cell Isotope Dilution Femtosecond Laser Ablation ICPMS**; *Analytical Chemistry*, 80 (2008), 6981-6994

[341] J. Heilmann, S. F. Boulyga, K. G. Heumann: **Development of an isotope dilution laser ablation ICP-MS method for multi-element determination in crude and fuel oil samples**; *Journal of Analytical Atomic Spectrometry*, 24 (2009), 385-390

[342] J. Kragten: **Tutorial review. Calculating standard deviations and confidence intervals with a universally applicable spreadsheet technique** ; *Analyst*, 119 (1994), 2161-2165

[343] C. G. Fraga: **Relevance, essentiality and toxicity of trace elements in human health**; *Molecular Aspects of Medicine*, 26 (2005), 235-244

[344] J.-L. Todoli, J.-M. Mermet: **Study of polymer ablation products obtained by ultraviolet laser ablation-inductively coupled plasma atomic emission spectrometry**; *Spectrochimica Acta, Part B: Atomic Spectroscopy*, 53 (1998), 1645-6156

[345] D. A. Frick, D. Günther: **Fundamental studies on the ablation behaviour of carbon in LA-ICP-MS with respect to the suitability as internal standard**; *Journal of Analytical Atomic Spectrometry*, 27 (2012), 1294-1303

[346] Y. Chen, G. Mehta, V. Vasiliou: **Antioxidant defenses in the ocular surface**; *Ocular Surface*, 7 (2009), 176-185

[347] **http://www.wikipedia.org**; 16^{th} September 2013

[348] A. Spector: **Oxidative stress-induced cataract: Mechanism of action**; *The FASEB Journal*, 9 (1995), 1173-1182

[349] A. Izzotti, A. Bagnis, S. C. Saccà: **The role of oxidative stress in glaucoma**; *Mutation Research - Reviews in Mutation Research*, 612 (2006), 105-114

[350] J. G. Hollyfield, V. L. Bonilha, M. E. Rayborn, X. Yang, K. G. Shadrach, L. Lu, R. L. Ufret, R. G. Salomon, V. L. Perez: **Oxidative damage-induced inflammation initiates age-related macular degeneration**; *Nature Medicine*, 14 (2008), 194-198

[351] V. B. Voleti, J.-P. Hubschman: **Age-related eye disease**; *Maturitas*, 75 (2013), 29-33

[352] H. Bloemendal, W. De Jong, R. Jaenicke, N. H. Lubsen, C. Slingsby, A. Tardieu: **Ageing and vision - Structure, stability and function of lens crystallins**; *Progress in Biophysics and Molecular Biology*, 86 (2004), 407-485

[353] A. H.Wagner, V. N. Anand, W. H. Wang, J. E. Chatterton, D. Sun, A. R. Shepard, N. Jacobson, I. H. Pang, A. P. DeLuca, T. L. Casavant, T. E. Scheetz, R. F. Mullins, T. A. Braun, A. F. Clark: **Exon-level expression profiling of ocular tissues**; *Experimental Eye Research*, 111 (2013), 105-111

[354] M. Ronci, S. Sharma, T. Chataway, K. P. Burdon, S. Martin, J. E. Craig, N. H. Voelcker: **MALDI-MS-imaging of whole human lens capsule**; *Journal of Proteome Research*, 10 (2011), 3522-3529

[355] B. H. Grahn, P. G. Paterson, K. T. Gottschall-Pass, Z. Zhang: **Zinc and the Eye**; *Journal of the American College of Nutrition*, 20 (2001), 106-118

[356] A. Loh, M. Hadziahmetovic, J. L. Dunaief: **Iron homeostasis and eye disease**; *Biochimica et Biophysica Acta - General Subjects*, 1790 (2009), 637-649

[357] M. Goralska, J. Ferrel, J. Harned, M. Lall, S. Nagar, L. N. Fleisher, M. C. McGahan: **Iron metabolism in the eye - A review**; *Experimental Eye Research*, 88 (2009), 204-215

[358] M. Ugarte, N. N. Osborne: **Zinc in the retina**; *Progress in Neurobiology*, 64 (2001), 219-249

[359] A. S. Borges-Giampani, J. Giampani Junior: **Glaucoma - Basic and Clinical Aspects**; *InTech*, http://www.intechopen.com (2013); 17^{th} September 2013

[360] B. G. Katzung (Ed.): **Basic & Clinical Pharmacology**; *McGraw-Hill Medical*, http://basic-clinical-pharmacology.net (2009); 17^{th} September 2013

[361] A. Vogel, V. Venugopalan: **Mechanisms of Pulsed Laser Ablation of Biological Tissues**; *Chemical Reviews*, 103 (2003), 577-644

[362] K. M. Matsuda, J.-Y. Chung, S. M. Hewitt: **Histo-proteomic profiling of formalin-fixed, paraffin-embedded tissue**; *Expert Review of Proteomics*, 7 (2010), 227-237

[363] S. Magdeldin, T. Yamamoto: **Toward deciphering proteomes of formalin-fixed paraffin-embedded tissues**; *Proteomics*, 12 (2012), 1045-1058

[364] S. Bohic, K. Murphy, W. Paulus, P. Cloetens, M. Salomé, J. Susini, K. Double: **Intracellular chemical imaging of the developmental phases of human neuromelanin using synchrotron X-ray microspectroscopy**; *Analytical Chemistry*, 80 (2008), 9557-9566

[365] M. V. Zoriy, M. Kayser, A. Izmer, C. Pickhardt, J. S. Becker: **Determination of uranium isotopic ratios in biological samples using LA-ICP-SF-MS with cooled ablation chamber**; *International Journal of Mass Spectrometry*, 242 (2005), 297-302

[366] W. Müller, J. M. G. Shelley, S. O. Rasmussen: **Direct chemical analysis of frozen ice cores by UV-laser ablation ICPMS**; *Journal of Analytical Atomic Spectrometry*, 26 (2011), 2391-2395

[367] J. S. Becker, M. V. Zoriy, M. Dehnhardt, C. Pickhardt, K. Zilles: **Copper, zinc, phosphorus and sulfur distribution in thin section of rat brain tissues measured by laser ablation inductively coupled plasma mass spectrometry: possibility for small-size tumor analysis**; *Journal of Analytical Atomic Spectrometry*, 20 (2005), 912-917

[368] M. V. Zoriy, J. S. Becker: **Imaging of elements in thin cross sections of human brain samples by LA-ICP-MS: A study on reproducibility**; *International Journal of Mass Spectrometry*, 264 (2007), 175-180

[369] E. Moreno-Gordaliza, C. Giesen, A. Lázaro, D. Esteban-Fernández, B. Humanes, B. Cañas, U. Panne, A. Tejedor, N. Jakubowski, M. M. Gómez-Gómez: **Elemental bioimaging in kidney by LA-ICP-MS as a tool to study nephrotoxicity**

and renal protective strategies in cisplatin therapies; *Analytical Chemistry*, 83 (2011), 7933-7940

[370] J. A. T. Pugh, A. G. Cox, C. W. McLeod, J. Bunch, B. Whitby, B. Gordon, T. Kalber and E. White: **A novel calibration strategy for analysis and imaging of biological thin sections by laser ablation inductively coupled plasma mass spectrometry**; *Journal of Analytical Atomic Spectrometry*, 26 (2011), 1667-1673

[371] M. B. Fricker, D. Kutscher, B. Aeschlimann, J. Frommer, R. Dietiker, J. Bettmer, D. Günther: **High spatial resolution trace element analysis by LA-ICP-MS using a novel ablation cell for multiple or large samples**; *International Journal of Mass Spectrometry*, 307 (2011), 39-45

[372] R. Agarwal, I. Iezhitsa, P. Agarwal, A. Spasov: **Magnesium deficiency: Does it have a role to play in cataractogenesis?**; *Experimental Eye Research*, 101 (2012), 82-89

Appendix

Chemicals

A prerequisite for any successful analysis is to prevent contamination of the sample, the eluent, but also of the analytical system as contamination of any kind can increase the detection limit or lead to misinterpretation of the data. In this respect, the used chemicals are of particular importance. Therefore, all chemical substances used during this study were of highest grade of purity available to avoid contamination. In *table 7.1* the compounds are listed together with their corresponding grade of purity and supplier. For all solutions, high purity Milli-Q water (Millipore, Bedford, USA) and/or was used . For preparation, the desired amount of solid or liquid was weighed using an analytical balance and afterwards dissolved in the respective solvent. Standard solutions for calibration of the instruments were also made by weight.

Table 7.1: List of reagents used throughout this work.

Chemicals		
Reagent	Degree of purity	Supplier
Acrylamide	≥99.5%	Fluka
Ammonium bicarbonate	puriss	Sigma Aldrich
Ammonium persulfate	98+%	Sigma Aldrich
Bromophenol Blue		Merck
Citric acid monohydrate	p.a.	Merck
Coomassie® Brilliant Blue R-250		Bio-Rad
Glycine	>99%	Sigma Aldrich
Iodine	≥99.8%	Sigma Aldrich
Iron(III) chloride hexahydrate	p.a.	Sigma Aldrich
Lithium iodide	99%	Sigma Aldrich
N,N'-Methylenebisacrylamide	>98%	Sigma Aldrich
Propiolamide	97%	USBiological

Chemicals		
Reagent	Degree of purity	Supplier
Sodium bicarbonate	p.a.	Merck
Sodium carbonate	99.9%	Merck
Sodium chloride	p.a.	Merck
Sodium dodecyl sulfate	∼99%	Sigma Aldrich
Sodium hydroxide	p.a.	Merck
Sodium phosphate	>98%	Sigma Aldrich
Sodium sulfate	p.a.	Merck
Sodium thiosulfate	≥98.0%	Sigma Aldrich
Tetramethylethylenediamine	p.a.	Merck
Tris(hydroxymethyl)aminomethane	p.a.	Merck
Trisodium citrate anhydrous		Sigma Aldrich

Solvents		
Reagent	Degree of purity	Supplier
Acetone	Rectapur	VWR
Acetonitrile	Optima®	Fisher Scientific
Dichloromethane	Chromasolv®	Riedel-de Haën
Diethyl ether	p.a.	Merck
Ethanol	AnalaR Normapur	VWR
Ethyl acetate	99.9%	Sigma Aldrich
Glycerol	85%, p.a.	Merck
Hexane	99%	VWR
Hydrochloric acid	37%, p.a.	Merck
Methanol	Gradient Grade	VWR
Nitric acid (subboiled)	Suprapur	Merck
Pyridine	p.a.	Merck

Proteins		
Reagent	Degree of purity	Supplier
Albumin, human	96-99%	Sigma Aldrich
Human serum		HUCA, Spain
Human serum ERM®-DA470k/IFCC	CRM	JCR-IRMM

Proteins		
Reagent	Degree of purity	Supplier
IEF Standards		Bio-Rad
Prestained SDS-PAGE Stds, low range		Bio-Rad
Transferrin, apo-, human	≥98%	Sigma Aldrich
Transferrin, holo-, human	≥97%	Sigma Aldrich

Stable isotopes		
Element	Abundancy	Supplier
Calcium (1000μg g^{-1})	nat.	Merck
Chlorine (1000μg g^{-1})	nat.	Merck
Copper (1000μg g^{-1})	nat.	Merck
Gallium (1000μg g^{-1})	nat.	Merck
Gold (1000μg g^{-1})	nat.	Merck
Iron (1000μg g^{-1})	nat.	Merck
Magnesium (1000μg g^{-1})	nat.	Merck
Phosphorus (1000μg g^{-1})	nat.	Merck
Sulfur (1000μg g^{-1})	nat.	Merck
Zinc (1000μg g^{-1})	nat.	Merck
Copper enriched in ^{65}Cu	90.0%	Spectrascan
Iron enriched in ^{54}Fe	96.8%	CIL Inc.
Iron enriched in ^{57}Fe	94.4%	CIL Inc.
Sulfur enriched in ^{34}S	99.9%	Euriso-top
Zinc enriched in ^{68}Zn	86.5%	Isoflex

Gases		
Gas	Degree of purity	Supplier
Argon	99.999%	Air Liquide
Helium	99.999%	Air Liquide
Nitrogen	99.999%	Air Liquide

Publications

In the following, all scientific of publications derived directly from this dissertation are summarized.

1. I. Konz, B. Fernández, R. Pereiro, M. L. Fernández, A. Sanz-Medel: **P, S and Cl trace detection by laser ablation double-focusing sector field ICP-MS to identify local defects in coated glasses**; *Journal of Analytical Atomic Spectrometry*, 26 (2011), 1526-1530

2. I. Konz, B. Fernández, M. L. Fernández, R. Pereiro, A. Sanz-Medel: **Absolute Quantification of Human Serum Transferrin by Species-Specific Isotope Dilution Laser Ablation ICP-MS**; *Analytical Chemistry*, 83 (2011), 5353-5360

3. I. Konz, B. Fernández, M. L. Fernández, R. Pereiro, A. Sanz-Medel: **Laser ablation ICP-MS for quantitative biomedical applications**; *Analytical and Bioanalytical Chemistry*, 403 (2012), 2113-2125

4. I. Konz, B. Fernández, M. L. Fernández, R. Pereiro, H. González, L. Álvarez, M. Coca-Prados, A. Sanz-Medel: **Gold internal standard correction for elemental imaging of soft tissue sections by LA-ICP-MS: element distribution in eye microstructures**; *Analytical and Bioanalytical Chemistry*, 405 (2013), 3091-3096

5. B. Fernández, I. Konz, A. Castañeda, M. L. Fernández, R. Pereiro, A. Sanz-Medel: **Celda de ablación criogénica con control de la temperatura de la muestra**; Patent No. P201300559 (2013) Spanish Patent Pending

6. I. Konz, B. Fernández, M. L. Fernández, R. Pereiro, A. Sanz-Medel: **Design and evaluation of a new Peltier-cooled laser ablation cell with on-sample temperature control**; *Analytica Chimica Acta*, (2013)

7. I. Konz, B. Fernández, M. L. Fernández, R. Pereiro, H. González, M. Coca-Prados, A. Sanz-Medel: **Quantitative bioimaging of trace elements in the human lens by LA-ICP-MS**; *Analytical and Bioanalytical Chemistry*, submitted

JAAS

View Online
Dynamic Article Links

Cite this: *J. Anal. At. Spectrom.*, 2011, **26**, 1526

www.rsc.org/jaas

TECHNICAL NOTE

P, S and Cl trace detection by laser ablation double-focusing sector field ICP-MS to identify local defects in coated glasses

Ioana Konz, Beatriz Fernandez,* Rosario Pereiro, M. Luisa Fernandez and Alfredo Sanz-Medel*

Received 22nd December 2010, Accepted 11th February 2011
DOI: 10.1039/c0ja00271b

Glass defects are always undesired because of their significant costs to manufacturing industries. Laser ablation inductively coupled plasma mass spectrometry (LA-ICP-MS) is a versatile technique for local trace element analysis in a wide variety of solid samples. Furthermore, the coupling of laser systems to double-focusing sector field mass analyzers provides low limits of detection with a high mass resolving power, allowing the accurate analysis of P, S and Cl traces in local defects of coated glasses. Three different types of defects, depending on the impurities identified at the LA-ICP-MS profiles, were found in the selected coated glasses (with metallic and oxide films in the low nanometre range), enabling the unambiguous identification of the contamination source that produces the local defects.

Introduction

Various types of glass defects (*e.g.* knots, striate, crystals, metallic inclusions, bubbles, *etc.*) may occur in the production of homogeneous and coated glasses, endangering their function and usage (*e.g.* by reducing the mechanical strength, inducing stress or producing optical inhomogeneities which may lower its functional properties) and, thereby, the quality of the product. In general, characterization of such defects presents a real challenge due to their complex chemical and mineralogical properties and, therefore, a multimethod approach is required.[1,2]

The fast and reliable depth profiling analysis of local defects in coated glasses is of critical importance to assist the optimization of the synthesis procedures as well as to evaluate their manufacturing quality. Therefore, novel or advanced analytical techniques capable of characterizing such samples at the microscale level are currently required. In this sense, laser ablation inductively coupled plasma mass spectrometry (LA-ICP-MS) has been widely investigated as a powerful analytical technique for the direct analysis of different types of materials.[3–5] According to its unique features, LA-ICP-MS allows element and isotopic analyses of solids, including microanalysis and depth profiling, with good lateral and depth resolution at trace concentration levels.[6,7] Moreover, the coupling of the laser systems to double-focusing sector field mass analyzers provides comparatively low detection limits and high mass resolving power. Thus, the common problems related to polyatomic interferences on analyte ions,[8] so usual in quadrupoles, can be circumvented.

Most of the earlier work on glass analysis using LA-ICP-MS has been focused on sampling strategies, evaluation of laser parameters and development of quantification methodologies for the analysis of homogeneous glasses.[9–14] However, studies on depth profiling analysis of coated glasses by LA-ICP-MS are still scarce[15,16] and few attempts have been done for the characterization of local defects in thin films.[17,18] In such cases, only major components of glass specimens (Na_2O, Al_2O_3, SiO_2, K_2O, ZrO_2 and BaO) were investigated and the sources of defects were attributed to high intrinsic compressive stress in the thin films.

Preliminary analysis of the coated glasses selected in this work were performed by the manufacturing company using electron probe microanalysis (EPMA) and P, S, and Cl were found to be possible impurities in the local defects. However, due to the low concentration of such elements and the limited depth resolution of EPMA for the analysis of thin films in the nanometre range, it was not possible to distinguish the position of the impurities in the samples and only averaged information on the composition was obtained, which was not enough to define the possible contamination sources.

In this study, the presence of P, S and Cl trace impurities in relevant local defects of coated glasses is investigated by using LA-ICP-MS. Several coated glasses with metallic and oxide layers in the nanometre range were selected for the study. As local defects (with a size in the range of 200–800 μm in diameter) appear during the temperate treatments, used to increase the strength of the glasses, the main goal of this work is to identify the nature of the impurities that promote the local defects as well as their position (*i.e.* at the glass substrate, the interface or the coating) in order to identify possible contamination sources, an aspect of critical importance in the glass manufacturing process.

Experimental

Samples

A set of coated glasses with antireflective and thermal properties from a glass manufacturing company was employed in this study.

Department of Physical and Analytical Chemistry, Faculty of Chemistry, University of Oviedo, Cl Julian Clavería 8, 33006 Oviedo, Spain. E-mail: fernandezbeatriz@uniovi.es; asm@uniovi.es; Tel: +34 98510 3474

All the selected glasses had local defects, not easily detected by the human eye due to their reduced size (200–800 μm diameter). In all cases, the glass substrates were 6 mm thick and had several metallic and oxide layers in the nanometres range (below 200 nm overall thickness) deposited on the surface. Detailed information about the composition of the thin films cannot be given due to confidentiality agreements. Fig. 1 shows three of the local defects detected in the coated glasses by using the optical microscope of the laser system.

Instrumentation

A double-focusing sector field ICP-MS instrument (Element 2, Thermo Fischer Scientific, Germany) coupled with a commercial laser ablation system LSX-213 (Cetac Technologies, USA) was used. A laser ablation chamber with an effective volume of 60 cm^3 was employed throughout the experiments, ensuring a reasonable fast washout time (less than 2 s). Measurements of Mg, P, S, Cl, and Ca were performed for all the samples. Thus, the analyses of the possible non-metal impurities present in the local defects (P, S and Cl) as well as of two of the major components of glass substrates (Mg and Ca) were always investigated. In order to separate the potential polyatomic interferences from analyte ions all measurements were performed at medium mass resolution in the Element 2 ($m/\Delta m = 4000$).[19,20]

The laser-generated aerosol is transported through a high-purity tube of 6.4 mm external diameter and 3.2 mm internal diameter (Tygon® tubing) into the ICP torch by using He as carrier gas. The optimized operating LA-ICP-MS conditions are given in Table 1.

Crater depths produced in the different glasses were measured with a profilometer (KLA-Tencor/P-15, USA) by measuring two profile traces in different directions across the centre of each crater. The morphology of the craters was investigated by scanning electron microscopy (SEM) with a JEOL JSM 6360 instrument (JEOL Ltd, Japan). The electron beam voltages used were 10 kV and 15 kV.

Results and discussion

First, the optimization of the LA-ICP-MS conditions and the selection of the ablation strategy was carried out. In order to perform depth profiling analysis and, therefore, identify the position of the impurities that produce the local defects (at the glass substrate, the interface, or at the thin films), the single point ablation mode was employed throughout the experiments. Moreover, a low laser repetition rate was used to avoid mixing of information coming from different laser pulses and, thus, 30 s of delay time was employed between two laser pulses. Craters of 200 μm in diameter were selected for the analysis as a compromise between high sensitivity, necessary to detect trace impurities, and good depth/diameter ratio.[6,15]

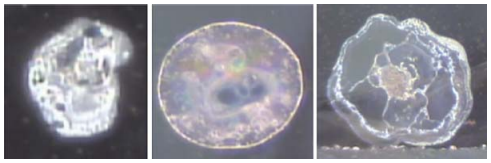

Fig. 1 Optical microscope images of three local defects in the coated glasses before LA-ICP-MS analysis.

Table 1 Operating conditions of the ICP-MS and LA system

ICP-MS	Thermo Element 2
RF Power	1325 W
Cooling gas	15 L min^{-1}
Auxiliary gas	0.8 L min^{-1}
Carrier gas (Ar)	0.4 L min^{-1}
Cones	Ni (Skimmer & Sampler)
Isotopes monitored	^{24}Mg, ^{43}Ca, ^{44}Ca (glass substrate), ^{31}P, ^{32}S, ^{34}S, and ^{35}Cl (local defects)
Sample time	0.02 s
Mass window	50%
Samples per peak	20
LA system	**Cetac LSX-213**
Laser energy	100% (~5.6 mJ)
Pulse duration	<6 ns
Repetition rate	0.033 Hz (1 shot and 30 s delay time)
Spot size	200 μm
Ablation mode	Single point
Carrier gas (He)	1 L min^{-1}

"Blank analyses" of the glasses in a location without defects was always performed to check the background levels of the impurities (P, S and Cl). Additionally, these analyses allowed us to get preliminary information about the thickness of the coating. Fig. 2 shows a typical profile obtained by LA-ICP-MS for the analysis of a coated glass without defects. As can be seen, a stable background signal was found for ^{32}S and ^{35}Cl, and only a slight increase of the ^{31}P ion signal was observed in the first laser pulse. ^{24}Mg and ^{44}Ca ion signals, coming from the glass substrate, progressively increased from the second to the fourth laser pulse, indicating that the homogeneous glass substrate was reached at the fourth laser pulse and, therefore, that the first, second and third pulses correspond to the analysis of the thin films and the coating/glass interface.

Next, the analysis of the local defects in the coated glasses was carried out for all the selected specimens. Three types of defects,

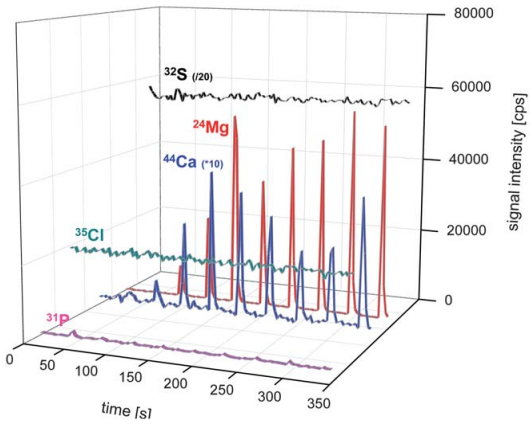

Fig. 2 LA-ICP-MS signals of ^{24}Mg, ^{31}P, ^{32}S, ^{35}Cl, and ^{44}Ca for a coated glass without defects.

depending on the impurities identified in the LA-ICP-MS profiles, were found in the samples. P, S and Cl impurities were identified at the local defects, whereas just background levels of those elements were always found in the glasses without defects. As an example, Fig. 3 shows the profiles obtained for the three different types of defects: with P and Cl (type-1), P, S and Cl (type-2) and Cl (type-3). LA-ICP-MS profiles of local defects denoted as type-1 and type-2 (Fig. 3a and b, respectively) showed ion signals significantly high for the corresponding impurities, whereas ^{35}Cl ion signals only showed a slight increase in the type-3 (Fig. 3c). Therefore, it could be concluded that the presence of P, S and Cl in the glasses seems to be critical for the samples, creating the unwanted defects.

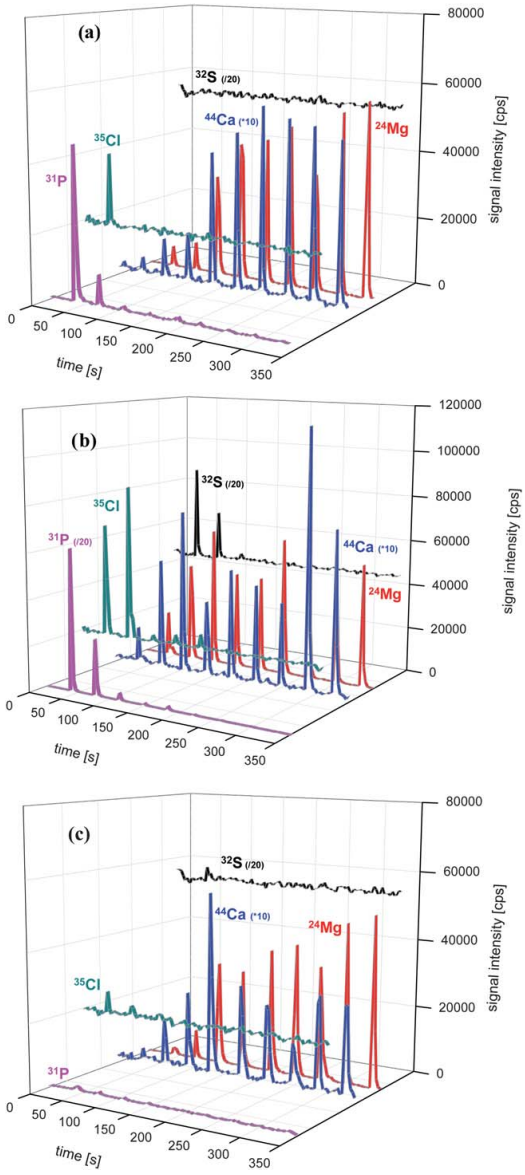

Fig. 3 LA-ICP-MS signals of ^{24}Mg, ^{31}P, ^{32}S, ^{35}Cl, and ^{44}Ca for the analysis of three coated glasses with local defects. (a) Type-1 (P and Cl); (b) Type-2 (P, S and Cl), and (c) Type-3 (Cl).

The main goal of this work is not only the identification of impurities present at the local defects (P, S and Cl) but also the recognition of their depth position (*i.e.* at the glass substrate, the interface, or the coating) to detect the possible contamination sources. As can be observed in Fig. 3, ^{31}P, ^{32}S and ^{35}Cl ion signals were always found in the two first laser pulses, where the signals coming from the glass substrate were negligible or rather low. Therefore, it could be stated that the impurities are located in the coating of the samples and not in the homogeneous glass substrate. Additionally, ^{31}P, ^{32}S and ^{35}Cl exhibited always the highest signals at the first laser pulse (*e.g.* ^{35}Cl was only found in the first peak for type-1 defects, Fig. 3a), which could also indicate that the impurities are in the thin metallic and oxide films and not in the coating/substrate interface.

Although the LA-ICP-MS technique shows promising performance for depth profiling analysis, it was not possible to precisely identify the position of P, S and Cl impurities due to the small thickness of the coating layers (metallic films in the order of 20–30 nm and oxide films around 100 nm). However, LA-ICP-MS profiles of selected glasses gave valuable information to the glass manufacturing company since P, S and Cl impurities were identified at the coating of the samples, indicating that contamination sources are mainly related to the thin films deposition process (*e.g.* pollutants derived from the oils used for the mechanical components of the sputtering lines: rollers, valves, rotating cathodes, *etc.*).

On the other hand, in order to evaluate if the ablation rate (nanometres per laser pulse) and, thus the depth of the craters, changed when analysing the local defects or the "blank" surfaces, the crater shapes were studied by profilometry. Fig. 4 shows the crater shapes obtained after LA-ICP-MS analysis for a glass without defects (Fig. 4a) and for two local defects (Fig. 4b and c; type-1 and -3 defects, respectively).

As can be seen, a rather Gaussian profile was obtained in all cases and some irregularities were found along the profiles of the craters inside the local defects, which could be attributed, at least partly, to the own structure of the defects. Moreover, the depth of the craters was different depending on the defects type (Fig. 4b and c), being in any case always in the range of 70–100 nm per pulse. For the analysis of glasses without defects (Fig. 4a), the craters depth was slightly lower compared to that obtained for the local defects, being the sputtering rate around 50 nm per pulse.

Such differences observed on the ablation rates for the glasses with and without defects can be mainly attributed to changes in the sample morphology (see Fig. 1) and, therefore, to an altered action of the laser beam during the analysis. Additionally, the possible mixing of the different layers of the coating (metallic and oxides films) inside the local defects could change the laser absorption characteristics of the glasses. Such mixing could be also responsible for the small ^{24}Mg and ^{44}Ca ion signals (coming from the glass substrate) observed at the first laser pulses (*i.e.* during the ablation of the coating). In any case, as can be seen in Fig. 4b and c, SEM images obtained for the craters inside the local defects showed craters with a well-defined structure and

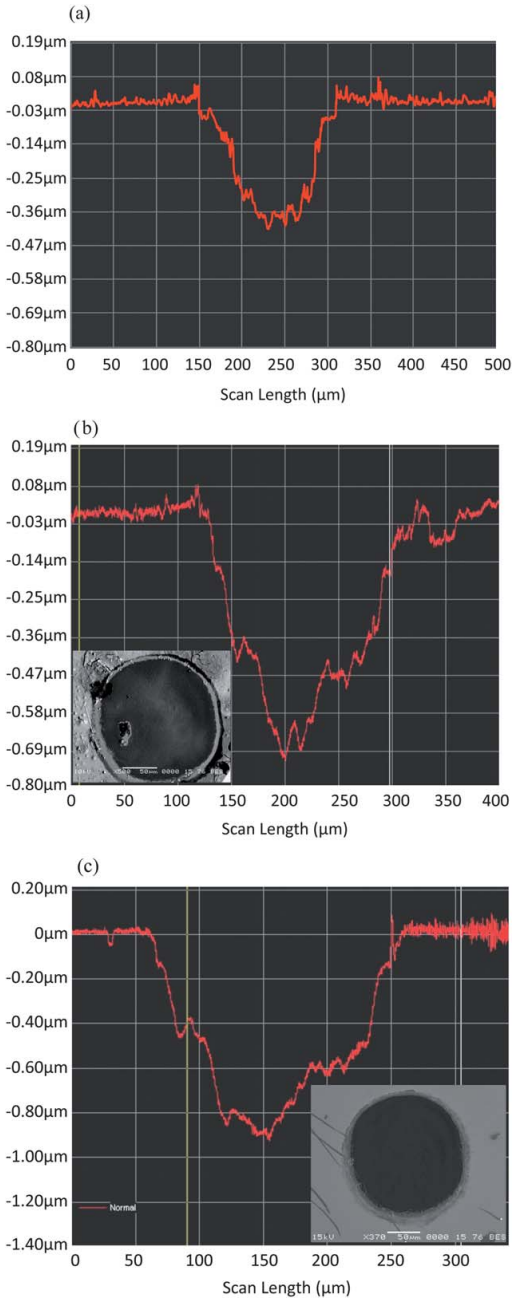

Fig. 4 Crater shapes and SEM images obtained for the coated glasses after LA-ICP-MS analysis. (a) Glass without defects; (b) Type-1 defect, and (c) Type-3 defect.

without big redeposited particles; only small particles can be observed in the SEM image of Fig. 4b and a negligible redeposition at the crater edges in the profiles measured by profilometry.

On the other hand, it is well-known that limits of detection (LODs) in LA-ICP-MS are a function of the background signal, the counting time per element and the sensitivity, this latter depending on the amount of the ablated material (*i.e.*, the spot size and the laser energy). Using a double-focusing sector field ICP-MS instrument (Element 2) and the optimized ablation strategy for depth profiling analysis, detection limits obtained by LA-ICP-MS were calculated by using the gas blank.[21] The 3s criterion ($3s_b/S$) was employed to calculate the LODs, where s_b is the standard deviation of five independent measurements of the blank value in cps and S is the sensitivity for the corresponding analyte isotope obtained by measuring the reference material NIST 610. It should be stated that indicative values for P, S and Cl concentrations suggested by GeoReM Max Planck Institute database[22] were employed for LODs calculation due to the lack of certified reference values. Detection limits obtained were in the low µg per g range in all cases (2.7 µg per g for ^{31}P, 3 µg per g for ^{35}Cl and 32 µg per g for ^{32}S), being the higher detection limit found for S related to the relatively high background.

Further investigations should be carried out for a more critical evaluation of the local defects morphology and structure and, thus, for clarifying the cause of the differences observed between the ablation rates of the local defect and without defect glasses. Moreover, due to the lack of appropriate certified reference materials, as well as to the different ablation rates observed for the defects, only qualitative information can be provided in this work. However, although such information can be sufficient for the contamination sources identification in the production stage of the glasses, quantitative profiles would allow us to obtain further valuable information about the incorporation of the impurities in the sample (*e.g.* if the impurities content depends or not on the temperature and pressure conditions).

Conclusions

This work demonstrates that LA-ICP-MS can be a highly valuable analytical tool for a fast and sensitive qualitative depth profile characterization of local defects in glasses coated with thin films. Moreover, the inherent capability of double-focusing sector field ICP-MS instruments to separate most polyatomic interferences from the analyte ions in the low mass range, working at a mass resolving power of 4000 has allowed the detection of ^{31}P, ^{32}S, and ^{35}Cl impurities located preferentially in the local defects. Thus, three different types of defects were successfully identified on the basis of the impurities analysed in the experimental LA-ICP-MS profiles by comparison with background signals of glasses without defects; with P and Cl (denoted as type-1), P, S and Cl (type-2) and Cl (type-3).

Furthermore, the craters produced after LA-ICP-MS analysis of the coated glasses (with and without local defects) were investigated by profilometry. Several irregularities along the crater profiles as well as higher ablation rates were found inside the local defects compared to craters measured for the glasses without defects (70–100 nm per pulse and 50 nm per pulse, respectively).

Finally, it should be stressed that the identification of the impurities locations at the thin metallic and oxide films and not in the substrate or in the sample interface allows the identification of the P, S and Cl contamination sources, that is of critical

importance to assist the optimization of the synthesis procedures as well as to evaluate the routine manufacturing quality of the glasses.

Acknowledgements

Financial support from "Plan Nacional de I + D+I" (Spanish Ministry of Science and Innovation or MICINN, and FEDER Programme) through MAT2010-20921-C02-01 is acknowledged. Ioana Konz and Beatriz Fernandez acknowledge financial support from FPU and Juan de la Cierva Programs from MICINN, respectively. Finally, the authors thank PCTI Asturias through the project FC-09-EQUIP09-29 for the acquisition of laser instrumentation.

References

1 J. Li, Z. L. Wang and T. C. Hufnagel, *Phys. Rev. B: Condens. Matter Mater. Phys.*, 2002, **65**, 144201.
2 R. Falcone, P. Galinetto, B. Messiga, E. Negri, M. P. Riccardi, G. Sommariva and M. Verita, *Microchim. Acta*, 2008, **161**, 381.
3 B. Fernandez, F. Claverie, C. Pecheyran and O. F. X. Donard, *TrAC, Trends Anal. Chem.*, 2007, **26**, 951.
4 B. Giussani, D. Monticelli and L. Rampazzi, *Anal. Chim. Acta*, 2009, **635**, 6.
5 J. S. Becker, *Int. J. Mass Spectrom.*, 2010, **289**, 65.
6 J. Pisonero and D. Günther, *Mass Spectrom. Rev.*, 2008, **27**, 609.
7 J. Pisonero, J. Koch, M. Wälle, W. Hartung, N. D. Spencer and D. Günther, *Anal. Chem.*, 2007, **79**, 2325.
8 U. Gießmann and U. Greb, *Fresenius' J. Anal. Chem.*, 1994, **350**, 186.
9 I. Horn, M. Guillong and D. Günther, *Appl. Surf. Sci.*, 2001, **182**, 91.
10 L. M. Neufeld, *Spectroscopy*, 2005, **20**, 31.
11 T. Trejos and J. R. Almirall, *Talanta*, 2005, **67**, 388.
12 F. Claverie, B. Fernandez, C. Pecheyran and O. F. X. Donard, *J. Anal. At. Spectrom.*, 2009, **24**, 891.
13 M. Humayun, F. A. Davis and M. M. Hirschmann, *J. Anal. At. Spectrom.*, 2010, **25**, 998.
14 M. Wälle, J. Koch, D. Tabersky, K. Hametner, N. D. Zhigadlo, S. Katrych, J. Karpinski and D. Günther, *J. Anal. At. Spectrom.*, 2010, **25**, 193.
15 A. J. G. Mank and P. R. D. Mason, *J. Anal. At. Spectrom.*, 1999, **14**, 1143.
16 P. R. D. Mason and A. J. G. Mank, *J. Anal. At. Spectrom.*, 2001, **16**, 1381.
17 K. Bange, H. Müller and C. Strubel, *Mikrochim. Acta*, 2000, **132**, 493.
18 H. Müller, C. Strubel and K. Bange, *Scanning*, 2001, **23**, 14.
19 J. S. Becker, M. Zoriy, J. S. Becker, C. Pickhardt and M. Przybylski, *J. Anal. At. Spectrom.*, 2004, **19**, 149.
20 H. Österlund, I. Rodushkin, K. Ylinenjärvi and D. C. Baxter, *Waste Manag.*, 2009, **29**, 1258.
21 J. S. Becker, C. Pickhardt and H.-J. Dietze, *J. Anal. At. Spectrom.*, 2001, **16**, 603.
22 GeoReM Max Planck Institute database for reference materials of geological and environmental interest: georem.mpch-mainz.gwdg.de (15 December 2010).

analytical chemistry

ARTICLE

pubs.acs.org/ac

Absolute Quantification of Human Serum Transferrin by Species-Specific Isotope Dilution Laser Ablation ICP-MS

Ioana Konz, Beatriz Fernández,* M. Luisa Fernández, Rosario Pereiro, and Alfredo Sanz-Medel*

Department of Physical and Analytical Chemistry, Faculty of Chemistry, University of Oviedo, Julian Clavería, 8. 33006 Oviedo, Spain

Supporting Information

ABSTRACT: We report for the first time the absolute quantification of a metalloprotein separated by nondenaturing gel electrophoresis (GE) using laser ablation inductively coupled plasma mass spectrometry (LA-ICP-MS) in combination with species-specific isotope dilution mass spectrometry (IDMS). The proposed method is based on the use of an isotopically enriched ^{57}Fe-transferrin complex to quantify natural transferrin (Tf) in human serum samples. First, the saturation process of Tf with natural abundance or isotopically enriched ^{57}Fe was accomplished by using freshly synthesized Fe-citrate solutions. The stability of the metal-protein complex as well as its stoichiometry was investigated by spectrophotometry and ICP-MS, demonstrating a satisfactory stability over a period of at least one month and a molar ratio Fe:Tf of 1.94 ± 0.09, which is close to the expected value of 2. The species-specific IDMS method was compared with external calibration using the Fe-Tf (absolute Tf amount between 2 and 10 μg) and different sample preparation procedures (stained and nonstained gels) as well as two laser ablation strategies (single line ablation in the direction perpendicular or horizontal to the electrophoretic migration) were evaluated. The proposed species-specific GE-LA-ICP-IDMS method was tested for the analysis of a serum certified reference material (ERM-DA470k/IFCC). The results were in good agreement with the certified value with relative standard deviation values in the range of 0.9−2.7% depending on the data treatment procedure used. Furthermore, the analysis time has been drastically reduced in comparison with previous approaches to less than 15 min. The quantification by species-specific GE-LA-ICP-IDMS allowed us to obtain accurate and precise results not only by analyzing the protein spot in the middle position but also in the adjacent ablation line to the center.

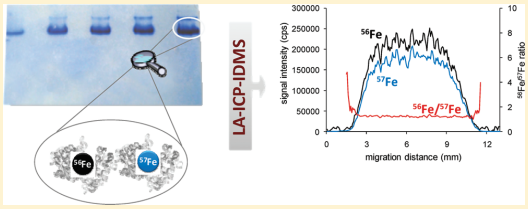

INTRODUCTION

Metals are present in more than one-third of all proteins, playing important biological functions. Thus, in recent years many research efforts have been focused on the comprehensive study of metalloproteins, mainly dealing with the structure and functions of the metal sites as well as the biological implications of those metal-biomolecule interactions. Metalloproteomics has become a key part of the more general concept of metallomics.[1,2] The main analytical tools for the analysis of metalloproteins and metal-binding proteins include chromatographic or electrophoretic separation of the target biomolecule and their subsequent identification by molecular mass spectrometric techniques, using an electrospray (ESI) or a matrix-assisted laser desorption ionization (MALDI) source.[3,4] Several alternative strategies have been developed to investigate the chemical speciation of the metal bound to the protein. Such techniques are based on the online coupling of high performance liquid chromatography (HPLC) with an elemental detector, particularly with an inductively coupled plasma-mass spectrometer (ICP-MS).[1,5,6] Unfortunately, the chromatographic selectivity of HPLC methods is crucial here but not always enough to separate all the proteins in complex biological samples before final elemental detection.

However, gel electrophoresis (GE), with its unique ability to resolve thousands of proteins in a single run, is a powerful tool used routinely in biochemical, medical, and molecular biology laboratories today.[7,8] In fact, such routine tool has contributed significantly to clarify key bioscience issues, opening many new biological and clinical avenues. Classical detection methods in GE employ more or less specific chemical reactions, resulting in visible spots in the gel. Then, the analyte biomolecule can be extracted from the spot in the gel and characterized by molecular MS.[9] One of the main limitations of GE techniques is to achieve in this way the absolute quantification of the corresponding protein. Therefore, it would be desirable to have a solid sample introduction device able to transport directly the separated protein from the spots to the ICP-MS for detection. It has been demonstrated that natural presence of a heteroelement in a given protein enables the application of elemental MS in the field of metalloproteomics, making possible a robust and sensitive approach to protein quantification.[6,10] So far, however, protein quantification studies are scarce due to their complexity.[4−6]

Laser ablation (LA) ICP-MS is currently regarded as one of the most versatile techniques for trace element and isotopic analyses of solid materials.[11] Additionally, since its first introduction by

Received: March 28, 2011
Accepted: May 19, 2011
Published: May 24, 2011

Neilsen et al.,[12] the combination of GE with LA-ICP-MS has been successfully applied for the detection of phosphorylated proteins, selenoproteins, and other metalloproteins[13−15] as well as for the imaging of total metals in biological tissues.[16] Previous studies on the application of GE with LA-ICP-MS have been mainly focused on the optimization of the basic conditions for the effective separation of metal-binding proteins, focusing on their stability during GE and postseparation gel treatment.[15,17] Furthermore, while qualitative and semiquantitative analyses are almost routine in LA-ICP-MS, accurate quantitative analysis still remains an important challenge for a large variety of solid samples. In particular, current calibration methods developed for metalloprotein determinations using GE-LA-ICP-MS include the use of known metal spiked gels or introducing a standard metal solution into the laser ablation cell.[18,19] However, those approaches are external calibration methods and neither consider the behavior of proteins under the conditions used for electrophoresis nor compensate for possible distribution inhomogeneities in a protein spot.

Isotope dilution mass spectrometry (IDMS) is internationally regarded as an absolute measurement method directly traceable to the International System of Units.[20] In contrast to other calibration strategies, the analytical result is not affected by signal drifts, matrix effects or analyte losses. The quantification of metalloproteins by HPLC-ICP-MS can be improved by the addition of an isotopically enriched protein at the beginning of the sample preparation procedure (species-specific spiking). In this way, current analytical procedures can be validated as the chromatographic separation, analyte losses,or transformations of the species will not affect the final results.[20−22] The use of IDMS in LA-ICP-MS can correct not only for such possible losses and transformations of the species but also for some common fractionation and matrix effects that cannot be controlled using other calibration procedures. Thus, the combination of LA-ICP-MS and IDMS has been successfully applied for the direct determination of trace elements in solid samples, such as soils and sediments, road dusts, hair samples, petroleum products, silicon wafers, etc.[23−25] So far, only one publication[26] dealing with the use of IDMS combined to GE-LA-ICP-MS for the analysis of metalloproteins (superoxide dismutase) has been reported. However, in such study, the absolute quantification capabilities of IDMS were not demonstrated, since the analysis of reference materials to validate the quantification approach was lacking.

Therefore, the aim of this work is the development and validation of a species-specific LA-ICP-IDMS methodology to achieve a sensitive, fast, and accurate absolute quantification of transferrin (Tf) metalloprotein in serum samples. Transferrin has been selected as model metalloprotein due to its important role in the iron metabolism of the human body. Physiologically, the majority of cells in the organism acquire iron from a well-characterized plasma glycoprotein; transferrin. The most common analytical approaches for absolute quantification of Tf in serum samples are based on separations by chromatography[5] or electrophoresis[27] techniques followed by an iron-specific detector such as ICP-MS. The proposed method is based on the use of an isotopically enriched ^{57}Fe-Tf complex to quantify natural Tf in human serum samples, after nondenaturing one-dimensional GE separation (1D-PAGE). A critical evaluation of novel external calibration strategies and the species-specific IDMS quantification method, in terms of precision, accuracy, and analysis time is presented. The proposed species-specific GE-LA-ICP-IDMS method was validated analyzing a certified reference serum material.

Table 1. Operating Conditions of the ICP-MS and Laser Ablation System

ICP-MS	thermo element 2
RF Power	1325 W
cooling gas	15.5 L min^{-1}
auxiliary gas	0.8 L min^{-1}
nebulizer gas (Ar)	0.9 L min^{-1} (ICP-MS)
	0.6 L min^{-1} (LA-ICP-MS; wet plasma)
cones	Ni (skimmer and sampler)
isotopes	^{13}C, ^{32}S, ^{34}S, ^{54}Fe, ^{56}Fe, ^{57}Fe, ^{58}Fe, ^{69}Ga, ^{71}Ga
sample time	0.01 s
mass window	100%
samples per peak	10
LA system	**CETAC LSX-213**
laser energy	100% (~5.6 mJ)
repetition rate	20 Hz
spot size	200 μm
scan speed	40 μm s^{-1}
ablation mode	single line scan
carrier gas (He)	0.8 L min^{-1}

EXPERIMENTAL SECTION

Standards, Reagents and Samples. All chemicals and reagents used in this work were of analytical grade and their detailed description is included as Supporting Information. The spike solutions of ^{57}Fe (94.42 ± 0.01% isotopic abundance) and ^{34}S (99.96 ± 0.01% isotopic abundance) were characterized in terms of isotopic composition and concentration by ICP-MS and reverse ICP-IDMS, respectively, and Fe and S concentrations were found to be 12.73 ± 0.26 μg g^{-1} for Fe and 66.81 ± 1.63 μg g^{-1} for S. The certified reference material (CRM) ERM-DA470k/IFCC was employed for the validation of the proposed quantification methodology.

Instrumentation. *Gel Electrophoresis.* The separation of protein standards and human serum samples was performed using a vertical mini-gel electrophoresis system (Mini-PROTEAN Tetra Cell, Bio-Rad Laboratories, Hercules, CA, U.S.). Gels were handcast in mini-gel cassettes as described in the Supporting Information. The running conditions were 300 V for 20 min or until bromophenol blue dye had migrated to the bottom of gel. For external calibration analyses a volume of 10 μL Fe-Tf standard (absolute amount of protein between 2 μg and 10 μg) was loaded into the gel. The serum proteins separation by 1D-PAGE was performed under nondenaturing conditions, avoiding the possible loss of metals associated to proteins.

Following electrophoresis, the gel cassettes were dismantled and the mini-gels were stained in freshly prepared and filtered Coomassie staining solution (10% acetic acid, 20% methanol) for 30 min. Next, the gels were destained in 10% acetic acid with 50% methanol until the gel background was clear. The gels were then placed in glycerol for 1 min and dried for at least 3 h in an oven at 70 °C on filter paper (Whatman paper) and covered with a transparent film (Saran Film) to protect them against contamination. Nonstained gels were carefully transferred into glycerol

(as the stained gels), but neither Coomassie solution nor acetic acid and methanol were added. For LA-ICP-MS measurements, the filter papers with the gels were transferred into the ablation cell and, in all cases, LA-ICP-MS analyses were performed on the same day of gel preparation to minimize any possible diffusion of the proteins within the gel or into the sample substrate.

Spectrophotometer (UV–vis). An UV–Vis spectrophotometer (Thermo Spectronic GENESYS 20, Thermo Scientific, Bremen, Germany) and an Agilent HPLC system model 1100 (Agilent Technologies, Tokyo, Japan) with a diode array detector were used for the studies of Tf saturation with Fe.

LA-ICP-MS. Element-specific detection was carried out using a double-focusing sector field ICP-MS (Element 2, Thermo Fisher Scientific, Bremen, Germany) at medium mass resolution (R = 4000), in order to avoid spectral interferences on Fe and S determination. For laser ablation analyses, a CETAC LSX-213 laser system (Cetac Technologies, Omaha, Nebraska, U.S.) was employed. The optimized conditions used for ICP-MS and LA-ICP-MS measurements are listed in Table 1. Taking into account the relatively long analysis time of the spots in the gels (around 5 min) as well as the homogeneity of the samples within the spots, each isotope is counted during one time slice of 100 ms per 2 s to improve the ions statistic and, therefore, to obtain a better precision in the isotope ratio measurements. The LA-ICP-MS coupling was carried out in wet plasma conditions using a homemade Y-piece of glass. The laser-generated aerosol was transported through a high-purity tube (Tygon tubing) into the ICP torch by the He carrier gas of the ablation cell. Before the introduction into the plasma, the laser-generated aerosol was mixed with a liquid aerosol (nebulized by means of a concentric nebulizer). This dual-flow introduction system enables a complete and easy optimization of the ICP-MS (gas flow rates, torch position, lens voltages, etc.) for high sensitivity by nebulizing a 1 ng g^{-1} multielement tuning solution. Moreover, LA-ICP-MS coupling was optimized daily using a SRM NIST 612 glass standard for high sensitivity, background intensity, and the $^{238}U/^{232}Th$ signal ratio that should be close to 1 to ensure a low fractionation effect due to the ICP ionization efficiency. $^{248}ThO/^{232}Th$ signal ratio was also measured for controlling oxide formation, being always below 0.5% at the selected optimized conditions. In addition, during laser ablation analyses, the plasma was kept under wet conditions by the continuous nebulization of a 10 ng g^{-1} Ga standard solution, which was used to correct for mass bias during the measurement of Fe isotope ratios.

Procedures. *Iron Saturation: Apo-Tf Standard Incubated with Fe-Citrate.* For the saturation of the Tf standard, a solution of ~31 μM Apo-Tf (typical Tf concentration in human serum samples) was prepared in a physiological medium, which consists of 50 mM Tris and 150 mM NaCl (pH 7.4). This solution was diluted 1:1 with a model solution containing 20 mM ammonium bicarbonate, 150 mM NaCl and 300 μM sodium citrate (pH 7.4). The Apo-Tf was then saturated with an appropriate amount of a freshly synthesized Fe-citrate solution (Fe-citrate was prepared at pH 7.4 using 0.03 g of an Fe standard solution and trisodium citrate 1 M to final concentrations of 100 μM Fe, being the optimum Fe-to-citrate molar ratio 1:1000[22,28]). The mixture was finally thoroughly stirred and incubated at room temperature during 1 h. Then, possible low weight impurities and the Fe-citrate excess after Tf incubation were removed by ultrafiltration through an Amicon centrifugal device (molecular cutoff of 10 kDa) at 14000 g. The protein fraction (retained in the upper

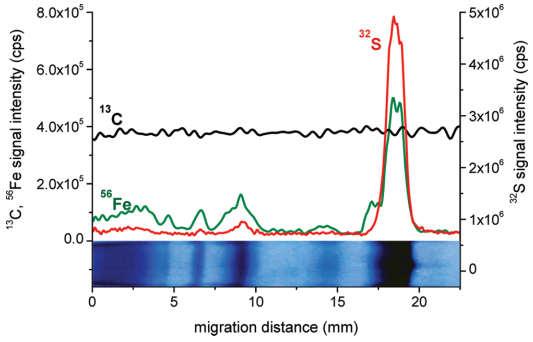

Figure 1. Electropherogram obtained by LA-ICP-MS for the analysis of a certified human serum sample (ERM-DA470k) after GE separation (nondenaturing 1D-PAGE, Coomassie stained gels).

side of the filter) was reconstituted with the physiological medium previously used in the incubation and then centrifuged again. Finally, the Fe-Tf complex was reconstituted in the model solution by inversion of the Amicon filter and a brief centrifugation at 1000 $\times g$. It should be stated that the same procedure used for the incubation of natural Fe-citrate with Apo-Tf standards was used for the incubation of real life serum samples.

Preparation of the Isotopically Enriched Fe-Saturated Tf. Concerning the synthesis of ^{57}Fe-Tf, 250 μL of an Apo-Tf standard solution in a physiological medium was diluted 1:1 with the model solution used for incubations. The Apo-Tf was then saturated with the ^{57}Fe-citrate solution previously synthesized (following the same incubation procedure used for the natural abundance Fe-citrate). The same strategy explained above was also applied for the purification of the ^{57}Fe saturated Tf. The isotopic composition of the ^{57}Fe-Tf spike was calculated by Fe isotope ratio measurements at medium resolution using the ICP-MS. The elemental concentrations of the isotopically enriched Fe-saturated Tf were determined by reverse ICP-IDMS using the corresponding standards of natural isotopic composition. The ^{57}Fe abundance was found to be 94.77 ± 0.12% and the obtained total concentration of Fe was 3.51 ± 0.05 μg g^{-1}. To demonstrate that the synthesized ^{57}Fe-Tf complex can be used over a large time scale for the analysis of different samples, its stability was studied over a period of one month. No significant changes on the isotopic composition were observed (more detailed information is presented in the Results and Discussion Section). Additionally, as previously described by del Castillo Busto et al.,[21] no replacement of ^{57}Fe by natural abundance Fe in the ^{57}Fe-Tf complex was found.

RESULTS AND DISCUSSION

Uptake of Fe by Tf under Physiological Conditions. Iron saturation of Apo-Tf has to be first established to avoid Fe isotopes exchange when applying IDMS to speciation analyses. Thus, the molar ratio Fe:Tf was first investigated using spectrophotometry and ICP-MS, both for the natural Fe-Tf and the isotopically enriched ^{57}Fe-Tf to demonstrate the Fe saturation. Furthermore, the complex stability and stoichiometry were evaluated spectrophotometrically. The detailed description of the methodology of Fe uptake used for the sample preparation is included as Supporting Information as well as the relationship

Table 2. Determination of Tf Concentrations in a Serum Reference Material by External Calibration GE-LA-ICP-MS[a]

sample preparation	laser ablation strategy	CRM [Tf][b] (g L^{-1})	RSD (%)	LOD Tf (g L^{-1})	analysis time[c]
stained gel (n = 3)	horizontally	2.45 ± 0.76	31	0.7	1.5 h
stained gel (n = 30)	horizontally	2.21 ± 0.10	5	0.7	18 h
stained gel (n = 3)	perpendicularly	2.07 ± 0.30	14	0.7	1.5 h
nonstained gel (n = 3)	perpendicularly	2.25 ± 0.18	8	0.2	4.5 h

[a] Comparison of different ablation strategies and sample preparation procedures. The precision of the measurements was calculated based on 1s-standard deviation from three independent replicates. [b] CRM ERM-DA470k: certified value 2.36 ± 0.08 g L^{-1} Tf [c] Including 5-points calibration and one sample (triplicate measurements)

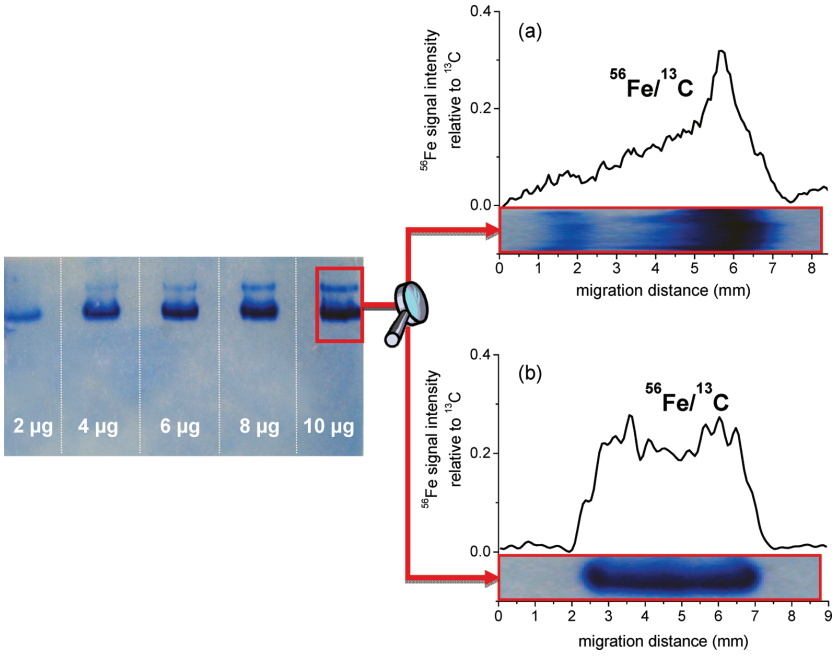

Figure 2. Nondenaturing gel after Coomassie blue staining of saturated Tf and ^{56}Fe/^{13}C profiles obtained by LA-ICP-MS. (a) Ablation of the protein spot horizontally to migration direction; (b) ablation of the protein spot perpendicular to migration direction.

observed between the absorbance measured at 465 nm and the Fe concentration used for incubation (Figure S1 of the Supporting Information, SI). The molar ratios of natural Fe:Tf and the ^{57}Fe:Tf spike were found to be 1.94 ± 0.09 and 1.88 ± 0.10, respectively, (close to the theoretical molar ratio of 2) and the Fe-Tf complex was stable during at least 4 weeks.

Quantification of Tf by External Calibration GE-LA-ICP-MS. The proposed species-specific IDMS method of quantification was compared with a conventional external calibration determination using our Fe-Tf standard solution. First, different sample preparation procedures and ablation strategies were evaluated. The external calibration was performed by using different concentrations of Fe-Tf to consider the behavior of the proteins under the selected electrophoretic conditions. The signal of ^{13}C (homogeneously distributed in the acrylamide gel) was employed as an internal standard to correct for any instrumental signal drift occurring during the ablation process. In all cases, triplicates of each Tf concentration (absolute amount between 2 and 10 µg) were submitted to gel electrophoretic separation using nondenaturing 1D-PAGE. Generally, after separation of proteins and Coomassie staining, the gel lanes were scanned by the laser beam in the electrophoretic migration direction, obtaining the corresponding electropherogram for the Fe, S, and C signal intensities as a function of the migration distance. For quantification purposes, signals were integrated with the *Origin* program and a reference serum sample (certified for total Tf) was analyzed. In this way, the accuracy and precision of LA-ICP-MS analyses was evaluated. Figure 1 shows the electropherogram obtained for the analysis of the CRM (3 µg of Tf). As can be seen, Fe was detected coordinated to Tf (~9 mm) as well as to albumin (~18 mm) to a high extent and to the immunoglobulins (0−5 mm) to a lower extent.

Four different external calibration approaches were investigated for the analysis of the certified serum sample, varying the ablation strategy (laser beam horizontal or perpendicular to the electrophoresis migration direction) and the sample preparation

(stained and nonstained gels). Table 2 shows a summary of the results obtained in these experiments aiming at the quantification of Tf in the CRM. Additionally, this table shows for comparison the observed required analysis time (LA-ICP-MS measurement time, excluding sample preparation time) and the limits of detection (LODs) for each calibration strategy. LODs were calculated by using the 3s criterion ($3s_b/S$), where s_b is the standard deviation of 5 independent measurements of the blank value (ablation of a pure polyacrylamide gel without protein spots) in cps and S is the sensitivity for the corresponding analyte isotope obtained by measuring the serum reference material. As can be seen in Table 2, the Tf concentrations determined by external calibration GE-LA-ICP-MS agreed quite well with the certified value (within the given uncertainties) in all cases. However, the required analysis time as well as the accuracy and precision were strongly dependent upon the conditions selected for the sample preparation and ablation strategy.

The Tf concentration determined by external calibration in stained gels using a single line ablation strategy (only one line per protein spot) in the same direction of migration (denoted as horizontally) showed results in agreement with the certified value, but a high standard deviation is apparent (relative standard deviation, RSD, ~30%). Figure 2a shows the electropherogram obtained for the analysis of a 10 μg Tf spot by LA-ICP-MS. As expected, increasing the number of analysis (10 single line ablations per protein spot) the precision obtained was significantly better (5% RSD). However, the sample analysis time (including a 5-point calibration and triplicate measurements of standards and sample) increase from 1.5 to 18 h for the multiple line ablation strategy. Thus, a different ablation strategy was investigated to overcome the inhomogeneous distribution of the protein inside the spot and its possible diffusion (due to the electrophoretic separation). As can be observed in Figure 2a, although no perfectly defined borders were visible for protein spots, the maximum intensity for ^{56}Fe signal was always identified at the center of the spot. Therefore, a single line ablation in the direction perpendicular of electrophoretic migration (only one line in the middle of each protein spot) was selected. Figure 2b collects the electropherogram obtained for the analysis of a 10 μg Tf spot using the perpendicular ablation strategy. As can be seen, ^{56}Fe profile was better defined than that obtained with the horizontal ablation and a 2-fold reduction in RSD value was found for the perpendicular strategy compared to the horizontal one (14% and 31% RSD, respectively). Such improvement in the precision could be attributed to a better counting statistics (the laser beam stays longer on the protein spot) and to a more homogeneous Fe distribution throughout the spot in this direction. It should be noted that the precision obtained for Tf quantification in this case was significantly worse than that for multiple ablation (14% vs 5%), but the analysis time was drastically reduced.

It has been recently reported by several authors[17,26] that Coomassie blue staining of the gels prior to LA-ICP-MS analysis can be a metals contamination source, which increase the Fe background in the gel and masks the real Fe content of the protein. Moreover, the reproducibility of the staining and destaining stages is quite low due to the concentration of the exogenous Fe, strongly depends on the duration and homogeneity of each stage. Aiming at avoiding such contamination source we also investigated the use of an external calibration in nonstained gels (and the proposed ablation strategy perpendicular to the migration direction). Since the proteins tend to diffuse in the gel after the electrophoretic separation, some actions must be taken to fix them in the gel. In our case, denaturation of the protein both chemically (by lowering the pH to 3) and thermally (by heating to 70 °C) were investigated. More accurate and precise results with the latter thermal strategy were observed. Figure 3 shows the Fe and S calibration curves obtained by LA-ICP-MS using the perpendicular ablation strategy. It should be stressed that as the spot (without staining) is currently not visible in the gels, a larger area had to be analyzed to ensure the protein spot ablation in its maximum. Thus, now the ablation of 3 lines per protein spot was carried out in all cases. As can be seen in Table 2, such calibration strategy allowed us to obtain not only a Tf concentration in agreement with the certified value, but with a good precision (similar RSD value to that obtain with n = 30) and in a reasonable analysis time. Additionally, Tf limit of detection was found to be 0.2 g L^{-1}, a value well below LODs recently reported by other authors.[26]

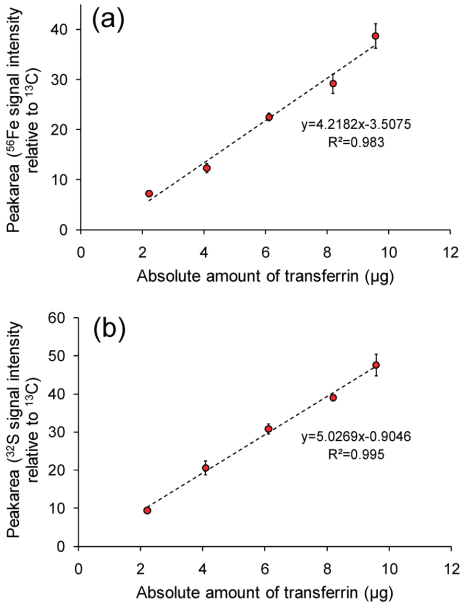

Figure 3. Calibration curves obtained for ^{56}Fe and ^{32}S (^{13}C as internal standard) by GE-LA-ICP- MS using a perpendicular ablation strategy (nondenaturing 1D-PAGE, nonstained gels). (a) ^{56}Fe; (b) ^{32}S.

Absolute Quantification of Tf by Species-Specific Isotope Dilution GE-LA-ICP-MS. Alternatively to external calibration, a species-specific quantification methodology based on the use of the previously synthesized isotopically enriched ^{57}Fe-Tf was tested. The ^{57}Fe-Tf spike was mixed up with the serum samples before the GE separation. Thus, matrix-matched quantification without any external standard with adequate corrections for all signal variations during the subsequent analysis (either derived from instrumental drift, varying mass ablation rates, etc.) was secured. Moreover, any possible analyte losses after the spiking (e.g., during sample handling and electrophoretic separation) will not affect the final concentration result. A successful isotope dilution analysis requires that the isotopically enriched ^{57}Fe-Tf added behaves chemically as the natural abundance Fe-Tf. Therefore, Apo-Tf saturated with natural Fe and isotopically

enriched ^{57}Fe-Tf were submitted to nondenaturing 1D-PAGE separations to compare their migration patterns. Figure 4a shows the protein spots observed corresponding to the natural and the isotopically enriched Fe-Tf standards, after Coomassie blue staining. As can be seen, the migration behavior was the same (expressed by a retention factor of $R_f = 0.25$), demonstrating that neither the charge nor the structure of the isotopically enriched protein was affected by the ^{57}Fe labeling procedure. In addition, it has to be stressed that no diffusion of the protein or protein cross contamination were observed.

For the analysis, a known amount of the ^{57}Fe-Tf spike was added to the certified human serum previously incubated with natural Fe-citrate for saturation. Samples were vortexed and left at room temperature during 5 min to guarantee the complete mixing and equilibration of Fe-Tf from the sample and the added isotopically enriched ^{57}Fe-Tf. Next, the CRM proteins were separated using nondenaturing 1D-PAGE and the nonstained gels were analyzed by LA-ICP-IDMS using the optimized ablation strategy perpendicular to the migration direction. As an example, Figure 4b shows the profile obtained for the analysis of the CRM (analyte/^{57}Fe-Tf spike ratio corresponding to a 1:1 proportion). Three different data treatment approaches to calculate the Fe isotope ratios were employed for comparison. First, ^{56}Fe and ^{57}Fe integrated areas within the protein spot along the LA-ICP-MS profiles (denoted as Integration in Table 3) were calculated. Second the ^{56}Fe/^{57}Fe point-by-point calculation of

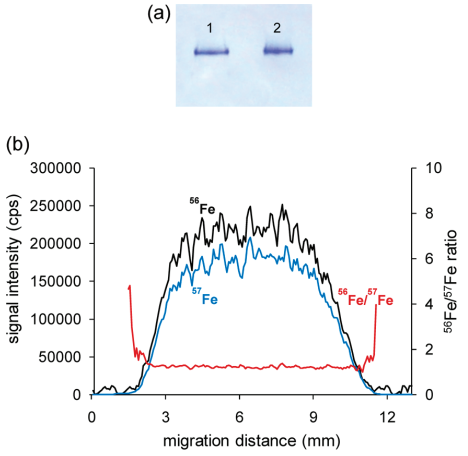

Figure 4. (a) Nondenaturing mini-gel after staining with Coomassie blue (2 μg Tf). Line 1- isotopically enriched ^{57}Fe-Tf; Line 2- natural abundance Tf. (b) Profiles obtained by LA-ICP-MS for ^{56}Fe, ^{57}Fe and their isotopic ratio using a mixture of the CRM and the isotopically enriched ^{57}Fe-Tf (13 μg natural Fe-Tf:14 μg ^{57}Fe-Tf).

average isotope ratios (point-by-point data in Table 3) was used to calculate the quantity of the natural Tf in the sample. Finally, a new strategy of isotopic ratios calculation recently described by Fietzke et al.[29] was also evaluated (corresponding to linear regression slope in Table 3). Here, we applied the described method for calculation of Fe isotope ratios using the INDEX LINEST function of MS EXCEL with the ^{56}Fe and ^{57}Fe signal intensities. This function calculates the statistics for a line by using the "least squares" method to determine a straight line that best fits the obtained data, and then returns an array that describes the line. In such a way, background correction and the subjective influence which may occur by setting the integration limits were avoided, simplifying enormously the evaluation of data. Although the linear regression slope treatment approach has been previously investigated for isotopic ratios measurements with a simultaneous detection by multicollector ICP-MS,[29,30] it should be highlighted that the present work shows, for the first time, the successful application of such signal processing using a slow signal acquisition detection.

Two mass bias correction approaches were investigated in this work by the measurement of natural abundance Fe isotope ratios in polyacrylamide gels of the human serum Tf standard (external correction) and by the continuous nebulization of a 10 ng g^{-1} natural abundance Ga standard solution (internal correction).[24] In both cases, the mass bias factor was calculated using the linear law model. The mathematical model used for the mass bias correction as well as the numerical differences observed between internal and external approaches are included as Supporting Information. As comparative studies showed similar results for internal and external mass bias correction strategies, the Ga standard solution was used for all the measurements. This means that the mass bias factor was performed in the same LA-ICP-MS profile by using a natural Ga standard with well-known isotopic composition. The final calculation of the GE-LA-ICP-IDMS results was carried out by using the conventional isotope dilution equation.[31]

The results obtained for the determination of Fe in the certified reference serum sample by species-specific GE-LA-ICP-IDMS are summarized in Table 3. As can be seen, the Tf concentration determined by the proposed species-specific IDMS method was in good agreement with the certified value, being the precision obtained significantly better than that obtained by external calibration; RSDs in the range of 0.9−2.7% depending on the data treatment procedure. The uncertainty for each individual measurement of Fe concentration was calculated according to the method proposed by Kragten.[31] A relative uncertainty (%) of 13.4% was obtained when external calibration was applied, whereas for the proposed species-specific IDMS methodology a relative uncertainty of 1.7% was found. Moreover, in order to study the influence of the different factors in the final uncertainty of the concentration values, we have calculated full uncertainty budgets for Fe in a representative analysis of the

Table 3. Determination of Tf Concentrations in a Serum Reference Material and Human Serum Samples by Species-Specific GE-LA-ICP-IDMS Using Three Different Data Treatment Approaches[a]

data treatment	CRM isotope ratio (^{56}Fe/^{57}Fe)	CRM [Tf][b] (g L^{-1})	human serum isotope ratio (^{56}Fe/^{57}Fe)	human serum [Tf][b] (g L^{-1})	analysis time[c]
integration	0.95 ± 0.03	2.40 ± 0.08	0.98 ± 0.02	2.48 ± 0.04	15 min
point-by-point	0.90 ± 0.01	2.28 ± 0.03	0.89 ± 0.01	2.24 ± 0.03	15 min
linear regression slope	0.92 ± 0.01	2.34 ± 0.02	0.93 ± 0.01	2.34 ± 0.04	15 min

[a] Standard deviation values are calculated from the mean of three measurements in three independent gels. [b] CRM ERM-DA470k: certified value 2.36 ± 0.08 g L^{-1} Tf [c] Triplicate measurements

dx.doi.org/10.1021/ac200780b |*Anal. Chem.* 2011, 83, 5353–5360

serum CRM. The corresponding uncertainty budgets demonstrated that the most important contributor to the uncertainty was the measurement of the $^{56}Fe/^{57}Fe$ isotope ratio for the isotope dilution procedure and the measurement of ^{56}Fe and ^{13}C signals and the y-intercept of the calibration curve for the external calibration. The uncertainty budget obtained for a representative analysis of the CRM by species-specific LA-ICP-IDMS can be observed in Table S1 of the SI.

Additionally, the analysis time (LA-ICP-MS measurement time, excluding sample preparation time) was drastically reduced to less than 15 min. Moreover, the quantification by species-specific GE-LA-ICP-IDMS provided accurate and precise results not only by analyzing the protein spot in the center position but also in adjacent ablation lines to the center with deviations from the certified value below 5%. It should be stressed here that by using the linear regression slope data treatment a significant improvement in the precision (0.9% RSD) and in the accuracy of the Tf concentration values were obtained (as compared to the results obtained by the other tested integration and point-by-point approaches). In addition, although a different instrumentation as well as ablation strategies were employed in previous IDMS approaches for the analysis of soils, sediments and crude and fuel oil samples, the precision obtained for the direct analysis of gels by species-specific LA-ICP-IDMS was significantly better that precisions reported in previous work using IDMS and LA-ICP-MS, where RSD values in the order of 15% were found.[23,24]

Finally, once the validation of the optimum quantification method was guaranteed by the analysis of the reference serum sample, the analysis of real life human serum samples from healthy volunteers was performed. A triplicate of a pool of serum samples was separated in nondenaturing 1D-PAGE following the Procedures section and the nonstained gels were analyzed by species-specific GE-LA-ICP-IDMS. Table 3 collects the results obtained using the three data treatment approaches. As can be observed, the Tf concentration obtained showed typical values reported for healthy human serum samples (similar to those obtained for the CRM). Although the comparison of the absolute amount of Tf from healthy volunteers and patients suffering from a disease affecting its concentration (e.g., hypotransferrinemia) would be an interesting application of the IDMS method for the evaluation as potential biomarker, such samples are not currently available in our laboratory.

CONCLUSIONS

While common GE-LA-ICP-MS is not a particularly accurate method, species-specific GE-LA-ICP-IDMS has been demonstrated here for the first time to provide an accurate, precise, and time-effective strategy for eventual absolute direct determinations of metalloproteins in serum samples (even at concentration of protein in the low gram per liter range). Compared with alternative quantification methodologies, no calibration curves or standard reference materials are necessary using the ID proposed method. Moreover, the sample analysis time is reduced to less than 15 min and precision and accuracy obtained for the analysis of a CRM were significantly better than those obtained by external calibration. The appropriate selection of the laser ablation strategy (single line ablation in the direction perpendicular to the electrophoretic migration) and of sample preparation (nondenaturing 1D-PAGE and nonstained gels) was found to be crucial to ensure a good precision and accuracy. Therefore, this enriched isotopes based analytical approach offers a tremendous potential to achieve reliable and direct metalloproteins quantification after conventional 1D and 2D gel electrophoretic separations. The use of such species-specific IDMS methods applied to LA-ICP-MS could open the door to meet the quality assurance requirements urgently needed in quantitative heteroatom-tagged protein analyses.[6] This work opens new avenues first, to uncover further potentialities of species-specific GE-LA-ICP-IDMS for other metalloproteins and, second, to apply such quantification potential of metal-biomolecules in biochemical, molecular biology, and medical sciences (e.g., detection of multiple proteins on one spot, immuno-microarray experiments, microarray-based multiplexed detection studies, etc.).

ASSOCIATED CONTENT

Supporting Information. The Supporting Information details the Experimental section of the manuscript concerning the description of the standards, reagents and samples employed in this work as well as a detailed explanation of the gel electrophoretic instrumentation and experimental conditions used. Furthermore, it includes a critical description of the Results and Discussion section of the Fe uptake by Tf under physiological conditions. A detailed explanation of the two models employed for the mass bias correction as well as the full uncertainty budget calculated for Fe in a representative analysis by species-specific LA-ICP-IDMS of the serum CRM are also included as Supporting Information. This material is available free of charge via the Internet at http://pubs.acs.org.

AUTHOR INFORMATION

Corresponding Author

*Tel/Fax: +34.985103474; E-mail: fernandezbeatriz@uniovi.es (B.F.); asm@uniovi.es(A.S.-M.).

ACKNOWLEDGMENT

Financial support from "Plan Nacional de I+D+I" (Spanish Ministry of Science and Innovation or MICINN, and FEDER Program) through MAT2010-20921-C02-01 and PCTI Asturias through the project FC-09-EQUIP09-29 is acknowledged. I.K. and B.F. are thankul for financial support from FPU and "Juan de la Cierva" Programs from the Ministry of Education and MICINN, respectively. Finally, the authors gratefully acknowledge the Laboratory for Clinical Analysis (Central University Hospital of Asturias, Spain) for providing the serum samples.

REFERENCES

(1) Mounicou, S.; Szpunar, J.; Lobinski, R. *Chem. Soc. Rev.* **2009**, *38*, 1119–1138.

(2) Lobinski, R.; Becker, J. S.; Haraguchi, H.; Sarkar, B. *Pure Appl. Chem.* **2010**, *82*, 493–504.

(3) Ballihaut, G.; Pécheyran, C.; Mounicou, S.; Preud'homme, H.; Grimaud, R.; Lobinski, R. *TrAC Trends Anal. Chem.* **2007**, *26*, 183–190.

(4) Becker, J. S.; Becker, J. S.; Lobinski, R. *Metallomics* **2009**, *1*, 312–316.

(5) Grebe, M.; Pröfrock, D.; Kakuschke, A.; Broekaert, J. A. C.; Prange, A. *Metallomics* **2011**, *3*, 176–185.

(6) Bettmer, J.; Montes-Bayón, M.; Ruiz-Encinar, J.; Fernández-Sánchez, M. L.; Fernández de la Campa, M.d.R.; Sanz-Medel, A. *J. Proteomics* **2009**, *72*, 989–1005.

(7) Sussulini, A.; Kratzin, H.; Jahn, O.; Banzato, C. E. M.; Arruda, M. A. Z.; Becker, J. S. *Anal. Chem.* **2010**, *82*, 5859–5864.

(8) Gauci, V. J.; Wright, E. P.; Coorssen, J. R. *J. Chem. Biol.* **2011**, *4*, 3–29.
(9) Becker, J. S.; Mounicou, S.; Zoriy, M. V.; Becker, J. S.; Lobinski, R. *Talanta* **2008**, *76*, 1183–1188.
(10) Nuevo Ordóñez, Y.; Deitrich, C. L.; Montes-Bayón, M.; Blanco-González, E.; Feldmann, J.; Sanz-Medel, A. *J. Anal. At. Spectrom.* **2011**, *26*, 150–155.
(11) Fernández, B.; Claverie, F.; Pécheyran, C.; Donard, O. F. X. *TrAC Trends Anal. Chem.* **2007**, *26*, 951–966.
(12) Neilsen, J. L.; Abildtrup, A.; Christensen, J.; Watson, P.; Cox, A.; McLeod, C. W. *Spectrochim. Acta B* **1998**, *53*, 339–345.
(13) Venkatachalam, A.; Koehler, C. U.; Feldmann, I.; Lampen, P.; Manz, A.; Roos, P. H.; Jakubowski, N. *J. Anal. At. Spectrom.* **2007**, *22*, 1023–1032.
(14) Ballihaut, G.; Kilpatrick, L. E.; Kilpatrick, E. L.; Davis, W. C. *J. Anal. At. Spectrom.* **2011**, *26*, 383–394.
(15) Raab, A.; Pioselli, B.; Munro, C.; Thomas-Oates, J.; Feldmann, J. *Electrophoresis* **2009**, *30*, 303–314.
(16) Becker, J. S.; Matusch, A.; Becker, J. S.; Wu, B.; Palm, C.; Becker, A. J.; Salber, D. *Int. J. Mass Spectrom.* 2011, DOI. 10.1016/j.ijms.2011.01.015
(17) Jiménez, M. S.; Rodríguez, L.; Gómez, M. T.; Castillo, J. R. *Talanta* **2010**, *81*, 241–247.
(18) O'Connor, C.; Sharp, B. L.; Evans, P. *J. Anal. Atom. Spectrom.* **2006**, *21*, 556–565.
(19) Pickhardt, C.; Izmer, A. V.; Zoriy, M. V.; Schaumlöffel, D.; Becker, J. S. *Int. J. Mass Spectrom.* **2006**, *248*, 136–141.
(20) Heumann, K. G. *Anal. Bioanal. Chem.* **2004**, *378*, 318–329.
(21) Del Castillo Busto, M. E.; Montes-Bayón, M.; Sanz-Medel, A. *Anal. Chem.* **2006**, *78*, 8218–8226.
(22) Sarmiento-González, A.; Encinar, J. R.; Cantarero-Roldán, A. M.; Marchante-Gayón, J. M.; Sanz-Medel, A. *Anal. Chem.* **2008**, *80*, 8702–8711.
(23) Heilmann, J.; Boulyga, S. F.; Heumann, K. G. *J. Anal. At. Spectrom.* **2009**, *24*, 385–390.
(24) Fernández, B.; Claverie, F.; Pécheyran, C.; Alexis, J.; Donard, O. F. X. *Anal. Chem.* **2008**, *80*, 6981–6994.
(25) Becker, J. S.; Sela, H.; Dobrowolska, J.; Zoriy, M.; Becker, J. S. *Int. J. Mass Spectrom.* **2008**, *270*, 1–7.
(26) Deitrich, C. L.; Braukmann, S.; Raab, A.; Munro, C.; Pioselli, B.; Krupp, E. M.; Thomas-Oates, J. E.; Feldmann, J. *Anal. Bioanal. Chem.* **2010**, *397*, 3515–3524.
(27) Sanz-Nebot, V.; González, P.; Toro, I.; Ribes, A.; Barbosa, J. *J. Chromatogr., B* **2003**, *798*, 1–7.
(28) Evans, R. W.; Rafique, R.; Zarea, A.; Rapisarda, C.; Cammack, R.; Evans, P. J.; Porter, J. B.; Hider, R. C. *J. Biol. Inorg. Chem.* **2008**, *13*, 57–74.
(29) Fietzke, J.; Liebetrau, V.; Günther, D.; Gürs, K.; Hametner, K.; Zumholz, K.; Hansteen, T. H.; Eisenhauer, A. *J. Anal. At. Spectrom.* **2008**, *23*, 955–961.
(30) Epov, V. N.; Berail, S.; Jimenez-Moreno, M.; Perrot, V.; Pecheyran, C.; Amouroux, D.; Donard, O. F. X. *Anal. Chem.* **2010**, *82*, 5652–5662.
(31) Heumann, K. G.; Rottmann, L.; Vogl, J. *J. Anal. At. Spectrom.* **1994**, *9*, 1351–1355.
(32) Kragten, J. *Analyst* **1994**, *119*, 2161–2165.

SUPPORTING INFORMATION

ABSOLUTE QUANTIFICATION OF HUMAN SERUM TRANSFERRIN BY SPECIES-SPECIFIC ISOTOPE DILUTION LASER ABLATION ICP-MS

Ioana Konz, Beatriz Fernández*, M. Luisa Fernández, Rosario Pereiro, Alfredo Sanz-Medel*

Department of Physical and Analytical Chemistry; Faculty of Chemistry; University of Oviedo; Julian Clavería, 8. 33006 Oviedo, Spain

*Corresponding author: fernandezbeatriz@uniovi.es; asm@uniovi.es

Abstract

The Supporting Information details the Experimental section of the manuscript concerning the description of the standards, reagents and samples employed in this work as well as a detailed explanation of the gel electrophoretic instrumentation and experimental conditions used. Furthermore, it includes a critical description of the Results and Discussion section of the Fe uptake by Tf under physiological conditions. The molar ratio Fe:Tf, complex stability and stoichiometry of natural Fe-Tf and isotopically enriched ^{57}Fe-Tf spike were evaluated by using spectrophotometry and ICP-MS. Figure S1 collects the relationship obtained between the absorbance measured at 465 nm and the Fe concentration used for incubation. Furthermore, a detailed explanation of the two models employed for the mass bias correction as well as the full uncertainty budget calculated for Fe in a representative analysis by species-specific LA-ICP-IDMS of the serum CRM are included as Supporting Information.

EXPERIMENTAL

Standards, Reagents and Samples. All chemicals and reagents used in this work were of analytical grade. Human serum Holo- and Apo-transferrin were purchased from Sigma-Aldrich (St. Louis, MO, USA). Tris(hydroxymethyl)-aminomethane (Tris), tetramethylethylenediamine (TEMED), sodium chloride, glycerol, bromophenol blue and sodium hydroxide were purchased from Merck (Darmstadt, Germany), whereas ammonium bicarbonate, sodium citrate, N,N'-methylene-bisacrylamide, glycine and acetic acid were from Sigma-Aldrich (St. Louis, MO, USA). Acrylamide was purchased from Fluka (Buchs, Switzerland) and ammonium persulfate (APS) and Coomassie® Brilliant Blue R-250 from Bio-Rad Laboratories (Hercules, CA, USA). Solvents, including methanol and ethanol were obtained from VWR Int. (Barcelona, Spain). Ga (1000 µg mL^{-1}) and Fe (1000 µg mL^{-1}) standard solutions were purchased from Merck (Darmstadt, Germany), while the S standard solutions were prepared from methionine (Sigma-Aldrich, St. Louis, MO, USA). All solutions were made up using high-purity deionized water from a Milli-Q system (18.2 MΩ cm^{-1} Millipore, Bedford, MA, USA).

The enriched isotopes ^{57}Fe (Fe_2O_3; 94.42 ± 0.01% ^{57}Fe) and ^{34}S (S; 99.96 ± 0.01% ^{34}S) were purchased from Cambridge Isotope Laboratories (Andover, MA, USA) and Euriso-top (Saclay, France), respectively. Spike solutions of ^{57}Fe and ^{34}S were prepared by dissolution of an accurately weighed amount of the solid enriched isotopes in nitric acid (Panreac, Barcelona, Spain). Isotope enriched spike solutions were then prepared from the corresponding stock solutions by dilution with Milli-Q water and acidifying with sub-boiled nitric acid. The spike solutions were characterized in terms of isotopic composition and concentration by ICP-MS. The elemental concentrations of the spike solutions were determined by reverse ICP-IDMS and were found to be 12.73 ± 0.26 µg g^{-1} for Fe and 66.81 ± 1.63 µg g^{-1} for S.

The certified reference material (CRM) ERM-DA470k/IFCC (serum protein reference material from JRC's Institute for Reference Materials and Measurements, Geel, Belgium) was employed for the validation of the proposed quantification methodology. Moreover, human serum samples from healthy volunteers were kindly provided by the Laboratory for Clinical Analysis (Central University Hospital of Asturias, Spain).

Instrumentation

Gel electrophoresis. The separation of protein standards and human serum samples was performed using a vertical mini-gel electrophoresis system (Mini-PROTEAN® Tetra Cell, Bio-Rad Laboratories, Hercules, CA, USA). Gels were hand-cast in mini-gel cassettes as follows: resolving gels were prepared at final concentrations of 8% acrylamide/0.2% bis-acrylamide, 375 mM Tris/HCl, pH 8.8 and 0.1% APS and TEMED. Stacking gels contained 5% acrylamide/0.1% bis-acrylamide, 63 mM Tris/HCl, pH 6.8 and 0.1% APS and TEMED. Both protein standards and serum samples were mixed in a 4:1 (*v*:*v*) ratio with 150 mM Tris/HCl, pH 8.8, 50% glycerol and bromophenol blue. Running buffer was prepared to final concentrations of 25 mM Tris and 200 mM glycine, pH 8.3. The running conditions were 300 V for 20 min or until bromophenol blue dye had migrated to the bottom of gel. For external calibration analyses a volume of 10 µL Fe-Tf standard (absolute amount of protein between 2 µg and 10 µg) was loaded into the gel. The serum proteins separation by 1D-PAGE was performed under non-denaturing conditions, avoiding the possible loss of metals associated to proteins.

Following electrophoresis, the gel cassettes were dismantled and the mini-gels were stained in freshly prepared and filtered Coomassie staining solution (10% acetic acid, 20% methanol) for 30 min. Next, the gels were destained in 10% acetic acid with 50% methanol until the gel background was clear. The gels were then placed in glycerol for 1 min and dried for at least 3 h in an oven at 70°C on filter paper (Whatman® paper) and covered with a transparent film (Saran™ Film) to protect them against contamination. Non-stained gels were carefully transferred into glycerol (as the stained gels), but neither Coomassie solution nor acetic acid and methanol were added. For LA-ICP-MS measurements, the filter papers with the gels were transferred into the ablation cell and, in all cases, LA-ICP-MS analyses were performed in the same day of gels preparation in order to minimize any possible diffusion of the proteins within the gel or into the sample substrate.

RESULTS AND DISCUSSION

Uptake of Fe by Tf under Physiological Conditions. Iron saturation of Apo-Tf has to be firstly established to avoid Fe isotopes exchange later on (a critical condition for any IDMS analyses). Thus, the molar ratio Fe:Tf was first investigated both using spectrophotometry and ICP-MS. Fe binding to Apo-Tf *in vitro* was prepared using a model solution containing Apo-Tf at the concentration level present in human blood serum (~ 31 µM) and this solution was incubated at room temperature with different amounts of Fe-citrate (between 2-40 µg g^{-1}). The saturation grade of Tf was first followed spectrophotometrically. A phenolate-to-Fe charge transfer transition at 465 nm arising from the binding of Fe to two tyrosine ligands is characteristic for the color of the Fe-Tf complex[i]. Therefore, a maximum in the absorbance at 465 nm is observed in the case of total saturation of Tf (molar ratio 2 Fe:1 Tf). In Figure S1, the absorbance measured at 465 nm is plotted against the Fe concentration used for saturation at different incubation times (up to 24 h). As can be observed, the absorbance reached a maximum value using Fe concentrations higher than 8 µg g^{-1} (2-fold excess) and 30 min of incubation time, remaining the absorbance constant independently of the Fe concentration and incubation time used. In order to guarantee Fe complete protein saturation a 4-fold excess of Fe^{+3} and 60 min incubation time were selected for all the subsequent measurements. The absorbance at 280 nm (amino acids with aromatic rings) was investigated as well to obtain additional information on the saturation grade and stability of the formed complex. In this case, the efficiency of Fe saturation was evaluated at room temperature and 37°C through the ratio of absorbance at 280 nm (total amount of protein) and 465 nm (saturation grade of Tf) by comparison with the ratio obtained for the totally saturated commercially available Holo-Tf. The results obtained indicated that the saturation of Tf at room temperature was more efficient than at 37°C and that the Fe-Tf complex was stable during at least 4 weeks when stored at 4°C.

The stoichiometry of the synthesized Fe-Tf complex was also investigated by ICP-IDMS after purification by ultrafiltration (as described in the Experimental Section). Three different solutions were selected for the study; the unfiltered solution of saturated Fe-Tf, the filtrate and the recovered residue in the filter. On one hand, the unfiltered solution was analyzed to obtain the total concentration of Fe and S in the sample, being the S concentration proportional to the amount of protein since all the S is bound to the protein. The Fe concentration reflects the amount of Fe used for

incubation, including the Fe bound to the Tf and the excess used for incubation. On the other hand, the filtrate should contain only the excess of Fe after incubation and the recovered residue should contain the purified Fe-saturated Tf. Fe and S concentrations were determined by ICP-IDMS using enriched ^{57}Fe and ^{34}S spike solutions, respectively. After quantification, the recovery of Fe and S, as well as the molar ratio of Fe to Tf, were calculated. The recoveries obtained for Fe (according to the amount of Fe used for the incubation) and S (corresponding to the weighed amount of protein) were always in the range of 95-105% and the molar ratio of Fe:Tf was found to be 1.94 ± 0.09, a value in agreement with the expected ratio and with the molar ratio calculated from Figure 1 (1.83 ± 0.04). Similarly the isotopically enriched ^{57}Fe-Tf was investigated for Fe saturation, complex stability and stoichiometry by spectrophotometry and reverse ICP-IDMS. The ^{57}Fe-Tf spike showed to be stable over a period of at least 4 weeks and the molar ratio Fe:Tf was found to be 1.88 ± 0.1.

Figure S1. *In vitro* study of the Tf saturation by Fe^{3+} added as natural Fe-citrate. Relationship between the absorbance measured at 465 nm and the Fe concentration used for incubation. Standard deviation values for 3 independent measurements below 2%.

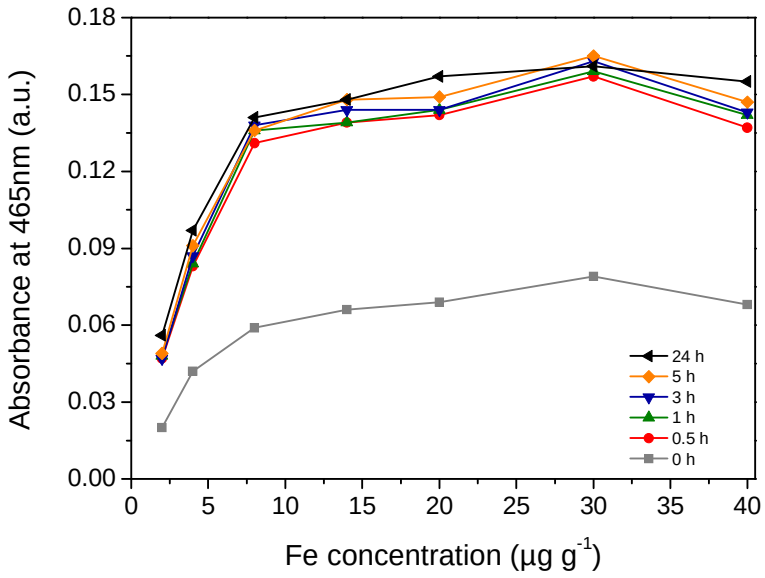

Mass Bias Correction. Two mass bias correction approaches were investigated in this work by the measurement of natural abundance Fe isotope ratios in polyacrylamide gels of a human serum Tf standard (external correction) and by the continuous nebulization of a 10 ng g^{-1} natural abundance Ga standard solution (internal correction)[ii]. In both cases, the mass bias factor, K, was calculated using the linear model with the equation:

$$K = \frac{(R_{exp} - R_{theo})}{R_{theo}\, x\, \Delta M}$$

where R_{exp} is the experimentally measured natural isotope ratio ($^{56}Fe/^{57}Fe$ for the external correction and $^{69}Ga/^{71}Ga$ for the internal correction), ΔM the mass difference between the isotopes and R_{theo} is the IUPAC tabulated 56/57 and 69/71 isotope ratios, respectively.

Comparative studies showed similar results for external and internal mass bias correction strategies and the calculated mass bias factor was found to be around -0.07 for the external correction and -0.06 for the internal correction. Thus, differences observed in the calculated Fe concentration by using the proposed species-specific LA-ICP-IDMS methodology were always below 1%. Since similar results were observed using the two strategies, the Ga standard solution was used for all the measurements. This means that the mass bias factor was performed in the same LA-ICP-MS profile by using a natural Ga standards with well-known isotopic composition.

Uncertainty Calculations. This section details the full uncertainty budget calculated for Fe in a representative analysis by species-specific LA-ICP-IDMS of the serum certified reference material. The standard uncertainty of each analysis was estimated using the spread sheet method of Kragten[iii], with the appropriate IDMS equation used as the model for these calculations.

Table S1. Relative contributions (%) of individual standard uncertainties to the total combined uncertainty for the determination of Fe by species-specific LA-ICP-IDMS in serum reference material ERM-DA470k/IFCC

UNCERTAINTY SOURCES Fe by Species-Specific LA-ICP-IDMS	**ERM-DA470k/IFCC**
Isotope Abundance for ^{56}Fe in the Sample	0.058
Isotope Abundance for ^{57}Fe in the Sample	<0.010
Isotope Abundance for ^{54}Fe in the Spike	<0.010
Isotope Abundance for ^{56}Fe in the Spike	0.038
Isotope Abundance for ^{57}Fe in the Spike	<0.010
Isotope Abundance for ^{58}Fe in the Spike	<0.010
Concentration of Fe in the Spike	0.28
Mass taken from the Sample	16.8
Mass taken from the Spike	25.9
Fe Atomic Weight in the Sample	0.046
Isotope Abundance for ^{69}Ga	0.98
Isotope Abundance for ^{71}Ga	2.2
Isotope Ratio of ^{69}Ga/^{71}Ga	0.62
Isotope Ratio of ^{56}Fe/^{57}Fe in the Mixture	53.0

REFERENCES

i. Quarles Jr., C. D.; Brumaghim, J. L.; Marcus, R. K. *Metallomics* **2010**, *2*, 792-799.

ii. Fernández, B.; Claverie, F.; Pécheyran, C.; Alexis, J.; Donard, O.F.X. *Anal. Chem.* **2008**, *80*, 6981-6994.

iii. Kragten, J.; *Analyst*, **1994**, *119*, 2161-2165.

Anal Bioanal Chem
DOI 10.1007/s00216-012-6023-6

REVIEW

Laser ablation ICP-MS for quantitative biomedical applications

Ioana Konz · Beatriz Fernández · M. Luisa Fernández · Rosario Pereiro · Alfredo Sanz-Medel

Received: 27 February 2012 / Revised: 27 March 2012 / Accepted: 4 April 2012

Abstract LA-ICP-MS allows precise, relatively fast, and spatially resolved measurements of elements and isotope ratios at trace and ultratrace concentration levels with minimal sample preparation. Over the past few years this technique has undergone rapid development, and it has been increasingly applied in many different fields, including biological and medical research. The analysis of essential, toxic, and therapeutic metals, metalloids, and nonmetals in biomedical tissues is a key task in the life sciences today, and LA-ICP-MS has proven to be an excellent complement to the organic MS techniques that are much more commonly employed in the biomedical field. In order to provide an appraisal of the fast progress that is occurring in this field, this review critically describes new developments for LA-ICP-MS as well as the most important applications of LA-ICP-MS, with particular emphasis placed on the quantitative imaging of elements in biological tissues, the analysis of heteroatom-tagged proteins after their separation and purification by gel electrophoresis, and the analysis of proteins that do not naturally have ICP-MS-detectable elements in their structures, thus necessitating the use of labelling strategies.

Published in the special issue *Young Investigators in Analytical and Bioanalytical Science* with guest editors S. Daunert, J. Bettmer, T. Hasegawa, Q. Wang and Y. Wei.

I. Konz · B. Fernández (✉) · M. L. Fernández · R. Pereiro · A. Sanz-Medel
Department of Physical and Analytical Chemistry,
Faculty of Chemistry, University of Oviedo,
Julian Clavería 8,
33006 Oviedo, Spain
e-mail: fernandezbeatriz@uniovi.es

Published online: 29 April 2012

Beatriz Fernandez obtained her European Ph.D. in 2006 at the University of Oviedo (Spain). She was awarded the Extraordinary Doctorate Prize (Analytical Chemistry) of the University of Oviedo and the San Alberto Magno Doctoral Thesis Award. Between 2006 and 2008 she was a postdoctoral researcher in the Laboratory of Bio-inorganic and Environmental Analytical Chemistry at the IPREM in Pau (France). Since September 2008 she has performed postdoctoral research in the Analytical Spectrometry Group in the Department of Physical and Analytical Chemistry of Oviedo University. Her main scientific interests are related to optical and mass spectrometry techniques for the direct analysis of solid materials. Her current research is mainly focused on elemental/molecular analysis of nanomaterials and thin films using GD-OES and GD-MS, and the analysis of biomedical, geological, and industrial samples by LA-ICP-MS.

Keywords Laser ablation inductively coupled plasma mass spectrometry · Gel electrophoresis · Quantitative bioimaging of heteroatoms · Heteroatom-tagged protein analysis · Protein labelling

Introduction

In recent years, much research effort has been directed towards the comprehensive study of metalloproteins, and many advances have been made in this field, mainly in relation to protein structures, metal site and function, and biological implications of metal–biomolecule interactions [1]. The great analytical challenge in this area is to combine specificity with high sensitivity. This is often difficult to achieve because of the complex compositions of biomedical

samples and the low concentration levels of the species of interest.

Mass spectrometry (MS) techniques offer great potential for the analysis of proteins and metalloproteins because they can provide unique elemental and molecular information that is of great value for enhancing our understanding of the roles of proteins in biological systems [2]. However, quantitative protein analysis is still one of the main challenges in the analytical and bioanalytical sciences [3]. Among the MS techniques available, laser ablation inductively coupled plasma mass spectrometry (LA-ICP-MS) is currently regarded as one of the most versatile inorganic MS tools for trace element and isotopic analyses of solids, including the analysis of heteroatom-tagged proteins in biological and medical tissues. The most striking features of LA-ICP-MS are its ease of use, high sensitivity, and its dynamic range, which covers up to twelve orders of magnitude, allowing the simultaneous acquisition of major, minor, and trace element constituents. Other useful features are its high spatial resolution (<1 μm) and small material uptake (<0.1 μg/s), which means that it is virtually nondestructive to samples on the macroscopic scale [4].

Biological heteroatom-relevant information can be addressed at different levels. Most often, bulk elemental analysis is carried out, so trace elements are determined after homogenisation of the biological sample, usually after an acid digestion. However, this approach is limited in many instances because it ignores not only the speciation of an element but also its spatial distribution. It can be stated that the meaning and value of trace element information in biological environments increases with the analytical sampling resolution, placing strict requirements on both the sensitivity and spatial resolution of the detection technique [5]. In this sense, during the last decade, LA-ICP-MS has established itself as a powerful tool for performing information-rich elemental analyses of biomedical samples.

The purpose of this review is to evaluate the progress of, recent developments in, and the most relevant applications of LA-ICP-MS for quantitative biomedical science and protein analysis. Thus, particular attention is paid to analytical quantification strategies, focusing on three areas of activity: elemental imaging in tissues, the analysis of naturally heteroatom-tagged proteins after their separation by gel electrophoresis, and the analysis of proteins that do not naturally possess ICP-MS-detectable elements in their structures, thus making it necessary to resort to labelling strategies.

Bioimaging of heteroatoms by LA-ICP-MS

Bioimaging analytical techniques are currently of great interest in life science studies, and have been rapidly growing in popularity for biomedical applications [6, 7]. To achieve a deeper understanding of complex biological processes at a tissue level, adequate analytical tools with spatial resolution in the nanometre region are increasingly needed. In this vein, LA-ICP-MS has demonstrated great potential, as it allows the spatially resolved analysis of heteroatoms (especially metals) in different types of tissues, including mouse kidney and heart tissues [8, 9], human lymph nodes and respiratory tissues [10, 11], as well as liver biopsy, breast cancer, and prostate tissues [12, 13]. The first work to report the analysis of fresh soft tissues by LA-ICP-MS was published in 2002 by Feldmann et al. [14], and it focussed on the analysis of thin sections of lamb's liver and kidney. The proof-of-concept for two-dimensional (2D) mapping was then reported for the analysis of Cu and Zn in sheep liver sections [15], showing the potential of LA-ICP-MS for the determination of nonuniform spatial distributions of elements throughout tissues. Since its introduction, LA-ICP-MS has found increasing use in studies of heteroatom distributions in biomedical tissues. In general, microlocal analysis is performed to study the accumulation of certain heteroatoms in the regions of interest, as well as to compare the distributions of different elements between control and diseased tissue.

In the last few years, LA-ICP-MS has been widely employed for metal and nonmetal imaging in brain tissue sections by the groups of McLeod [16], Doble [17, 18] and, particularly, Becker [19–23]. Metal accumulations in the brain appear to be directly linked to neurodegenerative processes (e.g. Alzheimer's, Parkinson's, or Wilson's diseases, ageing and ischaemia). Therefore, bioimaging of selected heteroatoms is a challenging (particularly in relation to metal quantification) and emerging field in brain research. Zoriy et al. [19] reported the quantitative imaging by LA-ICP-MS of element distributions in histological sections of glioblastoma multiforme, the most common primary human brain tumour. Frozen tissue sections were prepared from three different human glioblastoma specimens, and matrix-matched laboratory standards with defined concentrations of the analytes were prepared for calibration purposes. The Cu and Zn distributions showed similar localisations, which histologically corresponded to areas of intratumoral haemorrhage. Interestingly, both elements were found to be absent within the tumour. Moreover, the concentrations of all of the measured elements were lower in the glioblastoma multiforme tissue than in the control brain. In another quantification report, Matusch et al. [24] showed the potential of LA-ICP-MS to produce large series of quantitative maps of Cu, Zn, Fe, and Mn in native brain sections of mice that were subchronically intoxicated with the neurotoxin 1-methyl-4-phenyl-1,2,3,6-tetrahydropyridine (MPTP), as a model of Parkinson's disease. A defined sample area of brain tissue was ablated line by line with a focussed laser beam, and the distribution profiles of the metals were quantified using matrix-matched synthetic

laboratory standards. These calibration standards were prepared from brain homogenates of analogous control mice doped with the trace elements of interest at defined concentrations. Figure 1 shows quantitative LA-ICP-MS images reported for Cu, Zn, and Fe in brain sections from mice treated with the neurotoxin MPTP (2 h, 7 days, and 28 days after the last injection) compared to controls. Metal enrichments in different areas of the brain were observed in diseased mouse compared to the control brain.

So far, most of the quantitative works related to the imaging of heteroatoms in biomedical tissues by LA-ICP-MS have utilised synthetic laboratory standards for quantification. However, this is one of the most controversial aspects of quantitative imaging studies, from our point of view, due to the complexity of the sample matrix: careful control of the tissue thickness, water content, and density of each tissue region is required when synthesizing and selecting standards in order to avoid differences in the real laser–matter interaction and thus obtain precise and accurate measurements. Some critical points relating to the sample preparation step, the selection of instrumental parameters, and, particularly, reported normalisation approaches and quantification strategies when performing quantitative imaging by LA-ICP-MS are critically discussed in the following sections.

Sample preparation

The analysis of soft tissue samples by LA-ICP-MS is generally carried out using either paraffin-embedded or native frozen (stored at temperatures of around −70 °C) sections. The samples are sliced to about 20–200 μm in thickness and deposited on a flat surface (e.g. a glass slide). Both the thickness of the tissue and the laser parameters should be optimised for each specific application in order to ensure complete ablation of the tissue of interest, thus guaranteeing reproducible analyses. For the analysis of dried tissues, the laser ablation process can be performed at room temperature. However, the application of cooled laser ablation cells (commercially available from selected laser ablation companies or developed in research laboratories) has proved to be advantageous, not only for the analysis of cryopreserved materials, but also for dried biological samples [25, 26].

Two types of cooled ablation cells, developed originally by the working groups of Feldmann and Becker [14, 26], have been successfully employed for the elemental bioimaging of soft tissues [8, 15, 25]. Figure 2 shows schematic diagrams of these two ablation cells. Feldmann et al. [14] proposed a cryogenically cooled ablation cell with a temperature sensor and a copper cooling coil in the bottom of the cell. The sensor is connected to a temperature controller, which regulates the liquid nitrogen supply (stored in a dewar) to the ablation cell by a solenoid valve. In this case, the temperature can be controlled from −20 °C to −100 °C. On the other hand, Becker et al. [27] developed a cooled laser ablation cell. The cooling system is arranged such that two Peltier elements are connected serially under the target holder, made of Al. Using this setup, a target holder temperature of about −15 °C was observed. The use of cooled ablation cells led to higher signal stability and better sensitivity than seen for room temperature measurements, thus yielding precise and accurate analytical data.

However, most of the imaging studies reported by LA-ICP-MS are still carried out at room temperature, probably due to the high cost of commercial cooled systems. On the other hand, it should be noted that in both types of commercially available cells, the sensors do not measure the actual temperature of the sample—only that of the ablation cell surface. The measurement of sample temperature in situ is desirable, as it would allow better and faster control of the temperature in order to preserve sample integrity and the

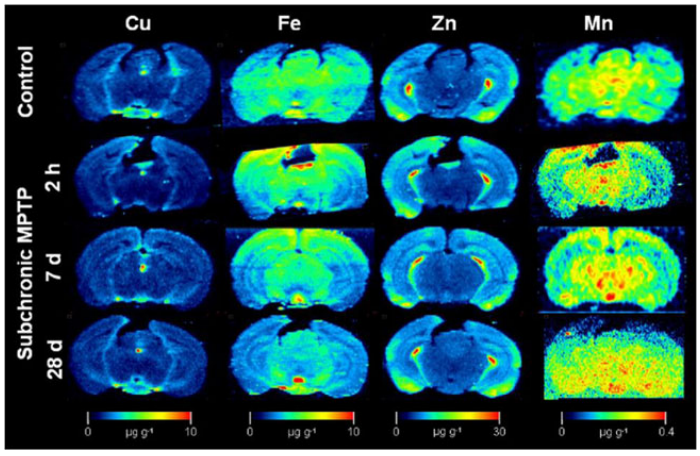

Fig. 1 Quantitative metal images of Cu, Zn, Fe, Mn representative of each group (control, 2 h, 7 days, and 28 days after the last of five daily MPTP injections). Sections obtained at a posterior level crossing the substantia nigra, the interpeduncular nucleus, and the hippocampus. From [24]; reproduced with the permission of the American Society for Mass Spectrometry

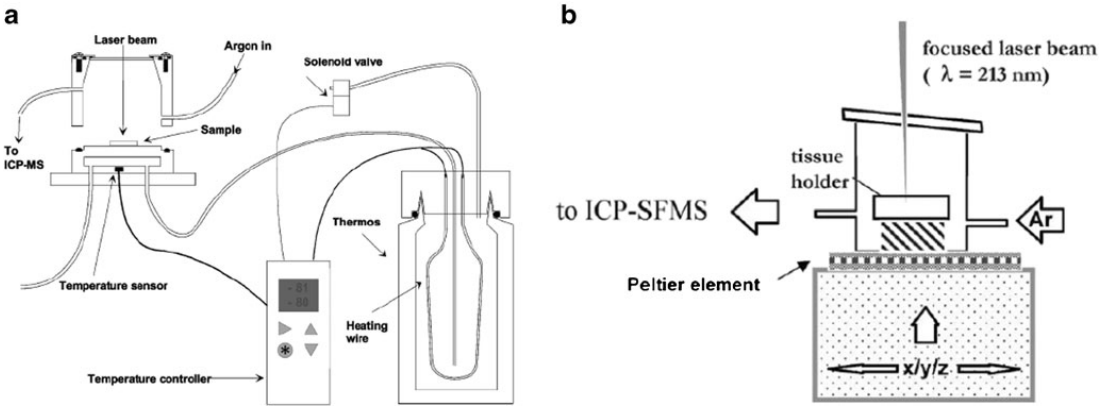

Fig. 2 **a**–**b** Schematics of the cryogenically cooled ablation cell (**a**) and the cooled PFA chamber (**b**) as proposed by the working groups of Feldmann and Becker, respectively. From [14, 27]; reproduced with the permission of The Royal Society of Chemistry

analytical conditions during the measurements (acquisition times of up to 30 h can easily be required for high-resolution imaging studies).

Optimisation of the laser and ICP-MS parameters

Despite the development of LA-ICP-MS for the imaging of elements in different types of tissues, spatial resolution, sensitivity, and data acquisition speed remain the main hurdles to achieving high-resolution images. Concerning spatial resolution, LA-ICP-MS analyses can easily be carried out using a 10 μm spot size, but achievable spatial resolution also depends on the integration time used and the washout time (through all of the transport system, including the ablation cell and transport tubing) of the laser-generated aerosol. Moreover, typical data acquisition times for a 5 mm^2 specimen can vary from over 2 h for a low-resolution image to more than 30 h for a more detailed image. As certain applications require high resolution, LA-ICP-MS requires significant reductions in analysis time to stay at the forefront of accessible μm-scale elemental imaging technology. Thus, the laser and ICP-MS parameters must be carefully selected for each particular sample to optimise the analytical conditions in terms of sensitivity, spatial resolution, and analysis time. Lear et al. [28] have recently investigated the relationship between laser scan speed, MS dwell time, and image resolution for the purpose of speeding up typical total acquisition times for constructing images of mice brain sections. It was observed that the original relative dimensions of the samples are maintained in LA-ICP-MS images if the laser scan speed is equal to the laser spot diameter divided by the scan cycle time in the MS. Thus, the maximum laser scan speed may be calculated from the dwell time, the number of *m*/*z* measured, and the detection limits required.

An interesting comparison between the elemental imaging capabilities of LA-ICP-MS and micro X-ray fluorescence (XRF) spectrometry was carried out for the model organism *Daphnia magna*, in terms of detection power and spatial resolution, by Gholap et al. [29]. Experimental results showed that the spatial resolution of LA-ICP-MS seems to be higher than that provided by micro-XRF. However, washout effects and spikes disturb the quality of the ICP-MS image to some extent. In the same way, Wang et al. [30] recently reported a complementary method for the high spatial resolution imaging of trace elements in heterogeneous media using LA-ICP-MS and synchrotron micro-XRF. It was observed that combining the outputs achievable by the two independent techniques enhances the imaging capabilities significantly. Nevertheless, it should be noted that the efficiency obtained using LA-ICP-MS measurements was comparatively low due to the slow washout of the ablation cell. In brief, a faster aerosol transportation system (to improve the spatial resolution) and the avoidance of signal deconvolution of experimental data (which has necessary up to now to obtain higher-quality imaging by decreasing the contribution of shot-to-shot overlap) would be aimed at.

Signal normalisation approaches

Different internal standards (IS) have been investigated for both qualitative and quantitative elemental bioimaging using LA-ICP-MS in order to account for matrix effects as well as variations in ablated mass, transported mass, and instrumental drift. An effective IS should behave in a similar manner to the analyte during the ablation process, during transport, and in the ICP. Additionally, it should be homogeneously distributed within the sample, which is one of the critical requirements to obtain accurate measurements in biomedical tissues. More conventional approaches to internal normalisation in elemental

bioimaging applications employ the ^{13}C signal [10, 15, 21]. However, ^{13}C is not always homogeneously distributed within the different structures of soft tissues, so it does not entirely satisfy the requirements of an IS. Moreover, ^{13}C is less sensitive to instrumental fluctuations than the analytes under investigation [31, 32].

Austin et al. [33] have recently reported a detailed study on the factors (e.g. laser spot diameter, mass bias, and cell sampling position) that affect IS selection for quantitative bioimaging of soft tissues. In that work, analyses of homogenised chicken breast sections were performed using ^{13}C, ^{52}Cr, ^{53}Cr and ^{101}Ru as internal standards. No single element was an ideal IS for all analytes; however, it was observed that normalisation greatly improved precision provided that the selected IS had a uniform distribution. Results showed that ^{13}C could be an acceptable IS for elemental bioimaging applications.

A new approach to elemental bioimaging by LA-ICP-MS that uses thin polymeric films spiked with elemental standards of the analytes and well selected ICP-MS internal standards (Ru and Y) as calibration standards has been recently proposed [34]. The tissue sample can be placed on top of a thin film containing an adequate IS. The use of Ru and Y internal standards improved the accuracy of quantification by LA-ICP-MS (whether no IS was used, or ^{13}C was employed as the IS).

Quantification strategies

Probably the more serious limitation of LA-ICP-MS for elemental bioimaging is the lack of reliable validated quantification strategies. On-line solution-based calibration has been investigated for quantitative analysis [25, 35]. The dual sample/standard approach was proposed to produce quantitative information in the absence of solid calibration standards: the laser-generated aerosol is combined with the aerosol generated by solution nebulisation of an aqueous calibration standard. Becker et al. reported two different solution-based calibrations for the bioimaging of heteroatoms in brain sections by inserting a micronebuliser into the laser ablation cell [25] and by introducing the two aerosols separately in the injector tube inside a special ICP torch [35]. In the first case, during the laser ablation of tissue, defined standard solutions with increasing concentrations were nebulised. In the second option, the dry aerosol produced by laser ablation of the sample and the wet aerosol generated by pneumatic nebulisation of standard solutions are carried by two separated flows of Ar and introduced directly into the injector tube of the ICP through two different apertures. The authors concluded that employing on-line solution-based calibration procedures leads to more standardised plasma conditions, and it buffers against the detrimental effects of sample loading. Obviously, these proposed external calibration approaches consider neither possible tissue inhomogeneities nor the different interaction between the laser beam and the biomedical tissue.

Most quantitative studies have relied upon certified reference materials (CRMs) or, especially, the preparation of matrix-matched laboratory standards. Examples of the former include the use of a CRM (LGC 7112) for single-point calibration in the quantification of trace elements in sheep liver [14] or the use of pressed pellets of CRMs (TORT-2, DOLT-2 and DORM-2) for the quantification of Cu, Zn and Fe in rat brain sections [31]. However, the most commonly employed calibration strategy is based on the use of matrix-matched standards prepared by spiking the tissues of interest with known amounts of aqueous standards [8, 19–22, 36–38]. Briefly, a set of matrix-matched homogenised laboratory standards with defined elemental concentrations are prepared. The homogenised tissue standards are frozen and cut into 20–100 μm sections and mounted on glass slides. The set of laboratory standards and the tissue are then analysed under the same experimental conditions. The final elemental concentrations in the prepared standards are verified (e.g. by ICP-MS) and their homogeneities can be investigated using LA-ICP-MS. Becker et al. [25] reported regression coefficients of the calibration curves of >0.9 using this methodology for the analysis of P, S, Fe, Cu, Zn, Th, and U in human brain samples. Nevertheless, it should be noted that this strategy does not take into account the inhomogeneity of the biomedical tissues and possible differences in water content and density within one tissue, so it is not possible to guarantee similar behaviour of samples and standards during the ablation process, during the transport of the laser-generated aerosol, and inside the ICP.

Two novel calibration approaches have been recently proposed for the quantitative elemental imaging of biomedical tissues by LA-ICP-MS. Austin et al. [34] investigated the use of thin film coated calibration standards prepared by spin coating for the quantification of Cu and Zn in chicken breast tissue. The tissues of interest were quantified using the calibration curves from the spin-coated standards (metal-spiked polymethylmethacrylate films) using Y and Ru as ISs. Figure 3a illustrates the concept of ablating the sample together with a film containing the IS and the workflow of the quantification process. The tissue samples were frozen and slices were cut precisely to a thickness of 20 μm and placed on top of spin-coated quartz. It was observed that the polymer matrix ablated in a similar way to soft tissue samples, and provided a much simpler, faster, and more reliable quantification methodology in comparison to homogenised tissue standards. On the other hand, Pugh et al. [39] proposed an alternative strategy for the quantitative imaging of Sr, Gd, and Pt. The approach is relatively simple and is based on spiking whole blood or blood serum with known amounts of elemental standards. Enriched aliquots are then frozen in a customised block and subjected to cryomicrotoming, thus

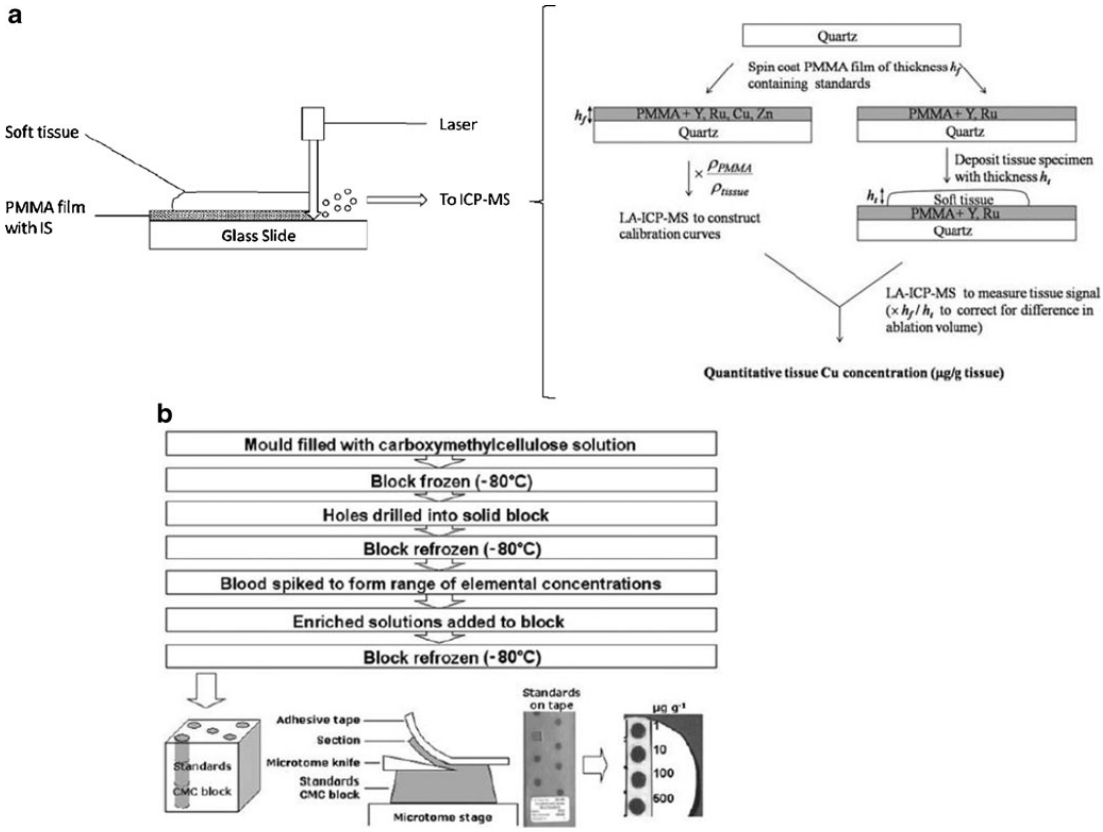

Fig. 3 **a**–**b** Schemes of the sample preparation and quantification processes used in two novel calibration strategies for the quantitative elemental imaging of biological soft tissues by LA-ICP-MS. **a** Internal standard scheme for elemental bioimaging and workflow of the quantification process with film standards. **b** Preparation of frozen matrix-matched standards. From [34, 39]; reproduced with the permission of The Royal Society of Chemistry

realising sections of comparable thickness to real samples (in the range of 20–60 μm). The preparation of thin section standards is presented in Fig. 3b. The proposed approach ensures that samples and standards are matched in terms of not only the chemical matrix but also the physical dimensions (i.e. section thickness). Moreover, lyophilisation, which is the norm in biological CRM production, is used during sample preparation, and this should permit the long-term storage and stability of prepared thin sections.

Analysis of heteroatom-containing proteins by LA-ICP-MS

The main analytical tools for the analysis of heteroatom-tagged proteins include chromatographic or electrophoretic separation of the target biomolecule and their subsequent identification by molecular MS techniques using an electrospray (ESI) or a matrix-assisted laser desorption ionisation (MALDI) source [40–42]. Several alternative elemental MS strategies have been developed to investigate the chemical speciation of the heteroatom bound to the protein, including LA-ICP-MS combined with a high-resolution separation technique.

Gel electrophoresis (GE), with its unique ability to resolve several thousands of proteins in a 2D run, is a powerful tool that is used routinely in biochemical, medical, and molecular biology laboratories today. Traditionally, detection of the heteroatom of interest relied on autoradiography, so radioactively labelled heteroatoms had to be used. An alternative technique to radioactive detection in the gels is LA-ICP-MS [43], the analytical potential of which has already been demonstrated for the detection of phosphoproteins, selenoproteins, and metalloproteins [41–45]. However, problems with GE-LA-ICP-MS analysis have been identified, which are related to both sample preparation and electrophoretic separation processes as well as to the laser–matter interaction [46]. In

spite of the significant number of studies dedicated to the optimisation of sample preparation and the effective separation of proteins (e.g. their stability during GE and post-separation gel treatment), accurate quantitative analysis still remains an important challenge.

Basic studies on gel electrophoresis LA-ICP-MS

GE-LA-ICP-MS has been applied for the qualitative and quantitative analysis of different types of heteroatom-containing proteins. Preliminary and basic studies performed over the last decade to assess its analytical potential have, however, focused on elemental analysis. The first work to explore the detection of trace elements in gels after electrophoretic separation using LA-ICP-MS was published in 1998 by Neilsen et al. [47], and centred on the analysis of Co-binding serum proteins. Chéry et al. [48] studied the capabilities of LA-ICP-MS for the detection of selenoproteins in red blood cell extracts and in yeast after 1D and 2D separations using polyacrylamide gels (PAGE). Limits of detection, linearity, and repeatability were evaluated for a whole range of elements using hydrated gels with standard solutions, and they showed that at least semiquantitative detection can be achieved.

A critical prerequisite in metal–protein speciation, however, is to maintain the integrity of heteroatom–protein binding during the whole sample preparation process, including the separation stage. In most applications reported for heteroatom–protein analysis by PAGE-LA-ICP-MS, the analytes were metal- or semimetal-containing proteins such as selenoproteins [48–51], as well as phosphoproteins [52–54]. In such cases the heteroelements are incorporated into the primary protein structure (pure covalent bonds), so the heteroatom–protein bond is not broken during electrophoretic separation. However, in metal–protein binding, the interactions are coordinative, and loss of the metal may occur during electrophoretic separation (especially when using denaturing PAGE). This is a serious pitfall that researchers need to tackle, so the development of new strategies for separating metalloproteins without breaking the metal–protein bond—or at the very least the discovery of accurate and precise quantification strategies that can correct for the possible losses—is urgently needed.

Several authors have reported studies on metal losses in proteins during GE [55–59]. In most cases, the use of native PAGE instead of denaturing PAGE was proposed as the best option to minimise the possible losses. For instance, McLeod's working group [55] investigated the behaviour of Pt-serum binding proteins by LA-ICP-MS after both native and denaturing PAGE. While clear Pt signals were obtained for the proteins of interest using native PAGE, no signals were found after using denaturing separation conditions (see Fig. 4). Those results showed that metalloprotein complexes

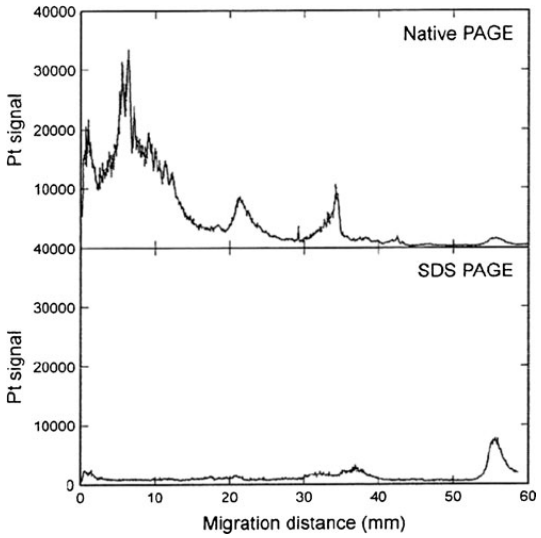

Fig. 4 ^{195}Pt profile obtained by LA-ICP-MS for the analysis of a Pt-enriched blood serum sample using native and denaturing PAGE. From [55]; reproduced with the permission of Wiley-VCH

may have limited conditional stability and, therefore, they should be studied under native rather than denaturing conditions. Moreover, it was found that denaturing PAGE was unsuitable for the absolute quantification of proteins via the metal due to its partial loss during separation (e.g. in coordinative metal-bound proteins, such as Fe in transferrin) [59]. An alternative approach is the use of GE in combination with electroblotting onto nitrocellulose or PVDF membranes. Proteins can be favourably detected using this technique, not only directly in agarose or polyacrylamide gels, but also after blotting onto membranes. This strategy looks particularly promising for the analysis of phosphoproteins by LA-ICP-MS: a matrix separation can be performed to reduce blanks from buffers used for sample preparation, and the proteins are enriched in a thin surface layer. Nevertheless, losses during blotting are often mentioned as a limiting factor as well [60–63], and these are particularly critical when aiming for accurate quantitative analyses.

However, other factors beyond the conditions of the electrophoretic separation can alter the observed metal–protein binding. Several studies have been devoted to investigating the stability of metalloproteins during GE and post-separation gel treatments [64–66]. Raab et al. [64] recently reported a study on the conditions necessary for effective and accurate application of GE-LA-ICP-MS in the analysis of metal-binding proteins. Experimental results showed some important points: (i) it is necessary to use nondenaturing separating conditions for most metalloproteins, since SDS and other denaturing agents can dissociate most metal–protein complexes; (ii) the use of

unstained gels is recommended, since elemental losses during staining procedures with silver or Coomassie Blue were generally observed; (iii) although several gel drying processes can be employed, the use of glycerol followed by heating proved to be a suitable drying method that did not result in extensive elemental loss; and (iv) elemental contamination of the gel surface should be avoided by using clean-room facilities when available. Therefore, it can be concluded that a separation protocol or speciation workflow that has been specifically selected for proteins cannot be directly extrapolated to metal–protein complexes. The separation conditions and the post-separation gel treatments for each specific application required should be carefully assessed.

Quantification strategies

Having gathered swathes of qualitative information over the last few decades, it is clear that studies performed in the field of proteomics is now turning quantitative [67]. The natural presence of a heteroatom in a given protein enables the application of elemental MS in the field of heteroatom-tagged proteomics, permitting a robust and sensitive approach to protein quantification [45, 55, 68]. In the case of proteins separated by GE using LA-ICP-MS, different calibration strategies have been investigated for protein quantitative analysis. The main proposed approaches have focused on external calibration and the use of isotope dilution mass spectrometry (IDMS).

External calibration methods have traditionally been used for quantitative protein analysis by GE-LA-ICP-MS using protein standards. Several examples can be found in the literature of the analysis of selenoproteins, phosphoproteins, and metalloproteins [40, 49, 52, 69–71]. External calibration is usually carried out by separating a standard model protein present at different concentration levels in the gels. Protein bands are then scanned by the laser beam in the direction of electrophoresis migration and the calibration curve is obtained by integrating LA-ICP-MS profiles of standards. The quantification of a given protein, such as the standard [71] or other proteins [49, 52, 69], has been reported. Also, hydrated gels with standard solutions containing increasing concentrations of the elements of interest have been used for calibration purposes [48, 72]. The main drawbacks of this strategy are the difficulty involved in ensuring a homogeneous distribution of the heteroelements in the gel, and the need for gel mineralisation afterwards to control the hydration efficiency. In addition, this strategy is clearly not applicable to proteins that are electroblotted onto nitrocellulose or PVDF membranes. Becker et al. [53] proposed a new quantification procedure using a solution-based calibration, where an ultrasonic nebuliser for the nebulisation of calibration standard solutions was coupled to the laser ablation chamber. It should be stressed, however, that such an approach can only be accurate if the particle size distribution of the laser-generated aerosol is well represented by the ultrasonically generated aerosol and is constant during ablation. Moreover, transport, vaporisation, and ionisation must be identical for both types of aerosol—a very difficult task to achieve.

However, these external calibration approaches do not consider the behaviour of proteins under the conditions used for electrophoresis, and do not compensate for possible inhomogeneities in a protein GE spot. Moreover, as stressed above, differences in the sampling rate and aerosol transport efficiency can occur using solution-based calibration, so the laser ablation of solid samples and simultaneous nebulisation of aqueous standards may not match each other. In the search for more accurate alternative quantification strategies, isotope ratio measurements (such as the use of IDMS) have been recently proposed for reliable quantitative protein analysis by GE-LA-ICP-MS. IDMS is internationally regarded as an absolute measurement method that is directly traceable to the International System of Units [73]. In contrast to other calibration strategies, the analytical result is not affected by signal drifts, matrix effects, or analyte losses. Therefore, the quantification of heteroatom-containing proteins by GE-LA-ICP-MS can be improved by adding an isotopically enriched protein at the beginning of the sample preparation procedure (so-called species-specific spiking). In this case, possible analyte losses during electrophoretic separation or transformations of the heteroatom-tagged species will not affect the final results. Additionally, LA-ICP-IDMS can also correct for some common fractionation and matrix effects that cannot be controlled using other calibration procedures. So far, however, only a few investigations have assessed the analytical performance of IDMS in combination with GE-LA-ICP-MS [71, 74, 75].

Deitrich et al. [75] reported the use of an isotopically enriched ^{65}Cu, ^{68}Zn-superoxide dismutase (SOD) complex in an attempt to quantify natural SOD in a spiked liver extract subjected to nondenaturing 1D-PAGE. The stability of the isotopically enriched metal–protein complex was carefully investigated. However, the absolute quantification capabilities of IDMS could not be demonstrated, as the reference materials needed to validate the proposed quantification approach were lacking. Recently, Konz et al. [71] carried out the absolute quantification of a metalloprotein (transferrin, Tf) that was separated by nondenaturing GE using LA-ICP-MS in combination with IDMS. The proposed methodology was based on the use of an isotopically enriched ^{57}Fe–Tf complex to quantify natural Tf in human serum. Figure 5 shows the profiles obtained by LA-ICP-MS for ^{56}Fe, ^{57}Fe, and their isotopic ratio using a mixture of the isotopically enriched ^{57}Fe–Tf complex and the sample of interest (a human serum CRM). Additionally, appropriate selection of the laser ablation strategy (single line ablation in

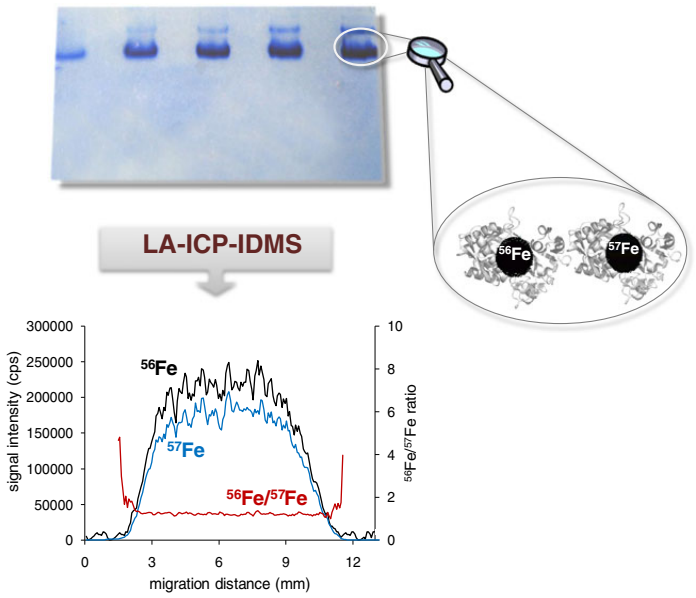

Fig. 5 Profiles obtained by LA-ICP-MS for $^{56}Fe^{+}$, $^{57}Fe^{+}$, and their isotopic ratio, using a mixture of a serum CRM and an isotopically enriched ^{57}Fe–Tf complex (13 μg natural Fe–Tf:14 μg ^{57}Fe–Tf). From [71]; reproduced with the permission of the American Chemical Society

the direction perpendicular to the electrophoretic migration), the sample preparation method (nondenaturing 1D-PAGE and unstained gels), as well as the data treatment approach (using a least squares method) was found to be crucial to ensuring good precision and accuracy. In contrast to alternative quantification methodologies, calibration curves are unnecessary, and the analysis time is reduced to less than 15 min [71].

Elemental tagging for peptides and proteins in LA-ICP-MS analysis

As explained in the preceding section, LA-ICP-MS has been successfully used for the measurement of heteroatoms that are naturally directly associated with proteins in tissues (e.g. P, S, Se, or metals). However, this technique could also be applied to the analysis of biomolecules that do not naturally have detectable heteroelements present in their structures, by using appropriate labelling strategies [76]. ICP-MS-detectable heteroatom tags can be bioconjugated to biomolecules [77, 78] to extend the applicability of "heteroatom (isotope)-tagged, or ICP-MS guided, targeted proteomics" [42]. Different labelling approaches have been investigated for the specific detection of proteins. Although there are many reports on elemental labelling for quantitative peptide and protein analysis in solution by ICP-MS [76, 78], in-depth investigations to assess the analytical potential of LA-ICP-MS in combination with labelling approaches are so far scarce.

Protein labelling with element-tagged antibodies for LA-ICP-MS

Immunoassays are currently the most popular analytical technique applied in clinical medicine for the detection and measurement of a large number of biomolecules (i.e. hormones, proteins, enzymes, drugs, nutritional factors, and disease markers) [79]. Immunoassays are simple, rapid, inexpensive, and versatile, and they are very amenable to automation and multiplexing. The capabilities of element-tagged immunoassay technology that employs ICP-MS detection of element-containing tags was first reported by Zhang et al. [80] and Baranov et al. [81]. Based on these pioneering works, several concepts and applications have been developed for protein determination by ICP-MS [76, 78]. In this paper, the use of element-tagged antibodies for protein detection by LA-ICP-MS is reviewed.

Lanthanides are the elements that are most widely used for this type of labelling study due to their absence in biological systems and the high stability of their chelate complexes. The labelling of three different polyclonal antibodies with lanthanides to enable the detection of those elements by LA-ICP-MS on Western blot membranes was reported by Waentig et al. [82]. An alternative to this strategy is to use metal clusters as the antibody tag; this approach has the advantage of increasing the detection limits for LA-ICP-MS measurements because the number of metal atoms per cluster is high [83].

Recent developments in element-tagged immunoassay technology employing ICP-MS have focused on multiplexed

immunoassays; that is, the detection and quantification of several analytes simultaneously [84]. In homogeneous immunoassays, in which the reagents are adsorbed onto surfaces, many handling steps are performed before the final measurement. The ability of LA to analyse solid samples directly provides a much simpler and faster method of analysing these immunoplates. The potential of immunoassays with element-tagged antibodies (or antigens) employed in combination with LA-ICP-MS detection for multiplexing assays has been demonstrated in several reports [82, 85, 86]. Waentig et al. [86] recently presented a method for the multiparametric and simultaneous quantitative determination of several cytochromes P450 in liver microsomes of untreated and inducer-treated (treated with various chemicals, including carcinogens and drugs) rats by LA-ICP-MS. Liver microsomal proteins were separated by SDS-PAGE and subsequently blotted onto nitrocellulose membranes. The resulting blots were simultaneously incubated with five different lanthanide-labelled antibodies, with an additional one used as an IS. The lanes were subsequently ablated by the laser beam and analysed by ICP-MS for ^{165}Ho, ^{169}Tm, ^{175}Lu, ^{153}Eu, ^{159}Tb, and ^{141}Pr. In this way, multiple isoforms of the cytochrome P450 enzymes could be simultaneously determined by LA-ICP-MS.

Protein microarrays provide a powerful multiplexing approach, when used in combination with laser sampling, for detecting proteins, monitoring their expression levels, and investigating protein interactions and functions. The potential of LA-ICP-MS combined with protein microarray technology and multielemental immunotags was recently explored by Hu et al. [87] for the detection of three model proteins. In that study, α-fetoprotein IgG (AFP), carcinoembryonic antigen (CEA), and human IgG were detected on the basis of sandwich-type immunoreactions on a microarray (with Sm^{3+} labelling for AFP, Eu^{3+} labelling for CEA, and Au nanoparticle labelling for IgG, respectively). Figure 6 shows a laser ablation sampling scheme for detecting three analytes on each spot of a microarray, and the transient signals obtained by LA-ICP-MS from spots of dried droplets on a glass slide when element-tagged antibodies were added. Experimental results proved that LA-ICP-MS can detect multiple proteins in each microarray spot with micrometre-range spatial resolution. Additionally, it was observed that the

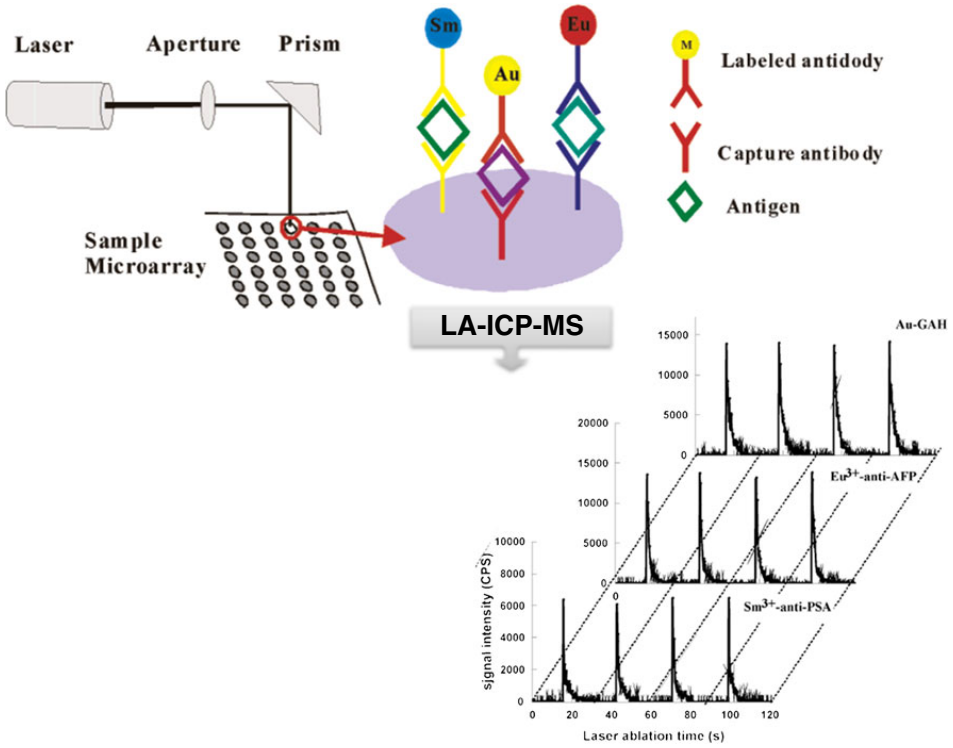

Fig. 6 Scheme for laser ablation sampling of a microarray with multiple analytes in each spot, and the transient signals obtained by LA-ICP-MS from spots of dried droplets on a glass slide when element-tagged antibodies were added: Eu^{3+}-labelled anti-AFP (α-fetoprotein antibody), Sm^{3+}-labelled anti-PSA (prostate-specific antigen), and colloidal Au-labelled GAH (goat-anti-human IgG). From [87]; reproduced with the permission of the American Chemical Society

detection limits of the proposed method (reported to lie in the range 0.012–0.2 ng mL^{-1} for a protein concentration of 1.0 ng mL^{-1}) decreased further still when nanoparticles were used as tags instead of rare-earth ion complexes.

A further application of LA-ICP-MS in this research area is the use of element-tagged immunoassays for imaging purposes, which provides a new strategy for not only mapping peptides and proteins in different types of tissues, but also for their possible quantification [13, 16, 88, 89]. In this vein, Hutchinson et al. [16] reported the imaging of amyloid precursor protein and Aβ peptide in histological sections of a transgenic mouse model of Alzheimer's disease using Eu- and Ni-coupled antibodies. Also, images and the distributions of endogenous metal trace elements in brain sections can be obtained simultaneously with the Eu and Ni measurements. Moreover, combining laser capture microdissection and ICP-MS provides a strategy for microanalysing immunohistochemical sections and an additional route for characterising Aβ deposits of associated trace elements in brain.

The analytical potential of immunohistochemistry combined with LA-ICP-MS has also been demonstrated for the imaging of cancer biomarkers [88, 89]. The distributions of two breast cancer-associated proteins (MUC-1 and HER2) were studied based on multiple line scanning of tissue sections by the laser beam and the subsequent measurement of relevant Au/Ag-tagged antibodies bound to the tissue. Results showed a good correlation between optical microscopy and LA-ICP-MS measurements in terms of feature information, and permitted analysis with a high sensitivity and sufficient resolution to permit fine-scale feature mapping at the cellular level.

Protein labelling using small molecules that form covalent bonds

As an alternative to element-tagged antibodies, proteins can be labelled by iodination, mercury-containing compounds, or metal chelates. Iodination has been widely used to label peptides and proteins, and has proven to be a simple, cheap, and efficient method based on the covalent binding of a heteroatom to a protein for solution ICP-MS detection. The reaction is based on the electrophilic substitution of iodine in histidine and tyrosine [90]. Different protocols for protein iodination have been applied for the LA-ICP-MS detection of intact proteins that have been separated by SDS-PAGE and electroblotted onto nitrocellulose membrane [91, 92]. The iodination efficiencies of single proteins (lysozyme, BSA, cytochrome C450, and β-casein), a whole proteome (microsomal proteome of rats), and antibodies (anti-bovine casein, anti-BSA) with potassium triiodide have been demonstrated, with minimal losses of antigen properties and antibody-binding ability observed [92]. Moreover, compared with previous experiences applying lanthanide-labelled antibodies for the detection of antigens, the iodine labelling of a whole proteome or of given markers looks very promising. Recently, Giesen et al. [13] reported the first application of iodination for imaging single cells in tissue sections by LA-ICP-MS. This method provides information on cell morphology. Mercury compounds can also be employed as protein ICP-MS tag reagents, since mercury can form highly stable covalent bonds with free sulfhydryl groups in proteins, as presented by Kutscher et al. [74]. In this work, the potential of a mercury tag for the sensitive detection of ovalbumin protein separated on PAGE gels, after labelling with *p*-hydroxymercuribenzoic acid (pHMB) and finally using LA-ICP-MS, was studied in detail. For quantification purposes, the use of label-specific IDMS (using ^{199}Hg-enriched pHMB) was found to improve the precision and accuracy of the quantitative results obtained.

An alternative labelling approach for the specific detection of proteins is to use metal chelates. A metal ion can be attached to a biological molecule via bifunctionalised chelating reagents; these contain a metal-chelating group (metal tag) and a second functional group that forms a covalent bond to the desired molecule (bioconjugation). Among several metal chelates described in the literature, lanthanide DOTA chelate (1,4,7,10-tetraazacyclododecane-1,4,7,10-tetraacetic acid) seems to be the most versatile [77]. Such a bifunctional chelate has been successfully applied by Jakubowski et al. for the multielement labelling of proteins separated by SDS-PAGE [93]. Detection was performed by LA-ICP-MS after electroblotting the target proteins onto nitrocellulose membranes. Two different proteins (BSA and hen egg white lysozyme) were labelled with the commercially available chelating compound DOTA containing stable isotopes of lanthanides (labelling with Eu, Tb, and Ho was successfully performed and studied). Compared to reported strategies that use iodine labelling [13, 92], the DOTA approach was found to be more laborious and time-consuming, but it is still promising, as it can be used to develop multiplexed procedures for proteins (and antibodies).

Conclusions

In recent years, LA-ICP-MS has been shown to be a powerful analytical tool for imaging (mapping) the distributions of metals and nonmetals in thin sections of biological tissues. Its high sensitivity, excellent spatial resolution, absolute quantification capability, robustness, and ability to carry out isotope ratio measurements with great accuracy are opening new avenues for the application of LA-ICP-MS in the life sciences [94–96].

Various quantification strategies have been reported so far, and there is no consensus regarding a preferred approach as yet. This is particularly important in relation to the growing

number of bioimaging applications that have appeared in the literature lately [97]. Thus, there is a clear need to develop reliable methodologies for LA-ICP-MS robust elemental determinations and to search for universal calibration methods for the absolute quantitative imaging of heteroatoms in tissues, and there is indeed a trend for studies focussing on these goals.

Concerning protein analysis, information provided by elemental LA-ICP-MS has been demonstrated to be complementary to that achieved by present molecular MS instruments (i.e. MALDI-MS or ESI-MS) [2, 98, 99]. It is worth highlighting, however, that combining LA-ICP-MS and protein fingerprinting methods ("integrated speciation" by heteroatom-tagged proteomics) helps to overcome some of the current limitations of the approaches more commonly used in proteomics. Information from both molecular and elemental mass spectrometry can be applied to discover new biomarkers and to study metal–biomolecule complexes and their interactions. In addition, new developments in imaging MS enable the spatial resolution of metalloproteins in tissues to be investigated. As an example, investigating interactions of proteins with small molecules by combining LA-ICP-MS and typical organic MS techniques will lead to precious information on the metal loading of proteins in diseased states, the identification of drug targets, and the development of new targeted proteomics approaches (e.g. via the quantification of appropriate biomarkers). It is expected that LA-ICP-MS will offer new insights into the molecular bases of diseases related to metals and other heteroatoms, and the differences between between normal and altered (disease) states. Moreover, multiplexed analytical methods based on LA-ICP-MS, which use metal-containing labels as elemental tags and possess great potential for the quantification of several biomarkers in microarrays, are currently being developed. Finally, LA-ICP-MS could provide a useful tool for obtaining valuable information for the early detection (diagnosis) and treatment (drug targets) of diseases, including cancer and neurodegenerative conditions [100].

Acknowledgements Financial support from "Plan Nacional de I + D + I" (Spanish Ministry of Science and Innovation or MICINN and the EU FEDER program) through MAT2010-20921-C02 and PCTI Asturias through the project FC-09-EQUIP09-29 is acknowledged. I. Konz and B. Fernandez are thankful for financial support from FPU and "Juan de la Cierva" Programs from the Ministry of Education and MICINN, respectively.

References

1. Mounicou S, Szpunar J, Lobinski R (2009) Chem Soc Rev 38:1119–1138
2. Careri M, Mangia A (2011) Anal Bioanal Chem 399:2585–2595
3. Bettmer J (2010) Anal Bioanal Chem 397:3495–3502
4. Koch J, Günther D (2011) Appl Spectrosc 65:155A–162A
5. Becker JS (2007) Inorganic mass spectrometry: principles and applications. Wiley, Chichester
6. Becker JS, Zoriy M, Matusch A, Wu B, Salber D, Palm C, Becker JS (2010) Mass Spectrom Rev 29:156–175
7. Qin Z, Caruso JA, Lai B, Matusch A, Becker JS (2011) Metallomics 3:28–37
8. Zoriy M, Matusch A, Spruss T, Becker JS (2007) Int J Mass Spectrom 260:102–106
9. Becker JS, Breuer U, Hsieh H-F, Osterholt T, Kumtabtim U, Wu B, Matusch A, Caruso JA, Qin Z (2010) Anal Chem 82:9528–9533
10. Hare D, Burger F, Austin C, Fryer F, Grimm R, Reedy B, Scolyer RA, Thompson JF, Doble P (2009) Analyst 134:450–453
11. Hare D, Tolmachev S, James A, Bishop D, Austin C, Fryer F, Doble P (2010) Anal Chem 82:3176–3182
12. Sarafanova AG, Todorov TI, Kajdacsy-Ballac A, Gray MA, Macias V, Centeno JA (2008) J Trace Elem Med Biol 22:305–314
13. Giesen C, Waentig L, Mairinger T, Drescher D, Kneipp J, Roos PH, Panneab U, Jakubowski N (2011) J Anal At Spectrom 26:2160–2165
14. Feldmann J, Kindness A, Ek P (2002) J Anal At Spectrom 17:813–818
15. Kindness A, Sekaran CN, Feldmann J (2003) Clin Chem 49:1916–1923
16. Hutchinson RW, Cox AG, McLeod CW, Marshall PS, Harper A, Dawson EL, Howlett DR (2005) Anal Biochem 346:225–233
17. Hare D, Reedy B, Grimm R, Wilkins S, Volitakis I, George JL, Cherny RA, Bush AI, Finkelstein DI, Doble P (2009) Metallomics 1:53–58
18. Hare DJ, George JL, Grimm R, Wilkins S, Adlard PA, Cherny RA, Bush AI, Finkelstein DI, Doble P (2010) Metallomics 2:745–753
19. Zoriy MV, Dehnhardt M, Reifenberger G, Zilles K, Becker JS (2006) Int J Mass Spectrom 257:27–33
20. Dobrowolska J, Dehnhardt M, Matusch A, Zoriy M, Palomero-Gallagher N, Koscielniak P, Zilles K, Becker JS (2008) Talanta 74:717–723
21. Zoriy M, Dehnhardt M, Matusch A, Becker JS (2008) Spectrochim Acta Part B 63:375–382
22. Matusch A, Bauer A, Becker JS (2011) Int J Mass Spectrom 307:240–244
23. Becker JS, Matusch A, Becker JS, Wu B, Palm C, Becker AJ, Salber D (2011) Int J Mass Spectrom 307:3–15
24. Matusch A, Depboylu C, Palm C, Wu B, Höglinger GU, Schäfer MK-H, Becker JS (2010) J Am Soc Mass Spectrom 21:161–171
25. Becker JS, Zoriy MV, Pickhardt C, Palomero-Gallagher N, Zilles K (2005) Anal Chem 77:3208–3216
26. Zoriy MV, Kayser M, Izmer A, Pickhardt C, Becker JS (2005) Int J Mass Spectrom 242:297–302
27. Becker JS, Zoriy MV, Dehnhardt M, Pickhardt C, Zilles K (2005) J Anal At Spectrom 20:912–917
28. Lear J, Hare D, Adlard P, Finkelstein D, Doble P (2012) J Anal At Spectrom 27:159–164
29. Gholap DS, Izmer A, De Samber B, van Elteren JT, Selih VS, Evens R, De Schamphelaere K, Janssen C, Balcaen L, Lindemann I, Vincze L, Vanhaecke F (2010) Anal Chim Acta 664:19–26
30. Wang HAO, Grolimund D, Van Loon LR, Barmettler K, Borca CN, Aeschlimann B, Günther D (2011) Anal Chem 83:6259–6266
31. Jackson B, Harper S, Smith L, Flinn J (2006) Anal Bioanal Chem 384:951–957
32. Todoli JL, Mermet JM (1998) Spectrochim Acta Part B 53:1645–1656
33. Austin C, Fryer F, Lear J, Bishop D, Hare D, Rawling T, Kirkup L, McDonagh A, Doble P (2011) J Anal At Spectrom 26:1494–1501
34. Austin C, Hare D, Rawling T, McDonagh AM, Doble P (2010) J Anal At Spectrom 25:722–725
35. Pozebon D, Dressler VL, Mesko MF, Matusch A, Becker JS (2010) J Anal At Spectrom 25:1739–1744
36. Becker JS, Zoriy M, Becker JS, Dobrowolska J, Dehnhardt M, Matusch A (2007) Phys Stat Sol 4:1775–1784

37. Myroslav V, Zoriy M, Becker JS (2007) Int J Mass Spectrom 264:175–180
38. Moreno-Gordaliza E, Giesen C, Lazaro A, Esteban-Fernández D, Humanes B, Canas B, Panne U, Tejedor A, Jakubowski N, Gómez-Gómez MM (2011) Anal Chem 83:7933–7940
39. Pugh JAT, Cox AG, McLeod CW, Bunch J, Whitby B, Gordon B, Kalber T, White E (2011) J Anal At Spectrom 26:1667–1673
40. Ballihaut G, Pécheyran C, Mounicou S, Preud'homme H, Grimaud R, Lobinski R (2007) Trends Anal Chem 26:183–190
41. Becker JS, Lobinski R, Becker JS (2009) Metallomics 1:312–316
42. Sanz-Medel A (2008) Anal Bioanal Chem 391:885–894
43. Cornelis R, Caruso JA, Crews H, Heumann KG (2003) Handbook of elemental speciation, 1st edn. Wiley, Chichester
44. Grebe M, Profrock D, Kakuschke A, Broekaert JAC, Prange A (2011) Metallomics 3:176–185
45. Bettmer J, Montes-Bayón M, Encinar JR, Fernández-Sánchez ML, De La Campa MDRF, Sanz-Medel A (2009) J Proteomics 72:989–1005
46. Sussulini A, Becker JS (2011) Metallomics 3:1271–1279
47. Neilsen JL, Abildtrup A, Christensen J, Watson P, Cox A, McLeod CW (1998) Spectrochim Acta Part B 53:339–345
48. Chéry CC, Günther D, Cornelis R, Vanhaecke F, Moens L (2003) Electrophoresis 24:3305–3313
49. Fan TWM, Pruszkowski E, Shuttleworth S (2002) J Anal At Spectrom 17:1621–1623
50. Tastet L, Schaumlöffel D, Lobinski R (2008) J Anal At Spectrom 23:309–317
51. Bianga J, Ballihaut G, Pecheyran C, Touat Z, Preud'homme H, Mounicou S, Chavatte L, Lobinski R, Szpunar J (2012) J Anal At Spectrom 27:25–32
52. Marshall P, Heudi O, Bains S, Freeman HN, Abou-Shakra FR, Reardon K (2002) Analyst 127:459–461
53. Becker JS, Boulyga SF, Becker JS, Pickhardt C, Damoc E, Przybylski M (2003) Int J Mass Spectrom 228:985–997
54. Becker JS, Zoriy MV, Przybylski M, Becker JS (2007) Int J Mass Spectrom 261:68–73
55. Ma R, McLeod CW, Tomlinson K, Poole RK (2004) Electrophoresis 25:2469–2477
56. Chéry CC, Moens L, Cornelis R, Vanhaecke F (2006) Pure Appl Chem 78:91–103
57. Polatajko A, Azzolini M, Feldmann I, Stuezel T, Jakubowski N (2007) J Anal At Spectrom 22:878–887
58. Becker JS, Mounicou S, Zoriy MV, Becker JS, Lobinski R (2008) Talanta 76:1183–1188
59. Garijo Añorbe M, Messerschmidt J, Feldmann I, Jakubowski N (2007) J Anal At Spectrom 22:917–924
60. Nesatyy VJ, Ross NW (2002) Analyst 127:1180–1187
61. Wind M, Feldmann I, Jakubowski N, Lehmann WD (2003) Electrophoresis 24:1276–1280
62. Venkatachalam A, Koehler CU, Feldmann I, Lampen P, Manz A, Roos PH, Jakubowski N (2007) J Anal At Spectrom 22:1023–1032
63. Pedrero Z, Madrid Y, Camara C, Schram E, Luten JB, Feldmann I, Waentig L, Hayend H, Jakubowski N (2009) J Anal At Spectrom 24:775–784
64. Raab A, Pioselli B, Munro C, Thomas-Oates J, Feldmann J (2009) Electrophoresis 30:303–314
65. Jiménez MS, Gomez MT, Rodriguez L, Martinez L, Castillo JR (2009) Anal Bioanal Chem 393:699–707
66. Jiménez MS, Rodriguez L, Gomez MT, Castillo JR (2010) Talanta 81:241–247
67. Ong S-E, Mann M (2005) Nat Chem Biol 1:252–262
68. Sanz-Medel A, Montes-Bayón M, De La Campa MDRF, Encinar JR, Bettmer J (2008) Anal Bioanal Chem 390:3–16
69. Ballihaut G, Claverie F, Pécheyran C, Mounicou S, Grimaud R, Lobinski R (2007) Anal Chem 79:6874–6880
70. Bandura DR, Ornatsky OI, Liao L (2004) J Anal At Spectrom 19:96–100
71. Konz I, Fernández B, Fernández ML, Pereiro R, Sanz-Medel A (2011) Anal Chem 83:5353–5360
72. Binet MRB, Ma R, McLeod CW, Poole RK (2003) Anal Biochem 318:30–38
73. Heumann KG (2004) Anal Bioanal Chem 378:318–329
74. Kutscher DJ, Fricker MB, Hattendorf B, Bettmer J, Günther D (2011) Anal Bioanal Chem 401:2691–2698
75. Deitrich CL, Braukmann S, Raab A, Munro C, Pioselli B, Krupp EM, Thomas-Oates JE, Feldmann J (2010) Anal Bioanal Chem 397:3515–3524
76. Bettmer J, Jakubowski N, Prange A (2006) Anal Bioanal Chem 386:7–11
77. Bettmer J, Montes Bayón M, Ruiz Encinar J, Fernández Sánchez ML, Fernández de la Campa MR, Sanz Medel A (2009) J Proteomics 72:989–1005
78. Tholey A, Schaumlöffel D (2010) TrAC Trends Anal Chem 2:399–408
79. Wild D (2005) The immunoassay handbook. Elsevier, Oxford
80. Zhang C, Wu F, Zhang Y, Wang X, Zhang X (2001) J Anal At Spectrom 16:1393–1396
81. Baranov VI, Quinn Z, Bandura DR, Tanner SD (2002) Anal Chem 74:1629–1636
82. Waentig L, Roos PH, Jakubowski N (2009) J Anal At Spectrom 24:924–933
83. Muller SD, Diaz-Bone RA, Felix J, Goedecke W (2005) J Anal At Spectrom 20:907–911
84. Quinn ZA, Baranov VI, Tanner SD, Wrana JL (2002) J Anal At Spectrom 17:892–896
85. Roos PH, Venkatachalam A, Manz A, Waentig L, Koehler CU, Jakubowski N (2008) Anal Bioanal Chem 392:1135–1147
86. Waentig L, Jakubowski N, Roos PH (2011) J Anal At Spectrom 26:310–319
87. Hu S, Zhang S, Hu Z, Xing Z, Zhang X (2007) Anal Chem 79:923–929
88. Seuma J, Bunch J, Cox A, McLeod C, Bell J, Murray C (2008) Proteomics 8:3775–3784
89. Giesen C, Mairinger T, Khoury L, Waentig L, Jakubowski N, Panne U (2011) Anal Chem 83:8177–8183
90. Markwell MAK (1982) Anal Biochem 125:427–432
91. Jakubowski N, Messerschmidt J, Garijo-Añorbe M, Waentig L, Hayen H, Roos PH (2008) J Anal At Spectrom 23:1487–1496
92. Waentig L, Jakubowski N, Hayen H, Roos PH (2011) J Anal At Spectrom 26:1610–1618
93. Jakubowski N, Waentig L, Hayen H, Venkatachalam A, von Bohlen A, Roos PH, Manz A (2008) J Anal At Spectrom 23:1497–1507
94. Murphy RC, Merrill AH (2011) Biochim Biophys Acta 1811:635–636
95. Eberlin LS, Liu X, Ferreira CR, Santagata S, Agar NYR, Cooks RG (2011) Anal Chem 83:8366–8371
96. Seeley EH, Caprioli RM (2008) Proteomics Clin Appl 2:1435–1443
97. Seeley EH, Caprioli RM (2012) Anal Chem 84:2105–2110
98. Castellino S, Groseclose MR, Wagner D (2011) Bioanalysis 3:2427–41
99. Matusch A, Fenn LS, Depboylu C, Klietz M, Strohmer S, McLean JA, Becker JS (2012) Anal Chem 84:3170–3178
100. Becker JS, Salber D (2010) TrAC Trends Anal Chem 29:966–979

Anal Bioanal Chem
DOI 10.1007/s00216-013-6778-4

TECHNICAL NOTE

Gold internal standard correction for elemental imaging of soft tissue sections by LA-ICP-MS: element distribution in eye microstructures

Ioana Konz · Beatriz Fernández · M. Luisa Fernández · Rosario Pereiro · Héctor González · Lydia Álvarez · Miguel Coca-Prados · Alfredo Sanz-Medel

Received: 13 November 2012 / Revised: 16 January 2013 / Accepted: 22 January 2013

Abstract Laser ablation coupled to inductively coupled plasma mass spectrometry has been developed for the elemental imaging of Mg, Fe and Cu distribution in histological tissue sections of fixed eyes, embedded in paraffin, from human donors (cadavers). This work presents the development of a novel internal standard correction methodology based on the deposition of a homogeneous thin gold film on the tissue surface and the use of the $^{197}Au^{+}$ signal as internal standard. Sample preparation (tissue section thickness) and laser conditions were carefully optimized, and internal normalisation using $^{197}Au^{+}$ was compared with $^{13}C^{+}$ correction for imaging applications. $^{24}Mg^{+}$, $^{56}Fe^{+}$ and $^{63}Cu^{+}$ distributions were investigated in histological sections of the anterior segment of the eye (including the iris, ciliary body, cornea and trabecular meshwork) and were shown to be heterogeneously distributed along those tissue structures. Reproducibility was assessed by imaging different human eye sections from the same donor and from ten different eyes from adult normal donors, which showed that similar spatial maps were obtained and therefore demonstrate the analytical potential of using $^{197}Au^{+}$ as internal standard. The proposed analytical approach could offer a robust tool with great practical interest for clinical studies, e.g. to investigate trace element distribution of metals and their alterations in ocular diseases.

Keywords Laser ablation · Biological samples · Mass spectrometry/ICP-MS

Electronic supplementary material The online version of this article (doi:10.1007/s00216-013-6778-4) contains supplementary material, which is available to authorized users.

I. Konz · B. Fernández (✉) · M. L. Fernández · R. Pereiro · A. Sanz-Medel (✉)
Department of Physical and Analytical Chemistry, Faculty of Chemistry, University of Oviedo, Julian Clavería 8, 33006 Oviedo, Spain
e-mail: fernandezbeatriz@uniovi.es
e-mail: asm@uniovi.es

H. González · L. Álvarez · M. Coca-Prados
Fundación de Investigación Oftalmológica, Instituto Oftalmológico Fernández-Vega, 33012 Oviedo, Spain

Published online: 05 February 2013

Introduction

Bio-imaging analytical techniques with adequate spatial resolution are today of crucial interest in life science studies to achieve a deeper understanding of the role of metals in biological systems [1, 2]. In this vein, the use of laser ablation coupled to inductively coupled plasma mass spectrometry (LA-ICP-MS) has demonstrated a great potential for spatially resolved analysis of heteroatoms (especially metals) in different types of tissues, including mouse kidney and heart [3, 4], human lymph nodes and respiratory tissues [5, 6], liver biopsy, breast cancer or prostate tissues [7, 8] and brain sections [9, 10]. In general, such micro-local analysis is performed to study the accumulation of certain heteroatoms in the regions of interest as well as to compare the differences of the elements' distribution between non-pathogenic and pathogenic tissues.

Both in qualitative and quantitative elemental imaging by LA-ICP-MS, different internal standards (IS) have been investigated to account for matrix effects as well as for variations in ablated mass, transported mass and instrumental drift normally present in laser-based analysis techniques [11]. More conventional approaches in elemental bio-imaging applications employ the $^{13}C^{+}$ signal for internal normalisation [5, 9, 10]. However, Frick et al. [12] have recently performed a detailed study of the ablation of carbon-containing matrices demonstrating the formation of two individual phases, a gaseous carbon-containing species and a carbon-containing particle phase. Such fundamental

findings line up with the hypothesis that carbon might not be a suitable IS even if a close matrix matching is performed. Austin et al. [13] proposed the use of thin polymeric films spiked with Ru and Y solutions as IS. The tissue sample can be placed on top of a thin film containing the adequate IS, but the complete ablation of the sample, including the polymeric film, has to be performed to ensure reproducible analysis. Moreover, a tedious and time-consuming step is added to the sample preparation process.

This work presents the development of a new internal standard correction methodology for qualitative elemental imaging by LA-ICP-MS using ocular tissue sections as model. The proposed strategy is based on the deposition of a homogeneous thin gold film on the tissue surface and the use of $^{197}Au^{+}$ signal as IS for normalisation. A structurally complex biological sample (eye section from a paraffin-embedded human eye of normal donors) was used as model tissue, and the bio-metal distribution ($^{24}Mg^{+}$, $^{56}Fe^{+}$ and $^{63}Cu^{+}$) was investigated by LA-ICP-MS in the structures of the anterior segment of the eye. Reproducibility studies with samples from both the same donor and different donor eyes were performed to investigate the potential of the novel IS correction approach with $^{197}Au^{+}$ as the internal standard signal.

Experimental

Standards, reagents and samples Chemicals and reagents used were of analytical grade. All solutions were prepared using distilled deionized water (18.2 $M\Omega cm^{-1}$) obtained from a Milli-Q water purification system (Millipore, Bedford, MA, USA). Iron, copper, magnesium and gold standard solutions (1,000 $\mu g mL^{-1}$) used for ICP-MS tuning were purchased from Merck (Darmstadt, Germany). All gases used for ICP-MS and LA analyses (argon and helium, each 99.999 % purity) were purchased from Air Liquide (Spain).

Ten eyes from normal donors (cadavers) were obtained 24 h post-mortem through the National Disease Research Interchange (Philadelphia, PA, USA). The procedures conformed to the tenets of the Declaration of Helsinki. Eyes were fixed in 10 % formalin and paraffin embedded (FFPE) following a conventional protocol [14]. The authors are well aware of the fact that this sample preparation might distort the initial metal concentration due to leaching of the metals from the tissue into the formalin solution or following paraffin embedding [2]. Nevertheless, this sample preparation was necessary in our case in order to ensure the sample's integrity. Sections through the eye bulbs in FFPE blocks (thicknesses between 10 and 160 μm) were prepared using a Microm HM550 cryostat (Thermo Fisher Scientific, Walldorf, Germany), mounted on microscope glass slides and dried for 24 h at 37 °C.

Instrumentation

LA-ICP-MS Element-specific detection of C, Mg, Fe, Cu and Au in ocular tissue sections was carried out using a double-focusing sector field ICP-MS (Element 2, Thermo Fisher Scientific, Bremen, Germany) at medium mass resolution (R=4,000) to avoid spectral interferences on the determination of the sought elements. For laser ablation analyses, a CETAC LSX-213 laser system (Cetac Technologies, Omaha, NE, USA) was employed. The optimized experimental parameters used for LA-ICP-MS measurements are summarized in Table 1. More details about the LA-ICP-MS system, other employed instrumentation as well as experimental conditions are provided as electronic supplementary material.

Procedures

Thin film Au deposition Thin sections (15 μm) of paraffin-embedded human eye tissues were metallized for 40 s with gold. The total duration of the thin film deposition was below 5 min, and no alteration was observed in the samples. Such metal coating was performed with a Balzers SCD 004 Sputter Coating Unit (Balzers, Bal Tec AG, Fürstentum, Lichtenstein) at the intensity current level of 20 mA under Ar atmosphere (7×10^{-2}atm). The Au layer thickness (9±1 nm) was determined on cross-sectioned witness samples by using a mechanical step profilometer (XP1–Ambios Technology, Santa Cruz, CA, USA).

Table 1 Operating conditions of the ICP-MS and laser ablation systems

ICP-MS	Thermo element 2
RF power	1,330 W
Cooling gas	15.5 $L min^{-1}$
Auxiliary gas	0.8 $L min^{-1}$
Nebuliser gas (Ar)	0.9 $L min^{-1}$
Cones	Ni (skimmer and sampler)
Isotopes	^{13}C, ^{24}Mg, ^{56}Fe, ^{63}Cu, ^{197}Au
Sample time	0.01 s
Mass window	100 %
Samples per peak	10
Scan time per pass	1.3 s
LA System	CETAC LSX-213
Output laser energy	100 % (5.6 mJ)
Repetition rate	20 Hz
Spot diameter	10 μm
Scan speed	6.5 $\mu m s^{-1}$
Ablation mode	Single line scan
Carrier gas (He)	1.0 $L min^{-1}$

Results and discussion

Optimization of sample thickness A basic requirement for a reliable bio-imaging analysis by LA-ICP-MS is the complete ablation of the sample matrix [15]. This task is even more challenging when inhomogeneous tissues with varying local distributions in the low micrometre range, such as ocular tissues, are investigated. In order to ensure the complete ablation of the sample and, therefore, to overcome a likely inhomogeneous and irreproducible ablation process, different section thicknesses between 10 and 160 μm were investigated. A detailed explanation about the studies carried out is collected as electronic supplementary material. The craters formed in the samples after LA-ICP-MS analysis were subsequently visualized by confocal laser scanning microscopy generating 3D images of the samples' surface (Fig S1, Electronic supplementary material). As can be seen in Fig. S2 (Electronic supplementary material), complete ablation of the sample could be only achieved in the case of tissue sections below 20 μm. Based on these results, all further imaging studies were performed with human eye tissue sections of 15-μm thickness.

Evaluation of thin gold film for internal standard correction The major source of error in imaging studies by LA-ICP-MS is usually related to inhomogeneities between different tissue structures. Therefore, the use of an effective IS correcting for matrix effects as well as variations in mass ablated, mass transported and instrumental drift is a must for reliable results. In order to experimentally demonstrate that at the optimized experimental parameters the signal intensity measured for $^{197}Au^+$ is stable, a glass reference material (NIST612) covered with a thin gold film was analysed. The signal intensities for the target elements and the internal standard were plotted as a function of time as well as the ratio of the target elements vs. $^{197}Au^+$ showing in all cases stable signals (data not shown). The temporal relative standard deviation was calculated to be below 20 %, presenting slight differences depending on the analysed element and/or measuring in low or medium resolution of the mass spectrometer.

Comparison of results for elemental distributions without normalisation, with $^{13}C^+$ and with $^{197}Au^+$ as internal standards A sample area of about 10 mm^2 of human eye tissue sections was selected containing different tissue structures of ophthalmological interest, such as ciliary body, ciliary muscle, iris, cornea and the outflow system, including trabecular meshwork (see Fig. 1a). Tissue structures differ very much in morphology, molecular composition and, as a consequence, also in water and solid matter content. Figure 1b shows the qualitative elemental distributions obtained by LA-ICP-MS for $^{24}Mg^+$, $^{56}Fe^+$ and $^{63}Cu^+$: with gas blank-corrected signal intensities (left), net signals corrected using $^{13}C^+$ (middle) and corrected with $^{197}Au^+$ (right) as IS. As can be seen in the left (gas blank-corrected) images, the three elements seemed to be present to different extents in the ocular tissue, while being totally absent in the paraffin matrix. Here, it should be pointed out that images of tissue sections without the Au layer on top showed the same elemental distributions for $^{24}Mg^+$, $^{56}Fe^+$ and $^{63}Cu^+$ (data not shown) than tissues with the Au layer on top. Nevertheless, significant increase in ablation efficiency was observed with the top Au layer. The use of internal standardization at this point is critical to ensure that the observed signal intensities are not artefacts due to matrix effects, as well as variations in ablated and transported mass or due to instrumental drifts. When the obtained signal intensities were corrected with the corresponding $^{13}C^+$ signal intensity (middle column), a drastic loss in structure definition (elemental contrast) was evident. Comparing the elemental distributions obtained after correction with $^{13}C^+$ signal with those obtained by correction with $^{197}Au^+$ signal (right), apparent conclusions from images are different: with $^{197}Au^+$ signal as IS, $^{24}Mg^+$ and $^{63}Cu^+$ seemed to be present in the cornea and ciliary muscle, while $^{56}Fe^+$ was clearly identified in the ciliary region. Such different conclusions for the elemental distributions of $^{24}Mg^+$, $^{56}Fe^+$ and $^{63}Cu^+$ in the tissue depending on the IS selected ($^{13}C^+$ or $^{197}Au^+$) raised the question of which of the obtained results reflect the real presence of the sought elements in the analysed zone of the ocular tissue section. To answer that key question, a closer look was taken to the elemental distributions obtained by LA-ICP-MS for $^{13}C^+$ and $^{197}Au^+$, and the results are included as electronic supplementary material. It was demonstrated that changes observed in signal intensities for $^{197}Au^+$ were not driven by selective accumulation of the gold in the different structures of ocular tissues but by changes in the ablation process itself, which depends on the sample composition at every structure.

Reproducibility studies After careful evaluation of the optimum laser ablation parameters and plasma conditions for imaging studies, the next step was a closer evaluation of the proposed Au-based normalisation strategy. Due to the lack of certified reference materials of biological tissues for elemental imaging purposes and the lack of information on distribution of metals in histological tissue sections, reproducibility studies through intra- and inter-donor comparisons were performed in order to assess the analytical potential of our approach using $^{197}Au^+$ as IS. It should be stressed that due to the long analysis time needed for obtaining high-resolution images (~15 h), the IS has to correct not only for matrix effects or tissue inhomogeneities within one analysis but also for instrumental drifts. Thus, elemental distribution maps of three ocular tissue sections of the same patient were performed firstly. Figure 2 shows the images obtained for $^{24}Mg^+$, $^{56}Fe^+$ and $^{63}Cu^+$ of three adjacent tissue sections after LA-ICP-MS analysis. The upper row represents the gas blank-corrected signals of the sought elements and the lower row, the same

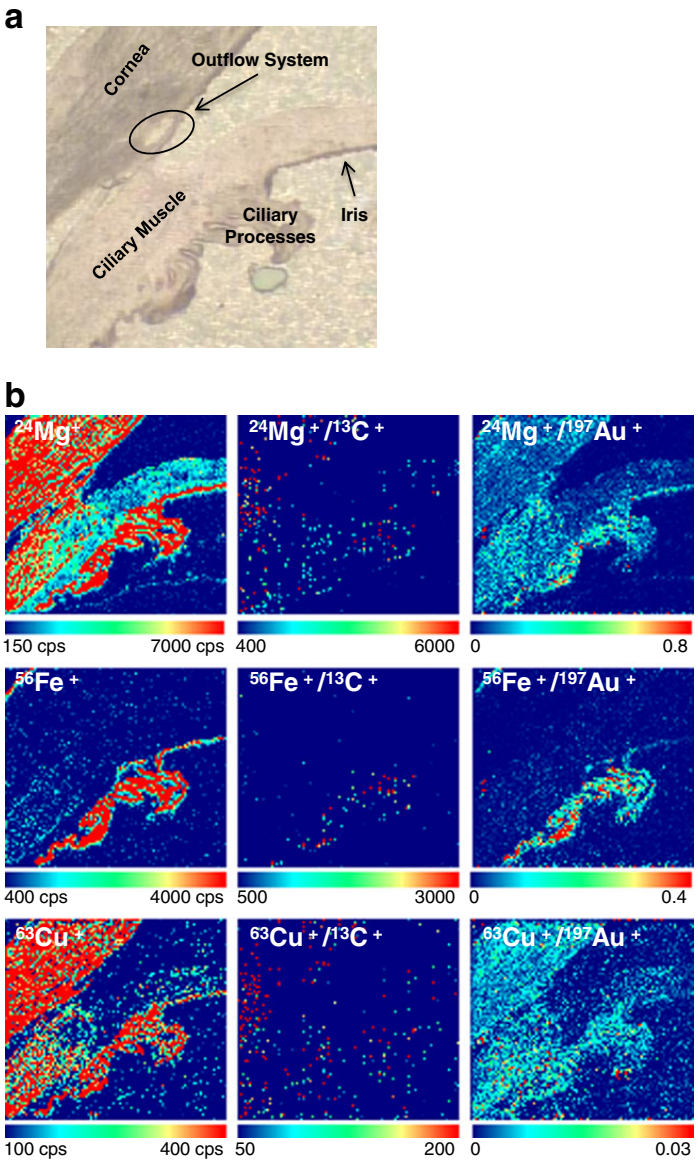

Fig. 1 **a** Histological image of a paraffin-embedded human eye tissue section of the anterior segment, analysed by LA-ICP-MS, showing the different structures of ophthalmological interest; **b** elemental distribution of $^{24}Mg^+$, $^{56}Fe^+$ and $^{63}Cu^+$ in the tissue section measured by LA-ICP-MS without internal standard correction (*left*), with $^{13}C^+$ (*middle*) and with $^{197}Au^+$ (*right*) as IS

images after IS correction with $^{197}Au^+$. As can be seen for the upper row (uncorrected images), differences in absolute signal intensities of one order of magnitude in the case of $^{24}Mg^+$, one and a half for $^{56}Fe^+$ and up to two orders of magnitude for $^{63}Cu^+$ could be observed for the three tissue sections scrutinized, which could lead to a distorted interpretation of the results. The great differences observed in intensities can be explained, at least partially, by daily variations in the laser ablation and ICP-MS systems, apart from real elemental differences in the three individual tissue sections. Such element-independent response variations could be compensated by applying the proposed approach of IS correction with $^{197}Au^+$. As can be seen in Fig. 2, differences in relative signal intensities were reduced drastically. In other words, using such IS methodology, the reproducibility of LA-ICP-MS analysis can be significantly improved allowing more reliable comparative studies among different laboratories.

Next, the study was extended to the comparison of $^{24}Mg^+$, $^{56}Fe^+$ and $^{63}Cu^+$ elemental distribution in sections of ten different eyes from normal donors. As an example, Fig. 3

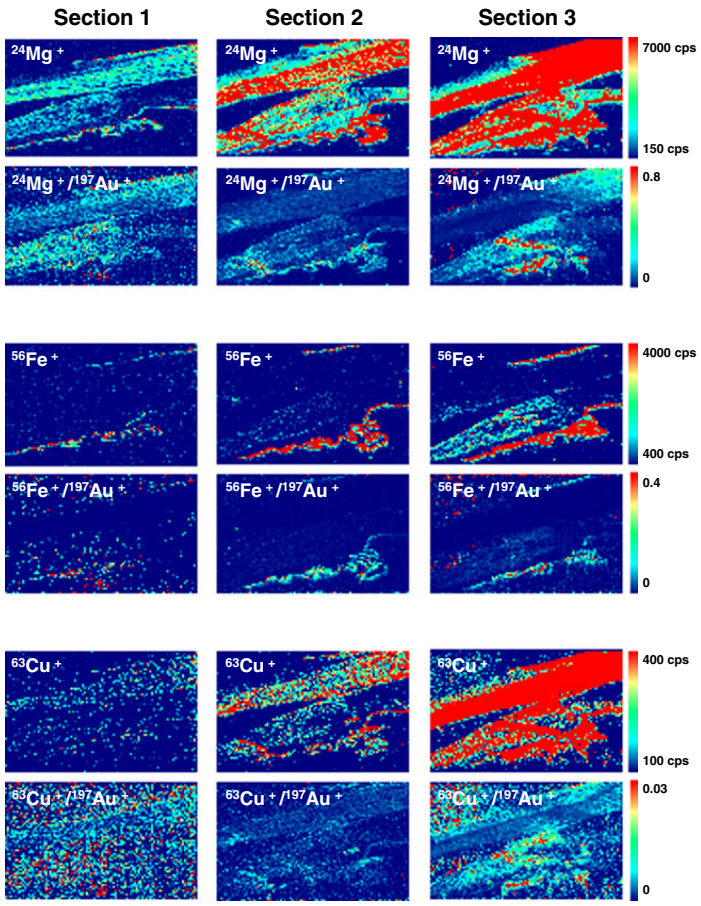

Fig. 2 Elemental distribution of $^{24}Mg^+$, $^{56}Fe^+$ and $^{63}Cu^+$ in three ocular tissue sections (similar to those shown in Fig. 1a) of the same donor (cadaver) measured by LA-ICP-MS without internal standard correction (blank-corrected signals) and using $^{197}Au^+$ as IS (*upper* and *lower row*, respectively)

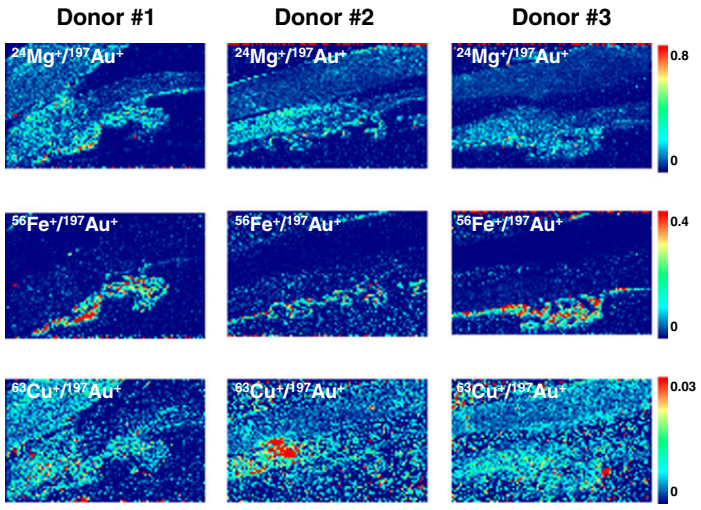

Fig. 3 Elemental distribution of $^{24}Mg^+$, $^{56}Fe^+$ and $^{63}Cu^+$ in human eye sections (similar to those shown in Fig. 1a) of three normal donors measured by LA-ICP-MS with corrected signal intensities using $^{197}Au^+$ as IS

collects images obtained by LA-ICP-MS for eye sections from three normal donors. Although slight differences between the elemental images can be observed, they could be attributed mainly to biological differences in elemental concentrations, characteristic for each individual. In any case, it should be stressed that the observed reproducibility in terms of relative signal intensities is still maintained. As can be seen in Fig. 3, $^{24}Mg^{+}$, $^{56}Fe^{+}$ and $^{63}Cu^{+}$ were not equally distributed along ocular structures: $^{56}Fe^{+}$ was found to be concentrated in the ciliary body, while $^{24}Mg^{+}$ and $^{63}Cu^{+}$ were mainly present in the ciliary body and muscle.

Conclusions

A new internal standard correction analytical strategy has been developed which affords more precise LA-ICP-MS imaging studies, and its performance has been checked for the first images of metal distributions in ocular tissue sections. The novel normalisation approach proposed here is based on the simple deposition of a thin and homogeneous gold film on the surface of the tissue section to be analysed and the use of the $^{197}Au^{+}$ signal as internal standard. This time-effective strategy offers the possibility for more robust direct and simultaneous qualitative determination of element distribution in tissue structures (having different compositions and morphology). Such strategy has been successfully checked here to improve the imaging of Mg, Fe and Cu in ocular tissue sections. In this work, the technique has been applied to different normal eye donors, and elemental images of the eye outflow system, iris, ciliary body and cornea regions have been obtained (see Figs. 2 and 3). To the best of our knowledge, those pictures represent the first published images of the likely distribution of the essential metals Mg, Fe and Cu in human eye microstructures.

Therefore, this work warrants further research to uncover Au as IS for LA-ICP-MS imaging and its application in biomedical research (e.g. more reliable comparative studies of normal and pathogenic tissues by IS elemental imaging can be anticipated).

Acknowledgments Financial support from "Plan Nacional de I+D+I" (Spanish Ministry of Science and Innovation or MICINN, and FEDER Program) through MAT2010-20921-C02-01 and PCTI Asturias through the project FC-09-EQUIP09-29 is acknowledged. I. Konz and B. Fernández thank the FPU programme (MICINN) and FC-11-COF11-21 project (PCTI Asturias), respectively, for financial support.

References

1. Becker JS, Zoriy M, Matusch A, Wu B, Salber D, Palm C, Becker JS (2010) Mass Spectrom Rev 29:156–175
2. Qin Z, Caruso JA, Lai B, Matusch A, Becker JS (2011) Metallomics 3:28–37
3. Zoriy M, Matusch A, Spruss T, Becker JS (2007) Int J Mass Spectrom 260:102–106
4. Becker JS, Breuer U, Hsieh H-F, Osterholt T, Kumtabtim U, Wu B, Matusch A, Caruso JA, Qin Z (2010) Anal Chem 82:9528–9533
5. Hare D, Burger F, Austin C, Fryer F, Grimm R, Reedy B, Scolyer RA, Thompson JF, Doble P (2009) Analyst 134:450–453
6. Hare D, Tolmachev S, James A, Bishop D, Austin C, Fryer F, Doble P (2010) Anal Chem 82:3176–3182
7. Sarafanov AG, Todorov TI, Kajdacsy-Ballac A, Gray MA, Macias V, Centeno JA (2008) J Trace Elem Med Biol 22:305–314
8. Giesen C, Waentig L, Mairinger T, Drescher D, Kneipp J, Roos PH, Panneab U, Jakubowski N (2011) J Anal At Spectrom 26:2160–2165
9. Zoriy M, Dehnhardt M, Matusch A, Becker JS (2008) Spectrochim Acta Part B 63:375–382
10. Kindness A, Sekaran CN, Feldmann J (2003) J Clin Chem 49:1916–1923
11. Hare D, Austin C, Doble P (2012) Analyst 137:1527–1537
12. Frick DA, Günther D (2012) J Anal At Spectrom 27:1294–1303
13. Austin C, Hare D, Rawling T, McDonagh AM, Doble P (2010) J Anal At Spectrom 25:722–725
14. Hewitson TD, Darby IA (2010) Histology protocols, methods in molecular biology, volume 611. Humana Press, New York
15. Konz I, Fernández B, Fernández ML, Pereiro R, Sanz-Medel A (2012) Anal Bioanal Chem 403:2113–2125

Analytical and Bioanalytical Chemistry

Electronic Supplementary Material

Gold internal standard correction for elemental imaging of soft tissue sections by LA-ICP-MS: element distribution in eye microstructures

Ioana Konz, Beatriz Fernández, M. Luisa Fernández, Rosario Pereiro, Héctor González, Lydia Álvarez, Miguel Coca-Prados and Alfredo Sanz-Medel

The Electronic Supplementary Material details the Experimental section of the manuscript concerning the description of the LA-ICP-MS system, other employed instrumentation and the selected experimental conditions used in this work. Furthermore, it includes a critical description of the Results and Discussion section for the optimization of tissue thickness measured by confocal laser scanning microscopy as well as the images obtained by LA-ICP-MS for $^{13}C^{+}$ and $^{197}Au^{+}$ throughout the tissue sections using two different sample preparation strategies.

EXPERIMENTAL

Instrumentation

LA-ICP-MS. Element-specific detection of C, Mg, Fe, Cu and Au in ocular tissue sections was carried out using a double-focusing sector field ICP-MS (Element 2, Thermo Fisher Scientific, Bremen, Germany) at medium mass resolution (R=4000) to avoid spectral interferences on the determination of the sought elements. For laser ablation analyses, a CETAC LSX-213 laser system (Cetac Technologies, Omaha, NE, USA) was employed. The LA-ICP-MS system was daily tuned using a SRM NIST-612 glass standard for high sensitivity, background intensity, and the $^{238}U/^{232}Th$ signal ratio

that should be close to 1 to ensure a low fractionation effect due to the ICP ionization efficiency. The optimized experimental parameters used for LA-ICP-MS measurements are summarized in Table 1 in the original manuscript. The laser ablation of the eye sections was performed using the commercial ablation chamber from Cetac with an effective volume of 60 cm^3, ensuring a reasonable fast wash-out time. The laser-generated aerosol was transported through a high-purity tube (Teflon-lined Tygon® tubing, ¼" OD, 1/8" ID) into the ICP torch by the He carrier gas of the ablation cell. It has been demonstrated in several works that wet plasma conditions (continuous nebulization of liquid during ablation events) can be advantageous for LA-ICP-MS analysis owing to the increased tolerance with respect to different plasma loads[i, ii]. Thus, dry and wet plasma conditions were investigated using a home-made Y-piece of glass to mix the laser-generated aerosol with a liquid aerosol nebulized by means of a concentric nebulizer. Elemental distributions obtained by LA-ICP-MS showed that, although an increase of the net signals (background corrected) for all sought elements could be obtained working in wet conditions, internal standard correction with $^{197}Au^+$ led to comparable results to those obtained using dry plasma. Hence, the simpler direct dry plasma conditions were selected for subsequent analyses.

Imaging measurements were performed by line scan ablation of eye tissue sections (line per line) using a small spot diameter of 10 µ m and 10 µ m distance between adjacent lines. In all experiments a gas blank was collected prior to ablation of the sample for background correction. The average analysis time for the imaging of one sample with the maximum resolution was about 15 h (sample area of 10 mm^2). Two dimensional images of elemental distributions in ocular tissue sections were created using *Origin*® software.

Confocal laser scanning microscopy. High-resolution 3D images from tissue sections analyzed by LA-ICP-MS were generated by sequential acquisition using a Leica TCS SP2 AOBS spectral confocal microscope (Leica Microsystems, Inc., Exton, PA, USA). The instrument is equipped with an Ar/Kr laser, at 488 nm in reflection mode and a Plan Apochromat 10X/0.40 CS objective lens (Leica Microsystems, Inc., Exton, PA, USA) operated in dry conditions, without band-pass filter. Stacks of images were collected every 1 µ m along the z-axis. 3D images and crater profiles were generated with Leica Confocal Software.

RESULTS AND DISCUSSION

Optimization of Sample Thickness. A basic requirement for a reliable bio-imaging analysis by LA-ICP-MS is the complete ablation of the sample matrix[iii]. This task is even more challenging when inhomogeneous tissues with varying local distributions in the low micrometer range, such as ocular tissues, are investigated. In order to ensure the complete ablation of the sample and, therefore, to overcome a likely inhomogeneous and irreproducible ablation process, different sections thicknesses between 10 and 160 µm were investigated. The precision of the thickness given by the provider of the Microm HM550 cryostat is of ± 1 µm although in our studies no such deviation from the desired thickness could be observed (determination by confocal laser scanning microscopy). As an example, Fig. S1 shows the results obtained for two of the investigated section thicknesses analyzed: 15 µm (Fig. S1A, S1B and S1C) and 50 µm (Fig. S1D, S1E and S1F). Furthermore, the ablation was performed comparing tissue structures with different compositions and morphology (see histological images in Fig. S1A and S1D). In order to investigate the penetration depth in different regions of the studied ocular tissue section, three adjacent lines were ablated at the optimum conditions selected for bio-imaging studies (see Table 1 in original manuscript). The craters formed in the samples after LA-ICP-MS analysis were subsequently visualized by confocal laser scanning microscopy generating 3D-images of the samples surface (Fig. S1B and S1E). The depth of those craters and their shape were also measured (Fig. S1C and S1F) to evaluate ablation efficiencies depending on the matrix composition as well as to select the optimum thickness tissue section.

As can be seen in Fig. S1, complete ablation of the sample along the entire line could be only achieved in the case of the 15 µm tissue section. Crater shapes with perpendicular walls and rather flat crater bottom were obtained for the three adjacent lines (Fig. S1C-1), showing a good reproducibility. Moreover, the crater profile performed along the whole ablation line showed also a flat bottom without unablated residues (Fig. S1C-2). In contrast, profiles obtained for the 50 µm tissue section clearly showed an incomplete and irreproducible ablation along the adjacent lines. Thus, it could be stated that the ablation was mainly dominated by the different laser-matter interaction due to the composition of the constituent biomolecules (see Fig. S1.F-1). Furthermore, as can be observed in Fig. S1.F-2, the crater profile along the entire line

showed preferential ablation in the structures containing melanin, resulting in higher penetration depth in this region.

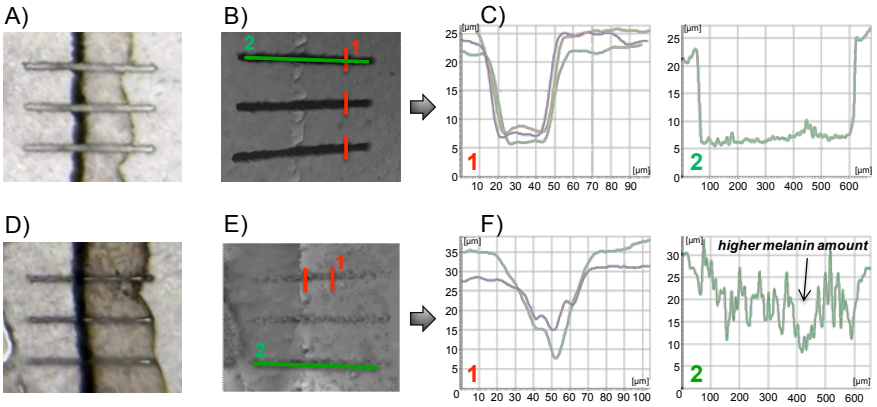

Fig. S1. Optimization of the thickness of human eye sections for LA-ICP-MS. Two thicknesses of tissue sections were investigated: 15 µm (A, B and C) and 50 µm (D, E and F)

A+D) Histological images obtained after laser ablation analysis;

B+E) 3D images obtained by confocal laser scanning microscopy;

C+F) Crater profiles obtained by confocal laser scanning microscopy (C1+F1 across ablated line and C2+F2 along ablated line)

Fig. S2 shows the relationship obtained between the measured penetration depth, after laser ablation analysis, and the analyzed tissue section thickness between 10 µm and 160 µm. The graphical representation shows a linear correlation for the first three points, indicating that up to 20 µm section thickness a complete ablation of the sample matrix takes place. For samples with thicknesses above 20 µ m the overall ablation efficiency decreased, reaching a maximum average penetration depth of about 30 µm (virtually independent of the tissue section thickness and much more irreproducible). Thus, the greater the section thickness (from 50 to 160 µm), the ablation process is more influenced by the inhomogeneous sample composition and morphology. Based on these results, all further imaging studies were performed with human eye tissue sections of 15 µm thick to ensure a complete ablation.

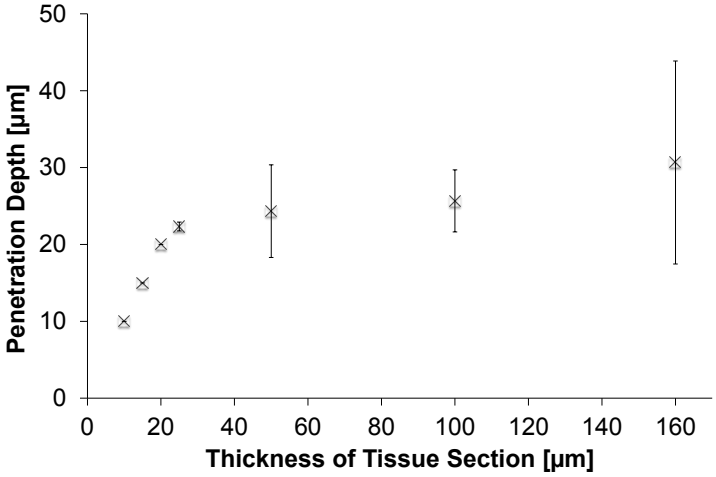

Fig. S2. Graphical representation of the penetration depth measured by confocal laser scanning microscopy versus tissue section thickness (10, 15, 20, 25, 50, 100 and 160 µm) for the analysis of ocular tissue sections by LA-ICP-MS. Standard deviation values were calculated from the mean of three independent measurements.

Comparison of Elemental Distributions without Normalization, using $^{13}C^{+}$ and $^{197}Au^{+}$ as Internal Standards. The different conclusions obtained for the elemental distributions of $^{24}Mg^{+}$, $^{56}Fe^{+}$ and $^{63}Cu^{+}$ in the tissue depending on the IS selected (see Fig. 1 in the original manuscript) raised the question of which of the obtained results reflect the real presence of the sought elements in the analyzed zone of the ocular tissue section. To answer that key question a closer look was taken to the elemental distributions obtained by LA-ICP-MS for $^{13}C^{+}$ and $^{197}Au^{+}$. Fig. S3A shows the results obtained for a tissue section with the thin gold layer deposited on the top of the tissue sample. As can be seen, in general terms both $^{13}C^{+}$ and $^{197}Au^{+}$ showed an elemental distribution which more or less fits to the corresponding histological image (left). In the case of $^{13}C^{+}$ this seems logical since the distinct tissue structures are characterized by different cell densities and water content (i.e. different carbon content). On the other hand, it was not expected that elemental distribution of $^{197}Au^{+}$ overlaps with the histological image of the analyzed zone as the thin Au film deposition process ensures a homogeneous distribution of Au within the tissue surface. Perhaps the observed distribution in the elemental image is caused by accumulation of Au in the different

tissue structures during or after the deposition process. Therefore, an alternative sample preparation procedure was investigated where the thin Au film was deposited directly on the glass substrate and subsequently covered with the ocular tissue section. After new LA-ICP-MS analysis, elemental maps for $^{13}C^{+}$ and $^{197}Au^{+}$ were obtained for this latter case (see Fig. S3B). As shown in Fig. S3B, elemental distribution obtained for $^{197}Au^{+}$ clearly defines again the morphology of the sampled ocular tissue section. Therefore, it appears that the changes observed in signal intensities for $^{197}Au^{+}$ were not driven by selective accumulation of the gold in the different structures of ocular tissues but by changes in the ablation process itself, which depends on the sample composition at every structure.

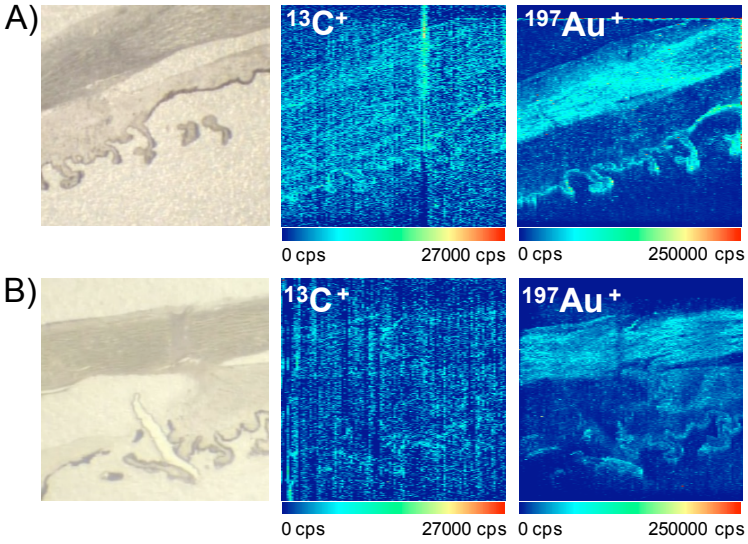

Fig. S3. Histological images of the analyzed zones (similar to those shown in Fig 1-A in original manuscript) in the ocular tissue sections (left) and corresponding elemental distribution of $^{13}C^{+}$ and $^{197}Au^{+}$ obtained by LA-ICP-MS

A) Sample with the thin Au layer deposited on the top of the tissue section;

B) Sample with the thin Au layer deposited directly on the glass substrate (below the tissue section)

REFERENCES

i. Kroslakova I, Günther D (2007) J. Anal. At. Spectrom. 22, 51-62.

ii. O'Connor C, Sharp BL, Evans P (2006) J. Anal. At. Spectrom. 21, 556-565.

iii. Konz I, Fernández B, Fernández ML, Pereiro R, Sanz-Medel A (2012) Anal. Bioanal. Chem. 403, 2113-2125.

(19) OFICINA ESPAÑOLA DE PATENTES Y MARCAS

ESPAÑA

(11) Número de publicación: **2 425 138**

(21) Número de solicitud: 201300559

(51) Int. CI.:

G01N 27/62 (2006.01)

(12) SOLICITUD DE PATENTE A1

(22) Fecha de presentación:

07.06.2013

(43) Fecha de publicación de la solicitud:

11.10.2013

(71) Solicitantes:

UNIVERSIDAD DE OVIEDO (100.0%)
C/ San Francisco 3
33003 Oviedo (Asturias) ES

(72) Inventor/es:

FERNÁNDEZ GARCÍA, Beatriz;
KONZ , Ioana;
VALENZUELA CASTAÑEDA, Adrián;
FERNÁNDEZ SÁNCHEZ, María Luisa;
PEREIRO GARCÍA, María Rosario y
SANZ MEDEL, Alfredo

(54) Título: **Celda de ablación criogénica con control de la temperatura de la muestra**

(57) Resumen:

Celda de ablación criogénica con control de la temperatura de la muestra (5) que comprende una tapa superior extraíble (2) con una ventana transparente al láser (3) y una base de la celda (4) con un sistema de refrigeración interno (12). El sistema también comprende un sistema de refrigeración externo (16), un sensor de temperatura (21), unos medios de control de la temperatura (22) y un sistema de ventilación externo (27). La celda se puede usar en combinación con otros dispositivos como, por ejemplo, un sistema de ablación láser acoplado a un sistema de plasma de acoplamiento inductivo con detección por espectrometría de emisión óptica o de masas.

De aplicación en aquellos sectores en los que se diseñen, produzcan o utilicen celdas de ablación, como por ejemplo el de la maquinaria y equipo mecánico, geología, biología, medicina, arqueología o química.

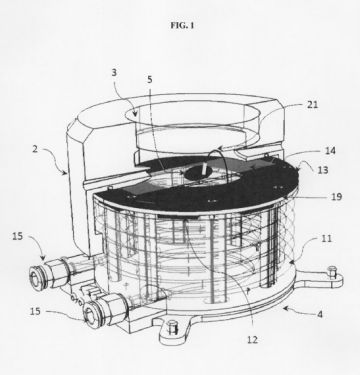

ES 2 425 138 A1

La presente invención se refiere a una celda de ablación con control de la temperatura de la muestra que comprende una tapa superior extraíble, una base de la celda que a su vez comprende en su interior un sistema de refrigeración interno, un sistema de refrigeración externo, un sensor de temperatura de la muestra, unos medios de control de la temperatura y un sistema de ventilación externo. La celda de la presente invención se puede usar en combinación con otros dispositivos como, por ejemplo, un sistema de ablación láser acoplado a un sistema de plasma de acoplamiento inductivo con detección por espectrometría de emisión óptica o de masas.

La invención resulta de aplicación en aquellos sectores en los que se diseñen, produzcan o utilicen celdas de ablación, como por ejemplo el de la maquinaria y equipo mecánico, geología, biología, medicina, arqueología o química.

ESTADO DE LA TÉCNICA

La celda de ablación criogénica propuesta en la invención está estrechamente relacionada con un método analítico para la detección de elementos traza en muestras sólidas mediante el arrancado de material de la muestra empleando un haz láser. Para la detección de los elementos de interés, una muestra a analizar se dispone en un sistema de ablación láser para ser sometida al arrancado de material por impacto del haz láser sobre su superficie. Posteriormente, el aerosol generado a partir de la muestra es transportado mediante un flujo de gas portador inerte (generalmente helio o argón) hacia un plasma de acoplamiento inductivo (ICP) donde se produce la atomización e ionización del aerosol, permitiendo posteriormente la detección de los iones generados con un espectrómetro de masas (MS).

Los componentes básicos de los que consta un equipo de ablación láser (LA) ICP-MS son: un sistema láser, donde se incluye una óptica de guía del haz láser

(conjunto de lentes y espejos que conducen el haz láser hasta la superficie de la muestra) y una celda de ablación donde se dispone la muestra a analizar, una interfase para el transporte del aerosol generado y, finalmente, un instrumento ICP-MS. Desde los primeros estudios realizados durante la década de 1980 (Gray AL "*Solid sample introduction by laser ablation for inductively coupled plasma source mass spectrometry*" *Analyst* 110 (1985) 551; Arrowsmith P, Hughes SK "*Entrainment and transport of laser ablated plumes for subsequent elemental analysis*" Appl. Spectrosc. 42 (1988) 1231), el interés por la técnica LA-ICP-MS ha ido en aumento, de tal modo que actualmente se emplea para el análisis elemental e isotópico en una gran variedad de materiales sólidos (Durrant SF, Ward NI "*Recent biological and environmental applications of laser ablation inductively coupled plasma mass spectrometry*" J. Anal. At. Spectrom. 20 (2005) 821; Pisonero J, Fernandez B, Günther D "*Critical Revision of GD-MS, LA-ICP-MS and SIMS as Inorganic Mass Spectrometric Methods for Direct Solid Analysis*" J. Anal. At. Spectrom. 24 (2009) 1145; Fernandez B, Claverie F, Pecheyran C, Donard OFX "*Direct analysis of solid samples by femtosecond laser ablation inductively coupled plasma mass spectrometry*" Trends Anal. Chem. 26 (2007) 951). Entre las principales ventajas de la técnica LA-ICP-MS se encuentran su facilidad de manejo, su alta sensibilidad (los límites de detección están en el intervalo comprendido entre los mg/kg y ng/kg) y un rango dinámico de hasta doce órdenes de magnitud, lo que permite la adquisición simultánea de componentes mayoritarios, minoritarios y traza. Además, otra de sus principales características es la elevada resolución espacial, tanto lateral (~5 μm) como en profundidad (del orden comprendido entre 500 nm y 2 μm dependiendo del tipo de láser empleado), por lo que se considera una técnica no destructiva a nivel macroscópico.

Una de las aplicaciones más importantes de la técnica LA-ICP-MS en los últimos años está relacionada con los estudios de "*imaging*". Esta técnica ofrece la posibilidad de obtener imágenes con una gran resolución lateral directamente de la superficie de la muestra, lo que permite estudiar la distribución elemental de los diferentes analitos (Becker JS, Zoriy M, Matusch A, Wu B, Salber D, Palm C, Becker JS "*Bioimaging of metals by laser ablation inductively coupled plasma mass spectrometry (LA-ICP-MS)*" Mass Spectrom. Reviews 2 (2010) 156). Este tipo de estudios resulta de gran interés en todos los campos relacionados con la biomedicina,

clínica y biología. Así, se ha demostrado su aplicabilidad a un tipo muy variado de muestras como corteza de árbol (Narewski U, Werner G, Schulz H, Vogt C "*Application of laser ablation inductively coupled mass spectrometry for the determination of major, minor, and trace elements in bark samples*" Fresenius' J. Anal. Chem. 366 (2000) 167), hojas de plantas (Cizdziel J, Bu K, Nowinski P "*Determination of elements in situ in green leaves by laser ablation ICP-MS using pressed reference materials for calibration*" Anal. Methods 4 (2012) 564), piezas dentales (Prohaska T, Latkoczy C, Schultheis G, Teschler-Nicola M, Stingeder G "*Investigation of Sr isotope ratios in prehistoric human bones and teeth using Laser Ablation ICP-MS and ICP-MS after Rb/Sr separation*" J. Anal. At. Spectrom. 17 (2002) 887) y otolitos (Huelga-Suarez G, Fernández B, Moldovan M, Alonso JIG "*Detection of transgenerational barium dual-isotopic marks in salmon otoliths by means of LA-ICP-MS*" Anal. Bioanal. Chem. 405 (2013) 2901).

Además, la técnica LA-ICP-MS también se emplea cada vez más para la determinación de metales y elementos traza en tejidos de interés biomédico, como tejidos de riñón y corazón (Zoriy M, Matusch A, Spruss T, Becker JS "*Laser ablation inductively coupled plasma mass spectrometry for imaging of copper, zinc, and platinum in thin sections of a kidney from a mouse treated with cis-platin*" Int. J. Mass Spectrom. 260 (2007) 102; Becker JS, Breuer U, Hsieh HF, Osterholt T, Kumtabtim U, Wu B, Matusch A, Caruso JA, Qin Z "*Bioimaging of metals and biomolecules in mouse heart by laser ablation inductively coupled plasma mass spectrometry and secondary ion mass spectrometry*" Anal. Chem. 82 (2010) 9528), ganglios linfáticos y tejidos respiratorios (Hare D, Tolmachev S, James A, Bishop D, Austin C, Fryer F, Doble P "*Elemental bio-imaging of thorium, uranium, and plutonium in tissues from occupationally exposed former nuclear workers*" Anal. Chem. 82 (2010) 3176), tejidos de cáncer de próstata y de mama (Giesen C, Waentig L, Mairinger T, Drescher D, Kneipp J, Roos PH, Panneab U, Jakubowski N "*Iodine as an elemental marker for imaging of single cells and tissue sections by laser ablation inductively coupled plasma mass spectrometry*" J. Anal. At. Spectrom. 26 (2011) 2160) y secciones de tejido cerebral (Zoriy M, Dehnhardt M, Matusch A, Becker JS "*Comparative imaging of P, S, Fe, Cu, Zn and C in thin sections of rat brain tumor as well as control tissues by laser ablation inductively coupled plasma mass spectrometry*" Spectrochim. Acta

Part B 63 (2008) 375). Dentro de los tejidos biomédicos, en los últimos años ha cobrado gran interés el empleo de la técnica LA-ICP-MS para evaluar tejidos de pacientes afectados por enfermedades neurológicas degenerativas como el Parkinson y el Alzheimer (Matusch A, Depboylu C, Palm C, Wu B, Höglinger GU, Schäfer MK-H, Becker JS "*Cerebral bioimaging of Cu, Fe, Zn, and Mn in the MPTP mouse model of Parkinson's disease using laser ablation inductively coupled plasma mass spectrometry*" J. Am. Soc. Mass Spectrom. 21 (2010) 161; Hutchinson RW, Cox AG, McLeod CW, Marshall PS, Harper A, Dawson EL, Howlett DR "*Imaging and spatial distribution of β-amyloid peptide and metal ions in Alzheimer's plaques by laser ablation–inductively coupled plasma–mass spectrometry*" Anal. Biochem. 346 (2005) 225).

Cuando se lleva a cabo el análisis de tejidos biológicos o biomédicos uno de los aspectos más importantes a tener en cuenta es la preparación de las muestras, así como la posible pérdida de metales de los tejidos durante este proceso. Actualmente, hay dos tipos de procedimientos estándar empleados en los laboratorios para la preparación de secciones de tejidos biomédicos: (i) fijación del tejido en formalina y posteriormente embebido del mismo en parafina y (ii) congelación de la muestra en el estado nativo a temperaturas inferiores a –40ºC. En el caso de las muestras embebidas en parafina se ha observado que puede haber pérdidas de algunos elementos durante el proceso de preparación de las muestras. De este modo, se ha demostrado que la concentración de algunos metales (p.ej. Fe) en muestras embebidas en parafina es inferior a las concentraciones detectadas en muestras criogénicas, preparadas de forma nativa (Qin Z, Caruso JA, Lai B, Matusch A, Becker JS "*Trace metal imaging with high spatial resolution: Applications in biomedicine*" Metallomics 3 (2011) 28). Este hecho podría deberse a la lixiviación de los metales de los tejidos en la disolución de formalina o durante el proceso de inclusión en parafina. Sin embargo, el método de congelación del tejido fresco protege el estado nativo de la muestra (especialmente con respecto a la preservación de los analitos que pueden difundir fácilmente). Por lo tanto, podría decirse que el método ideal para la preparación de las muestras es la congelación de las mismas, resultando en este caso imprescindible el empleo de una celda de ablación que permita trabajar a baja temperatura para asegurar de este modo tanto la integridad de las muestras como la exactitud de los análisis.

Por otro lado, aunque no resulta imprescindible emplear una celda criogénica para el análisis de otro tipo de muestras sólidas (p.ej. estructuras óseas, implantes o muestras geológicas), se ha observado que las prestaciones obtenidas empleando un control estricto de la temperatura de la muestra a lo largo del análisis son superiores a los análisis hechos sin control de la temperatura (Zoriy MV, Kayser M, Izmer A, Pickhardt C, Becker JS "*Determination of uranium isotopic ratios in biological samples using laser ablation inductively coupled plasma double focusing sector field mass spectrometry with cooled ablation chamber*" Inter. J. Mass Spectrom. 242 (2005) 297). De esta manera, el campo de aplicación de las celdas de ablación que operan a baja temperatura es muy amplio y no está únicamente restringido a muestras de tejidos biomédicos.

Actualmente existen varios tipos de celdas de ablación que permiten trabajar a baja temperatura, por ejemplo las descritas por Zoriy MV, Kayser M, Izmer A, Pickhardt C, Becker JS "*Determination of uranium isotopic ratios in biological samples using laser ablation inductively coupled plasma double focusing sector field mass spectrometry with cooled ablation chamber*" Int. J. Mass Spectrom. 242 (2005) 297, Müller W, Shelley JMG, Rasmussen SO "*Direct chemical analysis of frozen ice cores by UV-laser ablation ICPMS*" J. Anal. At. Spectrom. 26 (2011) 2391 y Feldmann J, Kindness A, Ek P "*Laser ablation of soft tissue using a cryogenically cooled ablation cell*" J. Anal. At. Spectrom. 17 (2002) 813. Sin embargo, en todas ellas, el control de la temperatura de la muestra y la refrigeración de la misma tienen lugar de manera indirecta, es decir, sin un control de la temperatura que se produce en la propia muestra sometida a la acción del haz láser.

En las celdas de ablación disponibles, el enfriamiento de la muestra tiene lugar sobre el soporte en el que se dispone la muestra a analizar y es la temperatura de este soporte la que es controlada por los sistemas de refrigeración. El control exacto y continuo de la temperatura de la muestra es un aspecto crucial para asegurar la integridad de la muestra durante el análisis (el cual puede llegar a durar más de 20 horas cuando se hacen estudios de *imaging*), especialmente tratándose de muestras de tejidos preparados en su forma nativa. Además, estas celdas de ablación no permiten monitorizar la temperatura de la muestra y, por lo tanto, ésta puede sufrir cambios

debido a los importantes efectos térmicos que ejerce el haz láser en la muestra durante el análisis. De este modo, los resultados obtenidos de los análisis por LA-ICP-MS carecen de exactitud y precisión y no son representativos de la muestra.

Por otro lado, un aspecto importante a la hora de hacer estudios de *imaging* sobre muestras con estructuras a escala micrométrica (p.ej. inclusiones en muestras geológicas o distribución de metales en secciones de tejidos humanos) es la necesidad de llevar a cabo una correcta visualización de la muestra. Las celdas de ablación que permiten trabajar a baja temperatura disponen de una base de la celda opaca por lo que la iluminación de la muestra se realiza únicamente a través de la parte superior de la celda, resultando en muchos casos insuficiente para llevar a cabo análisis con una buena resolución lateral y poder distinguir así microestructuras.

DESCRIPCIÓN DE LA INVENCIÓN

La presente invención se refiere a una celda de ablación con control de la temperatura de la muestra, que se puede usar en combinación con otros dispositivos como por ejemplo, un sistema de ablación láser acoplado a un sistema de plasma de acoplamiento inductivo con detección por espectrometría de emisión óptica o de masas.

La celda de ablación de la presente invención comprende:

- Una tapa superior extraíble que permite la disposición de una muestra dentro de la celda de ablación. La tapa a su vez comprende una ventana transparente al láser por donde penetra el haz que permite la ablación de la muestra. La tapa también dispone de al menos una abertura para la entrada de gas de arrastre y al menos una abertura para la salida de gas de arrastre. El gas de arrastre sirve para transportar el aerosol con partículas que se forma a partir de la ablación de la muestra hacia la salida de la celda de ablación. Este aerosol es apto para ser analizado por ejemplo empleando instrumentos de espectrometría de emisión óptica y de masas. Preferiblemente, el gas de arrastre es un gas inerte, como por ejemplo helio o argón, de forma que no interfiere en el análisis del material de interés.

- Una base de la celda que a su vez comprende en su interior un intercambiador de calor interno, un sistema de refrigeración interno, una placa refrigeradora sobre el sistema de refrigeración interno y un portamuestras sobre la placa refrigeradora. El intercambiador de calor interno proporciona un foco frío en el interior de la celda, que se enfría gracias al suministro constante de un fluido refrigerante que proviene del exterior. Por otra parte, el sistema de refrigeración interno permite regular de forma dinámica e inmediata la temperatura de la muestra que se sitúa sobre el portamuestras, manteniéndola dentro de un rango apropiado para el proceso de ablación. El sistema de refrigeración interno trasiega calor desde el foco frío al foco caliente, el cual aparece debido a la potencia del haz láser que incide sobre la muestra, calentándola. La placa refrigeradora transmite la temperatura de regulación proporcionada por el sistema de refrigeración interno al portamuestras, sobre el que se dispone la muestra. La base de la celda también comprende una ventana transparente a la luz y un sistema de conexión del intercambiador de calor interno y el sistema de refrigeración externo por el que penetra un fluido refrigerante.

- Un sistema de refrigeración externo que a su vez comprende un intercambiador de calor externo y unos medios de bombeo de un fluido refrigerante que permiten llevar a cabo la circulación del fluido refrigerante a través del intercambiador de calor interno de la base de la celda y del intercambiador de calor externo. A los efectos de esta invención y su descripción, los medios de bombeo pueden ser cualquier sistema para trasegar un fluido, como por ejemplo una bomba radial, controlada electrónicamente, asociada a unos conductos que transportan el fluido bombeado.

- Un sensor de temperatura de la muestra que permite controlar de forma directa su temperatura.

- Un sistema de ventilación externo que impulsa un fluido de ventilación sobre la ventana transparente al láser de la tapa superior extraíble. El sistema de ventilación permite mantener unas condiciones óptimas de

trabajo disminuyendo por ejemplo los efectos de difracción o reflexión asociados a fenómenos de condensación sobre la ventana transparente al láser.

- Unos medios de control de temperatura de todo el sistema.

En una realización preferida, la tapa superior extraíble y la base de la celda son de un material aislante térmico. La selección de un material con un coeficiente de transmisión térmica apropiado influye directamente en la cinética de trasmisión de calor debida al fuerte gradiente térmico que se puede dar entre el interior y el exterior de la celda. Este aspecto repercute directamente en el dimensionamiento y la configuración de los diferentes subsistemas de la celda, como por ejemplo en los medios de control de temperatura, el intercambiador de calor interno o el sistema de refrigeración interno. En una realización más preferida, el material aislante térmico es un compuesto de poliamida.

En otra realización preferida, la ventana transparente al láser comprende un cristal de cuarzo. El cristal de cuarzo ofrece unas propiedades ideales para la transmisión de un haz láser típicamente utilizado en procesos de ablación. Además, el cristal de cuarzo facilita la visión del interior de la celda y permite la iluminación de la muestra por la parte superior. En una realización más preferida, el cristal de cuarzo permite la trasmisión de una longitud de onda electromagnética en el rango comprendido entre 1064 nm y 193 nm.

En otra realización preferida, la abertura para la entrada de gas de arrastre consiste en un orificio único. En otra realización preferida, la abertura para la entrada de gas de arrastre consiste en cuatro orificios de entrada.

En otra realización preferida, la abertura para la salida de gas de arrastre consiste en un orificio único. En una realización más preferida, el orificio único tiene forma de embudo recolector. En otra realización preferida, la abertura para la salida de gas consiste en cuatro orificios de salida.

La selección entre uno o cuatro orificios para la entrada o la salida y la materialización de la salida en forma de embudo, depende del tamaño de la tapa y, por lo tanto, del volumen de la celda de ablación y, sobre todo, de las características del

gas de arrastre y los medios para impulsarlo. En algunas aplicaciones, como por ejemplo en estudios de *imaging*, la obtención de un flujo laminar del gas de arrastre con el aerosol es determinante para obtener un buen resultado analítico.

En una realización específica, el intercambiador de calor interno es un serpentín. Un intercambiador de calor en forma de serpentín es una solución muy eficiente, aumentando la capacidad de intercambio de calor en un volumen de espacio muy reducido. Por otro lado, permite además que el intercambiador de calor se pueda disponer en un espacio cercano a la pared interna de la celda, de forma que deja despejado un gran volumen en el interior de la misma.

Al igual que con la selección de materiales aislantes, otros componentes del sistema necesitan una selección de materiales de acuerdo a criterios de transmisión térmica, de forma que propicien una cinética térmica rápida. Entre los atributos que se ven relacionados con esta selección se encuentra la rapidez de reacción para el control de temperatura del sistema. Una selección de materiales optimizada permite limitar la variación térmica de la muestra en el tiempo con una precisión de, incluso, décimas de grado.

En una realización más específica, el serpentín es de un material conductor térmico. En una realización aún más específica, el material conductor térmico es un metal o una aleación de metales, como por ejemplo aluminio.

En otra realización específica, el sistema de refrigeración interno comprende al menos 4 elementos Peltier. Los elementos Peltier son dispositivos que permiten trasegar calor, regular la temperatura de la muestra y que además pueden estar controlados mediante señales de control. Preferidamente, los elementos Peltier se disponen de forma anular alrededor del eje vertical de la muestra, en un número de entre cuatro y ocho elementos. En una realización más específica, el sistema además comprende una placa aislante de un material aislante térmico que separa térmicamente la cara fría y la cara caliente de los elementos Peltier. En una realización aún más específica, el material aislante térmico es un compuesto de poliamida. La placa aislante de un material aislante térmico, como por ejemplo un compuesto de poliamida, tiene la función de aislar las dos caras de los Peltiers del sistema de

refrigeración interno con el fin de que no exista convección entre ambas zonas de borde. De esta manera es posible incrementar la eficiencia del conjunto y obtener una refrigeración óptima de la muestra.

En otra realización específica, la placa refrigeradora es de un material conductor térmico. En una realización más específica, el material conductor térmico es metal o una aleación de metales, como por ejemplo cobre.

En una realización preferida, el portamuestras es de vidrio. Además de tener unas propiedades térmicas adecuadas, el vidrio es un material traslúcido, que permite el paso de la luz exterior, como la que proviene de la ventana transparente a la luz situada también en la base de la celda, y de este modo una buena visualización de la muestra. En otra realización preferida, el sistema de conexión del intercambiador de calor interno y del intercambiador de calor externo comprende unos racores. En una realización más preferida, los racores son de metal o una aleación de metales.

En otra realización preferida, la ventana transparente a la luz de la base de la celda es un vidrio difusor.

En otra realización preferida, el intercambiador de calor externo también comprende elementos Peltier.

En una realización específica, el fluido refrigerante es polipropilenglicol. En otra realización específica, el fluido refrigerante es aceite de silicona.

En otra realización específica, el sensor de temperatura es un termopar en contacto con la muestra.

En otra realización específica, el sensor de temperatura es un pirómetro, que permite detectar directamente la temperatura de la muestra sin contacto, incluso situándose fuera de la celda, a través de la radiación de la misma.

En otra realización específica, el sistema además comprende unos medios de iluminación externos que iluminan la muestra a través de la ventana transparente a la luz. Este aspecto es relevante a la hora de analizar muestras con estructuras o defectos a escala micrométrica, donde es necesaria una buena visualización de la superficie de la muestra mediante el complemento con sistemas de visión artificial, como por

ejemplo cámaras o microscopios. En una realización más específica, los medios de iluminación externos comprenden un diodo emisor de luz, como por ejemplo un LED, PLED u OLED.

En otra realización específica, el sistema de ventilación externo comprende un ventilador accionado por unos medios motores los cuales pueden materializarse con cualquier sistema capaz de mover el ventilador, como por ejemplo un motor eléctrico electrónicamente controlado.

En otra realización específica, el sistema de ventilación externo comprende una cámara a presión que contiene el fluido de ventilación, una conducción que conduce el fluido de ventilación sobre la ventana transparente al láser y unos medios valvulares, como por ejemplo una electroválvula o un regulador hidráulico o neumático, para regular la salida del fluido de ventilación.

En otra realización específica, el sistema de ventilación externo comprende un compresor que comprime el fluido de ventilación, una conducción que conduce el fluido de ventilación sobre la ventana transparente al láser y unos medios valvulares para regular la salida del fluido de ventilación. En esta realización preferida, el fluido de ventilación puede ser el aire exterior de la celda, tratado térmicamente o no, comprimido por un compresor y proyectado sobre la ventana transparente al láser.

En una realización preferida, los medios de control de temperatura recogen y tratan señales analógicas o digitales capturadas por el sensor de temperatura y envían señales de control analógicas o digitales al sistema de refrigeración interno. En una realización más preferida, los medios de control de la temperatura además envían señales de control al sistema de refrigeración externo. En una realización más preferida, cuando los sistemas de la celda utilizan elementos Peltier, los medios de control de temperatura recogen y tratan señales analógicas o digitales capturadas por el sensor de temperatura y envían señales de control analógicas o digitales a los elementos Peltier, que modifican su dinámica de funcionamiento en función de estas señales eléctricas de control.

En otra realización más preferida, el tratamiento de las señales analógicas o digitales se realiza mediante bloques funcionales de programa o programas de software.

En otra realización más preferida, el tratamiento de las señales analógicas o digitales se realiza mediante algoritmos implementados en un ordenador. Este ordenador además puede centralizar el control de otros sistemas relacionados con la ablación, como por ejemplo el sistema láser o el sistema que proporciona el caudal de gas de arrastre.

La invención proporciona una celda con un sistema de refrigeración criogénico que permite realizar la ablación láser de muestras previamente criogenizadas a la vez que se mantiene la temperatura de la muestra dentro de un rango de ensayo predeterminado, a pesar de la perturbación térmica que se induce en la propia muestra durante el análisis debido al impacto del haz láser sobre la misma y a la circulación de un gas de arrastre no enfriado a través de la celda de ablación. De esta manera la celda de ablación permite el análisis de tejidos biológicos o biomédicos conservados en su forma nativa, asegurando la integridad de las muestras durante el tiempo en el que ésta se encuentre dispuesta en la celda de ablación.

La invención también proporciona una celda con un sensor de temperatura de la muestra que preferidamente puede ser un termopar en contacto directo con la superficie de la misma o un pirómetro dirigido sobre la superficie de la muestra. La medición de la temperatura de la muestra de forma directa permite un control instantáneo y continuo de la temperatura de la muestra durante el análisis sin necesidad de hacer aproximaciones o lecturas indirectas que podrían falsear los resultados. La medición directa de la temperatura de la muestra además hace que se pueda llevar a cabo un control muy riguroso de la dinámica de la ablación a lo largo del análisis, mediante el reajuste rápido de la temperatura de la muestra empleando el sistema de refrigeración interno.

La configuración que se emplea para llevar a cabo la refrigeración de la muestra dispuesta en la celda de ablación combina un sistema de refrigeración interno con un intercambiador de calor interno y un sistema de refrigeración externo. En una

realización preferida, tanto el sistema de refrigeración externo como el sistema de refrigeración interno comprenden elementos Peltier lo que permite llevar a cabo un ajuste de la temperatura de manera controlada, rápida y precisa. Los medios de control de temperatura recogen y tratan señales analógicas o digitales capturadas por el sensor de temperatura y envían señales de control analógicas o digitales al sistema de refrigeración interno. Los medios de control de temperatura hacen que, por una parte, se pueda monitorizar la temperatura de la muestra y, por otra, controlarla para que esté dentro del rango de trabajo óptimo en todo momento. Mediante una materialización de la invención con elementos Peltier, la respuesta rápida del sistema de refrigeración interno puede asegurar una variación térmica en la muestra de tan solo ± 0,2°C a lo largo de 17 horas de análisis con el láser. Preferidamente, el sistema de refrigeración interno está formado por ocho elementos Peltier dispuestos de manera anular en la base de la celda, lo que permite refrigerar internamente toda la muestra de manera muy homogénea y permitir además el paso de luz para una mejor visualización de la misma.

En una realización preferida de la invención, la tapa superior extraíble tiene una abertura para la salida de gas con una forma de embudo recolector lo que permite una extracción rápida y eficaz del aerosol generado a partir de la ablación de la muestra. De esta manera se asegura que en la celda de ablación haya un flujo laminar que repercute positivamente en la resolución lateral de los análisis, lo que resulta crucial en estudios de *imaging* al haber una menor mezcla de la información proveniente de diferentes partes de la muestra.

La ventana transparente a la luz permite mejorar la visualización de la muestra dentro de la celda de ablación sobre todo si se emplean medios auxiliares, como por ejemplo un monitor de video asociado al sistema de ablación láser, para optimizar la localización de la zona de impacto y ablación. De esta forma, no solo es posible iluminar la muestra por la parte superior, a través de la ventana transparente al láser, sino que también es posible retro iluminar la misma por la parte inferior, en el caso de que la ventana se disponga en el fondo de la base de la celda. Este aspecto es de crucial importancia a la hora de analizar muestras con estructuras o defectos a escala micrométrica donde es necesaria una buena visualización de la superficie de la

muestra. Para que la luz llegue de manera adecuada a la muestra por la parte inferior, además de la ventana transparente a la luz, en una realización preferida el sistema de refrigeración interno tiene forma de serpentín y el intercambiador de calor interno se dispone anularmente de tal forma que permiten pasar un haz de luz por el centro de la base de la celda.

La celda de ablación se complementa con un sistema de ventilación externo que impulsa un fluido de ventilación sobre la ventana transparente al láser evitando de este modo problemas de condensación y asegurando así la ablación de la muestra siempre en las mismas condiciones (para las mismas condiciones de contorno como la misma energía del haz láser), y por lo tanto la calidad y la repetibilidad de los experimentos.

La invención resulta de aplicación en aquellos sectores en los que se diseñen, produzcan o utilicen celdas de ablación, como por ejemplo el de la maquinaria y equipo mecánico, geología, biología, medicina, arqueología o química.

DESCRIPCIÓN DE LAS FIGURAS

La **Fig. 1** muestra una vista detallada de una sección de la celda de ablación (1) donde se pueden observar los diferentes componentes y sistemas de la base de la celda (4) y de la tapa superior extraíble (2). La tapa superior extraíble (2) tiene en el centro de la misma una ventana transparente al láser (3). En la base de la celda (4) se puede observar un intercambiador de calor interno (11) en forma de serpentín, un sistema de refrigeración interno (12) materializado en unos elementos Peltier, una placa refrigeradora (13) sobre el sistema de refrigeración interno (12), un portamuestras (14) sobre la placa refrigeradora (13), un sistema de conexión (15) en forma de racores del intercambiador de calor interno (11) y el sistema de refrigeración externo (16), el cual no se representa en esta figura, y una ventana transparente a la luz (17) que en la figura no se muestra al estar dispuesta en la cara oculta inferior de la base de la celda (4). La muestra (5) a analizar se coloca en la base de la celda (4) sobre un portamuestras (14) dispuesto sobre la placa refrigeradora (13). Tanto el portamuestras (14) como la ventana transparente a la luz (17) permiten llevar a cabo una correcta

visualización de la muestra (5) al poder iluminar la misma desde varias direcciones, a través de la ventana transparente al láser (3) y a través de la ventana transparente a la luz (17). De esta forma, unos medios de iluminación externos (18) que se pueden materializar mediante unos LED y que tampoco aparecen representados, emiten una radiación lumínica que se puede introducir por la ventana transparente a la luz (17), mejorando la visualización de la muestra (5). En cuanto a la refrigeración de la muestra, la placa refrigeradora (13), de un material que es buen conductor térmico, está colocada sobre el sistema de refrigeración interno (12) que comprende 8 elementos Peltier. En la figura también se muestra una placa aislante (19) de un material aislante térmico que separa térmicamente la cara fría y la cara caliente de los elementos Peltier. Por otro lado, la celda de ablación (1) dispone de un sensor de temperatura (21), que en la figura se representa mediante un termopar dispuesto directamente sobre la muestra (5), el cual permite llevar a cabo el control exacto y continuo de la temperatura de la misma.

La **Fig. 2** muestra una vista descompuesta de los diferentes componentes de la base de una celda (4) similar a la mostrada en la **Fig. 1**, dispuestos sobre un eje vertical imaginario. Como se puede observar, el sistema de refrigeración interno (12) representado mediante ocho Peltiers puede estar en contacto directo con la placa refrigeradora (13) donde se coloca el portamuestras (14) con la muestra (5). Por lo tanto, la refrigeración de la muestra (5) puede realizarse de manera directa y sin pérdidas. Por otra parte, esta figura muestra claramente la disposición de la placa aislante (19), separando la cara fría y la cara caliente del sistema de refrigeración interno (12), materializado en varios Peltiers, intercalándose con ellos. Además, se muestra en la parte inferior de la base de la celda (4), la ventana transparente a la luz (17) que permite llevar a cabo una correcta visualización de la muestra (5) al poder iluminarse la misma por la parte inferior utilizando unos medios de iluminación externos (18).

La **Fig. 3** muestra una vista de la tapa superior extraíble (2) de la celda de ablación (1). En ella se puede observar la ventana transparente al láser (3), la abertura para la entrada de gas (23) y la abertura para la salida de gas (24). Como se puede ver, la abertura para la salida de gas (24) es un orificio único que en la parte interior de la

tapa tiene forma de embudo recolector, lo que permite que el gas de arrastre que transporta un aerosol que comprende material arrancado a partir de la muestra (5) pueda ser extraído de la celda de ablación (1) de una forma rápida y eficaz. De este modo se puede mejorar la resolución lateral de los análisis, lo que resulta crucial en estudios de *imaging*.

La **Fig. 4** muestra una vista cenital general de la celda de ablación (1) y del sistema de refrigeración externo (16), demarcado por un rectángulo formado por una línea punteada. El sistema de refrigeración externo (16) comprende un intercambiador de calor externo (25) y unos medios de bombeo (26). Estos medios de bombeo (26) permiten llevar a cabo la circulación del fluido refrigerante (20) a través de unos conductos aislantes entre el intercambiador de calor interno (11), dispuesto en la base de la celda (4), y el intercambiador de calor externo (25). En la figura se muestran unas flechas que señalan la dirección de circulación del fluido refrigerante (20), el cual circula por el interior de unos conductos aislantes que se conectan con la base de la celda (4) mediante un sistema de conexión (15). De esta manera el fluido refrigerante (20) es enfriado por el intercambiador de calor externo (25) después de que éste haya extraído el calor del sistema de refrigeración interno (12), asegurando así que la temperatura de la muestra (5) permanece siempre constante.

La **Fig. 5** muestra una vista de la celda de ablación (1) dispuesta en un sistema de ablación láser. La celda de ablación (1) comprende una tapa superior extraíble (2) con una ventana transparente al láser (3) y una base de la celda (4) donde se coloca la muestra (5) a analizar. La base de la celda (4) puede estar montada sobre un soporte metálico, no representado en la figura, que se puede mover en las tres dimensiones (x, y, z) empleando unos medios motores. De esta manera se puede posicionar con precisión la celda de ablación (1), y por lo tanto la muestra (5), dentro del sistema de ablación láser, de forma controlada. El control del movimiento de la celda de ablación (1) se puede realizar con un software implementado en un ordenador del sistema láser (6). La zona de interés en la muestra (5) se define con exactitud empleando un monitor de vídeo (7), que también puede estar controlado con un software implementado en el ordenador del sistema láser (6). El láser (8) es enfocado mediante unas lentes de enfoque (9) sobre la superficie de la muestra (5). Tras el impacto del láser (8) se forma

un aerosol con partículas procedentes de la muestra (5) que es transportado mediante un flujo de gas de arrastre (10), contenido en un tanque, a través de unas conexiones flexibles. La celda de ablación (1) dispone de un sistema de ventilación externo (27) que impulsa un fluido de ventilación sobre la ventana transparente al láser (3) evitando de este modo problemas de condensación. La celda de ablación (1) se puede usar en combinación con otros dispositivos como, por ejemplo, un sistema de plasma de acoplamiento inductivo con detección por espectrometría de emisión óptica o de masas, donde se introduce el aerosol generado a partir de la muestra (5) y se detecta la presencia de los diferentes elementos de interés

La **Fig. 6** muestra dos diagramas con la evolución de la temperatura de la muestra (5) en la celda de ablación (1) durante un ciclo de enfriamiento hasta alcanzar la temperatura de -20°C. En ambos diagramas (a y b) el eje de ordenadas muestra el tiempo de análisis y el eje de abscisas muestra la temperatura de la muestra (5) medida con el sensor de temperatura (21). El diagrama a) muestra la evolución de la temperatura de la muestra (5) durante los primeros 40 min de análisis y el diagrama b) la evolución de la temperatura durante 17 h. Como se puede observar en el diagrama a), la temperatura de la superficie de la muestra (5) baja en menos de 20 minutos a -20°C. Además, cabe destacar que la temperatura se mantiene estable, con una desviación de solamente ± 0,2°C, a lo largo de 17 horas de análisis con el láser (8). De este modo, se puede asegurar la integridad de la muestra (5) así como que las condiciones de trabajo se mantienen constantes a lo largo de todo el análisis.

La **Fig. 7** muestra los perfiles de ablación obtenidos por LA-ICP-MS para los isótopos $^{107}Ag^{+}$ y $^{208}Pb^{+}$ en el análisis de un vidrio (SRM NIST 612) empleando la celda de ablación (1) de la invención en condiciones criogénicas y trabajando a temperatura ambiente (-20 y +20°C, respectivamente). En ambos perfiles el eje de ordenadas muestra el tiempo de análisis y el eje de abscisas la intensidad medida para cada elemento en el ICP-MS. Como se puede observar en el perfil a), la señal de $^{107}Ag^{+}$ se estabiliza con una desviación estándar temporal relativa (TRSD) menor del 12% trabajando a temperatura ambiente y en condiciones criogénicas. Además, se puede indicar que la precisión (RSD para tres medidas independientes) en la medida de las relaciones isotópicas de $^{109}Ag^{+}/^{107}Ag^{+}$ está por debajo de 1,7% con una

desviación del 1,3% de la relación isotópica natural. Para el caso del $^{208}Pb^+$ (perfil b), la señal se estabiliza con un TRSD del 8% siendo la precisión en la medida de la relación isotópica $^{208}Pb^+/^{206}Pb^+$ por debajo de 1% (con una desviación del 2,5% de la relación isotópica natural). Cabe destacar que la celda de ablación (1) permite obtener resultados comparables empleando ambas temperaturas de trabajo, en términos de precisión de las señales, exactitud en la medida de relaciones isotópicas y sensibilidad.

La **Fig. 8** muestra una representación de los tiempos de evacuación de la celda de ablación (1) para los elementos $^{59}Co^+$, $^{107}Ag^+$, $^{137}Ba^+$, $^{232}Th^+$ y $^{238}U^+$ en el análisis del vidrio SRM NIST 612 a dos temperaturas diferentes, +20°C y -20°C. El eje de ordenadas muestra los isótopos de cada elemento medidos en el ICP-MS y el eje de abscisas el tiempo de evacuación. Las barras de error de la figura indican la desviación estándar obtenida para 10 análisis independientes. El tiempo de evacuación se define como el tiempo que necesita la señal de cada uno de los isótopos para disminuir desde su máximo valor al 10% de la señal máxima. Este factor permite estudiar la rapidez con la que el aerosol generado en la celda de ablación (1) a partir de la muestra (5) abandona la celda de ablación (1) y es transportado, por ejemplo, a un equipo ICP-MS para su posterior análisis. Cuanto menor sea el tiempo de evacuación, mejor será la resolución lateral al haber una menor mezcla de la información proveniente de diferentes partes de la muestra (5). Como se puede observar en la figura, para todos los elementos se obtienen menores tiempos de evacuación trabajando a -20°C. Además, la reproducibilidad es también mejor a baja temperatura, indicando las óptimas prestaciones analíticas de la celda de ablación (1) en condiciones criogénicas.

La **Fig. 9** muestra las imágenes obtenidas a +20°C y -20°C para la distribución espacial de varios elementos traza ($^{56}Fe^+$, $^{63}Cu^+$, $^{64}Zn^+$ y $^{127}I^+$) en un material biológico sintético empleando la celda de ablación (1) conectada a un equipo ICP-MS. Las condiciones experimentales de análisis son: 50 µm diámetro del láser (8), 20 Hz de frecuencia de repetición, 5,6 mJ de energía y 32,5 µm/s velocidad de desplazamiento de la muestra (5). Como se puede ver en las imágenes, en todos los casos se puede observar una distribución homogénea de $^{56}Fe^+$, $^{63}Cu^+$, $^{64}Zn^+$ y $^{127}I^+$ en la muestra a ambas temperaturas de trabajo: para cada elemento en estudio las imágenes de la izquierda corresponden a los análisis a -20°C y las de la derecha a +20°C.

Comparando las intensidades obtenidas para los diferentes elementos se observa un aumento significativo en la señal de $^{127}I^{+}$ para los análisis realizados a -20°C. Además, cabe destacar que se obtiene una mejor resolución lateral trabajando a -20°C para todos los elementos (especialmente para el $^{64}Zn^{+}$) lo que indica una mejor conservación de la muestra durante el tiempo de análisis.

EXPLICACIÓN DE UNA FORMA DE REALIZACIÓN PREFERENTE

Para una mejor comprensión de la presente invención, se expone el siguiente ejemplo de realización preferente, descrito en detalle, que debe entenderse sin carácter limitativo del alcance de la invención.

EJEMPLO 1

La celda de ablación (1) fue integrada en un sistema de ablación láser acoplado a un equipo ICP-MS para llevar a cabo estudios de *imaging*. La celda de ablación (1) estaba formada por dos partes: una tapa superior extraíble (2) de un compuesto de poliamida con una ventana transparente al láser (3) y una base de la celda (4), también de un compuesto de poliamida por ser éste un compuesto con baja conductividad térmica. La tapa superior extraíble (2) se unía a la base de la celda (4) mediante una rosca. La ventana transparente al láser (3) se hizo de cuarzo con un recubrimiento exterior que permitía la trasmisión de una longitud de onda electromagnética de 213 nm. La base de la celda (4) se montó sobre un soporte metálico que se puede mover en las tres dimensiones (x, y, z) empleando un sistema auxiliar motorizado. De esta manera se consiguió posicionar con precisión la celda de ablación (1), y por lo tanto la muestra (5), dentro del sistema de ablación láser. El control del movimiento de la celda de ablación (1) se realizó con un software implementado en el ordenador del sistema láser (6). La zona de interés en la muestra (5) se pudo definir con exactitud empleando un monitor de vídeo (7), controlado también con un software implementado en el ordenador del sistema láser (6). El láser (8) se enfocó mediante unas lentes de enfoque (9) sobre la superficie de la muestra (5). Tras el impacto del láser (8) se formó un aerosol con partículas procedentes de la muestra (5), el cual se

pudo transportar mediante un flujo de gas de arrastre (10), constituido por helio inerte, a través de unas conexiones flexibles hasta el sistema ICP-MS. Para llevar a cabo el análisis, el láser (8) se disparó siempre en un mismo punto aunque fue posible variar la posición de la muestra (5) en las dimensiones x e y empleando el sistema auxiliar motorizado. Ésta es la estrategia de análisis habitualmente seleccionada para hacer estudios de *imaging* y obtener una buena resolución lateral. Las condiciones experimentales de análisis fueron: 150 µm diámetro del haz láser (8), 10 Hz frecuencia de repetición, 3,5 mJ de energía y 20 µm/s velocidad de desplazamiento de la muestra (5).

La tapa superior extraíble (2) tenía una abertura para la entrada de gas (23) y una abertura para la salida de gas (24). La abertura para la salida de gas (24) era un orificio único que en la parte interior de la tapa tenía forma de embudo recolector, lo que permitió que el gas de arrastre que transportaba el aerosol que comprendía material arrancado a partir de la muestra (5) pudiera ser extraído de la celda de ablación (1) de una forma rápida y eficaz. Como se muestra en la **Fig. 8**, empleando un vidrio SRM NIST 612 como muestra (5) se obtuvieron tiempos de evacuación menores de 4 segundos para todos los analitos investigados ($^{59}Co^{+}$, $^{107}Ag^{+}$, $^{137}Ba^{+}$, $^{232}Th^{+}$ y $^{238}U^{+}$), trabajando en condiciones de baja temperatura. De este modo se pudo mejorar la resolución lateral de los análisis empleando baja temperatura y una abertura para la salida de gas (24) con forma de embudo recolector, lo que resulta crucial en estudios de *imaging*.

En la base de la celda (4) se dispuso un intercambiador de calor interno (11) de aluminio en forma de serpentín, un sistema de refrigeración interno (12) materializado con 8 elementos Peltier distribuidos homogéneamente de forma anular, una placa refrigeradora (13) de cobre dispuesta sobre el sistema de refrigeración interno (12), un portamuestras (14) de vidrio sobre la placa refrigeradora (13), un sistema de conexión (15) en forma de racores entre el intercambiador de calor interno (11) y el sistema de refrigeración externo (16), y una ventana transparente a la luz (17) dispuesta en la parte inferior de la base de la celda (4). Además, entre el sistema de refrigeración interno (12) y la placa refrigeradora (13) se dispuso una placa aislante (19) de un compuesto de poliamida que tiene la función de aislar las dos caras de los 8 elementos

Peltier con el fin de que no existiese convección entre ambas en las zonas de borde, incrementando de esta manera la eficiencia del conjunto. De esta manera, el sistema de refrigeración interno (12) permitió alcanzar temperaturas en la muestra (5) de hasta -20ºC, lo que aseguraba la integridad de la muestra (5) durante el análisis. Además, para el buen funcionamiento del sistema de refrigeración interno (12) se empleó un serpentín de aluminio como intercambiador de calor interno (11). Un fluido refrigerante (20), formado por polipropilenglicol, circulaba a través del intercambiador de calor interno (11) proporcionando un foco frio a los 8 elementos Peltier para un funcionamiento más eficaz de los mismos. El sistema de conexión (15) de racores metálicos permitió la circulación del fluido refrigerante (20) entre el intercambiador de calor interno (11) y el sistema de refrigeración externo (16).

El sistema de refrigeración externo (16) comprendía un intercambiador de calor externo (25) materializado en un elemento Peltier y unos medios de bombeo (26) materializados mediante una bomba hidráulica de impulsión radial controlada electrónicamente. Estos medios de bombeo (26) permitieron llevar a cabo la circulación del fluido refrigerante (20) a través de unos conductos aislantes entre el intercambiador de calor interno (11) y el intercambiador de calor externo (25). El fluido refrigerante (20) circulaba a través del intercambiador de calor interno (11) proporcionando un foco frío a los 8 elementos Peltier y para enfriar de nuevo este fluido refrigerante (20) se hacía llegar el mismo al intercambiador de calor externo (25).

Se empleó como sensor de temperatura (21) un termopar en contacto directo con la superficie de la muestra (5) para controlar y poder ajustar así la temperatura de análisis. Los medios de control de la temperatura (22) estaban constituidos por un software que recogía y trataba señales digitales capturadas por el sensor de temperatura (21) y enviaba señales de control digitales tanto a los Peltier del sistema de refrigeración interno (12) como al Peltier y la bomba del sistema de refrigeración externo (16). Empleando este sistema de refrigeración controlado en la celda de ablación (1) se pudo llevar a cabo un enfriamiento rápido de la muestra (5). Como se recoge en la **Fig. 6**, la temperatura de la superficie de la muestra (5) bajó en menos de

20 minutos a -20°C. Además, esta temperatura se mantuvo estable, con una desviación de ± 0,2°C, a lo largo de 17 horas de análisis con el láser (8).

Para un correcto funcionamiento de la celda de ablación (1), se empleó un sistema de ventilación externo (27) que impulsaba un fluido de ventilación sobre la ventana transparente al láser (3). El sistema de ventilación externo (27) consistió en un ventilador accionado por un motor eléctrico. Este sistema de ventilación externo (27) permitió mantener unas condiciones óptimas de trabajo eliminando los fenómenos de condensación sobre la ventana transparente al láser al trabajar a baja temperatura.

REIVINDICACIONES

1. Celda de ablación que comprende:

   - una tapa superior extraíble (2) que permite la disposición de una muestra (5) dentro de la celda de ablación (1) que a su vez comprende una ventana transparente al láser (3), una abertura para la entrada de gas (23) de arrastre y una abertura para la salida de gas (24) de arrastre;

   - una base de la celda (4) que a su vez comprende en su interior un intercambiador de calor interno (11), un sistema de refrigeración interno (12), una placa refrigeradora (13) sobre el sistema de refrigeración interno (12), un portamuestras (14) sobre la placa refrigeradora (13), un sistema de conexión (15) del intercambiador de calor interno (11) y el sistema de refrigeración externo (16) y una ventana transparente a la luz (17);

   - un sistema de refrigeración externo (16) que a su vez comprende un intercambiador de calor externo (25) y unos medios de bombeo (26) de un fluido refrigerante (20) que permiten llevar a cabo la circulación del fluido refrigerante (20) a través del intercambiador de calor interno (11) de la base de la celda (4) y del intercambiador de calor externo (25);

   - un sensor de temperatura (21) de la muestra (5);

   - un sistema de ventilación externo (27) que impulsa un fluido de ventilación sobre la ventana transparente al láser (3) de la tapa superior extraíble (2);

   - unos medios de control de temperatura (22).

2. Sistema según la reivindicación 1 caracterizado por que la tapa superior extraíble (2) y la base de la celda (4) son de un material aislante térmico.

3. Sistema según la reivindicación 1 caracterizado por que la ventana transparente al láser (3) comprende un cristal de cuarzo.

4. Sistema según la reivindicación 3 caracterizado por que el cristal de cuarzo permite la trasmisión de una longitud de onda electromagnética en el rango comprendido entre 1064 nm y 193 nm.

5. Sistema según la reivindicación 1 caracterizado por que la abertura para la entrada de gas (23) de arrastre consiste en un orificio único.

6. Sistema según la reivindicación 1 caracterizado por que la abertura para la entrada de gas (23) de arrastre consiste en cuatro orificios de entrada.

7. Sistema según la reivindicación 1 caracterizado por que la abertura para la salida de gas (24) de arrastre consiste en un orificio único.

8. Sistema según la reivindicación 7 caracterizado por que el orificio único tiene forma de embudo recolector.

9. Sistema según la reivindicación 1 caracterizado por que la abertura para la salida de gas (24) consiste en cuatro orificios de salida.

10. Sistema según la reivindicación 1 caracterizado por que el intercambiador de calor interno (11) es un serpentín.

11. Sistema según la reivindicación 10 caracterizado por que el serpentín es de un material conductor térmico.

12. Sistema según la reivindicación 1 caracterizado por que el sistema de refrigeración interno (12) comprende al menos 4 elementos Peltier.

13. Sistema según la reivindicación 12 caracterizado por que además comprende una placa aislante (19) de un material aislante térmico que separa térmicamente la cara fría y la cara caliente de los elementos Peltier.

14. Sistema según la reivindicación 2 ó 13 caracterizado por que el material aislante térmico es un compuesto de poliamida.

15. Sistema según la reivindicación 1 caracterizado por que la placa refrigeradora (13) es de un material conductor térmico.

16. Sistema según la reivindicación 11 ó 15 caracterizado por que el material conductor térmico es metal o una aleación de metales.

17. Sistema según la reivindicación 1 caracterizado por que el portamuestras (14) es de vidrio.

18. Sistema según la reivindicación 1 caracterizado por que el sistema de conexión (15) comprende unos racores.

19. Sistema según la reivindicación 18 caracterizado por que los racores son de metal o una aleación de metales.

20. Sistema según la reivindicación 1 caracterizado por que la ventana transparente a la luz (17) es un vidrio difusor.

21. Sistema según la reivindicación 1 caracterizado por que el intercambiador de calor externo (25) comprende elementos Peltier.

22. Sistema según la reivindicación 1 caracterizado por que el fluido refrigerante (20) es polipropilenglicol.

23. Sistema según la reivindicación 1 caracterizado por que el fluido refrigerante (20) es aceite de silicona.

24. Sistema según la reivindicación 1 caracterizado por que el sensor de temperatura (21) es un termopar.

25. Sistema según la reivindicación 1 caracterizado por que el sensor de temperatura (21) es un pirómetro.

26. Sistema según la reivindicación 1 caracterizado por que además comprende unos medios de iluminación externos (18) que iluminan la muestra (5) a través de la ventana transparente a la luz (17).

27. Sistema según la reivindicación 26 caracterizado por que los medios de iluminación externos (18) comprenden un diodo emisor de luz

28. Sistema según la reivindicación 1 caracterizado por que el sistema de ventilación externo (27) comprende un ventilador accionado por unos medios motores.

29. Sistema según la reivindicación 1 caracterizado por que el sistema de ventilación externo (27) comprende una cámara a presión que contiene el fluido de ventilación, una conducción que conduce el fluido de ventilación sobre la ventana transparente al láser (3) y unos medios valvulares para regular la salida del fluido de ventilación.

30. Sistema según la reivindicación 1 caracterizado por que el sistema de ventilación externo (27) comprende un compresor que comprime el fluido de ventilación, una conducción que conduce el fluido de ventilación sobre la ventana transparente al láser (3) y unos medios valvulares para regular la salida del fluido de ventilación.

31. Sistema según la reivindicación 1 caracterizado por que los medios de control de temperatura (22) recogen y tratan señales analógicas o digitales capturadas por el sensor de temperatura (21) y envían señales de control analógicas o digitales al sistema de refrigeración interno (12).

32. Sistema según la reivindicación 31 caracterizado por que los medios de control de la temperatura (22) además envían señales de control al sistema de refrigeración externo (16).

33. Sistema según las reivindicaciones 12 ó 21 caracterizado por que los medios de control de temperatura (22) recogen y tratan señales analógicas o digitales capturadas por el sensor de temperatura (21) y envían señales de control analógicas o digitales a los elementos Peltier.

34. Sistema según la reivindicación 31, 32 ó 33 caracterizado por que el tratamiento de las señales analógicas o digitales se realiza mediante bloques funcionales de programa o programas de software.

35. Sistema según la reivindicación 31, 32 ó 33 caracterizado por que el tratamiento de las señales analógicas o digitales se realiza mediante algoritmos implementados en un ordenador.

ES 2 425 138 A1

FIG. 1

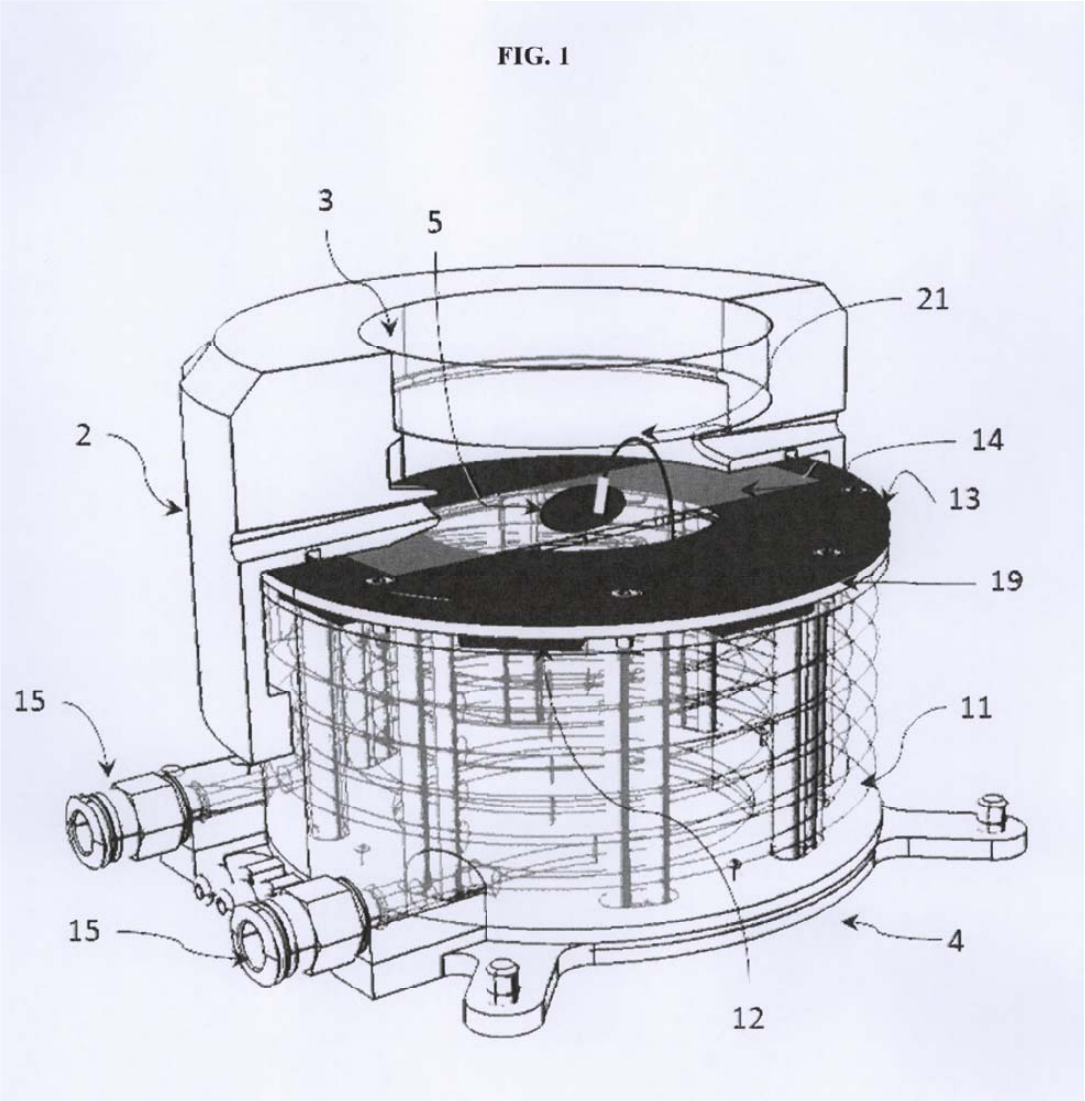

FIG. 2

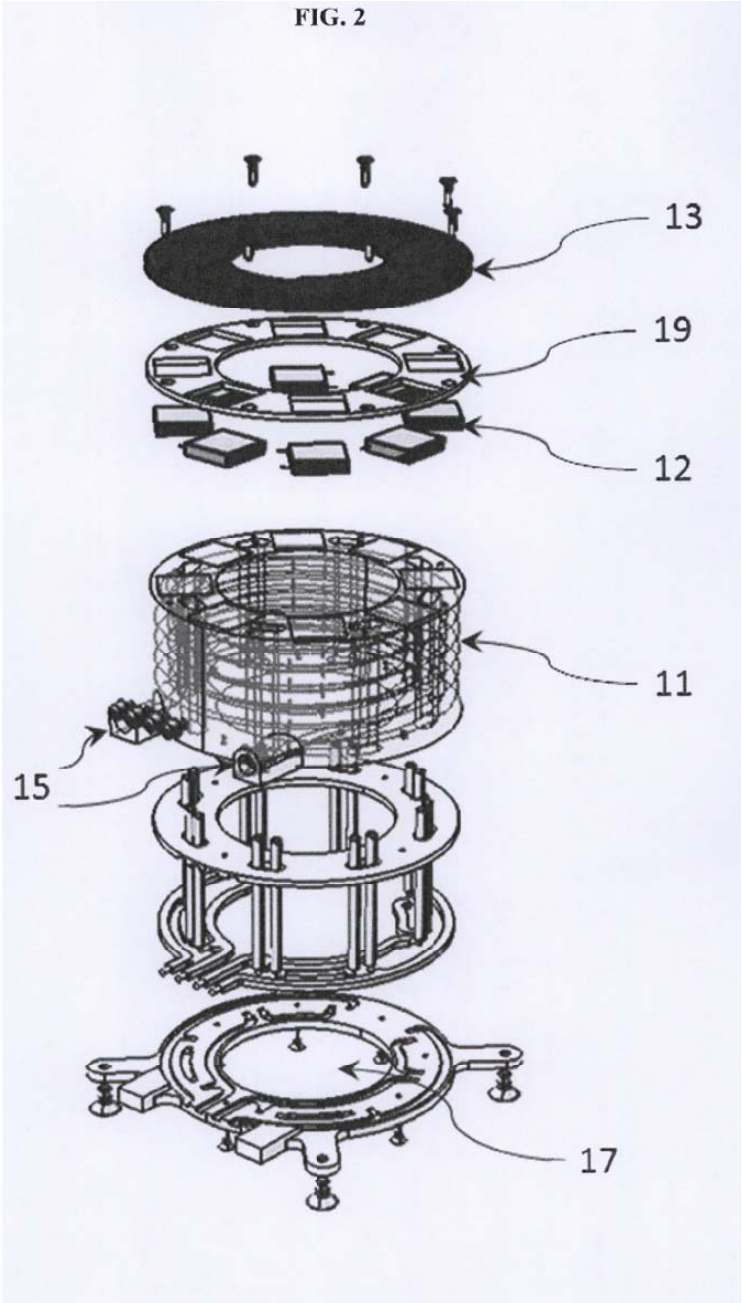

FIG. 3

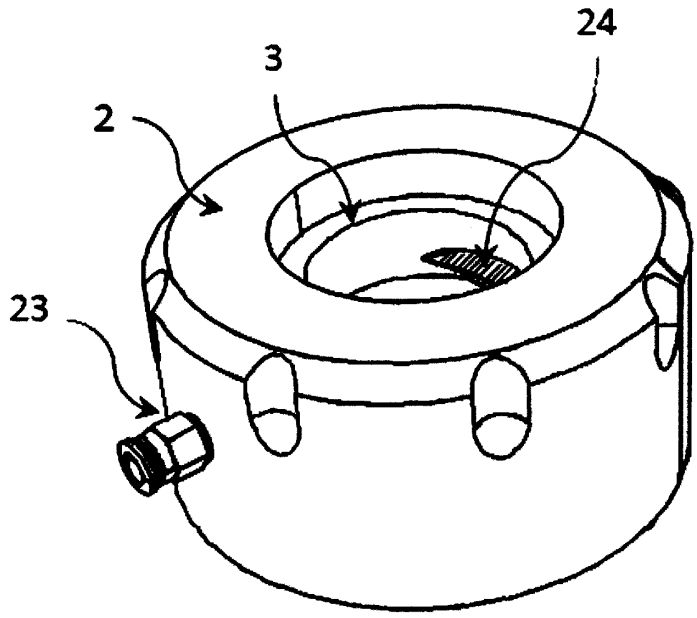

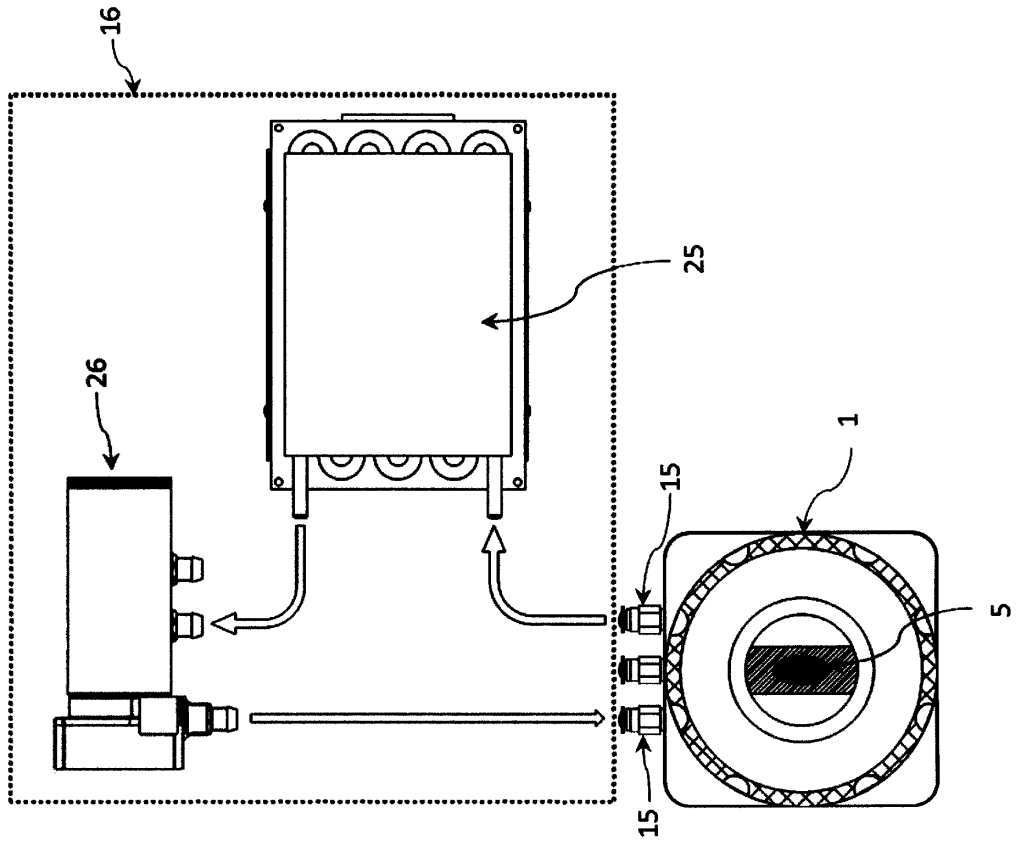

FIG. 4

ES 2 425 138 A1

FIG. 5

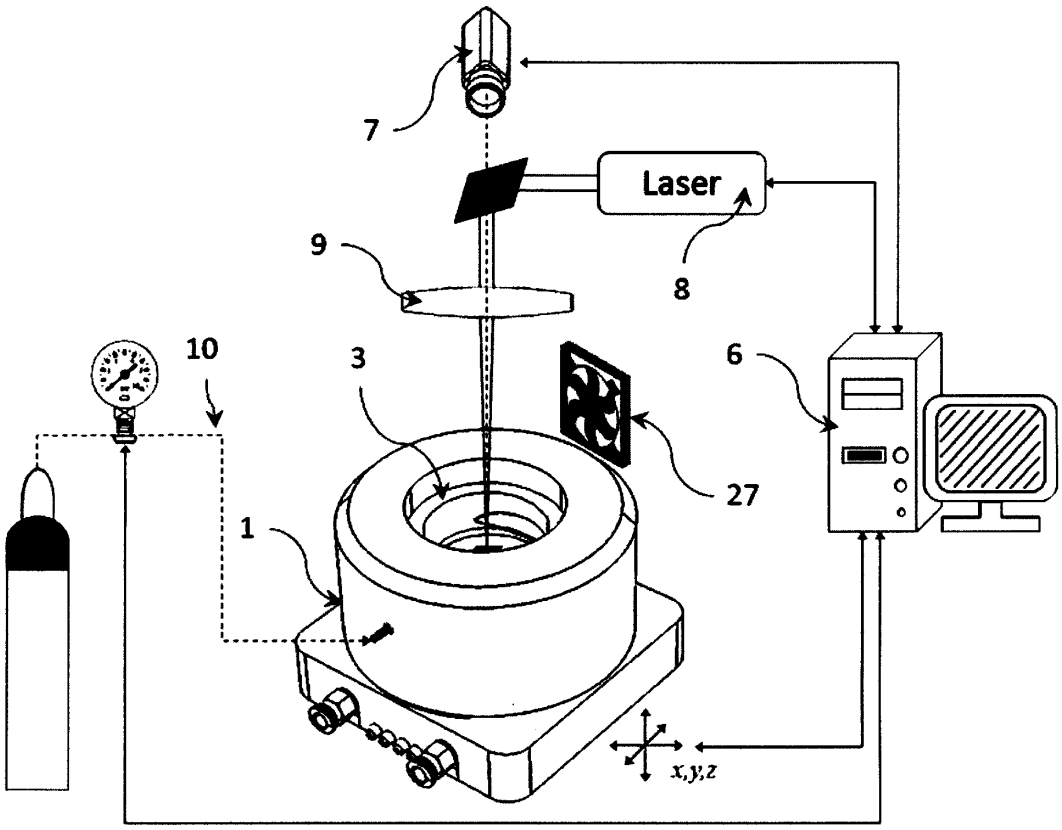

FIG. 6

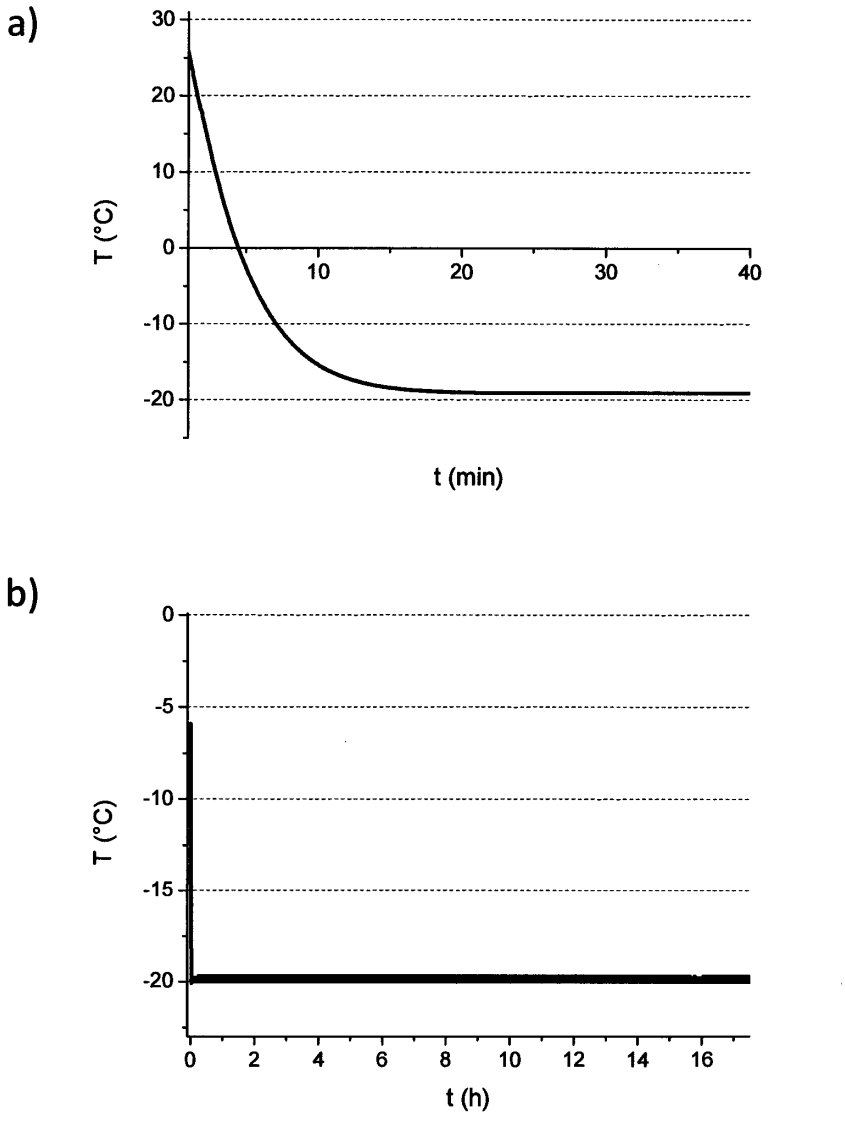
a)
30
20
10
0
-10
-20
T (°C)
10
20
30
40
t (min)
b)
0
-5
-10
-15
-20
T (°C)
0
2
4
6
8
10
12
14
16
t (h)

ES 2 425 138 A1

FIG. 7

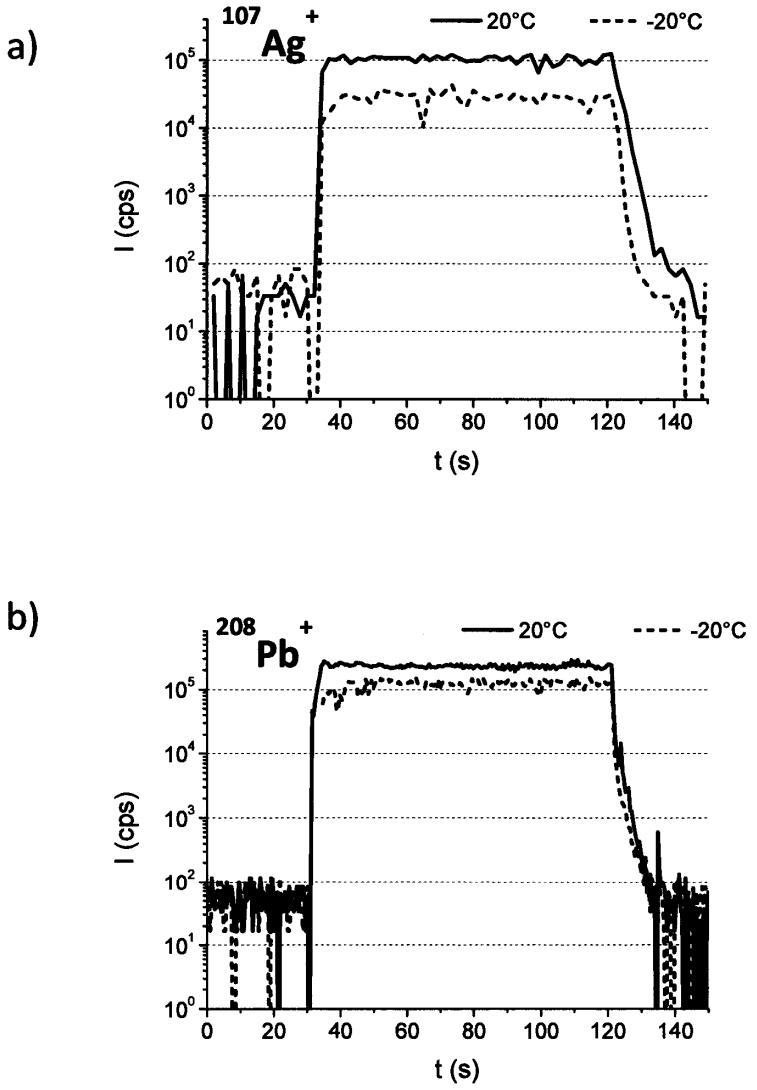

FIG. 8

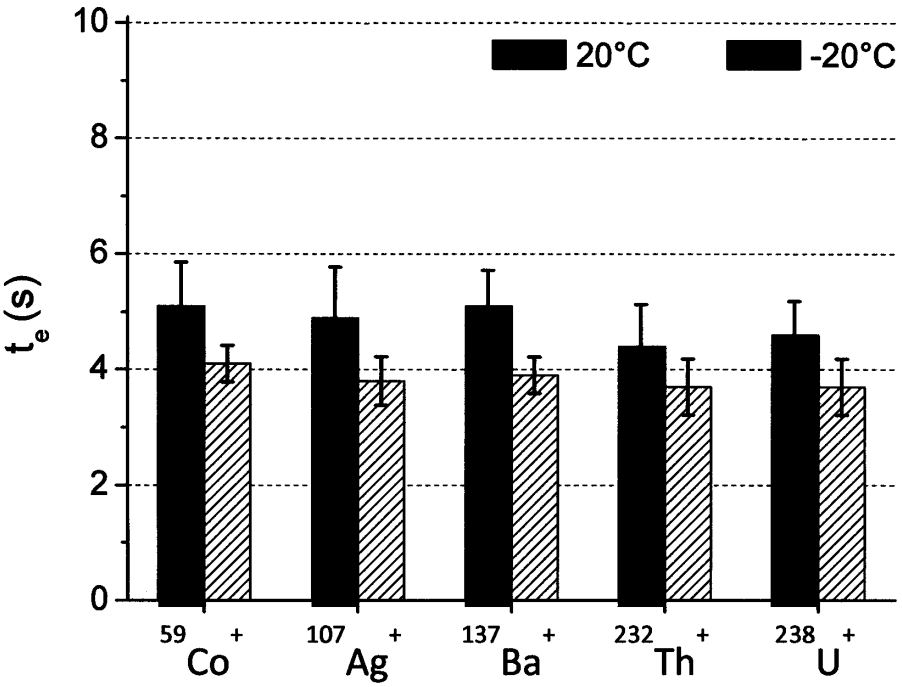

ES 2 425 138 A1

FIG. 9

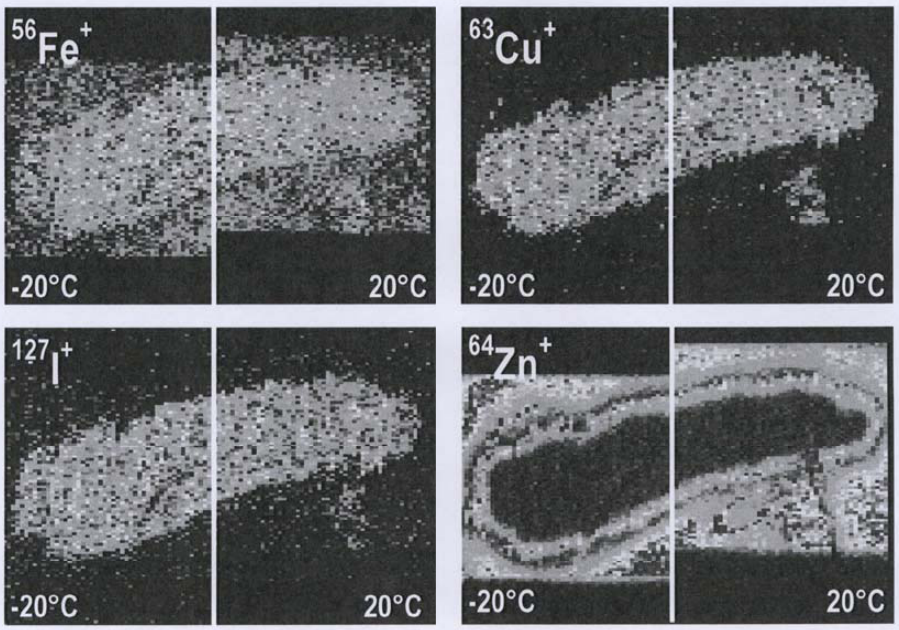

OFICINA ESPAÑOLA
DE PATENTES Y MARCAS

ESPAÑA

(21) N.º solicitud: 201300559

(22) Fecha de presentación de la solicitud: 07.06.2013

(32) Fecha de prioridad:

INFORME SOBRE EL ESTADO DE LA TECNICA

(51) **Int. CI. :** ***G01N27/62*** (2006.01)

DOCUMENTOS RELEVANTES

Categoría	(56) Documentos citados	Reivindicaciones afectadas
A	US 20040045497 A1 (KRIEWS) 11.03.2004, resumen; párrafos [0010]-[0013],[0015]-[0016],[0019]-[0021],[0032]-[0033],[0038]-[0042]; reivindicaciones 1,3,5,7,8; figuras 1,7,9.	1-35
A	WO 2006106265 A1 (CENTRE NATIONAL DE LA RECHERCHE SCIENTIFIQUE ET UNIVERSITE DE PAU ET DES PAYS DE L'ADOUR) 12.10.2006, resumen; página 4, líneas 16-23,32-35; página 5, líneas 1-26; página 7, líneas 28-35; página 8, líneas 4-9; reivindicación 1.	1-35
A	US 20120104244 A1 (UNIVERSITY OF NORTH TEXAS) 03.05.2012, todo el documento.	1-35
A	US 20120074307 A1 (SABINE BECKER AND AGMAR SALBER) 29.03.2012, resumen; párrafos [0014]-[0019]; figuras 1a;1b.	1-35
A	WO 2006076817 A1 (EMPA, EIDGENÖSSISCHE MATERIALPRÜFUNGS- UND FORSCHUNGSANSTALT) 27.07.2006, todo el documento.	1-35

Categoría de los documentos citados
X: de particular relevancia
Y: de particular relevancia combinado con otro/s de la misma categoría
A: refleja el estado de la técnica
O: referido a divulgación no escrita
P: publicado entre la fecha de prioridad y la de presentación de la solicitud
E: documento anterior, pero publicado después de la fecha de presentación de la solicitud

El presente informe ha sido realizado

☒ para todas las reivindicaciones ☐ para las reivindicaciones nº:

Fecha de realización del informe	Examinador	Página
30.09.2013	M. J. García Bueno	1/5

INFORME DEL ESTADO DE LA TÉCNICA	Nº de solicitud: 201300559

Documentación mínima buscada (sistema de clasificación seguido de los símbolos de clasificación)

F25B, G01N

Bases de datos electrónicas consultadas durante la búsqueda (nombre de la base de datos y, si es posible, términos de búsqueda utilizados)

INVENES, EPODOC, WPI, GOOGLE

OPINIÓN ESCRITA

Nº de solicitud: 201300559

Fecha de Realización de la Opinión Escrita: 30.09.2013

Declaración

Novedad (Art. 6.1 LP 11/1986)	Reivindicaciones	1-35	**SI**
	Reivindicaciones		**NO**
Actividad inventiva (Art. 8.1 LP11/1986)	Reivindicaciones	1-35	**SI**
	Reivindicaciones		**NO**

Se considera que la solicitud cumple con el requisito de aplicación industrial. Este requisito fue evaluado durante la fase de examen formal y técnico de la solicitud (Artículo 31.2 Ley 11/1986).

Base de la Opinión.-

La presente opinión se ha realizado sobre la base de la solicitud de patente tal y como se publica.

OPINIÓN ESCRITA

Nº de solicitud: 201300559

1. Documentos considerados.-

A continuación se relacionan los documentos pertenecientes al estado de la técnica tomados en consideración para la realización de esta opinión.

Documento	Número Publicación o Identificación	Fecha Publicación
D01	US 20040045497 A1 (KRIEWS)	11.03.2004
D02	WO 2006106265 A1 (CENTRE NATIONAL DE LA RECHERCHE SCIENTIFIQUE ET UNIVERSITE DE PAU ET DES PAYS DE L'ADOUR)	12.10.2006
D03	US 20120104244 A1 (UNIVERSITY OF NORTH TEXAS)	03.05.2012
D04	US 20120074307 A1 (SABINE BECKER AND AGMAR SALBER)	29.03.2012
D05	WO 2006076817 A1 (EMPA, EIDGENÖSSISCHE MATERIALPRÜFUNGS- UND FORSCHUNGSANSTALT)	27.07.2006

2. Declaración motivada según los artículos 29.6 y 29.7 del Reglamento de ejecución de la Ley 11/1986, de 20 de marzo, de Patentes sobre la novedad y la actividad inventiva; citas y explicaciones en apoyo de esta declaración

La presente solicitud de invención consiste en una celda de ablación que comprende una tapa superior extraíble, una base de la celda, un sistema de refrigeración externo, un sensor de temperatura de la muestra, un sistema de ventilación externo y unos medios de control de temperatura.

La tapa superior extraíble comprende una ventana transparente al láser, una abertura para la entrada de gas de arrastre y otra abertura para la salida de dicho gas.

La base de la celda comprende un intercambiador de calor interno, un sistema de refrigeración interno, una placa refrigeradora, un porta muestras, un sistema de conexión del intercambiador de calor interno y el sistema de refrigeración externo y una ventana transparente a la luz.

Además, el sistema de refrigeración externo comprende un sistema de intercambiador de calor externo y medios de bombeo de un fluido refrigerante (reivindicaciones 1-35).

El documento D01 se considera el más representativo del estado de la técnica y consiste en una celda de ablación con una tapa superior extraíble de material aislante que comprende una ventana transparente al láser de cristal de cuarzo que permite la transmisión de una longitud de onda electromagnética de 1064 nm, una abertura para la entrada de gas de arrastre y una abertura para la salida de dicho gas.

El sistema de ablación divulgado en el documento también comprende una base de la celda que comprende un intercambiador de calor en forma de serpentín de material conductor térmico, un sistema de refrigeración, una placa refrigeradora, un portamuestras, y un sistema de conexión del intercambiador de calor con el sistema de refrigeración (ver resumen, párrafos [0010]-[0013], [0015]-[0016], [0019]-[0021], [0032]-[0033], [0038]- [0042], reivindicaciones 1, 3, 5, 7, y 8, y figuras 1, 7 y 9).

El fluido refrigerante utilizado es aceite de silicona (ver párrafo [0013]).

El documento D02 consiste en un aparato laser de análisis directo para el microanálisis de muestras, que comprende una cámara de ablación con una ventana óptica, un orificio de entrada del gas de arrastre y un orificio de salida, unos medios de enfoque y un porta muestras entre otros (ver resumen, página 4, líneas 16-23 y 32-35, página 5, líneas 1-26, página 7, líneas 28-35, página 8, líneas 4-9, y reivindicación 1).

El documento D03 consiste en un sistema LA-ICP-MS para muestras refrigeradas antes del análisis (ver todo el documento).

El documento D04 consiste en una cámara de ablación por láser adecuada para su uso en una unidad de disección micro asistida por láser convencional (ver resumen, párrafos [0014]-[0019] y figuras 1a y 1b).

El documento D05 consiste en un dispositivo para el análisis de la ablación por láser que comprende una boquilla giratoria que gira alrededor de un eje de rotación. El gas de arrastre se expulsa a la cámara de ablación y su trayectoria es helicoidal asegurando un buen lavado de la cámara y aumentando el porcentaje de partículas sometidas a la ablación en el analizador (ver todo el documento).

OPINIÓN ESCRITA

Nº de solicitud: 201300559

1.- NOVEDAD (Art. 6.1 Ley 11/1986) Y ACTIVIDAD INVENTIVA (Art. 8.1 Ley 11/1986).

La presente solicitud de invención difiere de los documentos D01-D05 en que los sistemas de ablación divulgados no comprenden los sensores y medios de control de temperatura, ni una ventana transparente a la luz en la base de la celda.

Dichas características implican un efecto mejorado comparado con el estado de la técnica, ya que el control exacto y continuo de la temperatura de las muestras de tejidos es un aspecto crucial para asegurar la integridad de la muestra durante el análisis siendo los resultados más exactos y precisos, y, por otro lado, la iluminación de la muestra mejora con la ventana en la zona de la base de la celda consiguiendo así una buena resolución lateral y una mejor distinción de las microestructuras.

Además, no se considera obvio que un experto en la materia obtenga la invención a partir de los documentos mencionados anteriormente.

Por lo tanto se considera que las reivindicaciones 1-35 son nuevas e implican actividad inventiva en el sentido de los artículos 6.1 y 8.1 Ley 11/1986.

G Model
ACA-232970; No. of Pages 9
ARTICLE IN PRESS
Analytica Chimica Acta xxx (2013) xxx–xxx
Contents lists available at ScienceDirect
Analytica Chimica Acta
journal homepage: www.elsevier.com/locate/aca

Design and evaluation of a new Peltier-cooled laser ablation cell with on-sample temperature control

Ioana Konz, Beatriz Fernández*, M. Luisa Fernández, Rosario Pereiro, Alfredo Sanz-Medel*

Department of Physical and Analytical Chemistry, Faculty of Chemistry, University of Oviedo, Julian Clavería, 8, 33006 Oviedo, Spain

HIGHLIGHTS

- Development of a cryogenic laser ablation cell with on-sample temperature control.
- Ablation cell combines small internal volume and laminar gas flow pattern.
- Refrigeration is composed of two Peltier systems (internal and external).
- Peephole under the sample enables its optimum visualization.
- Analytical performance was studied analyzing inorganic and biological tissues.

GRAPHICAL ABSTRACT

A cryogenic laser ablation cell with a small internal volume was designed and successfully tested for imaging studies by LA-ICP-MS of inorganic materials and biological samples.

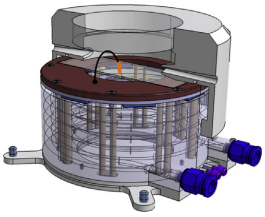

ARTICLE INFO

Article history:
Received 4 September 2013
Received in revised form
11 November 2013
Accepted 16 November 2013
Available online xxx

Keywords:
LA-ICP-MS
Cryogenic ablation cell
Imaging
Biological tissue

ABSTRACT

A new custom-built Peltier-cooled laser ablation cell is described. The proposed cryogenic cell combines a small internal volume (20 cm^3) with a unique and reliable on-sample temperature control. The use of a flexible temperature sensor, directly located on the sample surface, ensures a rigorous sample temperature control throughout the entire analysis time and allows instant response to any possible fluctuation. In this way sample integrity and, therefore, reproducibility can be guaranteed during the ablation. The refrigeration of the proposed cryogenic cell combines an internal refrigeration system, controlled by a sensitive thermocouple, with an external refrigeration system. Cooling of the sample is directly carried out by 8 small (1 cm × 1 cm) Peltier elements placed in a circular arrangement in the base of the cell. These Peltier elements are located below a copper plate where the sample is placed. Due to the small size of the cooling electronics and their circular allocation it was possible to maintain a peephole under the sample for illumination allowing a much better visualization of the sample, a factor especially important when working with structurally complex tissue sections. The analytical performance of the cryogenic cell was studied using a glass reference material (SRM NIST 612) at room temperature and at −20 °C. The proposed cell design shows a reasonable signal washout (signal decay within less than 10 s to background level), high sensitivity and good signal stability (in the range 6.6–11.7%). Furthermore, high precision (0.4–2.6%) and accuracy (0.3–3.9%) in the isotope ratio measurements were also observed operating the cell both at room temperature and at −20 °C. Finally, experimental results obtained for the cell application to qualitative elemental imaging of structurally complex tissue samples (e.g. eye sections from a native frozen porcine eye and fresh flower leaves) demonstrate that working in cryogenic conditions is critical in such type of direct sample analysis.

* Corresponding authors. Tel.: +34 985103474; fax: +34 985103474.
E-mail addresses: fernandezbeatriz@uniovi.es (B. Fernández), asm@uniovi.es (A. Sanz-Medel).

0003-2670/$ – see front matter © 2013 Elsevier B.V. All rights reserved.
http://dx.doi.org/10.1016/j.aca.2013.11.040

Please cite this article in press as: I. Konz, et al., Design and evaluation of a new Peltier-cooled laser ablation cell with on-sample temperature control, Anal. Chim. Acta (2013), http://dx.doi.org/10.1016/j.aca.2013.11.040

G Model
ACA-232970; No. of Pages 9
ARTICLE IN PRESS

1. Introduction

Since the first efforts carried out in the 80s, interest in laser ablation coupled to inductively coupled plasma mass spectrometry (LA-ICP-MS) has been continuously increasing [1,2]. In fact, LA-ICP-MS is currently used for elemental and isotopic analysis in a wide variety of applications, including environmental, geological, biomedical and materials sciences samples [3–5]. The main advantages of LA-ICP-MS include ease of use, relatively high sensitivity (detection limits in the range of the mg kg^{-1}–μg kg^{-1}) and a dynamic range of up to twelve orders of magnitude. This allows the simultaneous acquisition and measurement of major, minor and trace elements while offering a high spatial resolution in the low micrometers range (this technique can be then considered as non-destructive at macroscopic scale).

One of the most important applications of LA-ICP-MS in the last years is related to surface imaging studies. The technique offers the possibility of obtaining isotopic images directly from the sample surface with a high lateral resolution (~5 μm), which allows obtaining the elemental distribution of multiple analytes [6]. By now LA-ICP-MS has demonstrated its applicability to elemental imaging analysis of an extensive variety of samples, including tree bark [7], plants [8], otoliths [9] and teeth [10]. Furthermore, LA-ICP-MS is also used increasingly for the determination of elemental distribution of trace metals in tissues of biomedical interest, including mice kidney and heart [11,12], lymph nodes and tissues from human respiratory system [13,14], prostate and breast cancer [15,16] and in brain sections [17,18]. In this last field, there are numerous studies that employ LA-ICP-MS to evaluate tissues from patients affected by neurological degenerative diseases such as Parkinson's and Alzheimer [19].

One of the crucial points analyzing biological or biomedical tissues by laser ablation is the sample preparation and the possible metal losses during such process. Currently, there are two types of standard procedures used in laboratories for the preparation of biomedical tissues for imaging studies: (i) fixation of tissue in formalin followed by embedding in paraffin, and (ii) freezing of the sample in its native state. In the first case it has been demonstrated that it is possible to induce some metal losses during sample preparation [6]. It was recently reported that the concentration of some metals (e.g. Fe) in samples embedded in paraffin was lower than the concentrations detected in cryogenic samples. This fact could be attributed to leaching of metals from tissues in formalin solution or during the process of inclusion in paraffin [6]. On the other hand, freezing the tissue in its fresh state preserves the native status of the sample (especially with regard to diffusible ions). Additionally, it requires less sample preparation reducing the risk of contamination of the samples. In this latter case, the use of a laser ablation cell working at controlled low temperatures is essential to ensure the integrity of the biological samples throughout the entire ablation process and analysis time (a requirement for good lateral resolution and to ensure reliable elemental analysis).

To the authors knowledge there are currently three commercially available cryogenic laser ablation cells denoted as: (1) Cryocell System 10, from GeoMed Analytical, LLC (Boston, USA); (2) CryoLAC, from W. Ludolph GmbH (Bremerhaven, Germany); and (3) Cryocell, from New Wave Research, Inc. (Fremont, CA, USA). In addition, three other designs have been proposed by Feldmann et al. [20], Becker et al. [21] and Müller et al. [22]. Despite their different designs and cooling mechanisms, all of them have in common that temperature control is carried out in the structural components of the cell such as the target holder and not in the sample itself. During a laser ablation process significant thermal effects occur, which may affect the sample, both directly in the irradiated surface and in adjacent areas. Therefore, a direct and precise control and an adjustment of the sample temperature throughout LA-ICP-MS analysis is mandatory (particularly when working with biological samples which have to be preserved in cryogenic conditions during the long analysis time generally needed for obtaining high-resolution images).

In this work we present a new laser ablation cell specifically designed for the analysis of cryogenic tissues. The here proposed Peltier-cooling system allows the direct control of the temperature on the sample surface. Additionally, the circular design of the refrigeration system permits to illuminate the sample from the bottom of the cell, allowing an optimum visualization of the actual structures of the samples. In order to guarantee an adequate design for imaging applications the internal volume of the ablation cell as well as the shape of the gas inlet and outlet have been optimized for maximum sensitivity and reasonable washout times. The analytical performance of the proposed ablation cell has been evaluated through the analysis of both, inorganic glass samples and biological tissues.

2. Experimental

2.1. Instrumental set-up

A commercially available Nd-YAG laser with an excitation wavelength of 213 nm was used (CETAC LSX-213, Cetac Technologies, Omaha, NE, USA). The laser system was coupled to a double-focusing sector field ICP-MS (Element 2, Thermo Fisher Scientific, Bremen, Germany). In order to avoid spectral interferences on Fe, Cu and Zn, the mass spectrometer was operated at medium resolution ($R = 4000$). In this work, a commercial ablation cell from CETAC was replaced by the developed cryogenically cooled ablation cell (Spanish patent application pending [23]). The ablation cell was in-house built and specially designed for the analysis of cryogenic tissue sections. The different components of the ablation cell are indicated in Fig. 1. Fig. 1a shows the entire corpus of the ablation cell (1) which was made from polyamide due to the excellent thermal and electrical insulating properties offered by this material. In the center of the lid a specially coated quartz crystal (2) is mounted. The sample to be analyzed is placed on a microscope slide (3) which in turn is arranged in the space holder of a high purity copper plate (4). The copper plate is cooled by a circular internal refrigeration system that includes eight small Peltier elements (5) placed right beneath the plate. Additionally, an internal heat exchanger (7), in this case a cooling coil, is placed below the internal refrigeration system. The internal refrigeration system is controlled by a sensitive thermocouple (6). Such temperature sensor is a thin and flexible wire allowing to be placed at any desired position (e.g. directly on the sample surface). In this vein, a rigorous temperature control of the sample surface can be assured down to −25 °C. Custom-built software has been developed for the continuous temperature control, offering additionally the possibility to extract the data from the cooling cycles. As can be observed in Fig. 1b, a refrigerant fluid (8) (polypropylene glycol) is pumped through the cooling coil (7) which is placed below the eight Peltier elements of the internal refrigeration system for extracting the generated heat. This refrigerant fluid in turn is cooled by an external refrigeration system (9) that includes an external Peltier system (10) that employs air as cooling media and an electrical motor (11) to pump the refrigerant fluid throughout the system.

Concerning the dimensions of the ablation cell, the total volume of the cell into which the laser aerosol expansion takes place is about 20 cm^3. Moreover, the gas inlet has a circular entrance of 2 mm diameter and the gas outlet has a specifically designed funnel shape, ensuring a laminar gas flow inside the cell.

The ICP-MS was daily tuned using a 1 ng g^{-1} Li, I and U solution for maximum signal intensity and low oxide formation (ThO^+/Th^+).

Please cite this article in press as: I. Konz, et al., Design and evaluation of a new Peltier-cooled laser ablation cell with on-sample temperature control, Anal. Chim. Acta (2013), http://dx.doi.org/10.1016/j.aca.2013.11.040

G Model
ACA-232970; No. of Pages 9
ARTICLE IN PRESS
I. Konz et al. / Analytica Chimica Acta xxx (2013) xxx–xxx

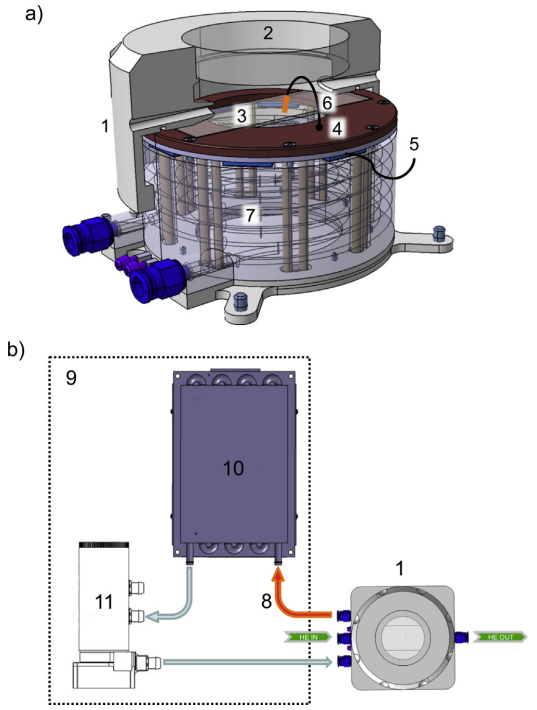

Fig. 1. Schematic set-up of the cryogenic laser ablation cell. For detailed description see the text. (a) Ablation cell including the internal refrigeration system; (b) Ablation cell with the external refrigeration system and the circuit followed by the refrigeration fluid.

Table 1
Operating conditions of the ICP-MS and laser ablation systems.

ICP-MS		Thermo Element 2
RF Power		1330 W
Cooling gas		15.5 L min^{-1}
Auxiliary gas		0.8 L min^{-1}
Nebulizer gas (Ar) – *NIST 612*		0.5 L min^{-1}
Nebulizer gas (Ar) – *Biological tissue*		0.9 L min^{-1}
Cones		Ni (skimmer and sampler)
Isotopes		^{56}Fe, ^{59}Co, ^{63}Cu, ^{64}Zn, ^{107}Ag, ^{109}Ag, ^{135}Ba, ^{137}Ba, ^{206}Pb, ^{208}Pb, ^{232}Th, ^{238}U
Sample time		0.01 s
Mass window		100%
Samples per peak		10
Acquisition time per pixel		1.3 s
LA System		**CETAC LSX-213**
Laser energy	*NIST 612*	70% (~3.5 mJ)
	Eye section	100% (5.6 mJ)
	Flower leaf	30% (~1.7 mJ)
Repetition rate	*NIST 612*	10 Hz
	Eye section	20 Hz
	Flower leaf	10 Hz
Spot diameter	*NIST 612*	50 μm
	Eye section	10 μm
	Flower leaf	200 μm
Scan speed	*NIST 612*	32.5 μm s^{-1}
	Eye section	6.5 μm s^{-1}
	Flower leaf	50 μm s^{-1}
Ablation mode		Single line scan
Distance between lines (*eye section/flower leaf*)		10 μm/60 μm
Cryogenic cell temperature (*eye section/leaf*)		−20 °C/−5 °C
Carrier gas (He) (*NIST 612/biological samples*)		1.0 L min^{-1}/0.9 L min^{-1}

The laser ablation ICP-MS was daily tuned by continuous ablation of a reference glass sample (SRM NIST 612) for maximum intensity of $^{59}Co^+$, $^{139}La^+$, $^{232}Th^+$ and $^{238}U^+$ and low elemental fractionation effects (by optimizing the $^{238}U^+/^{232}Th^+$ ratio to 1). The laser ablation conditions for the analysis of cryogenic tissues were optimized for $^{56}Fe^+$, $^{63}Cu^+$ and $^{64}Zn^+$ using frozen tissue sections of porcine eye. The optimized conditions are summarized in Table 1.

Imaging measurements were performed by line scan ablation of eye tissue sections and flower leaves (line per line) using a spot diameter of 10 μm and 200 μm, respectively. In all experiments a gas blank was collected prior to ablation of the sample for background correction. Two dimensional images of elemental distributions in ocular tissue sections and flower leaves were created using Origin® software.

2.2. Standards and samples

For testing the performance of the proposed laser ablation cell, the reference glass sample SRM NIST 612 was placed on a microscope slide in the center of the cell. Multiple line ablations were performed in order to evaluate signal intensity and stability, reproducibility, accuracy for isotope ratio measurements and washout times. All experiments were performed at room temperature and at −20 °C for comparison.

The design of the ablation cell allows fitting of a microscope slide, normally the sample substrate for imaging studies of tissue sections, directly on the cupper plate without further cutting, preserving a small internal cell volume of 20 cm^3. Two biological samples of different matrices have been investigated as model tissues: a structurally complex sample with structures in the micrometer range (eye section from a native frozen porcine eye) and fresh tomato leaves. The bio-metal distribution of $^{56}Fe^+$, $^{63}Cu^+$ and $^{64}Zn^+$ in the structures of the anterior segment of the eye was investigated by LA-ICP-MS at room temperature and at −20 °C in order to assess the necessity for cryogenic analysis temperatures. Porcine eyes, provided by the Fundación de Investigación Oftalmológica – Instituto Oftalmológico Fernández-Vega (Oviedo, Spain), were collected from a butcher shop and directly frozen at −80 °C. For LA-ICP-MS, the eyes were embedded in Optimal Cutting Temperature compound and cut in a Microm HM550 cryostat (Thermo Fisher Scientific, Walldorf, Germany) at −20 °C (tissue thickness 20 μm). Tomato leaves (*Solanum lycopersicum* L. cv. "Tres-Cantos") were provided by the Department of Plant Nutrition, Experimental Station of Aula Dei, Spanish National Council for Scientific Research (CSIC) (Zaragoza, Spain). Plants were grown in a controlled environment chamber with a photosynthetic photon flux density at leaf height of 350 mmol m^2 s^{-1} photosynthetic active radiation and a 16 h–22 °C/8 h–19 °C, day/night regime. Leaves were harvested immediately before the laser ablation analysis to avoid drying and shrinking of the sample and they were fixed on microscope slides using double-sided tape.

3. Results and discussion

3.1. Computational fluid dynamic modeling

Numerous investigations have shown that the geometry and volume of a laser ablation cell will affect size and distribution of laser-generated particles, dispersion and transport efficiency of the aerosol, gas flow pattern and velocity and eventually the ICP-MS signal response [24–28]. Furthermore, it was also shown that ablation under turbulent gas-flow conditions is undesirable

Please cite this article in press as: I. Konz, et al., Design and evaluation of a new Peltier-cooled laser ablation cell with on-sample temperature control, Anal. Chim. Acta (2013), http://dx.doi.org/10.1016/j.aca.2013.11.040

G Model
ACA-232970; No. of Pages 9
ARTICLE IN PRESS
4 I. Konz et al. / Analytica Chimica Acta xxx (2013) xxx–xxx

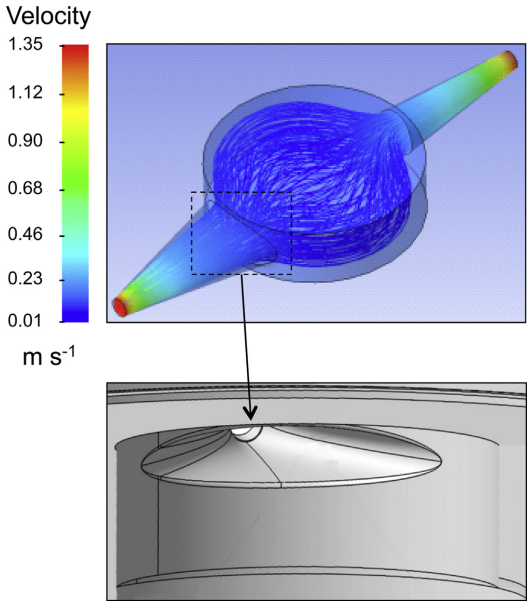

Fig. 2. Gas flow model studied for the proposed cryogenic laser ablation cell showing gas velocity (m s^{-1}) at the ablation area. The inset of the figure shows a diagram of the funnel-shaped gas outflow.

since the ablated particles follow the flow lines of the gas and are redistributed over the whole volume of the ablation chamber, resulting in longer wash-out times. In contrast, if the ablation takes place under laminar flow conditions, much shorter wash-out times could be achieved [25]. In this vein, a cylindrical ablation cell with an internal volume of 20 cm^3 was designed here. To validate the assumptions about the gas flow patterns within the ablation cell, the gas flow dynamics were modeled with Ansys CFX 11.0 using an optimized fine numerical grid of about 0.8 million elements. The fluid was set to helium at standard temperature and pressure. The boundary conditions, i.e. inflow and outflow were based on experimental data and set to a mass flow of 2.9767×10^{-3} g s^{-1} at 25 °C (1 L min^{-1}).

As can be seen in Fig. 2, a laminar gas flow could be obtained with the proposed cell design (single circular gas inflow and funnel-shaped gas outflow). A detailed schematic of the funnel-shaped outflow can be seen in the inset. Although not shown in the paper, different cell designs were investigated with four side-by-side circular gas inflows and single circular gas outflow instead the proposed funnel-shaped. In any case, LA-ICP-MS experiments analyzing a SRM NIST 612 at room temperature showed that higher signal intensities, with smaller relative standard deviations and higher accuracy and precision in the measured isotope ratio were obtained using the cell design proposed (compared to the other investigated configurations). Additionally, single shot analyses have been performed using SRM NIST 612 to evaluate if the ablation depends on the sample position inside the cell. The silicate glass was placed in three different positions (near the cell exit, in the middle of the cell and next to the gas inflow) and $^{56}Fe^+$ signal was monitoring. Experimental results showed that neither the absolute intensity nor the washout times were influenced by the position of the sample in the cell and, thus, it can be concluded that the ablation is location-independent.

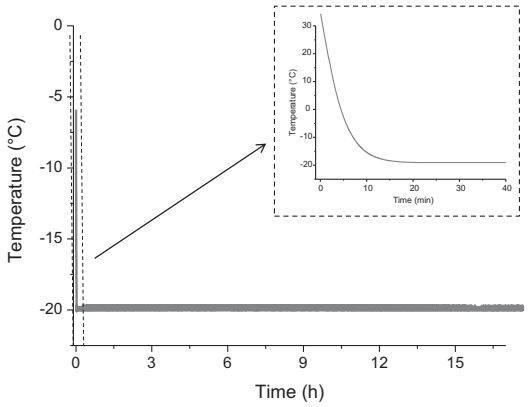

Fig. 3. Temperature diagram of a cooling cycle in a long-time test (17 h). The first 40 min are zoomed-in in the inset.

3.2. Characterization of the analytical performance

Some elemental imaging analyses can last up to several hours depending on the sample size and required lateral sample resolution. During this time a reliable control of the sample temperature has to be ensured. For this reason, the stability of the temperature measurement was first evaluated in a long-time test using the glass sample (SRM NIST 612). Fig. 3 shows the temperature diagram obtained during a cooling cycle of the cryogenic cell for an analysis of 17 h. The inset shows a zoom of the first 40 min of the cooling cycle. As can be seen, the sample surface reaches a temperature of −20 °C in less than 20 min. In addition, it is noteworthy that the working temperature is stable, with a deviation of ±0.2 °C over the 17 hours period. Thus, the sample integrity and also constant working conditions can be ensured throughout the entire analysis time. Furthermore, temperature fluctuations can be corrected by placing the temperature sensor directly on the sample surface. This possibility was neglected in the previously reported cell designs where the temperature sensor is localized below the target holder. Temperature fluctuations, e.g. caused by the helium carrier gas flow [22], would result in a warming of the sample surface and even in a temperature gradient within the sample. A similar problem arises when thick samples with low thermal diffusivity (e.g. bones, teeth) are analyzed: temperature of the sample surface (where the ablation process takes place) does not necessarily correlate with the temperature in the target holder and, thus, reliability and reproducibility of analysis conditions cannot be ensured. Both aspects are taken into account and those parameters can be instantly corrected by using the proposed cryogenic cell with on-sample temperature control.

Initial experiments performed on the glass reference material were focused on features as absolute signal intensity, stability along the analysis time as well as on reproducibility, accuracy and precision of isotope ratio measurements at different temperatures. The employed LA-ICP-MS conditions are summarized in Table 1. Different ablation strategies were employed: (i) long-term (6 min) single line ablation to evaluate signal stability (temporal relative standard deviation), and (ii) consecutive single line ablations (n = 10) to evaluate reproducibility. Fig. 4a shows the time resolved signal intensities obtained for $^{59}Co^+$, $^{139}La^+$, $^{232}Th^+$ and $^{238}U^+$ from a single line ablation over a period of 6 min at room temperature. As can be seen, stable signals were obtained for the investigated elements with temporal relative standard deviations (TRSDs) below 7%. The LA-ICP-MS profile obtained for $^{59}Co^+$ and $^{238}U^+$ in 10 consecutive

Please cite this article in press as: I. Konz, et al., Design and evaluation of a new Peltier-cooled laser ablation cell with on-sample temperature control, Anal. Chim. Acta (2013), http://dx.doi.org/10.1016/j.aca.2013.11.040

G Model
ACA-232970; No. of Pages 9
ARTICLE IN PRESS
I. Konz et al. / Analytica Chimica Acta xxx (2013) xxx–xxx

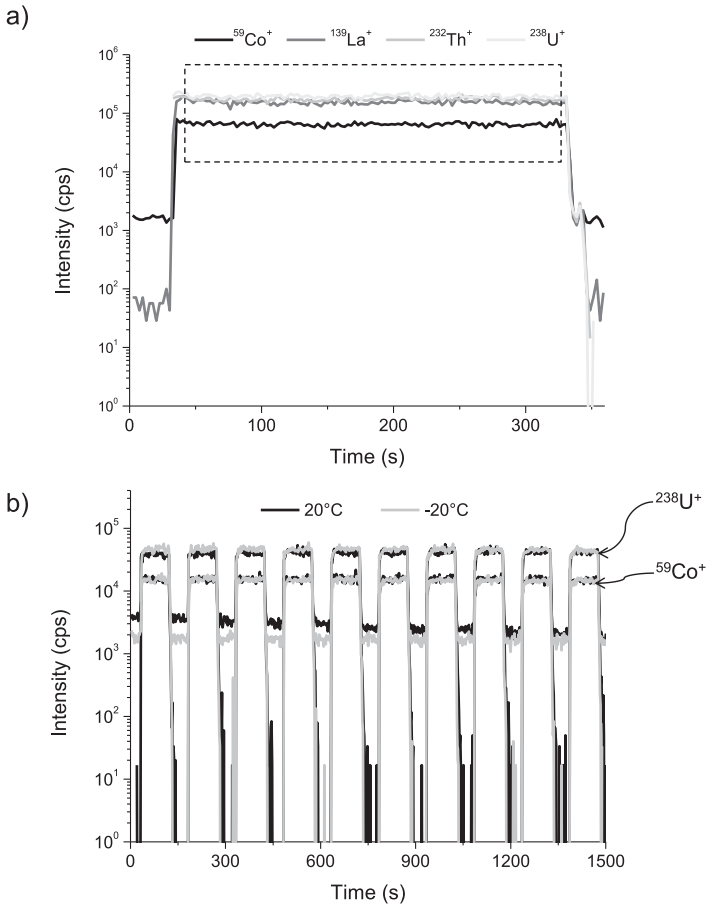

Fig. 4. (a) LA-ICP-MS profile obtained for $^{59}Co^+$, $^{139}La^+$, $^{232}Th^+$ and $^{238}U^+$ in a long-term stability test using the ablation cell at room temperature. Selected area (dashed line) was used for calculation of TRSD; (b) Raw intensities of $^{59}Co^+$ (lower signal intensity) and $^{238}U^+$ (higher signal intensity) in dependence of the analysis temperature (20 °C black line and −20 °C gray line) obtained for LA-ICP-MS analysis of glass SRM NIST 612.

single lines (in this case the individual analysis time was 90 s) at two different temperatures is represented in Fig. 4b. Relative standard deviations (RSD) of signal intensities over the entire analysis time for all investigated masses ($^{59}Co^+$, $^{107}Ag^+$, $^{109}Ag^+$, $^{135}Ba^+$, $^{137}Ba^+$, $^{232}Th^+$ and $^{238}U^+$) were found to be below 3.7% at room temperature and below 3.1% when the sample is maintained at −20 °C. Furthermore, individual signal stability of the elements under study ranged between 7.3 and 12.4% working at room temperature and between 6.6 and 11.7% at cryogenic conditions. Taking into account the ICP-MS drift (about 4% for liquid nebulization during 5 min analysis) the TRSD obtained for LA-ICP-MS analysis with the proposed cryogenic cell can be considered quite good.

The accuracy and precision of natural isotope ratios measurement were also measured at different temperatures for silver, barium and lead using SRM NIST 612. The obtained results are presented in Table 2. Experimental results showed that with the ablation cell at room temperature, the accuracy (deviation from the natural isotope ratio) was in the range 1.3–4.5%. Comparable results were obtained when the ablation cell was operated under cryogenic conditions (−20 °C). Here, the determined accuracy turned out to be 0.3–3.9%. The precision (relative standard deviation, $n = 10$) of the analyses at both investigated temperatures was also comparable. Since a glass reference material was used in this experiment no significant temperature influence on the analytical performance was expected. However, these results confirm that the proposed ablation cell does not contribute to loss of isotope signals by working at cryogenic conditions and that changes in analytical signals are purely sample dependent. Hence, the obtained results demonstrate the applicability of the designed ablation cell not only in cryogenic but also at room temperature conditions.

Fast washout of the laser ablation cell and efficient transport of the laser-generated particles to the ICP are crucial parameters for LA-ICP-MS imaging with high spatial resolution. Hence, the washout time should be as short as possible to avoid mixing of the aerosol coming from different spots and, therefore, ensure discrimination of information from adjacent sampling positions. This can be achieved on one hand using a laminar gas flow with gas flow vectors pointing toward the gas outlet at all positions and, on the other hand, securing a small volume of the laser ablation cell [26,27]. In order to evaluate the washout time in our ablation cell, line scans were performed using the glass SRM NIST 612 at room temperature and at −20 °C. As an example, Fig. 5a collects the first and last

Please cite this article in press as: I. Konz, et al., Design and evaluation of a new Peltier-cooled laser ablation cell with on-sample temperature control, Anal. Chim. Acta (2013), http://dx.doi.org/10.1016/j.aca.2013.11.040

G Model
ACA-232970; No. of Pages 9
ARTICLE IN PRESS
6 I. Konz et al. / Analytica Chimica Acta xxx (2013) xxx–xxx

Table 2
Precision and accuracy obtained for silver, barium and lead isotope ratio measurements at two analysis temperatures using the glass SRM NIST 612.

Temperature	Isotope ratio	Measured isotope ratio	SD	Accuracy (%)	Natural isotope ratio
Room temperature (20 °C)	$^{107}Ag/^{109}Ag$	1.028	0.024	4.5	1.076
	$^{135}Ba/^{137}Ba$	0.611	0.013	4.1	0.587
	$^{206}Pb/^{208}Pb$	0.466	0.001	1.3	0.460
−20 °C	$^{107}Ag/^{109}Ag$	1.034	0.018	3.9	1.076
	$^{135}Ba/^{137}Ba$	0.602	0.015	2.6	0.587
	$^{206}Pb/^{208}Pb$	0.461	0.002	0.3	0.460

part of the LA-ICP-MS profiles obtained for $^{59}Co^+$, $^{107}Ag^+$, $^{137}Ba^+$, $^{232}Th^+$ and $^{238}U^+$ at −20 °C. As can be seen, the time required for the signal rise after switching on the laser was only 2 s. Moreover, a decay of the signals to background level (i.e. the time required for the signal to decay from 100 to 1%) within less than 10 s was observed for all elements, both for higher and lower signal intensities. The obtained washout times are in good agreement with those reported by other authors using cells with a similar internal volume [28,26]. It is worth mentioning that the washout times obtained with the proposed ablation cell are higher than those recently published by Wang et al. [29]. However, it should be highlighted that the focus in the design of the present ablation cell was placed on the cooling system rather than on reducing the washout times to obtain high resolution imaging analyses. Fig. 5b summarizes the obtained washout times for the investigated isotopes ($^{59}Co^+$, $^{107}Ag^+$, $^{137}Ba^+$, $^{232}Th^+$ and $^{238}U^+$) at room temperature (black columns) and at −20 °C (gray columns). Faster washout times were obtained in all cases under cryogenic conditions and better reproducibility (error bars from 10 consecutive analyses) was also observed.

3.3. Application to elemental imaging of native eye tissue sections

After the above thorough characterization of the proposed laser ablation cell for a model inorganic sample, the influence of the

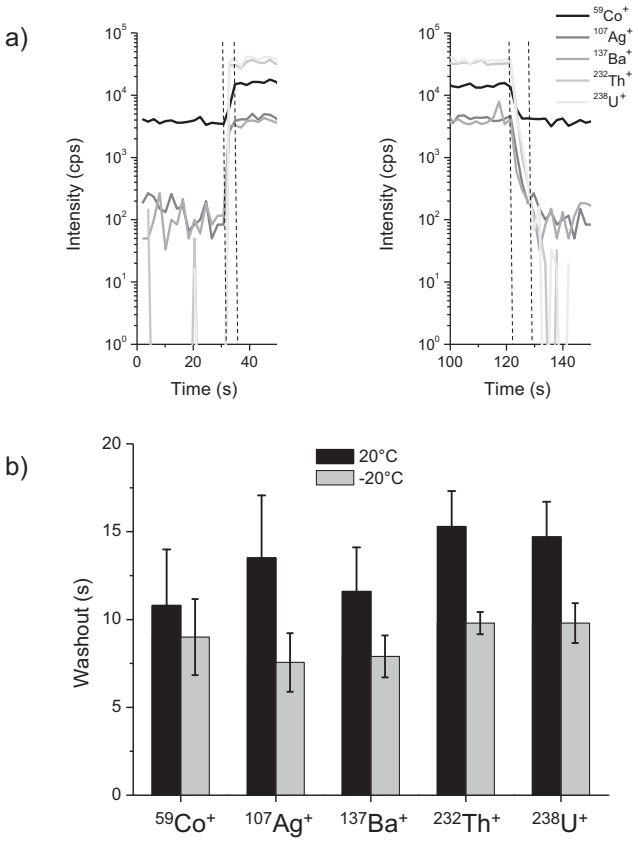

Fig. 5. (a) Zoom of signal rise and decay at −20 °C for the LA-ICP-MS profile of $^{59}Co^+$, $^{107}Ag^+$, $^{137}Ba^+$, $^{232}Th^+$ and $^{238}U^+$ in glass SRM NIST 612. Selected area (dashed lines) was used for calculation of the washout times (signal decay to background level); (b) Comparison of the laser-generated aerosol washout times obtained for $^{59}Co^+$, $^{107}Ag^+$, $^{137}Ba^+$, $^{232}Th^+$ and $^{238}U^+$ after 90 s of laser ablation at room temperature (black) and −20 °C (gray).

Please cite this article in press as: I. Konz, et al., Design and evaluation of a new Peltier-cooled laser ablation cell with on-sample temperature control, Anal. Chim. Acta (2013), http://dx.doi.org/10.1016/j.aca.2013.11.040

G Model
ACA-232970; No. of Pages 9
ARTICLE IN PRESS
I. Konz et al. / Analytica Chimica Acta xxx (2013) xxx–xxx

sample temperature was studied for biological tissues analysis. The analysis of soft tissue samples by LA-ICP-MS is generally carried out using either formalin-fixed or paraffin-embedded (FFPE) or native frozen sections (stored at temperatures around −70 °C). FFPE has been in use for over a century for histologic preparations of clinical tissue samples. Formalin fixation results in crosslinking of proteins, but when paired with impregnation with paraffin and the exclusion of water, results in a remarkably stable biospecimen [30]. Furthermore, FFPE processing provides an ideal architectural preservation and stabilization of cellular details. Such morphological features, however, can be affected when the tissue is preserved by freezing [31]. Nevertheless, as already mentioned before, due to the numerous washing and embedding steps in a conventional FFPE protocol [32], a distortion of the existing initial metal concentration might occur (e.g. via metal leaching, especially for diffusible metal ions).

As LA-ICP-MS analysis seeks the robust determination of those metals, native freezing sample preparation procedure is preferred. Additionally, analysis of frozen tissue sections reduces errors in LA-ICP-MS analysis due to fractionation effects, molecular ion formation and evaporation of the water from the vicinity of the laser shot [21]. Interestingly, improvements in precision and accuracy of isotopic ratios measurements using cool ablation cell temperatures were reported in 2005 for flower leaves in comparison to the analysis at room temperature [21]. Nevertheless, animal or human and plant tissues differ profoundly in composition and morphology. Therefore they might have different behaviors during LA-ICP-MS, particularly using different sample temperature. Thus, in our work here an investigation to compare the behavior of animal tissue sections at different sample temperatures during LA-ICP-MS analysis was undertaken.

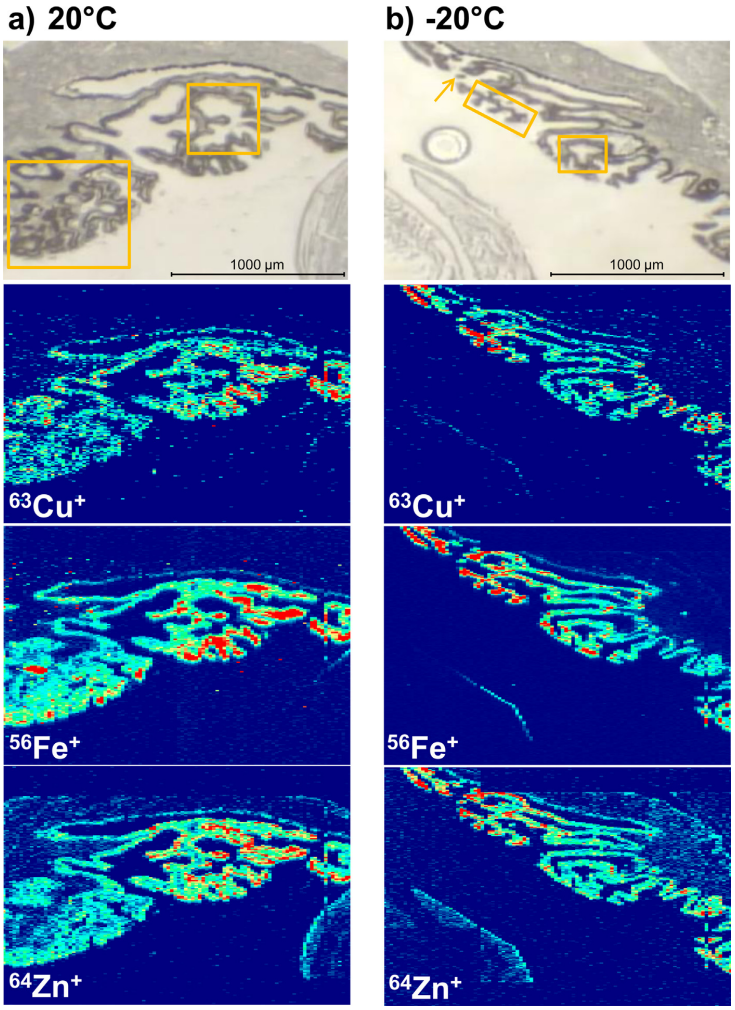

Fig. 6. Histological images of native tissue section of an anterior segment of the porcine eye and elemental images obtained by LA-ICP-MS for $^{56}Fe^+$, $^{63}Cu^+$ and $^{64}Zn^+$. (a) Room temperature conditions; (b) Analysis at −20 °C. The area included in the framed zones and spot indicated by the arrow highlight zones of special interest, where the slight improvement in lateral resolution is remarkable.

Please cite this article in press as: I. Konz, et al., Design and evaluation of a new Peltier-cooled laser ablation cell with on-sample temperature control, Anal. Chim. Acta (2013), http://dx.doi.org/10.1016/j.aca.2013.11.040

G Model
ACA-232970; No. of Pages 9
ARTICLE IN PRESS
8 I. Konz et al. / Analytica Chimica Acta xxx (2013) xxx–xxx

A morphologically complex tissue sample was selected: the structures of the anterior segment of porcine eye sections, including the iris, ciliary body, cornea and trabecular meshwork. The experimental operating parameters for the analysis of those histological sections of the eye are summarized in Table 1. In Fig. 6 the histological images of the analyzed samples and the qualitative elemental images obtained by LA-ICP-MS for $^{56}Fe^+$, $^{63}Cu^+$ and $^{64}Zn^+$ at room temperature and at −20 °C (Fig. 6a and b, respectively) are presented. As can be seen, a slight enhancement of the lateral resolution was obtained when working in cryogenic conditions. The elemental images obtained for $^{56}Fe^+$, $^{63}Cu^+$ and $^{64}Zn^+$ are less blurred when the sample temperature was fixed at −20 °C. This cryogenic effect is especially clear in the highlighted zones of the histological images (orange squares and arrow in Fig. 6). For the analysis at room temperature (see Fig. 6a), the areas in the highlighted zones showed a poorer lateral resolution in the elemental images with slightly broadened microstructures.

Conversely, when similar areas were analyzed at −20 °C the microstructures obtained by LA-ICP-MS images are better defined in terms of morphology and size. The spot indicated by the arrow shows how small (low μm range) and close microstructures (single spot between two ciliary processes) were resolved in the elemental images just by maintaining the sample in cryogenic conditions. To summarize, the microstructures formed by the ciliary processes were slightly better resolved at −20 °C than using the elemental images obtained at room temperature. This could be explained by less heat dissipation into adjacent structures during the laser impact and, therefore, less tissue damage. Furthermore, favorable ablation efficiency might result in less re-deposition of the ablated aerosol particles (leading to less contamination of neighboring ablation lines).

3.4. Application to elemental imaging of fresh flower leaves

In the light of the described results for LA-ICP-MS imaging of soft ocular tissue sections, the proposed cryogenic cell was extended to flower leaves (other type of harder biological samples, widely investigated by LA-ICP-MS). In this case, freshly harvested plant leaves from *S. lycopersicum* (tomato plant) were selected and the center part of the leaf was chosen for imaging purposes, covering zones of leaf blade, midvein and veins. The experimental conditions employed for LA-ICP-MS analysis are also summarized in Table 1. The results for the elemental distribution obtained for $^{63}Cu^+$ and $^{127}I^+$ in the flower leaves at room temperature and at −5 °C are presented in Fig. 7a and b, respectively. The same laser ablation conditions were employed at both temperatures, namely a laser beam diameter of 200 μm and a distance between adjacent lines of 60 μm. A comparison of the microscope images of the leaves analyzed at room temperature and −5 °C (Fig. 7a and b, respectively) shows, at first sight, a clear improvement in the preservation of the sample integrity when maintaining the sample temperature slightly below the freezing point. Due to strong thermal effects provoked by the laser impact, an expansion of the formed crater after laser ablation is observed when the sample is analyzed at room temperature, enlarging the original crater from 200 μm to approximately 300 μm (zoom of microscope image in Fig. 7a). Furthermore, the generation of small and volatile leaf artifacts was observed during the ablation process. As can be seen in the elemental images

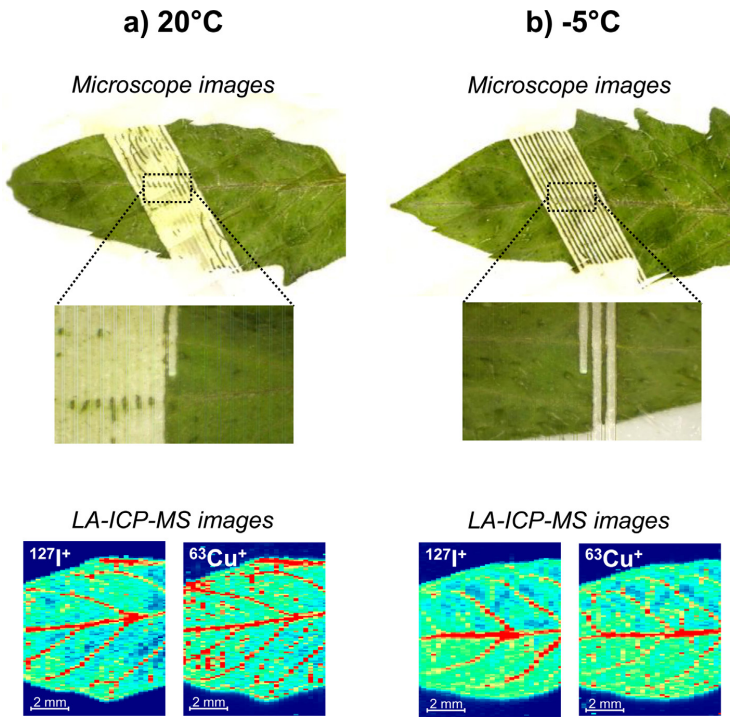

Fig. 7. Microscope images of fresh leaves from *Solanum lycopersicum* and elemental images obtained by LA-ICP-MS for $^{63}Cu^+$ and $^{127}I^+$ (a) Room temperature conditions; (b) Analysis at −5 °C.

Please cite this article in press as: I. Konz, et al., Design and evaluation of a new Peltier-cooled laser ablation cell with on-sample temperature control, Anal. Chim. Acta (2013), http://dx.doi.org/10.1016/j.aca.2013.11.040

G Model
ACA-232970; No. of Pages 9
ARTICLE IN PRESS
I. Konz et al. / Analytica Chimica Acta xxx (2013) xxx–xxx

obtained by LA-ICP-MS (Fig. 7a), both effects have a direct influence in the ablation of adjacent lines leading to cross-contamination and thus noisy LA-ICP-MS profiles. On the other hand, maintaining the sample temperature slightly below the freezing point results in an excellent preservation of the formed laser crater without any thermal expansion, ensuring the integrity of the sample (zoom of microscope image in Fig. 7b). Additionally, working at low temperatures showed to prevent cross-contamination due to leaf artifacts and, therefore, no mixing of elemental information from adjacent lines was obtained (resulting in elemental images with less noise).

4. Conclusions

A cryogenic laser ablation cell with a small internal volume was designed, assembled and successfully tested for imaging by LA-ICP-MS of inorganic material (glass) and for biological samples. The most remarkable feature of the developed cryogenic cell includes its on-sample temperature control, achieved by using a flexible thermocouple for continuous, robust and reliable control of the temperature on the sample surface throughout the entire analysis time (up to several hours in imaging analysis). Fluctuations of the sample temperature could be so corrected instantly while ablation conditions and sample thermal stability are ensured.

Experimental results showed that the proposed ablation cell is able to provide good elemental sensitivity and reproducibility, as well as high accuracy and precision for isotope ratio measurements, both at room temperature and using cryogenic conditions (−20 °C). The image analysis of a morphologically complex soft tissue section in its native frozen state showed a slight enhancement in lateral resolution when maintaining the sample temperature at −20 °C compared to the elemental distribution obtained at room temperature. Furthermore, the analysis of harder tissues (freshly harvested flower leaves) showed a better preservation of the sample integrity all along LA imaging analysis if the sample temperature was maintained below the freezing point.

Acknowledgements

Financial support from “Plan Nacional de I+D+I” (Spanish Ministry of Science and Innovation or MICINN, and FEDER Program) through MAT2010-20921-C02-01 and PCTI Asturias through the project FC-09-EQUIP09-29 is acknowledged. I. Konz thanks the FPU program (MICINN) for financial support. The authors gratefully acknowledge the Fundación de Investigación Oftalmológica, Instituto Oftalmológico Fernández-Vega (Oviedo, Spain) for providing the ocular tissue sections. Sandra Carrasco Gil from the Department of Plant Nutrition, Experimental Station of Aula Dei, Spanish National Council for Scientific Research (CSIC) (Zaragoza, Spain) is also acknowledged for providing the tomato plant.

References

[1] A.L. Gray, Analyst 110 (1985) 551–556.
[2] P. Arrowsmith, S.K. Hughes, Anal. Chem. 59 (1987) 1437–1444.
[3] S.F. Durrant, N.I. Ward, J. Anal. At. Spectrom. 20 (2005) 821–829.
[4] J. Pisonero, B. Fernández, D. Günther, J. Anal. At. Spectrom. 24 (2009) 1145–1160.
[5] B. Fernández, F. Claverie, C. Pecheyran, O.F.X. Donard, Trends Anal. Chem. 26 (2007) 951–966.
[6] Z. Qin, J.A. Caruso, B. Lai, A. Matusch, J.S. Becker, Metallomics 3 (2011) 28–37.
[7] U. Narewski, G. Werner, H. Schulz, C. Vogt, Fresenius J. Anal. Chem. 366 (2000) 167–170.
[8] T. Punshon, B.P. Jackson, P.M. Bertsch, J. Burger, J. Environ. Monit. 6 (2004) 153–159.
[9] G. Huelga-Suarez, B. Fernández, M. Moldovan, J.I.G. Alonso, Anal. Bioanal. Chem. 405 (2013) 2901–2909.
[10] T. Prohaska, C. Latkoczy, G. Schultheis, M. Teschler-Nicola, G. Stingeder, J. Anal. At. Spectrom. 17 (2002) 887–891.
[11] M. Zoriy, A. Matusch, T. Spruss, J.S. Becker, Int. J. Mass Spectrom. 260 (2007) 102–106.
[12] J.S. Becker, U. Breuer, H.F. Hsieh, T. Osterholt, U. Kumtabtim, B. Wu, A. Matusch, J.A. Caruso, Z. Qin, Anal. Chem. 82 (2010) 9528–9533.
[13] D. Hare, F. Burger, C. Austin, F. Fryer, R. Grimm, B. Reedy, R.A. Scolyer, J.F. Thompson, P. Doble, Analyst 134 (2009) 450–453.
[14] D. Hare, S. Tolmachev, A. James, D. Bishop, C. Austin, F. Fryer, P. Doble, Anal. Chem. 82 (2010) 3176–3182.
[15] A.G. Sarafanov, T.I. Todorov, A. Kajdacsy-Ballac, M.A. Gray, V. Macias, J.A. Centeno, J. Trace Elem. Med. Biol. 22 (2008) 305–314.
[16] C. Giesen, L. Waentig, T. Mairinger, D. Drescher, J. Kneipp, P.H. Roos, U. Panneab, N. Jakubowski, J. Anal. At. Spectrom. 26 (2011) 2160–2165.
[17] M. Zoriy, M. Dehnhardt, A. Matusch, J.S. Becker, Spectrochim. Acta B 63 (2008) 375–382.
[18] A. Kindness, C.N. Sekaran, J. Feldmann, Clin. Chem. 49 (2003) 1916–1923.
[19] M.W. Bourassa, L.M. Miller, Metallomics 4 (2012) 721–738.
[20] J. Feldmann, A. Kindness, P. Ek, J. Anal. At. Spectrom. 17 (2002) 813–818.
[21] M.V. Zoriy, M. Kayser, A. Izmer, C. Pickhardt, J.S. Becker, Int. J. Mass Spectrom. 242 (2005) 297–302.
[22] W. Müller, J.M.G. Shelley, S.O. Rasmussen, J. Anal. At. Spectrom. 26 (2011) 2391–2395.
[23] B. Fernández, I. Konz, A. Castañeda, M.L. Fernández, R. Pereiro, A. Sanz-Medel, Patent No. P201300559 (2013) Spanish Patent Pending.
[24] J. Koch, M. Wälle, R. Dietiker, D. Günther, Anal. Chem. 80 (2008) 915–921.
[25] E.L. Gurevich, R. Hergenröder, J. Anal. At. Spectrom. 22 (2007) 1043–1050.
[26] M.B. Fricker, D. Kutscher, B. Aeschlimann, J. Frommer, R. Dietiker, J. Bettmer, D. Günther, Int. J. Mass Spectrom. 307 (2011) 39–45.
[27] D. Bleiner, D. Günther, J. Anal. At. Spectrom. 16 (2001) 449–456.
[28] C.C. Garcia, H. Lindner, K. Niemax, Spectrochim. Acta B 62 (2007) 13–19.
[29] H.A.O. Wang, D. Grolimund, C. Giesen, C.N. Borca, J.R.H. Shaw-Stewart, B. Bodenmiller, D. Günther, Anal. Chem. (2013), http://dx.doi.org/10.1021/ac400996x.
[30] K.M. Matsuda, J.-Y. Chung, S.M. Hewitt, Expert Rev. Proteomics 7 (2010) 227–237.
[31] S. Magdeldin, T. Yamamoto, Proteomics 12 (2012) 1045–1058.
[32] T.D. Hewitson, I.A. Darby, Histology Protocols, Methods in Molecular Biology, vol. 611, Humana Press, New York, USA, 2010.

Please cite this article in press as: I. Konz, et al., Design and evaluation of a new Peltier-cooled laser ablation cell with on-sample temperature control, Anal. Chim. Acta (2013), http://dx.doi.org/10.1016/j.aca.2013.11.040

QUANTITATIVE BIOIMAGING OF TRACE ELEMENTS IN THE HUMAN LENS BY LA-ICP-MS

Ioana Konz[1], Beatriz Fernández*[1], M. Luisa Fernández[1], Rosario Pereiro[1], Héctor González-Iglesias[2], Miguel Coca-Prados[2], Alfredo Sanz-Medel*[1]

1. *Department of Physical and Analytical Chemistry; Faculty of Chemistry; University of Oviedo; Julian Clavería, 8. 33006 Oviedo, Spain*
2. *Fundación de Investigación Oftalmológica, Instituto Oftalmológico Fernández-Vega, Avenida Doctores Fernández-Vega, 34. Oviedo 33012, SPAIN*

*Authors to whom correspondence should be addressed

Corresponding authors: fernandezbeatriz@uniovi.es; asm@uniovi.es;
Tel/ Fax: +34.985103474

0

ABSTRACT

Laser ablation inductively coupled plasma mass spectrometry (LA-ICP-MS) was used for the quantitative imaging of Fe, Cu and Zn in cryostat sections of human eye lenses and for depth profiling analysis in bovine lenses. To ensure a tight temperature control throughout the experiments, a new Peltier-cooled laser ablation cell was employed. For quantification purposes, matrix-matched laboratory standards were prepared from a pool of human lenses from eye donors and spiked with standard solutions containing different concentrations of natural abundance Fe, Cu and Zn. An internal standardisation was also carried out to correct matrix effects, lack of tissue homogeneity and/or instrumental drifts using a thin gold film deposited on the sample surface. Quantitative images of cryo-sections of human eye lenses analysed by LA-ICP-MS revealed a homogeneous distribution of Fe, Cu and Zn in the nuclear region and a slight increase in Fe concentration in the outer cell layer (i.e. lens epithelium) at the anterior pole. These results were assessed also by isotope dilution mass spectrometry (IDMS) and Fe, Cu and Zn concentrations determined by ID-ICP-MS in digested samples of lenses and lens capsules.

KEYWORDS.- Laser Ablation; Mass Spectrometry / ICP-MS; Quantitative Elemental Bio-Imaging; Internal Standard; Biological Samples.

INTRODUCTION

In recent years, laser ablation (LA) coupled to inductively coupled plasma mass spectrometry (ICP-MS) was introduced as a promising tool for elemental imaging of biological tissue sections [1-5]. However, several obstacles need to be taken into consideration when reliable analytical results are aimed at, particularly when quantitative images are required. Due to the complexity of the sample matrix, tissue thickness and water content of different tissue regions could affect the analytical signals. Therefore, the selection of an appropriate internal standard becomes crucial to achieve precise and accurate measurements. In addition, the experimental conditions have a great influence on the analytical results obtained by LA-ICP-MS for the analysis of biological tissue sections. It has been demonstrated that cryogenic conditions, both for the sample preparation step and the LA-ICP-MS analysis, are preferable for metal determination in biological samples [6,7].

The aim of the present work was the quantitative determination of trace elements and their spatial distribution in bovine and human eye lenses by LA-ICP-MS. The direct depth profiling analysis was first performed by LA-ICP-MS on freshly dissected bovine lenses without any sample pre-treatment. Based on this analysis, the quantitative imaging of Fe, Cu and Zn was performed in eye lens sections from eye donors (cadavers) using matrix-matched laboratory standards for external calibration and using $^{197}Au^{+}$ as internal standard. These results were assessed and compared with an alternative more conventional quantitative approach: isotope dilution mass spectrometry (IDMS) combined to conventional nebulisation ICP-MS on digested lenses and lens capsule samples.

EXPERIMENTAL SECTION

LA-ICP-MS Instrumentation. LA-ICP-MS analyses were carried out using a CETAC LSX-213 laser system (Cetac Technologies, Omaha, NE, USA) coupled to a double-focusing sector field ICP-MS (Element 2, Thermo Fisher Scientific, Bremen, Germany). The commercial ablation cell from CETAC was replaced by a novel Peltier-cooled ablation cell built in-house [8,9]. Cell temperature was kept constant at -20°C for the analysis of frozen sections of human eye lens samples. Further details about the LA-ICP-MS system as well as the optimized experimental parameters used for LA-ICP-MS measurements are provided as Supporting Information.

Imaging measurements were performed by line scan ablation of cryostat lens sections (line per line) using a spot diameter of 50 µm and 20 µm distance between adjacent lines (in order to reduce the risk of cross-contamination).

Reagents and Samples. Chemicals and reagents used were of analytical grade and are provided as Supporting Information. Concerning the samples, for depth profiling analysis bovine eyes were collected from a local slaughterhouse (Matadero Central de Asturias, Oviedo, Spain) and lenses were dissected prior LA-ICP-MS analysis without any further treatment. A total of 20 human eyes from adult normal donors (cadavers) ranging in age from 45 to 65 years were also used in this study. Human eyes were obtained 24 h post-mortem through the Hospital Universitario Central de Asturias

(HUCA, Oviedo, Spain). The procedures adhere to the tenets of the Declaration of Helsinki, and full ethical approval was obtained from the Clinical Research Ethics Committee at the HUCA. Dissected human lenses were directly frozen at -80°C, embedded in Optimal Cutting Temperature Compound, cut in a Microm HM550 cryostat (Thermo Fisher Scientific, Walldorf, Germany) at -20°C (tissue thickness 80 µm) and mounted on microscope glass slides. For internal standardization [10], frozen lens sections were metallised during 40 s with Au.

Matrix-Matched Standard Preparation. Matrix-matched laboratory standards were prepared for the calibration of images obtained by LA-ICP-MS. The preparation procedure of the synthetic matrix-matched standards was similar to previously published ones [11,12] and is summarised in Figure S1 in the Supporting Information. Eye lenses from human donors (10 lenses) were homogenised using an Art-Micra D-8 homogeniser (ART Prozess- & Labortechnik GmbH & Co. KG, Müllheim, Germany). The homogenate (total weight 1.8 g) was divided into four aliquots (200 mg each). Three of them were spiked (total volume 150 µL) with increasing concentrations of the desired standard metal solutions (~300 □g g^{-1}); to the forth sample the same volume of 0.1% HNO_3 was added and was used as blank. The total weight of the final samples was about 350 mg. All samples were carefully homogenised and centrifuged at 12,000 g for 5 min and then filled into 0.5 cm^3 plastic histology moulds and frozen at -80°C. To evaluate the Fe, Cu and Zn concentration in the prepared matrix-matched standards an aliquot of 50 mg of each standard was digested in 3 mL HNO_3 and 1.5 mL H_2O_2 in an ultrasonic bath for one hour (or until the resulting solution turned colourless). The digested solutions were analysed by ICP-MS (external calibration) for determination of the multi-element concentrations. The frozen matrix-matched tissue standards were cut in a cryostat at -20°C to 80 µm tissue thickness and metallised with Au following the procedure described for the lens sections.

Quantitative Analysis of Human Eye Lens by ID-ICP-MS. The quantitative measurement of Fe, Cu and Zn levels in eye lens and lens capsules from human donors were assessed separately by conventional nebulisation ICP-MS. Five eye lenses were digested in 3 mL of concentrated HNO_3 and 1.5 mL H_2O_2. The corresponding lens capsules were digested using 300 µL HNO_3 and 150 µL H_2O_2. Digested samples were diluted in 1% (v/v) HNO_3 prior to ICP-MS analysis and finally the metal concentrations were determined by IDMS. As controls, preparatory blank tubes (no tissue added) were treated in the same manner as the samples. The proposed mineralisation procedure for the human eye lenses and lens capsules produced homogeneous solutions and no insoluble residues were observed.

RESULTS AND DISCUSSION

Depth Profiling Analysis of Freshly Dissected Eye Lenses. So far, investigations related to metal content distribution of mammalian lens throughout its different structures have not been performed. To reveal possible trace element distribution in the lens, depth profiling analysis of freshly

dissected bovine lenses was conducted. Fig. 1a shows a representative cross-section scheme of a mammalian lens. The lens is primarily composed of highly elongated fibre cells that are regularly packed to form a spheroidal mass. Anteriorly, the fibre cells are covered by a monolayer of cuboidal epithelial cells, and the complete structure is covered by a thick membrane, the lens capsule. The anterior and posterior poles of the lens face distinct environments, the anterior pole faces the front of the eye whereas the posterior pole the vitreous and back of the eye. Depth profiling analysis of the trace elements (i.e., Fe, Cu and Zn) through the central anterior-to-posterior pole axis of the lens was attempted using the single point ablation mode (200 □m, 5.6 mJ, 20 Hz, 2000 burst counts). As shown in Fig. 1b, and following the red line, $^{56}Fe^{+}$ and $^{63}Cu^{+}$ were detected mainly in the outer layers of the lens (i.e. capsule and/or epithelial cells). To verify whether the detected signals in the lens were restricted to the capsule and/or the epithelial cells we applied LA-ICP-MS analysis to the lens with and without capsule: in the back part of the lens, where the epithelial cell layer is absent but the capsule is present, and in the front part of the lens without the capsule (Fig. 1b, blue and black lines, respectively). The LA-ICP-MS profiles suggested that $^{56}Fe^{+}$ and $^{63}Cu^{+}$ were associated preferentially to the epithelial cell layer of the lens and not to the capsule. Furthermore, LA-ICP-MS profiles also showed no differences in the distribution of $^{64}Zn^{+}$ throughout the lens. That is, the profile of $^{64}Zn^{+}$ along the anterior-to-posterior poles of the lens appears to be homogenous.

Quantitative Bioimaging of Fe, Cu and Zn in Frozen Human Eye Lens Sections by LA-ICP-MS. Next we determined the quantitative trace elements (i.e. $^{56}Fe^{+}$, $^{63}Cu^{+}$, $^{64}Zn^{+}$) distribution in human lenses by the analysis of transversal frozen sections using LA-ICP-MS. Quantification by external calibration using matrix-matched tissue standards were performed (details on the calibration procedure are provided as Supporting Information). Fig. 2 shows a microscope image of the analysed lens section and the quantitative images for $^{56}Fe^{+}$, $^{63}Cu^{+}$ and $^{64}Zn^{+}$. A relatively homogeneous distribution of these elements throughout the human lens was observed. The element concentrations for Fe, Cu and Zn in the lens fibres (i.e. nuclear and cortical) were ~0.36 µg g^{-1}, 0.30 µg $g^{-1}$and 9.1 µg g^{-1} of wet tissue, respectively (see Table 1). The average concentration for Fe, Cu and Zn in the capsule at the anterior pole of the lenses were ~1.35 µg, 0.42 µg and 9.0 µgper g^{-1} of wet tissue, respectively. Thus, there was a slight increase in Fe concentration in the capsule when compared to the lens fibres.

Overall we observed that Zn was present in the entire lens to a higher extent than Fe and Cu. This observation is in general agreement with reported previous findings [13]. As shown in Fig. 2, $^{63}Cu^{+}$ and $^{64}Zn^{+}$ were homogeneously distributed throughout the entire lens, whereas $^{56}Fe^{+}$ was homogeneously distributed only in the nuclear and cortical fibres and its concentration was higher in the anterior pole of the lens. Although bovine and human lenses correspond to different species, LA-ICP-MS images obtained for human lenses were partly in agreement with the results obtained for depth profiling analyses performed in freshly dissected bovine lenses. We did not find significant

difference in the distribution of $^{64}Zn^{+}$ between the inner and the outer cortical fibres, whereas $^{56}Fe^{+}$ was clearly identified in the anterior pole of the lens. Conversely, the detection of $^{63}Cu^{+}$ observed in the anterior pole of the bovine lens could not be confirmed by similar analysis in the human lens. This could suggest a significant species difference in the distribution of $^{63}Cu^{+}$ in the lens.

Determination of Fe, Cu and Zn in Human Eye Lenses by ID-ICP-MS. We corroborated the Fe, Cu and Zn concentrations determined in human eye lens frozen sections using an alternative quantification approach. We used IDMS, which is internationally regarded as an absolute measurement method directly traceable to the International System of Units [14], in combination with conventional nebulisation ICP-MS. A total of five human lenses from adult human eye donors (cadavers) were used for total elemental determinations, after acidic mineralisation of the entire lens without capsule and lens capsule, separately. The digested samples were quantified by ID-ICP-MS using the corresponding enriched isotopes at appropriate concentrations. Table 1 summarises the Fe, Cu and Zn concentrations obtained by ID-ICP-MS and LA-ICP-MS in lens fibres and lens capsule. As shown in Table 1, the estimated concentrations of Fe, Cu and Zn from the LA-ICP-MS image of the human lens were in very good agreement with those determined by the reference technique of ID-ICP-MS. In addition, no significant differences in Cu and Zn concentrations between lens without capsule and lens capsule were found by the two employed quantification methodologies. It should be stressed here that the increase of Fe concentration localised by LA-ICP-MS in the lens capsule was also confirmed by ID-ICP-MS measurements (as well as the higher amount of Zn present in the human lens compared to Cu and Fe levels). Slight differences observed between LA-ICP-MS and ID-ICP-MS results could be mainly attributed to biological differences characterising each individual.

Finally, the difference observed for Cu between bovine and human lenses (Cu was present in the bovine outer layer of the lens whereas it was absent in the human lens) was also verified by applying the same quantification approach. A total of five bovine lenses and the corresponding lens capsules were quantified by ID-ICP-MS after acidic mineralisation of the samples. Fe, Cu and Zn concentrations were respectively found to be 0.11 ± 0.02 □g g^{-1}, 0.015 ± 0.007 □g g^{-1} and 10.74 ± 0.86 □g g^{-1} in lens without capsule and 0.98 ± 0.26 □g g^{-1}, 1.32 ± 0.25 □g g^{-1} and 3.95 ± 1.22 □g g^{-1} in lens capsule. According with the data obtained in human lenses, in bovine animals a significantly higher Fe concentration was observed in the lens capsule, compared to the content in lens fibres. Additionally, in contrast to the results obtained from the human samples, Cu was found to be present in the lens capsule with a 100-fold higher concentration than in the lens itself. These results confirm our previous qualitative depth profiling analysis results observed in freshly dissected bovine lens.

CONCLUSIONS

A recently developed Peltier-cooled laser ablation cell was used, in combination with matrix-matched calibration using $^{197}Au^{+}$ as internal standard, for the quantitative bioimaging of Fe, Cu and Zn contents in frozen eye lens sections from human and bovine eyes. The proposed direct tissue quantitative analysis revealed detection limits for Fe, Cu and Zn sufficiently low (in the range of 60-200 ng g^{-1}) for the determination of the analytes in the lens. Despite the homogeneous distribution observed for Fe, Cu and Zn in the lens without capsule, the applied methodology was sensitive enough to differentiate between lens fibres and lens capsule, showing an increase in Fe concentration in the anterior part of the lens. Quantitative LA-ICP-MS results for Fe, Cu and Zn have been successfully assessed in human lens and lens capsule by isotope dilution analysis ICP-MS after acid digestion of the samples.

This work provides insight information into the spatial distribution and image quantification of metals in human and bovine eye lenses. The data may lead to a better understanding on the role of trace elements in antioxidant mechanisms and in ocular diseases.

ACKNOWLEDGEMENTS

Financial support from "Plan Nacional de I+D+I" (Spanish Ministry of Science and Innovation or MICINN, and FEDER Program) through MAT2010-20921-C02-01 and PCTI Asturias through the project FC-09-EQUIP09-29 is acknowledged. I. Konz and B. Fernández thank the FPU program (MICINN) and FC-11-COF11-21 project (PCTI Asturias), respectively, for financial support. M. Coca-Prados and H. González-Iglesias acknowledge financial support from "Fundación de Investigación Oftalmológica", "Fundación Rafael del Pino" and "Fundación Mª Cristina Masaveu Paterson". Finally, the authors gratefully acknowledge Lydia Alvarez from Fundación de Investigación Oftalmológica, Instituto Oftalmológico Fernández-Vega.

REFERENCES

1 Becker JS, Zoriy M, Matusch A, Wu B, Salber D, Palm C, Becker JS (2010) Mass Spectrom Rev 29:156–175

2 Qin Z, Caruso JA, Lai B, Matusch A, Becker JS (2011) Metallomics 3:28–37

3 Gholap D, Verhulst J, Ceelen W, Vanhaecke F (2012) Anal Bioanal Chem 402:2121-2129

4 Austin C, Hare D, Rawling T, McDonagh AM, Doble P (2010) J Anal Atom Spectrom 25:722-725

5 Hare D, Austin C, Doble P (2012) Analyst 137:1527-1537

6 Zoriy MV, Kayser M, Izmer A, Pickhardt C, Becker JS (2005) Int J Mass Spectrom 242:297-302

7 Feldmann J, Kindness A, Ek P (2002) J Anal At Spectrom 17:813-818

8 Konz I, Fernández B, Fernández ML, Pereiro R, Sanz-Medel A (2013) Anal Chim Acta accepted for publication (18 November 2013).

9 Fernández B, Konz I, Castañeda A, Fernández ML, Pereiro R, Sanz-Medel A (2013) Spanish patent application pending (P201300559)

10 Konz I, Fernández B, Fernández ML, Pereiro R, González H, Álvarez L, Coca-Prados M, Sanz-Medel A (2013) Anal Bioanal Chem 405:3091-3096

11 Becker JS, Zoriy MV, Pickhardt C, Palomero-Gallagher N, Zilles K (2005) Anal. Chem. 77:3208-3216

12 Hare DJ, Lear J, Bishop D, Beavis A, Doble PA (2013) Anal Methods 5:1915-1921

13 B.H. Grahn, P.G. Paterson, K.T. Gottschall-Pass, Z. Zhang, J. Am. Coll. Nutr. 2001, 20, 106-118

14 García Alonso JI, Rodríguez-González P (2013) "*Isotope Dilution Mass Spectrometry*" The Royal Society of Chemistry, Cambridge

Table 1. Comparison of Fe, Cu and Zn concentrations (µg g^{-1}) in human lens without capsule (nuclear and cortical) and lens capsule obtained by LA-ICP-MS and ID-ICP-MS. LA-ICP-MS concentrations correspond to the estimated values form the image (Fig. 2). ID-ICP-MS uncertainties show result from standard deviations of the mean of five independent analyses.

	Lens without capsule (nuclear & cortical) (µg g^{-1} wet tissue)		**Lens capsule (µg g^{-1} wet tissue)**	
	LA-ICP-MS	**ID-ICP-MS**	**LA-ICP-MS**	**ID-ICP-MS**
Fe	0.35 - 0.37	0.27 ± 0.10	1.29 - 1.40	1.65 ± 0.41
Cu	0.29 - 0.32	0.23 ± 0.04	0.40 - 0.44	0.39 ± 0.12
Zn	8.7 - 9.5	9.4 ± 1.1	8.7 - 9.3	9.8 ± 2.5

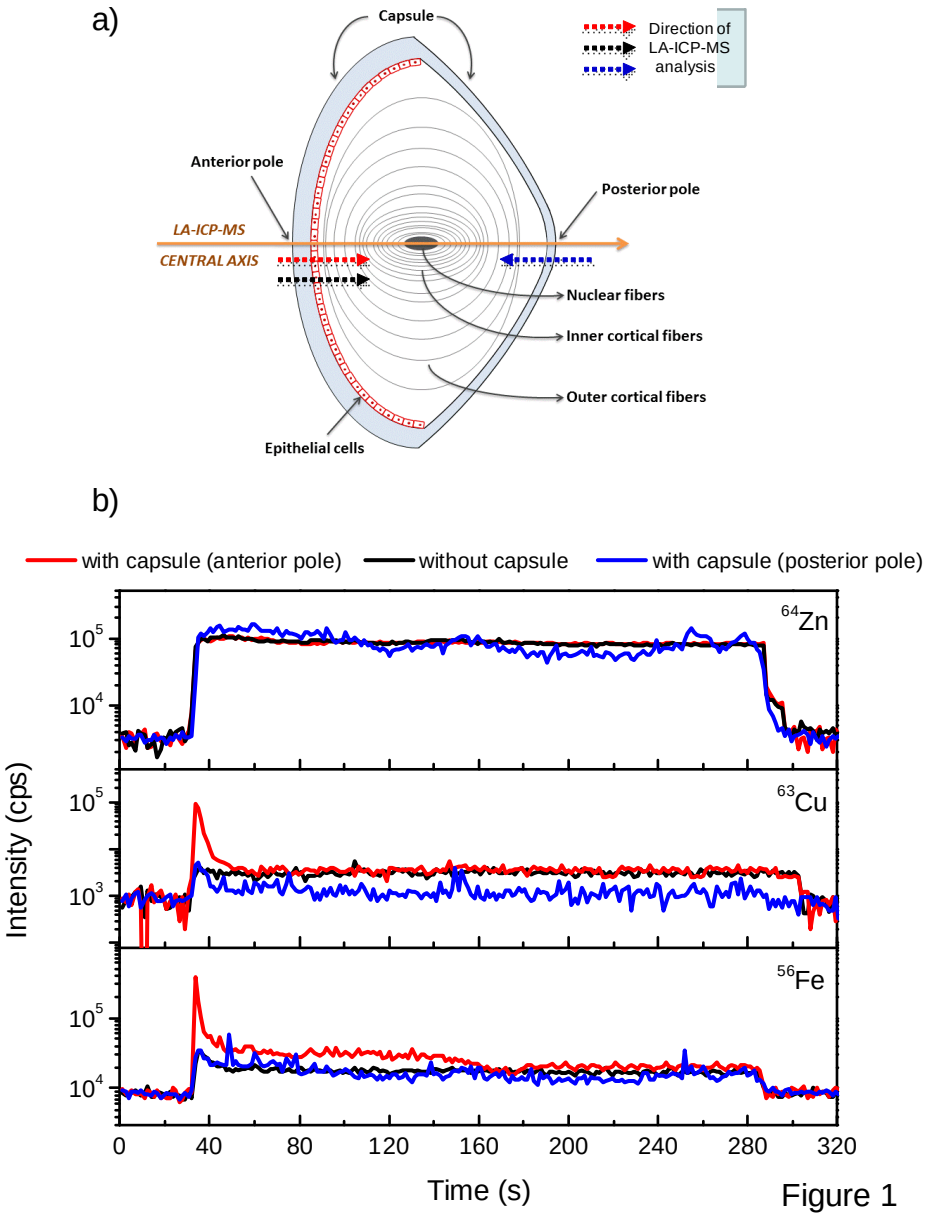

Figure 1.- a) Schematic diagram of the structures in a lens cross-section. The color arrows indicate the direction of the ablation in the different analysis; b) Depth profiles obtained for $^{56}Fe^{+}$, $^{63}Cu^{+}$ and $^{64}Zn^{+}$ in freshly dissected bovine lens by LA-ICP-MS: lens analysed in the anterior pole with the capsule (red line), in the anterior pole without the capsule and the epithelial cell layer (black line) and on the posterior pole of the lens (blue line).

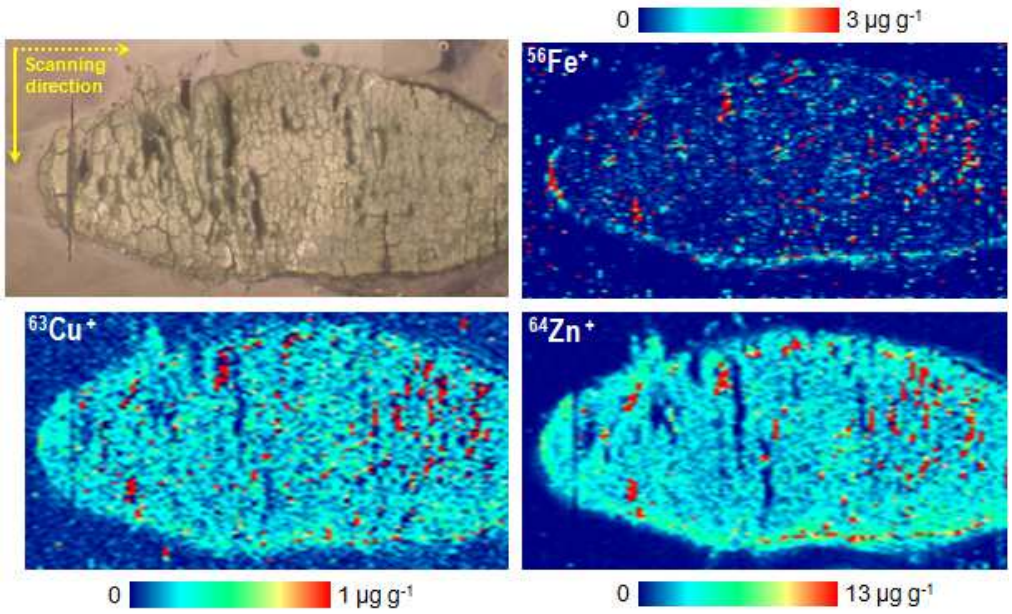

Figure 2.- Microscope image of analysed human eye lens section (up left) and quantitative images (linear scale) obtained by LA-ICP-MS for $^{56}Fe^{+}$, $^{63}Cu^{+}$ and $^{64}Zn^{+}$ distributions (external calibration using matrix-matched laboratory standards and $^{197}Au^{+}$ signal as internal standard).

Supporting Information

QUANTITATIVE BIOIMAGING OF TRACE ELEMENTS IN THE HUMAN LENS BY LA-ICP-MS

Ioana Konz[1], Beatriz Fernández*[1], M. Luisa Fernández[1], Rosario Pereiro[1], Héctor González[2], Miguel Coca-Prados[2] and Alfredo Sanz-Medel*[1]

1. Department of Physical and Analytical Chemistry; Faculty of Chemistry; University of Oviedo; Julian Clavería, 8. 33006 Oviedo, Spain

2. Fundación de Investigación Oftalmológica, Instituto Oftalmológico Fernández-Vega, 33012, Oviedo, Spain

*Corresponding authors: fernandezbeatriz@uniovi.es; asm@uniovi.es

Abstract

The Supporting Information details the Experimental section of the manuscript concerning the description of the LA-ICP-MS system, the selected experimental conditions and the chemicals and reagents used in this work. It also includes a description of preparation procedure of the matrix-matched tissue standards.

Furthermore, it provides a details description of the Results and Discussion section for the external calibration procedure.

EXPERIMENTAL

LA-ICP-MS Instrumentation. LA-ICP-MS analyses were carried out using a CETAC LSX-213 laser system (Cetac Technologies, Omaha, NE, USA) coupled to a double-focusing sector field ICP-MS (Element 2, Thermo Fisher Scientific, Bremen, Germany). ICP-MS measurements were carried out at medium mass resolution (R=4000) to avoid spectral interferences on the determination of the sought elements. The commercial ablation cell from CETAC was replaced by a novel Peltier-cooled ablation cell built in-house [i, ii]. Cell temperature was kept constant at -20°C for the analysis of frozen sections of human eye lens samples. The total volume of the cell into which the laser aerosol expansion takes place is about 20 cm³. The laser-generated aerosol was transported through a high-purity tube (Teflon-lined Tygon® tubing, ¼" OD, 1/8" ID) into the ICP torch by the He carrier gas of the ablation cell. The ICP-MS was daily tuned using a 1 ng g^{-1} Li, I and U solution for maximum signal intensity and low oxide formation (ThO^+/Th^+). The LA-ICP-MS system was daily tuned by continuous ablation of a reference glass sample (NIST SRM 612) for maximum intensity of $^{59}Co^+$, $^{139}La^+$, $^{232}Th^+$ and $^{238}U^+$ and low elemental fractionation (by optimising the $^{238}U^+/^{232}Th^+$ ratio to 1). Monitored isotopes and optimised operating parameters used for LA-ICP-MS measurements are summarised in Table S1.

Table S1. Operating conditions of the ICP-MS and laser ablation system.

ICP-MS	**Thermo Element 2**
RF Power	1330 W
Cooling gas	15.5 L min^{-1}
Auxiliary gas	0.8 L min^{-1}
Nebuliser gas (Ar)	0.9 L min^{-1}
Cones	Ni (skimmer and sampler)
Isotopes	^{54}Fe, ^{56}Fe, ^{63}Cu, ^{65}Cu, ^{64}Zn, ^{68}Zn, ^{197}Au
Sample time	0.01 s
Mass window	100%
Samples per peak	10
LA System	**CETAC LSX-213**
Laser energy	5% (~0.3 mJ ≙ 1.5 J cm^{-2})
Repetition rate	10 Hz
Spot diameter	50 µm
Scan speed	32.5 µm s^{-1}
Ablation mode	single line scan
Carrier gas (He)	0.9 L min^{-1}
Cryogenic cell temperature	-20°C

Imaging measurements were performed by line scan ablation of cryostat lens sections (line per line) using a spot diameter of 50 µm and 20 µm distance between adjacent lines (in order to reduce the risk of cross-contamination). In all experiments a gas blank was collected prior to ablation of the sample for background correction. The average analysis time for the imaging of one sample with the required resolution was about 10 h (sample area of 40 mm²). Two-dimensional images of elemental distributions in eye lens were created using Origin® software.

Chemicals and Reagents. High purity standard solutions of Fe, Cu, Zn and Au (1000 µg mL-1) were purchased from Merck (Darmstadt, Germany). Acid digestion of tissue samples was performed using nitric acid (67% NORMATOM® for trace metal analysis, VWR BDH Prolabo) and hydrogen peroxide (30% ARISTAR® for trace metal analysis, VWR BDH Prolabo). Enriched stable isotopes of ^{54}Fe (96.8 ± 0.2% isotopic abundance), ^{65}Cu (90.03 ± 0.03% isotopic abundance) and ^{68}Zn (86.5 ± 0.2% isotopic abundance) were purchased from Cambridge Isotope Laboratories (Andover, MA, USA), Spectrascan (Teknolab AS, Dröbak, Norway) and Isoflex (San Francisco, CA, USA), respectively. Spike solutions were prepared by dissolving an accurately weighed amount of the solid enriched isotopes in nitric acid. Isotope enriched spike solutions were then prepared from the corresponding stock solutions by dilution with Milli-Q water and acidifying with sub-boiled nitric acid. The spike solutions of ^{54}Fe, ^{65}Cu and ^{68}Zn were characterised in terms of isotopic composition and concentration by ICP-MS and reverse ID-ICP-MS, respectively. Fe, Cu and Zn concentrations were respectively found to be 1.022 ± 0.012 µg g-1, 5.77 ± 0.03 µg g-1 and 13.23 ± 0.74 µg g-1. All solutions were prepared using ultrapure water (18.2 MΩ cm-1) obtained from a Milli-Q water purification system (Millipore, Bedford, MA, USA). The gases used for ICP-MS and LA analyses (Ar and He, each 99.999% purity) were purchased from Air Liquide (Spain).

Matrix-Matched Standard Preparation. Matrix-matched laboratory standards were prepared for the calibration of images obtained by LA-ICP-MS. The preparation procedure of the synthetic matrix-matched laboratory standards is summarised in Figure S1.

RESULTS AND DISCUSSION

External Calibration by LA-ICP-MS using Matrix-Matched Laboratory Standards. The proposed quantification approach ensured that samples and standards were similar not only in terms of chemical matrix but also in physical dimensions (i.e. section thickness). In the present work, the thickness of frozen tissue sections was optimised to 80 µm, thus ensuring complete sample ablation without the ablation of the subjacent sample substrate. One potential source for error, using a laboratory standard in the quantification of biological specimens by LA-ICP-MS,

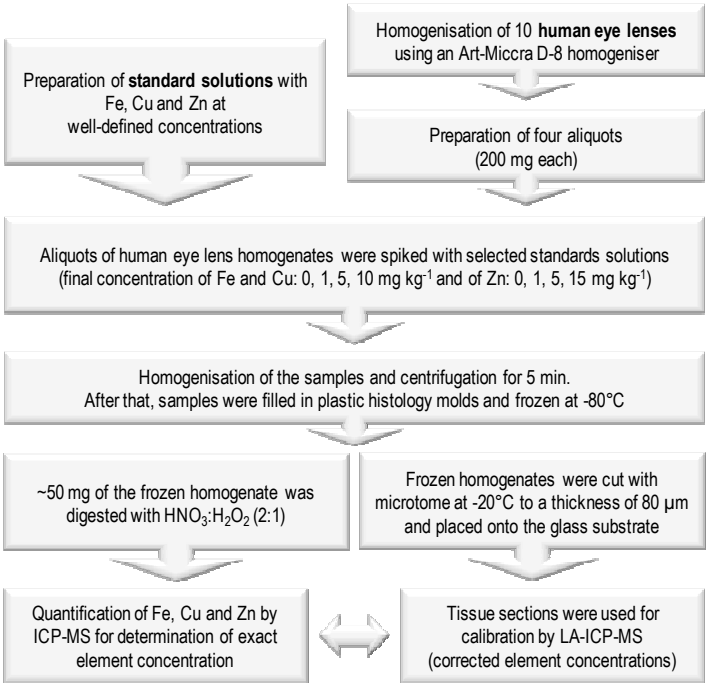

Figure S1.- Workflow of the preparation of matrix-matched laboratory standards used for quantification of images obtained by LA-ICP-MS.

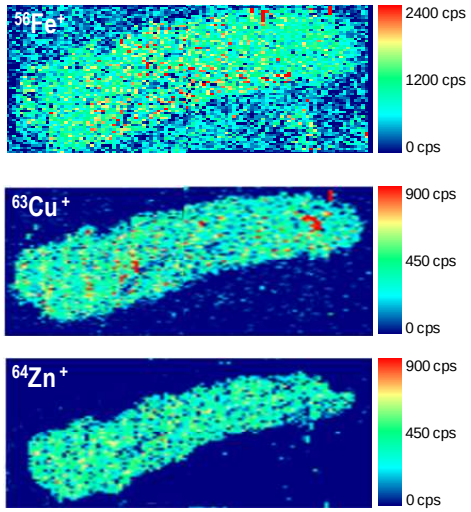

Figure S2.- Elemental distribution obtained for $^{56}Fe^{+}$, $^{63}Cu^{+}$ and $^{64}Zn^{+}$ in a thin section of a matrix-matched tissue standard by LA-ICP-MS.

is the lack of homogeneity in the sample. Therefore, the homogeneous distribution of the spiked elements in the prepared matrix-matched standards needs to be ensured. LA-ICP-MS elemental images were obtained for laboratory standards under the conditions summarised in Table S1. Fig. S2 shows representative images obtained for the standard with the lower concentrations of trace elements (~0.6 µg g^{-1} of Fe, Cu and Zn). As shown, a homogenous distribution was observed in our prepared tissue standards for the three elements of interest. Thus, the ICP-MS signals obtained from the ablation of the standards were representative of the corresponding concentrations, independently of the ablation position.

The matrix-matched laboratory standards were carefully characterised and their concentrations were calculated by conventional nebulisation ICP-MS after acidic digestion of each corresponding aliquot. Fe, Cu and Zn concentrations obtained for the three standards are summarised in Table S2.

Table S2. Fe, Cu and Zn concentration (□g g^{-1}) of the matrix-matched laboratory standards (homogenised human eye lens) obtained by conventional nebulisation ICP-MS. Uncertainties show result from standard deviations of the mean of three independent analyses.

	Laboratory Standard	Concentration determined by ICP-MS
Fe	(1)	0.77 ± 0.03
	(2)	4.72 ± 0.15
	(3)	9.19 ± 0.01
Cu	(1)	0.642 ± 0.004
	(2)	3.85 ± 0.02
	(3)	8.35 ± 0.02
Zn	(1)	< LOD
	(2)	5.285 ± 0.007
	(3)	14.07 ± 0.05

Calibration curves were constructed by plotting the signal intensity of $^{56}Fe^{+}$, $^{63}Cu^{+}$ and $^{64}Zn^{+}$ (after normalisation with $^{197}Au^{+}$ signal) obtained by LA-ICP-MS vs. the standards concentration (see Fig. S3). The correlation coefficients of calibration curves were found to be 0.9999, 0.9980 and 0.9855 for $^{56}Fe^{+}$, $^{63}Cu^{+}$ and $^{64}Zn^{+}$, respectively. Using the obtained linear regressions, each data point (or pixel) resulting from the LA-ICP-MS images of human eye lens was converted from normalised intensities into concentrations, allowing the production of high resolution quantitative images. Additionally, the limits of detection (LODs) for Fe, Cu and Zn were calculated according to the 3s criterion of IUPAC using the matrix-matched laboratory standards. LODs determined by LA-ICP-MS were found to be 100 ng g^{-1} for Fe, 60 ng g^{-1} for

Cu and 200 ng g^{-1} for Zn in the experimental conditions used. These values are sufficiently low for the determination of the trace metals in the sought tissues and comparable or slightly lower than those reported by other authors using similar LA-ICP-MS conditions.

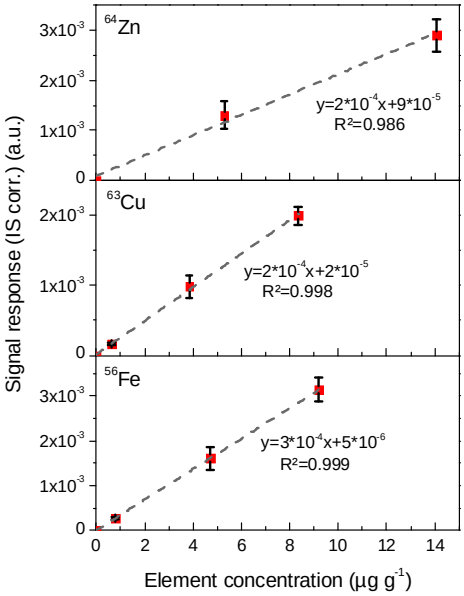

Figure S3.- Calibration curves obtained for $^{56}Fe^{+}$, $^{63}Cu^{+}$ and $^{64}Zn^{+}$ ($^{197}Au^{+}$ as internal standard) by LA-ICP-MS using three matrix-matched laboratory standards of human eye lens homogenates. Standard deviation values are calculated from the mean of ten independent analyses.

REFERENCES

i. Konz I, Fernández B, Fernández ML, Pereiro R, Sanz-Medel A (2013) Anal Chim Acta accepted for publication (18 November 2013).

ii. Fernández B, Konz I, Castañeda A, Fernández ML, Pereiro R, Sanz-Medel A (2013) Spanish patent application pending (P201300559)